europhysics
conference
abstracts

14 th European Conference on

Controlled Fusion and Plasma Physics

Madrid, 22 - 26 June 1987

Editors: F. Engelmann, J. L. Alvarez Rivas

Contributed Papers
Part II

Published by: European Physical Society

Series Editor: Prof. S. Methfessel, Bochum

Managing Editor: G. Thomas, Geneva

VOLUME
11 D
PART II

14 th European Conference on

CONTROLLED FUSION

AND PLASMA PHYSICS

Madrid, 22-26 June 1987

XIV
FUSION
MADRID
1987

Contributed Papers, Part II

Editors: F. Engelmann, J.L. Alvarez Rivas

VOLUME 11D

EUROPHYSICS CONFERENCE ABSTRACTS is published by the
European Physical Society, 1987

The 14th European Conference on Controlled Fusion and Plasma Physics was held in Madrid, Spain from 22 to 26 June 1987. It was organized by Centro de Investigaciones Energéticas Medioambientales y Tecnológicas (CIEMAT), Madrid, Spain on behalf of the Plasma Division of the European Physical Society (EPS).

The following topics for poster sessions were taken into consideration:

A. Tokamaks
B. Stellarators
C. Alternative Magnetic Confinement Systems
D. Inertial Confinement
E. Plasma Edge Physics
F. Plasma Heating and Current Drive
G. Tokamak and Basic Fusion Plasma Theory
H. Diagnostics

The orally presented contributed papers were grouped into four sessions covering:

Confinement and Heating in Toroidal Plasmas
Plasma Edge Physics
Inertial Confinement

The Conference Programme included 18 invited lectures, 19 orally presented contributed papers and more than 400 papers presented in poster sessions. In addition, an evening lecture on the Status of Fusion Research was given by R.S. Pease.

The contributed papers of this 3-volume publication are photographically reduced in size from the originals provided by the authors.

Programme Commitee/Paper Selection Committee

F. Engelmann (Chairman), FOM (The Netherlands), NET (German Fed. Rep.)
J.L. Alvarez Rivas, CIEMAT (Spain)
K. Appert, CRPP (Switzerland)
R. Behrisch, IPP (German Fed. Republic)
G. Briffod, CEN (France)
A. Gibson, JET (United Kingdom)
M. Key, Chilton Lab. (United Kingdom)
D.D. Ryutov, Inst. Novosibirsk (USSR)

The invited papers will be published by Pergamon Press in the journal "Plasma Physics and Controlled Fusion" and sent free of charge to each registered participant.

TABLE OF CONTENTS

TITLE LIST

A. Tokamaks

E. Plasma Edge Physics

G. Tokamak and Basic Fusion Plasma Theory

H. Diagnostics

C

ALTERNATIVE MAGNETIC CONFINEMENT SYSTEMS

FIRST SPEED2 Z-PINCH DISCHARGES ON SOLID STATE FIBRES

G.Decker,K.Gasthaus,W.Kies,M.Mälzig,C.van Calker,G.Ziethen and A.E.Robson+,J.D.Sethian+
Physikalisches Institut I, Universität Düsseldorf
+ Naval Research Laboratory,Washington DC,USA

Abstract
Solid state fibres(CD_2 and frozen D_2, diameter $<10^{-4}$m) have been applied to the pulseline POSEIDON (500kA,500kV) at NRL and recently also to the capacitive driver SPEED2 (1.5MA,300kV) at Düsseldorf university in order to generate thermal Z-pinch plasmas for nuclear fusion. The neutron yield ($>10^{10}$ for POSEIDON and $\sim 10^9$ for SPEED2) is mainly due to beam-target reactions initiated by disruptive instabilities that have been found in the POSEIDON experiments to appear as $\dot{I}$ goes to zero. In SPEED2 experiments the pinch is disrupted after typically 400ns and 250ns for CD_2 and D_2 respectively although the pinch current keeps rising up to 1.5MA with CD_2 and 900kA with D_2 after 700ns. Early pinch expansion leads to too low density ($<10^{27}m^{-3}$) and plasma temperature (<100eV) for nuclear fusion. There is evidence that not only initial electric field and current rise but also the fibre length are crucial parameters for discharge initiation and current concentration to the pinch - a necessary condition for high pinch energy density.

300KV capacitive driver SPEED2

SPEED2 is a capacitive driver originally meant as a current generator for an initially low inductance dynamical pinch (Z-pinch, plasma focus) (Decker et al.1986). First discharges on a high inductance (15nH/cm) stationary pinch (CD_2 fibre) revealed that the original voltage rise of this driver (4kV/ns) was too low to fast enough initiate the discharge along the fibre surface. Therefore a steepening switch was integrated providing a voltage rise of 20kV/ns comparable to the POSEIDON pulseline (Sethian et al.1987). A pinch current maximum of 2 MA with a rise time of 750ns is available for a 3cm long pinch.

Pinches for nuclear fusion?

Pinches are comparatively simple configurations generating fusion plasmas (Haines 1982). The energy W coupled into the discharge at any time can be given in terms of pinch inductance L, resistance R and current I

$$W(t)=1/2LI^2 + 1/2 \int_0^t \dot{L}I^2 dt' + \int_c^t RI^2 dt'. \qquad (1)$$

Dynamical pinches efficiently make use of the second term via an increasing inductance generating a nonthermal plasma component (Deutsch,Kies 1987) that finally governs the pressure equilibrium (modified Bennett equilibrium)

$$\mu_0 I^2/8\pi = N_b \langle W_b \rangle + 2NkT \qquad (2)$$

where N_b, N denote line densities of the nonthermal (beam) and thermal (target) plasma components and $\langle W_b \rangle$, $T=T_e=T_i$ the mean energy of fast particles (typically 100keV) and the bulk plasma temperature, respectively. These fast particles have the advantage of causing many beam-target fusion reactions but they limit target density ($<10^{26}m^{-3}$) and temperature (<keV). Unfortunately, the extrapolation of fusion efficiency of dynamical pinches above break-even-conditions requires target data (density $10^{28}m^{-3}$, lifetime 10^{-7}s and temperature >10keV) hardly achievable since fast particles primarily settle the final equilibrium. Furthermore, dynamical pinches are prone to impurity problems at discharge initiation especially in high power experiments (Kies 1986).

Stationary pinches are supposed to generate purely thermal plasmas avoiding ion runaway and acceleration mechanisms. The plasma is generated 'on axis' and ohmically heated since the second term of eq.(1) vanishes and eq.(2) reduces to the normal Bennett-relation. For a given temperature (e.g.10keV) the line density can be matched to the pinch current available from the driver. However, there is hardly an ab initio stable pressure equilibrium maintained beyond current maximum (more than 700ns in our case). Initially pinch expansion is very likely because of effective ohmic heating while later during the discharge when the plasma resistance is low rapid contraction (localised) may happen so that fast particles can also be generated. Therefore, not only line density but also initial density profile and especially initial voltage and current rise are important parameters.

SPEED2 stationary Z-pinch experiments

Based on experiments carried out on the pulseline POSEIDON first Z-pinch discharges on CD_2 and frozen D_2 fibres (diameter 70µm, length 2 to 4cm) have been investigated at SPEED2. Experimental set-ups have been chosen such that initial conditions (vacuum 10^{-5}mbar, initial voltage rise 20kV/ns, electric field at breakdown 10^5V/cm, initial current rise 3kA/ns) are comparable to the POSEIDON experiments with the exception of current rise time (130ns -> 700ns) and current maximum (500kA -> 1.5MA).

Figure 1 shows image converter and X-ray pinhole pictures. The visible pinch structures (400ns (a) and 200ns (b) after discharge initiation) can only be identified in the X-ray picture (behind 10µm Be) in the case of CD_2 but not with D_2 where only the anode edge and copper plasma are seen. This means that the plasma temperature is low (<100eV) and that the neutrons ($<10^9$ for CD_2 and $\gtrsim 10^9$ for D_2) are not of thermonuclear origin but due to fast deuterons accelerated by

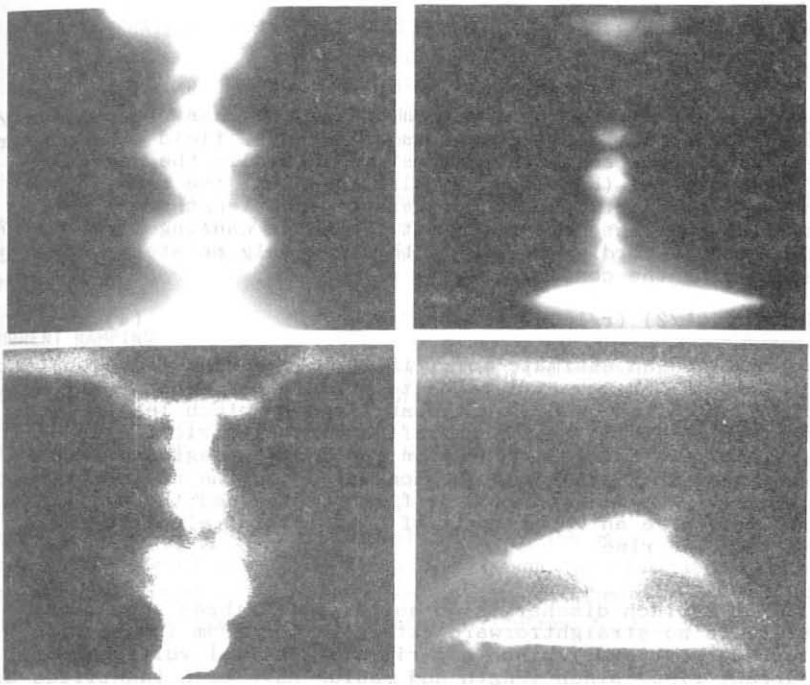

Fig.1: Image converter (upper,10ns exposure) and X-ray pinhole pictures (lower, time integrated) of Z-pinch discharges on CD_2 (a) and frozen D_2 (b) fibres.

pinch disruption\$typically taking place 400ns and 250ns after discharge initiation for CD_2 and D_2 fibres respectively although the pinch current is steadily rising up to 1.5MA (CD_2) and 900kA (D_2). Pinch expansion by a factor of$\sim$10 occurs and the current is not totally concentrated to the visible pinch. The different pinch behaviour in the POSEIDON experiments (expansion less than twice the initial radius) is hard to understand since the only obvious difference is the pinch length (POSEIDON 5cm). (Leak discharges develop only after the current maximum thus not affecting the pinch phase). We consider a collisionless moving electron being accelerated. Starting in the cathode region at radial position r and gyrating in the self magnetic field B it can only be prevented from directly crossing the gap if its larmor radius is much smaller than the pinch length l_p. This yields a condition for

the pinch voltage

$$U << (e/m_e)\,(B l_p)^2 \qquad (3)$$

where e and me are the electron charge and mass, respectively. This means that first electrons released by field or secondary emission never reach the axis since initially the magnetic field is zero. (Equation (3) also says that the same initial breakdown conditions with different pinch lengths are not available.) These electrons hit the anode causing X-ray emission. According to eq.(3) this can only be stopped by satisfying the condition

$$I_A >> (10^3/2)\,(r/l_p)\sqrt{U_k v} \qquad (4)$$

which gives an estimate for $\breve{I}$ if it is regarded as a constant ($I=\int \breve{I} dt \sim \breve{I} t$). However, $\breve{I}$ tends to drive the discharge off axis. Since pinch inductance is almost fixed by pinch length $\breve{I} \sim U$. Even if condition (4) is satisfied high electric fields can also cause axial ion runaway in low density regions where electrons are magnetized but ions are not. The necessity that initially the radial E x B drift should exceed the axial one can also give an upper limit of both initial electric field and current rise.

Conclusions

SPEED2 Z-pinch discharges on solid state fibres show that there is no straightforward extrapolation from low to high current stationary pinch experiments. Initial voltage and current rise, pinch length and radius have been identified as important parameters the optimum values of which have not yet been experimentally determined. Parameter estimates based on equilibrium conditions are uncertain since initial pinch expansion is unavoidable. Fast stopping of this expansion and subsequent contraction needs higher initial current rise (>3kA/ns) and longer fibres (>5cm) than presently available with SPEED2 but there might be also upper limits. It seems also likely that a shorter current rise time (<500ns) is necessary to avoid pinch disruptions prior to reaching the current maximum. The latter requirement is beyond SPEED2 limits but within accessible modern driver technology.

Support by EC is gratefully acknowledged.

References

G.Decker et al.(1986) Nucl.Instr.Methods A 249
J.Sethian et al. (1987) to be published in Phys.Rev.Lett.
R.Deutsch,W.Kies (1987) to be published in Plasma Physics
W.Kies (1986) Plasma Physics Vol.28 No.11
M.G.Haines (1982) Phys.Scripta T2/2 380

PLASMA BEHAVIOUR DURING PROGRAMMED CURRENT DECAY AND RAMPING IN THE REVERSED FIELD PINCH

P G Noonan, C G Gimblett and A A Newton
Culham Laboratory, Abingdon, Oxon, OX14 3DB, UK
(UKAEA/Euratom Fusion Association)

In this paper we summarise investigations of Reversed Field Pinch (RFP) with rising and falling current on HBTX1B (R/a = 0.8/0.26 m) with 156 graphite tile limiters and toroidal equilibrium given by a conducting shell.

CURRENT RAMPING

The usual method of start up in HBTX1B is the matched mode. A large loop voltage, V_L, of 200-500 V is applied to produce plasma current, I, of 120-440 kA in a risetime, τ_I, of 0.7 to 1.4 ms. The loop voltage is then clamped at 30-60 V to sustain a flat top current. The toroidal field, B_ϕ, is programmed so that the toroidal magnetic flux in the vacuum vessel is constant during start up. Thus the pinch parameter, θ, rises with the current and reversal of the toroidal field at the edge of the plasma occurs late during the current rise. Although the resistance of the non-reversed discharge is high (a few mΩ) the risetime is sufficiently short for it to make only a minor contribution to the volt second consumption, $\Delta\phi = \int_0^{\tau_I} V_L \, dt$.

Attempts to produce a plasma current of 200 kA with a lower V_L of 80-120 V and a risetime of 5 ms in the matched mode have failed. The maximum current I <100 kA is achieved early in time and thereafter the plasma resistance increases with time to several mΩ. Reversal of the toroidal field is not obtained.

Therefore we have investigated current ramping (sometimes called the constant θ mode) [1,2] in which field reversal and the peak θ are produced early in the current rise, in 2 ms at currents of 30-40 kA. Figure 1 compares waveforms for a ramped discharge and normal start up matched mode with a flat top. To ensure breakdown at low V_L a high initial B_ϕ is required which is quickly reduced by programming in the first 1 ms of the current rise. Switching to a passive poloidal current crowbar causes the small discontinuity in the current rise seen in Fig 1a. For most of the time the plasma resistance is <1 mΩ and in this case the current is ramped to 140 kA at constant θ in 7 ms. It can be seen that in the flat top part

of each discharge the plasma resistance $R_p = V_L/I$ is independent of the mode of start up.

During the ramp the inductive contribution to V_L can be subtracted to obtain the true plasma resistance. The magnetic energy is calculated using a Modified Bessel Function Model where the cutoff radius, r_1, is determined from the measured values of F and θ at the plasma surface. The resistance is found to be independent of dI/dt. In Fig 2 we show that the resistance falls with current ($R_p \propto I^{-1}$) and has the same value in the ramp and in the flat top.

After field reversal the volt seconds, which contains inductive and resistive terms, is given by $\Delta\phi = RIl_i + C\tau_I/a^2$, where l_i the plasma inductance inside the vessel = 1.1 x 10^{-6} H/(m of major radius) and C = 3.8 Vm^2.

The magnetic fluctuation level at the plasma edge is found to be independent of dI/dt in both the ramping and flat top cases and is related to I, decreasing from 6% to 2% as I increases from 50 to 150 kA. It was expected that ramping would require more dynamo activity than the matched mode [2], but this is not seen in present conditions.

The R_p vs I behaviour can be analysed in terms of $R_pI = V_s + \delta V$ where V_s is due to the collisional conductivity and δV = 45 to 55 V is the anomaly arising from the intersection of field lines with material objects [3,4]. The value of δV is significantly reduced in the flat top when the equilibrium is corrected by B_v and the limiters removed [3,4]. We expect that if the equilibrium could be centered during ramping with no limiters the volts seconds consumption would be reduced.

DECAYING CURRENTS

Rapid termination of the RFP with large induced V_L occurs when the reversed B_ϕ is lost (see Fig 1). It has been shown that control of V_θ during current decay maintains $B_\phi < 0$ until the current falls from 200 to 30 kA [5]. During this "controlled rundown" measurements of asymmetry factor (Shafranov's Λ) suggested that β_θ increases to 50% with improved energy confinement [5]. Such improved confinement and reduction in fluctuations is predicted when current and toroidal flux are decaying at the same rate because the magnetic field configuration will be closer to the BFM [6] and has been observed on ZETA [7].

Here we report experiments where V_L and V_θ were varied over a wide range (V_L = -50 to +70 V, V_θ = -8 to 1 V) and data taken as the current falls between 180 and 140 kA with θ nearly constant in the range 1.3-1.4. Figure 3 shows the normalised OV intensity fluctuations decreasing from 30 to 15% as V_L is reduced. The OV and CV mean intensities are reduced by a factor of 5 although the electron density remains constant at n_e = 1.3 x 10^{19} m^{-3}. Magnetic field fluctuations also decrease about a factor of 2 with more negative V_L.

The energy confinement time, τ_E, was estimated from T_i measured by an NPA assuming $T_e = T_i$. A scan of V_L over many shots shows T_i constant at 330 eV. Energy confinement increases due to the reduction of ohmic heating in the plasma volume as V_L is made negative. The results are sensitive to a number of assumptions including the temperature and magnetic profiles being the same as those in the flat top.

CONCLUSION

Start up by ramping to currents of $\leq$160 kA in 4-7 ms (τ_i/a^2 = 65-110 ms/m^2) with loop voltages of 80-125 V has been demonstrated and the plasma resistance found to be independent of the dI/dt in the range 0 to 30 MA/s. A typical ramp uses $\Delta\phi/IR \simeq 1.6$ Vs/MA.m which is consistent with the 3 Vs/MA.m at τ_I/a^2 = 120 ms/m^2 specified for RFX (R/a = 2.0/0.5 m, I = 2 MA) under construction. With decaying currents some improvement in confinement with lower fluctuations is seen, although the effect is at present short lived.

ACKNOWLEDGEMENT

We would like to thank our colleagues for ion temperature measurements, spectroscopic and density data.

REFERENCES

[1] J A Phillips et al: Los Alamos Report LA-10060-MS (1984)
[2] A A Newton & J W Johnston: Proc RFP Theory Workshop (1980) Paper IIIA-1
[3] T R Jarboe, B Alper: Phys Fluids 30 (1987) 1177
[4] B Alper and H Y W Tsui: this conference
[5] A A Newton, P G Noonan: Nuc Instr & Methods in Physics Res, A245 (1986) 167
[6] J W Long, A A Newton, C G Gimblett: 11th Euro Conf on Cont Fusion & Plasma Physics (Aachen 1983) 159
[7] D C Robinson, R E King: Proc IAEA Conf Novosibirsk 1(1969) 263

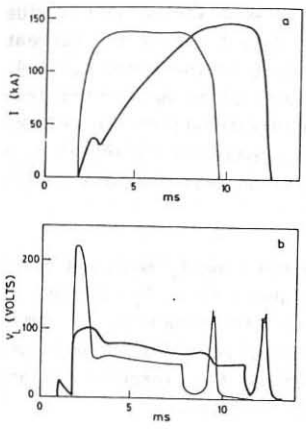

Fig 1 Waveforms for ramped start up (thick line) and matched mode (thin line).
a - toroidal current
b - loop voltage
c - toroidal field reversal
d - pinch parameter

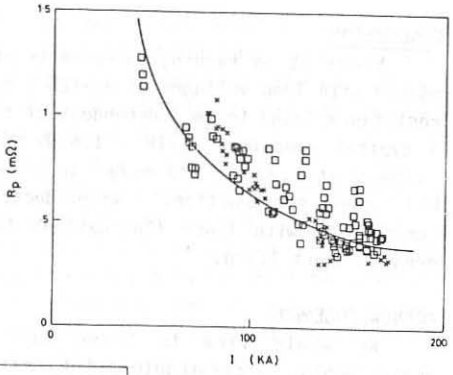

Fig 2 R_p vs I. □ Ramped I. X Flat top I. The curve is $R_p = 60/I$

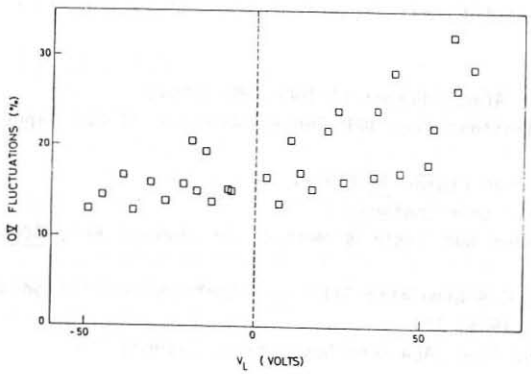

Fig 3 Normalised OV fluctuations vs V_L for decaying plasma.

EFFECT OF A MOVEABLE TILE LIMITER ON THE LOOP VOLTAGE IN HBTX1B RFP

B Alper and H Y W Tsui
Culham Laboratory, Abingdon, Oxon, OX14 3DB, UK
(UKAEA/Euratom Fusion Association)

INTRODUCTION

Results are presented of detailed investigations of the dependence of the loop voltage, V_{loop}, in a steady state Reversed Field Pinch (RFP) on the quantity of flux intercepted by a carbon tile limiter when inserted progressively into the edge of the plasma in HBTX1B.

Models based on magnetic helicity balance in relaxed state systems [1,2] or the interception of current flow [3] have been proposed to explain the dependence of V_{loop} on field errors and on the insertion of limiters. In models [1,2] it is proposed that the helicity dissipation in the edge regions dominate the impedance of present day RFPs. Following ref [2] the increase in loop voltage (δV) over that expected classically is given by: $\delta V = \delta\chi\ (\theta/\pi a^2)A$, where $\delta\chi$ is the potential difference between the boundaries where field lines enter and leave the plasma and A is the projected area of such surfaces normal to the field lines.

In the studies outlined below we vary A in a controlled manner and are able to separate the effect on V_{loop} due to helicity dissipation at the plasma boundary from that of impurities in the plasma core.

RESULTS

A long graphite tile 5 cm wide by 0.5 cm thick was inserted progressively into the edge of the plasma. The effect on the increase in loop voltage during current flat-top discharges from ~33 V at I_ϕ = 220 kA is shown in Fig 1 for two examples; firstly when the tile intercepts the maximum flux at the plasma edge and secondly when it intercepts the minimum flux (ie rotated through 90°). In both cases the loop voltage is seen to increase linearly with the distance of the tile insertion beyond the existing limiters (1 cm in from the liner) with about a factor of three greater increase in the first case. When taking due account of the changing angle of the field lines at the edge with insertion depth, the increase in loop voltage for both cases is proportional to the flux intercepted by the tile. (In these discharges $F \approx -0.1$ and $\theta \approx 1.4$ at the edge.) Similar measurements were carried out at other plasma currents. The variation with I_ϕ of $\delta V/A$ was small; ($\delta V/A$ represents the increase in loop voltage per unit area of tile normal to the field beyond the fixed limiters). Values of $\delta V/A$ were 0.5 ± 0.1 V/cm^2 at 175 kA, 0.5 ± 0.2 V/cm^2 at 220 kA rising to 0.7 ± 0.15 V/cm^2 at 280 kA.

The resistivity of the graphite (10 $\mu\Omega$.m) is comparable with that of the plasma in the edge region. To investigate any effect of varying the tile conductivity whilst minimising any change in the impurity composition (see next section), a "pyrolytic" graphite tile, with anisotropic conductivity, of identical dimensions was used. For this tile the electrical resistivity across the face was (3 mΩ.m), ie about a factor of 300 higher. Values of $\delta V/A$ were 40% $\pm$ 25% higher with the pyrolytic graphite being 0.7 $\pm$ 0.1 V/cm^2 at 175 kA and 0.9 $\pm$ 0.2 at 220 kA.

The current flowing through the tile is measured to be ~2A/cm^2 which is of the order of the ion saturation current in the edge region. The deuterium ion temperature (see [4] this conference) rose with insertion depth. (Electron temperature and Z_{eff} changes are discussed below.)

IMPURITY AND TEMPERATURE EFFECTS

An increase in carbon impurities and a possible fall in T_e with limiter insertion could contribute (classically) to increases in V_{loop}. This possibility was studied in detail for the case of a 4 cm graphite limiter insertion at I_ϕ = 280 kA. For this case, Fig 2(a) shows the signal from a bolometer which has a direct view of the neighbourhood of the limiter. The curve shows the integrated radiated power (P_{rad}) as a function of time compared with a normal discharge with no tile present (shown as a dotted line). The discharge starts at t = 2 ms. From 2 ms to ~5 ms the values of P_{rad} are about equal but at around 5 ms a rapid increase in P_{rad} occurs for the data with the tile in. At about the same time radiation from CV (see Fig 2(b)) as measured by a visible spectrometer located 90° around the torus also shows a rapid rise with little or no increase above standard discharges (dotted line) at earlier times. Similarly, in Fig 3, the central electron temperature T_e, measured by a Si(Li) detector, deviates significantly from values found in normal discharges (dotted line) only at later times when it is seen to fall - in direct contrast to the increase in T_i noted earlier.

These results indicate that impurities do not play a significant role in these discharges at early times when any contribution from changes in Z_{eff} and T_e on δV_{loop} is small [5]. This has been confirmed by studies using a computer model which takes account of all electromagnetic energy energy flows into and out of the plasma during the discharges. The effective value of the loop voltage (V_{eff}) required to maintain constant current and profiles is shown for these discharges in Fig 4. An increase in V_{eff} of ~10 volts over normal discharges (dotted line) is present at early times before impurity and T_e effects are believed to contribute. This increase, we attribute to helicity dissipation effects in the region

of the tile-plasma boundary. The same dependence of V_{loop} with time was confirmed experimentally by varying the power-crowbar (driving loop-voltage) to obtain current-flat-tops at various times in the discharge and measuring V_{loop} at these times. In general, the onset time for the commencement of impurity influxes was earlier the higher the current and the deeper the limiter insertion depth. Also with the pyrolytic limiter, influxes were earlier and higher than that with the corresponding graphite conditions.

The values of δV quoted in the previous section were taken at these earlier times, ie before or just at the time that impurity influxes were observed. In the case studied here (4 cm in at 280 kA) the measured value of δV was 12.5 volts. In general we conclude that impurities etc contribute 25% ± 10% to the measured increase in loop voltage quoted in the previous section.

DISCUSSION OF RESULTS

These results have shown that a sharp rise in loop voltage occurs when a relatively small object is inserted into RFP discharges and that this rise in loop voltage of ~0.5 V/cm^2 of graphite tile insertion is additional to any effect from changes in Z_{eff} and T_e and is proportional to the magnetic flux intercepted by the object. This is in good accord with recent models which propose that helicity dissipation in the plasma edge regions where field lines intersect material objects increases the plasma loop voltage. The potential differences ($\delta\chi$) across the tile required to account for the observed values of δV_{loop} are in the range 400-800 volts.

Further confirmation that limiters contribute significantly to V_{loop} in RFP discharges has recently been obtained in HBTX1B where a reduction of ~30% in V_{loop} was obtained with the removal of 156 graphite tile limiters which covered 8% of the liner 1 cm in from the surface.

These studies demonstrate that future RFPs must be carefully designed to have correct equilibrium with no obstructions protruding beyond the first conducting wall.

REFERENCES

[1] T R Jarboe & B Alper: Phys of Fluids 30 No 4 (1987) p1177
[2] H Y W Tsui: this conference
[3] R S Pease: Private Communication
[4] P G Carolan, A R Field et al: this conference
[5] P G Carolan, C A Bunting et al: this conference

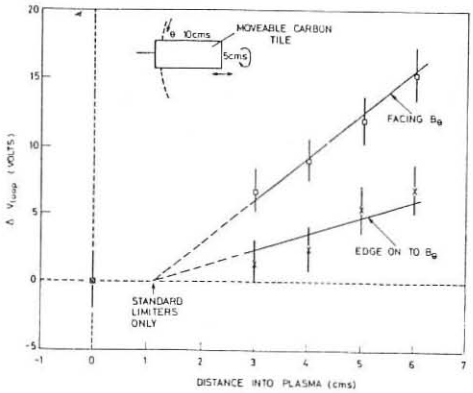

Fig 1 Increase in loop voltage with insertion depth for two tile orientations

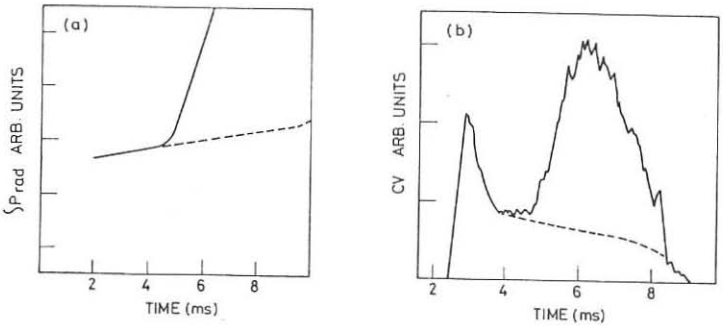

Fig 2 Time-integrated total radiation (a), and CV line intensity (b), with tile inserted 4 cms (solid lines) and tile withdrawn (dotted)

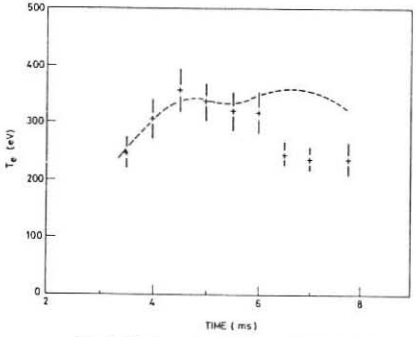

Fig 3 Electron temperature with tile (+) and without tile (---)

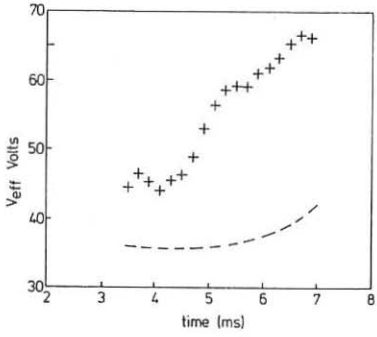

Fig 4 Loop voltage with tile (+) and without tile (---)

DIVERTOR EQUILIBRIUM OF REVERSED FIELD PINCH

Kichiro Shinya
Toshiba Research and Development Center
4-1 Ukishima-cho, Kawasaki-ku, Kawasaki 210, Japan
Kiyoshi Ogawa
Electrotechnical Laboratory
1-1-4 Umezono, Sakura-mura, Niihari-gun, Ibaraki 305, Japan

1. Introduction

Recently impurity control has been recognized as one of the crucial issues to realize reactor relevant plasmas even in the reversed field pinches (RFP). The poloidal divertor seems to be an attractive tool for this purpose from both the physical and engineering view points. Active shaping by the external equilibrium coils is required for attaining divertor plasma configuration, which results in necessity of precise estimation of the equilibrium coil current distribution by 2-dimensional equilibrium analysis beforehand.

The purpose of this paper is to describe how to obtain divertor configuration of the RFP plasma for prescribed plasma parameters by numerically solving the Grad-Shafranov equation. Plasma parameters are chosen of the TPE-RX which is planed as a next step machine succeeding to the TPE-1RM15 at the Electrotechnical Laboratory. Both the normal and inverse-dee double null divertor configurations will be described.

2. Formulation

The MHD code EQUCIR, which was developed to analyse tokamak plasma equilibria, was modified to calculate RFP plasma. In this code the plasma cross section, null point locations, average plasma pressure and plasma current are required inputs. On the other hand equilibrium coil currents are resultant outputs.

The Grad-Shafranov equation which rules over the axisymmetric plasma equilibrium is written in the cylindrical coordinate (R,ϕ, Z) as

$$\frac{\partial^2\Psi}{\partial R^2} - \frac{1}{R}\frac{\partial\Psi}{\partial R} + \frac{\partial^2\Psi}{\partial Z^2} = \mu_0 R j_\phi(R,\Psi) \tag{1}$$

$$j_\phi(R,\Psi) = R\frac{dP}{d\Psi} + \frac{1}{\mu_0 R}\frac{d}{d\Psi}\left(\frac{f^2}{2}\right) \tag{2}$$

where j_ϕ is the toroidal plasma current density. In solving the Grad-Shafranov equation the functional form of the plasma pressure $p(\Psi)$ and toroidal magnetic field $f(\Psi) = RB_{TOR}$ should be identified. In this paper $p(\Psi)$ and $f(\Psi)$ are selected as

$$p(\Psi) = p_0\tilde{\Psi}^{m_p} \quad \text{and} \quad f(\Psi) = f_0(1 + c_f\tilde{\Psi}^{m_f}) \tag{3}$$

where $\tilde{\Psi} = (\Psi - \Psi_S)/(\Psi_M - \Psi_S)$ is the normalized poloidal flux with Ψ_M the flux at the magnetic axis and Ψ_S the flux at the plasma surface.

Iterative method is used to solve the Grad-Shafranov equation because of its nonlinearity. Starting from flat plasma current distribution, the

poloidal flux distribution is then calculated by the Green's function method. The contribution of the external equilibrium coil currents to the poloidal flux are modified to minimize the following square error which is evaluated at the prescribed plasma surface points

$$E = \sum_{k}^{N_S} (\Psi_k - \Psi_S)^2 W_k + \sum_{j}^{N_C} \gamma_j N_j^2 I_j^2 + \sum_{k}^{N_n} \sigma_k (B_{Rk}^2 + B_{Zk}^2) \tag{4}$$

where Ψ_k is the poloidal flux at the k'th plasma surface point, which is the sum of the plasma current contribution Ψ_{pk} and the external coil contribution Ψ_{Ek}, $N_j I_j$ is the ampere-turns of the j'th coil and B_{Rk} and B_{Zk} are the magnetic fields at the prescribed k'th null point in the R and Z direction, respectively. The plasma current distribution of the next iteration step can be calculated by equation (2). C_f in equation (3) is modified so that the integral of j_ϕ over the plasma cross section is equal to the plasma current I_p. Note that C_f should be less than -1 throughout the iterations to ensure RFP configuration.

Another iteration loop is engaged in the code to converge plasma pressure to the prescribed value. This loop works per several j_ϕ iterations, the number of j_ϕ iteration being dependent upon the covergence level.

Once convergence is attained for both plasma current distribution and plasma pressure, the characteristic quantities of the RFP plasma can be evaluated as follows:

(i) F and Θ

$$F = \frac{B_T(S)}{\langle B_{TOR} \rangle} \qquad \Theta = \frac{B_P(S)}{\langle B_{TOR} \rangle} \tag{5}$$

(ii) Safety factor

$$q^\Psi = \frac{f(\Psi)}{2\pi} \int \frac{d\ell_P}{R^2 B_{POL}} \tag{6}$$

The current density, magnetic field and safety factor are calculated on magnetic surfaces divided into equal flux difference. In the equation (5) $B_T(S)$ and $B_P(S)$ mean line-averaged toroidal and poloidal magnetic fields on the plasma surface, respectively, which are written as

$$\begin{aligned} B_T(S) &= \int \frac{B_{TOR}(S)}{B_{POL}(S)} d\ell_P \Big/ \int \frac{d\ell_P}{B_{POL}(S)} \quad , \\ B_P(S) &= \int B_{POL}(S) d\ell_P \Big/ \int d\ell_P \quad . \end{aligned} \tag{7}$$

$\langle B_{TOR} \rangle$ is averaged toroidal magnetic field over the plasma cross section, i.e.,

$$\langle B_{TOR} \rangle = \int B_{TOR} dA \Big/ \int dA \quad . \tag{8}$$

For nested magnetic surfaces with equal flux difference the equation (8) reduces to line average on the magnetic surface as follows

$$\langle B_{TOR} \rangle = \sum_i \int \frac{B_{TOR}}{B_{POL}} d\ell_P \Big/ \sum_i \int \frac{d\ell_P}{B_{POL}} \quad . \tag{9}$$

3. Results

Two different divertor configurations with same plasma parameters but null point locations are examined, i.e., normal divertor and inverse-dee

divertor. The proposed plasma parameters of the TPE-RX are; $R_p = 1.5$ m, $a = 0.3$ m, $I_p = 2$ MA, $\bar{n}_e \sim 1.5 \times 10^{14}$ m^{-3} and $T_e \sim T_i \sim 1$ keV. The axial position of the null points Z_N for both divertor configurations are same as ± 0.36 m, but the radial poitions R_N are 1.36 m for the normal divertor and 1.75 m for the inverse-dee divertor. The corresponding triangularities are 0.6 and -0.83, respectively.

Figure 1 shows (a) the normal divertor and (b) the inverse-dee diverter plasma configurations for the average plasma pressure of $\bar{P} = 4.8 \times 10^4$ N/m^2 which corresponds to $\bar{n}_e = 1.5 \times 10^{14}$ m^{-3} and $T_e = T_i = 1$ keV. The vacuum toroidal magnetic field at the major radius R_p is fixed at $B_{TO} = -0.2$ T throughout this paper. The total ampere-turns of both configurations are almost equal to 4.5 MAT, but divertor coil ampere-turns for the normal divertor is twice larger than for the inverse-dee divertor, i.e., 1.3 MAT and 0.7 MAT, respectively.

The magnetic field distributions are shown in Fig. 2 for three different plasma pressures; (a) 4.8×10^4 N/m^2, (b) 2.4×10^5 N/m^2 and (c) 4.8×10^5 N/m^2. The toroidal magnetic field decreases with increasing plasma pressure while keeping the profile constant. This decrease corresponds to the decrease of the poloidal plasma current shown in Fig. 3. The depletion of the toroidal magnetic field in the plasma brings about the reduction of the average toroidal magnetic field $\langle B_{TOR} \rangle$ resulting in the increase of F and Θ values.

The poloidal magnetic field is kept almost constant due to the constancy of the total plasma current I_p. The toroidal plasma current distribution becomes broader as the plasma pressure increases. Force free assumption is not a good approximation for RFP plasmas with high plasma pressure.

Figure 4 shows the F-Θ trajectory as the plasma pressure increases. When the plasma pressure is low F and Θ values exist on the curve predicted by the Bessel function model (BFM), while at higher pressures the values deviate from the BFM. It should be noted that the vacuum toroidal magnetic field B_{TO} is kept constant throughout the analysis. The F-Θ trajectory may therefore be different for changing value of B_{TO}.

Table 1 summarizes the results including a comparison between the normal and inverse-dee divertors. It might be concluded that there is little difference between the normal and inverse-dee divertors. The average decay index of the equilibrium magnetic field is defined by

$$\langle n \rangle = \frac{1}{\bar{B}_Z} \int j_{TOR} B_Z \, n \, dRdZ \qquad (10)$$

where

$$\bar{B}_Z = \frac{1}{I_p} \int j_{TOR} B_Z \, dRdZ \, .$$

$\langle n \rangle$ takes positive value of 0.33 for the normal divertor plasma at $\bar{P} = 4.8 \times 10^4$ N/m^2, while it decreases to -0.52 for the inverse-dee divertor plasma. The negative value of $\langle n \rangle$ inevitably brings about the positional instability in the vertical direction. The null point location should therefore be lowered to stabilize the positional instability at the expense of the increase of the equilibrium coil currents. The normal divertor configuration is preferable for suppressing the positional instability.

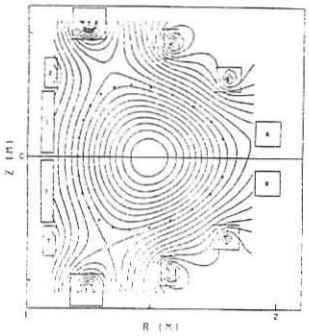

(a) Normal divertor

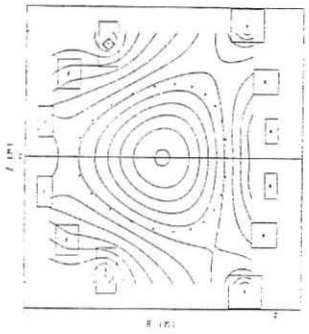

(b) Inverse-dee divertor

Fig. 1 Plasma configuration

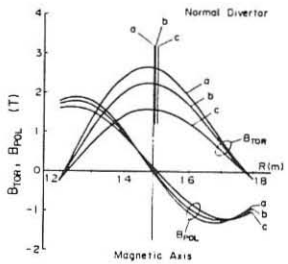

Fig. 2 Magnetic field

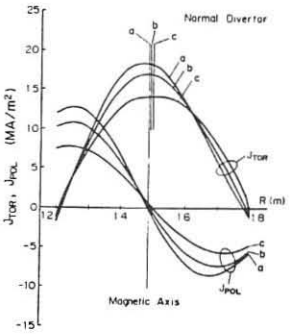

Fig. 3 Plasma current

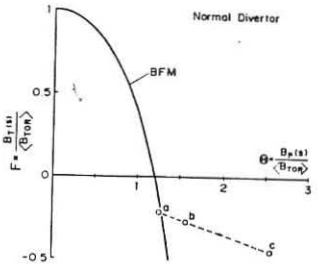

Fig. 4 F-Θ diagram

Table 1

Comparison of Plasma Parameters between Normal and Inverse Dee Divertor

Divertor	Normal			Inverse Dee		
P (N/m²)	4.8×10^{4}	2.4×10^{5}	4.8×10^{5}	4.8×10^{4}	2.4×10^{5}	4.8×10^{5}
I_P (MA)	2.0	←	←	←	←	←
B_{TO} (T)	-0.2	←	←	←	←	←
B_{PO} (T)	1.37	←	←	←	←	←
B_{TOR} (T)	1.00	0.79	0.48	0.93	0.77	0.51
B_T (SXT)	-0.21	-0.21	-0.21	-0.19	-0.19	-0.19
B_P (SXT)	1.26	1.24	1.23	1.23	1.22	1.21
F	-0.21	-0.27	-0.45	-0.20	-0.24	-0.37
θ	1.26	1.57	2.56	1.32	1.59	2.39
$q^{\psi}(0)$	0.15	0.14	0.11	0.14	0.13	0.09
$q^{\psi}(S)$	-0.05	-0.05	-0.05	-0.05	-0.05	-0.05
I_{PR} (MA)	0.10	0.55	1.23	0.12	0.62	1.29
$I_{FF'}$ (MA)	1.90	1.45	0.77	1.88	1.38	0.71

$$I_{PR}=\int R\frac{dP}{d\psi}\,dS \quad , \quad I_{FF'}=\int\frac{1}{\mu_0 R}\frac{d}{d\psi}\left(\frac{F^2}{2}\right)dS$$

FREE BOUNDARY MHD STABILITY OF RFP CONFIGURATIONS

D. Merlin, S. Ortolani, R. Paccagnella

Istituto Gas Ionizzati del C.N.R.
EURATOM-ENEA-CNR Association, Padova, Italy

INTRODUCTION

In a previous article [1] a fixed boundary MHD stability analysis of force-free RFP profiles was described. In this paper we present an extension of the analysis including the effect of a vacuum region separating the plasma from the conducting shell.

An ideal MHD eigenvalue code and a resistive code, based on the Δ' criterium, are employed to study the stability, for current driven modes, of force-free equilibria obtained from a μ radial distribution of the form:

$$\mu(r) = \mu_0 \frac{\vec{J} \cdot \vec{B}}{B^2} = \frac{2\Theta_0}{a} \left[1 - \left(\frac{r}{a} \right)^{\alpha} \right]$$

where a is the plasma minor radius.

The equilibrium distributions are therefore parametrized through the two quantities α and Θ_0 which define respectively the form and the on axis value of the μ distribution.

The present study considers a plasma-vacuum interface at $r = a$ and a vacuum region for $a < r \leq b$. At $r = b$ we assume the presence of a perfectly conducting wall. The analysis is performed with different values of the ratio $\delta_v = (b - a)/a$, i.e. different proportion of the extension of the vacuum region with respect to the plasma radius. Poloidal numbers $m = 0, 1, 2$ and a wide range of toroidal wave numbers, k, are analysed.

RESULTS

For the fixed boundary case the results for $m = 1$ modes [1], which have been found to pose the more severe constraints for stability, are reported in Fig. 1 in a $\alpha - \Theta_0$ plane. In this diagram the region of existence for the RFP configuration is bounded by the curve $F = 0$ and $F = -\infty$, F being the ratio between the toroidal field at the plasma surface and the mean toroidal field over the plasma cross section. In Fig. 2 it is seen that, for the free boundary case, the main differences with respect to the fixed boundary one are due to the external modes, that is modes resonant outside the radius of reversal of the toroidal field. In fact with a vacuum region of 5% extension, the marginal stability curve for these modes moves

to lower values of Θ_0 (for a fixed value of α). Moreover the ideal and resistive external modes boundaries, which were practically indistinguishible without vacuum, become now separated; the boundary for resistive modes being in this case well below the ideal one. When the extension of the vacuum region is increased to 10% of the plasma radius it is found that, beyond the ideal stability limit, modes resonant in the vacuum and also non resonant develop, with growth rates of the order of $\gamma \tau_A = 0.5 \cdot 10^{-1}$. From Fig. 2 it is also seen that with this vacuum extension the stable region, limited on one side by the external modes and on the other side by the internal modes, is drastically reduced. Furthermore, as can be expected, the effect of the vacuum is quite small on the internal modes (which are resonant inside the field reversal point).

In general in the free boundary case the m = 0 modes, resonant at the toroidal field reversal surface, are found to play a much more important role than in the fixed boundary case. In Fig. 3 it is shown the stability region for these modes when a vacuum region of 3% is present. The curves refer only to resistive modes because ideal m = 0 modes are found to be stable. In this case we see that two limits are found for stability. An upper limit similar to that found for m = 1 modes and a lower limit near the F = 0 curve. However the most important result from the m = 0 mode analysis is that there is no stable region in the $\alpha - \Theta_0$ plane if the extension of the vacuum region exceeds 4%.

Finally, m = 2 modes, both ideal and resistive, are found to be completely stable.

DISCUSSION AND CONCLUSIONS

We have analysed the effect of a vacuum region, separating the plasma from the conducting boundary, on the MHD stability of force-free configurations. While in the fixed boundary case the m = 1 modes set the more stringent limit on stability, with the vacuum region the m = 0 modes become more relevant and they are completely destabilized when the vacuum region extends by more than $\sim 4\%$ of the plasma minor radius. This result appears to be very similar to that found in a previous analysis [2], in which a limit of 4% of extension of the vacuum region for the MHD stability of both m = 0 and m = 1 modes has been determined. However, in reference [2], a current density profile which does not vanish at the plasma edge was used and, to study the free-boundary properties, it was therefore necessary to modify the current profile, by introducing a matching region between plasma and vacuum. In this way m = 1 unstable modes were artificially produced by this matching region.

To discuss the relevance of m = 0 and m = 1 modes for stability, we have also compared the characteristic growth rates for m = 0 and m = 1 external modes. In Fig. 4 the values of $(\gamma \tau_A)^{-1}$ and Δ' vs. $\tilde{k} = ka$ for the case

$\alpha = 5$, $\Theta_0 = 1.8$ with $\delta_v = 0.1$ and $S = 10^4$ are shown. It is evident that the $m = 1$ modes have in general shorter growth times. This aspect is obviously relevant since, if the $m = 0$ modes grow on a time scale comparable to the resistive diffusion of the equilibrium configuration, then the $m = 1$ modes remain the most important also when a vacuum region is present. Furthermore, for a configurations characterized only by the presence of $m = 0$ unstable modes, the Δ' values are very low and the corresponding linear growth times are a significant fraction of the resistive diffusion time.

Finally, in the fixed boundary case [1] we noted that the destabilization of internal modes, due to the diffusive on axis current peaking, can also be a good candidate to explain the large fluctuations and current redistributions observed in RFP's [3, 4]. In the present case, with a vacuum region surrounding the plasma, we observe that external modes can also play an important role in the plasma behaviour. This fact can be illustrated by plotting the stability boundaries for $m = 1$ modes in the $q(a)\cdot(R/a) - q(0)\cdot(R/a)$ plane (q being the safety factor) together with typical experimental points (Fig. 5). It can be seen that in the case of $\delta_v = 0.1$, some experimental points lie outside the stability limit due to the external modes. The mechanism by which these external modes can act on the plasma evolution is not clear; however these modes have closely spaced resonant surfaces and their multiple interaction can easily produce a region of stochastic magnetic field near the plasma edge.

In conclusion, the effect on the MHD stability of a vacuum interspace between the plasma boundary and the conducting shell has been found to be very significant and could become particularly important in larger higher current machines where limiters armours and/or divertors can be necessary.

REFERENCES

[1] Antoni, V., Merlin, D., Ortolani, S., Paccagnella, R., Nuclear Fusion 26 (1986) 1711.

[2] Robinson, D.C., Nuclear Fusion 18 (1978) 939.

[3] Watt, R.G., Nebel, R.A., Phys. Fluids 26 (1983) 1168.

[4] Antoni, V., Martin, P., Ortolani, S., Plasma Phys. Contr. Fusion 29 (1987) 279.

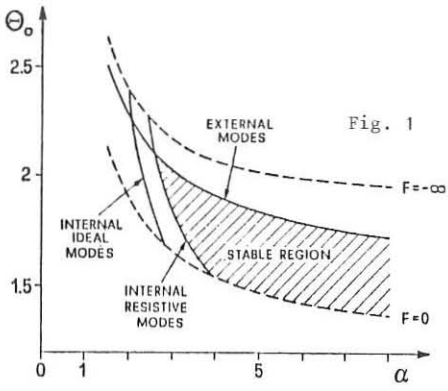

Fig. 1

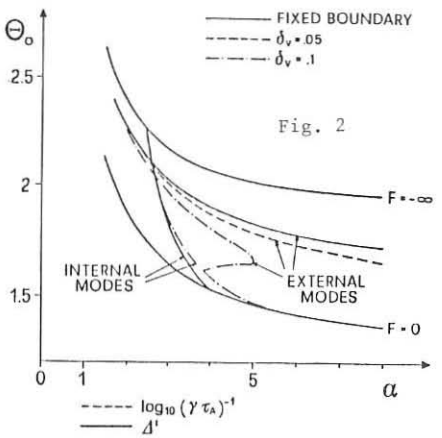

Fig. 2

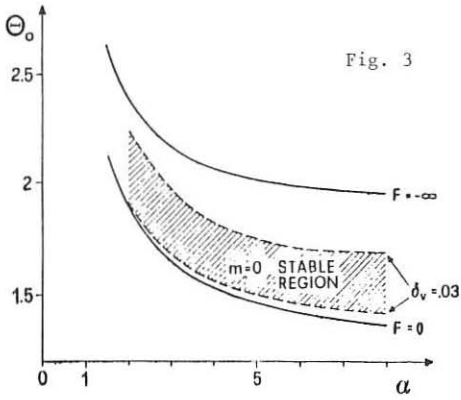

Fig. 3

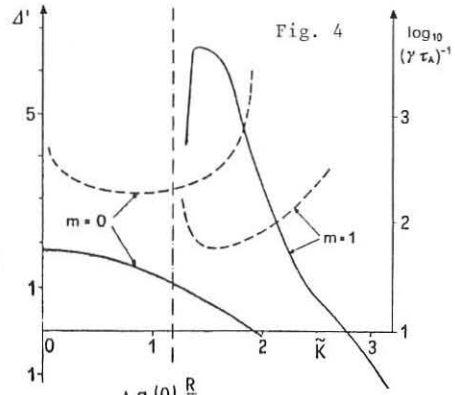

Fig. 4

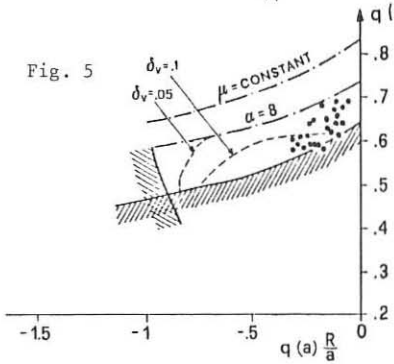

Fig. 5

EXPERIMENTAL STUDY OF FRC PLASMA WITH AXIAL CURRENT APPLICATION

T. Takahashi*, M. Ohara*, S. Shimamura*, Y. Nogi*, M. Machida†

*Nihon University, Japan - †Campinas University, Brazil

With recent progress on the Field Reversed Configuration (FRC) research, large scale devices has been constructed[1,2]. The axial current application on the FRC machines adresses the better control of the plasma during the field reversal in a slow rising main field, increasing the trapped bias flux, and the plasma equilibrium against the n = 2 rotational instability.

In the Nihon University's NUCTE-II machine[3], the FRC plasma is produced by using a field reversed theta-pinch device of 1.7 m long, 16 cm bore coil. It's feature is the existence of an internal z-discharge electrodes for the axial current generation. When the negative bias field reaches $\sim$ 630 G, the positive main field (12 kG) is applied to the plasma preheated by the axial current I_{z_1}. In order to study the effects of the axial current, a second current I_{z_2} is added few microseconds before the main bank discharge.

The I_{z_2} current flows through the well ionized plasma paramagnetically, increasing the axial bias field. This amplification effect has been compared with the calculations under the assumption of the force-free current profile having boundary conditions $B_z = -630$ G and $B_\theta = \mu_0 I_z / 2\pi r_w$ at the tube wall r_w. The experimental results agree well with the theoretical predictions, indicating that the bias flux amplification follows the force-free current model.

Although the amplification of bias field is possible by factor of three with application of 30 kA current in our experiment, the FRC is strongly affected in the equilibrium phase by the amount of this current.

We find that there are two limiting values of I_{z_2} to obtain the long-lived plasma. The first is the magnitude of the current existent at the moment when the main field is applied in the formation phase. For the current below 4kA the plasma lifetime is longer or at least same as in the case without current, but above this value the lifetime dacays sharply. The reason for this limit is not undertood well yet although, the FRC formation is seemed to be disturbed by the asymmetry of the bias field and the plasma condutivity in the reconnection regions near the coil ends, further studies are needed.

The second limit is predominant at the confinement phase. Even if the first limit is satisfied, there is another condition to be obeyed in this stage. The FRC plasma produced by this method has strong axial field B_e and additional azimuthal field produced by the axial current flowing near the separatrix

radius. And it is known that the stability of the plasma in a magnetic field system composed of axial and azimutal fields is governned by the Krushal-Shafranov limit or safety factor q. In our case this stability condition can be written by:

$$q = \frac{2\pi r B_e}{\mu_0 \ell_p I_z / 2\pi r} > 1 \qquad (1)$$

where ℓ_p and μ_0 are the separatrix length and the permeability of the FRC plasma respectively. The I_z is total axial current on the annular sheet. The parameters in eq.(1) are time dependent, and the FRC is destroyed when the q value becomes less than one during the confinement phase.

Many discharge datas have been taken within two limits above and compared to the cases where no axial (I_{z2}) current was applied. The monitoring of the plasma parameters were done by flux excluded and Rogowskii loops, line integrated He-Ne (3, 39 μm) laser interferometry and photodiode radial and axial arrays.

For the ordinary case with no I_{z2}, the initial equilibrium radius of the plasma is 2.3 ∿ 2.6 cm (x_s = 0.29 - 0,33) and the lifetime taken by e-holding time of the initial plasma cross-section, πr_s^2, is 28 ∿ 56 μs.

When the I_{z2} is applied, the plasma radius becomes larger, 2.5 ∿ 2.9 cm (x_s ≅ 0.31 - 0.36) and the lifetime is improved to 48 - 64 μs. The longest lifetime (65 μs) corresponds to the decay time of the main field. The start of the I_{z2} is about 5 μs before the main field, so that the current reaches 1.5 ∿ 2.5 kA at the moment of the FRC formation.

The increase of the poloidal flux Φ_p trapped in the FRC is calculated from a rigid rotor equilibrium model[4]:

$$\Phi_p = \frac{\pi r_s^3}{2\sqrt{2}\, r_w} B_e \qquad (2)$$

which gives the increase of about 30 % in the trapped poloidal flux during the equilibrium phase.

The n = 2 rotational instability has been measured by the interferometric and photodiode systems. The instability grows within 25 ∿ 30 μs after the start of the main field in the case of ordinary FRC operation. When I_{z2} is applied the onset time of the instability is delayed to 35 - 40 μs, and the amplitude of the oscilation is modified to lower levels. This indicates the possibility of the stabilization of n = 2 instability besides the usual external multipole system used in other machines[5,6].

So far, the total supression of the n = 2 instability is not possible due to lower current limit (< 4 kA) imposed by q value. The estimatives of current necessary for complete supression was calculated by the radial force balance between centrifugal force of the plasma and Lorentz force due to the axial current gething I_{zs} = 13 kA. Therefore what we have

observed in NUCTE-II is the slight change on the behavior of the n = 2 instability.

|1| D.C. Barnes et al; 11th Int. Conf. Plasma Phys. Cont. Nuclear Fusion, IAEA - CN - 47/D-V-9, Kyoto, Japan (1986).

|2| A.L. Hoffman et al; 11th Int. Conf. Plasma Phys. Cont. Nuclear Fusion, IAEA - CN - 47/D-IV-2-1, Kyoto, Japan (1986).

|3| S. Shimamura, Y. Nogi; Fusion Technology, 9, 69, (1986).

|4| W.T. Armstrong et al; Phys. Fluids 24, 2068, (1981).

|5| S. Ohi et al, Phys. Rev. Lett., 51, 1042, (1983).

|6| T. Ishimura, Phys. Fluids, 27, 2139, (1984).

SLOW, LOW VOLTAGE GENERATION OF ANNULAR FRC'S*

G.C. Vlases, Z.A. Pietrzyk, R.D. Brooks, K.D. Hahn, R. Raman, R.J. Smith
University of Washington, Seattle WA 98195, U.S.A.

Introduction Significant progress has been made in FRC research in the past few years, with the achievement of $n\tau_E > 4 \cdot 10^{11} cm^{-3} sec$ in 40 cm diameter plasma tubes.[1] Conventional FRC generators, which are descendants of reversed field linear θ-pinch devices, require very high voltages and fast pulse technology. We report here on an FRC generation technique designed to circumvent these difficulties, which we call the Coaxial Slow Source.[2] This CSS consists of coaxial θ coils, with radii of 7 and 22 cm, an active length of 95cm, and with plasma formed in the annular space between the coils (Fig. 1). The outer coil is of conventional single turn design, while the inner coil, which is cantilevered from one end of the device to allow translation of the plasma out the other end, is a four turn design consisting of close-fitting coaxial two-turn coils wound in the opposite sense to cancel axial currents and provide for a symmetric current feed. The coils are powered by a 2 kV, 800 μF bank and an 8 kV, 1200 μF bank, respectively. The resulting loop voltage of 2 kV maximum is 1/50th of that used in the similarly-sized FRX-C device[1] and the rise-time of 25 μs is about 10 times that of FRX-C. The vacuum vessel is of quartz, with metal end flanges, and the base pressure is $2 \cdot 10^{-8}$ Torr. The operating scenario is as follows: The inner coil is discharged "negative" through one quarter-cycle (18 μs), during which a weak glow discharge is normally operating. As the inner coil current begins to decrease in magnitude, the plasma acts to prevent reduction of the flux linking it, effectively transferring reversed flux from the inside of the core to the region between the core and the plasma, forcing it outwards. After a delay of ~ 2 to 12 μs, the outer coil is energized in the forward direction ($\tau_{1/4}$= 24μs), forcing flux inwards. The field lines on the two sides of the plasma, being oppositely directed, connect at the ends of the plasma, building in time a set of nested near-vacuum flux surfaces around the plasma, which is heated both ohmically and compressionally.

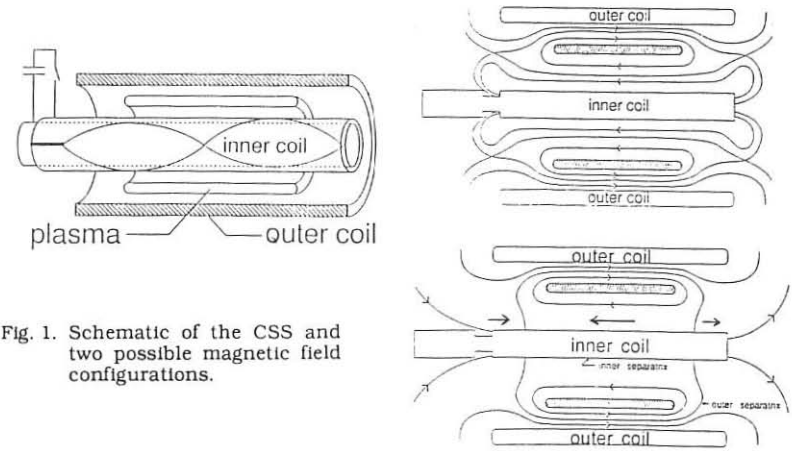

Fig. 1. Schematic of the CSS and two possible magnetic field configurations.

The main diagnostics consist of several axial arrays of 11 B_z probes each along the inner and outer coils, and flux loops on each coil. An array of 12 internal probes, spaced about 1 cm apart radially, and translatable in the axial direction, has been used in a few runs. The magnetic measurements are supplemented by interferometry, spectroscopy, and fast photography. In addition, a 2-D resistive mhd code written by Barnes[3] is used to predict and interpret the experiment performance.

Results The desired reversed field configuration forms within one or two μs of the time the outer coil is energized, and persists for times of 40 - 60 μs, depending on fill pressure. Such formation has been observed for pressures from 60 mT to 8 mT, limited at the low end by a poor preionization system, and with inner coil voltages from 4 to 8 kV. Figure 2 shows recently obtained internal probe data, where the formation and radial growth of the reversed field configuration can be seen. If one of the separatrices is assumed to be on a coil (which must be true at least until the field within the inner coil reverses or if the field along the coil changes sign) the location of the other separatrix can be determined from purely "external" probe measurements. Even if one of these conditions is not met, simulations show that any error incurred by assuming one separatrix always to be on a coil is very small. The radial position of the separatrices and the plasma can be controlled by varying the ratio of outer to inner coil voltages; the outer coil acts analogously to the vertical field coils in a Tokamak.

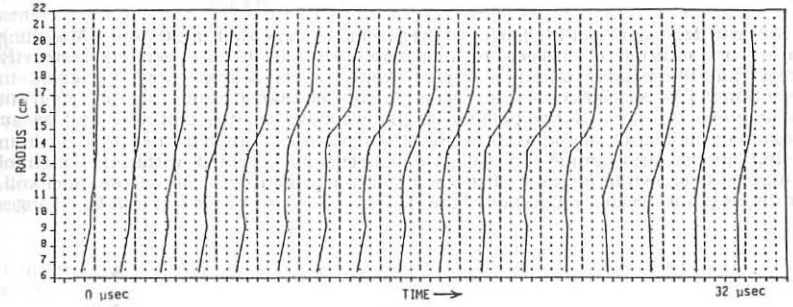

Fig. 2. Magnetic field (B_z) versus radius every 2 μs at the midplane from internal probe array and probes between the vacuum walls and coils. The first curve is at the outer coil start time. (0.1 Tesla/div, V_{out}=1.7 kV, V_{in}=6.0 kV, 9 mT of He)

Once the positions of the separatrices at the midplane are known, the poloidal flux enclosed within them can be estimated by assuming a model profile. For this purpose we use a rigid rotor model[4] constrained by the axial equilibrium condition, which for the CSS geometry is $\langle\beta\rangle = 1-\frac{1}{2}\frac{r_{so}^2-r_{si}^2}{r_o^2-r_i^2}$. The resulting values of flux are shown on Fig. 3. It can be seen that the flux builds up continuously over a period of about 20 μs, and attains a value of 7 mWb, somewhat greater than that which is trapped in a typical FRX-C shot. The flux decays rather rapidly, however, with an e-folding time of ~12 μs. This corresponds to an average resistivity at the magnetic axis of $\sim 2\cdot 10^{-4}$ Ω-m.

Values of average electron density have been obtained by single chord, axial-viewing interferometry and, in addition, for a limited number of shots the radial profile at a given instant was determined by axial holographic interferometry. For the shot shown in Figs. 2 and 3, $\int n_e dl = 9 \cdot 10^{16}$ cm^{-2} corresponding to $\langle n_e \rangle = 9 \cdot 10^{14}$ cm^{-3} if the plasma length is assumed to be 1 m. For field lines with negligible curvature at the midplane, a radial pressure balance estimate of the temperature then gives $T_e + T_i = 120$ eV. Total temperatures determined in this manner over the entire operating range of fill pressures quoted above vary from ~60 to 220 eV.

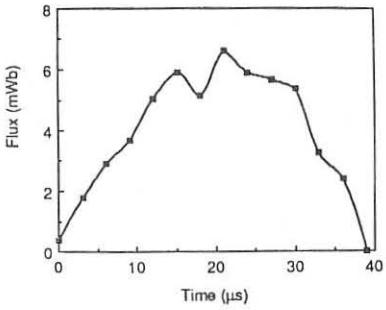

Fig. 3. Flux within the separatrix versus time. (V_{out}=1.7 kV, V_{in}=6.0 kV, 9 mT of He)

The time dependence of the length of the plasma is somewhat mysterious. Modelling with either a multiple of classical or anomalous drift-parameter-dependent resistivity predict that the plasma should contract axially, as is nearly always observed in conventional FRC's. Since simple measurements of diamagnetism do not yield an unambiguous measure of the plasma length, we have used a plot of $B_z(z,t)$ as an approximate indication of the axial extent of our plasmas, supplemented by data from the simulations. An example of a plasma which remains "confined" within the length of the magnet is shown in figure 4. It is clear that the x-points remain on the inner coil, near the ends, for the entire duration of the shot, as evidenced by the fact that B_Z changes

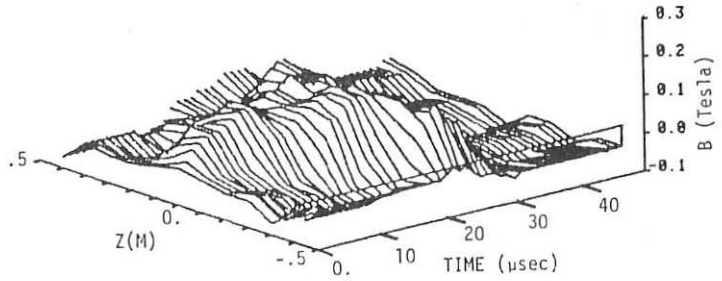

Fig. 4 Magnetic field ($-B_z$) along the inner coil versus time. The field at the ends is directed opposite to that at the midplane for all times indicating that the separatrix is always on the inner coil. (V_{out}=1.95 kV, V_{in}=5.0 kV, 8 mT of D_2)

sign along the coil from + to - and back to +. On the other hand, when $|B_z|$ remains approximately constant and negative along the whole length of the coil, one may surmise that the plasma extends beyond the length of the coil, and is not well-confined axially. These two types of configuration are sketched in fig. 1. The axial contraction of the plasma expected theoretically is seldom seen. At higher pressures in both D_2 and He, the length is approximately the coil length, and changes relatively little in time. At lower fill pressures, the plasma seems to form near the midplane, and then to expand axially, often beyond the coil length. This tendency to form near the center is not yet understood, but may result from the axial profile of the initial plasma which results from the glow pre-preionization, combined with the first quarter cycle induced θ p.i. It seems to be less likely to occur when a more energetic z-discharge p.i. system is used. The axial growth of the plasma suggests that the plasma energy content at any time is too great for the amount of enclosed flux, as in conventional FRC's.

Conclusions We have demonstrated that the desired "annular FRC" configuration can be formed over a wide range of initial pressures, using voltages about 1/50th of those conventionally employed in FRC research, and on time scales 10 times longer. This should ease the technological requirements for scaling FRC generators to larger sizes, provided the annular plasma can be successfully translated and re-formed into a true FRC. The plasmas generated, however, suffer from rather rapid decay rates, which may result in part from the relatively low magnetic fields, and correspondingly low plasma temperatures, employed in the present experiments. Although spectroscopic measurements have been carried out to identify impurities, quantitative measurements of radiative loss rates have not yet been made. The plasma radial position can be effectively controlled by adjusting the external "vertical field" coil voltage for a fixed inner coil voltage. The plasma axial dynamics depend sensitively on the filling pressure, type of gas used, and preionization technique, and are not yet adequately understood. Termination of the configuration occurs 45-60 μs after initiation, fairly independent of initial pressure. Termination may result either from radial diffusion, expansion out the ends, or a combination of the two. The device is currently being upgraded to allow for higher fields, longer risetimes, lower fill pressure operation through improved preionization, and active mirroring of the outer coil to control the axial dynamics.

Acknowledgments The authors wish to thank D.C. Barnes for allowing generous use of his simulation code, and for stimulating discussions concerning the experimental results.

References

1. R.E. Siemon et. al., Fusion Technology **9**, 13 (1986).
2. G.C. Vlases et. al. Bull. Am. Phys. Soc. **29**, 1360 (1984).
3. D.C. Barnes & D.D. Schnack, Bull Am. Phys Soc. **30**, 1455 (1985).
4. W.T. Armstrong et. al., Phys. Fluids **24**, 2068 (1981).

*Work supported by U.S. Department of Energy

HIGH DENSITY Z PINCH FORMED FROM A SOLID DEUTERIUM FIBER

J. E. Hammel and D. W. Scudder

Los Alamos National Laboratory, Los Alamos, NM, USA

I. Introduction

The linear Z pinch is among the simplest plasma configurations and was one of the first considered for controlled fusion applications. After an initial period of investigation, however, this research was largely abandoned because of observations and theoretical predictions of instabilities. Research on z pinches as radiation sources has continued.

Despite the troubled history of linear z pinches, they offer some great advantages, if ways can be found to tame their unstable nature. Since an unstabilized pinch in equilibrium is inherently a $\beta = 1$ plasma, it can be ohmically heated to fusion temperatures and thus requires no auxiliary heating sources. Since the heating current also provides the confining field, no magnetic field coils are required. Hence the two most expensive and complicated subsystems of a fusion reactor are eliminated. In addition, practical systems are expected to be inherently compact and small, involving only about 200 kJ of stored energy.

The greatest issue in making a practical z pinch is thus how to achieve sufficient stability. Present experiments aim to tackle this problem in at least two ways.

The first approach is that of the equilibrium pinch. Most z pinches have been formed by a discharge initiated on the cylindrical boundary of a comparatively low density gas, either on a wall, the outside of a gas puff, or in a wire array. The pinch effect then drives an implosion, culminating in assembly to high density on axis where the implosion kinetic energy is converted into thermal energy. Such a pinch has the current flowing in a current sheath on its edge. An equilibrium pinch, in contrast, is formed in a dense channel on the axis of the device, and the current rate of rise is programmed to keep that channel at or near radial pressure equilibrium at all times. Figure 1 illustrates the current profile theoretically required to maintain this equilibrium.

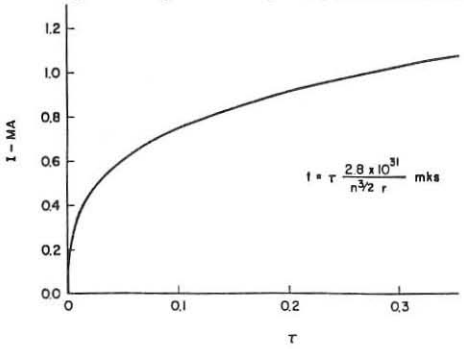

Figure 1

In an equilibrium pinch all of the heating is ohmic, and the current has the opportunity to penetrate into the center of the column. Kadomtsev[1] and Suydam[2] have shown that a z pinch can be stable to $m = 0$ modes if the

plasma beta falls of with radius at a sufficiently slow rate. Thus an equilibrium pinch would be expected to form a more nearly stable configuration than an implosion pinch.

The second technique for achieving sufficient stability is to make the density of the column as high as possible. The rate at which the fastest growing instabilities grow is typically $\sim v_{therm}/r$. However, the radially integrated reaction rate is $\propto n^2\pi r^2 \propto N^2/r^2$ where N is the density integrated across the column cross section. Thus if a given N is heated at smaller radius and hence higher density, more reactions will be generated before instabilities can grow to disruptive amplitudes. This approach amounts to reducing to a minimum the time that the magnetic fields must hold the plasma beyond the inertial confinement time. The experiments described here are performed at solid density, which is a practical limit for an equilibrium pinch.

This paper describes experiments that have been performed on a high density z pinch a Los Alamos National Laboratory over the last two years with plasma currents of 250 kA. Also described is an experiment under construction which will increase the plasma current to over 1 MA.

II. Experimental Techniques

The current generator for the 250 kA experiments is a 12 kJ, 600 kV Marx bank charging a 1.6 Ω, 100 ns water transmission line switched to the load by a self-breaking multipont water switch. The plasma chamber is maintained at a vacuum of $10^{-6}-10^{-7}$ Torr. The plasmas are created from fibers of cryogenic deuterium with diameters ranging from 20 to 40 μm and a length of 5 cm. The fibers hang in the vertical anode-cathode gap of the plasma chamber (see figure 2), and are ionized, heated, and confined by application of the 600 kV voltage pulse. The resulting voltage and current profiles are shown in figure 3.

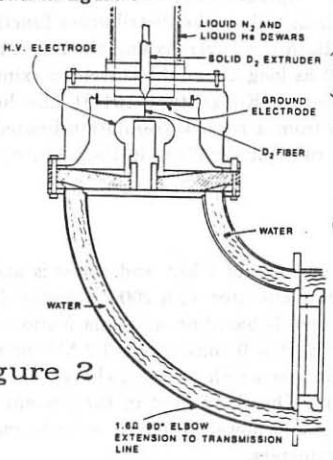

Figure 2

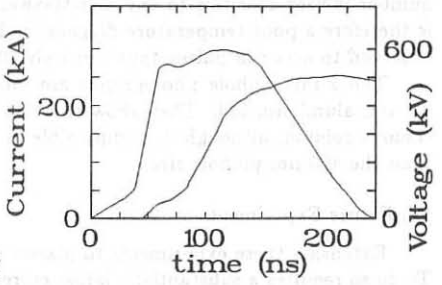

Figure 3

Diagnostics of the pinch include a multi-frame fast schlieren camera giving seven images, one every ten nanoseconds, neutron counting with a silver counter, and neutron time history using a scintillator/photomultiplier tube arrangement, differential absorber XRD soft x-ray detectors, and an x-ray pinhole camera.

III. Results at 250 kA

The fibers are observed to begin current conduction typically at the peak of the voltage pulse, although the time of initial conduction can vary by up to 50 ns. The resulting plasma columns expand at a velocity less than 1/10 of thermal velocity despite the fact that the current rate of rise is well below what figure 1 would imply is necessary to maintain radial equilibrium. The columns are free from visible instabilities for typically 80 ns into the current discharge, at which time the instability growth times would be expected to be ≈ 1 ns. After approximately 80 ns $m = 0$ modes become apparent, which ultimately disrupt the column. However, $m = 1$ modes are not observed.

Plasma parameters are inferred from a number of diagnostics. Since the initial fiber diameters are known, the average plasma density can be obtained from measurements of the column diameter. The initial solid density is 5×10^{28} m^{-3}, which drops to 2×10^{27} m^{-3} before the onset of instability.

Peak plasma temperature measured with differential absorber XRDs is 150 eV. The Bennett relation

$$\mu_0 I^2 = 16\pi NkT$$

fives temperatures which range from 150 eV to 600 eV for fiber diameters of 40 μm down to 20 μm. The number of neutrons per shot varies from several 10^6 to 10^8. The larger neutron numbers would imply plasma temperatures of ≈ 300 eV. However, this number is very sensitive to any non-Maxwellian tail on the distribution function and is therefore a poor temperature diagnostic. Both the neutrons and the soft x-rays are observed to occur in pulses approximately 50 ns long about the current maximum.

The x-ray pinhole photographs are taken on Kodak type 101-01 film behind a 0.5 μm aluminum foil. They show emission from a narrow (resolution-limited), continuous column, although it is impossible to rule out structure in the pictures smaller than the 400 μm pinhole size.

IV. Future Experiment

Extension these experiments to plasma currents of 1 MA and above is underway. To do so requires a substantially larger current generator with 200 kJ of stored energy and a voltage of 3 MV. The design we have used is based on a Sandia National Laboratories, Albuquerque generator, named MITE. It will consist of a 3.2 MV marx bank feeding a 32 nF intermediate store water capacitor which, in turn, charges a 1.9 Ω, 50 ns vertical transmission line to drive the same fiber load used in the present experiments. Our approach is to use conservative pulsed power design in order to maximize the probability of achieving the intended parameters.

The vertical tranmission line has been fabricated and tested with the existing MITE marx bank and intermediate store at Sandia. These tests achieved a current of 0.93 MA in a plastic fiber load. By optimizing the design of the intermediate store and the interconnections between stages, achievement of currents up to 1.2 MA is expected.

Bennett scaling of the plasma parameters predicts that a 20 μm diameter fiber at 1 MA would have a temperature of 10 keV. If such a plasma at or near solid density, if it demonstrated the same stability properties as have been observed in present experiments, would be capable of producing significant thermonuclear burn in a comparatively modest experiment.

V. Summary

Experiments in which 250 kA have been passed through a z-pinch column formed from a thin fiber of cryogenic solid deuterium have demonstrated unexpectedly stable behavior. It has been shown that it is possible to maintain a z pinch in near radial equilibrium while it is ohmically heated from 16° K to several hundred eV.

These encouraging results have motivated an effort to increase the plasma current to 1 MA and above, giving the potential of producing reactor-relevant plasmas capable of significant thermonuclear burn. Such a megamp experiment has been designed, partially fabricated, and successfully tested with an existing generator.

---

[1] B. B. Kadomtsev, "Hydromagnetic Stability of a Plasma," in *Reviews of Plasma Physics* (Consultants Bureau, New York, 1965) Vol. 1, p. 205.

[2] B. R. Suydam, Los Alamos Scientific Laboratory Report No. LA-7809-MS, May 1979.

LINEAR IDEAL MHD STABILITY OF THE Z–PINCH

M. Coppins
Blackett Laboratory, Imperial College, London SW7 2BZ, UK

Abstract

Solutions of the ideal MHD linear eigenvalue problem for the m= 0 and m= 1 modes in two important types of Z−pinch equilibrium are presented. The spatial structure of the instabilities, the dependence of the growth rate on wavelength and the effect of a surrounding conductor are described. A comparison of the theoretical results with recent experiments is given.

1 Introduction

Ideal magnetohydrodynamic (MHD) linear stability theory is the most extensively studied and familiar theoretical treatment of low frequency gross instabilities in plasmas. The Z−pinch is particularly susceptible to this type of instability. However, in spite of some early work (1,2) a comprehensive study of the application of the theory to the device has not been undertaken previously. Apart from its direct relevance to experiments such a study provides a firm basis for more elaborate theoretical work.

Because of (a) the relatively high degree of collisionality of many Z−pinch plasmas, and (b) the absence of mode rational surfaces in the device (implying that purely resistive instabilities do not arise), ideal MHD should provide a good description of Z−pinch stability. A comparison with recent experimental results is given in Section 3.

2 Theoretical results

We use a 1−D shooting code (a modified version of a code originally written by C. Davies in 1979) to solve the ideal MHD linear eigenvalue equation. A formulation of the eigenvalue problem is used in which the equation is rewritten as a pair of coupled first order ordinary differential equations for $r\xi_r$ ($\underline{\xi}$ is the plasma displacement) and P^*, the total (thermal + magnetic) pressure (3,4). Both growth rates and the spatial structure of instabilities can be obtained.

We assume that the pinch, equilibrium radius a, is surrounded by a vacuum which extends to a perfectly conducting wall at $r = r_w$. For m= 0 the perturbed magnetic field ($\underline{B}_1$) in the vacuum is identically zero and the plasma is decoupled from the outer region. The existence of a conducting wall outside the plasma therefore has no effect on the linear m= 0 mode. For all other m numbers the eigenfunctions in the plasma are coupled into the vacuum region through the plasma edge boundary condition and thus growth rates can be modified by changing the value of r_w/a.

The solutions given here are for a compressible ($\Gamma = 5/3$) plasma. Growth rates are given normalised in terms of the radial thermal transit time.

Two important types of Z−pinch equilibrium have been studied. The first is characterised by a uniform current density. This equilibrium is unstable to m= 0 and m= 1, but stable for $m \geq 2$ (2). Figure 1 shows the dependence of growth rate on ka (k is the axial wavenumber of the instability) for the two unstable modes. The m= 0 mode grows faster over almost the whole range of ka. Figure 2 shows the components of $\underline{\xi}$ and $\underline{B}_1$ in the case of m= 1, ka= 4.0. The instability is peaked near the plasma edge.

The second type of equilibrium to be studied satisfies the Kadomtsev Criterion (5) i.e. it is unstable to m= 1 only. This type of equilibrium is characterised by a centre peaked current density. Figure 3 shows the components of $\underline{\xi}$ and $\underline{B}_1$ of the m= 1, ka= 4.0 mode

in this case. The instability is peaked on axis.

These solutions have been obtained with the assumption of a vacuum of infinite extent surrounding the plasma. The existence of a conducting wall seperated from the plasma by a vacuum of finite extent does not affect the linear $m=0$ mode, but can reduce the $m=1$ growth rate if the wall is close to the pinch. Figure 4 shows the dependence of $m=1$ growth rate on the ratio r_w/a in the uniform current density case, for three different values of ka. Long wavelength (low ka) modes are affected the most, and in the limit of $r_w/a=1$ (corresponding to fixed boundary modes) absolute stability to $m=1$ is found for values of ka below 1.58. A qualitatively similar effect is found for the Kadomtsev stable profile.

3 Comparison with experiment

A detailed interpretation of recent experimental results from the compressional and gas embedded pinches at Imperial College (6,7,8) in the light of this theoretical work has been carried out. We estimate that the observed lifetime of the compressional pinch is equivalent to approximately 20 $m=0$ or 11 $m=1$ growth times, where the growth times correspond to peak current. This surprising degree of stability may be due to rapid cooling which would reduce the growth rate. Large initial perturbations in the number density profile are not observed to grow and we attribute this phenomenon to the conducting wall stabilising effect described above. In this case a plasma layer which forms inside the insulating wall of the pinch chamber, the existence of which is inferred from the maintenance of the equilibrium beyond current reversal, acts as a conducting wall close to the plasma.

The main features of the observations on instabilities in the gas embedded pinch are (a) the complete absence of the $m=0$ mode, (b) an apparent delay in the onset of the $m=1$ mode, and (c) the $m=1$ mode when first seen is peaked on axis. The first of these phenomena suggests that the equilibrium is of the Kadomtsev stable type and our theoretical study indicates that this view is confirmed by the observed spatial structure of the instabilities. Thus although the form of the current density profile cannot be obtained experimentally we infer from the nature of instabilities that it is centrally peaked. Such a current profile would probably be associated with a centrally peaked temperature profile which could arise naturally in the gas embedded pinch through cooling of the outer region of the plasma due to thermal conduction to the surrounding gas and/or accretion of neutrals. We suggest that this mechanism offers an explanation for the apparently universal absence of the $m=0$ mode in gas embedded Z-pinches. Finally we suggest that the apparent delay in the onset of the instability is a manifestation of exponential growth with a growth rate which is increasing with time during the current rise.

References

1. M. Kruskal and M. Schwarzschild, Proc. Roy. Soc. A223, 348 (1954).
2. R.J. Tayler, Proc. Phys. Soc. B70, 31 (1957).
3. K. Appert, R. Gruber and J. Vaclavik, Phys. Fluids 17, 1471 (1974).
4. G. Bateman, MHD Instabilities (MIT Press, 1978).
5. B.B. Kadomtsev, in Reviews of Plasma Physics, Vol 2, ed M.A. Leontovitch (Consultants Bureau, New York, 1966).
6. M.G. Haines et al., Eleventh Int. Conf. on Plasma Physics and Controlled Nuclear Fusion Research, (Kyoto.1986), Paper IAEA-CN-47/D-IV-4.
7. A.E. Dangor et al, Phys. Rev. A27, 2751 (1983).
8. M.B. Favre Dominguez, PhD Thesis (London, 1985)

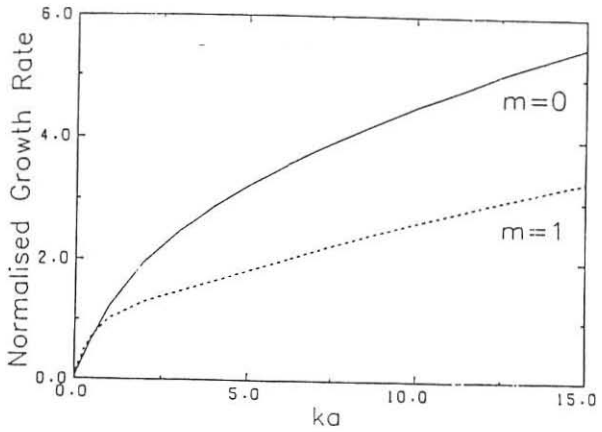

Figure 1 Flat current; infinite vacuum. Dependence of growth rate on ka for m=0 and m=1 modes.

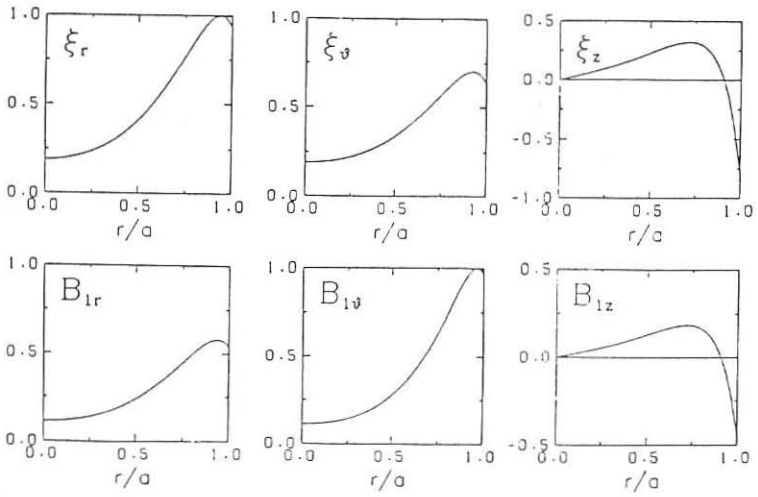

Figure 2 Flat current; infinite vacuum; m=1; ka=4.0. Components of displacement and perturbed magnetic field.

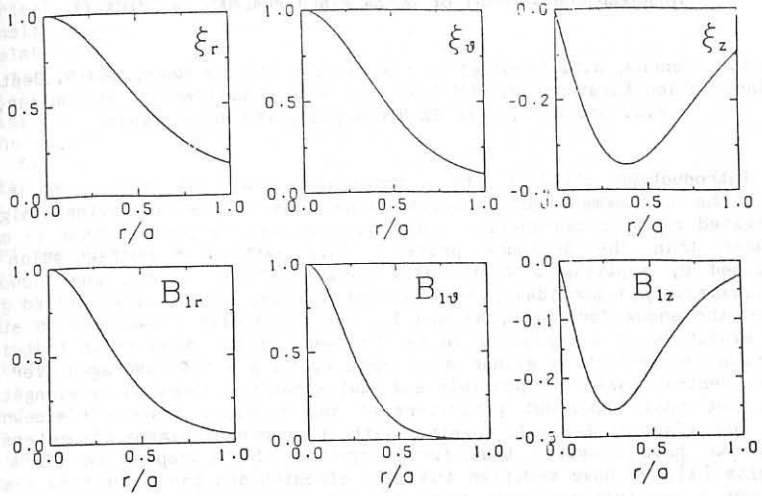

Figure 3 Kadomtsev stable equilibrium; infinite vacuum; m=1; ka=4.0. Components of displacement and perturbed magnetic field.

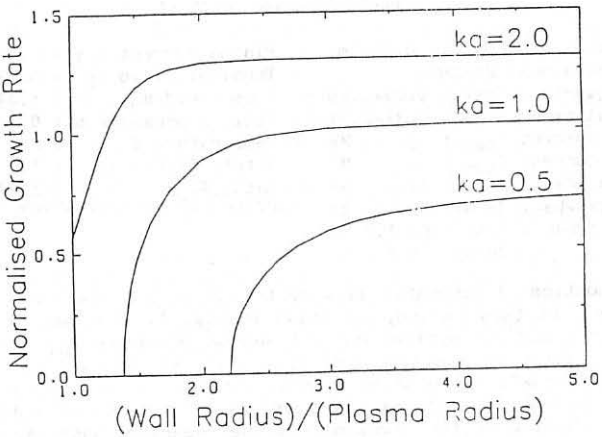

Figure 4 Flat current; m=1. The effect on growth rate of a conducting wall, for three values of ka.

IMPROVED CONFINEMENT OF SCREW PINCH PLASMAS IN SPICA II

A.A.M. Oomens, H.S. Lassing, J. Lok, A.F.G. van der Meer, and D. Oepts
Association Euratom-FOM, FOM-Instituut voor Plasmafysica, Rijnhuizen,
P.O. Box 1207, 3430 BE Nieuwegein, The Netherlands.

1. **Introduction** SPICA II is a toroidal screw-pinch device, built to study the confinement and stability properties of plasmas having a highly elongated minor cross-section and a current density profile that is much broader than the pressure profile. This particular configuration is produced by applying a fast-rising toroidal field B_T to, and inducing simultaneously a toroidal plasma current I_{pl} in, a partially ionized gas. After the shock formation, B_T and I_{pl} are (actively) crowbarred to study the evolution of the plasma. In earlier work it has been shown that in a circular cross-section stable discharges up to $\beta = 15\%$ (averaged over the dense central part) are possible and that β can be increased by elongation [1]. The most important parameters of the machine, described elsewhere [2], are given in Table I, together with the range of plasma parameters in which we have operated thus far. Since the first report on SPICA II results [3], we have modified the main circuits and the preheating system in such a way that now each discharge can be routinely passively crowbarred, with a decay time of 0.35 ms, leading to reduced plasma-wall interaction prior to and during the main discharges.

TABLE I

PARAMETERS OF SPICA II

Major radius R	: 0.45 m	Plasma current I_{pl}	: 0.3 - 0.45 MA
Minor dimensions: 2b×2h:		Toroidal field B_T	: 0.72- 1.1 T
inside quartz vessel	: 0.29×0.69 m	Bias field B_o	: 0.03- 0.14 T
inside aluminium shell	: 0.31×0.71 m	Filling pressure p_o	: 0.2 - 2 Pa (D_2)
Poloidal current I_{pol}	: 3 MA	Temperature T_e	: 20 -80 eV
Toroidal current I_{tor}	: 2 MA	Safety factor q_I	: 1.5 - 3
Rise time T/4	: 11.3 µs	Beta (%) β	: $\lesssim 25$
Passive crowbar: decay:	0.35 ms	Degree of preionization α: 10-70%	
Active crowbar : flat top:	1.2 ms		
decay	: 7 ms		

2. **Diagnostics** A schematic view of the distribution of the diagnostics, operational in this period, is shown in Fig. 1. The name "Faraday loop" stands for a magneto-optical current sensor measuring I_{pl} by means of the Faraday rotation in a single-mode fibre [4]. At the position indicated by "poloidal streak", the aluminium shell contains a large number of viewing holes to observe the plasma light emission by means of optical fibres. Digital recording of the signals from the separate channels, using photodiodes and transient recorders, offers the possibility to further process these signals after the shot. In this way one acquires, in addition to a quantified streak picture shown in Fig. 2 the possibility to apply a

numerical reconstruction technique, to get a cross-section of the intensity distribution. The results of preliminary attempts to check the correlation of the emission with the electron density are shown in Fig. 3. The temporary vidicon detection system for the multi-point Thomson scattering was replaced by an intensifier-CCD combination. The proximity-focussed, micro-channelplate image intensifier allows operation of the detector system at the photo-electron noise limit and also operates as a fast shutter (~ 100 ns) with a shutter ratio better than 10^9. The spatial resolution is 2 mm with a field of view of 115 mm, while the spectral resolution is ~ 10 nm with a spectral range of 140 nm.

3. **Plasma operation** In Ref. [3], it was reported that a rapid loss of density, within 50 μs, of the main column after crowbarring was always observed. Since then we have operated over a wide range of preheating conditions (B_o, p_o, α) and at different q_I at the wall. Unfortunately, we have not yet found a clear connection between the preheating conditions and the behaviour of the main discharge. Since the SPICA II experiment will be terminated at the end of 1987, the first priority now is to collect data. However, some general observations, based upon the results of the interferometer, Thomson scattering and pick-up coils can be made. At high p_o (~ 2 Pa), it is possible to confine plasmas during several hundreds of μs without gross instabilities. Some of the results for such a discharge are shown in Fig. 4. The displacement of the column is small ($\Delta/a \leq 0.14$) and q_ψ increases slowly from 1.7 to 2.2. The average density in the horizontal plane remains roughly constant at 2×10^{21} m^{-3}, but the temperature is low (T_e ~ 20 eV). At low p_o and high α, thus at stronger shock heating, we very often observe a high elongation already early in the discharge, which leads either to an up/down instability or to a breaking up of the main column into several filaments. Anyway, under these conditions, there is a sharp decrease in density along the horizontal and vertical chords, the pick-up coils indicate large excursions of the current centre, mostly in inward direction, and wall contact is obvious from the digital streak picture and the VUV spectrometer. At low p_o and low α, it is possible to produce plasmas with high β (up to 25%, Fig. 5), but in that case the cross-section of the column is almost circular (b/a = 0.08/0.065).

To draw quantitative conclusions, however, a more detailed analysis, especially of the magnetic data and the density distribution, has to be made.

Acknowledgements The authors wish to thank Mrs. B.J.J. Grobben, W. Kooijman, W.J. Mastop, B.J.H. Meddens and P.H.M. Smeets for operation of the machine and their assistance in diagnostics and data-handling.

This work was performed under the Euratom-FOM association agreement with financial support from ZWO and Euratom.

References

[1] C. Bobeldijk et al., Nucl. Fusion 25 (1985) 1093.
[2] SPICA II Team, Nucl. Instrum. Methods **207** (1983) 61.
[3] SPICA II Team; C. Bobeldijk et al., Proc. 12th Eur. Conf. on Contr. Fusion and Plasma Phys., Budapest (1985) Vol. 9F-I, p. 594.
[4] H.S. Lassing et al., to be published in Applied Optics, June 1987.

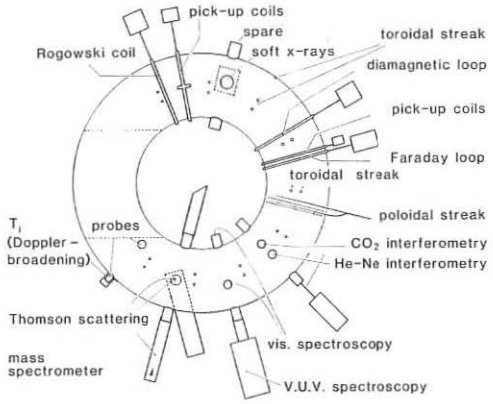

Fig. 1.
Schematic view of SPICA II torus with the diagnostics set-up.

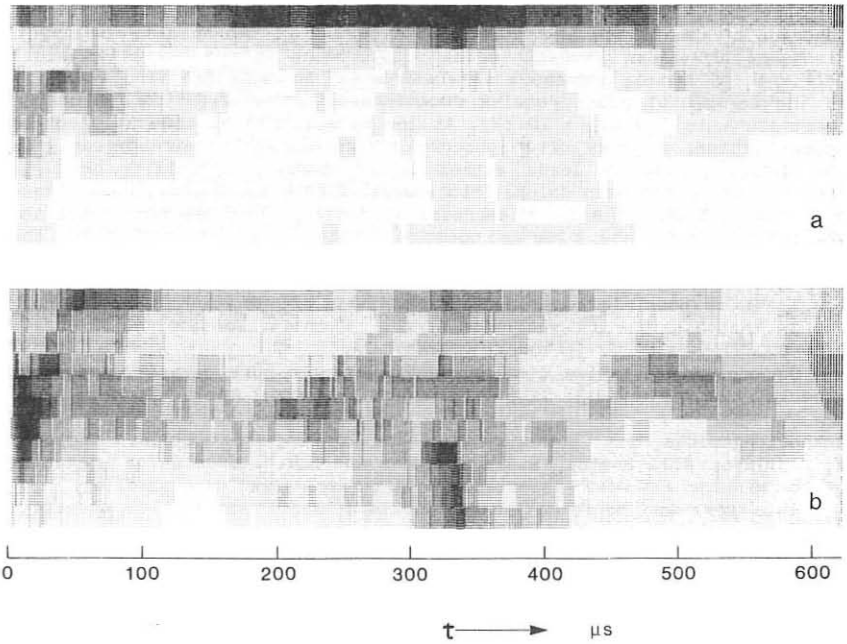

Fig. 2. A digital streak picture of the discharge of Fig. 5. The implosion and wall contact at t ~ 330 μs can be distinguished.
(a: top view; b: side view).

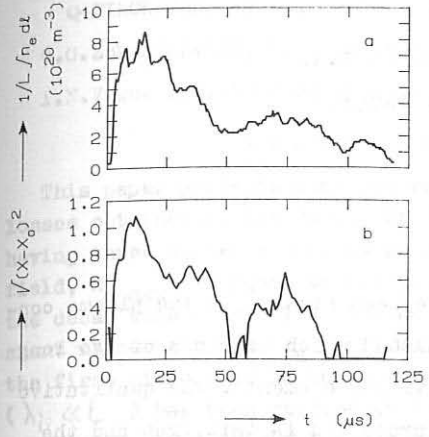

Fig. 3. a. Electron line density measured by means of interferometry. b. The square root of the corrected infrared emission.

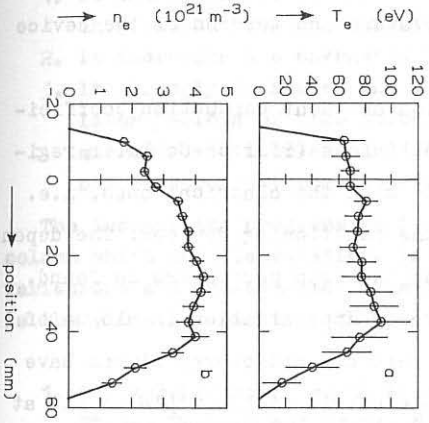

Fig. 5. T_e- and n_e-profile in the equatorial plane at 10 μs for a discharge with p_o = 0.5 Pa, B_o = 0.03 T and B_T = 0.87 T.

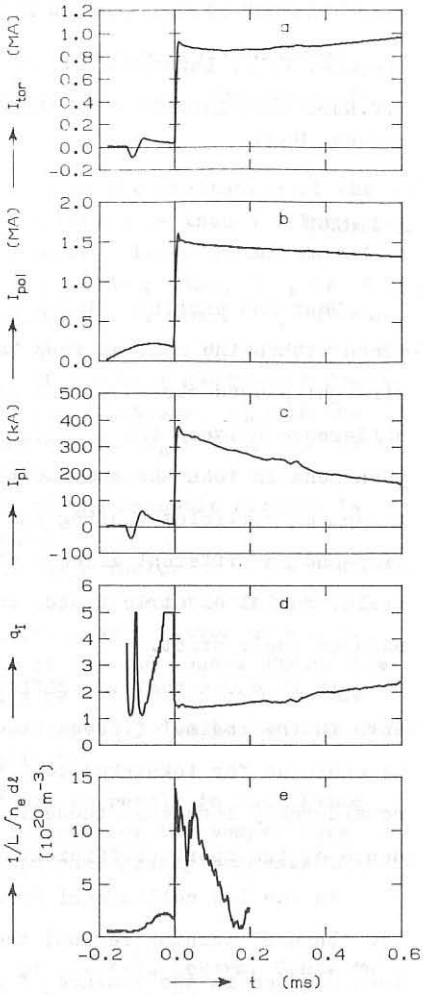

Fig. 4. Some parameters of a discharge at p_o = 1.5 Pa and with active power crowbar: a. The primary toroidal current. b. The primary poloidal current (1.5 MA α B_T = 0.67 T). c. The plasma current. d. q_I at the wall. e. $1/L \int n_e dl$ along a vertical chord.

DIFFUSIVE PLASMA LOSSES IN THE CLOSED MAGNETIC TRAP "DRACON" WITH A SPATIAL AXIS

Glagolev V.M., Lazarev S.L., Trubnikov B.A.

I.V.Kurchatov Institute of Atomic Energy,
Moscow, USSR

ABSTRACT

Heat and particle fluxes have been studied in the plasma confined within the spatial trap "DRACON" which consists of two long straight pieces closed with curvilinear elements. The qualitative difference between the diffusive processes in this trap and the phenomena in tokamaks and stellarators is in the presence of many groups of particles-passing and trapped at different pieces of the trap-and in different effects of a rippled longitudinal magnetic field, radial electric field, curvature and torsion of the device axis on their drift.

It is shown that the diffusion and heat conduction coefficients in the regime of frequent collisions (Pfirsch-Schluter regime analogue for tokamaks) coincide with the classical ones, i.e. considerably less than those in the functioning devices. The dependence of transport coefficients on the trap parameters is found.

In the low collisional frequency approximation (analogue of the "banana" tokamak region) the particle and energy fluxes have been studied in the absence of an electric field in plasma and at the ambipolar nature of diffusion. It is shown that the elongation of straight pieces improves a thermal plasma insulation in spite of the resonant nature of ion diffusion there. A radial electric field strongly reduces the fluxes and the transport coefficients

A STUDY OF PLASMA CONFINEMENT AND STABILITY IN AN OPEN Q-PINCH TRAP WITH THE MAGNETIC MIRRORS.

G.G.Zukakishvili, L.L.Goldinov, E.K.Tichanov, Z.P.Chkuaseli

I.N.Vekua Institute of Physics and Technology, Tbilisi, USSR.

A B S T R A C T

This paper presents some new results on the limitation of the end losses obtained on the device KP-1M, a linear Q-pinch 1 m long, [1] having three magnetic mirrors at the ends. A longitudinal magnetic field, $H_{z\ max}$ is equal to 2.2 Tl, its build-up time, τ , is 4 μs, the decay time is equal to 100 μs after the crowbar. A quasi-constant magnetic field, $H_{n\ max}$, is equal to 6 Tl. The mirror ratio in the first mirror, K, is in the range of 2 - 6. A gasdynamic regime ($\lambda_{ii} \ll \ell$) has been studied at the concentrations, n_e= in the range of 2 - 6.10^{16}cm^{-3} and the temperatures $T_e + T_i \leq$ 200 eV in the presence of the mirrors and without them.

It is shown that the introduction of the magnetic mirrors is advantageous for the following reasons:

1. It increases the energy content by a factor of 1.5 - 2 at the initial stage which is proportional to the mirror ratio.
2. It increases the energetic lifetime by a factor of 4 - 5.
3. It strongly decreases the rate of the end losses during the later periods of time which may be attributed both to the mirror ratio increase and plasma cooling due to the longitudinal electronic thermal conductivity.

The instability progression is found to result in the plasma column shift and its rotation. The analysis of the temperature variations and end-and-side high-speed photography suggests that it is the MHD -instability with m = 1.

1. G.G.Zukakishvili, et al Proc. of the X-th Intern. Conf. on Plasma Physics and Contr. Nucl. Fusion, London, section II, p.93, 1984.

NATURE OF ANOMALOUS ELECTRON TRANSPORT ACROSS MAGNETIC FIELD IN A TRAP WITH STEEP DENSITY FALL

M.S.Ioffe, B.I.Kanaev, V.P.Pastukhov, V.V.Piterskij, E.E.Yushmanov

I.V.Kurchatov Institute of Atomic Energy, Moscow, USSR

ABSTRACT

The results of studying the mechanism of anomalous transverse electron transport in Atoll device are presented. The device is a ring cusp with electrostatically-plugged gaps. Its main characteristics are as follows: magnetic field is of quadrupole shape, field intensity in the gaps is up to 30 kGs, gap width is 2 mm, plugging potential is about 5 kV, mean plasma ring radius is 48 cm, plasma density $\lesssim 10^{12}\,cm^{-3}$, $Te \simeq T_i \gtrsim 100$ eV, plasma volume is about 50 l.

As was shown earlier, the electron field-parallel losses can be completely suppressed. Under such conditions the quality of confinement is determined by an electron cross-field transport rate. This transport proved to be governed by microinstabilities driven by steep density gradient rather than by a classical diffusion process and appeared to be three orders of magnitude more intense than the classical one.

The knowledge of instabilities acting has been obtained on the basis of a detailed investigation of frequency and wave characteristics of the oscillations observed. The characteristics are compared with those predicted theoretically for Atoll. It is found that for the central plasma region, where the magnetic field ununiformity is strong enough, the long-wave ion-sound (LWIS) instability plays the principal role. In the external regions the drift low-hybrid (DLH) instability replaces LWIS. Experimental plasma density profile is in agreement with the theoretical idea about the existence of a "marginal stability profile" for each instability mentioned above.

The mechanism of anomalous electron transport revealed in Atoll might also be responsible for collisionless formation of the sheath separating a field-free plasma from a vacuum magnetic field in some other traps having $m = 1$.

STUDIES ON MAGNETIC HELICITY AND MHD BEHAVIOUR IN A COMPACT TOROID (+)

S.SINMAN
Middle East Technical University, Electrical and Electronic Engineering Department, Plasma Engineering Laboratory, Ankara - Turkey

A.SINMAN
Ankara Nuclear Research and Training Center, Nuclear Fusion Laboratory, Ankara - Turkey

ABSTRACT

A spheromak plasma has been produced by means of the C-guns located inside the floating octagonal flux conserver of 40 litres. The C-gun is a novel and alternative version of a magnetically driven shock tube. The vertical electrode pairs at the toroidal plane in the flux conserver and the back-strap outside of the flux conserver are the main structure of the C-gun. The electrical characteristics of the C-gun have conformed with the critical damping and under damping modes depending upon the back-ground gas pressure ranges of 40-70 mTorr and 75-250 mTorr respectively. The experimental results have indicated existence of the minimum energy state ($k=\mu_o J/B$ = constant). It has been observed from the oscillograms taken from the diagnostic devices that the current channel of the toroid ($\bar{n}_e = 5\times10^{14}\,cm^{-3}$, T_e= 30-50 eV, B_ϕ= 800 G, $\bar{b}_v$= 0.12 and t_{fm}= 20 ms) produced in the critical damping mode of operation of the C-gun is modulated by the drift wave in the frequency range of 16-25 kHz. In return at the under damping mode of the C-gun, a spheromak plasma in MHD behaviour ($\bar{n}_e = 10^{14}\,cm^{-3} - 5\times10^{15}\,cm^{-3}$, T_e= 20-35 eV, B_ϕ= 450-600 G and $\bar{b}_v$= 0.085) has been obtained. According to the total flux measurements, the resistive decay times of the toroid have been determined in the range of 3.5-5 ms.

INTRODUCTION

The compact toroid (CT) researches /1-2/ are complementary to tokamak researches and will improve the understanding of plasma physics in toroidal devices, as the overall optimization of the toroidal experimental arrangements.

Concepts in this class, which includes spheromak /3-5/ and field reversed configuration /6-7/ offer reactor advantages that result from simplified geometries of the confinement chamber. In the case of the spheromak requirement is the entrapment of the desired toroidal flux within the separated

poloidal flux region. The plasma currents are largely force-free and the toroidal and poloidal fluxes are comparable.

In our previous study; it has been experimentally demonstrated that in the flux conserver by means of a C-gun, the CT particularly in two different behaviour may be formed /8/.

Especially in spheromak, as at the Los Alamos (CTX) and Osaka (CTCC) devices, the toroidal field at the flux conserver is produced by the poloidal field injection (co-axial gun) through the flux conserver. This is a flux conversion mechanism and it can be interpreted by the magnetic helicity concept /9/.

At the mentioned C-gun; the shock heated warm electrons (5-20 eV) in the plasma belt, interacting with the toroidal magnetic field produced by the current passing through the plasma belt and back-strap closed loop, a helical plasma current channel is created. Thus without a toroidal-poloidal flux conversion, a toroidal field together with a current channel (E-layer) at the flux conserver may be generated. This procedure fits to the principle of minimum energy equilibrium /9/. On the other hand, the helicity existence rate is $(dK/dt) = 2V_g\phi_{ex}$, where V_g is the voltage applied to the C-gun, ϕ_{ex} is the net flux on the area framed by the plasma belt and the wall of the flux conserver.

When the experimental data obtained from the CT produced by the C-gun and above considerations are compared and evaluated, they have been understood that as in the other magnetized co-axial plasma guns, in the C-gun too the helicity injection and current drive mechanisms /10/ can be come into existence. Below the thermal energies of 15 eV for the shock heated electrons in the C-gun, the reconnection probability is lower than 70 %. To produce the helical electron ring for 15 eV, it is necessary one microsecond duration. In this duration, the toroidal field generated by C-gun, is not sufficient.

At a distance of 7 cm from the wall of the flux conserver, the toroidal and the poloidal magnetic flux densities were very close being about 600-800 G. The decay times of the fields have changed between 2.2 - 3.5 ms which has been calculated by the expression of $t_B = B/(dB/dt)$.

SYSTEM DESCRIPTION

By the main points, the experimental arrangement has an octagonal 40 litres floating flux conserver which is the vacuum chamber at the same time. The back-pressure in the flux conserver is 5×10^{-6} Torr. Four C-guns have been inserted around the flux conserver with 90° aparts.

The system consists of 2 kJ capacitor bank for each C-gun, the spark-gap switches controlled by self generated UV ring and other needed diagnostic measuring equipments.

shock heated electrons having helical orbits and being at the energy level capable to ionize the back-ground gas, causes to generate an E-layer. This matter has been determined by the resistivity probe measurements.

According to the magnetic probe signals at the distance of 7 cm from the wall of flux conserver, the ratio of the toroidal and poloidal magnetic field variations in time are constant. This result verifyes the mimimum energy criterion.

It has been understood from the experimental data that C-gun can translate the energy on capacitor bank to the plasma inductance with an efficiency of 0.12 - 0.18.

Probable in the first step, the shock heated electrons and in the second phase, the ion cyclotron wave damping and subsequently the ohmic heating mechanisms have caused the temperature increasing of the spheromak plasma produced in MHD behaviour.

(+) This work was performed under cooperative agreement between Turkish Atomic Energy Authority and IAEA Vienna, the Division of Research and Laboratory, under Contract No.: 3823/R2/RB.

REFERENCES

/1/ Proc. of the 7th CT Symposium, May 21-23, 1985 Santa Fe.
/2/ Yamada, M., in Advances in Compact Torus Research, (Proc. IAEA Techn. Committee Meeting on Advances in Compact Torus Research Sydney, 1985), IAEA Vienna (1986) 175.
/3/ Jarboe, T., et al., Phys. Rev. Lett. 45(1980)1264.
/4/ Goldenbaum, G., et al., Phys. Rev. Lett. 44(1980)393.
/5/ Yamada, M., et al., Phys. Rev. Lett. 46(1981)188.
/6/ Siemon, R.E., et al., in Plasma Physics and Controlled Nuclear Fusion Research (Proc. 9th Int. Conf. Baltimore, 1982) Vol.2, IAEA Vienna (1983)283.
/7/ Rej, D.J., et al., in Ref. /1/.
/8/ Sinman, S., and Sinman, A., in Plasma Physics and Controlled Nuclear Fusion Research (Extended Synopses, 11th Int. Conf. Kyoto, 1986)137.
/9/ Taylor, J.B., Phys. Rev. Lett. 33(1974)1139.
/10/Bellan, P.M., in Ref. /8/, p. 48.

The main diagnostic techniques used are: the Langmuir electrical probes; the magnetic probes and loops; L-R fast operational integrators; the paramagnetic loop including a fast integrator; the resistivity probe; the charge-exchange cell and the visible light spectrum analyzer.

Besides, the fast storage oscilloscope of HP-1744/A and the other conventional fast oscilloscopes of HP-180/C and Tektronix 454/A have been used during data recording.

RESULTS OBTAINED

The operating period of the C-gun at under damping mode (UDM) was about 10-12 microseconds but at the critical damping mode (CDM) it was only 2-3 microseconds. The electrical characteristics related with UDM was periodic whereas that of CDM was aperiodic. The UDM was in MHD property on the other hand in CDM the drift wave instability accompanying with the current drive mechanism have been observed.

Utilizing from either the magnetic probes or total magnetic flux loop, data taken at UDM have shown that in the first two microseconds which is the quarter of a period, C-gun generates an ion cyclotron wave. Through first half period, ion cyclotron wave damping and the reconnection have occured. Just after the reconnection, it has been understood that the toroid has come into equilibrium phase.

On the oscillograms by this mechanism they have been determined that in the first half period, the toroidal magnetic flux variation has began with a zero average (reference line) and then gained a positive or a negative off-set value and finally in 3 - 5 ms decayed exponentially back-down to zero average.

In CDM too such as in UDM there exist the ion cyclotron wave mechanism. Correlating the signals taken from magnetic probes, loops and charge-exchange cell, it has been concluded that the current channel is closed and modulated by the drift wave in a frequency range of 15-25 kHz.

This toroid produced depending on the gas pressure (40-60 mTorr) and its own physical characteristics have been confined for a life time of 5 - 20 ms. The magnetic field configurations at CDM have not yet been investigated.

CONCLUSIONS

Without any flux conversion, by means of a magnetically driven C-gun, it seems to be possible to produce a toroidal magnetic field in a floating flux conserver. Thus it can be said that the magnetic helicity injection is also valid for the C-gun.

For a toroid in MHD behaviour, this mechanism has realized in the pressure range of 70 - 250 mTorr.

Interacting with above mentioned magnetic field, the

POWER BALANCE OF IONS IN THE HBTX REVERSED FIELD PINCH

P G Carolan,A R Field*,A Lazaros‡,M G Rusbridge‡,H Y W Tsui & M K Bevir
Culham Laboratory, Abingdon, Oxon, OX14 3DB, UK
(UKAEA/Euratom Fusion Association)
*Royal Holloway and Bedford New College, London
‡UMIST, Manchester

ABSTRACT

An ion power balance model, with simple assumptions, is presented which reproduces the main experimental results - viz $T_{io} \simeq T_{eo}$ at $\theta = 1.35$ and 156 limiter tiles in position, $T_{io}/T_{eo} > 1$ when a moveable limiter is inserted and $T_{io}/T_{eo} < 1$ with tile removal.

INTRODUCTION

Since the electrons and ions are collisionally decoupled in RFP plasmas they can be treated separately in power balance considerations. The input power remaining, after joule heating of the electrons, is assumed to heat the ions. This power is associated with the fluctuations which drive the dynamo electric field required to sustain the RFP configuration. The first part of the model is to determine the sharing of input power between electrons and ions and it is found important to include edge effects. The second part is to model the ion loss term. It is assumed that this is dominated by diffusion losses. When the neutral particle density distribution, $n_0(r)$, is known the diffusion coefficient, $D(r)$, can be calculated from particle balance considerations. However, the absolute neutral profile is available for only a few selected cases although the relative profile is sufficiently reproducible to allow a calculation of the relative $D(r)$ profile. The value of D on axis is obtained, assuming ambipolarity, from the axial power balance of the electrons, obtained experimentally. The ion temperatures can then be calculated and related to T_e and the loop voltage.

POWER BALANCE MODEL

The total input power density is: $W = \underline{E}\cdot\underline{j} = \eta j^2 - \underline{u} \times \underline{B}\cdot\underline{j}$, which in the presence of fluctuations (eg $\underline{j} = \underline{j}_0 + \underline{\tilde{j}}$) becomes, $W = \underline{E}_0\cdot\underline{j}_0 = \eta j_0^2 - \langle\underline{\tilde{u}} \times \underline{\tilde{B}}\rangle\cdot\underline{j}_0$ where $\langle\underline{\tilde{u}}\times\underline{\tilde{B}}\rangle$ is the dynamo electric field, η is the Spitzer resistivity (obtained from T_e and Z_{eff}), $\underline{E}_0$ is the mean electric field and j_0 is the current density (obtained from the Modified Bessel Function Model). The power input to the electrons is simply ηj_0^2 and it is assumed that the remaining dynamo power, $-\langle\underline{\tilde{u}}\times\underline{\tilde{B}}\rangle\cdot\underline{j}_0$, is dissipated locally into the ions.

The $\mu(r)$ profile can be estimated from the measured F and θ and making some assumption about the $\mu(r)$ distribution (eg $\mu(r) = \mu_0 (1-(r/a)^\beta)$). When edge effects are ignored the resistivities obtained from electrical measurements, assuming helicity balance, are about a

factor of 3-4 higher than those measured from Z_{eff} and T_e. However an imperfect boundary (eg tiles or field errors) acts as a sink for helicity [1,2], or presents current blockages [3], and so requires an enhanced dynamo field to sustain the configuration or in practical terms an increased loop voltage. An important feature of this effect is that the associated power is dissipated in the plasma bulk rather than at the boundary. If η^k is the resistivity obtained from helicity balance, but ignoring edge effects, it can easily be shown that when these are included we get $\eta = \eta^k(V_\phi - V_{wall})/V_\phi$, where V_ϕ is the loop voltage and V_{wall} the voltage associated with an edge helicity sink. The quantity V_{wall} is difficult to measure directly but is estimated to be at least 14 volts (with the tiles in position) for $\theta = 1.35$ and is apparently insensitive to plasma current[7]. The resistivity then obtained electrically agrees within the experimental uncertainties with the Spitzer value. This result simplifies the treatment since the residual dynamo power can now be calculated from electrical measurements and assuming a relative T_e profile.

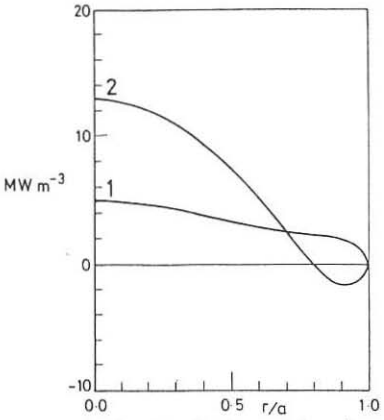

Fig 1 Distributions of input power densities into the electrons (1) and ions (2)

An example of the ohmic and dynamo power input distributions is shown in Fig 1 (I_ϕ=200 kA, $\bar{n}_e$=2 x 10^{19} m^{-3}, V_ϕ=30 volts, $T_e = T_{e0}\{1-(r/a)^6\}$, T_{e0}=250 eV, Z_{eff}=2). Assuming the dynamo power goes into the ions it can be seen that on axis it is 2-3 times the ohmic power going into the electrons and in the outer regions, power is taken from the ions. (The total integrated powers are similar with only about 20% extra for the ions.)

To obtain the ion temperature the ion energy losses must be modelled. The power loss, W_i, is assumed to be dominated by diffusion where $W_i(r) = (1/r)\cdot d/dr\{rG_i(r)\}$, and $G_i = -D(r)\, d/dr\, U_i(r)$, where U_i is the ion energy density. Ionisation of the neutrals is the only source of ions so that knowing the neutral density distribution, the diffusion coefficient, D(r), can be obtained from particle balance considerations. In practice, the absolute neutral density is difficult to measure and has been obtained in only a few selected cases in HBTX by fluorescence scattering [4].

However, the relative neutral density profile is sufficiently reproducible to calculate a relative D(r) distribution. This is confirmed by many Monte Carlo simulations of the neutral particle transport for the appropriate range of T_e, T_i and n_e. The problem remains to obtain a local

absolute value of D(r). To obtain D(r) on axis we appeal to the experimental electron power balance and assume ambipolar diffusion (ie $D_i(0) \equiv D_e(0) = D(0)$). On HBTX, as generally found in RFPs, the $T_e(r)$ has a flatter profile than $n_e(r)$ so that diffusion losses become of relatively greater importance, compared with conduction losses as the axis is approached. Assuming diffusion losses dominate on axis, the D(0) is obtained from the axial ohmic input power and the n_e distribution ($n_e(r) \simeq n_{eo}\,[1-(r/a)^2]$. The remaining conduction power loss (radiation losses are negligible), obtained from the difference of ohmic input and diffusive losses, is comparable to the latter. If the conduction losses were much larger then it would be difficult to justify our calculation of D(0). However, the absolute values of D(r) obtained (~50 m^2s^{-1} on axis rising to ~300 m^2s^{-1} at the periphery) is consistent with the spectroscopic determinations [5].

RESULTS

From power balance on axis we obtain $D_e(0) \propto W_{ohmic}(0)/n_{eo}T_{eo}$ and $D_i(0) \propto -\langle \underline{\tilde{u}} \times \underline{\tilde{B}} \rangle \cdot j_0/n_{io}\,T_{io}$. For most of the data obtained from current scaling in HBTX, T_{eo} ~ constant for I_ϕ = 150-400 kA and Z_{eff} is small (~2-3) so that η remains fairly constant. This is consistent with V_{wall} ~ constant in these conditions. Also $\mu(r)$ is insensitive to I_ϕ. The consequence is that the ratio $W_{ohmic}(0)/\langle \underline{\tilde{u}} \times \underline{\tilde{B}} \rangle \cdot j$ ~ constant and then from ambipolarity, $D_e(0) = D_i(0)$, it follows that $T_{io} \propto T_{eo}$ as has been observed experimentally [6].

The model of ion power balance can also predict absolute ion temperatures and a comparison between measured (deduced from an NPA spectrum) and calculated $T_i(r)$ profiles is shown in Fig 2. Note that the peaked values of measured and modelled T_{io} agree and that the narrower $T_i(r)$ compared with $T_e(r)$ is reproduced by the model.

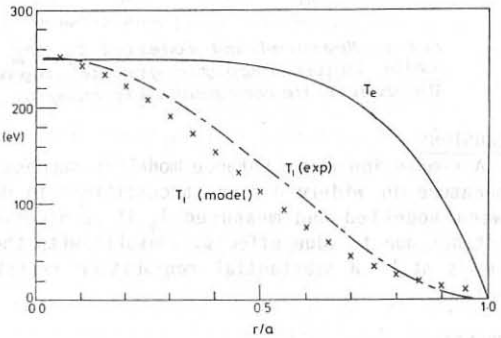

Fig 2 Distributions of electron and ion temperatures

The mobile limiter experiments [7] provide a further test of the model. If the V_{wall} used previously in relating η to η^k is supplemented with the additional loop voltage required to sustain the plasma with limiter insertion, the power into the ions can be calculated. A comparison between measured and calculated values of the ratio T_{io}/T_{eo} is

shown in Fig 3. The conclusion is that the extra voltage is not associated with edge power dissipation but is available to heat the ions. Removal of the 156 tiles results in $T_{io}<T_{eo}$ ($T_{io} \sim 200$-250 eV, $T_e \sim 350$-700 eV). However, T_{io} is still about a factor of 2 higher than that expected from helicity balance with a perfect edge (and an order of magnitude higher than from ion-electron collisions). These results suggest that there are remaining edge effects giving rise to an additional non-Spitzer plasma resistance together with the corresponding ion heating.

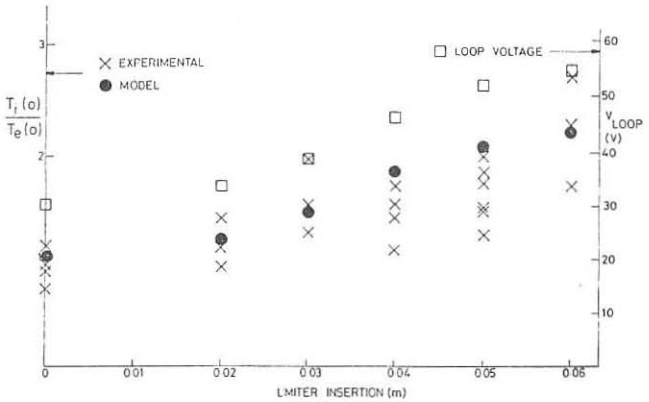

Fig 3 Measured and modelled T_{io}/T_{eo} with insertion of a mobile limiter (pyrolytic graphite) beyond the limiter tiles. Also shown are the corresponding loop voltages.

CONCLUSIONS

A simple ion power balance model is successful in reproducing the ion temperature in widely different conditions in HBTX. To obtain agreement between modelled and measured T_i it is necessary to include non-Spitzer resistance due to edge effects. Results with the removal of tiles suggest there is still a substantial non-Spitzer resistance present due to edge effects.

REFERENCES

[1] T R Jarboe and B Alper: Phys Fluids 30 No 4 (1987) 1177
[2] H Y W Tsui: this conference
[3] R S Pease: private communication (1986)
[4] D A Evans et al: Rev of Sci Instrum 56 (1984) 1012
[5] P G Carolan, C A Bunting et al: this conference
[6] B Alper et al: 11th Int Conf on Plasma Phys and Controlled Nuclear Fusion (Kyoto, 1986) IAEA-CN-47/D-II-1
[7] B Alper and H Y W Tsui: this conference

HELICITY TRANSPORT AND ANOMALOUS RESISTANCE IN THE REVERSED FIELD PINCH

H Y W Tsui
Culham Laboratory, Abingdon, Oxon, OX14 3DB, UK
(UKAEA/Euratom Fusion Association)

ABSTRACT

The behaviour of the Reversed Field Pinch (RFP) is discussed in terms of the balance and transport of magnetic helicity. The analysis shows that the departure from the Taylor's fully relaxed state is caused by energy losses from the fluctuations associated with helicity transport. Within this framework, there are two energy flow channels supported by the external power input: the classical resistive dissipation and the power throughput coupled to the $\tilde{u}\times\tilde{B}$ fluctuations. The second channel corresponds to the anomalous resistivity reported from experiment and may give rise to ion heating. The anomalous loop voltage can be interpreted in terms of helicity loss to the wall or limiters where field lines intersect material objects. A model which shows that such leakage depends on the flux intercepted and the local electron temperature is presented and applied to explain the loop voltage anomaly observed in HBTX experiment.

INTRODUCTION

The importance of magnetic helicity [1] in determining the behaviour of RFP was first discussed in the relaxation theory by Taylor [2]. When reconnections are allowed, the plasma relaxes to a minimum energy state subjected to the constraint that the global helicity is invariant. At this fully relaxed state, the field configuration satisfies $\nabla\times B = \mu B$ with uniform μ. In experiments, $\mu(r)$ is not uniform but decreasing towards the plasma edge. It has been suggested [4] that such departure is caused by the energy throughput coupled to the fluctuations which takes place in a second energy flow channel in addition to that involving electron heating through Spitzer resistivity. It is well known in the mean field magnetohydrodynamic theory that fluctuations can lead to an effective electric field and that the Ohm's law for RFP be modified [5,6] to include their contributions. Although these fluctuations do not dissipate helicity and therefore do not affect the global balance [7], they can dissipate energy. It has been shown that when fluctuations are ignored the global helicity balance is more correct than the global energy balance in computing the plasma resistivity [8,4].

HELICITY TRANSPORT AND FLUCTUATIONS

The magnetic helicity in an RFP [9] is $K = \int_V \underline{A}\cdot\underline{B}\,d\tau - \oint_S \underline{A}\cdot d\underline{\alpha} \oint \underline{A}\cdot d\underline{\beta}$ where α and β are the poloidal and toroidal distance on the surface S bounding the volume V. With variables separated into the mean and fluctuating components such as $\underline{A}(r,\alpha,\beta,t) = \underline{A}_0(r,t) + \tilde{\underline{A}}(r,\alpha,\beta,t)$ where $\underline{A}_0 = \langle\underline{A}\rangle$ and $\langle\ldots\rangle$ denotes the appropriate average over α, β and time, the helicity balance equation in a steady state RFP is

$$V_\phi \Phi_0(r) = \int_V \eta \underline{j}_0\cdot\underline{B}_0\, d\tau + \int_S \chi_0 \underline{B}_0\cdot(d\underline{\alpha}\times d\underline{\beta}) + H \qquad (1)$$

where $\Phi_0 = \oint \underline{A}_0\cdot d\underline{\alpha}$ is the toroidal flux, χ_0 is an electrostatic potential and H is the outward helicity flow across the mean flux surface S due to fluctuations. By defining $\{\ldots\}$ as the average over α and β and $\tilde{\underline{A}}' = \tilde{\underline{A}} - \{\tilde{\underline{A}}\}$, H can be expressed as

$$H = \langle\dot{\tilde{\Phi}}\dot{\tilde{\Psi}}\rangle + \int_S \langle\tilde{\chi}\tilde{\underline{B}}\rangle\cdot(d\underline{\alpha}\times d\underline{\beta}) + \tfrac{1}{2}\int_S \langle\tilde{\underline{A}}'\times\dot{\tilde{\underline{A}}}'\rangle\cdot(d\underline{\alpha}\times d\underline{\beta}) \qquad (2)$$

where $\tilde{\Phi} = \oint\{\underline{A}\}\cdot d\underline{\alpha}$ and $\tilde{\Psi} = \oint\{\underline{A}\}\cdot d\underline{\beta}$. The first term is the helicity flow associated with fluctuating flux as in F-Theta pumping current drive [9]. After substituting $\eta\underline{j}_0 = \underline{E}_0 - \langle\tilde{\underline{u}}\times\tilde{\underline{B}}\rangle$ and $\int_V \underline{E}_0\cdot\underline{B}_0\,d\tau = V_\phi\Phi_0$, eq(1) becomes

$$\int_V \langle\tilde{\underline{u}}\times\tilde{\underline{B}}\rangle\cdot\underline{B}_0\, d\tau = -\int\chi_0\underline{B}_0\cdot(d\underline{\alpha}\times d\underline{\beta}) - H \qquad (3)$$

When the fluctuating radial field vanishes at the plasma edge, it can be shown from $\tilde{\underline{B}}' = \nabla\times\tilde{\underline{A}}'$ that H=0. And if $\underline{B}_0\cdot(d\underline{\alpha}\times d\underline{\beta})=0$, equ(3) reduces to

$$\int_V \langle\tilde{\underline{u}}\times\tilde{\underline{B}}\rangle\cdot\underline{B}_0\, d\tau = 0 \qquad (4)$$

This means that fluctuations do not dissipate helicity while transporting it within the plasma bounded by a perfectly conducting wall.

ANOMALOUS LOOP VOLTAGE

When there is an equilibrium shift or objects protrude into the plasma the helicity loss arises from field lines which intersect material objects is described by the surface term in equ(1). This loss or leakage is caused by the potential difference which is generated by the obstruction to current flow [10], between the boundaries connected by the field lines. An additional ("anomalous") loop voltage is needed to increase the helicity input and transport to compensate the loss.

The current flow along the field lines is limited by the presence of an obstruction in a similar way to the current saturation phenomenon in sheath or probe theories. This arises when the surfaces do not emit charged particles, even though they may emit neutrals. The current density which is generated by the difference in the sheath potential drops ($\delta\chi$) and electron flux to the two sides is limited by the ion flux. In one dimensional approximation,

$$\bar{v}_e n[e^{-e(\phi_f-\delta\chi/2)kT_e} - e^{-e(\phi_f+\delta\chi/2)kT_e}] = \bar{v}_e n\, e^{-e\phi_f/kT_e}$$

where $\bar{v}_e$ is the averaged velocity of the electrons flowing towards the surface, ϕ_f is the mean floating potential. The solution gives

$$\delta\chi \simeq 1.8\, kT_e/e$$

Thus the helicity loss and the increase in loop voltage (δV_ϕ) depend on the local electron temperature and the amount of magnetic flux intercepted. These properties differ from those when helicity dissipation in the edge volume [11]. According to this model δV_ϕ due to plasma shift (Δ) and obstruction (eg limiter) with projection area wd are

$$\delta V_\phi = \delta\chi\,(\frac{4R\Theta}{a^2})\Delta \qquad \text{and}$$

$$\delta V_\phi = \delta\chi(\frac{\theta}{\pi a^2})wd$$

where θ is the pinch parameter. When plasma wall contact is increased due to the plasma shift, a higher loop voltage (Fig 1) is observed [12] as expected from the theory. The value of $\delta\chi$ obtained is 18 volts corresponding to an edge electron temperature of 10 eV. A reduction of 8 volts is expected when the limiters are removed, which is consistent with the ~10 volts observed in experiment [13].

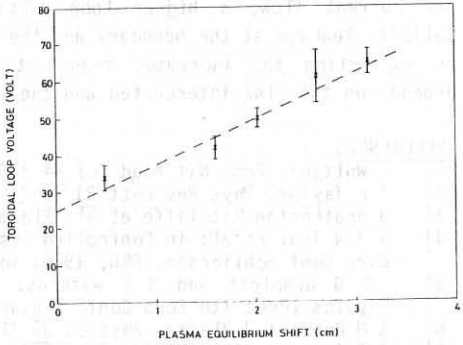

Fig 1 The variation of toroidal loop voltage (V_ϕ) with plasma equilibrium displacement (Δ)

The energy balance in a steady state RFP is

$$V_\phi I_\phi \simeq \int_V \eta j_0^2\, d\tau + \int_S \chi_0 \underline{j}_0 \cdot (d\underline{\alpha} \times d\underline{\beta}) - \int_V \langle \underline{\tilde{u}} \times \underline{\tilde{B}} \rangle \cdot \underline{j}_0\, d\tau \qquad (5)$$

and $$-\int_V \langle \tilde{u} \times \tilde{B} \rangle \cdot j_0 \, d\tau = \int_S \langle \tilde{E} \times \tilde{B} \rangle \cdot (d_\alpha \times d_\beta) + \int_S \langle \tilde{p}\tilde{u} \rangle \cdot (d_\alpha \times d_\beta) + \{\text{losses from fluctuations}\} \quad (6)$$

represents the transport of energy by fluctuations. This integral which depends on the μ profile is not necessarily zero at the plasma edge [7]. It is zero when the plasma is fully relaxed with uniform μ (from eq(4)). The departure from the fully relaxed state is related to the energy losses from the fluctuations in transporting helicity. These losses can arise from the non-vanishing fluctuating radial velocity at the edge or viscous damping, for instance in heating the ions. When there is helicity leakage, a higher loop voltage is needed to compensate the energy loss in supporting the increased helicity transport and leads to the observed loop voltage or resistance anomaly.

CONCLUSION

The balance and transport of magnetic helicity due to fluctuations in the RFP has been discussed. Energy loss from these fluctuations causes departure from the fully relaxed state. It is shown that the anomaly in loop voltage or resistance observed in HBTX experiment can be explained on this basis. When field lines intersect material objects which obstruct the current flow, a higher loop voltage is needed to compensate the helicity leakage at the boundary and the energy loss from the fluctuations in supporting the increased transport. The increase in loop voltage depends on the flux intercepted and the local electron temperature.

REFERENCES

[1] L Woltjer: Proc Nat Acad Sci 44 (1958) 489
[2] J B Taylor: Phys Rev Lett 33 (1974) 139
[3] D Brotherton-Ratcliffe et al: Plasma Phys & Cont Fus 29 (1987) 161
[4] H Y W Tsui et al: in Controlled Fusion and Plasma Physics (Proc 13th Euro Conf Schliersee, FRG, 1986) Vol 10C, Part 1, 345
[5] C G Gimblett and M L Watkins: in Controlled Fusion and Plasma Physics (Proc 7th Euro Conf, Lausanne 1975) Vol 1, 103
[6] A H Boozer: J Plasmas Physics 35 (1986) Part 1, 133
[7] H R Strauss: Phys Fluids 28 (1985) 2786
[8] K F Schoenberg et al: Phys Fluids 27 (1984) 1671
[9] M K Bevir and J W Gray: in Proc of Reversed Field Pinch Theory Workshop, Los Alamos Report LA-8944-LC 1981, p176
[10] R S Pease: private communication
[11] T R Jarboe and B Alper: Phys Fluids 30 No. 4 (1987) p1177
[12] B Alper et al: in Plasma Physics and Controlled Nuclear Fusion Research (Proc 11th Int Conf, Kyoto, 1986), IAEA-CN-47/D-II-1
[13] B Alper and H Y W Tsui: this conference

REVERSED FIELD PINCH OPERATION WITH A THIN SHELL

S. Ortolani, V. Antoni, and S. Martini
Istituto Gas Ionizzati del C.N.R.
EURATOM-ENEA-CNR Association, Padova, Italy

and

R. LaHaye, M. Schaffer, T. Tamano, and P. Taylor
GA Technologies, San Diego, California, USA

Reversed Field Pinches (RFP) have typically been studied in experiments where a thick conducting shell tightly surrounds the plasma. This feature has been dictated by the theoretical belief that MHD plasma instabilities would otherwise grow and destroy plasma confinement. On the other hand, the presence of the thick conducting shell prevents accurate active plasma position control, which is important for minimizing plasma-wall interactions. Furthermore, in a reactor the discharge length will of necessity be longer than the shell time constant and the possibility of using a thin conducting shell will make the prospect of the fusion reactor more attractive.

Already in the design of the new generation of devices such as RFX [1], ZT-H [2], OHTE II [3], TPE-RX [4], the decision of whether or not to continue installing thick conducting shells is a very important and difficult one to make. In particular, it is now believed that accurate equilibrium control, edge plasma properties, plasma-wall interactions and impurity contamination can play a dominant role in determining the loop voltage necessary for maintaining the RFP distributions, and therefore the energy confinement time, since for an ohmically heated system like the RFP, the simple relationship holds: $\tau_E = 3/8\, \mu_o\, R\, \beta_\theta\, I/V$.

The present OHTE device has the unique feature of utilizing an electrically thin conducting shell in which discharge lenghts much longer than the shell time constant for the vertical field have already been achieved [5].

Due to the interest in the construction and operation of future larger experiments, a joint Padova/GA experimental program was therefore carried out to further examine the scientific and technical features of the OHTE thin shell operation. In particular, an attempt was made to prolong the pulse lenghts through finer tuning of the equilibrium control using an additional vertical field (B_v) circuit thereby further assessing the plasma sensitivity to position control as opposed to inherent MHD stability limitations due to the lack of a perfectly conducting shell.

The OHTE device (R = 1.24 m, a = .18 m) [5] has been operated in the RFP mode. The thin shell is made of brass ($\eta = 6 \cdot 10^{-8}\ \Omega \cdot m$) and is 0.8 mm

thick with a minor radius of 0.2 m. The vertical field time constant is 1.5 ms whereas the toroidal field time constant is $\lesssim$ 0.25 ms. The experiments reported here have been made at currents of 150-200 kA. Typical plasma parameters are $\bar{n} = 5 \cdot 10^{19}$ m^{-3}, $T(0) \cong 150$ eV corresponding to $I/N \cong 3\text{-}4 \cdot 10^{-14}$ A · m and to the OHTE temperature scaling of approximately 1 eV/kA [5]. The loop voltage is of $\sim$100 volts corresponding to plasma resistances $V/I \gtrsim 0.5$ mΩ. The total vertical field necessary for centering the OHTE plasma is approximately $1.6 \cdot 10^{-7} \cdot I\,T$ (i.e., ~ 0.03 T at the current level we operated). The basic toroidal equilibrium control is achieved by mismatching the currents in the primary poloidal field coils [5]. In addition, an independently powered vertical field coil system was used for fine B_v tuning and plasma positioning. In this vertical field control experiment, variations of a few gauss in B_v were explored and the corresponding plasma pulse lenghts were analysed. In particular, we present here two sets of measurements: a) a comparison between discharges with and without the use of vertical field control; b) a comparison between discharges with opposite orientation of the toroidal field.

This last experiment was done to examine the existence of any direct coupling with the external helical coils leading to effective stabilization.

RESULTS - An example of a typical current waveform and of the corresponding plasma displacement is shown in Fig. 1 for a case without (1a) and one with (1b) the vertical field control where B_v was ramped at the rate of 10 G/ms starting at 3 ms. Systematic prolongation of the current pulse is achieved, typically from 6-8 ms to 10-11 ms. An example of a discharge where the vertical field was initiated before current start is shown in Fig. 2. This mode of operation resulted in more reproducible discharges and on average gave even longer pulse lenghts of $\sim$12 ms. The addition of a second bank to maintain the current flat-top has already been used in the past [5]. In the recent measurements, after having done some B_v optimization, the second flat-top bank was applied and resulted in discharge lenghts $\gtrsim$ 14 ms (see Fig. 3). A summary of the results is presented in Fig. 4 in which the plasma displacement at the beginning of the current termination is plotted versus discharge duration. The results for the discharges without vertical field control are shown in Fig. 4a. In this case, the plasma is always displaced outward and terminated. Fig. 4b shows the results with vertical field control demonstrating the prolongation of the discharge compared to the case without B_v control. The large number of discharges with small displacement indicates that termination is caused by insufficient sustaining voltage while a smaller set of discharges is terminated because of excessive inward displacement. In the present OHTE set-up, just outside the shell at $r = 0.215$ m, there are 4 cm thick helical coils. In order to examine whether or not these coils can provide some plasma stabilization by acting

as a sort of discrete thick shell, the sign of the B_ϕ field was changed to reverse the relative pitch between magnetic field lines and external coils. The coil q is 0.2 and it is nowhere resonant in the plasma, which is characterized by q values < 0.1. Indeed, the change in sign did not apparently change the MHD stability properties of the discharge, and fluctuation spectra were very similar in both cases. It should also be noted that resistive MHD stability theory indicates that increasing the size of the vacuum interspace between the plasma and the conducting wall rapidly cancels the stabilizing effect of even a perfect wall [6]. It seems therefore unlikely that with an approximately 20% vacuum interspace from the plasma the discrete coils could produce a significant effect.

CONCLUSIONS - The pulse lenght in OHTE, operating with a thin conducting shell, has been prolonged by finer control of the plasma position. The plasma sensitivity to equilibrium control further proves the absence of any intrinsic limitation on the plasma performance due to the lack of a perfectly conducting shell. The addition of the external vertical field control has extended the discharge lenghts from ~ 8 ms to ~ 14 ms, with a simultaneous increase in discharge reproducibility. Although MHD linear theory predicts that RFP plasmas are unstable with a resistive shell boundary, no change in gross MHD modes is observed experimentally. However, a toroidally localized kink mode ("slinky" mode) due to non-linear couplings of several internal kink modes has been found [7]. The experimental indication that a relatively resistive shell ($\tau_{shell} \approx 1/10\, \tau_{pulse}$) can provide an adequate MHD stability boundary introduces the possibility of major simplifications and optimizations in the design and construction of the next generation of RFP experiments. In particular, field error constraints on gaps and portholes become much less important and active accurate plasma positioning becomes possible. The latter may prove to be a crucial issue in RFP research where the dissipation in the outer plasma regions can largely determine the loop voltage and therefore the energy confinement time.

This work was supported by the U.S. DOE under Grant No. DE-FG03-86ER53228.

REFERENCES

[1] Malesani, G. and Rostagni, G., Proc. 14th Soft, Avignon (1986).
[2] Los Alamos Internal Report, LA-UR842601 (1985).
[3] T. Tamano, private communication.
[4] K. Ogawa, private communication.
[5] R.R. Goforth, et al., Nuclear Fusion, 26, 4 (1986) 515.
[6] D. Merlin, S. Ortolani, R. Paccagnella, this conference.
[7] T. Tamano, et al., GA-A Report 18821 (1987).

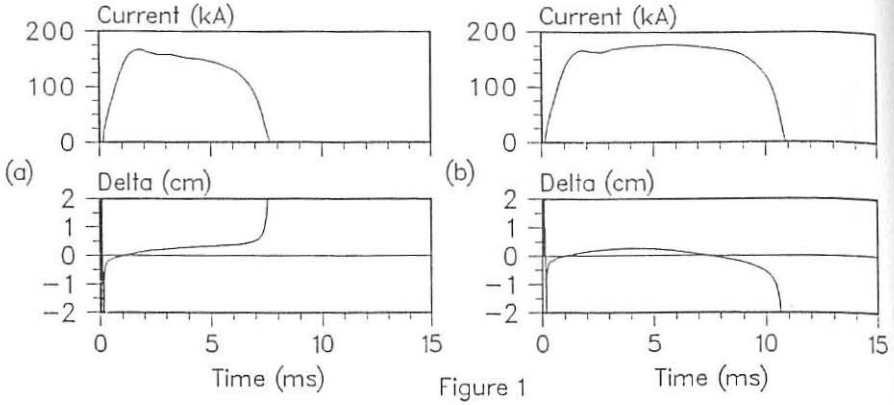

Figure 1

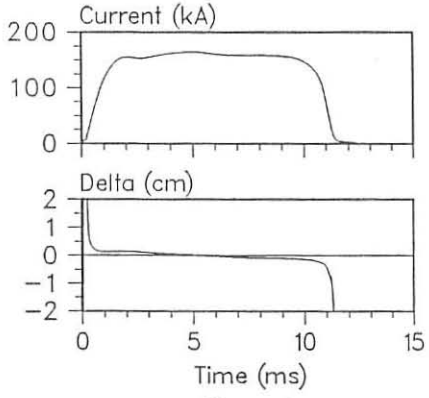

Figure 2

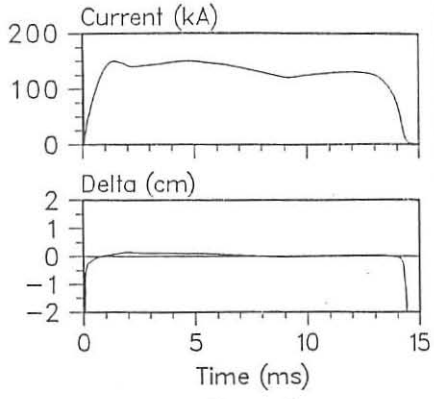

Figure 3

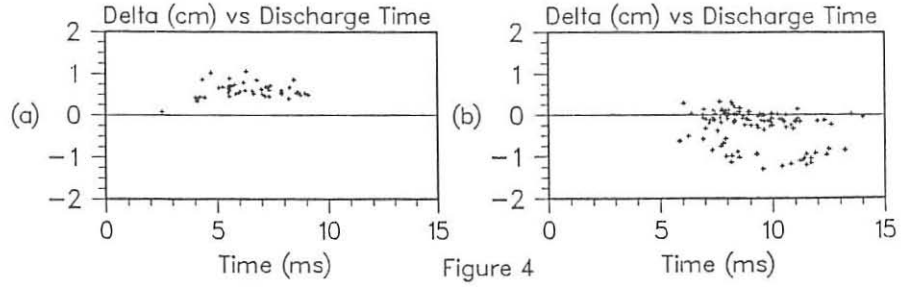

Figure 4

REVERSED FIELD PINCH EXPERIMENTS IN ZT-40M AND ZT-P

K. F. Schoenberg, J. C. Ingraham, R. Ellis*, P. G. Weber, J. N. Downing, C. P. Munson, G. A. Wurden, D. A. Baker, C. J. Buchenauer, L. C. Burkhardt, T. E. Cayton, R. E. Chrien, J. N. DiMarco, P. R. Forman, R. F. Gribble, R. B. Howell, G. Miller, R. W. Moses, Jr., R. A. Nebel, J. A. Phillips, M. M. Pickrell, W. A. Reass, A. E. Schofield, D. M. Weldon.

Los Alamos National Laboratory
Los Alamos, NM 87545, U.S.A.
*University of Maryland, College Park, MD

INTRODUCTION

Experimental research on the Los Alamos ZT-40M and ZT-P experiments is addressing issues vital to the design and operation of the next generation Reversed Field Pinch (RFP) devices.[1] These issues include: density and profile control by pellet injection and gas puffing,[2] the exploration of Oscillating Field Current Drive (OFCD) as a mechanism to provide steady-state RFP operation by low frequency field modulation,[3]the investigation of magnetic field programming, dynamic equilibrium control, no shell operation and field error effects in air core systems, and a study of edge plasma physics and limiter design for effective impurity control and wall protection. The following paper summarizes our most recent work on the ZT-40M edge plasma studies.

EDGE PLASMA AND LIMITER EXPERIMENTS

The design of effective wall protection hardware depends on a knowledge of the plasma conditions in the discharge edge; specifically the perpendicular scale length of the scrape-off plasma and the edge plasma density and temperature. Experiments performed on ZT-40M have addressed this question by examining the edge plasma poloidally downstream from a single local limiter with several diagnostics. Simultaneous measurements were made of the principal global plasma parameters, with a view to understanding the effects of edge plasma conditions on RFP confinement.

The limiter is a 11.4 cm by 9.1 cm graphite tile, that is inserted into the toroidal RFP plasma from above. The inner limiter surface, which faces the plasma, is flat, whereas the outer limiter surface conforms to the toroidal vacuum vessel curvature. A 1.3 cm recess in the vacuum vessel, at the position of the limiter, allows the limiter to be withdrawn such that its inner surface is flush with the vacuum vessel wall. The limiter tile is grounded to the vacuum vessel through an external cable and is instrumented with a current probe and a thermocouple.

An infrared camera observes the surface of the graphite tile that is exposed to the plasma. Peak surface temperatures of $300°C$ have been observed for insertions of 19 mm inside the geometrical shadow of the vacuum vessel using 120 kA, 15 ms discharges. For this insertion, the tile typically collects a peak electron current of 750 A during plasma formation, and 300 A during the 120 kA plasma current flat-top phase.

Localized measurements of the scrape-off plasma are made at the outer horizontal midplane in the same toroidal section as the limiter tile. The pitch angle of the edge magnetic field lines is kept nearly poloidal by imposing a shallow reversal (F=–0.08, where F is defined as the ratio of toroidal magnetic field at the plasma edge over the mean toroidal magnetic field). In this way, the field lines that are affected by the limiter are sampled by the downstream diagnostics. The poloidal distance between the graphite tile and the local probes is about 0.3 m.

A double Langmuir probe is used to measure the density and temperature of the bulk plasma in the edge. Results in this paper were obtained with 1 mm diameter, 1 mm long platinum probe tips, oriented such that the imaginary line joining the tips was perpendicular to the local magnetic field vector. The probe was driven with both a dc voltage bias and an ac voltage bias modulated at 2 kHz. Results for the two cases were comparable.

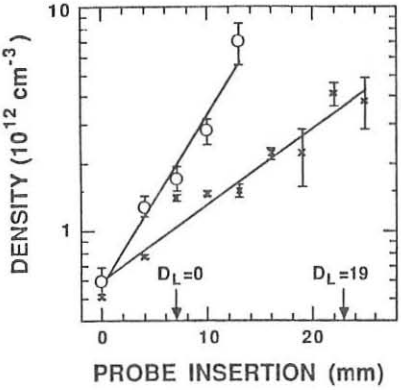

FIG. 1. Plasma density profile for (o) limiter withdrawn, $D_L = 0$, and (x) limiter inserted, $D_L = 19$ mm. Probe insertion is measured from the end of the diagnostic tubulation, 12.7 mm outside of the vacuum vessel bellows inner surface.

Figure 1 shows the electron density profile in the edge plasma, inferred from the probe's ion saturation current, for two cases. In case one, denoted by (o), the inner surface of the limiter tile was flush with the vacuum vessel wall ($D_L = 0$). In case two, denoted by (x), the limiter tile was inserted 19 mm into the plasma ($D_L = 19$ mm). The probe insertion is related to the magnetic mapping of the limiter position as indicated by the arrows on the graph. The error bars reflect the expected error of the mean of the data, with 4 to 15 data points for each location at $D_L = 0$, and 2 to 3 data points per location for $D_L = 19$ mm. It should also be

noted, that large plasma fluctuations are observed on the ion saturation current when the probe is within 5 to 10 mm of the magnetic mapping of the limiter edge. These fluctuations are presumably due to severe momentary increases of the plasma density from a lower bound or "pedestal" value. The density data plotted here reflect the "pedestal" values of j_{sat}, and would be increased by a factor of 2 to 3 if the mean value of these fluctuations were included. The largest densities plotted in Fig. 1 are comparable to the line averaged electron densities obtained from an interferometric measurement at the equivalent location of a 4 cm probe insertion.

In Figure 1, very distinct effects of the limiter are seen. Most clearly, the density behind the limiter is much smaller than that with the limiter withdrawn. That is, a scrape-off plasma is established with a characteristic perpendicular scale length of 1.3 cm. This compares to a characteristic scale length of 0.6 cm with the limiter withdrawn, where limiter action is attributed to other vacuum vessel hardware. Although the connection length for the limiter has not been firmly established, the scrape-off region at a position 0.3 m from the limiter is roughly equal to the limiter insertion distance. Thus, the connection length is probably much longer than 0.3 m. Further experiments are planned to elucidate this question.

Electron temperatures, which can be inferred reliably only when the probe is well-shadowed, are shown in Figure 2 for $D_L = 19$ mm. T_e ranges from 10 to 25 eV, increasing with the insertion distance. For an unshadowed probe, the edge electron temperature is between 10 eV and 40 eV, but data scatter masks the profile information.

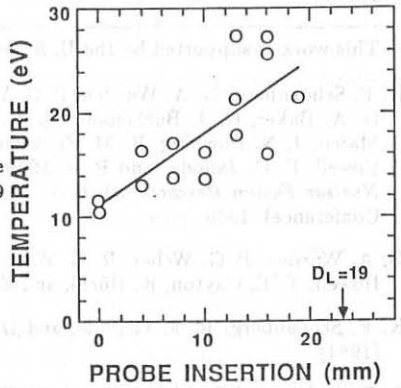

FIG. 2. Plasma electron temperature profile for limiter insertion of 19 mm.

Non-thermal electrons have been measured with a new collimating electrostatic energy analyzer designed to eliminate the effects of ions, space charge and secondary electrons. The analyzer is radially movable and can be rotated in

the plane perpendicular to the radius. Geometric constraints limit the range of accurate energy analysis to electrons whose perpendicular energy is less than 100 eV.

The major findings of the edge electron energy analysis may be summarized as follows: (1) A dilute suprathermal electron tail is detected with a temperature of 300 eV and a density of 1% of the cold, thermal density. (2) The energetic electrons primarily stream very nearly parallel to the edge magnetic field, and in a direction consistent with the model that they are accelerated in the interior of the discharge by the applied toroidal electric field. (3) The energetic electron density steadily increases in time from the beginning of the shot until saturation at 5 ms into the discharge. (4) The energetic electron density increases with distance from the wall, but at a slower rate than the cold density. (5) Insertion of the limiter tile considerably reduces the suprathermal electron density in the edge.

Global plasma parameters are not affected by tile insertions of up to 19 mm. The global parameters include the electron density, electron temperature by Thomson scattering on axis, ion temperature by Doppler broadening of impurity lines, impurity concentrations (carbon and metals), radiated power (bolometry), bulk plasma resistivity, toroidal loop voltage, and other electrical discharge parameters. This result is in contrast to that observed in HBTX-1B,[4] when that device was operated with a rail limiter structure inserted 5 cm into the plasma edge. Although our graphite tile is significantly smaller than the HBTX-1B structure, the documented the production of a scrape-off volume with significant dimensions relative to the normal ZT-40M edge volume should have caused an observable effect. We anticipate inserting the tile to greater depths, and using a larger limiter structure in an effort to further study this hypothesized phenomenon.

This work is supported by the U. S. Dept. of Energy.

[1]K. F. Schoenberg, G. A. Wurden, P. G. Weber, J. C. Ingraham, C. P. Munson, D. A. Baker, C. J. Buchenauer, L. C. Burkhardt, T. E. Cayton, J. N. DiMarco, J. N. Downing, R. M. Erickson, P. R. Forman, A. Haberstich, R. B. Howell, F. C. Jahoda, and R. S. Massey, in *Plasma Physics and Controlled Nuclear Fusion Research, 1986*, p. (IAEA, Vienna, 1987), Volume I (Kyoto Conference), 1986.

[2]G. A. Wurden, P. G. Weber, R. G. Watt, C. P. Munson, J. C. Ingraham, R. B. Howell, T. E. Cayton, K. Büchl, and E. J. Nilles, Nucl. Fusion **6**, (1987).

[3]K. F. Schoenberg, R. F. Gribble, and D. A. Baker, J. Appl. Phys. **56**, 2519 (1984).

[4]T. R. Jarboe and B. Alper, Physics of Fluids **30**, 1177 (1987).

FIELD-REVERSED CONFIGURATION FORMATION AND CONFINEMENT STUDIES ON THE LSM DEVICE *

R. E. Siemon, G. A. Barnes, R. E. Chrien, W. N. Hugrass,
Y. Ito†, D. J. Rej, M. Tuszewski and B. Wright
Los Alamos National Laboratory, University of California,
Los Alamos, New Mexico 87545, USA.

LSM is an upgrade of the FRX-C/T[1] device in which the diameter of the θ-pinch coil has been increased by 50% and two quasi-steady cusp coils have been added at each end. Parameters are given in Table 1 and diagnostics in Table 2. The FRC formation sequence in LSM is as follows. The quartz discharge tube is filled with deuterium gas and a reversed (with respect to the main field) bias magnetic field is applied. The neutral gas is then preionized by means of a low-power rf discharge followed by a ringing θ-pinch discharge. When the forward fast-rising main magnetic field is applied, a closed magnetic field configuration is formed. LSM can be operated in both tearing and non-tearing formation modes. For tearing formation, the closed field lines initially extend well beyond the θ-pinch coil. The plasma outside the coil is pushed axially out while the plasma under the coil is pushed further in. The evacuation of the region near the coil ends is accelerated by means of passive mirror sections (which are regions of reduced coil radius) until a change of topology (tearing/reconnection) occurs and an FRC is formed. Non-tearing formation[2] in LSM is implemented using two quasi-steady coils that form a cusp at each end during the bias phase. In this case a closed field line configuration which does not extend far beyond the coil ends is formed initially. Provided that the current in the cusp coils is sufficiently high, the plasma is pushed axially in under the coil and an FRC is formed without tearing.

Early experiments on LSM were carried out using a θ-pinch coil which had a passive mirror section at each end. It was therefore possible to compare tearing and non-tearing formation. Non-tearing formation was achieved when the cusp field exceeded a threshold value ($\simeq .1 - .2$ T) and led to earlier, stronger and more symmetric axial contraction and in some cases to enhanced flux trapping. Later, a straight θ-pinch coil was installed and only non-tearing formation was possible.

Experiments at high fill pressure ($\simeq 10 mTorr$) were carried out mainly with passive mirrors. They showed poor reproducibility with regard to confinement, and qualitatively appeared to represent poor FRC formation independent of the use of cusp coils. These results are not presently understood.

Experiments at low fill pressures ($2 - 4\ mTorr$) showed much improved reproducibility and confinement compared with high fill pressures ($5 - 10\ mTorr$). These experiments were carried out mainly using a straight θ-pinch coil and cusp fields (non-tearing formation). For the optimum pre-ionization and bias conditions at $4 mTorr$ fill pressure, FRCs with the following average parameters were formed : average density, $n \simeq 1.2 \times 10^{21}\ m^{-3}$, pressure balance temperature, $T_e + T_i \simeq 430\ eV$, closed magnetic flux, $\phi_p \simeq 4.1\ mWb$, number of local gyro-radii between the field null and the sep-

aratrix, $s \simeq 2$, ratio of the separatrix to the coil radii, $x_s \simeq 0.45$, flux confinement time, $\tau_\phi \simeq 160\,\mu s$, energy confinement time, $\tau_E \simeq 80\,\mu s$ and particle confinement time, $\tau_N \simeq 160\,\mu s$. Particle confinement time is consistent with the R^2/ρ_{io} scaling[3] observed in FRX-B and FRX-C, where R is the radius of the field null and ρ_{io} is the ion Larmor radius in the magnetic field outside the separatrix at the mid-plane.

Figure 1 shows the time evolution of the external magnetic field B_e, the separatrix radius r_s, the average density n, and the average temperature $T_i + T_e$ for a typical 4 $mTorr$ shot. Note that the high-frequency oscillations in the density and temperature traces at $t \simeq 0 - 10\,\mu s$ are due to radial oscillations caused by the radial implosion. These do not appear in the separatrix radius trace because the response of the instruments is not fast enough. The-low frequency oscillations which appear in the density and temperature traces for $t \geq 50\,\mu s$ do not reflect real variations in these quantities but are manifestations of the $n = 2$ rotational instability. No corresponding oscillations are observed in B_e and R_s because the separatrix apparently deforms without a significant change in the area of its cross section. The inferred value of the closed flux at $t = 30\,\mu s$ is $\phi_p = 4.2\,mWb$ and $s = 1.7$. The confinement times are: $\tau_\phi = 260\,\mu s$, $\tau_E = 73\,\mu s$ and $\tau_N = 130\,\mu s$.

It is desirable to form FRCs with the largest possible closed flux, ϕ_p and hence largest number of local gyro-radii between the field null and separatrix so that reactor relevant transport and stability regimes can be studied. So far, the pursuit of this objective has been difficult. The equilibrium closed flux in FRCs with good confinement properties could not be increased by simply increasing the reversed bias magnetic field. It was observed on LSM as well as on FRX-C[1,4] that, in agreement with theoretical predictions[5], the axial implosion wave became stronger as the effective bias field was increased. The minimum elongation (defined as the ratio of the separatrix diameter to the full-width half-maximum length as measured using the interferometer array) provided a sensitive quantitative measure of the strength of the axial implosion in any particular device. Good confinement was not observed on LSM whenever the minimum elongation was less than 1.6-2 and this effectively set the upper limit on the closed flux that could be achieved.

Upcoming experiments scheduled on LSM this year include a continuation of formation studies in order to better understand the observed fill density limit. Later, we will begin launching the LSM plasmas into, and trapping them inside of, the 0.4-diam FRX-C/T translation region. FRC translation will allow one to: (1) better diagnose any internal disturbances that may appear; (2) increase the s parameter; (3) determine more unambiguously the influence of plasma parameters on confinement.

The LSM device will be modified in 1988 to permit magnetic compression experiments. Heating by adiabatic magnetic compression allows one to address FRC physics at higher temperatures in a more collisionless regime and to assess the important transport issue of anomalous electron thermal conduction believed to be present in FRCs. In contrast to earlier liner-compression experiments,[2] these high-power heating

studies will utilize external flux compression. LSM plasmas will be translated out of the source and into an adjacent compressor (0.5-m-id, 4-m-long coil); subsequently, the plasma will be compressed by increasing the compressor guide field five-fold to 2 T in less than 50 μs. The compressed plasma will be finally translated into a 0.3-m-diam magnetized confinement region where it will then decay away. Adiabatic theory predicts significant power input (1 GW) at levels that exceed the plasma losses by almost an order of magnitude. 0-D modeling has been used to estimate the parameters that could be achieved by compression. For example, using optimal LSM source conditions at 4 mTorr and transport based on LHD diffusion we predict: $n \simeq 7 \times 10^{21}\, m^{-3}$, $T_i \simeq 1\, keV$, $r_s \simeq 0.10\, m$, $n\tau_E \simeq 10^{18}\, m^{-3} s^{-1}$. The engineering design of the magnetic compression experiment is presently underway. Construction will start this year with installation and initial operation scheduled for fall 1988.

* Work supported by the USDOE

† Permanent Address: Osaka University, Osaka, Japan.

REFERENCES

[1]R. E. Siemon *et al.*, Proc. 12th European Conf. (Budapest 1985), I, pp.590

[2]V. V. Belikov *et al.*, in Plasma Phys and Contr Nucl Fus Res 1982 (IAEA, Vienna, 1983), II,p.343

[3]K. F. McKenna *et al.*, Phys. Rev. Lett., 50, 1787 (1983).

[4]M. Tuszewski, Proc. 7th Symp. on CT Research (Santa Fe, 1985) Los Alamos Nat. Lab Report LA-10830-C (1986) pp.142

[5]L. C. Steinhauer, Phys. Fluids, 26, 2254 (1983)

Table 1. LSM PARAMETERS

θ-Pinch Coil Length (overall)	2.01 m
Coil Central Diameter (1.4 m long)	0.76 m
Passive Mirror Diameter (0.3 m each end)	0.66 m
Straight θ-Pinch Coil Diameter	0.70 m
Quartz Tube Inner Diameter	0.60 m
Main Field Swing (vacuum)	0.6 T
Main Field Rise Time ($\tau/4$)	6.7 μs
Main Field Decay Time (L/R)	500 μs
Bias Field (maximum)	0.13 T
θ-Preionization Field Amplitude	0.08 T
Cusp Field (maximum on axis)	0.40 T
Cusp Field Rise Time ($\tau/4$)	4.0 ms

Table 2. LSM DIAGNOSTICS

Diagnostic	Measured Quantity
Magnetic Loop and Probes	Magnetic Field
	Separatrix Shape
	Closed Flux (inferred)
Interferometers (side-on)	$\int ndl$
Framing Camera (end-on)	Symmetry

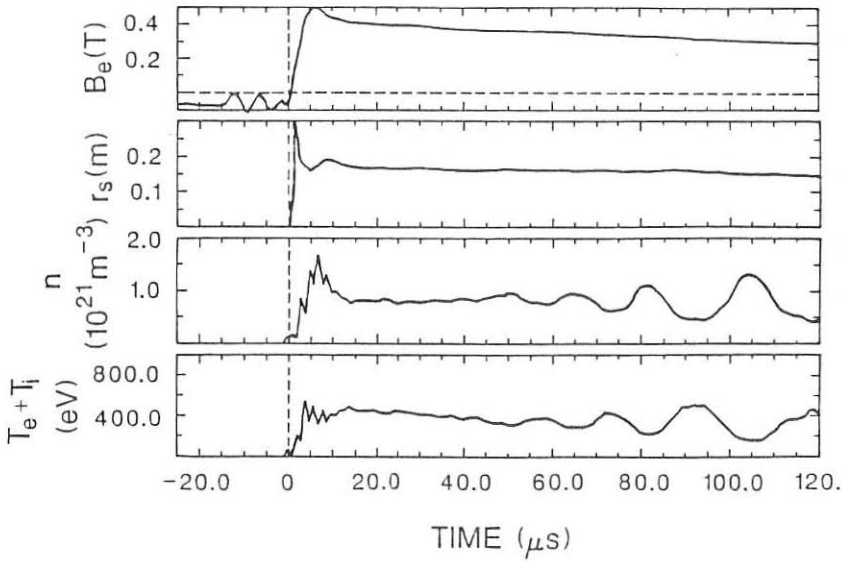

Figure 1. The time evolution of the external magnetic field B_e, the separatrix radius r_s, the average density n and the average temperature $T_i + T_i$ for a typical $4\,mTorr$ shot.

NONLINEAR MOTION AND BIFURCATED EQUILIBRIA OF THE EXTRAP Z-PINCH

C. Wahlberg

Uppsala University, Department of Technology, Box 534,
S- 75121 Uppsala, Sweden

1. INTRODUCTION. In the Extrap configuration, stable confinement of a pure z-pinch ($B_z = 0$) over many Alfvén periods has been demonstrated experimentally /1/ . Linear, ideal MHD theory predicts that equilibria centered at the symmetry axis of the configuration are unstable both in position and with respect to long kink modes /2/ , and no satisfactory explanation of the observed stability of the plasma has been given. In the present work , previous ideal MHD stability calculations are extended into the nonlinear regime , and an equation describing relatively slow plasma motions near the symmetry axis is derived. Various consequences , such as nonlinear stabilization for plasma motions in certain directions , existence of bifurcated equilibrium points , and the importance of including inertial effects in future Extrap theory , are discussed.

2. NONLINEAR EQUATION OF MOTION. We consider z-independent , incompressible and irrotational motions of a surface current z-pinch in an external poloidal magnetic field $\mathbf{B}_C = -\mathbf{e}_z \times \nabla \Psi_C(r,\varphi)$. Writing the plasma surface as $r_S = R_P + \eta(\varphi,t)$, such motions are described exactly by the equations /2/

$$\Delta\Phi = 0 \quad (r < r_S) \ , \ \Delta\Psi' = 0 \quad (r > r_S) \tag{1a,b}$$

and boundary conditions (BC 1-3)

$$1.\ \Phi_{rs} = \eta_t + \eta_\varphi \Phi_{\varphi s}/r_s^2 \qquad 2.\ \Psi_s = C_1(t) \tag{2a,b}$$

$$3.\ (\Psi_{\varphi s}/r_s)^2 + (\Phi_{\varphi s}/r_s)^2 + \Psi_{rs}^2 + \Phi_{rs}^2 + 2\Phi_{ts} = C_2(t) \tag{2c}$$

where Φ defines the velocity field in the plasma as $\mathbf{v} = \nabla\Phi$ and $\Psi = \Psi_C + \Psi'$ is the total flux function in the vacuum region. The quantities above are normalized according to $r \to r\,R_P$, $\eta \to \eta\ R_P$, $t \to t/\omega_A$, $\Phi \to \Phi\omega_A R_P^2$ and $\Psi \to \Psi\mu_0 I_P/2\pi$ where $\omega_A = I_P(\mu_0/\rho_m)^{1/2}/2\pi R_P^2$, ρ_m is the mass density and I_P the total pinch current.

As a first step towards a description of the nonlinear mean plasma motion (m = 1) we Fourier decompose the functions η , Φ and Ψ' as

$$\eta = \eta_0(t) + \sum_{m=1}^{\infty} \eta_m(t) \cos m\varphi' + \sum_{m=2}^{\infty} \tilde{\eta}_m(t) \sin m\varphi' \tag{3a}$$

$$\Phi = \sum_{m=1}^{\infty} r^m [\Phi_m(t) \cos m\varphi' + \tilde{\Phi}_m(t) \sin m\varphi'] \tag{3b}$$

$$\Psi' = -\ln r + \sum_{m=1}^{\infty} r^{-m} [\Psi_m(t) \cos m\varphi' + \tilde{\Psi}_m(t) \sin m\varphi'] \tag{3c}$$

respectively , where $\varphi' \equiv \varphi - \theta(t)$ and $\theta(t)$, the mean polar displacement of the plasma, is definied by the absence of the component $\tilde{\eta}_1$ in the Fourier decomposition (3a) of η.

Next we introduce an ordering scheme into the problem based on the two (assumed) small quantities η_1, the radial plasma displacement, and $\varepsilon \equiv (R_P/R_C)^4$, the plasma size parameter of the Extrap configuration /2/. We assume $\eta_1 = O(\varepsilon^{1/2})$ and choose the time scale as $\partial_t = O(\varepsilon)$. Then , writing $\eta_1(t) = \delta \cdot \eta(t)$, with $\eta = O(1)$, the m-values contributing to the m=1 equation of motion (BC 3) up to $O(\delta^7)$ are given by:

BC 1	BC 2,3
δ^3 : 1	δ : 1
δ^4 : 0 2	δ^2 : 0 2 4
δ^5 : 1	δ^3 : 1 3 5
	δ^4 : 0 2 4 6
	δ^5 : 1 3 5
	δ^6 : 0 2
	δ^7 : 1

The m=4 , $O(\delta^2)$ component in BC 2,3 is due to the external field $\Psi_C = \varepsilon\rho\, r^4 x \cos(4\varphi) + \ldots$ of the Extrap configuration /2/, ρ being the current ratio I_C/I_P.

Finally , inserting appropriate Ansatzes for η_m , $\tilde{\eta}_m$, Ψ_m , $\tilde{\Psi}_m$ and Φ_m , $\tilde{\Phi}_m$ into the boundary conditions (2), solving them order by order and Fourier component by Fourier component , we end up with the following cos φ' and sin φ' components of BC 3 , respectively: ($\delta \cdot \eta \rightarrow \eta$)

$$\left(1+\tfrac{3}{8}\eta^2\right)\left[\eta_{tt}-\eta\theta_t^2-8\varepsilon\rho\cos(4\theta)\eta^3\right] = 192\,\varepsilon^2\rho^2\eta + 936\,\varepsilon^2\rho^2\eta^3 \qquad (4a)$$

$$\left(1+\tfrac{1}{8}\eta^2\right)\left[\eta\theta_{tt}+2\eta_t\theta_t+8\varepsilon\rho\sin(4\theta)\eta^3\right] = 0 \qquad (4b)$$

The calculations leading to eqs. (4a,b) have been performed with the help of REDUCE. It is seen that the square brackets contain the equation of motion $md^2\mathbf{r}/dt^2 = I_P\mathbf{e}_z x(\nabla\Psi_C x\mathbf{e}_z)$ for an infinitely thin plasma (line-current) in the external Extrap field. Furthermore , the first term on the RHS of eq. (4a) yields the previously calculated linear instability of the surface current Extrap z-pinch /2/ , while the second term gives the corresponding nonlinear contribution , also seen to be destabilizing.

The relatively simple description of the nonlinear plasma motion obtained here is due to the slow time scale $\partial_t = O(\varepsilon)$ involved ("quasi-static approximation" , QSA) , which essentially ignores inertial effects of the $m\geq 2$ components.

3. CONSEQUENCES. Particularly illustrative cases of nonlinear motion occur for θ-independent motions along the symmetry lines $\theta = \theta_0 = n\cdot\pi/4$, $n=0,1, \ldots$ With $\theta_t=0$, eq. (4a) can for such motions be written $\eta_{tt} + V'(\eta)=0$, with the potential $V(\eta)$ given by

$$V(\eta) = -96\,\varepsilon^2\rho^2\eta^2 - \left[2\varepsilon\rho\cos(4\theta_0) + 216\,\varepsilon^2\rho^2\right]\eta^4 \qquad (5)$$

So , when $\rho\cos(4\theta_0) > 0$ all terms in the potential are destabilizing , and the weakly nonlinear evolution of the linear instability becomes of "explosive" type /3/. In the opposite case , $\rho\cos(4\theta_0) < 0$, the η^4 term is stabilizing provided $R_P < R_P^{max} = (108\,|\rho|)^{-1/4}R_C$. $R_P^{max} \approx 0.22\,R_C$ for the experimental value /1/ $\rho = -4$. The nonlinear stabilization above is associated with the existence of <u>bifurcated equilibrium points</u> /3/ $\eta_{eq}^2 = 24\,\varepsilon|\rho|/(1-108\,\varepsilon|\rho|)$ on the symmetry lines. These equilibria are easily seen to be radially stable but azimuthally unstable. Writing $\eta = \eta_{eq} + \eta'$, $\theta = \theta_0 + \theta'$ and linearizing eqs.(4a,b) around the equilibrium , we get

$$\omega_r^2 = 384\,\varepsilon^2\rho^2 + \ldots \quad , \quad \omega_\theta^2 = -\,786\,\varepsilon^2\rho^2 + \ldots \qquad (6a,b)$$

With $R_P = 0.2\,R_C$ and $\rho = -4$ one obtains $\eta_{eq} = 0.70$, $\omega_r = 0.13$, and $\omega_\theta = i0.18$.

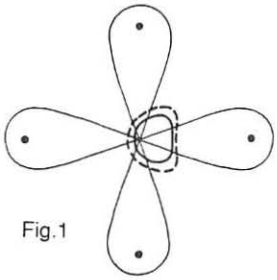

Fig.1

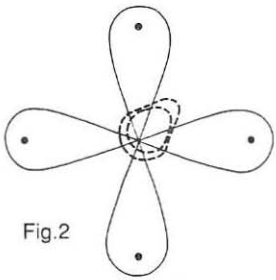

Fig.2

Fig.1 (solid curve) shows a bifurcated equilibrium corresponding to $\theta_0 = 0$, $R_P = 0.2\ R_C$ and $\rho = -4$. The larger plasma (dashed curve) in the same figure corresponds to the same values of θ_0 , ρ and plasma center but $R_P = 0.25 R_C$ (no equilibrium, plasma is moving outwards). Similarly , Fig.2 illustrates the plasma shape in the unstable motion out between the conductors in the case $\theta_0 = \pi/4$, $\rho = -4$, $R_P = 0.2\ R_P$ and $0.25\ R_C$, respectively. Obviously , the physical mechanism behind the destabilizing influence of the Extrap multipole field on the quasi-static z-pinch can be identified here: As the plasma moves away from the axis the external field pushes the plasma out from the regions where the **jxB** force is directed inwards ("private flux" regions of the multipole field for $\rho < 0$) and into the regions where the **jxB** force pulls the plasma outwards ("common flux" regions) , resulting in a net force on the plasma which is directed outwards.

Although the QSA is adequate for the description of the weakly nonlinear development of the linear instability , it is important to be aware of the limitations imposed by this approximation. Other choices of ∂_t are possible and probably necessary in the strongly nonlinear regime of the instability. Furthermore , the near-axis motion may as well require a different ordering of the time scale in order to give an adequate description of "equilibria" which are not completely at rest. For instance , precessional motion of the pinch around the symmetry axis at some angular frequency Ω would lead to substantial inertial effects on the $m \geq 2$ modes already for $16\Omega^2 \sim \omega_m^2$, where $\omega_m^2 = m(m-1)$ are the eigenfrequencies of the circular pinch /2/.

/1/. Drake, J.R. Plasma Phys. and Contr. Fusion **26** , 387 (1984)
/2/. Brynolf, J. , Ring, R. and Wahlberg, C. Plasma Phys. and Contr. Fusion **27** , 1255 (1985)
/3/. Pao, Y. Phys. Fluids **21** , 765 (1978)

A 2-D MODEL FOR TOROIDAL EXTRAP BREAKDOWN

Jin Li and Michael Tendler
Royal Institute of Technology, 100 44 Stockholm, SWEDEN

Abstract The breakdown process in a strongly inhomogeneous poloidal field and a weak toroidal field is modelled with a 2-D continuity equation. The breakdown mechanism, which seems plausible for Extrap, is discussed and a parametric study of breakdown voltage versus filling pressure is obtained using a computer code.

Extrap device is a toroidal pinch with an externally applied poloidal field (the octupole field), produced by four conductor rings as shown in Fig.1. In its original type there is no toroidal field, however a weak toroidal field is necessary for the startup. The octupole field is very strong and varies by several orders of magnitude along the minor radius, and has a 'magnetic well' structure, as shown in Fig.2. The simple breakdown analyses of the 0-D model [1] and 1-D model [2] do not seem suitable to the Extrap configuration because the poloidal field is essentially two dimensional.

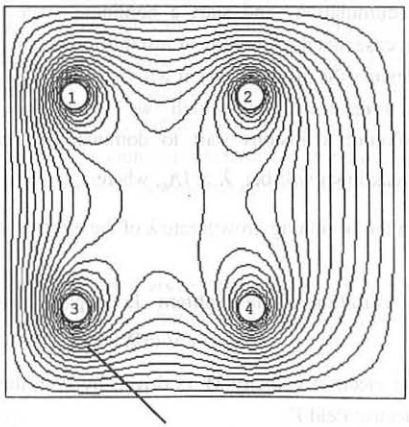

Fig.1 Flux contour of the poloidal field, produced by the four octupole rings.

Breakdown Mechanism Apparently the Townsend mechanism (secondary emmision) is not applicable to the toroidal Extrap discharge[3]. Also the streamer mechanism is not expected in the early stage of the discharge, because the filling density is usually fairly low for fusion plasmas so that space charge effects can be omitted at least in the very beginning of the discharge (Lorentz limit, for Extrap given by $n_e \ll 10^7 V_{loop} cm^{-3} volt^{-1}$). This implies that the problem can be decoupled from the Poisson equation. Like the tokamak discharge, the Extrap discharge is

also a diffusion controlled discharge due to its large gap length and small cross section. At the very beginning of a discharge there is a linear stage when the electron density obeys a linear equation. If loop voltage is higher than the spark voltage, the electron density will grow exponentially during the linear stage: $n(t) = n_0 e^{\lambda t}$; eventually the discharge will meet some kinds of ionization instabilities (ex. caused by distribution function deformation or space charge accumulation) and start a nonlinear stage. In case that these nonlinear instabilities do not destroy the discharge[4], it will finally lead to a breakdown, by which we mean that coloumb collisions start to dominate. Therefore the necessary condition for plasma breakdown will be: $\lambda > 1/t_c$, where t_c is some kind of characterastic time, it depends only on the beginning growth rate λ of the electron density

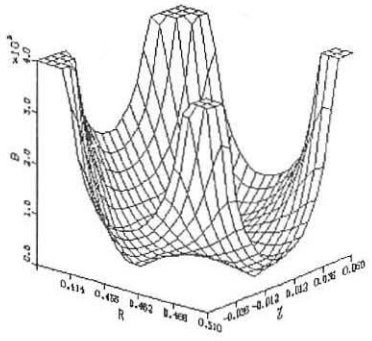

Fig.2 Octupole field strength distribution has a 'well' structure. Generally there are three poloidal magnetic field nulls.

Fomulation of the Problem In the particle balance equation for electron density n

$$\partial n/\partial t + \nabla\cdot(n\mathbf{W}) = \nu_{ioni}\, n \tag{1}$$

the electron velocity **W** is driven by both the density gradient and the externally applied electric field **E**

$$\mathbf{W} = -\mathbf{D}\cdot(\nabla n/n + e\mathbf{E}/kT_e) \tag{2}$$

where **D** is the diffusion coefficient tensor, given by the integral

$$\mathbf{D} = 4\pi \int_0^\infty \mathbf{M}^{-1} c^4 f_0(c)\, dc / 3 \tag{3}$$

$$\mathbf{M}^{-1} = \frac{1}{\nu(\nu^2+\omega^2)} \begin{pmatrix} \nu^2+\omega_R^2 & -\nu\omega_z+\omega_R\omega_\varphi & \nu\omega_\varphi+\omega_z\omega_R \\ \nu\omega_z+\omega_R\omega_\varphi & \nu^2+\omega_\varphi^2 & -\nu\omega_R+\omega_\varphi\omega_z \\ -\nu\omega_\varphi+\omega_z\omega_R & \nu\omega_R+\omega_\varphi\omega_z & \nu^2+\omega_z^2 \end{pmatrix} \tag{4}$$

where in matrix $\mathbf{M}^{-1}$, given in cylindrical coordinates R, ϕ, z, ω is gyrofrequency

$$\omega = eB/m \tag{5}$$

$f_0(c)$ is 0-th order velocity distribution function, which is taken as Maxwellian in our calculations. The ionization rate ν_{ioni} is given by

As can be seen in (3) and (6), the calculations of the coefficients ν_{ioni} and **D** rely on the

$$\nu_{ioni} = 4\pi N \int_0^\infty \sigma_{el}(c)\, f_0(c)\, c^3\, dc \tag{6}$$

distribution function, and then the knowledge of electron temperature T_e is needed. This can be obtained either from experimental data or by coupling the energy equation into the problem. The data obtained from general gas discharge experiments are not so suitable to our case. Because in the ordinary gas discharge experiments the main energy loss mechanism is heat conduction to cold gas, and T_e is determined by the local electric field. But Extrap discharge has very strong energy and particle interactions between the inner and outer regions, which means more convection losses. No doubt this will affect the energy balance, and then the temperature distribution, and consequently leads to different estimates for spark voltage. However, as a first step we still use the experimental data [5] to estimate T_e as a function of E/N, where N is the filling gas density.

Eigenvalue Problem With the approximations mentioned above, the problem is linear with respect to the electron density n, so the electron density should have exponential time dependence

$$n(R,z,t) = n_0(R,z)\, e^{\lambda t} \tag{7}$$

then (1) can be rewritten as an eigenvalue problem

$$L\, n = \lambda n \tag{8}$$

where L is a elliptic operator given by

$$L = D_{RR}\partial^2/\partial R^2 + (D_{Rz}+D_{zR})\partial^2/\partial R\partial z + D_{zz}\partial^2/\partial z^2 + F_4\partial/\partial R + F_5\partial/\partial z + F_6 \tag{9}$$

The electron density is natually set to zero at the boundary of the computing domain. However, the density profile is not so sensitive to the choice of the computing domain. Due to the 'well' structure of the poloidal magnetic field, the density distribution should be mostly concentrated inside the well region and this implies that the electron density profile is determined mainly by the drastically changing diffusion coefficients. But this dosen't mean that the electrons are well confined in the 'magnetic well'. The interaction of the inner and outer region is still very strong because electron velocity becomes very large at the strong

field region although density is very low there. Only the largest eigenvalue and corresponding eigenfunction are interesting for breakdown study.

Numerical method A difference technique is used to approximate the Eq.(9) by

$$L_{kl}\, n^l = \lambda n^k \qquad (k = 1, N*M) \qquad (10)$$

where the vector (n^k) is an approximation of the 2-D distribution of the electron density

$$n^k = n_{ij} = n\,(R_i, z_j) \qquad (11)$$

$$k = j*(M-1) + i \qquad (i = 1, M;\ j = 1, N) \qquad (12)$$

where M and N are the numbers of grids in R and z directions respectively. Instead of solving an eigen-problem of a differential operator L we need only to solve the eigen-problem of a matrix (L_{kl}). The iteration method dosen't seem to converge, which is probably the consequence of the drastic variation of the octupole field. So a direct method is used to solve (10). This method demands very large computer storage and quite a lot CPU time, especially for calculation of the eigenfunction, which then actually limits the values of M and N.

Parametric Study A model problem is studied in order to see how the breakdown voltage varies versus filling density, with rod currents I1=2.5kA, I1/I3 = 1.76, toroidal field B_t = 0.1Tesla

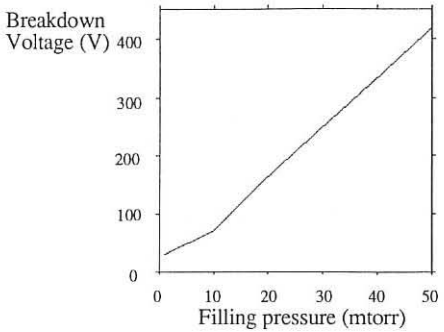

Fig. 3 Breakdown voltage versus filling pressure.

References

[1] Papoular, R., 1976, Nucl. Fusion **16** (1) 37

[2] Rose, D.J. and Clark, M. Jr, 1961, in *Plasmas and Controlled Fusion*, pp.72-75

[3] Drake J.R., 1984, Plasma Phys. and Contr. Fusion **26** (2) 387

[4] Tendler, M., 1987, Europhys. Lett. **3** (4) 467

[5] Huxley, L.G.H. and Crompton, R.W., 1974, in *The Diffusion and Drift of Electrons in Gases*, pp.615-616

FORMATION OF HIGH-BETA PLASMAS IN VARIOUS MODES OF OPERATION IN TPE-2

A.A.M. Oomens
Association Euratom-FOM, FOM-Instituut voor Plasmafysica, Rijnhuizen,
P.O. Box 1207, 3430 BE Nieuwegein, The Netherlands.

H. Hayase, I. Hirota, H. Kiyama, S. Kiyama, Y. Maejima, Y. Sato,
E. Yahagi, M. Kito
Electrotechnical Laboratory, Sakura-mura, Niihari-gun, Ibaraki, Japan

1. Introduction

The main objective of the ETL-TPE-2 device is to study the confinement and stability properties of high-beta plasmas. TPE-2 is a toroidal screw-pinch machine with an elliptic minor cross-section and a small aspect ratio (A = 3.0). In the usual mode of operation, the screw-pinch configuration is created by exposing a magnetized plasma column to fast-rising (T/4 ~ 3 μs) toroidal and poloidal magnetic fields, and maintained by actively crowbarring the fields when the peak values are reached. Some parameters of the machine, which has been described elsewhere [1], are listed in Table I, together with the operating range.

TABLE I

TPE-2 PARAMETERS

Major radius R_o	: 0.4 m
Minor dimensions	: 0.26 × 0.42 m
Discharge vessel	: alumina with Ti-coating
Toroidal field B_t	: 0.6 - 0.75 T (flat top: ~ 0.6 ms)
Plasma current I_p	: 40 - 175 kA (programmable)
Safety factor q_I	: 1.3 - 4.0
Filling pressure p_o	: 0.16 - 1.13 P_a (D_2)
Electron density $\bar{n}_e$	: $1\text{-}10\times10^{21}$ m^{-3}
Temperature $\bar{T}$	: 30-400 eV

The filling gas is magnetized by a slowly rising predischarge current in the presence of a positive bias field ($\leq$ 0.15 T). The circuits for the toroidal and poloidal field components are independent, so various modes of operation are possible. In the following sections, we will briefly discuss the relevant diagnostics and data analysis, summarize the results obtained in the usual mode of operation and finally present the initial results of the "matched screw-pinch" mode. In this mode, the bias field and predischarge current are combined with the power-crowbar circuits in such a way, that B_t and I_p increase almost simultaneously to their maximum values in about 0.5 ms at a nearly constant value of q_I at the wall. For both modes, the time evolution of a typical discharge is shown in Fig. 1.

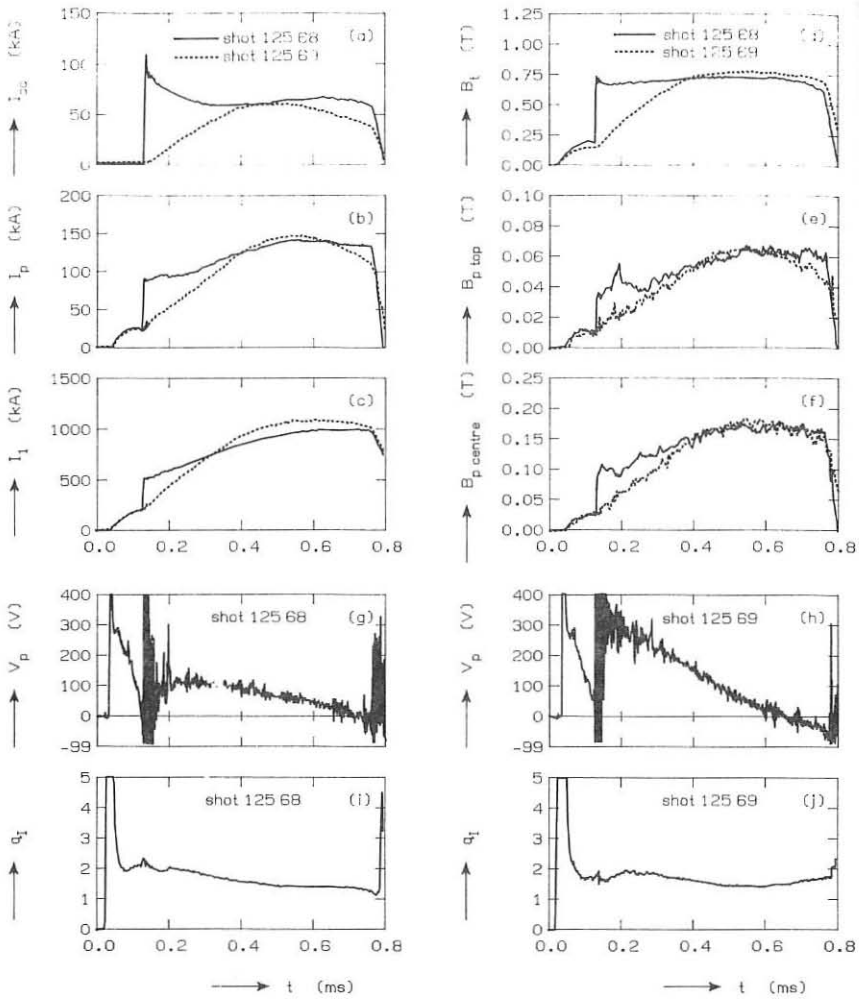

Fig. 1. A comparison of the time behaviour of a typical discharge with fast field programming (shot 12568, solid line) and in the "matched screw-pinch" mode (shot 12569, dashed line):
(a) the current in the compensating coils, resulting in a vertical field, (b) the plasma current, (c) the primary toroidal current, (d) the toroidal field, (e) the poloidal field at the wall in the top, (f) the poloidal field at the wall in the midplane at the outside, (g,h) the one-turn surface voltage, (i,j) the safety factor at the wall.

2. Diagnostics and data analysis

To diagnose the plasma in TPE-2, the following parameters are measured in each discharge: the primary currents, the plasma current I_p, the toroidal one-turn voltage V_p, the diamagnetic signal, the poloidal field B_p at the wall at 11 positions for one toroidal angle and at 5 positions for five other toroidal angles, the field in the feeding flange, the radial field at the wall at a single position, the emission in various lines: Ti-II, CII, CIII, CV and D_β (2×), the electron line density in a vertical plane by a HeNe- and a CO_2-interferometer, the output of an SXR-monitor, and of a bolometer. The observations for discharges with fast field programming are also based on measurements with the Thomson-scattering diagnostic, an optical sensor array, a magnetic probe movable along a horizontal chord and on measurements of $T_i(r)$ by Doppler broadening. An on-line data-analysis programme calculates, from the poloidal magnetic field data, the distribution of the flux surfaces and related quantities such as q_ψ, ℓ_i and the shift. The values of poloidal beta, β_p, and average total beta, $\bar{\beta}_t$, are obtained from the well-known Shafranov contour integrals, using the ℓ_i-value from the q-profile analysis [2]. These calculations agree within 20% with the outcome of the diamagnetic loop measurement. T_e is usually estimated from the plasma conductivity, and is in accordance with or slightly below the result of the Thomson scattering (if available).

3. Results with fast field programming

The results on confinement and stability of high-beta plasmas produced by fast field programming are reported in Refs [3] and [4]. The most relevant conclusions are summarized. The initial value of $\bar{\beta}_t$ is determined by the preheating conditions and the implosion heating. Under comparable conditions $\bar{\beta}_t$ is larger for higher p_o and independent of I_p. However, at later times ($t > 0.15$ ms) $\bar{\beta}_t$ is independent of p_o and increasing when the ohmic input exceeds the energy loss. The initial value of β_p can be very high (~ 2.5), or low ($\beta_p < 1$), but in the quasi-stationary phase β_p is always about 1. In this phase, also the q_ψ-profile is always of the same shape, it only changes during the transition of $q_I \sim 2$. The toroidal current density profile, calculated from the q_ψ-profile, is nearly flat over the cross-section. This profile is essential for the good stable confinement of high-beta plasmas. If the initial configuration deviates substantially, the transition is not successful.

4. Results in the "matched screw-pinch" mode

Since in the usual mode the early phase only seems important for the transition, we tried to operate in the "relaxed" state from the beginning and to rely solely on joule heating to get a high $\bar{\beta}_t$. In Fig. 1, the time behaviour of some plasma parameters is compared. As can be seen, V_p is much higher in the early phase, which is partly due to the formation of the magnetic configuration, but the variations in B_p are less and the q_I-trace is smoother. From the magnetic field data, it is concluded that after roughly 0.3 ms, the plasmas are similar. The average value of ℓ_i is ~ 1, due to the broad current profile and the elliptical cross-section, and $\bar{\beta}_t$ is high (≤ 0.1, $\beta_p \sim 1$). If q_I decreases in the preheating phase

from ∞ to 1.5-2 and if this matches the value in the power-crowbar phase, then the level of impurities is low and the average electron density reaches a plateau level of ~ 3×10^{20} m^{-3} (at p_0 = 0.5 Pa). If the transition is not smooth, large m=2-oscillations ($\tilde{B}_p/B_p \geq 10\%$) are observed on the B_p-coils and the line radiation from carbon is increased. In both modes, operation below the limit q_I ~ 1.3 is only possible with a very high energy dissipation and a sharply increasing amount of impurities. Of course this investigation is still very preliminary and a lot of questions are unanswered, of which the most important maybe are the shape of density, temperature and current- density profiles. However, from these initial attempts we conclude that the matched mode is not better than the fast formation mode, but it might have the major advantage that high-beta tokamak-like plasmas can be produced and stably confined in metal discharge vessels.

Acknowledgement

One of the authors (AO) is grateful to the Science and Technology Agency of the Japanese Government for their support and to the members of the Plasma Section of ETL for their hospitality. Part of this work was performed under the Euratom-FOM association agreement with financial support from ZWO and Euratom.

References

[1] Y. Sato et al., Proc. 11th Symp. on Fusion Technology, Oxford (1980) p. 615.
[2] S. Kiyama et al., Bull. Electrotechnical Laboratory **50** (1986) 95.
[3] S. Kiyama et al., Proc. 10th Int. Conf. on Plasma Phys. and Contr. Nucl. Fusion Res., London (1984) Vol. I, p. 393.
[4] K. Hayase et al., Proc. 11th Int. Conf. on Plasma Phys. and Contr. Nucl. Fusion Res., Kyoto (1986) paper D-IV-3.

CURRENT RAMP-UP WITH COLLISIONLESS ELECTRONS IN Z-PINCHES

J.A. Heikkinen, S.J. Karttunen and R.R.E. Salomaa*
Technical Research Centre of Finland, Nuclear Engineering Laboratory, SF-00181 Helsinki, Finland

*Helsinki University of Technology, Department of Technical Physics, SF-02150 Espoo, Finland

ABSTRACT: Starting the Z-pinch current with fast collisionless electrons to avoid the strong ohmic heating during the early stage of the pinch formation is investigated, The appropriate magnetohydrodynamic equations are solved numerically to illustrate this scheme.

1. INTRODUCTION: In an ideal case of a high density Z-pinch the cylindrical plasma column should be compressed from the initial radius of the order of 100 μm [1] to its final value before MHD-instabilities set on. This requires extremely fast current rise of $10^{14}\,As^{-1}$ during the first few nanoseconds to keep the magnetic pressure above the kinetic pressure. Presently achieved current rise rates, determined by the voltage and pinch inductance, are still too slow ($<10^{13}\,As^{-1}$) to prevent expansion of the pinch due to rapid ohmic heating in the early phases of the discharge [1, 2].

We have recently suggested [3] to use a beam of fast electrons (0.1 - 1 MeV) injected axially into the plasma channel so that the corresponding current enhances the main pinch current induced by the external voltage V_{ext}. Due to the low collisionality of the high energy electrons a weak ohmic heating results if the fast electron current dominates over the ohmic current. As is appearant from the circuit equations for the total current I and voltage V, $I = V/R+I_f$ and $V = -L\dot{I}+V_{ext}$, correspondingly (R is the plasma resistance and L the total inductance of the circuit), there is no ohmic current if the fast electron current I_f has the time dependence $V_{ext}t/L$, i.e., it rises at the rate of V_{ext}/L. In this case the inductive voltage $-V_{ext}$ due to $\dot{I}_f$ exactly cancels the external voltage. The current is exclusively driven by the fast, nearly collisionless electrons.

The purpose of this paper is to study the electrodynamics of this scheme in more detail. To calculate the radial profiles and the time dependence of the plasma parameters and the electromagnetic fields the corresponding magnetohydrodynamic equations are solved numerically.

2. NUMERICAL MODEL: We assume the plasma channel to have been initiated for example by a laser beam and to be fully ionised and surrounded by a nonconducting cold gas. Magneto-hydrodynamic approach is taken and the equations describing the plasma density n, radial plasma velocity v, electron temperature T, axial electric field E, atsimuthal magnetic field B and axial current densities j and j_f, read in cylindrical geometry as

$$Dn = -(n/r)\,\partial_r(rv) \tag{1}$$

$$MnDv = -2\partial_r(nT) - B(j+j_f) \tag{2}$$

$$3/2DT = -(T/r)\partial_r(rv) + (1/rn)\partial_r(k_e r\partial_r T) + \eta j^2/n \tag{3}$$

$$\partial_r E = \partial_t B \tag{4}$$

$$(1/r)\partial_r(rB) = \mu_0(j+j_f)\ , \tag{5}$$

where D denotes the convective derivative $\partial_t + v\partial_r$, r is the radial coordinate, M the ion mass, j and j_f are the current densities for the ohmic and fast electron current, respectively. Electron and ion temperatures have been taken to be equal, and cylindrical symmetry is assumed. $k_e = 1.38\times10^{22}T^{5/2}s^{-1}m^{-1}$ and $\eta = 8.4\times10^{-4}T^{-3/2}Vm/A$ are the heat conductivity and the plasma resistivity, correspondingly. The Spitzer resistivity has been chosen although this is propably not well justified at such low temperatures as 1eV due to the low number of plasma particles in the corresponding Debye sphere. In addition to Eqs. (1) - (5) we have Ohms law for the ohmic current

$$E + vB = \eta j. \tag{6}$$

We solve Eqs. (1) - (6) with appropriate initial and boundary conditions and assume the externally injected fast electron beam to have a constant radius larger than the plasma radius and a constant current rise rate. Axial effects are omitted in the beam propagation. The beam and the external electric field are set on instantaneously at t = 0. The influence of various profiles for plasma parameters has been studied.

3. RESULTS: Fig. 1a presents the temporal evolution of plasma radius and temperature (its radial maximum) for the case where the inductive electric field $-(1/2)\ln(r_b/r_f)r_f^2\mu_0\partial_t j_f$ due to the fast electron current density cancels the external electric field E_{ext} = 11.6 MV/m at $r = r_f$ (here r_b is the radius of the wall where E = 0

holds). As initial conditions we have assumed radially homogeneous plasma parameters ($n = 3\times10^{26}m^{-3}$, $T = 2eV$). The corresponding curves are given also for the case of no fast electron beam with the same E_{ext}. There is a strong contrast in ohmic heating of the plasma between these cases. The temperature increases up to 80 eV and the radius of the plasma channel doubles in the absence of the fast beam. When $j_f \neq 0$, the temperature even slightly decreases (due to the expansion, which is now only 30 % in radius). The radial profile of the electric field during the calculation for the case of fast electrons shows a good agreement with a simple analytical estimate

$$E \sim E_{ext}+(\mu_0/4)(r^2-r_f^2)\partial_t j_f-(1/2)\ln(r_b/r_f)r_f^2\mu_0\partial_t j_f, \quad (7)$$

which is readily obtained from Eqs. (4) - (6) in the limit of large resistivity and $vB \sim 0$ at the steady-state. In Figs. 1b to 1d the radial profiles of the electric field, magnetic pressure, plasma pressure and velocity are plotted at the onset of implosion in the presence of fast electrons. With the given parameters E is less than 10 % of E_{ext} according to Eq. (7) and, hence, the ohmic current is respectively greatly reduced. It is interesting to note that an exact cancellation of the external field is never possible according to Eq. (7). There always remains a non-zero ohmic current density, the magnitude of which depends on the relative values of E_{ext} and $\partial_t j_f$. With the given beam radius 150 μm and E_{ext} = 11.6 MV/m the corresponding hot electron current rise rate is 10 kA/ns, the magnitude of the hot current being about 30 kA at the beginning of implosion while the ohmic current amounts to only about 100 A.

In the case of parabolic density profile one obtained a strong ohmic heating and a skin current formation at the low density edge of the plasma when no fast electrons are applied. With fast electrons this is eliminated and a low temperature plasma with small ohmic currents is obtained.

4. SUMMARY By a correctly timed fast electron beam with an appropriate current rise rate it is possible, according to the magnetohydrodynamic model, to strongly suppress the ohmic heating at the early current formation phase of a Z-pinch. The benefit of the method discussed would be a more efficient and stable compression.

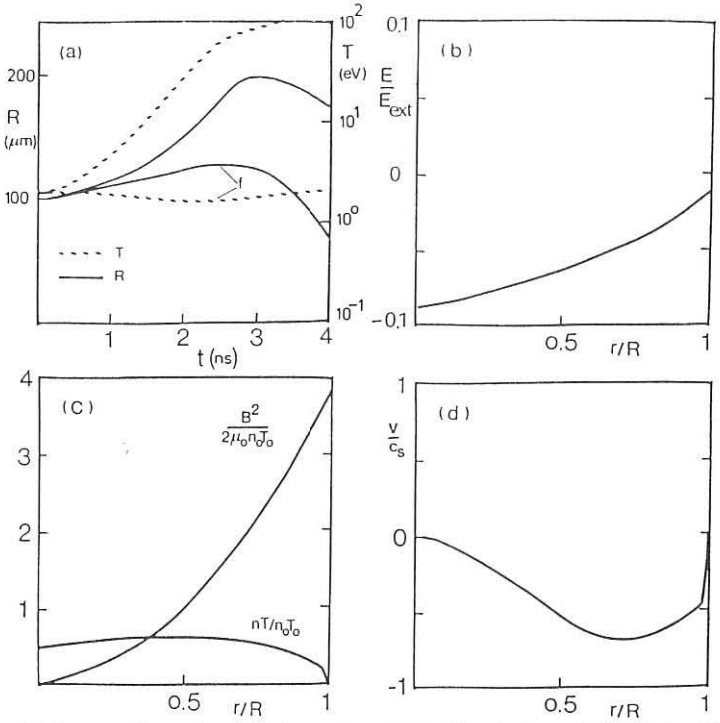

Fig. 1. (a) Plasma radius and maximum temperature during the start-up of the pinch with a fast electron beam (denoted by f) and without. Radial profiles of the electric field (b), plasma and magnetic pressure (c), and radial plasma velocity (d) calculated at the onset of implosion at t= 2.6ns for the case of fast electrons. The parameters were: E_{ext}= 11.6MV/m, n_o= $3\cdot10^{26}m^{-3}$, T_o= 2eV, r_o= 100μm, r_f= 150μm, r_b= 5cm, I_f= 10kA/ns. Homogeneous initial profiles with abrupt boundaries were assumed. $c_s=(T_o/M)^{1/2}$.

REFERENCES:

[1] Haines, M.G., Phys. Scripta T2/2, 380(1982).

[2] Hammel, J.E., Scudder, D.W., Shlachter, J.S., Nucl. Instr. and Methods 207, 161(1983).

[3] J.A. Heikkinen, S.J. Karttunen and R.R.E. Salomaa, "Feasibility Studies of Fast Electron Driven Dense Z-pinch Fusion Reactor", in 4th Int. Conf. on Emerging Nuclear Energy Systems, 1986, Madrid (Editors, G. Velarde and E. Minguez). World Scientific, 426(1987).

THE DISSIPATIVE DRIFT INSTABILITY IN A HOT ELECTRON PLASMA

Huang Chaosong, Ren Zhaoxing, Qiu Lijian
Institute of Plasma Physics, Academia Sinica
P. O. Box 26, Hefei, China

1. INTRODUCTION

In a magnetically confined plasma, the presence of density gradient is inevitable[1]. The drift wave causes anomalous transport. The core plasma in a hot electron plasma can drive drift wave. The hot electron ring has profound effects on the fluctuation and transport of the core plasma[2-4].

The MHD equations are used to derive the dispersion relation of drift wave. Electron-ion collisions (resistivity) and ion-ion collisions (viscosity) are considered. Exciting region, fluctuation level and radial loss of the drift wave are measured experimentally.

2. DISPERSION RELATION AND ANALYSIS

We make the rigid ring approximation and use a slab model. Equilibrium magnetic field is $\vec{B}=B_0(1+\varepsilon x)\vec{e}_z$. The gradients of magnetic field and plasma density are in the x direction. The curvature of field line is simulated by a gravitational field $\vec{g}=g\vec{e}_x$, and $g=-2T/MR_c$. Only electrostatic perturbations are discussed. The wave form of $\exp(iky+ik_{\parallel}z-i\omega t)$ is taken.

Using the linearized MHD equation, we find the dispersion relation of the drift wave driven by the density gradient of the core plasma[5]:

$$\omega^2+(i\frac{k_{\parallel}^2\Omega_e\Omega_i}{k^2\nu_{ei}}-\omega_{*i})\omega+\frac{2(\omega_{*i}-\omega_{di})\omega_{di}}{k^2a_i^2}+i(\omega_{*i}-\omega_{di})\frac{k_{\parallel}^2\Omega_e\Omega_i}{k^2\nu_{ei}}=0 \qquad (1)$$

where,

$$a_i=\frac{V_i}{\Omega_i},\quad \omega_{*i}=\frac{kT_i}{M_i\Omega_i}\left(\frac{2}{R_c}+\frac{1}{r_p}\right),\quad \omega_{di}=\frac{kT_i}{M_i\Omega_i}\left[\frac{2}{R_c}-\frac{1}{2}\beta\left(\frac{2}{R_c}+\frac{1}{r_p}\right)\right],$$

ν_{ei} is the electron-ion collision frequency, R_c is the curvature of field lines, $r_p^{-1}=d(\ln N_0)/dx$, $\beta=\beta_i+\beta_h\cong\beta_h$, beta value of the hot elections. For simplicity, $T_i=T_e$ is assumed, and the stabilizing viscosity is neglected.

Set $\omega=\omega_r+i\omega_i$, and suppose $\omega_i<<k_{//}^2\Omega_e\Omega_i/k^2\nu_{ei}$. The solution of Eq. (1) is

$$\omega_r = -\omega_{*i} , \tag{2}$$

$$\omega_i = \left[\omega_{*i}^2 + \frac{(\omega_{*i}-\omega_{di})\omega_{di}}{k^2 a_i^2} \right] \frac{2k^2\nu_{ei}}{k_{//}^2\Omega_e\Omega_i} . \tag{3}$$

The special growth rate is defined as

$$\gamma = \frac{\omega_i(\beta_h)}{\omega_i(\beta_h=0)} . \tag{4}$$

The β_h dependence of the growth rate is calculated with $r_p/R_c=0.1$ at different ka_i, as shown in Fig.1. The marginal stability is $\beta_h=0.33$ if $ka_i<0.1$, corresponding to $\omega_{di}\simeq 0$. The stability requires $\omega_{di}>0$, that is

$$\beta > \frac{4\xi}{1+2\xi} , \quad \left(\xi = \frac{r_p}{R_c}\right) . \tag{5}$$

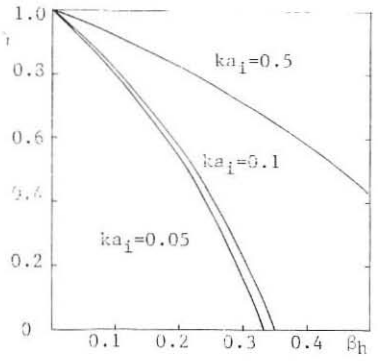

Fig.1 Growth rate as a function of β_h

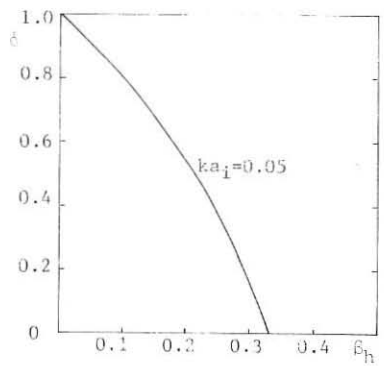

Fig.2 Transport flux as a function of β_h

The density and potential fluctuations cause the anomalous transport of plasma in the x direction. The transport flux of the cold electrons is

$$\Gamma_e = \frac{ekN_0/2T_iB}{\omega_{*i}^2 + (k_{//}^2T_i/M_e\nu_{ei})^2} \left[-\omega_{di}\frac{k_{//}^2T_i}{M_e\nu_{ei}} - (\omega_{*i}-\omega_{di})\omega_i \right]\phi^2 . \tag{6}$$

We have known in the calculation on growth rate that the stability require $\omega_i<0$, $\omega_{di}>0$. $\Gamma_e<0$ for the stable mode is assured under the same condition. The transport of ions is caused by ambipolarity diffusion.

The effect of beta of the hot electrons on the anomalous transport is shown in Fig. 2. δ is the special flux defined as

$$\delta = \frac{\Gamma_e(\beta_h)}{\Gamma_e(\beta_h = 0)} \quad . \tag{7}$$

The hot electron ring reduces the anomalous transport of core plasma.

3. EXPERIMENTAL RESULTS

The experiments were carried out in a simple mirror to investigate the drift instability. The hot electron plasma is produced by microwave source with power 15KW at 20.4 GHz. The data were analyzed by computer. There is a coherent fluctuation at 35KHz in the core plasma. In Figs. 3 and 4, $\Delta I/I_0$ is the normalized levels of the 35KHz fluctuation measured in r=4cm where the fluctuation grows most rapidly. W_h is the stored energy of the hot electrons. N_i is the ion density near the cavity wall. $N_e l$ is the line density of the cold plasma on the axis of mirror.

The data in Fig.3 were obtained at a neutral pressure of 1.6E-5 torr, and B_0 is the strength of magnetic field at the center of mirror. As the stored energy of the hot electrons increases, the plasma fluctuation level is reduced, and density of the core plasma inside the ring is higher. The fluctuation propagates in the direction of electron diamagnetic drift.

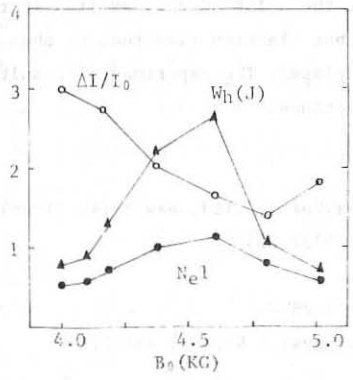

Fig. 3 B_0 dependences of W_h, $N_e l$, $\Delta I/I_0$

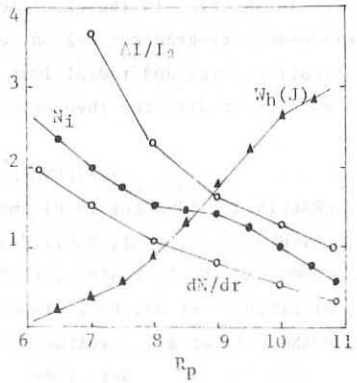

Fig.4 Influences of the probe on W_h, N_i, dN/dr, $\Delta I/I_0$

In Fig. 4, Rp is radial position of a movable probe. dN/dr is density gradient of the core plasma at r=4cm. When the probe is inserted into the plasma to destroy the hot electron ring, the radial loss of plasma increases, and the local density gradient enlarges. The enhanced fluctuation results in the decrease of plasma density in the middle and the increase of the particle flux escaping to the cavity wall.

The experimental results indicate that the plasma fluctuation at 35KHz has three distinct characteristics. (1) The fluctuation is driven by the density gradient, and propagates in the direction of electron diamagnetic drift. (2) The high fluctuation levels are closely related to the enhanced radial losses. (3) The hot electron ring reduces the density gradient, fluctuation level, and radial loss of the plasma. According to the theoretical analysis, the fluctuation is the drift wave of plasma.

4. CONCLUSIONS

The low frequency dissipative drift wave in the hot electron plasma is studied theoretically and experimentally. The conclusions are as follows.

The hot electron ring can reduce the growth rate, and suppress the anomalous transport of plasma. The resistivity and the viscosity have destabilizing and stabilizing effect on the drift wave, respectively.

It is observed in the experiment that the drift wave is excited in the maximum-density-gradient region, and the hot electron ring reduces the fluctuation level and radial loss of the plasma. The experimental results are consistent with the theoretical predictions.

REFERENCES

[1] KRALL,N.A., Advances in Plasma Physics,Vol.1,P.153, New York, (1968).

[2] BATCHLOR,D.B. et al, Nucl. Fusion 19(1979) 235.

[3] KOMORI,A., Nucl. Fusion 24(1984) 1173.

[4] HILLIS,D.L. et al, Phy. Fluids 28(1985) 2848.

[5] HUANG,C.S. et al, Institute of Plasma Physics Report, ASIPP/25, Oct. 1986.

PARABOLOMAK: A SPHEROMAK TYPE MHD EQUILIBRIUM CONFIGURATION

G. N. Throumoulopoulos and G. Pantis

Department of Physics, University of Ioannina, Ioannina, Greece

A b s t r a c t

Under the boundary conditions of a perfectly conducting wall an exact class of spheromak type MHD equilibria is obtained for finite pressure pofiles. Analytic force-free equilibria which satisfy approximately the plasma-vacuum interfact boundary conditions are also determined. Simple force-free configurations are identified which ensure plasma confinement within two intersecting paraboloids(parabolamak).

The spheromak, a compact toroid with poloidal and toroidal component of the magnetic field has been increasingly considered as a fusion plasma container in the last few years. The main attractive feature of spheromak is the fact that internal poloidal plasma currents generate entirely the toroidal field component, thus resulting in the lack of the toroidal field coils linking the toroid. The physics of spheromak has been reviewed by several authors (see f. e., Goldenbaum [1] and Jardin [2]. Spheromak equilibrium and stability in general, depends on plasma shape [4], [7]. For this reason analytic equilibria have been studied in various coordinate systems [3]- [7].

Presently we have obtained an analytic class of finite pressure spheromak type equilibria in parabolic coordinates. In particular, force-free equilibria are defined in such a way that the plasma is confined in the interior of two intersecting paraboloids (parabolomak).

The Grad-Shafranov equation in the cylindrical coordinates (z,r,φ) takes the familiar form

$$r\frac{\partial}{\partial r}\left(\frac{1}{r}\frac{\partial\psi}{\partial r}\right)+\frac{\partial^2\psi}{\partial z^2}=-\left[r^2\frac{dP}{d\psi}+I(\psi)\frac{dI(\psi)}{d\psi}\right] \qquad (1)$$

Equation (1) determines the flux function ψ and thus the magnetic field if the kinetic pressure P and the poloidal current I are known functions of ψ. In parabolic coordiantes with appropriate boundary conditions ([5] [6]) the general solution for ψ in the non negative z half plane reads

$$\psi=-\frac{a}{b^2}\eta^2\xi^2+d\,F_0\left(j,\frac{\eta^2\sqrt{b}}{2}\right)F_0\left(-j,\frac{\xi^2\sqrt{b}}{2}\right) \qquad \eta\geq\xi \qquad (2)$$

where F_0 is the regular Coulomb wave function of zero order, λ is the separation constant, $j=\lambda/4\sqrt{b}$ and d is an arbitrary constant. The solution in the non positive z half plane ($\xi \geq \eta$) which is symmetric about the r-axis, is then immediately determined by permuting ξ and η in eq. (2). Eq. (2) for a = 0 determines force-free configurations. They can be easily recognized because the separatrix is a closed surface of revolution of two intersect-

ing parabolas $\xi = c$ and $\eta = c$, ($c \neq$ constant), where this constant is equal to the first zero of $F_0(j, x^2\sqrt{b/2})$ (parabolomak). If the separation constant is set equal to zero eq. (2) takes the simpler form

$$\psi = -\frac{a}{b^2}\,\xi^2\eta^2 + \psi_0 \sin\left(\frac{\xi^2\sqrt{b}}{2}\right)\sin\left(\frac{\eta^2\sqrt{b}}{2}\right) \qquad (3)$$

where ψ_0 is the value of the force-free flux function on the magnetic axis. The force-free configuration of the last equation is plotted in figure.

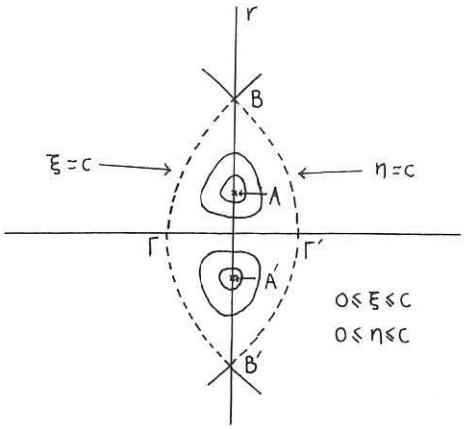

Parabolomak. A force-free compact toroid which confines the plasma in the interior of two interesting poraboloids $\eta = \xi = \sqrt{2\pi/\sqrt{b}} \equiv c$. The points A, A', lying on the axis r at a distance $r_m = \pi/\sqrt{b}$ from the axis z, indicate the magnetic axis.

The parabolomak is apparantly oblate and the plasma elongation is equal to

$$e = \frac{\ell_z}{\ell_r} = \frac{1/2\, c^2}{c^2} = \frac{1}{2} \qquad (4)$$

where $\ell_z(r_z)$ is the configuration cut on the z (r) axis. This result is also valid for any force-free equilibrium of eq. (2) and it does not depent on λ and b.

Let us assume now that an indefinitely extended vacuum magnetic field region match the plasma surface. Although it is not the way external coil positions are determined it gives a first step approximation of the external magnetic field topology. Then the Grand-Shafranov equation can also be solved analytically in the vacuum region. In fact the plasma pressure vanishes there and no toroidal component of the external magnetic field exists. The vacuum solution of eq. (1) is

$$\psi = \xi\eta\, Z_1(a\xi)\bar{Z}_1(a\eta) \qquad (5)$$

where $Z_1(\bar{Z}_1)$ is a Bessel (Modified Bessel) function. It is seen that the solution fullfils the boundary condition for the flux-function. However, the additional boundary condition of the pressure balance on the plasma-vacuum interface can only be fullfiled approximately. As an example we give below a simple vacuum solution for the parabolomak of eq. (3).

$$\psi_{out} = \frac{\psi_0 b}{4} (\xi^2 - c^2)(\eta^2 - c^2) \qquad (5)$$

Although ψ_{out} is an unbounded function, it is physically acceptable as the vacuum magnetic field

$$B_{\xi,out} = -\frac{b\psi_0}{2\sqrt{\xi^2+\eta^2}} \frac{1}{\xi} (\xi^2 - c^2) \qquad (6)$$

$$B_{\eta,out} = \frac{b\psi_0}{2\sqrt{\xi^2+\eta^2}} \frac{1}{\eta} (\eta^2 - c^2) \qquad (7)$$

is finite throughout the vacuum region. By expanding the sinusoidal term in eq. (3) around the point $\xi = c$ ($\eta = c$) one can see that on the plasma surface the pressure of the internal magnetic field balances approximately the pressure of the external magnetic field given by eq. (6) ((7)). The approximation is better as one moves on the separatrix from the points Γ and Γ' to the points B and B' . (see figure). Alternatively an inverse approximation which gives better values around the points Γ and Γ' can be obtained by using in the vacuum region the function

$$\psi_{out} = \begin{cases} (\psi_0 b/4)\,\xi^2 (\eta^2 - c^2) & 0 \leq \xi < \infty \qquad \eta \geq c \qquad (8) \\ (\psi_0 b/4)\,\eta^2 (\xi^2 - c^2) & 0 \leq \eta < \infty \qquad \xi \geq c \qquad (9) \end{cases}$$

which is also a solution of the homogeneous part of eq. (1).

We finally note that the parabolomak of eq. (3) defines a minimum magnetic energy state (Taylor State) in which according to Taylor's theory the plasma relaxes retaining the global magnetic helicity invariant [8]. Therefore, it is stable against all the ideal magnetohydrodynamic perturbations [9], and because of its oblate shape it is also expected to remain stable under the tilting mode [7]. Although spheromak plasma relaxation to a Taylor state has been verified experimentally [10], results of other investigators [11] show that relaxation may occure to states which are significantly different from the Taylor states. In this respect it appears that an extension of Taylor's theory inclunding finite pressure gradients as well as geometries with no conducting walls would be essential.

References

[1]. G. C. Goldenbaum, Physica Scripta T2/2 (1982) 359.

[2]. S. J. Jardin, Europhysics News 17 (1986) 73.

[3]. H. L. Berk, J. H. Hammer and H. Weitzner, Phys. Fluids 24 (1981) 1758.

[4]. S. Kaneko, A. Kamitani and A. Takimoto, J. Phys. Soc. Jpn. 54

(1985) 3347.

[5]. G. N. Throumoulopoulos and G. Pantis, Nuclear Fusion 26 (1986) 1501.

[6]. G. N. Throumoulopoulos and G. Pantis, to appear in Phys. Lett. A.

[7] M. N. Rosenbluth and M. N. Bussac Nuclear Fusion 19 (1979) 489.

[8]. J. B. Taylor, Phys. Rev. Lett. 33 (1974) 1139.

[9]. J. B. Taylor, Rev. Mod. Phys., 58 (1986) 741.

[10]. G. W. Hart, A. Janos, P.D. Meyerhofer, M. Yamada, Phys. Fluids 29 (1986), 1994.

[11]. S. O. Knox, Cris W. Barnes, G. L. Marklin, T. R. Jarboe, I.Henins, H. W. Hoida and B. L. Wright, Phys. Rev. Lett. 56 (1986) 842.

GENERATION OF D.C. CURRENTS IN A MAGNETIZED PLASMA BY R.F. FIELDS

M. Kühnapfel, R. Tabersky and H. Tuczek

Universität Essen - GHS, FB Physik, D-4300 Essen 1
F.R. Germany

In order to produce a compact torus configuration current drive by rotating magnetic fields is studied.
The rotating field is generated according to the "Rotamak" concept proposed by I. R. Jones, or utilizing the "Blevin-Thonemann End Effect" by a linearly polarized r.f. field.
Experiments are performed which allow to investigate both configurations. The r.f. fields are produced up to a power level of 5 MW for a pulse period up to 1.5 msec at a frequency of 1 MHz.
In both cases a toroidal current can be driven producing a stable compact torus configurations during the whole pulse duration. But contrary to the explanation of the "Blevin-Thonemann End Effect" the toroidal current may also have the direction opposite to the diamagnetic current, depending on the plasma density.
We therefore assume that magnetoacoustic eigenmodes are excited in the plasma. To describe this behaviour a simple theoretical model is presented.

1. Introduction

Compact torus configurations can be produced by applying an external rotating magnetic field to a magnetized plasma (fig. 1). When the electrons are tied to the rotating magnetic field lines and the ions form a stationary background, a toroidal electron current in the direction of rotation /1/ is generated. Basing on observations of Blevin and Thonemann /2/ Miller /3/ speculated that only a single linearly polarized r.f. field is required to produce a rotating magnetic field within the plasma ("Blevin-Thonemann end effect"). This speculation has been proved experimentally /3 - 5/ and described by a model of Hugrass /6/. The resulting electron current was found to be diamagnetic.

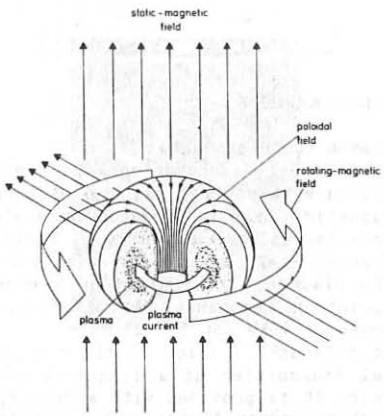

Fig. 1: Rotamak principle

In contradiction to these experiments there has been some evidence, that under certain conditions a current in the opposite direction is produced leading to an enhancement of the external steady field /4/. Such an observation is not compatible with either the Blevin Thonemann

mechanism nor the Hugrass theory. Therefore in the present paper, the production of toroidal d.c. currents by a linearly polarized alternating and a rotating magnetic field was investigated in some detail. We especially look for conditions, where the transition of one current direction to the opposite one occurs.

2. Apparatus

The experiments are performed on the Rotamak-E I /7/ and the Rotamak-E II device.

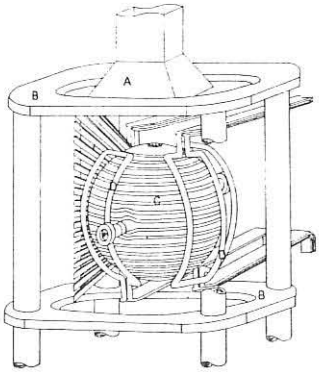

Fig. 2: Rotamak-E I

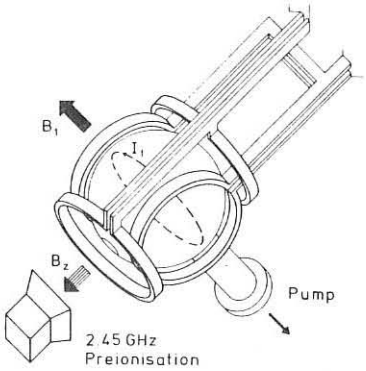

Fig. 3: Rotamak-E II

Common technical data:
A spherical discharge vessel of glass which has a diameter of 20 cm is filled with neutral gas (H_2) at a pressure of 10^{-4} to 10^{-2} mbar. A static magnetic field is produced by a slow capacitor bank discharge which is crow-barred for a programmed field decay. The field varies from 88 mT down to 6 mT for the preionisation and the main discharge respectively. The plasma is preionized by a microwave pulse working at the electron cyclotron resonance. A commercial 2.45 GHz magnetron is pulsed to a power of 4 kW for 5 - 23 ms.
At Rotamak-E I (fig. 2) the r.f. power is supplied by a 5 MW two-channel transmitter at a frequency of 1 MHz for a pulse duration of 1.5 msec. It is provided with a coil system, which allows to apply rotating high frequency fields as well as linearly polarized fields. At this experiment 0.1 to 1 MW can be coupled into the plasma maintaining a stable reversed field configuration for about 1.2 msec. An initial plasma heating is achieved by discharging a capacitor bank of 4.3 kJ at a frequency of 220 kHz through 2 coils surrounding the discharge vessel.
At the Rotamak-E II (fig. 3) a high frequency field is supplied by a pulsed transmitter, which delivers 1 MHz with a power of 500 kW for 200 µs. The maximum amplitude of the alternating field is 6 mT.

3. Measurements

Previous investigations indicated, that stable compact torus configurations can be established at densities below 10^{14} cm^{-3} by applying a uniform rotating magnetic field /4/ to the magnetized plasma. Using a only linearly polarized r.f. field, a threshold behaviour of the plasma is observed. At low densities the magnetic field $B_0(t)$ in the center of the plasma is reversed, while at high pressures it is enhanced. Figure 4 shows the inversion and figure 5 the amplification of the static magnetic field and the plasma currents, at Rotamak-E II. In these examples the electron densities n_e, determined by microwave interferometry, are $n_e = 4.2 \cdot 10^{13}$ cm^{-3} and $n_e = 8.7 \cdot 10^{13}$ cm^{-3}, respectively.

A similar behaviour is observed, if the coil geometry for the rotating field creates large gradients producing higher harmonics of the rotating r.f. field (Rotamak-E I). Even if the field rotates in the "wrong" direction inversion and amplification of the static magnetic field can be achieved, depending on the density domain.

In both cases (fig. 6 & 7) the axial and radial distribution of the magnetic field configuration B_z are measured. In the case of amplification of the static magnetic field a current distribution of two concentric currents of different directions is determined.

Since in these experiments the balance between kinetic plasma pressure an magnetic field is not fulfilled a cooling of the plasma is observed during the main discharge. The temperature of the plasma T_i, evaluated from Doppler broadening of impurity ions, indicates 40 eV in the preionisation and 20 eV in the main discharge.

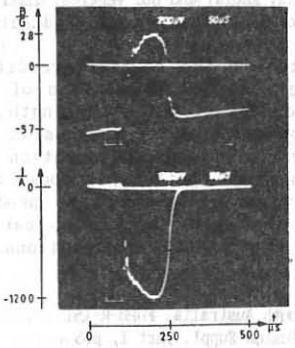

Fig. 4: Magn. field and plasma current at low pressure as a function of time

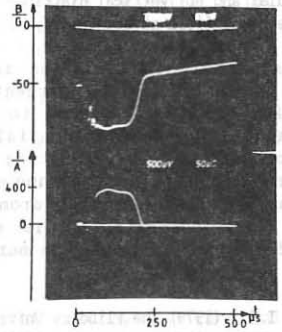

Fig. 5: Magn. field and plasma current at high pressure as a function of time

4. Theoretical model

It was tried to find a description of the rotamak by means of hydromagnetic waves. Assuming a cold plasma, infinite conductivity and small amplitudes of the waves, fields of the type

$$B = B_0 + B^{(1)}(r) \cdot e^{i(kz - \Omega t + m\vartheta)} + B^{(1)}(r) \cdot e^{-i(kz - \Omega t + m\vartheta)}$$

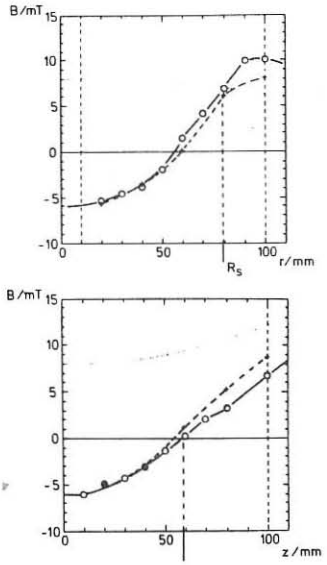

Fig. 6a:Radial and 6b: vertical distribution of the magn. field at low density

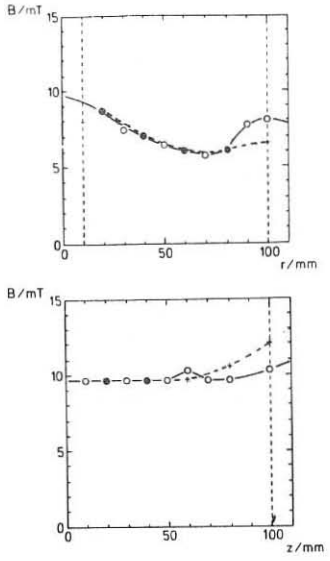

Fig. 7a: Radial and 6b: vertical distribution of the magn. field at high density

are investigated. The solution is subjected to the boundary condition $j_n = 0$, where j_n is the current flowing through the surface of the plasma. Its shape was assumed to be cylindrical with finite length. By linearization of the differential equation an analytic expression for $B^{(1)}$ can be derived. The resulting magnetic r.f. field configuration has a component rotating in the same direction as in the Hugrass model /6/. It can be concluded, that hydromagnetic waves are capable to produce toroidal d.c. currents. It is expected that the wave model can be further developed to reproduce more of the experimental observations.

References

/1/ Jones, I.R., (1979) The Flinders University of South Australia, FUPH-R-151
/2/ Blevin, H.A. and Thonemann P.C., (1962) Nuclear Fusion Suppl. part I, p55
/3/ Miller, R.B. (1968) Ph. D. thesis. University of New England N.S.W. Australia
/4/ Tuczek, H. (1982) Proc. of the 3rd Int. Conf. on Heating in Toroidal Plasma, Grenoble G17
/5/ Durance, G. (1983) Ph.D.thesis. Flinders University, S.A., Australia
/5/ Jones, I.R. and Hugrass,W.N., (1981) J. Plasma Phys. 26 , 441
/6/ Hugrass, W.N. (1982) I. Appl. Phys. 53, 2800
/7/ Frank, M., Hardtke, A., Jogwich, M., Kühnapfel, M., Plennis, K. and Tuczek, H., (1985) 12th European Conference on Controlled Fusion and Plasma Physics, Budapest, Suppl. 9F, 84

MAGNETIC EDGE FLUCTUATIONS IN THE HBTX1B REVERSED FIELD PINCH

H Y W Tsui, J Cunnane*, and D E Evans
Culham Laboratory, Abingdon, Oxon. OX14 3DB, England
(UKAEA/EURATOM Fusion Association)
* University College, Cork, Ireland

ABSTRACT

Normal θ = 1.4, F = -0.1 discharges display magnetic modes with m<2 and $|n|$ = 6, 10, 13, 16 resonant within the reversal surface. Rotation velocities $v_\phi = 5.6 \times 10^4 ms^{-1}$, $v_\theta = 3.0 \times 10^4 ms^{-1}$ in the direction of the conventional currents are measured. In deep reversal, θ>1.6, F<-0.35, sawtooth-like activity at 5kHz is seen in m=0, sinusoidal oscillations in m=1, with $|n|$ = 4 and 6 or 7, and a group velocity $v_\phi = 5 \times 10^4$ and $v_\theta = 4.7 \times 10^4 ms^{-1}$. In about 5% of discharges with graphite tile limiter removed, B_θ and B_ϕ edge coils exhibit strong coherent signals periodic at 1kHz, reflecting a non-rotating m=1, $|n|$ = 5 disturbance which may be a resistive wall mode.

INTRODUCTION

Magnetic fluctuations are associated with self-reversal and sustainment of reverse field pinch (RFP) electric plasmas.

In the RFP, the most dangerous MHD instabilities [1,2] have poloidal modes m=0, m=1 and a variety of possible mode numbers n. Thus toroidal mode structure is of great interest in the RFP.

This investigation is confined to the sustainment phase of the plasma pulse, when toroidal current I_ϕ is approximately constant and the gross plasma properties appear to be unchanging. Before removing the limiter, which was composed of about 156 5cm x 10cm graphite tiles covering approximately 8% of the internal surface of the stainless steel vacuum vessel, a study was carried out of normal 220kA discharges with pinch ratio $\theta \simeq 1.4$ and field reversal ratio $F \simeq -0.1$, as well as deeply reversed discharges with $I_\phi \simeq 170$kA, θ>1.6, and F<-0.35. The increase in global resistance V_ϕ / I_ϕ seen in deep reversed discharges is found to depend more on F than on θ, implying the dominant influence of the plasma edge.

This was borne out when removing the tile limiter led at once to a reduction in V_ϕ at all currents of about 14 volts, accompanied by electron temperatures rising during sustainment up to above 700eV while T_i remained constant or fell somewhat. Changes were accordingly expected in the character of the magnetic fluctuations.

TECHNIQUE

Small search coils are distributed poloidally and toroidally around the periphery of the HBTX vacuum vessel to detect magnetic field at the surface of RFP plasmas. The toroidal array lies in the interspace between the vacuum vessel (R = 0.8 metres, a = 0.26 metres) and the conducting aluminium shell (inner minor radius 0.29 metres). Five poloidal arrays, each capable of measuring B_θ, B_ϕ, and B_r at 16 equally spaced poloidal angles θ are available. Two are in the interspace region, and three are internal to the vacuum vessel, recessed into special sections provided for them. Two internal poloidal arrays separated by 40° in ϕ have been the chief source of the rotation information.

MAGNETIC EDGE FLUCTUATIONS IN NORMAL DISCHARGES, TILES IN PLACE

Fluctuations are 1-2% of the total edge field amplitude and toroidal component fluctuations predominate by 3-5 times over those of the poloidal component: B/B = 1-2%, B_ϕ/B_θ = 3-5. Fluctuations power is concentrated mainly below 150kHz. The poloidal mode distribution is dominated by m=0, m=1. Evidence from the toroidal array shows most n activity in the range 5-17. Higher resolution shows modes numbered n=6, 10, 13, 16 are favoured in the toroidal component B_ϕ, as can be seen in Fig 1a.

In B_θ (Fig 1b) n=0, corresponding to a toroidal current fluctuation, is dominant. This behaviour is substantially the same as was seen in HBTX1A [3], suggesting that it is intrinsic to the RFP and not an artifact of field error, which was considerably reduced in 1B relative to 1A [4].

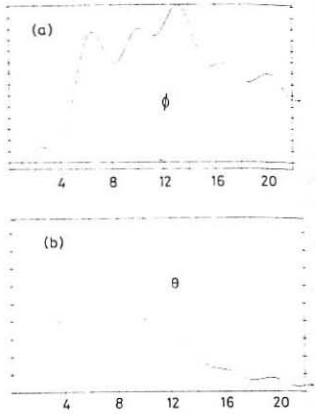

Fig 1 Relative power distribution of toroidal modes (a) B_ϕ, (b) B_θ, in a normal discharge viz θ=1.4, F=-0.1, I_ϕ=220 kA

Two poloidal arrays separated by 40° in toroidal angle, were used to investigate propagation through correlation analysis between the spatially-resolved poloidal m modes. Toroidal and poloidal rotation speeds found in this way are v_ϕ = 5.6 x $10^4 ms^{-1}$, v_θ = 3.0 x $10^4 m^{-1}$, directed in the same sense as the conventional ie, positive, current components. Plasma velocity measured spectroscopically using the CV 2271Å line [4] gave smaller values, viz v_ϕ = 1.4 x $10^4 ms^{-1}$, v_θ = 0.6 x $10^4 ms^{-1}$, but in the same directions.

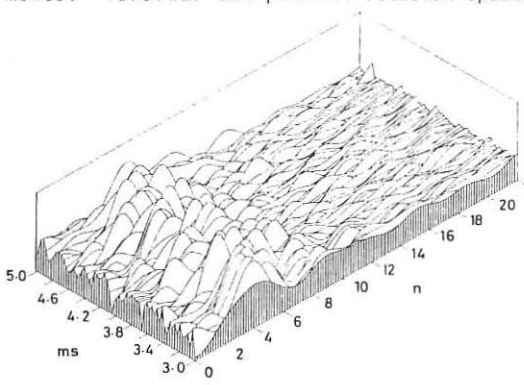

Fig 2 Evolution of n-spectrum in a normal discharge. Scale to the left is time in ms, that to the right is mode number. Each trace is an average over 0.03 ms.

The modes were shown to be resonant inside the reversal surface.

The temporal behaviour of the toroidal modes was investigated by evaluating n-spectra over many successive short time intervals. Such an analysis performed from HBTX1A produced evidence for cyclical behaviour in the n-spectrum evolution [3]. Nothing of the same

kind has been found in HBTX1B discharges. Time variation of the n-spectrum with the dominant mode changing apparently at random among the favoured n numbers occurs on a time scale much shorter than the 0.3ms of the earlier study shown in the accompanying diagram in which mode number n is horizontal and time vertical (Fig 2). Averaging HBTX1B data over such a time span resulted in behaviour that looked neither cyclical nor even progressive.

DEEP REVERSAL DISCHARGES, TILES IN PLACE

Edge coil signals in deeply reversed discharges display an unmistakable periodicity absent in normal discharges. The relative amplitude of the fluctuations is greater: $\tilde{B}/B$ = 5-10%, and the toroidal component fluctuations are larger than those of the poloidal components by two to three times: B_ϕ/B_θ = 2-3.

Analysing signals into m=0, m=1 modes reveals sawtooth-like oscillations recurring with about 5kHz frequency in the former, while sinusoidal oscillations with frequency varying in the range 20-80kHz are to be seen on the latter. Two principal toroidal modes $|n|$ = 4 and 6 or 7, of which the first is the stronger, dominate these fluctuations. This is confirmed in a dispersion analysis of the toroidal array signals (Fig 3) which gives $v_\phi = 5 \times 10^4 ms^{-1}$ and $v_\theta = 4.7 \times 10^4 ms^{-1}$. This describes a helical structure that bears some resemblance to the lowest energy asymmetric solution in cylindrical coordinates of the equation $\nabla \times \underline{B} = \mu \underline{B}$, which corresponds to m=1, n=4 in HBTX [5]. There is evidence too for some activity at the m of the opposite sign.

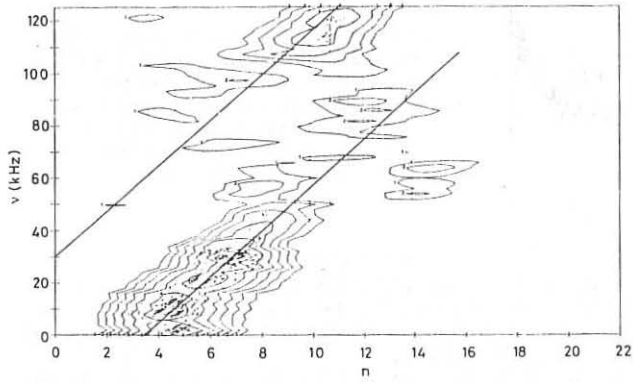

Fig 3 Dispersion relation for m =1 activity in deep reversal (θ=1.7, F=-0.6) discharges, constructed from toroidal array measurements. Diagonal lines represent $\nu=(v_\phi/2\pi R)n \pm (mv_\theta/2\pi a)$.

NORMAL DISCHARGES, TILES REMOVED

Operating with graphite tiles removed, B_θ and B_ϕ coils exhibit a tendency to periodic oscillation that develops strongly at ~1kHz in about 5% of all discharges. As an example Fig 4 shows signals on three B_ϕ coils displaced each from the last by ϕ = 18° approximately. These signals

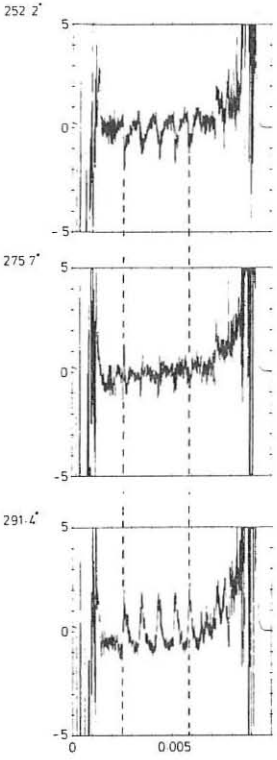

occur on dB/dt rather than the integrated signals B, and are m=1. It can be seen that peaks occur at precisely the same time at each coil position, implying zero rotation, and that the pair separated by about 36° are in antiphase with a minimum amplitude signal of indeterminant phase half way between them consistent with a toroidal mode number $|n| = 5$. Coherent fluctuations in the emission from some impurities lines, viz CII, FeII, OI and CrI all near the plasma edge, accompany these magnetic fluctuations. It has been conjectured [6] that these observations might be explained by a hitherto unobservable resistive wall mode whose growth time undergoes a massive decrease bringing it into the observable range because a trifling change in the equilibrium occasioned by removing the tiles has brought its marginal radius from outside the conducting shell (penetration time = 80ms) into the space between the shell and the liner (time constant < 0.1ms).

Fig 4 Records of dB/dt on B_ϕ coils at three toroidal-angle positions (upper left hand corner). The ordinate is in the same arbitrary units in each case. Abscissa is time during discharge in secs. Vertical dashed lines emphasize time coincidence of extrema from which non-rotation is inferred.

REFERENCES

[1] D C Robinson: Nuclear Fusion 18, 939 (1978)
[2] D C Robinson, Plasma Physics 13, 439 (1971)
[3] I H Hutchinson, M Malacarne, P Noonan and D Brotherton-Ratcliffe: Nuclear Fusion 24, 59 (1984).
[4] B Alper et al: 11th Int Conf on Plas Phys & Cont Nuc Fus Res, Kyoto 1986, IAEA-CN-47/D-II-1
[5] J B Taylor: International School of Plasma Physics, Varenna September 1983, EUR 8961 EN Vol II, p501
[6] C G Gimblett and T C Hender: Internal Culham Laboratory Report TPGN/233 (1987).

IMPURITY BEHAVIOUR AND Z_{EFF} IN THE HBTX EXPERIMENT

P G Carolan, C A Bunting, A M Manley* and A Patel*
Culham Laboratory, Abingdon, Oxon, OX14 3DB, UK
(UKAEA/Euratom Fusion Association)
*Royal Holloway and Bedford New College, London

ABSTRACT

It is shown that impurities cannot explain the loop voltage, V_{loop}, with 150 limiter tiles in position nor the increase in V_{loop} on insertion of a moveble limiter and the decrease when the tiles are removed. The plasma resistance obtained from T_e, Z_{eff} and helicity balance is less by about a factor of 3-4 than that measured electrically when the 150 tiles are in position. Removal of the limiter tiles increases the Z_{eff} by about 50% although the loop voltage decreases from ~30 V to ~20V.

RESULTS

The diagnostics used include a multichord soft X-ray (SBD's) system, a polychromator (600-4500Å) and absolutely calibrated bolometers and normal incidence (500-3500Å) spectrometer. The SBD's are filtered to detect the short wavelength transitions of CV (mainly 40.27Å, 34.97Å and 40.73Å). A collisional radiative model [1] is used to calculate the line intensities over the range of n_e and T_e, relevant to HBTX. For $T_e \simeq$ 150-500 eV the line intensity of CV 2271 Å is only marginally dependent on T_e (±10% variation) and has an approximate linear dependence on n_e. Only weak burn through of CV is observed in HBTX so on dividing the CV line intensity by n_e, an approximate measure of the CV density is obtained.

The distribution of the measured CV density, with the 156 graphite tiles in position, is shown in Fig 1 for I=220 kA and I/N = 7 x 10^{-14}A.m together with 1D simulations (SANCO1 code [2]). In all cases a constant diffusion coefficient, D, is assumed where the particle flux, Γ_k, is given by $\Gamma_k = -D\nabla n_k$. As illustrated in Fig 1, simulations from D = 100-200 m^2s^{-1} approximate the experimental curve.

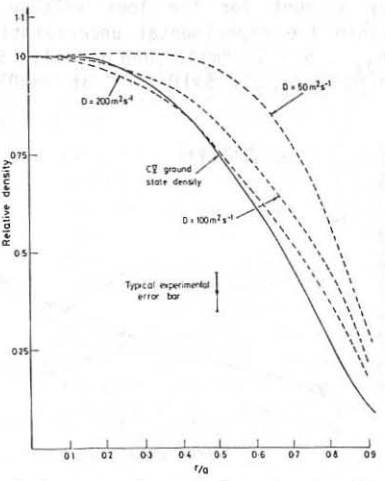

Fig 1 Measured and simulated density distributions of CV (220 kA, $\bar{n}_e = 2x10^{19}m^{-3}$, 156 tiles in position)

Using a fixed D value (100 m^2s^{-1}) the emission profiles of the other carbon and oxygen ion states are calculated, from which the densities are obtained using the normal incidence spectrometer. The concentrations obtained are 3% oxygen, 1% carbon and 0.1% iron with an overall uncertainty of about 70%. (The sum of oxygen and carbon radiative powers is used to estimate the concentration of metallics, mainly iron, from the bolometer results.)

From the impurity ion state distributions the spatial profile of the Z_{eff} is calculated and is shown in Fig 2. These values of Z_{eff}, and using $T_e(r) = T_{eo}\{1-(r/a)^4\}$ with $T_{eo} \sim 250$ eV, yield a plasma resistance which is less by a factor of 3-4 than that obtained electrically and including helicity balance but ignoring edge effects [3]. The Z_{eff} profile is in contrast to that measured in ηβII [4] which exhibits $Z_{eff} \sim 1$ in the plasma bulk and $Z_{eff} \sim 4$ at the periphery. With the lower T_e values found in ηβII such a profile may account for the loop voltage within the experimental uncertainties. However, the high oxygen density ($n_{OV} \sim 5 \times 10^{18} m^{-3}$) seen in ηβII [5] at the periphery is much higher than in HBTX ($n_{OV} \sim 5 \times 10^{16} m^{-3}$ at r=20 cm), so that impurity effects together with a narrower T_e profile in ηβII indicate qualitatively different plasmas, as regards resistance, in the two devices.

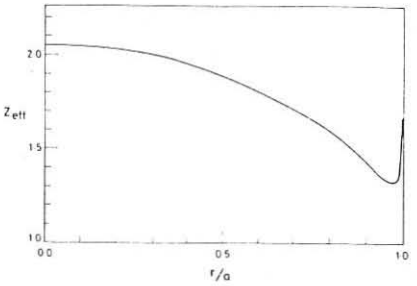

Fig 2 Z_{eff} profile obtained from impurity ion state distributions (220 kA, $\bar{n}_e = 2 \times 10^{19} m^{-3}$, 156 tiles in position)

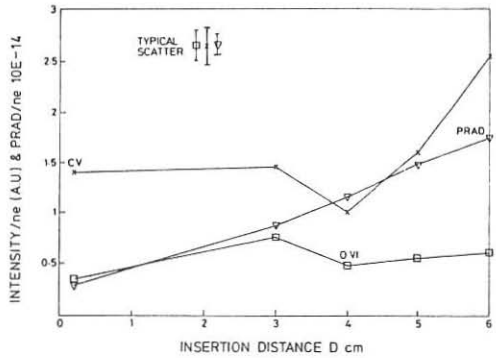

Fig 3 Electron density normalised line intensities of CV (2271Å) and OVI (1038Å) and total radiation, P_{rad}, versus limiter (graphite) insertion distance beyond the tiles position

The impurity behaviour is examined when a variety of mobile limiters are inserted [3]. In Fig 3 are shown the behaviour of CV (2271Å), OVI (1038Å) and total radiation as a function of limiter insertion distance from the tiles for $I_\phi \sim 220$ kA. The results were obtained during the sustainment period (t ~ 4 ms) and averaged over 6 discharges. The total

radiation is from a bolometer in the vicinity of the mobile limiter while the spectral line intensities are from a polychromator displaced toroidally by about 90°. The radiated power increases almost linearly with limiter insertion distance indicating local impurity contamination whereas remote from the limiter only the CV density shows any significant change and then only when the limiter (graphite) is inserted over 5 cm. (The limiter was orientated to intercept maximum magnetic flux for this data set which requires the greatest loop voltage to sustain the current [3]). Since T_e and n_e remained largely unaffected by the limiter insertion the impurities are not responsible, at least globally, by an increase in Z_{eff}, for the additional loop voltages seen with limiter insertion.

A useful check on the generally small influence of Z_{eff} on loop voltage is provided by the experiments using a pyrolytic graphite limiter. An example is shown in Fig 4 where the pyrolytic limiter is inserted 3 cm beyond the tiles with an initial increase of 12 V in loop voltage. The bolometer in this case is 20° toroidally displaced from the limiter. There is a sudden increase in the total radiation, P_{rad}, at t~2 ms

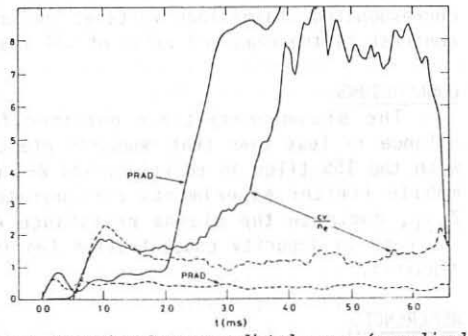

Fig 4 Comparison between radiated powers (normalised to n_e) with (full lines) and without a pyrolytic limiter inserted 4 cm

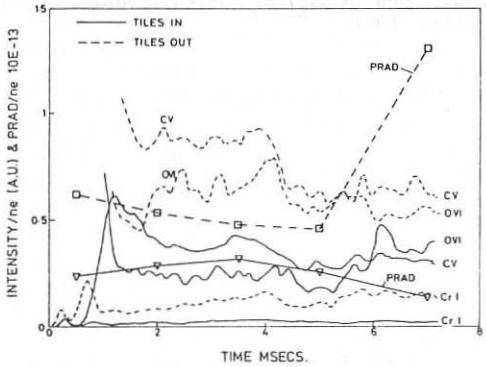

Fig 5 Radiated powers (normalised to n_e) with (full lines) and without the 156 graphite tiles in position (I_ϕ ~ 220 kA, $\bar{n}_e = 2x10^{19}m^{-3}$)

preceding that from CV and presumably due to burn through of the lower carbon states. At t ~ 4 ms the discharge is essentially a carbon plasma with Z_{eff} ~ 4 and T_e ~ 220 eV compared with Z_{eff} ~2 and T_e ~270 eV at t=1.5 ms. The consequent further increase in loop voltage at t ~ 4 ms is about 20 V which is close to that observed [3]. (The 20 V includes the larger dynamo electric field necessary to sustain the RFP with the increase (factor of ~2.2) in resistivity). These results

confirm that the much lower impurity injection with the mobile graphite limiter, or in the early phase using a pyrolytic limiter, has only a marginal influence on the loop voltage.

Comparisons of the radiation with and without tiles are shown in Fig 5. The total radiation per electron has increased by between 50% and 100% which corresponds to an increase of Z_{eff} from about 2 to between 2.5 and 3 for the same relative distributions of impurity ionisation states. There is about a factor of 2 increase in the CV and OVI concentrations and about a fourfold increase in CrI influx. The latter suggests a similar increase in the metallic concentration. Scaling from previous results, where absolutely calibrated spectrometers were available, the impurity concentrations are ~6% Ox, 2% C and 0.5% Fe with a resultant Z_{eff} = 3. The corresponding plasma loop voltage, including helicity balance, is ~8 V in contrast to the measured value of ~24 V at these conditions.

CONCLUSIONS

The plasma resistance obtained from T_e and Z_{eff} using helicity balance is less than that measured electrically by about a factor of 3-4 with the 156 tiles in position, and 2-3 without tiles. Measurements from mobile limiter experiments corroborate that edge effects, rather than Z_{eff}, dominate the plasma resistance except when there is a very large increase in impurity concentration (eg increase by a factor of ~10 in CV density).

REFERENCES

[1] H Gordon and H P Summer: Culham Laboratory Report CLM-R250 (1985)
[2] D G Muir and M L Watkins: Internal JET Report DPA(08)87 (1987)
[3] B Alper and H Tsui: this conference
[4] L Gabellieri et al: to be published in Nuclear Fusion (1987)
[5] P Scarin: private communication (1987)

FLUCTUATION STUDIES ON THE ETA-BETA II EXPERIMENT

Antoni V., De Simone P., Innocente P., Martin P., Martini S.,
Ortolani S., Paccagnella R., Puiatti M.E.,
Scarin P., Valisa M., Villoresi P.

Istituto Gas Ionizzati del C.N.R.
EURATOM-ENEA-CNR Association, Padova, Italy

INTRODUCTION

The RFP configuration is intrinsically turbulent since many MHD instabilities are simultaneoulsy allowed [1]. It has been suggested that these instabilities underlie the profile sustainment process and also limit the plasma confinement [2]. The non-linear interaction of these instabilities results in an enhanced fluctuation level for all of the plasma quantities, such as magnetic field, plasma density and temperature. In the past the magnetic fluctuations have been measured in ETA-BETA II and their properties discussed [3].

In this paper we compare the properties of the measured fluctuations of the magnetic field, density and radiation emission. In particular the change in their characteristics during the sustainment of the plasma density by pellet injection has been studied.

EXPERIMENTAL RESULTS

With the current in the range 150-180 kA, the plasma density has been varied from a few 10^{19} m^{-3}, for a normal discharge, up to $1.5 \cdot 10^{20}$ m^{-3} (almost constant in time) for the discharges sustained by pellet injection [4]. The plasma density was measured by a two colour CO_2 interferometer and the radiation emission by a single chord SBD and a multichord Ebert spectrometer. An example of the waveforms of plasma current, electron density and of D_α line emission for the central and the innermost chord is shown in Fig. 1 for a discharge without (a) and with pellet injection (b). For the discharges with pellet, larger fluctuations are observed on the density and on the D_α signals.

In Fig. 2 the comparison between the average power spectrum of density fluctuations for discharges with and without pellet is shown. As found for the magnetic fluctuations [3], the power spectrum is peaked at low frequency ($\sim$ 10 KHz) where most of the power density is concentrated. Fig. 3 shows the typical amplitude of normalized density fluctuations, $\frac{\tilde{n}}{n}$, as a function of plasma density. The rms of the density signal (averaged over a millisecond during the flat-top phase of the discharge and over many shots)

is about 5 % and does not show any clear dependence on density. For the same discharges in Fig. 4 and 5 are plotted the amplitude of the normalized fluctuations of the toroidal magnetic field at the wall, b_ϕ / B_ϕ , and of the SXR signal from the SBD detector. In particular the amplitude of the SXR fluctuations increases for discharges with pellet, whereas b_ϕ / B_ϕ does not show a clear change.

The cross-correlation analysis of the density fluctuations with magnetic, SXR and D_α fluctuations shows in any condition a poor correlation (typically < 20%) for frequencies higher than 5 KHz. The fluctuation amplitude measured by the multichord spectrometer shows for the D_α emission an increase by a factor of 2 between the normal and the density sustained discharges but no substantial change in the profile. On the other hand, considering the correlation between the central and the other chords, it is found, as shown in Fig. 6, that, with pellet, there is a large radial correlation length (of the order of the minor radius a), whereas, without pellet, the correlation length is still large but reduces to a/2. This value is comparable with the radial correlation length ($\sim a/2$) found by insertable probes for the magnetic fluctuations at low frequency.

DISCUSSION

From the ETA-BETA II results the density fluctuations are characterized by an amplitude of 5 %, which is substantially higher than that of magnetic fluctuations (typically 1-2 % when normalized to the total magnetic field). Moreover the density fluctuations have a poor correlation with those of the other quantities (typically less than 20 %). At high densities obtained by pellet injection, the correlation is still poor and the amplitude does not change. This behaviour is different from that of magnetic, SBD and D_α fluctuations and suggests that, in the parameter range of ETA-BETA II, the density fluctuations are weakly coupled with the other fluctuations in particular with that of the magnetic field.

REFERENCES

/1/ B.B. Kadomtsev, 6th Int. Conf. Pl. Phys. Contr. Fus. Res., IAEA (1976).

/2/ V. Antoni, S. Martini, S. Ortolani, EPS 86 Schliersee, Vol. 1, 385.

/3/ V. Antoni, S. Ortolani, Plasma Physics, 25, 799 (1983).

/4/ V. Antoni, et al., "D_2 pellet injection in ETA-BETA II plasma", this Conference.

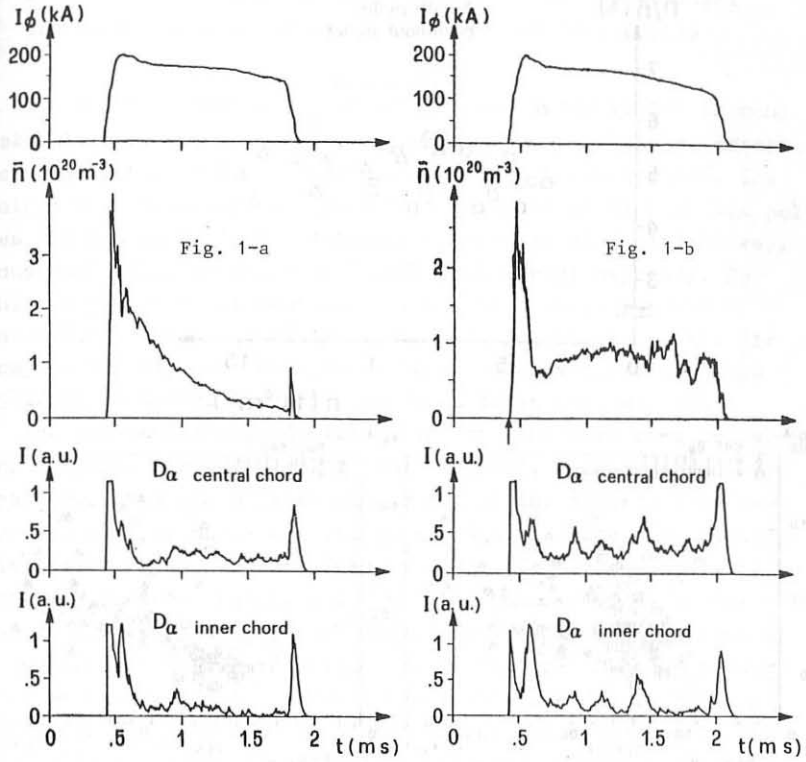
Iφ (kA)
200
100
0
n̄ (10^20 m^-3)
3
2
1
0
Fig. 1-a
I (a.u.)
Dα central chord
1
.5
0
I (a.u.)
Dα inner chord
0 .5 1 1.5 2 t(ms)
Iφ (kA)
200
100
0
n̄ (10^20 m^-3)
2
1
0
Fig. 1-b
I (a.u.)
Dα central chord
1
.5
0
I (a.u.)
Dα inner chord
0 .5 1 1.5 2 t(ms)

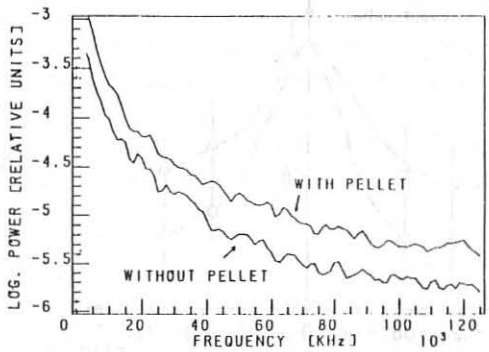
LOG. POWER (RELATIVE UNITS)
-3
-3.5
-4
-4.5
-5
-5.5
-6
WITH PELLET
WITHOUT PELLET
0 20 40 60 80 100 120
FREQUENCY (KHz) 10^3

Fig. 2

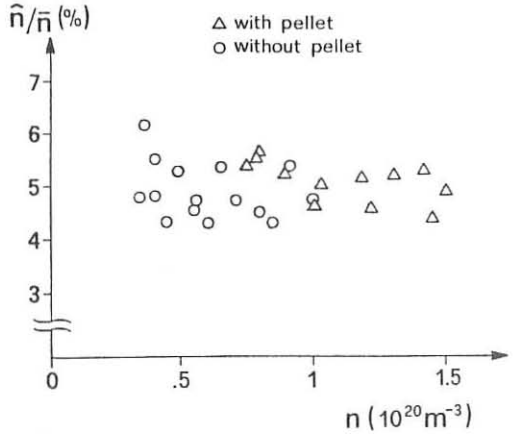

Fig. 3

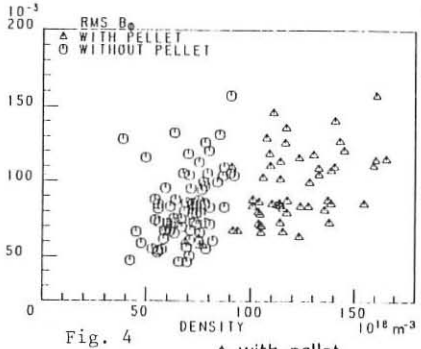

Fig. 4

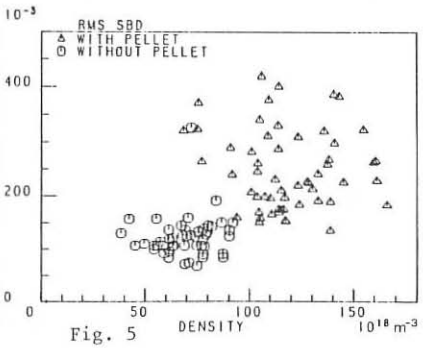

Fig. 5

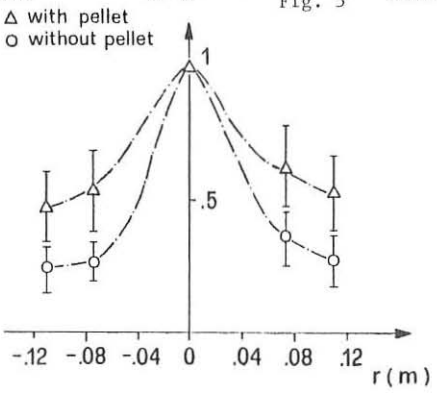

Fig. 6

STUDIES ON ION EMISSION FROM PLASMA FOCUS FACILITIES

M. Sadowski, J. Żebrowski, E. Rydygier, and J. Kuciński
Institute for Nuclear Studies, 05-400 Świerk, Poland

Abstract

Ion emission from PF machines has been investigated in many laboratories, but no exact scaling has been established except for empiric power laws describing the energy spectra /1/. The main aim of this work was to extend previous studies of ion pulses /2/ and to perform detailed measurements of fast />50 keV/ ions emitted by PF devices of different energy capacity. For this purpose use has been made of a small 3.6-kJ PGN device and a large PF-360 facility /3/ operated at about 200 kJ. For comparative studies the results obtained previously with the 25-kJ PF-20 device /2/ have also been taken into account.

Angular- and energy-distributions of ions have been measured and compared for the machines investigated. Also compared were space-resolved ion pinhole pictures. Special efforts have been done to compare mass- and energy-spectra of deuterons and impurity ions, which were obtained by means of Thomson analyzers. The mean deuteron energy and the total numbers of deuterons /above the threshold 330 keV/ have also been found by means of a nuclear activation technique using $^{12}C/d,n/^{13}N$ and $^{27}Al/d,p/^{28}Al$ reactions and the known thick-target yields. Particular attention has been paid to time-resolved ion measurements realized with miniature scintillation detectors placed behind the ion pinhole camera and the Thomson analyzer.

It has been found that the ion emission from the PF devices demonstrates some similarity features, but evident differences depend strongly on parameters and the operation mode of the machine. Interesting new results have concerned the fine structure of ion pulses, and the ion emission from the PGN device operated at a higher repetition rate.

/1/ W. Stygar, G. Gerdin, F. Venneri, J. Mandrekas; Nucl. Fusion 22 /1982/ 1161-1172.
/2/ M. Sadowski, J. Żebrowski, E. Rydygier, H. Herold, U. Jäger, H. Schmidt: Phys. Letters 113A /1985/ 25-31.
/3/ M. Sadowski, L. Jakubowski, E. Rydygier, J. Żebrowski; Proc. 12th European Conf. CF PP /Budapest 1985/ Part I, pp. 538-541.

NEW RESULTS OF PLASMA-FOCUS NEUTRON EMISSION OPTIMIZATION

A.Jerzykiewicz,M.Bielik,Sz.Brandt,K.Kocięcka,L.Kociński,
J.Kuciński, W.Nawrot
Institute for Nuclear Studies, 05-400 Świerk,Poland.

A b s t r a c t

The paper presents the results of neutron emission investigations performed with PF-360 and PGN devices.

As it was reported previously /1/ there was an upper energy limit observed at which the neutron yield from PF-360 device decreased rapidly. To overcome this limitation and to study influence of the start-up-phase initial conditions on the neutron emission, an additional circuit has been installed in parallel to the main capacitor bank. This circuit includes 24 uF, 25kV, 7.5 kJ condensers which can be switched on before the main discharge. The crest value of the predischarge current reaches up to 175 kA /about 10% of the main crest value/. The influence of the predischarge has been investigated using several sets of electrodes and insulators, changing the deuterium pressure, the predischarge current value and polarity, as well as the delay between the both discharges. Integral and time-resolved neutron measurements have been performed under above specified conditions.

The results of measurements can be summarized as follows:
- the application of the predischarge enables the neutron emission at higher energy to be obtained, but it is still smaller than resulting from the energy scaling low;
- the maxima of characteristics of neutron yield as the function of the pressure, as obtained with the predischarge, are shifted to a lower pressure;
- duration of the inverse pinch is shorter for the courses realized with the predischarge;
- the neutron yield decrease when the predischarge current of opposite polarity is applied.

The 8-kJ PGN plasma-focus device has also been used to neutron emission investigations at the repetition rate elevated up to 8 p.p.s. The neutron yield at the elevated repetition and continuous deuterium flow through the device vacuum chamber, is higher than that observed for the single shot operation. The dispertion of neutron yield does not exceed 30%, and the shapes of subsequent neutron pulses are more similar. The average neutron flux amounts to 10^9 n/s.

/1/ A.Jerzykiewicz et.al. Nuclear Fusion Suppl.1985,V.2,p.591

NEW ASPECTS OF THE STABILITY OF EXTRAP DEVICE.

M.TENDLER,DEPARTMENT OF PLASMA PHYSICS & FUSION RESEARCH,ROYAL INSTITUTE OF TECHNOLOGY,S-10044,STOCKHOLM 70,SWEDEN

1.GENERAL DISCUSSION.

EXTRAP is a classical Z-pinch with a divertor[1].In its original version there is no toroidal magnetic field[2].The poloidal magnetic field has magnetic field nulls(the absolute value of the magnetic field is equal to zero at these nulls) and the plasma surrounding these nulls is unmagnetized[3].The latter constitutes a very important difference with all other major configurations under consideration in fusion research.Nulls fall on the axis and on a magnetic field line separatrix.Field lines beyond the separatrix nulls are diverted.

Obviously the kinetic approach is imperative to assess the issue of a strongly inhomogeneous Larmor radius.Therefore all attempts to unravel the physics of EXTRAP by employing models based on the ideal MHD approach have further confused rather than clarified the problems.

A physically correct model has to incorporate a separate analysis of the following regions[3]:

1).the layer where electrons and ions are unmagnetized:

2) the layer with magnetized electrons and unmagnetized ions

3) the main body of the plasma,where both species are magnetized.The stability is adequately described by the well known local perturbation analysis of a magnetized plasma,based upon integration of the Vlasov equation along characteristics[4]:

Solutions,restricted by the first order quasi-neutrality constraints in each of these regions,have to be obtained and matched to each other.

The stringent matching of these solutions is the key to the assessment of this problem.

The consistency of solutions in these regions,governed by a completely different physics,is much more important than the subtle details of solutions obtained,including an arbitrary number of terms in each one of these regions.Phenomena of this kind are widely known in other branches of physics.As examples;the tunneling effect in quantum mechanics[5] or the effect of inelastic collisions with molecules on the electron distribution function[6],might be mentioned.The idea that to match solutions is more essential for the assessment of the problem than to consider some subtle details of solutions in each one of them,was overlooked in the majority of studies on this subject[2].

Two important implications of the fact,related to the above-mentioned existence of areas with unmagnetized plasmas are considered.The first is the line tying effect,arising due to the magnetic field being frozen into an ideal conductor.Here,the role of an ideal conductor is played by hot unmagnetized plasmas,surrounding nulls.In its simplest interpretation the line tying effect[7] imposes a concave form on the boundary due to the "frozen in " condition into metallic rods.Thence magnetic field lines are immovably fastened to these rods and potentially unstable perturbations are suppresed.In EXTRAP either the solid copper rods or current spikes,flowing around nulls might affect a plasma in a similar fashion.The latter implies that both of these equilibria are easily attainable in EXTRAP.On the other hand it is difficult to make to make a transition between them,because both of them are stable.In order to gain a significant stabilization effect the magnetic field pressure outside the current rods should significantly exceed the pressure of a confined plasma.The form of the plasma surface in the both equilibria is governed by the stability constraints and has a concave shape between these rods,as shown in Fig.1a &b.

Although it is often declared that EXTRAP is meant to be a high ß configuration,the influence of a high ß value in the inner core has never been properly accounted

for.Operating the device with a high filling pressure leads to the expulsion of a magnetic field from the dense area and thus to the expansion of a field free unmagnetized plasma around the O-point.A very similar effect arises,when a low ß plasma,with a magnetic field frozen into it,is lost from the core,owing to a mass flow or,in other words,due to the finite particle confinement time there[3].

The second utterly important point,following from the existence of unmagnetized plasmas in EXTRAP is the issue of a Larmor radius and its impact on the stability of the latter configuration.Since early days of fusion research there is little doubts that perturbations with high mode numbers in a classical Z-pinch are efficiently stabilized by the FLR effects[4].It is also well known that these effects do not affect rigid perturbations with low mode numbers at any significant rate.

The latter leads to a notorious reputation of a Z-pinch of being violently unstable.The lifetime of a Z-pinch is usually limited by approximately Alfven time scale.On the other hand,discharges in EXTRAP seem to last longer.

2.THE INFLUENCE OF UNMAGNETIZED PLASMAS.

In the present study we aim to show,that unmagnetized plasmas, surrounding nulls at the periphery are responsible for the latter effect.

Following our previous study[3],we distinguish the above mentioned three different areas.Assuming a low ß value of a plasma in the vicinity of the separatrix,we consider only electrostatic perturbations.We solve the Vlasov equation approximately in each region,integrate over the velocity space and impose the quasi-neutrality constraint on the first order density perturbations of both species.Matching these solutions,we require the smoothness of eigenfunctions at transition points.The latter means that arbitrary constants are determined by the conditions imposed on the continuity of the functions and their derivatives at the boundaries of the regions.Ramifications of this procedure reduce quite significantly the number of unstable modes.

In the core of the plasma,where both electrons and ions are magnetized,we adopt the existing solution,keeping in mind a non-local form of ion responce due to the integration of the potential structure along an ion Larmor radius.This yields:

$$f_{1i}(t)=-ef_0\phi(t)/T+(ef_0/T+(e\partial f_0/\partial x_0)/m_i\Omega_{Hi})<\phi> \qquad (1)$$

where $f_0(\varepsilon,x_0)$ is a Maxwellian function of integrals of motion and$<\phi>=\int dt\ \phi[x(t),y(t),t]$ taken along the unperturbed characterisics.Thus,the ion response,given by Eq.(1) is non-local everywhere,owing to to the integration of the potential along an ion Larmor radius.

The latter here,might be a large LLR[2] or a small FLR[4]depending on the region under consideration. On the other hand,using the idea,suggested by us before[6],the contribution of the potential perturbation appears in the dispersion relation under the double integral sign.Therefore,the form of the solution for magnetized plasma (region 3) is only slightly sensitive(i.e.probably not sensitive at all) to the fine details of ion orbits in the unmagnetized area.

Thus,in the core where the scale lengths of all plasma parameters are larger than a local ion Larmor radius,the expansion of the potential is justified and the local formulation suffices.Following [4],in this region we include the ion polarization drift,the classical averaging of the potential over an ion Larmor orbit and the Doppler shift due to the curvature drifts into the calculation of the first order of the ion density perturbation.Then we impose the quasi-neutrality condition.

Turning to the solution of the problem in the region (1)(both electrons and ions are

unmagnetized),we assume for electrons the purely Boltzmann response to the induced potential perturbation.For ions,the source term,given by Eq.(1),is modelled by a d-function,owing to the abrupt jump of the potential there.

The most difficult part of the problem is in the second area,where electrons are magnetized,but not the ions.However,the form of the solution is not sensitive to fine details of the potential structure as emphasized before.Therefore,we consider the inhomogeneity to be a constant and compute the latter from the condition of the quasi-neutrality.This procedure is a solution by the generalized method of Galerkin moments.

Matching these three solutions,obtained by different means,we arrive to the following worthy of being remembered conclusion.

Contrary to the earlier beliefs,the finite pressure gradient has to be maintained at the periphery in order to fully exploit the effect of the nulls(fig.2).The physical reason seems to be the essentiality to communicate the beneficial effect of nulls to a maximum available plasma volume during a wave period.

On the other hand the plasma pressure gradient at the edge is determined primarily by the edge neutral density,the parallel and the perpendicular confinement times and the energy influx[8].Therefore to control this pressure gradient does seem to be much of a problem in EXTRAP.

3.The passive feedback stabilization by currents flowing through X-point nulls.

It is suggested long wave kinks in EXTRAP are stabilized by image currents flowing through X-points due to the unstable behaviour of ordinary Z-pinch plasmas.These currents represent singular spikes in the current profile,antiparallel to the current in the pinch.The electrical conductivity of the plasma at these X-points is larger than in the rest,owing to the well-known Spitzer relation $\sigma = 2\,\sigma_{\perp}$.Image current spikes in the area around X-points are induced due to the expanding or weakly unstable pinch current.These currents are governed by the relation $\dot{\Phi} = \sigma j_{x,}$ where $\dot{\Phi}$ is the rate of the magnetic flux change,σ is the plasma conductivity at the X-point and j_x is the respective current density.It is obvious that if the plasma temperature is high and thence σ goes to infinity then a current singularity arises at X points.

On the other hand, positions of the X-points are very weak function of both the pinch and rod currents,given by:

$$a_s=a_v(I_p/I_r)^{1/4} \qquad (2)$$

where a_s and a_v are radial distances to X-points and rods,I_p and I_r are currents in the pinch and rods.

In the steady state the rate of change of the magnetic flux in the X-point layer is equal to the rate of change of the magnetic flux of the plasma core (primarily the flux,generated by the pinch current).Therefore the image currents are linear functions of a perturbation and its derivatives:

$$I_{im}=-c\,\xi \qquad (3)$$

where c is a constant,varying from 0 to 1.The latter depends on the efficiency of coupling between the pinch current and the unmagnetized plasma,surrounding nulls.

Using Eq.(3) as the boundary condition,we get for the modified growth rate of the kink instability in a Z-pinch:

$$\Gamma=\sqrt{[-k^2H_e^2(\ln kR/2+\gamma)/(4\pi\rho)+(ck)/(R\rho)]} \quad (4)$$

Here,notations are the usual.Eq.(4) yields that the stabilization might be attained,if:

$$I_{im} \approx I_{pl}\xi/4R \quad (5)$$

Finally,this effect should be easy to observe experimentally by putting Rogowski coils around X-points and correlating the signal with the level of magnetic fluctuations of the Z-pinch.

References.

1.L.Spitzer,Project Sherwood,The U.S.Program in Controlled Fusion(1951)
2.B.Lehnert,TRITA-PFU-87-02,1987 and references cited therein
3.M.Tendler,Nucl.Inst.& Meth. **207**,233,1983
4.M.N.Rosenbluth et al.Plasma Physics&ControlledNuclearFusion (Proc.Int.Conf.Salzburg,1961),Nucl.Fus.Suppl.Pt.1,IAEA,Vienna,143,1962& Phys.Fluids 8,1300,1965
5.L.Landau & E.Lifschitz.Quantum Mechanics,Pergamon Press,London,1958
6.R.Lagushenko & M.Tendler.Sov.J.Plasma Phys.**1**.458.1975
7.B.Kadomtsev in Plasma Physics and the Problem of Controlled Thermonuclear Reactions,v.4,Pergamon Press,London,417,1960
8.M.Tendler.Nuc.Fus.**24**,937,1984 &J.Nuc.Mat.**128.**100.1984

Figure Captions.

Fig.1.Two types of equilibria a & b of EXTRAP
Fig.2.The normalized maximum allowed growth rate stabilized by the pressure gradient at the separatrix.

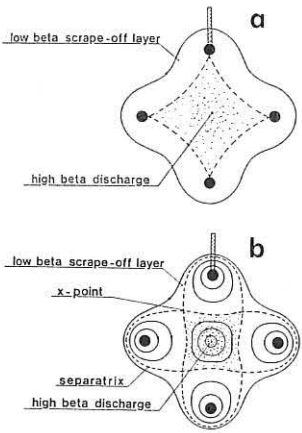

Fig.1

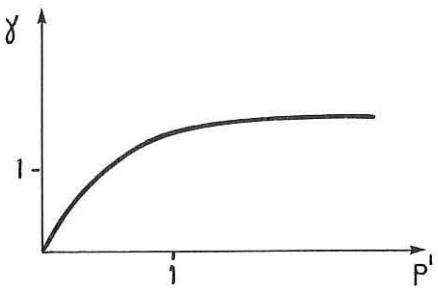

Fig.2

A KELVIN-HELMHOLTZ INSTABILITY ASSOCIATED WITH AN INTERSECTION OF TWO DISPERSION CURVES

J. A. Elliott and G. D. Conway*

Physics Department, UMIST, Manchester M60 1QD, U.K.
* Research School of Physical Sciences, Australian National University, Canberra

1. Introduction

In this paper we report observations of a large amplitude coherent density perturbation within the private flux regions of a linear quadrupole which forms as a result of the filling mechanism.

We present evidence that this is essentially a Kelvin-Helmholtz instability driven by a velocity shear. However, there are other important features, including evidence of a mode which we have been unable to identify, and which is not described by the very thorough theoretical survey of Hastie and Taylor (1971).

2. The Quadrupole System

Fig 1. shows the quadrupole magnetic field configuration. The flux surface which passes through the neutral field axis is the separatrix, and it defines the shared flux (field lines encompassing both conductors) and the two private flux (field lines encompassing only one conductor) regions. A full description of the device together with details of the main plasma parameters and features is given by Phillips et al (1978).

Each field line can be identified by the coordinates (ψ, z) where z is the distance along the axis and ψ the flux per unit axial length contained between the field line and the separatrix. Dividing by the quadrupole current I gives the dimensionless parameter ψ/I (c.g.s. units) which is defined to be zero at the separatrix, and thus negative for field lines in the private flux and positive in the shared flux. The hydrogen plasma is injected on the axis from a duoplasmatron source at one end of the device. It rapidly fills the layer $-0.05 < \psi/I < 0.01$ (hot plasma layer) and thence traverses the length of the device under the influence of the $\underline{E} \times \underline{B}$ and ∇B drifts. In this region $n \approx 10^9$ cm^{-3} and $T_e \approx 10 - 13$ ev. The ends of the device, and all internal surfaces of the plasma chamber, are separately earthed.

The outer regions of the device are filled by secondary processes described by Daly and Elliott (1982). The general flow pattern is illustrated in Fig.2.

Potential measurements reveal the existence of several velocity shear layers in the device, but this paper is concerned with that which appears close to the conductors, at a position denoted by $\psi/I = -0.17$.

The instability observed on this shear layer is flute-like in form, for which the field curvature should be highly stabilising. It appears that the velocity shear is strong enough to overcome this effect and result in a net growth of the mode amplitude.

All the measurements presented in this paper were made with biased or floating single langmuir probes, usually in pairs. Two channels of fluctuating signals were sampled simultaneously by a transient recorder (variable sample

rate), digitized and transfered to a mini-computer for storage on disc and subsequent processing.

Spectral densities and correlation measurements used the procedures of Smith, Powers and Caldwell (1974). Full descriptions of the processing techniques, are given in separate papers by Conway and Elliott (1985 and 1987, a,b).

3. Experimental evidence

3.1 Potential Profiles.

A typical potential ϕ_f profile (fig. 3.) displays a minimum at $\psi/I = -0.03$, close to the boundary between the fast (2 x 10^4m/s) hot electrons streaming downtank (direct injected plasma) and the fast cold electrons and ions streaming uptank (reflected plasma) (Daly and Elliott 1982). In addition the profile shows a level region or plateau in ϕ_f close to the conductor surfaces ($\psi/I < -0.20$); this saturation region is marked by a sharp transition or knee implying a second shear layer.

3.2 Survey of density fluctuations

A complete survey of density fluctuation distribution and power spectra for the private flux region is given in Conway and Elliott (1987a). The mode here discussed exhibited a single spatial peak in the range $-0.23 < \psi/I < -0.17$, at a frequency of about 12kHz. At the maximum, $\tilde{n}/n$ was of the order 20 - 25%. Correlation measurements have shown that the fluctuations maintain uniform phase around a closed field line, and propagate across the field, longitudinally down the machine in the direction of the ion diamagnetic drift with a velocity in the laboratory frame of 2.6 ± 0.4 km s^{-1}. Coherence length is comparable to the mean wavelength. All these observations are consistent with the fluctuation being an $m \mp 0$ flute-like instability.

The plasma flow velocities have been estimated from the transverse scans of floating potential. We have no reliable method for correcting for the effect of plasma temperature, in order to obtain a more accurate estimate of the true plasma potential. However, we observe that in the vicinity of the shear, temperature is varying only slowly, so floating potential gradients are likely to yield a reasonable estimate of the true electric field, with the possibility of over-estimation. On this basis we estimate the velocities on either side of the shear to be 21 ± 2.5 km s^{-1} at $\psi/I = -0.15$ on the fast side, and essentially zero in the region close to the conductor surface. A classic K-H wave should propagate at the mean velocity i.e. ~ 10 km s^{-1}, or greater than the observed mode velocity by a factor of 4. This discrepancy has not been resolved, and must await a detailed analysis of the K-H mode in a quadrupole field.

3.3 Dispersion analysis

Four different methods were used to obtain the dispersion information, and these are discussed and contrasted by Conway and Elliott (1987b). One of these methods gave more detailed information than the others, the method of Beall et al (1982). The method computes the spectral density as a function of ω and k simultaneously, and is sensitive to low power fluctuations in the region of k-values of interest. The result is shown in fig.4 as a contour map in the ω-k plane, with the mode peak normalised to 1000. There are clearly two distinct branches to the dispersion curve, which cross at (ω,k) = (70 krad/s, 24 krad/m), the point at which the instability shows a very strong sharp maximum. Other methods of dispersion analysis yielded only the dispersion curves for the low k (< 24 krad/m) region, and did not directly display the cross-over. The physical mechanism for

the instability is not yet understood, but it is expected to relate to the intersection occurring at that point.

The lower branch is linear (non-dispersive) from 0 to 18 kHz and is identified as the K-H mode. Theory shows that K-H modes are non-dispersive when unstable, but have non-linear curves when stable. The upper branch, from 8 to 32 kHz exhibits a broadly reciprocal form, but has a very low spectral intensity except at the mode peak at the cross-over. This mode has not yet been identified: it appears not to be described by the comprehensive analysis of Hastie and Taylor (1971) for multipoles. (Two illustrative curves are fitted to fig.5: $k \propto 1/\omega$ and $k \propto 1/\omega^2$.)

4. Stability

We can estimate the relative strengths of the destablising shear and stabilising curvature effects in the following way. For a simple oscillator described by an equation of the form $\ddot{y} + \omega^2 y = 0$, the system oscillates stably if ω^2 is + ve, but exhibits unstable growth for ω^2 – ve. There will be an ω^2 value for the shear-driven (K-H) oscillations, and also for the curvature driven (flute) oscillations, and by considering these effects to be independent the ω^2 values add in a linear fashion: $\omega^2_{tot} = \omega_f^2 + \omega^2_{KH} + \ldots\ldots$ For a K–H mode (Gerwin 1968) $\omega^2_{KH} = -(\tfrac{1}{2}ku)^2$ where u is the velocity difference across the shear. We estimate $\omega^2_{KH} = -1.4 \times 10^{11}\ s^2$. Hastie and Taylor (1971) give a dispersion relation for low frequency, low k flute oscillations in a quadrupole field which yields $\omega^2_f = 1.9 \times 10^{12}\ s^{-2}$ for our conditions. This value needs to be adjusted to take account of finite k. For both cases, finite radial boundaries should also be taken into account. Nevertheless, this order of magnitude analysis shows that the system is close to marginal stability, justifying the conclusion that we are probably observing a K-H instability.

5. Discussion

Although the upper mode as yet remains unidentified, we can make general observations concerning certain features of the dispersion diagram. The fact that the instability is spatially located at the shear layer indicates that this is the energy source. The K-H mode showing a linear dispersion indicates an unstable mode; however, the strong peak appears at the coincidence point with the upper mode, indicating that a non-linear interaction of the modes is primarily responsible for the large amplitude. We suggest that the upper mode is itself intrinsically stable: it is very weak away from the peak. Non-linear interactions can allow the oscillation at the peak frequency ω_o to split into two secondary frequencies ω_1 and ω_2, provided $2\omega_o = \omega_1 + \omega_2$ and $2k_o = k_1 + k_2$. For a negatively sloping curve as observed (ω,k) values are available that will allow this. We therefore suggest that the weak oscillations of the upper mode are non-linear 'spreading' of the peak along the dispersion curve.

We believe this to be an unusually clear example of this type of reactive instability, essentially driven by a non-linear interaction of two separate modes.

References

Beall J.M. Kim Y.C. and Powers E.J. (1982) J. Appl. Phys. 53, 3933
Conway G.D. and Elliott J.A. (1987a) to be published in Plasma Physics and CF
Conway G.D. and Elliott J.A. (1987b) to be published in J. Phys. E.
Daly E.J. (1984) PhD Thesis, Univ. of Manchester.
Daly E.J. & Elliott J.A. (1982) Plasma Phys. 24, 923
Gerwin R.A. (1968) Rev. Mod. Phys. 40 (3). 652

Hastie R.J. & Taylor J.B. (1971) Plasma Phys. 13, 265
Phillips K. Rusbridge M.G. & Young K.M. (1978) Plasma Phys. 20, 653
Smith D.E. Powers E.J. & Caldwell G.S. (1974) IEEE Trans. Plas Sci. PS–2, 263.

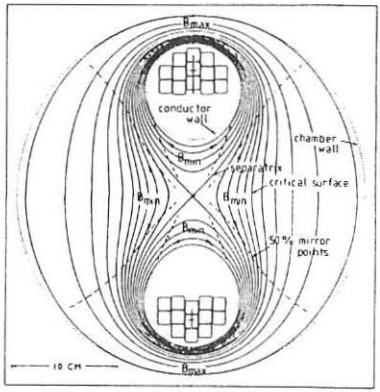

Fig 1 The Quadrupole Field

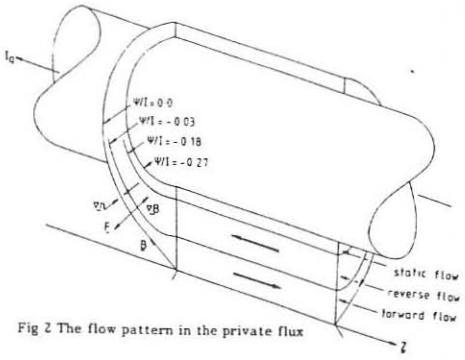

Fig 2 The flow pattern in the private flux

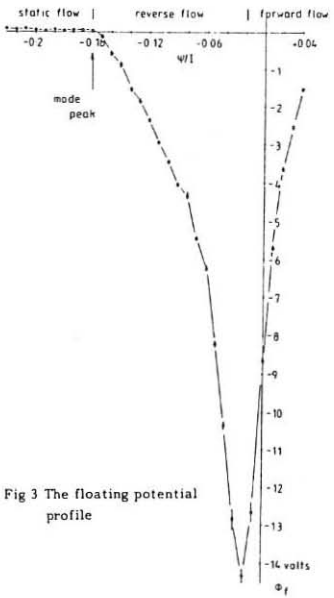

Fig 3 The floating potential profile

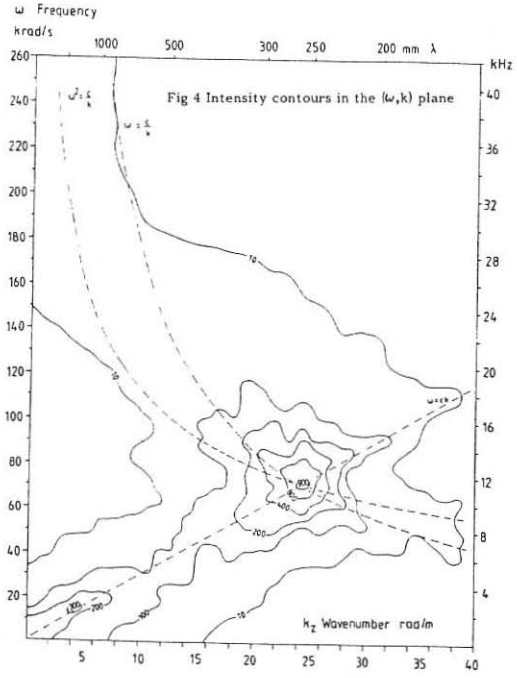

Fig 4 Intensity contours in the (ω,k) plane

OPTIMIZATION OF INITIAL GAS DISTRIBUTION IN PLASMA FOCUS DISCHARGES.

R.G.Salukvadze, E.Yu.Khautiev, N.G.Reshetnyak, V.I.Krauz, A.A.Batenyuk, A.Ch.Chkhaidze.

I.N.Vekua Institute of Physics and Technology, Sukhumi, USSR.

Energy build-up in power sources (W) for plasma focus (PF) discharge systems is accompanied by thermal flux increase on the electrodes and insulator and may lead to discharge current leakage from the plasma layer compressed beyond the inner electrode end. As a result of this, the current in the PF does not grow as $W^{1/2}$, and the neutron output (N) increasingly falls behind the value which corresponds to the well-known scaling $N \sim W^2$. In the systems with l>d (Mather type), matching is preferably accomplished by increasing the operating gas pressure. On using bigger-size electrodes, either the interelectrode gap "magnetic insulation" is reduced, or the current undergoes an additional decrease. However, in practice, the pressure may be increased up to a certain limit only, the discharge parameters remarkably degrading later on.

In the KPF-3 (40kV, 250kJ, l=24cm, d=11cm) and KPF-IM (22kV, 36kJ, l=24cm, d=8cm) devices, initial phases and PF discharge parameters have been studied versus the operating gas composition and pressure for stationary filling and as a function of neutral gas density distributions along the electrodes for pulsed filling of the interelectrode gap.

Two types of breakdowns and plasma sheath formations are found. In monoatomic gases (He, Ar), breakdowns take place along the insulator and an azimuthally homogeneous plasma layer is formed (Fig.1a). For molecular gases (N_2, CO_2, air), at relatively high initial pressures (>5Torr), from the very beginning layer is typically split into radial filaments which are almost uniformly distributed along the azimuth over the plane crossing the insualtor-inner electrode interface (Fig. 1b). For P=1-5Torr N_2 or CO_2 at the same W the breakdown types indicated above contest with each other. The filament formation process is vaguely observed in monoatomic gases as well, but only for extremal experimental conditions with the highest pressure and the lowest power. Under the ordinary conditions, even the slightest impurities of molecular gases in monoatomic ones result in formation of filament within the uniform current layer typical of pure monoatomic gases. The current fraction flowing through the filaments builds up with increase in impurity levels untill the current along the insulator becomes totally depressed (Fig.1c).

For pure deuterium, the initial discharge evolution phase has certain specifics. For low pressure (~2Torr), an uniform small-scale structure develops/1/which afterwards immediately levels out (Fig.2a). With the pressure being further in-

creased, within the small-scale structure background, a large-scale structure begins to evolve and there arise filaments similar to those observed in heavier molecular gas discharges but with less defined boundaries. For P~4Torr, these filaments immediately split into smaller ones and further on, the layer behaves almost in the same manner as for low initial pressures but a certain azimuthal nonuniformity remains. For P>8Torr the larger-scale structure becomes prevalent (Fig.2b). It should be noted that for P=8-10Torr at W~100kJ under the present conditions there exists the upper limit for optimum deuterium pressures with rather high neutron outputs still recorded for them.

The results obtained indicate that in molecular gas discharges, the breakdown types and plasma sheath shapes depend upon the W/P ratio. On increasing this ratio, e.g. by diminishing P, one can obtain conditions for uniform plasma layer formation.

The experiments conducted lead us to the conclusion that PF discharges have two optima of the initial pressures. At considerably low pressures an uniform plasma layer is formed, which drags the gas efficiently from the initial region of the discharge volume. Simultaneously, at the beginning of the interelectrode gap the electrical strength is essentially increased, this being necessary for spiking the discharge power in the end stage. The growth of intensity and total duration of hard X-radiation component generation testify this. Neutron outputs in low-pressure modes are smaller and less reproducible in a discharge-to-discharge series. Since the PF generated ion beam intensities (during an unstable period) grow, the trend indicated may be due to the fact that the low-pressure modes do not lead to the formation of a cumulative jet dense and prolonged enough, which serves as a plasma target/2/. As distinct from above situation, higher pressures result in degrading the conditions for ion beam generation because of various current leakages from the main channel, the neutron outputs being somewhat increased but not reaching the scaling values.

One of the ways for overcoming this contradiction is to create profiled initial gas distributions with lowered density near the insulator region. For this purpose, during the experiments on the KPF-IM device, deuterium was filled either through the system of apertures in the middle of the outer electrode or via the axial channel in the internal electrode. In the second case, the coaxial outlet was plugged by means of a cylindrical copper cap, its bottom being 7cm away from the inner electrode end. Gas amount and its distribution along the electrodes have been adjusted within the certain limits by varying the delay (τ) between the opening time for the electrodynamic valve and the discharge onset.

For radial fillings at small τ, the discharge behaviour is similar to the low-pressure mode described above. During t= = 0,6-0,8μs, a whole number of discharge current drops and

corresponding voltage spikes is observed accompanied by the intense flashes of hard X-rays. The current layer becomes already instable at the stage of radial compression and splits up into a number of filaments; current transfer in each of the filaments is accomplished by electron beams/2/. On increasing τ, the instable phase duration is reduced. The neutron output over the whole operating range of delays remains at the low level ($\sim 10^9$ n/ discharge at w=36kJ).

Fig.3 shows the deuterium pressure variation within the insulator region (dashed line) and near the electrode ends versus τ, for the second type of filling with two values for pressure within the undervalve region: 1 atm. and 3 atm. Fig.4 shows N versus τ for the same time-scale as in Fig.3. It is seen that on increasing the gas amount, neutron outputs rapidly grow untill the optimum pressure difference is mantained. When the pressure near the insulator begins to overgrow the pressure near the electrode ends neutron outputs become smaller than those for stationary fillings (horizontal line).

Thus, on using the axial feeding method for the operating gas, one can obtain the best optimal conditions for initial discharge phase evolution and for increasing the neutron generation efficiency.

REFERENCES.

1. Yu.A.Kolesnikov, N.V.Philippov, T.I.Philippova. Proc.7 Int.Conf. on Ionis.Phenomena in gases, Belgrad, 1965, v.2, pp.833-837.
2. V.I.Krauz, R.G.Salukvadze, E.Yu.Khautiev. Fizika Plazmy, v.11, N3, 1985, pp.281-287.

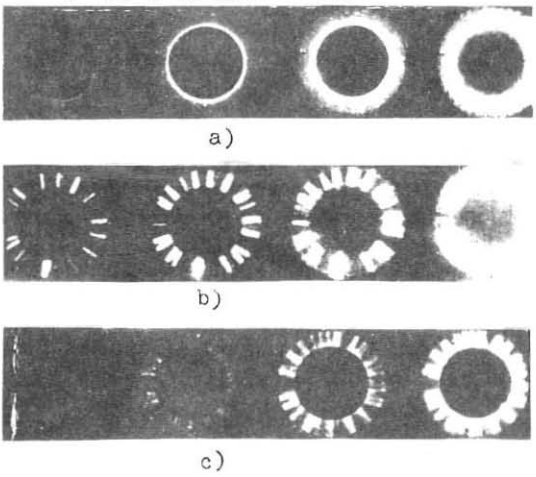

a)

b)

c)

Fig.1. W= 36 kJ, Exposure time 0,5 μs

a) 10 Torr Ar;

b) 15 Torr N_2;

c) 12 Torr Ar + + 4 Torr of air.

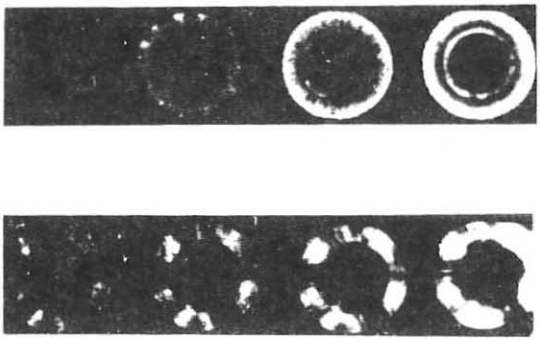

Fig. ... λ = ... nm, exposure time ... μs;
a) 2 Torr D_2;
b) 16 Torr D_2;

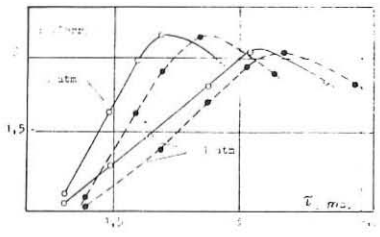

Fig.3

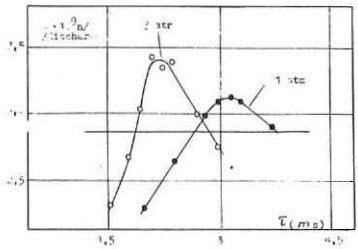

Fig.4

EMERGENCE OF CHARGED PARTICLE ANISOTROPY IN THE MAGNETIZED PLASMA DUE TO ION-ION COLLISIONS

Vikhrev V.V., Dobryakov A.V., Rozanova G.A., Yushmanov P.N.

I.V.Kurchatov Institute of Atomic Energy, Moscow, USSR

ABSTRACT

In a plasma confined by a magnetic field the ion-ion collisions can result in the emergence of anisotropy in their distribution function. This effect emerges, when the collisions provide the particle distribution different from the initial one. In particular, the anisotropy should be observed at the relaxation of the isotropic, but not equilibrium, distribution to the Maxwellian one. The anisotropy can also emerge from the Maxwellian distribution of particles, when inelastic scatterings, resulting in the transformation of these particles into another ones, occur. The emergence of anisotropy in the charged fusion products at their isotropic birth in a plasma can serve as an example.

The anisotropy emergence effect is manifested most vigorously in the systems with high β, when the Larmor radius of particles is comparable with the effective dimensions of the system. The calculations of the charged particle distribution anisotropy in the Z-pinch plasma are given in the paper. Both the relaxation to the Maxwellian distribution and the birth of charged particles in the plasma as a result of nuclear collisions are considered. It is shown that in the non-skinned Z-pinch, at the currents $\sim$1MA, more than 90% of all trit ons and He^3-nuclei, as a result of α-α-reaction in the Z-pinch, move towards a cathode. The deuteron distribution function in the Z-pinch is found to become anisotropic due to elastic scattering among themselves at the relaxation in this case, the particles with an energy higher than the average thermal one move mainly to the cathode; with the lower one, drift to an anode. High energy particles, responsible for neutron radiation, drift to the cathode with a velocity exceeding the thermal velocity of these particles in the plasma. As a result, the fusion neutron radiation from the Z-pinches can be anisotropic.

CONFINEMENT STUDIES OF RFP'S IN HIGH DENSITY REGIMES IN ETA-BETA II

Antoni V., Buffa A., Carraro L., Costa S.,
Flor G., Flora F., Gabellieri L., Giudicotti L., Innocente P.,
Martini S., Ortolani S., Paccagnella R.,
Puiatti M.E., Scarin P., Valisa M.

Istituto Gas Ionizzati del C.N.R.
EURATOM-ENEA-CNR Association, Padova, Italy

The sustainment of the plasma density is one of the crucial issues in RFP plasma confinement. In fact at low densities, though high temperatures are easily achieved, β_e values are smaller and confinement times are usually degraded [1], corresponding to plasma electrical resistivities largely exceeding the classical value [2].

Pellet injection has already proven to be an efficient plasma fuelling technique [2, 3]. In this paper recent results obtained with the injection of large pellets [4] into ETA-BETA II discharges are discussed in terms of electron temperature, β_e, electrical resistivity and energy confinement time. Depending on the time of pellet injection, on the background filling density and on gas wall loading conditions, various density versus time behaviours can be obtained [4]. Therefore two sets of high density discharges with slightly different time behaviours obtained with pellet injection [4] have been analysed and compared with two sets with no density control.

The electron density has been measured by means of a two colour CO_2 interferometer and the electron temperature by both a soft x-rays Si(Li) detector and a 7-point Thomson scattering system. All the data are averaged over several similar discharges and also over time intervals of about 200 μs in order to get sufficient photon statistics for the PHA.

Figures 1 and 2 show the electron densities and the corresponding temperatures versus time. The sets with pellet injection are identified by symbols in full. The differences in temperature though significant appear to be less pronounced than those in density: this systematically results in higher $\beta_{\theta e}$ values at higher densities. This is illustrated in Fig. 3, where $\beta_{\theta e} \equiv \langle nT_e \rangle / (B_\theta^2(a) / 2\mu_o)$ takes into account the experimental T_e profiles shown in Fig. 4 and 5 for the cases with and without pellet respectively.

The time variation of the resistivity anomaly factor Z^*_{eff} [1, 2] is shown in Fig. 6. In fact a value of 4 for Z^*_{eff} can be easily justified by computing the resistivity from an helicity balance model [2]. When the density is sustained and maintained about constant the resistivity remains practically classical. When the density is not controlled higher values are

observed at late times, which, as observed in the past [1] could be due to both and increase of the ion effective charge and a change in the profiles of Z_{eff}, T_e and current density. The differences in β and resistivity combine into the energy confinement time $\tau_{Ee} \equiv \langle nT_e \rangle / VI \propto \beta T_e^{3/2} / Z^*_{eff}$ so that improved confinement is also associated to the higher densities.

The dependence of $\beta_{\theta e}$, Z^*_{eff} and τ_{Ee} on I/N observed in the past [1] is confirmed also by these results. It must be emphasized that in the density sustained discharges the I/N parameter can now be kept constant in time at $\sim 3.5 \cdot 10^{-14}$ Am. This is favourable to the prospects of new experiments [5] and indicates the plasma current termination as probably due to lack of equilibrium. It would be therefore very important to confirm also in ETA-BETA II the possibility of extending the pulse length by improving the equilibrium control [6].

ETA-BETA II equilibrium relies on a conducting shell with b = 0.145 m, $\rho = 5 \cdot 10^{-8}$ Ωm. Therefore one might expect [7] a plasma displacement of $\sim$ 8 mm immediately after the setting up phase and subsequently increasing with a velocity of $\sim$0.5 mm/ms. The time behaviour of the plasma shift during a standard discharge, as derived from poloidal flux measurements is shown in Fig. 7(a) (solid line). The initial value is close to the theoretical prediction, whereas the subsequent rate of increase is greater by a factor $\sim$4, which is probably due to the presence of 12 poloidal gaps in the conducting shell. The discharge generally terminates when the shift is $\sim$ 10% of the minor radius.

Some preliminary equilibrium control has been obtained by varying the ratio of the currents in the internal and external poloidal field inductors. This system has no flexibility and, due to the increasing flux needed to power crow-bar the discharge, produces a B_v ramping from $\sim$2 to $\sim$3 times the one theoretically required without a shell, B_v^0 [7]. Nevertheless, since the diffusion of this field through the shell is relatively slow (< 20% penetrates after 1 ms), during the first part of the discharge its effect is beneficial to the plasma behaviour. Indeed, as shown in Fig. 7(a), for a discharge with vertical field (dashed line) the plasma shift is < 1 cm for $\sim$1 ms. As a consequence, the plasma resistance is lower by $\sim$ 10-15% (see Fig. 7(b)). A clear improvement in terms of allowed range of field and density programming is also observed, which allows e.g. to obtain discharges without the initial density "pump-out" (see Fig. 8). On the other hand the discharge is always prematurely terminated after $\sim$ 1.4 ms, when the penetrated vertical field ($\sim$20-30% of B_v^0) causes a large inward shift.

In conclusion, sustaining the density by pellet injection in ETA-BETA II results in higher β and improved plasma confinement. Preliminary experiments with a vertical field indicate that this performance could be furtherly improved by a better equilibrium control.

/1/ Alper, B., et al. Nucl.Fus. **26** (1986) 1256.

/2/ Antoni,V., et al. Proc. 11th IAEA Conf. (1986) to be published.

/3/ Shoenberg, K.F. et al. ibidem.

/4/ Antoni, V. et al. "D_2 pellet injection in ETA-BETA II plasma" This Conference.

/5/ Antoni,V. et al. 13th EPS Conf. Vol.10C, Part I, 385.

/6/ Ortolani,S. et al. "RFP operation with a thin shell". This Conf.

/7/ Mukhovatov,V.S., Shafranov,V.D., Nucl.Fus.**11** (1971), 605.

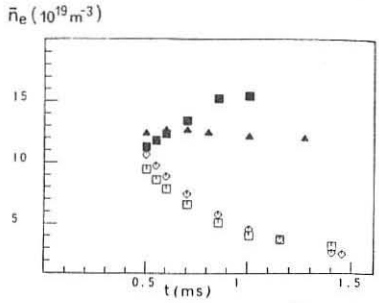

FIG.1

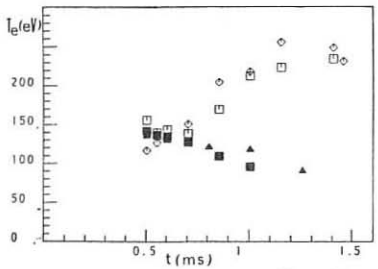

FIG.2

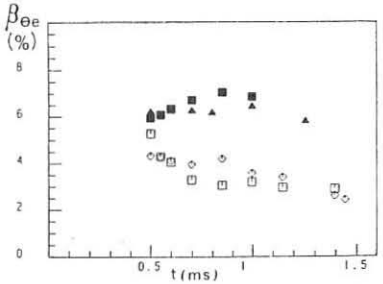

FIG.3

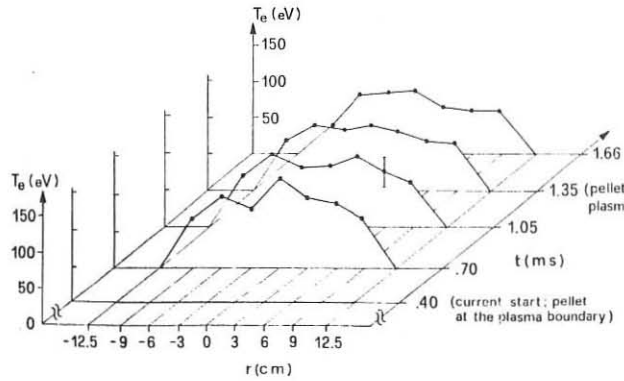

FIG.4

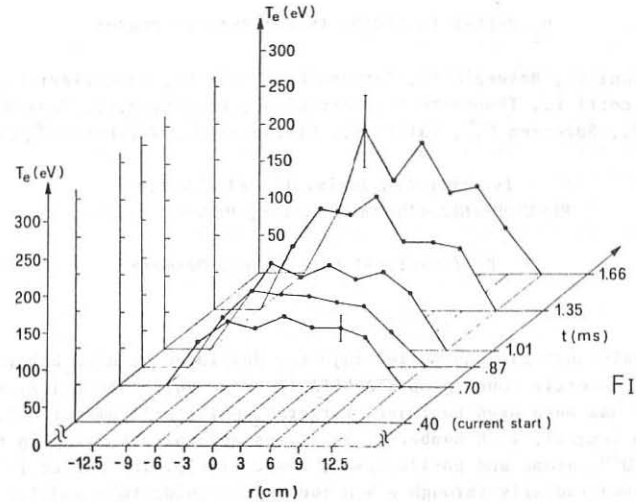

FIG.5

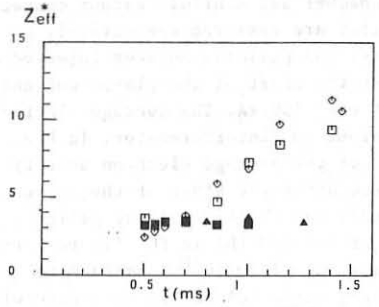

FIG.6

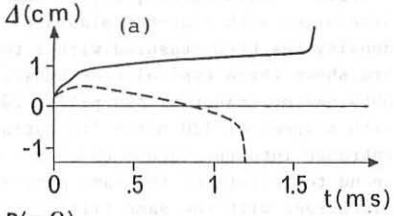

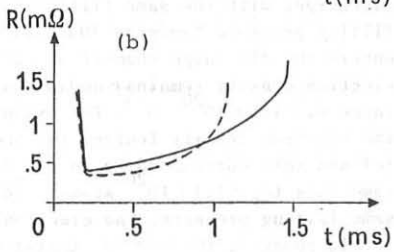

FIG.7

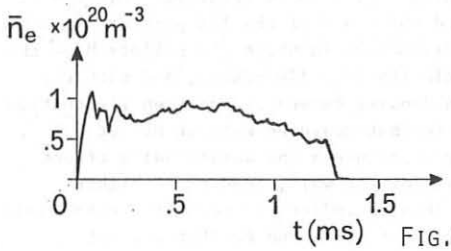

FIG.8

D_2 PELLET INJECTION IN ETA-BETA II PLASMA

Antoni V., Baseggio E., Carraro L., Flora F., Gabellieri L., Giudicotti L., Innocente P., Martini S., Puiatti M.E., Sass B.*, Scarin P., Sørensen H.*, Valisa M., Villoresi P., Weisberg K.*, Zago S.

Istituto Gas Ionizzati del C.N.R.
EURATOM-ENEA-CNR Association, Padova, Italy

* Risø National Laboratory, Denmark

A single-shot gas gun pellet injector developed by Risø Laboratory has been satisfactorily running on ETA-BETA II since July 1986 [1]. Recently the system has been used to inject larger D_2 pellets (diameter < 1.4 mm and 2.5 mm length), with number of particles and speed varying in the range $0.2\text{-}1.2 \cdot 10^{20}$ atoms and 60-170 m/sec, respectively. The pellet is injected in the plasma radially through a 4 m long nylon guide tube and 1.2 m of free flight in a differential pumping chamber and manifold vacuum connection. The speed and the mass of the pellet are measured respectively by optical detectors and a microwave cavity. The pellets have been injected at different times before, during and after the start of the plasma current in discharges with flat-top plasma current of $\sim$ 150 kA. The average electron density has been measured with a two-colour CO_2 interferometer. In Fig. 1 are shown three typical time behaviours of the average electron density obtained by injecting the pellet 200 μsec after the start of the current with a speed of 120 m/sec (the arrow indicates the time of the pellet entrance into the vacuum chamber). Curves (a) and (b) in the figure correspond to pellets of the same nominal mass ($m_p = 1.2 \cdot 10^{20}$ atoms) and to discharges with the same filling pressure; curve (c) refers to a case with filling pressure lower by 30% and $m_p = 8 \cdot 10^{19}$ atoms. When the pellet enters the discharge chamber at the start of the plasma current, the electron density remains constant during the discharge, with a value in the range $0.7\text{-}1.5 \cdot 10^{20}$ m^{-3}. For example, Fig. 2 shows the time evolution of the electron density (curves (a) and (b)) and of the I/N parameter (curves (c) and (d)) corresponding to two discharges in which the pellets have the same mass ($m_p = 1.1 \cdot 10^{20}$ atoms), velocity ($v_p = 110$ m/sec), and with the same filling pressure. The electron density curves show a high fluctuation level; however, the $\delta n/n$ is similar to that measured without pellet [2].

The density sustained discharges produce a gas wall-loading effect that gives a significant gas influx from the wall, leading to higher densities also in the edge region. This is indirectly seen from the visible line emission of low ionization stages of C, Cl and Fe that are not

observed in non-sustained standard discharges.

The time behaviour of the D_α line measured through a dump in front of the entrance pipe of the pellet is quite different in discharges with and without pellet. In particular, with pellet, the emission persists during the discharge (Fig. 3). With small pellets the effect consists only in the addition of a spike in the emission, suggesting that the pellet is poloidally deflected and moved out of the line of sight [3]; with larger pellets, however, the emission persists, possibly indicating a smaller deflection. In the latter case it is possible to infer that the ablation time is comparable to pulse lenght ($\sim$ 1 msec).

The effect of the pellet is also seen in the time behaviour of line emission in the XUV spectral range. For example, Fig. 4 shows a comparison of OVI emission with and without pellet. In general a higher emission from impurities and deuterium is observed. The radial emission profile of OIII and OIV, obtained by inverting the signals measured by a multichord Ebert spectrometer, are not too different from those measured without pellet (Fig. 5). In fact, the emission after the ionization peak, comes from the external region of the plasma, both for discharges with and without pellet, consistently with the outward shifted equilibrium of the ETA-BETA II plasma, which has no vertical magnetic field control [4]. However with the pellet, the D_α line emission comes from a region wider than without pellet (Fig. 5), indicating that neutral atoms are present in a wider edge region. The average neutral density, however, is, within a factor of two, similar to that without pellet ($\sim 10^{18}$ m^{-3}).

The electron temperature profiles remain fairly flat throughout the discharge and, compared with discharges without pellet, the central temperature increases little [4]. However the resistivity remains almost classical and higher β_θ values are achieved.

REFERENCES

[1] Antoni V., et al., 11th Int. Conf. Pl. Phys. Contr. Nucl. Fus. Res., Kyoto (1986), to be published.

[2] Antoni V., et al., "Fluctuation studies on ETA-BETA II experiment", this Conference.

[3] Schoenberg K.F., et al., 11th Int. Conf. Pl. Phys. Contr. Nucl. Fus. Res., Kyoto (1986), to be published.

[4] Antoni V., et al., "Confinement studies of RFP's in high density regimes in ETA-BETA II", this Conference.

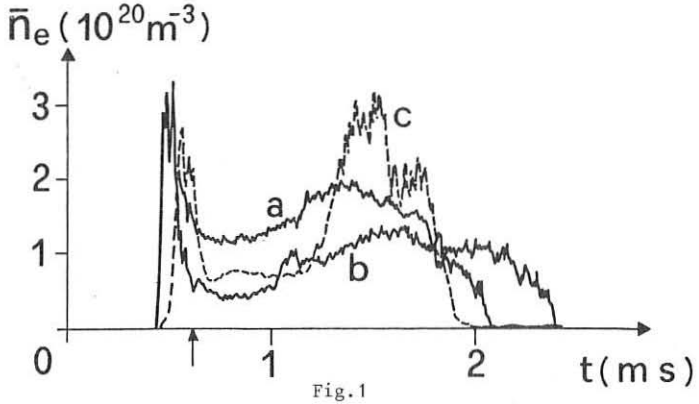

Fig.1

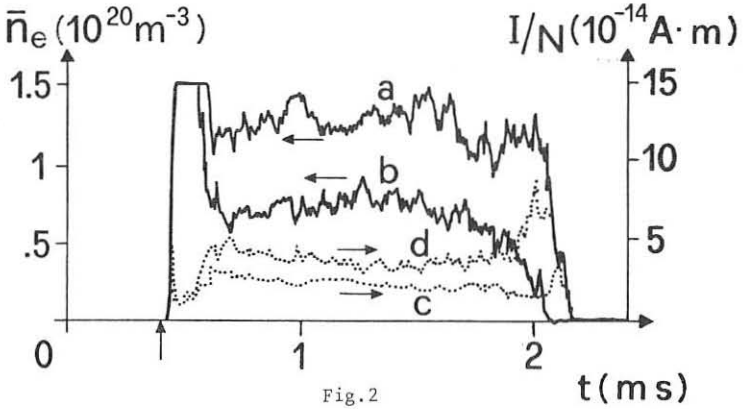

Fig.2

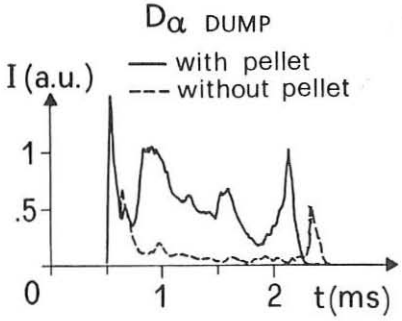

Fig.3

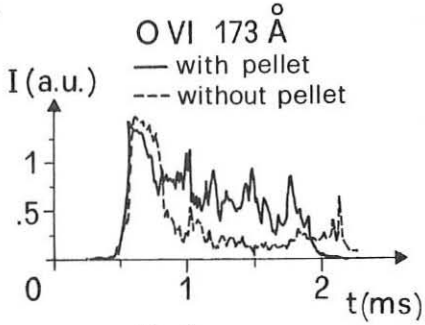

Fig.4

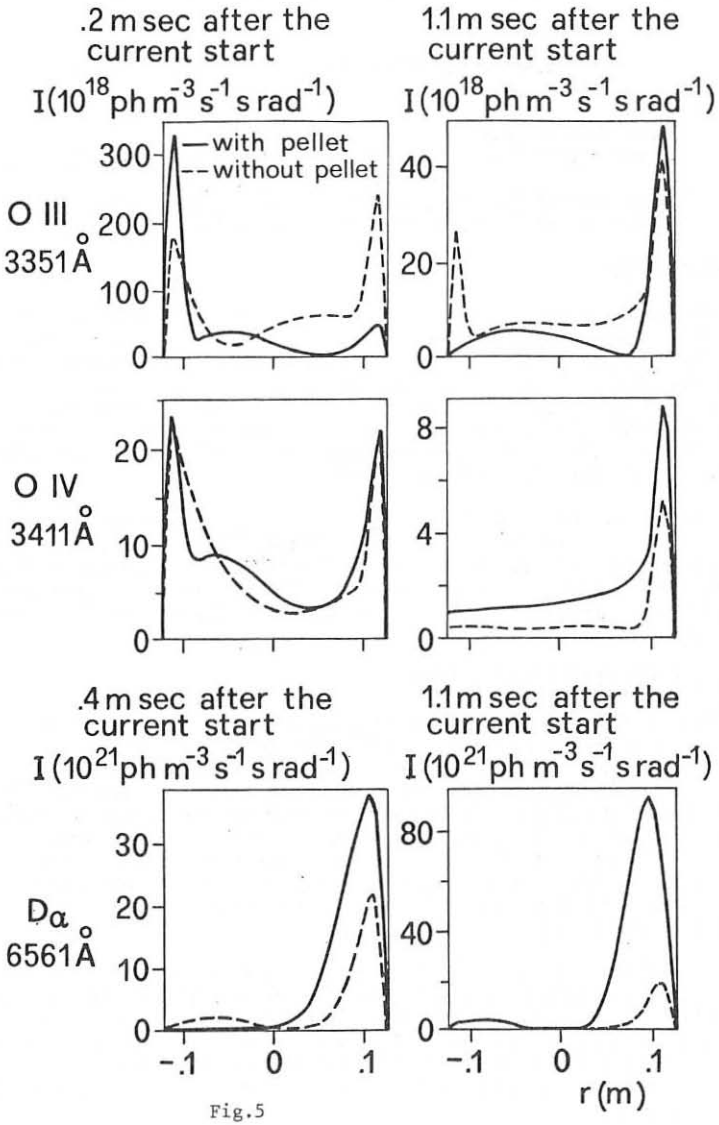
.2 m sec after the current start
1.1 m sec after the current start
I(10^18 ph m^-3 s^-1 s rad^-1)
—with pellet
--without pellet
O III 3351 Å
O IV 3411 Å
.4 m sec after the current start
1.1 m sec after the current start
I(10^21 ph m^-3 s^-1 s rad^-1)
Dα 6561 Å
r (m)

Fig.5

SOFT X-RAY ARRAY RESULTS ON REPUTE-1 REVERSED FIELD PINCH

N.Asakura, Y.Nagayama, S.Shinohara, H.Toyama
K.Miyamoto, N.Inoue*

Department of Physics, Faculty of Science,
University of Tokyo, Hongo 7-3-1, Bunkyo-ku, Tokyo 113, Japan

*Department of Nuclear Engineering, Faculty of Engineering,
University of Tokyo, Hongo 7-3-1, Bunkyo-ku, Tokyo 113, Japan

1. INTRODUCTION

Recently, many experiments have shown that the RFP plasma can be maintained for a long time than the magnetic diffusion time and that total toroidal magnetic flux is generated in the sustainment phase of the RFP discharge /1,2/. Experimental and numerical results indicate that these phenomena are due to a relaxation process leading to the lower energy state and that this process is closely related to MHD instabilities or fluctuations /3,4,5/. The primary interest in RFP physics has concerned on the causal mechanism of this relaxation process.

Soft X-ray measurements have been made with Surface Barrier Diode (SBD) arrays in REPUTE-1 RFP device (R/a = 82/22 cm) /6,7/. Applying the tomography technique to the soft X-ray data, we can reconstruct the 2-dimensional images of the soft X-ray emissivity and can investigate the dynamic mechanism of the relaxation process in the RFP plasma, experimentally.

2. SOFT X-RAY MEASUREMENT SYSTEM

Figure 1 shows the schematic view of the soft X-ray measurement system. The arrays of 7 SBDs and 11 SBDs are arranged to view a minor cross section of the plasma from the vertical and horizontal diagnostic ports at the same toroidal position, respectively. The soft X-rays emitted from the plasma are imaged on each diode array, passing through a circular pinhole of 5 mm diameter. In front of each detector, 4μm polypropylene foil filter is placed in order to cut off visible and VUV photons due to the line radiation of light impurities. The line-averaged soft X-ray data are reconstructed to the cross-sectional emissivity profile by the tomography technique /8/.

In addition to these arrays, 2 sets of simple arrays consisting of 2 SBDs with 4μm polypropylene filter and viewing $\pm$7 cm off-axis in the poloidal direction, are located at different toroidal positions. Toroidal propagation of the soft X-ray fluctuation can be observed by them. The magnetic fluctuation measurements are also carried out by the use of magnetic probes which are set at the plasma boundary, simultaneously.

3. EXPERIMENTAL RESUNTS

Figure 2 shows typical time evolution of the plasma parameters and line-of-sight soft X-ray emission. In the sustainment phase of the RFP plasma discharge, the field reversal ratio F and pinch parameter Θ remain -0.4 and 2.2, respectively. The intensity of the soft X-ray emission depends mainly on the plasma current I_p and filling pressure P_f. In the case of relatively low filling pressure (P_f < 1.6 mtorr) and high plasma current (I_p > 200 kA) discharge, the soft X-ray emissivity increases enough to be observed. When the value of I/N exceeds 5×10^{-14} Am, the characteristic fluctuations appear in the soft X-ray signals as shown in Fig.2.

Figure 3 shows the profiles of the soft X-ray emissivity in the period of t = 1.21 - 1.28 ms for the same shot as Fig.2. The emissivity increases rapidly in the hot core region from t = 1.24 ms. In this phase, the displacement of the hot core is small and the contour of the emissivity profile is almost axisymmetrical. After a few precausal oscillations, an abrupt large crash of the emissivity profile starts from t = 1.27 ms. Figure 4 shows the time evolution of the emissivity profile during the large crash. The displacement of the hot core becomes large ($\Delta r/a > 0.2$) and the emissivity profile is distorted. In the period of t = 1.280 - 1.286 ms, the emissivity profile changes to a hollow one. This result indicates the reconnection of the magnetic flux surfaces. After the crash, the profile of the soft X-ray emissivity increases in the outer region of the plasma ($r/a > 0.7$).

The toroidal propagation of the soft X-ray fluctuation can be measured by the additional SBD detectors. The result suggests that the toroidal mode of the large crash has very low n number.

The magnetic fluctuation measured at the plasma boundary has dominant m = 1 mode with the frequency of ~100 kHz. The amplitude of the m = 1 magnetic fluctuation and the differential signal of the toroidal magnetic flux are increasing as the soft X-ray emissivity profile peaks in the central hot region. Corresponding to the succeeding crash process of the emissivity profile, the amplitude of the m = 1 magnetic fluctuation decreases rapidly and m = 0 magnetic fluctuation appears for several μs.

4. SUMMARY

In the sustainment phase of the RFP discharge, the characteristic fluctuation of the soft X-ray emissivity repeats several times. There happen the peaking and subsequent large crash of the emissivity profile after a few precausal oscillations. One period of the soft X-ray fluctuation ranges from 60 to 100 μs. The amplitude of the soft X-ray fluctuation increases and the period becomes shorter as the plasma current increases in the same discharge. Whereas the duration of the large crash always remains about 30 μs (corresponding to $\sim100\times t_A$ in REPUTE-1 experiments) and toroidal mode of this fluctuation has very low n number.

In this crash process, the specific distortion of the emissivity profile can be observed. This result indicates the reconnection of the magnetic flux surfaces which is predicted by MHD non-linear reconnection model /4,5/. The behavior of the magnetic fluctuations correlate very well to this soft X-ray fluctuations. We find that the soft X-ray fluctuations observed in our experiments reflect the relaxation mechanism of the RFP plasma. These phenomena are considered to be driven by the global MHD activities.

REFERENCES

/1/ D.A. Baker et al. : 10th Int. Conf. Plasma Phys. Contr. Nucl. Fusion Res., London 1984, Report IAEA-CN-44/D-II-2.
/2/ P.G. Carolan et al. : 10th Int. Conf. Plasma Phys. Contr. Nucl. Fusion Res., London 1984, Report IAEA-CN-44/D-II-3.
/3/ R.G. Watt, R.A. Nebel : Phys. Fluids 26 (1983) 1168.
/4/ K. Kusano, T. Sato : Nucl. Fusion 26 (1986) 1051.
/5/ D.D. Schnack, E.T. Caramana, R.A. Nebel : Phys. Fluids 28 (1985) 321.
/6/ H. Toyama et al. : 12th European Conf. on Contr. Fusion and Plasma Phys. 9F (1985) 602.
/7/ N. Asakura et al. : Plasma Phys. 28 (1986) 805.
/8/ S. Tsuji et al. : Nucl. Fusion 22 (1982) 1082.

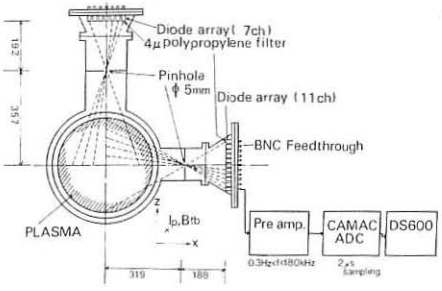

Fig. 1. Schematic view of SBD arrays; the arrays of 7 SBDs and 11 SBDs are installed on the vertical and horizontal ports, respectively. The soft X-rays emitted from the plasma are imaged on each SBD array, passing through an imaging pinhole of 5 mm diameter.

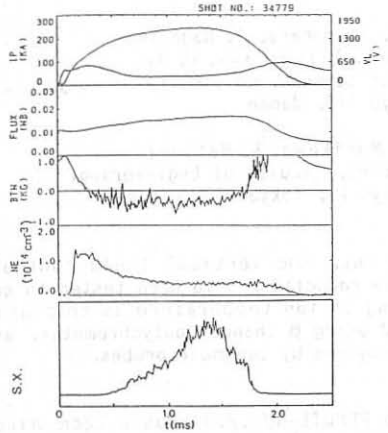

Fig. 2. Time evolution of the RFP plasma parameters for high I/N discharge; I/N ~ 5×10^{-14} Am in the sustainment phase. Plasma current I_p, loop voltage V_l, toroidal magnetic flux Φ_t, toroidal magnetic field at the wall B_{tw} and soft X-ray signal are shown.

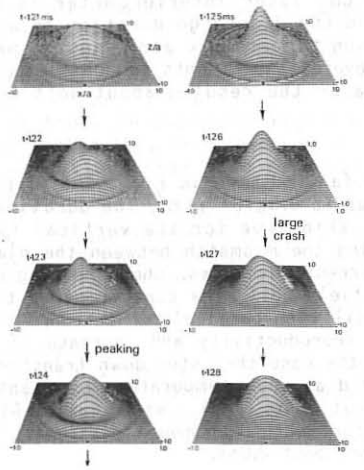

Fig. 3. Profiles of soft X-ray emissivity in the period of t=1.21-1.28 ms for the same shot as Fig.2.

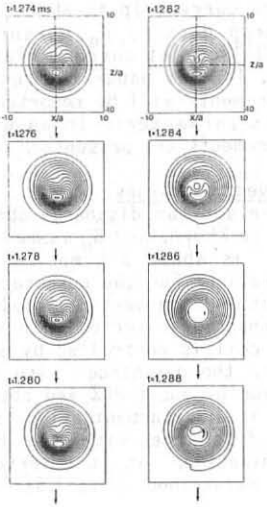

Fig. 4. Contours of the soft X-ray emissivity profile in the large crash as shown in Fig.3.

RECENT EXPERIMENTS OF THE RFP DEVICE, REPUTE-1

H. Toyama, K. Miyamoto, S. Shinohara, Y. Nagayama
K. Yamagishi, N. Asakura, A. Fujisawa, H. Ji
Department of Physics, Faculty of Science, University of Tokyo
Bunkyo-ku, Tokyo 113, Japan

N. Inoue, Z. Yoshida, J. Morikawa, K. Hattori
Department of Nuclear Engineering, Faculty of Engineering,
University of Tokyo, Bunkyo-ku, Tokyo 113, Japan

Abstract

The various operational conditions, the vertical field control, carbonization and toroidal field ripple reduction, have been tested to get better plasma discharges. The scaling of ion temperature as to plasma current and density has been obtained using 8 channel polychrometer, and the edge plasma properties have been studied by Langmuir probes.

Introduction

The reversed field pinch device REPUTE-1/1,2,3/ has a 22cm minor radius and an 82cm major radius. Ordinarily the discharges are done without limiters, and the main plasma parameters are as follows: the plasma current Ip is about 200kA at that flat top, the chord-averaged electron density $\bar{n}_e$ measured with CO_2 laser interferometer is 0.2-0.6x10^{14}/cm^3 at current flat top, and the discharge duration is about 2.2ms. In this paper the results of ion temperature and Langmuir probe measurements will be reported after several experiments to achieve better plasma parameters. In an another paper the results about soft X-ray measurements are presented. /4/

Improved discharges

The optimum discharge obtained so far is shown in Fig.1. The flat top of Ip is 250kA, and $\bar{n}_e$ is maintained up to 0.5x10^{14}/cm^3. The duration of 3.2ms is about 3 times of shell's skin time for the vertical field penetration. For the purpose of reducing the mismatch between the plasma current and the vertical field coil current waveforms, ohmic heating coil is connected in series with vertical field coil. The current of vertical field coil is controlled by a shunt coil with parallel connection. As the result, the discharges with improved reproductivity and increase of the duration by about 20% are obtained in the case that step down transformer ratio is 4:1. Carbonization is performed at room temperature by means of glow discharge with the H_2-CH_4 (ratio is 7:3) mixed gas. After carbonization, it is observed that 'pump-out' phenomenon disappears and $\bar{n}_e$ is maintained up to 1.5x10^{14}/cm^3 for about 2.0ms.

Ripple reduction experiments

To reduce toroidal field ripple, trimming coils have been wound at the outer side of the torus between each toroidal coil. As a rough estimate these trimming coils are expected to reduce toroidal field ripple from 1.5% to 0.3% at the plasma edge. The trimming field is applied 1ms after the plasma initiation, when the plasma is in the RFP-configuration phase.

Consequently, one-turn loop voltage decreases from 260V to 230V with the increase of the plasma current from 220kA to 230kA. Furthermore, the low frequency part ranging from 4kHz to 10kHz of toroidal field fluctuations is found to be reduced, especially outside the reversal surface, which is mainly m=1 mode and has good coherence in space and time.

Measurements of ion temperature

The ion temperature Ti has been measured from Doppler bloadening of OV line(2781A), and the dependence of ion temperature on plasma parameters has been studied at current flat top. Figure 2 shows the time evolution of oxygen lines. For comparison, the central electron temperature of plasma Te is calculated from Spitzer's formula. In typical discharges Ti is more than 100eV, which is higher than Te around 60eV to 80eV. It is found that Ti increases with the decrease of $\bar{n}_e$, with the increase of Ip. As the result, it is shown that Ti is proportional to $Ip^{0.5}/\bar{n}e$(fig.3); the range of the parameters is following; Ip from 100kA to 250kA, $\bar{n}_e$ from 0.1 to $2.5\times10^{14}/cm^3$ at the current flat top. As for the dependence of Ti on the drift parameter, which is defined as the ratio of electron drift velocity to its thermal velocity, it is shown that Ti increases linearly with increase of the drift parameter from 0.0 to 1.0×10^{-2}.

Edge plasma

Langmuir probes, which consist of four cylindrical molybdenum tips, are used as double probes or single probes to measure radial profiles of ion saturation current I_{sat}, floating potential V_f and their fluctuations. At the reversal surface region, (1) I_{sat} has a steep gradient; (2) V_f has minimum value in radial direction; (3) fluctuation level of toroidal and poloidal magnetic fields, I_{sat} and V_f, are higher than those in the other regions. Moreover, a frequency spectrum and a wavenumber-frequency spectrum is measured for both potential and density fluctuations near the reversal surface (Figs.4 and 5). Potential and density fluctuations show quite different properties at the same spatial point, which suggests electromagnetic characterstics. For Ip = 110kA case, the fluctuation level at the central region is also measured. It is shown that fluctuations have almost the same level at the edge region as the central region, which is typically 2-6% for magnetic fields, and around 20% for density.

Conclusion

The discharges of REPUTE-1 have been improved by means of the vertical field control, carbonization and toroidal field ripple reduction. The ion temperature is proportional to $Ip^{0.5}/\bar{n}_e$, and the results of fluctuation's spectrum by Langmuir probe measurements are presented.

Reference

/1/ H. Toyama et al., Proc. 12th EPS. Conf. Controlled Fusion and Plasma Phys., Budapest, 1, 602(1985)
/2/ N. Asakura et al., Plasma Phsyics and Controlled Fusion, 28, 805(1985)
/3/ N. Asakura et al., Proc. 11th Int. Conf., Kyoto(1986)
/4/ N. Asakura et al., Proc. 14th EPS. Conf. Controlled Fusion and Plasma Phys., Madrid(1987)

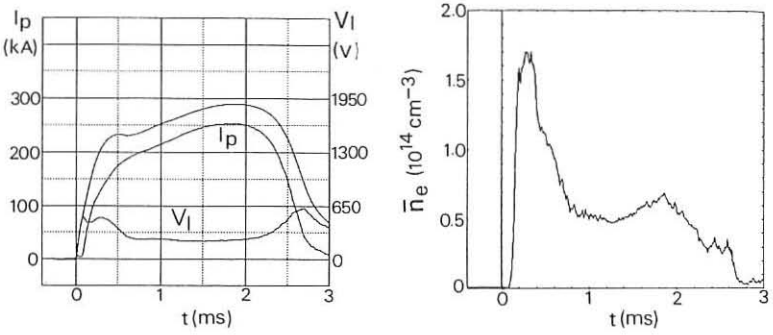

Fig.1. Plasma current, one-turn loop voltage(left) and chord-averaged electron density(right) of the optimum discharge in REPUTE-1.

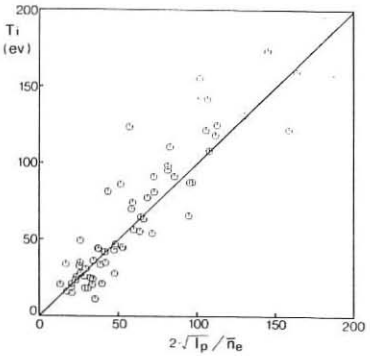

Fig.3. Dependence of ion temperature from Doppler bloadening on plasma current in kA units and density in 10^{14}/cm^3 units.

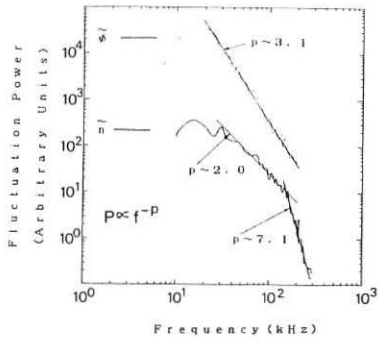

Fig. 4. Frequency spectrum for density and potential fluctuations near the reversal surface.

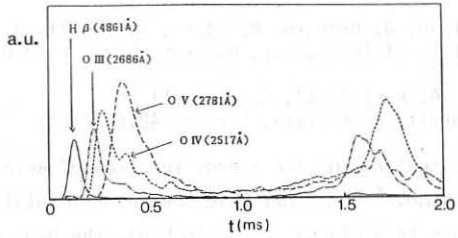

Fig.2. Time evolution of oxygen lines of typical discharges.

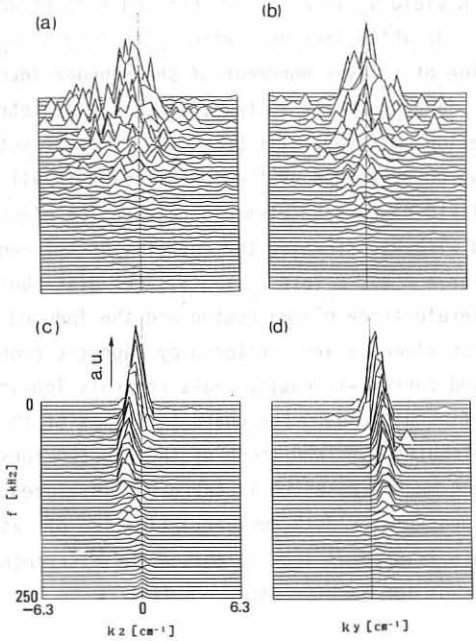

Fig. 5. Wavenumber-frequency spectrum for density((a),(b)) and potential((c),(d)) fluctuations near the reversal surface. Here, y and z indicate poloidal and toroidal directions.

Enhanced Confinement of Accelerated Ions in Focused Discharges

V. Nardi, L. Bilbao, J. Brzosko, M. Esper, C. Powell, D. Zeng
Stevens Institute of Technology, Hoboken, New Jersey 07030

A. Bortolotti, F. Mezzetti
Universita di Ferrara, Ferrara 48100 Italy

Characteristic features of the energy spectrum of accelerated D^+ ions with energy 0.3 MeV $\lesssim E \lesssim$ 7 MeV have been experimentally determined for the confined ions in a plasma focus pinch via the D-D neutron spectrum and for the ejected ions via a variety of ion spectrometers, with or without nanosec time resolution. A strong correlation exists between (i) neutron yield y_n in a single shot and (ii) escaping ion-beam fluence $d^2\phi/d\omega\, dE$ which increases with y_n as long as $y_n \lesssim 2\,\bar{y}_n$, where $\bar{y}_n$ is the mean value of y_n over hundreds of shots under identical conditions of pressure, capacitor-bank voltage, electrode geometry. In shots with $y_n > 3\,\bar{y}_n$ the ion emission falls below the limit of detectability. This is verified by observations of the ion emission in all directions. The insertion of field distortion elements between the electrodes increases $\bar{y}_n$ by a factor > 3 without affecting the correlation between ion fluence and y_n ($\bar{y}_n > 10^9$ for a 6 kJ, 6 Torr D_2 shot). The distribution of the current in the interelectrode plasma region and the induced variations via field distortion elements are monitored by magnetic probes. The magnitude of the observed current-intensity peaks controls ion-accelerating fields and ion confining fields. The characteristics of the confined population of accelerated ions and those of the ejected ions are consistent with an acceleration mechanism which is extremely localized in space (< 100μm). In parallel with spectrometer data nuclear activation of gaseous targets and of solid targets is used as further method for discriminating among different processes of ion acceleration.

NUMERICAL OPTIMIZATION OF DENSE PLASMA FOCUS

M.ZAKAULIAH, T.J.BAIG and G.MURTAZA
Deptt. of Physics, Quaid-i-Azam Univ. Islamabad, Pakistan.

A generalized snowplow momentum equation describing the dynamic behaviour of high density Z-pinch based on ideal MHD model is used for numerical optimization of a Mather-type Plasma Focus as a function of the physical parameters like aspect ratio, radius ratio, charging voltage, capacitance of the bank, external inductance of the circuit, filling pressure, breakdown interval, length of the insulator sleeve, and specific heats ratio γ. The results are found to be in agreement with the empirical values of the existing devices. They also suggest that the figure of merit $n\tau$ may be enhanced manifold by choosing suitably the experimental parameters.

Dense plasma focus is a simple functional device. However, its theoretical understanding is not very satisfactory. Potter (1971) and Maxon et al. (1978) developed a two dimensional MHD code and determined the dynamics and structure of the current sheath. Although their study was very helpful in understanding the physics of the machine, yet it could not be employed for designing a device. Using ideal MHD equations, we have developed a model for the dynamical behaviour of a Mather-type plasma focus with a view to achieve numerical optimization of the device vis a vis variation of different experimental parameters. The dynamics of the plasma focus exhibit three distinct phases - breakdown and formation of the current sheath, axial rundown to the tip of the central electrode and finally the radial collapse to the z-axis.

The current sheath structure during the axial rundown phase is governed by the equations

$$\frac{d^2Z}{dT^2} = \frac{(\alpha^2 i^2/R^2)\sin\theta - (dZ/dT)^2}{Z} \qquad (1a)$$

$$\frac{d^2R}{dT^2} = \frac{(\alpha_0^2 i^2/R^2)\cos\theta - (dR/dT)^2}{R - R_0} \qquad (1b)$$

alongwith the current equation

$$\frac{di}{dT} = \frac{1 - \int i\, dT - \eta(dZ/dT)}{1 + \eta Z} \qquad (2)$$

where $i = I/I_0$, $T = t/t_0$, $I_0 = V_0(C_0/L_0)^{\frac{1}{2}}$, $t_0 = (L_0C_0)^{\frac{1}{2}}$, V_0 is the charging voltage, C_0 the capacitance of the capacitor bank and L_0 the external inductance of the circuit. Z and R represent the position of the current sheath normalized with the accelerator length z_0 and outer radius b respectively, $\alpha = (\mu_0 V_0^2 C_0^2 / 4\pi\rho_0 b^2 z_0^2)^{\frac{1}{2}}$, $\alpha_0 = \alpha(z_0/b)$ and $\eta = (\mu_0 z_0/2\pi L_0)\ln(b/a)$ appear as dimensionless scaling parameters, a is the radius of the inner electrode and ρ_0 the ambient gas density in the accelerator. $R_0=(a/b)$ and θ is the angle which the canted current sheath makes with the z-axis.

For the study of radial collapse phase, generalized snowplow momentum equation as derived from the ideal MHD model [Zakaullah et al. (1987)] is used. Besides the terms of the original snowplow momentum equation, some new terms accounting for the tension due to azimuthal magnetic field lines, kinetic pressure and compressible nature of the plasma column, arise. For the radial collapse phase of the plasma focus, the equation takes the form

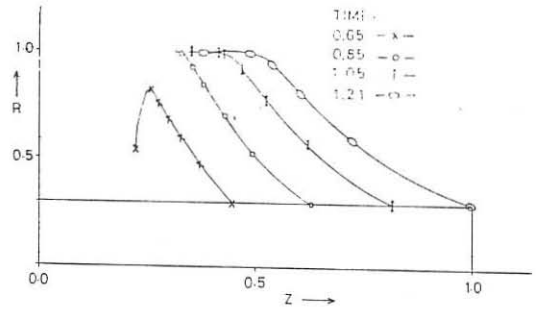

Fig. 1: Temporal development of current sheath during the axial rundown phase.

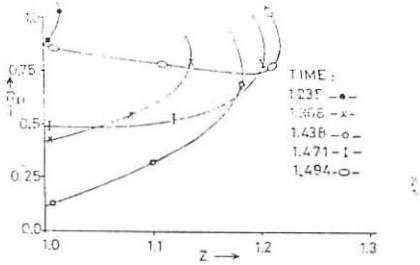

Fig. 2: Evolution of focus plasma in the radial collapse phase.

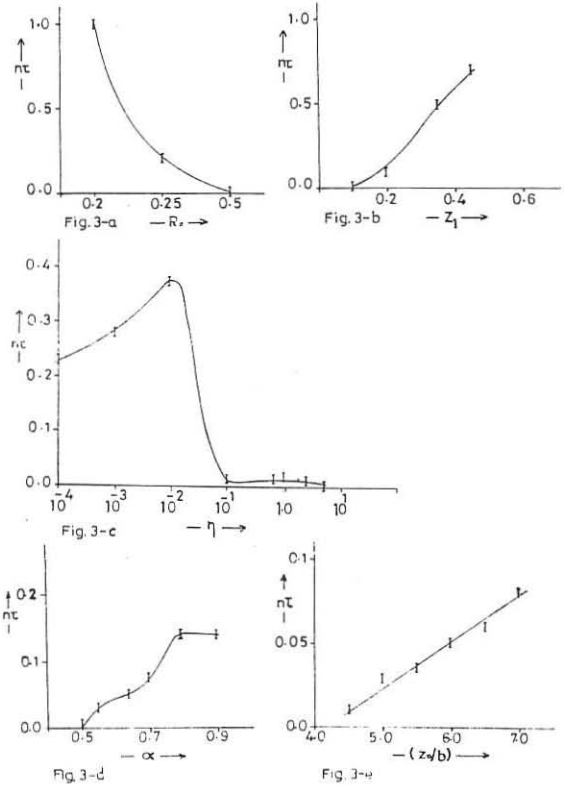

Fig. 3: Behaviour of nτ as a function of various scaling parameters.

Table 1: Experimental Parameters of different devices.

	DEVICE	C_o (μF)	L_o (nH)	$a = \left(\frac{\mu_o V_o^2 C_o^2}{4\pi^2 r_o^2 b^2 z_o^2}\right)^{\frac{1}{2}}$	$f = \frac{2L_o C_o P_o}{\pi_o a^2}$	$n = \frac{L_o z_o}{2\pi L_o} \ln(b/a)$	$\frac{z_o}{b}$	b/a	REFERENCE
1.	Los Alamos Scientific Lab. Univ. of California	45	33	~ 0.65 - 0.85	~ 0.017	~ 0.99	5.2	1.92	Mather (1965)
2.	Los Alamos Scientific Lab. Univ. of California	90	16	~ 0.69	~ 0.017	~ 1.7	4.0	2.0	Mather et al. (1968)
3.	National Aeronautics and Space Administration, Langley Research Centre, Virginia.	125	18	~ 0.9	~ 0.025	~ 2.3	6.0	2.0	Jalufka et al. (1972)
4.	Applied Physics, Technische Hochschule Darmstadt F.R.G.	6.7	24	~ 0.3	~ 0.02	~ 0.94	4.0	3.125	Michel et al. (1974)
5.	Lab. de Fisica del Plasma, Univ. de Buenos Aires Argentina.	6	51,43,33	~ 0.35	~ 0.025	~ 0.31-0.61	4.1	2.65	Gratton et al. (1977)
6.	UM DPF Univ. Malaya, Malaysia.	60	90	~ 0.65	~ 0.25	~ 0.46	4.0	3.4	Lee et al. (1984)
7.	UNU/ICTP DPF Univ. Malaya, Malaysia.	30	110	~ 0.64	~ 0.245	~ 0.39	4.9	3.4	Lee et al. (1986)
8.	SPEED 2, Physikalisches Institut I Universitat Dusseldorf F.R.G.	4	10	~ 0.79	~ 0.00008	~ 2.6	2.0	3.0	Kies (1986)

$$\frac{d^2R}{dT^2}p = \left(-\alpha_1^2 \frac{i^2}{R_p}\Big|_{R_i}^{R_p} - \alpha_1^2 \int i^2 \frac{dR}{R_p^2}p - \beta \int \left(\frac{R_i}{R_p}\right)^{2\gamma} dR_p + \beta \left\{ R_p \left(\frac{R_i}{R_p}\right)^{2\gamma} - R_i \right\} - 2 \int \frac{R_i^2}{R_p} \left(\frac{dR}{dT}p \right) d\left(\frac{dR}{dT}p\right) + \right.$$

$$\left. + 2R_p \left(\frac{dR}{dT}p\right)^2 \right) \Big/ \left(R_i^2 - R_p^2 \right) \qquad - (3)$$

where R_p is the time dependent radius of the plasma column and R_i its initial radius when pinching just started, both normalized by the radius of the inner electrode, and γ is the specific heats ratio. The associated equation for the current in the circuit may be written as

$$\frac{di}{dT} = \frac{1 - \int i\, dT + \eta_1 i (dZ_p/dT) \ln(R_0 R_p)/U + \eta_1 i Z_p (dR_p/dT)/(UR_p)}{1 + \eta - \eta_1 Z_p \ln(R_0 R_p)/U} \qquad - (4)$$

where $U = (z_0/a)$, $\alpha_1 = (\mu_0 V_0^2 C_0^2/4\pi^2 \rho_0 a^4)^{\frac{1}{2}}$, $\beta = (2p_0 L_0 C_0/\rho_0 a^2)$ and $\eta_1 = \dfrac{\mu_0 z_0}{2\pi L_0}$

are dimensionless scaling parameters, p_0 is the ambient pressure in the accelerator and Z_p the length of the pinched plasma filament.

We shall solve the equations (1-4) numerically using one hundred point mesh in Lagrangian coordinate system. If we choose the parameters $\alpha = 0.64$, $\beta = 0.2$, $\eta = 0.5$, $z_0/b = 6.0$, $R_0 = 0.3$, $D = 0.05$, $Z_1 = 0.15$ and $\gamma = 5/3$, the numerical solution describes the formation of a current sheath and its evolution during the axial phase as well as the radial collapse phase. This is depicted in figures 1 and 2. The choice of the scaling parameters is for the purpose of illustration and is based on the empirical data summarized in table 1. D represents the time interval for breakdown and formation of current sheath normalized by t_0 and Z_1 is the ratio of the length of the insulator sleeve and the accelerator. The numerical model is also employed to study the individual effect of the scaling parameters on the behaviour of the pinch ratio and the confinement time of the focus plasma. We have specifically estimated the nT value as a function of the parameters R_0, Z_1, η, α and z_0/b. The effect of remaining parameters is rather weak. The results are summarized in figure 3 and can be useful as a guide in designing a dense plasma focus of appropriate characteristics.

Acknowledgement: This work is partially supported by the PSF Project C-QU/Phys.(50) and the PAEC.

REFERENCES:

Gratton R. et al. (1977) Phys. Lett., 62A, 422.
Jalufka N.W. et al. (1972) Phys. Fluids, 15, 1954.
Kies W. (1986) Plasma Phys., 28, 1645.
Lee S. et al. (1984) in Laser & Plasma Technology, p. 37, World Scientific, Singapore.
Lee S. et al. (1986) J. Fiz. Mal., 7, 1.
Mather J.W. (1965) Phys. Fluids, 8, 366.
Mather J.W. et al. (1968) Phys. Fluids, 11, 611.
Michel L. et al. (1974) App. Phys. Lett, 24, 57.
Maxon S. et al. (1978) Phys. Fluids, 21, 1855.
Potter D.E. (1971) Phys. Fluids, 14, 1911.
Zakaullah et al. (1987) to be published.

EXPERIMENT INVESTIGATION OF ELECTROSTATIC PLUGGING IN MAGNETIC CUSP DEVICE

TIAN ZHONG-YU MENG MING-TIU CHAO XIAO-GUN FENG XIAO-XIEN

Southwestern Institute of Physics, Leshan, Sichuan, China

Electric fields can be used to diminish end losses of an open magnetic confinement system [1]. The electrostatic plugging has been studies in some device[2].An electrostatic plugging magnetic cusp device, MM-4 , which was described elsewhere [3] has been in operation since 1983 at Southwestern Institute of Physics Leshan.A combination of magnetic and electrostatic field are employed to enhance plasma confinement.A magnetic configuration is formed by two contrary engaged solenoids.An annular gap and two end holes are blocked by electrostatic mirrors.Its main parameters are as follows: Magnetic field 0.5T at line cusp, Plugging electrostatic field 20KV/cm at line cusp and at point cusp,Spacing between point cusps 20cm, Radius of line cusp 10cm, Base pressure of the device 5.10^{-4}Pa.

Hydrogen plasma is produced by a pulsed electron beam.The density of plasma is measured by means of an electron current collected at the anode. Typical densities are about $4.7.10^{11}cm^{-3}$. The ion temperature is estimated from the characteristics of the grid energy analyzer and is typically about 80eV. Plasma potential is about -300V.The results of recent experiments can be summarized as follows :

1) Confinement time is 3ms to 5ms and theoretical result is 4.6ms at same condition.The sag of the potential in the anode region is about -200V.

2) The relation that the injection electron velocity is proportional to peak axial magnetic field is obtained in our experiment (See Fig.1,here I is magnet current).The optimum injection position obtained experimentally is 27.5 ± 0.5cm from the centre of the machine.

3) Experiments have demonstrated that the life time of plasma increased by the order of 10^3 can result in significant reductions in plasma end losses.The electrostatic field provides this plugging.

4) The scalling law between the density and the magnetic field ($n \propto B^2$)has been proved.Same law has been achieved in similar kind of devices in other countries.Fig.2 shows theoretical limited density(1) and experimental results at the diffirent injection energy of 92W(2) and 31W(3).Another properties of plasma confinement have been also determined,for example, the density versus the injection energy,the life time versus the magnetic field and the injection energy and so on.

5) The potential sag profile in the anode region has been measured(See Fig.3,here an arrowhead indicates the stopping injection time).The result shows that there is a potential shielding in this kind of device.It will influence the effect of the plugging.How to reduce space electron charge in the anode region is very important topic for this kind of device.

The energy spectra of ions and electrons have been measured and two kinds of ion temperature have been observed in the experiment.The results are diffirent from another devices.As shown in Fig.4,they are 80eV and 140eV during a period from 1ms to 4 ms,where t=0 corresponds to the electron gun turned on,t=4ms corresponds to turning off,but only sigle temperature appears at 0.3ms after turning on and at 0.3ms after turning off.We think an electron beam-plasma interaction is a possible reason.We are going to study these problems in detail this year.

Next step,we plan to develop the device into an electrostatial plugging end plug with a negative potential in an axisymmetric tandem mirror.

We thank Feng Chun-Fang,Lin Ling,Qian Jia-Huang,Jiu Yi-Hua,Yin Miu-Jun for taking part in this work.

References: 1. G.A.Lawrentiev, AEC-TR-7002

2. Ю.И. Панкратьев, ЖТФ. А.Э. 32,2(1972)13

3. Tian Zhong-Yu, Nuc. Fusion and Pl. Phys. 5,2(1985)108

Figure Captions:

Fig. 1 the limiting condition of electron injection

Fig. 2 the scalling law of plasma density

Fig. 3 the potential sag in anode region

Fig. 4 the ion energy spectrum

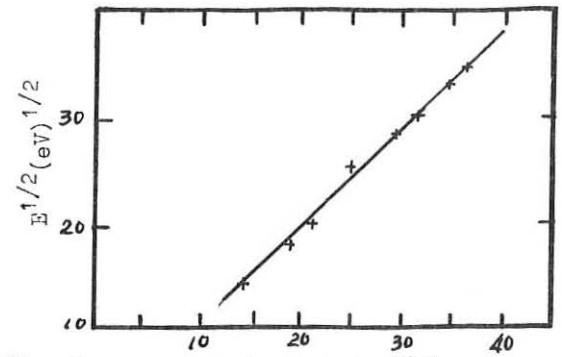

Fig. 1

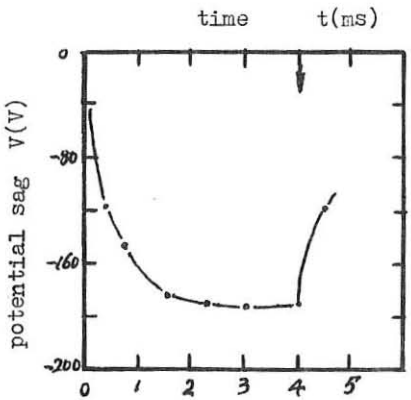

Fig. 3

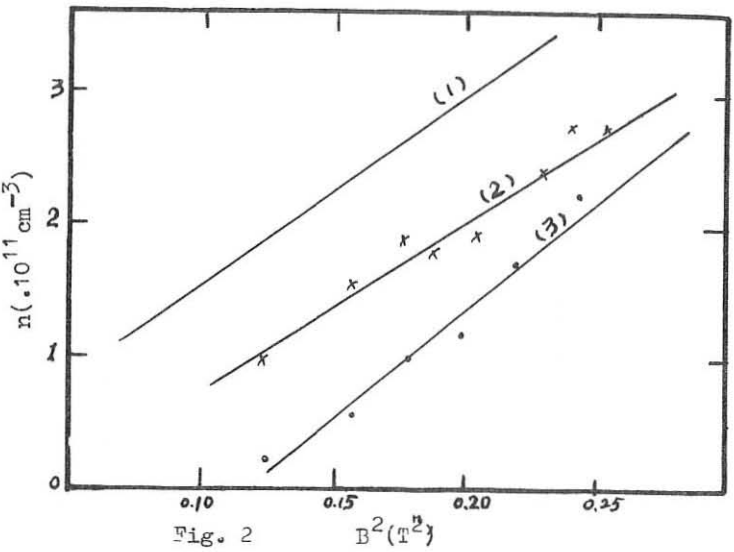
n(.10^11 cm^-3)
3
2
1
0
(1)
(2)
(3)
0.10
0.15
0.20
0.25
B^2(T^2)

Fig. 2

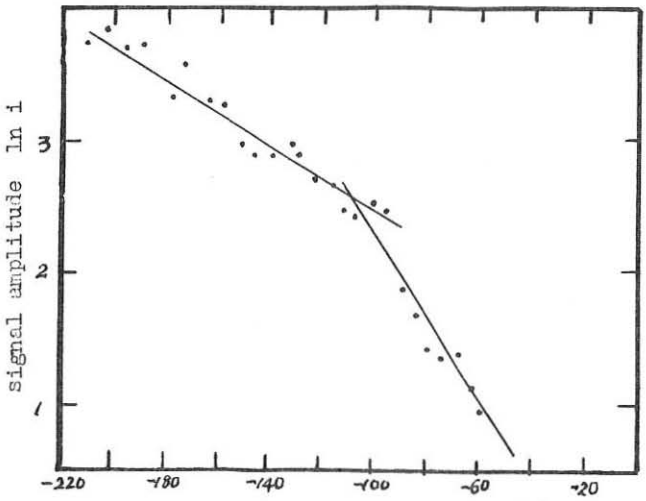
signal amplitude ln i
3
2
1
-220
-180
-140
-100
-60
-20
analysing voltage V(V)

Fig. 4

ICRF HEATING AND CONFINEMENT EXPERIMENTS ON TANDEM MIRROR GAMMA 10

M.Ichimura, S.Adachi, T.Cho, M.Inutake, K.Ishii, A.Itakura, M.Fujita, J.Jeong, T.Kariya, I.Katanuma, Y.Kiwamoto, T.Kondoh, A.Mase, S.Miyoshi, Y.Nakashima, T.Saito, K.Sawada, F.Tsuboi, N.Yamaguchi and K.Yatsu

Plasma Research Center, University of Tsukuba, Ibaraki 305, Japan

ABSTRACT

ICRF heating experiments using antennas installed in the central cell in GAMMA 10 are reported. The plasma is sustained when the resonance of $\omega/\omega_{ci}=1$ exists near the midplane of the anchor cell. The plasma of which density is 10^{13} cm^{-3} is produced by arranging the phases between antennas. The particle confinement time increased remarkably up to 0.45sec with the combinations of ECH and NBI in the parameters of $n=3.5\times10^{12}cm^{-3}$ and $\overline{T_i}$ =1.2keV.

INTRODUCTION

The concept of tandem mirror with thermal barrier has been demonstrated by TMX-Upgrade/1/ and GAMMA 10/2/. The efficient formation of a plug potential has been realized in association with a thermal barrier and the decay of the thermal barrier has been mainly due to the classical processes in GAMMA 10 experiments/3/. The higher central cell ion temperature and the lower barrier density plasma is required in the startup phase of the tandem mirror. The plasma startup by using ICRF is reported by several devices/4,5,6/. In this paper, we describe the plasma startup by using ICRF which is suitable for the GAMMA 10 type tandem mirror characterized with inboard minimum-B anchor and axisymmetrized plug/barrier cells.

EXPERIMENTAL RESULTS

The schematic drawing of the magnetic field configuration of GAMMA 10 and locations of ICRF antenna is shown in Fig.1. So-called Nagoya Type-III antennas without Faraday shield and ceramics cover are installed in both ends of the central cell. The conventional double half turn antenna, DHT, is set near the west Type-III antenna. The cyclotron resonance layers of $\omega/\omega_{ci}=1$, where ω is the applied

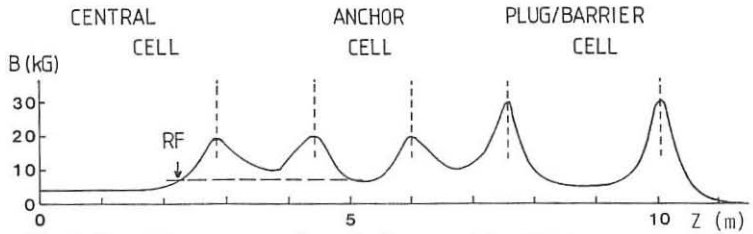

Fig.1 The schematic drawing of the magnetic field of GAMMA 10

frequency and ω_{ci} the ion cyclotron frequency, exist both in the central cell and in the anchor cell at a same time as shown in Fig.1. Gas-puffers only in the central cell are used. The plasma can be sustained by the central cell ICRF in the case that the $\omega/\omega_{ci}=1$ resonance exists in the anchor cell, the ions streaming from the central cell are heated and trapped in the anchor cell. Then the plasma to the plug/barrier region is reduced. The strong ion heating has been observed in the anchor cell from the charge exchange neutral measurement.

To clarify the mechanism of the plasma sustainment, we have done the experiments under the conditions of the fixed frequency and changing the magnetic field strength. By changing the magnetic field strength of the central cell and anchor cell independently, we confirmed the essential condition of the plasma sustainment is the existence of the $\omega/\omega_{ci}=1$ resonsnce near the anchor midplane. The line density of the central cell obtained by changing the whole fields, changing the anchor field and changing the central field with fixed others are summarized in Fig.2, as a function of B/B_{res}, where B is the magnetic field strength at the anchor midplane or that under the Type-III antenna and B_{res} the resonance magnetic field strength. Both the wave-excitation and the resonance in central cell have no contributions to the plasma sustainment. These experiments have been done by using only Type-III antennas. As shown in Fig.2(c) the line density in the central cell increases as the value of B/B_{res} decreases.

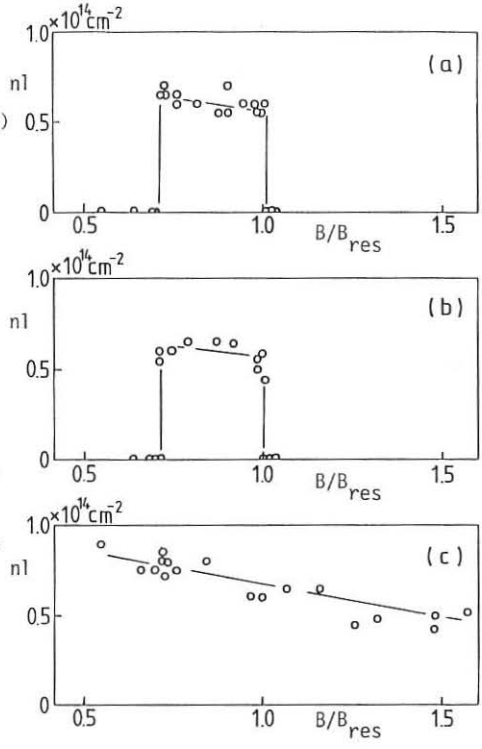

Fig.2
Central cell line density obtained by (a) changing the whole fields, where B is the magnetic field strength at the anchor midplane, (b) changing the anchor field with fixed central field and (c) changing the central field with fixed anchor one, where B is the magnetic field strength under Type-III antennas

In the condition of $B/B_{res}<1$, the slow wave can not be excited. Then the fast wave is considered to be effective for the higher density plasma production. Because the Type-III antenna is more effective for the slow wave excitation, we have added a DHT antenna for the fast wave excitation. In Fig.3, the maximum density obtained in the central cell are shown as a function of ω/ω_{ci} under the DHT. The density up to $10^{13}cm^{-3}$ is obtained by the combination of Type-III and DHT antennas.

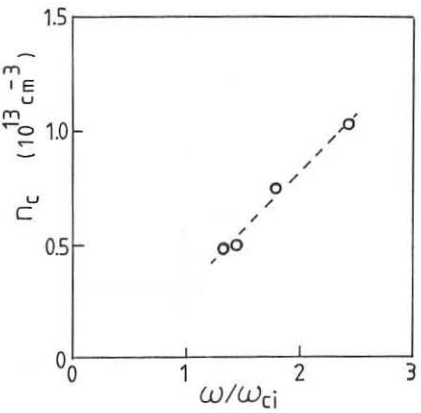

Fig.3 Central cell density as a function of ω/ω_{ci} under the DHT antenna

Because the rf currents on two elements of the DHT flow in the opposite phase, the right hand polarized fast mode, m=+1, is excited mainly in present experimental conditions. The Type-III antennas also excite m=+1 modes. Then the two types of antennas couples strongly with each other. The effect of the coupling appears on the loading resistances of each antenna. Figure 4 shows the temporal variations of the central cell line density and the loading resistances of the DHT antenna. It is noted that the peaks of the loading resistance correspond to humps of the line density. The loading resistances of the east and west Type-III antennas have out-of-phase dependences aginst the line density. The peaks on the loading resistance of DHT antenna appear between those of both Type-III antennas. The phasing between the DHT and Type-III antennas is sensitive for the density increase. The fast modes are possibly excited strongly, when the DHT antenna enhance the mode which is oscillated by east and west Type-III antennas.

The plugging experiments in ICRF heated plasma have been done and the parallel confinement time of 0.45sec has been achieved on the parameters of $n=3.5\times10^{12}cm^{-3}$ and $\overline{T_i}=1.2keV$. We are now proceeding the higher density plugging experiments up to $10^{13}cm^{-3}$.

SUMMARY

The plasma startup with the central cell ICRF antenna is realized under the condition that the resonance exists in the anchor cell. The ions which pass through the anchor cell are heated and trapped. The target plasma for the NBI is formed without any gas-puffing in the anchor cell. The fast wave is effective to the higher density plasma formation in the central cell of the tandem mirror.

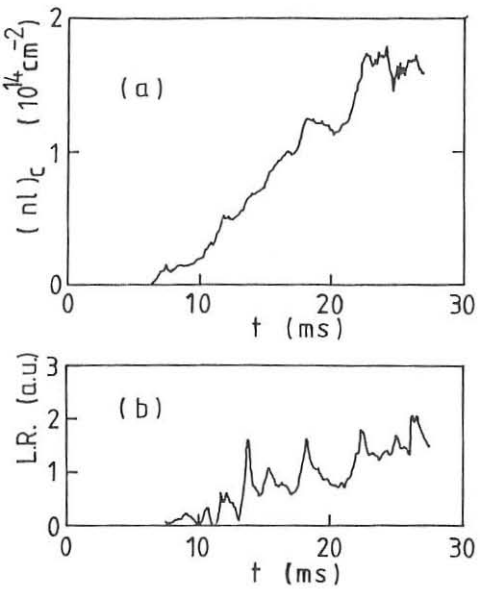

Fig.4 Temporal variations of (a) central cell line density and (b) the loading resistance of the DHT antenna under the condition of $\omega/\omega_{ci}=2.5$

REFERENCES

/1/ D.P. Grubb, et al., Phys. Rev. Lett. 53 (1984) 783.
/2/ M. Inutake, et al., Phys. Rev. Lett. 55 (1985) 939.
/3/ T. Cho, et al., 11th International Conference on Plasma Physics and Controlled Nuclear Fusion Research, Kyoto (1986) CN-47/C-I-2.
/4/ R. Breun, et al., Phys. Rev. Lett. 47 (1981) 1833.
/5/ S. Okamura, et al., Nuclear Fusion 26 (1986) 1491.
/6/ R.S. Post, et al., Nuclear Fusion 27 (1987) 217.
/7/ M. Ichimura, et al., to be submitted

Function of the Conducting Wall on Stabilities of the Hot Electron Ring

Ren Zhaoxing Ding Liancheng Fang Yude Huang Chaosong Qiu Lijian
Institute of Plasma Physics, Academia Sinica,P.O.Box 26, Hefei, China

Abstract

In this paper, functions of the conducting wall on stabilities of the hot electron ring in the simple mirror are described in both experiment and theory. The fluctuations of cold plasma and hot electron depend closely on the radius of hot electron ring and have the minimum amplitude and coherence when R_h/R_w is about 0.8. Here, R_h and R_w are the radii of hot electron ring and conducting wall, respectively.

I Introduction

The experimental and theoretical investigations on the stabilities of hot electron plasma have been performed. But because it is more complex, the satisfactory result can not be obtained untill now[1].

According to the theories[2,3] on hot electron stabilities in a hot electron plasma, the fluctuation of its interchange mode is stabilized by the cold plasma. This condition is always satisfied to operate at T-model. However the hot electron β_h operated in lower magnetic field strength at the mirror centre is lower than that in optimum strength. But in case of the former, the second harmonic resonance layer is nearer the magnetic axis of mirror, it seems advantage for stabilizing interchange mode of hot electron. Which factor cause the energy loss of it, then?

II Experiments

The experiments were performed in a axisymmetric mirror machine named HER with some parameters: central field strength B_0 being from 4 KG to 5 KG, mirror ratio being 2.2 and the radius of stainless steel chamber being 12cm. The plasma is produced by the microwave from a gyrotron launcher (P_μ=15 KW, f_μ=20.4 GC, H_{01}mode). The parameter of the cold plasma can be measured by a multiple-monochromater set one end of mirror, two fixed Langmuir probes near the conducting wall and a movable probe which is able to destroy the hot electron ring at the midplane of mirror. The parameters of the hot electeon

can be measured by diamagnetic loops, a hard X-ray spectrometer and two ECE receivers.

(1) The functions of B_0 on the parameters of the hot electron ring

When B_0 increases, the radius R_h and 3cm ECE power P_{ECE} of the ring also increase. But when R_h is closely conducting wall R_w, P_{ECE} reduce(Fig.1). The dependence of R_h on B_0 can be explained by the function of B_0 on the position of second harmonic resonance layer. And the dependence of P_{ECE} on B_0 will be investigated in the following.

(2) Function of B_0 on the fluctuations of the cold plasma

The normalized fluctuation amplitude $\Delta I/\bar{I}$ of the cold plasma near the hot electron ring can be stabilized by it. The ring with higher β_h can also reduce the $\Delta I/\bar{I}$ of whole plasma. Since β_h depend on B_0, then $\Delta I/\bar{I}$ still depend on B_0.

(3) Hot electron fluctuations caused by cold plasma

The fluctuation frequency of hot electron interchange mode is near its drift frequency. But the signals from 3cm ECE receiver involve mainly the drift wave fluctuations frequency of the cold plasma. An important case is that the coherence between $\Delta I/\bar{I}$ near the conducting wall and P_{ECE} is reduced contineusely when the hot electron ring is closely it.

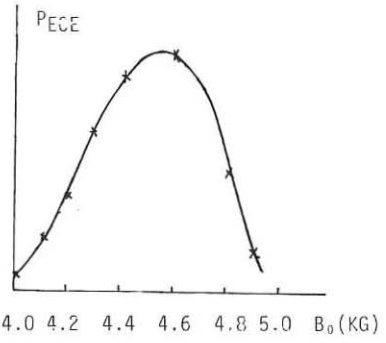

Fig.1 ECE power P_{ECE} of hot electron ring varying with B_0

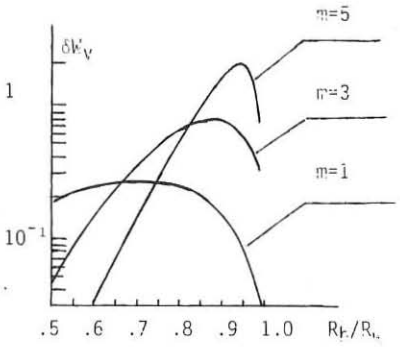

Fig.2 The variation of vacuum energy varying with R_h/R_w for different m

III Theoretical analysis

It has been known that, in the past theories on stabilized hot electron fluctuations, the cold plasma effect on its stabilization is only considered and the function of conducting wall is neglected. Now we consider a reversed case that the former can be neglected and the latter is the only stabilizing mechanism, which is mainly dominated by the variation of vacuum energy in the MHD energy principle. In the vacuum region inside the ring, the scalar potential of the perturbed field may be written as

$$\phi_1(\vec{r})=AI_m(kr)\exp[i(kz+m\theta)] \tag{1}$$

Here, I_m is a modified Bassel function, and m and k are the azimuthal and axial mode numbers, respectively. A is a constant determined by the boundary condition.

In the vacuum region between wall and ring, it is

$$\phi_2(\vec{r})=C[I_m(kr)-(I_m'(kR_w)/K_m'(kR_w))K_m(kr)]\exp[i(kz+m\theta)] \tag{2}$$

Where C also is a constant, and the prime denotes a derivation with respect to the argument.

Considering the actual thickness of the ring measured in the experiment, we assume the thin-ring approximation. Therefore, the fluctuation of it can be considered as a surface current and its fluctuation has the form of surface profile. Thus, considering the boundary conditions of the perturbed magnetic field, we can determine the A and C in equation (1) and (2)

If the ring is long and thin($kR_h<<1$, $kR_w<<1$), we may finally obtain

$$\delta W_V=-\frac{1}{2}\pi m\mu_0^2 L^3\overline{(\delta\alpha_{h\theta})^2}(R_h/R_w)^{2m}[1-(R_h/R_w)^{2m}] \tag{3}$$

Here, L is the length of it and $\overline{(\delta\alpha_{h\theta})^2}$ is the current fluctuation averaged over parameter z.

According to relation (3), we may draw following conclusions:

(1) δW_V is always positive and, therefore, the conducting wall always plays stabilizing rote for the hot electron fluctuations;

(2) For a certain azimuthal mode number, there is the optimum rate of R_h/R_w for stabilizing ring fluctuations by conducting wall. The R_h/R_w approaches to 1, as the azimuthal mode increases (Fig.2).

IV Discussion

Our researches provide the new evidence in both experiment and theory for the problem related in section I. The analysis in the section III well corresponds with the experiment.

(1) The energy loss of the ring can be caused not only by hot electron interchage mode, but also by fluctuations of cold plasma;

(2) The fluctuations of the ring can be stabilized by the conducting wall near it. During R_h/R_w=0.8, the fluctuations of whole plasma were reduced apparently;

(3) The optimum position of the ring also was derived from the interaction between it and wall;

(4) Up to now, this stabilizing mechanism isn't clear and should be further investigated.

References

[1] D. L. Hillis, et al., Phys. Fluids, Vol. 28, No. 9 (1985);

[2] H. L. Berk, et al., Phys. Fluids, Vol. 26, 201 (1983);

[3] Adel El-Nadl, Phys. Fluids, Vol. 25, 2019 (1982).

ELECTRON HEATING IN A RAREFIED PLASMA OF A THETATRON DISCHARGE

M.A. Bourham, H.A. El Gamal, R.N. El Sherif and A.M. Shagar

Plasma Physics Department, Nuclear Research Centre,
Atomic Energy Authority, Atomic Energy 13759, Cairo, Egypt

Abstract

In a Thetatron discharge with a plasma of anisotropic electron energy distribution, due to electron acceleration by the induced electric field, instability is developed and gives rise to the excitation of electromagnetic waves. The epithermal transverse emitted electromagnetic waves are due to the transformation of the longitudinal electrostatic oscillations, and propagate at a right angle to the direction of the magnetic field. The electrons are heated significantly due to the electric field fluctuations, as the plasma in hand becomes turbulent, and collisionless mechanisms become to be effective.

Introduction

The generation of electromagnetic waves from an anisotropic plasma is studied theoretically and experimentally in a number of previous works[1-6]. Kinetic instabilities were observed in a number of experiments where the electric field is perpendicular to the magnetic field, associated with the generation of electromagnetic radiation[7,8]. The non-linear effects might arrise due to the existance of electron oscillations and electric field with large amplitudes, and the generated waves would be in the neighbourhood of the upper hybrid resonance frequency[9,10], and plasma becomes turbulent as instabilities are excited[11,12] resulting in the heating of the plasma particles[12].

Experimental Set-up

Measurements are carried on a plasma produced in a Thetatron discharge of 4KJ stored energy. The discharge current of up to 150KA is allowed to pass through a single turn coil of 14 splitted sections, total length of 80 cm and 8.5 cm diameter surrounding the discharge tube. The working gas (H_2) is allowed to entre the discharge tube via a controlling valve, and a ring glow discharge serves for preheating. Magnetic probes, double electrical probes and microwave detection antennae could be freely move axially and radially for diagnostics purposes. Full details of the system is described in a previous work[13].

Experimental Results and Discussion

Measurements of the emitted electromagnetic radiation for the wave length 8 and 4 mm showed that they originate from the plasma itself, and their relative intensities increase with the increase of the bank stored energy. Fig.(1) shows the variation of the relative intensity against the stored energy. The emitted waves have also a dependence on the initial gas pressure as shown in Fig.(2), showing that the radiation takes place between 0.1 and 0.001 mmHg . At higher pressures, the most excitable harmonics correspond to λ = 8mm while at lower pressures the harmonics which correspond to λ = 4mm are excited.

The radial distribution of the emitted wave relative intensity, Fig.(3), shows that the plasma is a source of intensive electromagnetic radiation with a characteristic frequency $\omega_{rad} \sim 2.4 \times 10^{11}$ Sec^{-1} for λ = 8mm, and for λ = 4mm $\omega_{rad} \sim 4.7 \times 10^{11}$ Sec^{-1}, and the excitation takes place at the layer where the plasma is inhomogeneous and the electron density falls rapidly as shown in Fig.(4). The plasma electron temperature has its maximum at the axis of the discharge, and decays rapidly near the tube walls. The harmonic structure of the generated waves showed that the most excitable is the 8th for λ = 8mm , and the 10th for λ = 4mm, as shown in Fig.(5) and Fig.(6) . The harmonic structure revealed that the radiation takes place at the neighbourhood of the upper hybrid resonance frequency, which fulfill the form $\omega_{rad} = \omega_{hl} = n\omega_{ce} = (\omega_{pe}^2 + \omega_{ce}^2)^{1/2}$ for λ = 8mm, and $\omega_{rad} = 2\omega_{hl}$ for λ = 4mm. The calculation of the upper hybrid frequency for λ = 8mm shows that $\omega_{hl} = 2.38 \times 10^{11}$ Sec^{-1} and ω_{rad} for the same wavelength is 2.36×10^{11} Sec^{-1} , and for λ = 4mm the hybrid frequency is 2.4×10^{11} Sec^{-1} while the radiation frequency is 4.71×10^{11} Sec^{-1} . This reveales that the radiation takes place near the upper hybrid resonance frequency with a radiation frequency of the order of $\omega_{rad} \sim \omega_{hl}$ or $\omega_{rad} \sim 2\omega_{hl}$ which conforms well with the theory, and indicating the possibility of the longitudinal oscillations to be transformed into electromagnetic radiation where one of the components of the complex permitivity tensor approaches zero [2] . Hence, a more generalized form will be $\omega_{rad} = n\omega_{ce} \ll \omega_{pe}$, and ω_{rad} is in the range of ω_{hl} or $2\omega_{hl}$.

The detected high frequency oscillations are in the frequency range of the ion cyclotron frequency, which is typical for low ß plasma, and thus the energy transfere which leads to the heating of the plasma electrons might be owing to the ion-cyclotron and the ion-sound instabilities.

The generated waves proved to propagate at a right angle to the direction of the axial magnetic field, as shown in Fig.(7), which predicts the excitation of the longitudinal oscillations of harmonic structure, and leading to the generation of electromagnetic radiation .

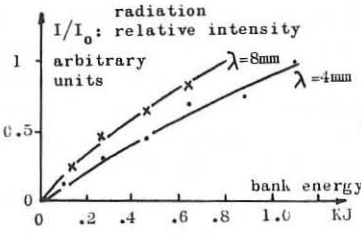

Fig.(1)

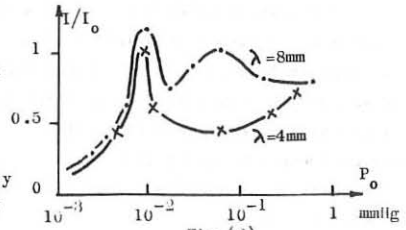

Fig.(2)

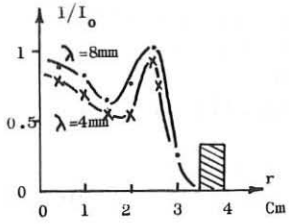

Fig.(3)

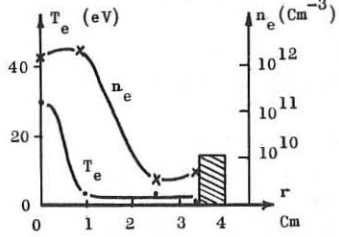

Fig.(4)

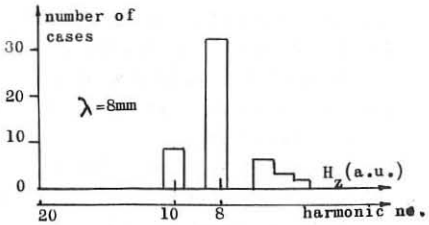

Fig(5)

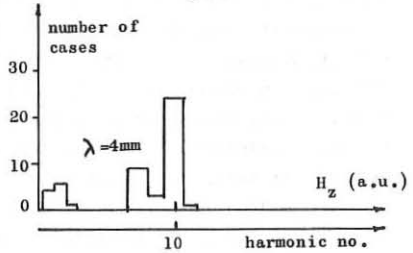

Fig.(6)

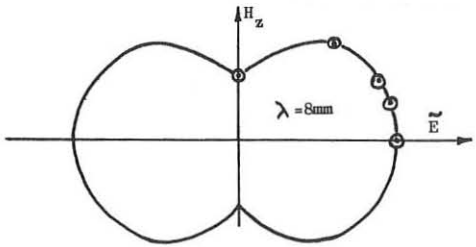

Fig.(7)

Conclusion

In a low ß inhomogeneous plasma of a Thetatron discharge, the longitudinal oscillations are transformed into transverse electromagnetic radiation with a characteristic frequency in the neighbourhood of the upper hybrid resonance, where one of the components of the complex permitivity tensor approaches zero.

Ion-cyclotron and ion-sound instabilities are responsible for the process of energy transfere, and resulting in the heating of plasma electrons.

The emitted radiation propagates at a right angle to the direction of the axial magnetic field.

References

(1) I.Yu. Adamov et al., Atomnia Energya, 16, 94 (1965).

(2) V.D. Shapiro and V.I. Shavchenko, Sov.Phys. JETP, 15, 1053 (1962)

(3) A.T. Altyntzev et al., Proc. IVth Int. Conf. Plasma Physics and Controlled Nucl. Fusion, Vol. II, p.309 (1971) .

(4) V.N. Tsytovich, "Non-linear Effects in Plasma", Plenum Press, New York (1970).

(5) V.V. Demchenko et al., Nuclear Fusion, 11, 245 (1971).

(6) W.P. Davis et al., Proc. IVth Int. Conf. Plasma Physics and Controlled Nucl. Fusion, Vol.III, p. 289 (1971) .

(7) T.A. El Khalafawy et al., 5th Europ. Conf. Controlled Fusion and Plasma Physics, Grenoble, France, I, 42 (1972) .

(8) M.A. Bourham et al., Bull. Phys. M'sia, 4, 161 (1983) .

(9) T.A. El Khalafawy et al., Plasma Physics, 10, 117 (1968) .

(10) F.F. Chen, Phys.Fluids, 1 , 430 (1959) .

(11) D.W. Forslund et al., Phys.Rev.Let., 25, 1225 (1970) .

(12) M.A. Bourham, Int.Conf. on Plasma Physics, ICPP, Lausanne, Switzerland, 27a: Pl, paper Pl-7, 27 June- 3 July (1984) .

(13) M.A. Bourham, " Experimental Investigation of Turbulent Plasma Heating in a Theta Pinch Discharge ", Ph.D. Thesis, Ain Shams Univ., Faculty of Engineering (1976) .

MHD STABILITY OF PLASMA IN AN AXISYMMETRIC OPEN-ENDED SYSTEM WITH NONPARAXIAL CELLS

V.V. Arsenin

I.V.Kurchatov Institute of Atomic Energy, Moscow, USSR

The flute instability in a low-pressure plasma within the chain of traps, including the cells with a transversal size comparable with a characteristic magnetic length, is studied. The stability-average minimum B Principle-is shown to be reached, in particular, in the combination of a fat simple mirror with an adiabatic cusp region. In this case, the requirements to the field decay rate on the equatorial plane in the simple mirror are less stringent than those in the known case, when the only fat simple mirror provides stabilization of the m =1 mode of oscillations. The stability conditions (requirements to the pressure profiles across the field) for the system with a ring-like mirror produced at the radial periphery of a throat with the flux expanding from the equatorial plane are derived.

D

INERTIAL CONFINEMENT

14th European Conference on Controlled
Fusion and Plasma Physics

Madrid, Spain, 22-26 June 1987

DIAGNOSTICS OF HYDRODYNAMIC IMPLOSION EFFICIENCY OF LASER-IRRADIATED SHELL TARGETS

A.S.Shikanov, G.V.Sklizkov, Yu.A.Zakharenkov

P.N.Lebedev Physical Institute, USSR Academy of Sciences, Moscow, USSR

ABSTRACT

Methods of experimental investigations of basic hydrodynamic processes relevant to the determination of laser-irradiated shell target implosion efficiency are considered. Diagnostics of mass abl tion rate and implosion velocity is analyzed. On the base of expe- rimental data (ion mass-spectrometry and critical density dynamic chronography) odtained at "Delfin-1" laser facility it is demonstr: ted that high-aspect ratio shell targets could be imploded with hydrodynamic efficiency of 10%.

SHOCK WAVE MOTION IN AN IDEALIZED MEDIUM

Carlos Alejaldre
Asociación Euratom/CIEMAT
CIEMAT, 28040 Madrid , Spain

Eli A. Mishkin
Polytechnic Institute of New York
New York 11201, U.S.A.

A spherical , or cylindrical , strong shock wave may move away from the center, or axis of symmetry , or be center , or axis of symmetry , bound. In the first case , the shock is due to a sudden release of a substantial amount of energy E at the center of the disturbance–an explosion. A sudden release of an evenly distributed energy far away from the center of the disturbance causes a strong implosion. Spherically imploding shocks acquired great importance with the emerging possibility of achieving matter densities well above those characteristic of the solid state . The mean free path of the very energetic α particles produced in a thermonuclear reaction is shortened then by several orders of magnitude, enabling thereby a self–sustained reaction. Implosion is viewed, therefore, as necessary in achieving controlled thermonuclear fusion by inertial methods[1].

The mass, momentum, and energy conservation equations of a spherical, $\nu=2$, or cylindrical, $\nu=1$, shock wave moving through an ideal gas with constant specific heats, $\gamma=c_p/c_v$ read[2],

$$\begin{aligned} d_t \rho + \rho(\partial_r u + \nu\frac{u}{r}) &= 0 \ , \\ d_t u + \frac{1}{\rho}\partial_r p &= 0 \ , \\ d_t(p\rho^{-\gamma}) &= 0 \ , \end{aligned} \qquad (1)$$

p,ρ and u, the pressure , density and velocity of the gas, respectively, are functions of r and t .

With the molecular structure of the gas neglected, there is no characteristic length, therefore eqs. (1) admit a self-similar solution [3],

$$p(r,t) = \rho_0 \dot{R}_s^2 P(\xi)\ ,\quad \rho(r,t) = \rho_0 \mathcal{R}(\xi)\ ,\quad u(r,t) = \dot{R}_s U(\xi) \qquad (2)$$

where $P(\xi)$, $\mathcal{R}(\xi)$ and $U(\xi)$ are the non-dimensional pressure, density and velocity , respectively, dependent only on the self-similar variable $\xi = r/R_s$. This solution reduces the partial differential equations (1) to the set of ordinary differential equations [4],

$$\begin{aligned} -(U-\xi)\, d_\xi \ln \mathcal{R} &= X + \nu Y \\ -\frac{C^2}{\gamma \xi}\, d_\xi \ln P &= X(\gamma - 1) + \lambda Y \qquad \lambda = \frac{R_s \ddot{R}_s}{\dot{R}_s^2} \qquad (3) \\ -(U-\xi)\, d_\xi \ln P &= \gamma X + \nu \gamma Y + 2\lambda \end{aligned}$$

where $Y = U/\xi$, $X = d_\xi U$ and the self-similar coefficient λ depends only on γ . $C^2(\xi)$ is the reduced speed of sound.

The representative curve of the state of the compressed gas [5] ,obtained from the fundamental equations (3),

$$X(\gamma-1)^2 + \lambda\gamma(\gamma-1) - (X + \nu Y + 2\lambda/\gamma)C^2/\xi = 0 \qquad (4)$$

is shown in fig. 1, together with the straight line that passes through the mapping of the front of the shock and of its tail. In this case, the approximate reduced pressure P, density $\mathcal{R}$, and velocity U reduce to simple closed expressions.

A physical solution must be single valued. An implosion experiment performed anywhere, at any time, must follow the same self-similar coefficient λ. The imploded ideal gas with the adiabatic constant γ, is characterized by a single-valued $\lambda(\gamma)$and a uniquely defined representative curve (4). Integrating equation (4), the

reduced functions $P(\xi)$, $R(\xi)$ and $U(\xi)$ are obtained. In fig. 2, a comparison is made between the values obtained for the gas pressure from a numerical solution of the nonlinear conservation equations with those obtained assuming a linear representative curve.

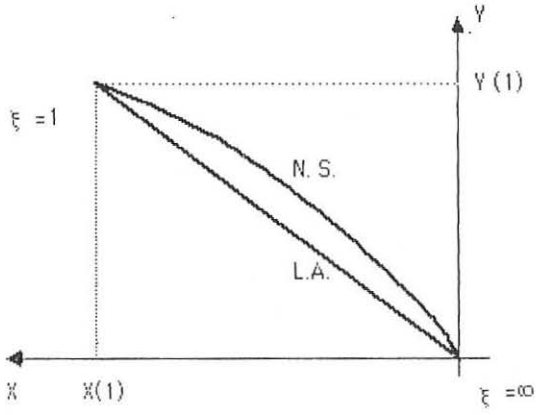

Fig. 1
The representative curve obtained from a numerical solution (N.S.) and a linear approximation (L.A.)

Through a study of the singularities of the characteristic curve, an analytic solution for the self-similar coefficient $\alpha=1/(1-\lambda)$ can be obtained. The difference between the values obtained analytically and those computed numerically[6], does not exceed 0.0015 (0.0012, when $\nu=1$), at $\gamma=5/3$ and 0.014 (0.008, $\nu=1$) at $\gamma=7/5$, with the analytical values being the smaller ones.

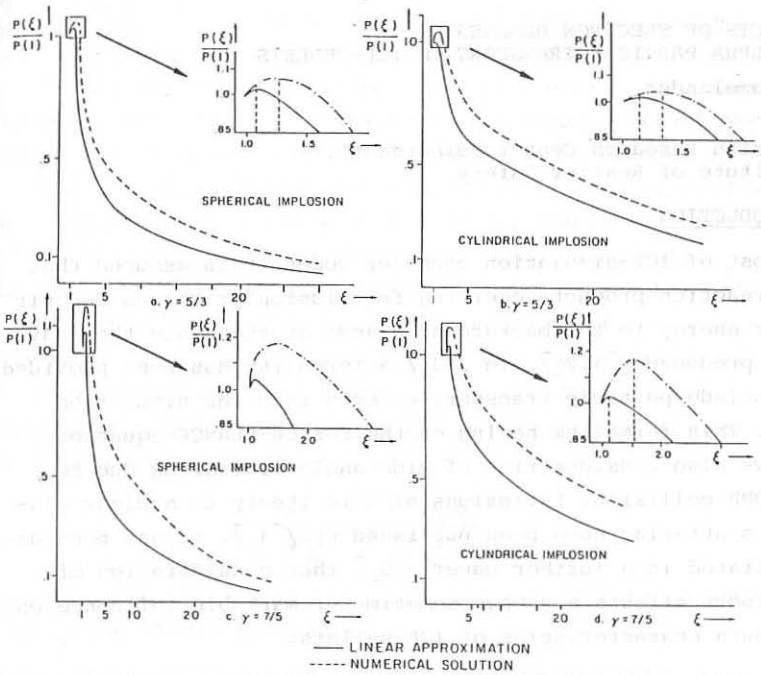

Fig. 2
The reduced pressure P(ξ) for γ=5/3 and γ=7/5

References:

[1] J. Nuckolls, L.Wood, A. Thiessen and G. Zimmerman, Nature,**239**, 139, (1972).

[2] Zel'dovich and Yu. P. Raizer, Physics of Shock Waves and High Temperature Hydrodynamic Phenomena ,Academic Press, New York, (1967).

[3] G. Guderley, Luftfahrtforschung **19** , 302,(1942).

[4] E.A. Mishkin and C. Alejaldre, Physica **124C** , 399,(1984).

[5] Y. Fujimoto, E.A. Mishkin and C. Alejaldre. Phys. Fluids, **28** (10), 3018(1985).

[6] K. V. Brushlinskii and Ya.M. Kazhdan, Usp.Mat.Nauk XVII ,**17**, 3, (1963), [Sov.Math. Surveys, **18**, 1, (1963)].

EFFECTS OF ELECTRON DEGENERACY ON ALPHA PARTICLE TRANSPORT IN ICF-PELLETS

G. Kamelander

Austrian Research Center Seibersdorf,
Institute of Reactor Safety

INTRODUCTION

In most of ICF-simulation computer codes it is assumed that the reaction products emerging from fusion processes deposit their energy to the background plasma at the place they have been produced [1,2]. In [3] a formalism has been provided to include particle transport effects into the simulation code. This formalism basing on the FOKKER-PLANCK-equation allows also consideration of wide angle scattering due to COULOMB collision. Extensions of this theory to nuclear elastic scattering have been published by [4]. It has been demonstrated in a further paper [5] that consideration of transport effects may have sometimes remarkable influence on the burn characteristics of ICF-pellets.

As a consequence of the high compression of the pellet at low temperatures the electron component is degenerate. Therefore the assumption of Maxwellian electron distributions for the evaluation of the FOKKER-PLANCK-coefficients in [1] to [5] is not justified. The effect of a degeneracy corrected transport equation on the burn characteristics of ICF-pellets is the subject of the present paper.

ANALYSIS

The collision term of the FOKKER-PLANCK-equation is given by

$$\left(\frac{\delta \varphi_a}{\delta t}\right)_c = \sum_b \left\{ \frac{\partial}{\partial E}\left[S_{ab}(\vec{r},E)\varphi_a(\vec{r},E,\mu)\right] + T_{ab}(\vec{r},E)\,\underline{\underline{\delta}}\,\varphi_a \right\} \qquad (1)$$

where φ_a is the test particle flux and $\underline{\underline{\delta}}$ equal to

$\frac{\partial}{\partial\mu}(1-\mu^2)\frac{\partial}{\partial\mu}$. The summation is extended over all plasma constituents. S_{ab} and T_{ab} are the FOKKER-PLANCK coefficients which are degeneracy-corrected for the electron component. A detailed analysis to calculate the corrected FOKKER-PLANCK coefficients is given by [6]. The evaluation bases on the FERMI-DIRAC distribution function which is approximated by well-known formulas for weak and strong degeneracy. For partial degeneracy the fugacity is approximated by tables stored in the computer code. The degeneracy-corrected FOKKER-PLANCK coefficients cannot be evaluated in a closed form but by numerical integration. Special care is taken to calculate the DEBYE-radius being an argument of the COULOMB-logarithm appearing as a factor of S_{ab} and T_{ab}. For strong degeneracy it is calculated by [7]

$$\frac{1}{\lambda_{De}^2} = \frac{4\pi n_e e^2}{k(T_e+T_F)} \qquad (2)$$

n_e being the electron density, T_e the electron temperature and T_F the FERMI-temperature.

The computational method to solve the FOKKER-PLANCK is similar to [3]. A degeneracy-corrected transport option has been included as an option into the simulation code MEDUSA-EUMOD.

RESULTS AND DISCUSSION

From [6] it is known that degeneracy correction leads to very significant modifications of the FP-coefficients for dense plasma. Nevertheless the degeneracy correction effects on burn characteristics of ICF-pellets are only important if the hot spot in the pellet is not sufficiently pronounced in the moment of maximum compression, i.e. the temperature profile is flat. Under these circumstances transport effects become important.

As an example a compressed DT-pellet with a density of $2,1.1o^7$ kg/m^3, and an initial temperature profile ranging from $1o^8$ ^oK to $4,6.1o^7$ ^oK is given. Fig. 1 shows the corresponding degeneracy parameter i.e. the fraction of FERMI-temperature and electron temperatur. Fig. 2 shows the stopping power of the plasma near to the boundary at the beginning of the burning phase. The fusion energy as a function of the time calculated by the corrected and the uncorrected models is presented in Fig. 3. It is demonstrated that the differences became very significant. Finally the corrected and the uncorrected stopping power at the plasma boundary is shown for the beginning and for an advanced state of the burning phase in Fig. 4. In Figures 2 to 4 the curves (a) refer to the degeneracy corrected and (b) to the not corrected calculations.

REFERENCES

/1/ J.P. CHRISTIANSEN et al., Comp.Phys.Comm. 7 (1974)

/2/ N.A. TAHIR, K.A. LONG, KfK 3454 (1983)

/3/ K. PRZYBYLSKI, J. LIGOU, Nucl.Sci.Eng. 81 (1982) p.98

/4/ G. KAMELANDER, Nucl.Sci.Eng. 86 (1984) p. 355

/5/ G. KAMELANDER, 12th Europ.Conf.on Controlled Fusion, Vol. II, p. 3o (1985)

/6/ G. KAMELANDER, Atomkernenergie-Kerntechnik, Vol. 48 (1986)

/7/ Y.T. LEE, R.M. MORE, Phys. Fluids 27 (1984) 5

This work has been supported by Austrian FONDS ZUR FÖRDERUNG ZUR WISSENSCHAFTLICHEN FORSCHUNG

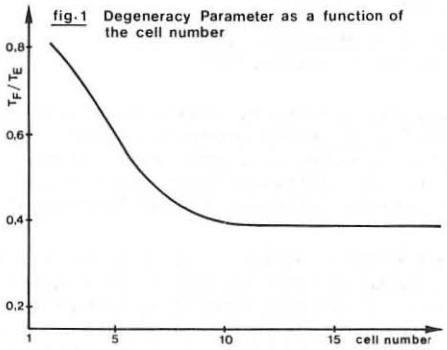

fig.1 Degeneracy Parameter as a function of the cell number

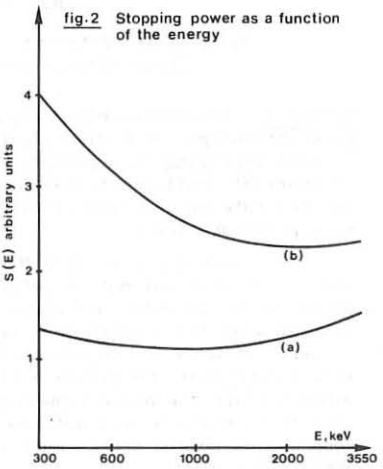

fig.2 Stopping power as a function of the energy

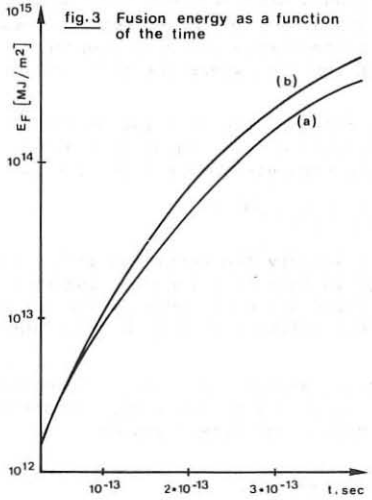

fig.3 Fusion energy as a function of the time

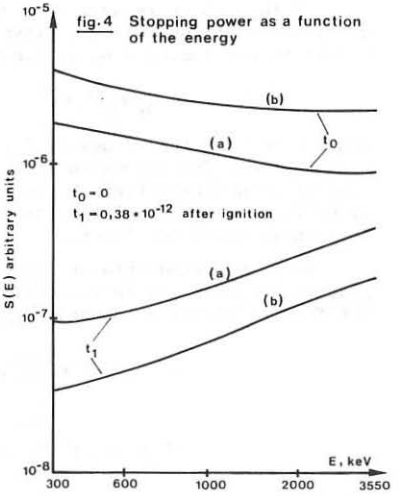

fig.4 Stopping power as a function of the energy

TIME LAW PULSE EFFECTS ON THE HYDRODYNAMICS OF ION BEAM FUSION

A. Barrero and A. Fernández

Department of Thermo and Fluid Mechanical Engineering,
University of Sevilla, 41012 Sevilla, Spain

ABSTRACT The self-similar expansion generated by an intense light ion beam pulse of energy per nucleon $E_b=E_o(t/\tau)^p$ and current intensity $I_b=I_o(t/\tau)^{2p-1}$ $(0<t<\tau)$ impinging on a planar target is considered. Quantities of interest in inertial confinement fusion such as the ablation pressure and the mass ablated rate as function of time for several values of the law time exponent p are obtained.

In a recent paper (FERNANDEZ and BARRERO 1986), the authors found that the one dimensional motion generated by an intense ion beam pulse impinging on an initially cold half space plasmas of electron density n_o becomes self-similar when the beam parameters (energy per nucleon E_b and current intensity per unit area I_b) depend on time as $E_b=E_o(t/\tau)^{2/3}$ and $I_b=I_o(t/\tau)^{1/3}$ $(0<t<\tau)$ They showed that the plasma motion depends on a dimensionless number $\alpha\sim n_o^{2/3}\tau^{2/3}I_o/E_o^{5/3}$ which contain the basic beam and plasma parameters. For $\alpha>>1$, results show that there exits a well defined ablation surface separating an isentropic compression region from a much wider expansion flow where the beam energy absorption occurs.

In this paper we have considered the effect of the time law on the hydrodynamics of the ion beam plasma interaction.To this end,we consider a planar target impinged by an ion beam whose parameters depend on time as

$$E_b=E_o(t/\tau)^p \qquad , \qquad I_b=I_o(t/\tau)^{2p-1} \qquad ,$$

and assume that the values of E_o, I_o and τ satisfy the condition $\alpha>>1$ (ablation regime). The expansion flows produced in this case , neglecting heat conduction and radiation, becomes self-similar since the restriction imposed by solid density is relaxed (density becomes infinity at the ablation surface as we shall see later).

We have assumed planar geometry, and a quasi-neutral collision-dominated plasma. The beam, which is considered both cold and neutralized, transfers to the free electrons a momentum R per unit volume and time given by

$$R = 4\pi e^4 Z_b^2 \ln\Lambda \frac{nn_b}{m_e v_b^2}\Phi\left[\frac{v_b}{(2kT/m_e)^{1/2}}\right] \qquad ,$$

$$\Phi(y) = 2\pi^{-1/2}\left[\int_o^y \exp(-t^2)dt - y\exp(-y^2)\right] \qquad ,$$

(MIYAMOTO 1980, JACKSON 1975); e, m_e and $\ln\Lambda$ are electron mass and charge and Coulomb logarithm respectively. Notice that we do not include the effect of the inelastic collisions on the stopping power, so that we should only consider low Z_i targets (NARDI et al.1977, MELHORN 1981, OLSEN 1985).

The beam pulse, starting at t=0, is incident from $x=-\infty$ on the solid half-space x>0; assuming that the beam parameters depend on time as

$$I_b(t) = eZ_b n_b(-\infty,t)v_b(-\infty,t) = I_o(t/\tau)^{2p-1} ,$$

and

$$E_b(t) = m_b v_b^2(-\infty,t)/2 = E_o(t/\tau)^p \quad , \quad (0<t<\tau) ,$$

we may introduce self-similar variables

$$v_b(\xi) = (eZ_b/I_o)(2E_o/m_b)^{1/2} n_b(x,t)(t/\tau)^{1-3p/2} ,$$

$$u_b(\xi) = v_b(x,t)/[(2E_o/m_b)^{1/2}(t/\tau)^{p/2}] ,$$

$$v(\xi) = [n(x,t)(t/\tau)^{1-3p/2}]/n_r ,$$

$$u(\xi) = v(x,t)/[(Z_i kT_r/m_i)^{1/2}(t/\tau)^{p/2}] ,$$

$$\theta(\xi) = T(x,t)/[T_r(t/\tau)^p] ,$$

$$\xi = x/[(Z_i kT_r/m_i)^{1/2}\tau(t/\tau)^{p/2-1}] ,$$

and then, the equations describing the expansion flow of a fully ionized plasma produced by impinging a solid target with an ion beampulse, are

$$v_b u_b = 1 \quad , \quad (1)$$

$$\frac{du_b}{d\xi} = -\frac{v}{u_b^3}\,\phi(\beta u_b/\theta^{1/2}) \quad , \quad (2)$$

$$(3\tfrac{p}{2}-1)v - (\tfrac{p}{2}+1)\xi\frac{dv}{d\xi} + \frac{d(vu)}{\xi} = 0 \quad , \quad (3)$$

$$v[\tfrac{p}{2}u - (\tfrac{p}{2}+1)\xi\frac{du}{d\xi} + u\frac{du}{d\xi}] = -\frac{Z_i+1}{Z_i}\frac{d(v\theta)}{d\xi} \quad , \quad (4)$$

$$v\left\{p(\frac{u^2}{2} + \frac{3}{2}\frac{Z_i+1}{Z_i}\theta) + [u-(\tfrac{p}{2}+1)\xi]\frac{d}{d\xi}(\frac{u^2}{2} + \frac{3}{2}\frac{Z_i+1}{Z_i}\theta)\right\} = -\frac{Z_i+1}{Z_i}\frac{d(vu\theta)}{d\xi} + \frac{v v_b}{u_b} , \quad (5)$$

where

$$\beta = (m_e E_o/m_b kT_r)^{1/2}$$

and to simplify the equations, we chose a convenient reference temperature and density

$$T_r = \frac{2\pi e^3 Z_b(\ln\Lambda)\tau I_o m_b}{m_e k E_o} \quad , \quad n_r = \left(\frac{m_e^3 m_i E_o^5}{2\pi^3 e^{11} Z_b^5 (\ln\Lambda)^3 \tau^3 m_b^3 Z_i I_o}\right)^{1/2} ,$$

and neglected terms of order of $[m_b Z_i kT_r/(2m_i E_o)]^{1/2}$ which are assumed small (the case of interest in ion beam fusion).

For $n_r \ll n_o$ (n_o being the solid density) there exits a well defined ablation surface separating the rarefied expansion flow, where the absorption energy occurs, from the high density compression zone in the right. It is worth to notice that inequality $n_r \ll n_o$ corresponds to condition $\alpha \gg 1$.

The implosion velocity of the ablation surface is slow when compared with velocities in the expansion flow, so that to analyze the expansion in the ablation regime, the ablation surface may be set at $\xi=0$, where to match with the cold high density compression region the density goes to infinity, both temperature and velocity vanish, and the pressure takes a finite value; then for values of the beam and plasma parameter such as $n_r \ll n_o$ we may write as boundary conditions $u=\theta=0$ and $\nu\theta=\gamma$ at $\xi=0$, where γ is an unknown constant defined in terms of the ablation pressure as:

$$\gamma = \frac{Z_i P_a (t/\tau)^{1-5p/2}}{(Z_i+1) n_r k T_r} \quad .$$

In addition, at the plasma vacuum interface $x_v(t)$ (which must satisfied the condition $dx_v/dt=v(x_v,t)$) we have zero density and undisturbed values of the beam parameter:

$$\nu=0 \quad , \quad \nu_b=u_b=1 \quad \text{at } \xi \to 2u/(p+2) \quad ;$$

notice that system (1)-(5) must be solved subject to six boundary conditions since γ is unknown.

It is easy to verify that the solutions of system (1)-(5) behave in the neighbourhood of $\xi=0$ as

$$\theta=A(-\xi)^{1/3} \quad , \quad \nu=(\gamma/A)(-\xi)^{-1/3} \quad , \quad u=-B(-\xi)^{1/3} \quad , \quad u_b=C(-\xi)^{1/6} \quad ,$$

where

$$C = [\frac{6\gamma}{A}\Phi(\beta C/A^{1/2})]^{1/4} \quad , \quad B=Z_i C^2/[5\gamma(Z_i+1)]$$

and A is an arbitrry constant.

Once the expansion is determined one may calculate the ablation pressure P_a and the ablated mass rate per unit area $\dot{m}$ as a function of the parameters of the problem:

$$P_a=[(Z_i+1)n_r k T_r/Z_i]\gamma(p)(t/\tau)^{5p/2-1} = \bar{P}_a \gamma(p)(t/\tau)^{5p/2-1} \quad ,$$

$$\dot{m}=(m_i k T_r/Z_i)^{1/2} n_r \frac{\gamma B(p)}{A(p)}(t/\tau)^{2p-1} = \bar{\dot{m}} \frac{\gamma B(p)}{A(p)}(t/\tau)^{2p-1} \quad ,$$

in terms of the beam and plasma parameters $\bar{P}_a$ and $\bar{\dot{m}}$ becomes

$$\bar{P}_a = 5.9\ 10^8 \frac{Z_i+1}{Z_i} [\frac{A_i E_o^3 I_o}{A_b Z_b^3 Z_i \tau}]^{1/2} \quad \text{Pa} \quad ,$$

$$\bar{\dot{m}} = 1.75\ 10^7 \frac{1}{Z_i} \frac{E_o^2 A_i}{A_b Z_b^2 \tau} \quad \text{kg m}^{-2}\text{s}^{-1} \quad ,$$

where E_o, I_o and τ are in Mev, Acm^{-2} and nanoseconds respectively, Figures 1 and 2 show the ablation pressure and the ablated mass rate as a function of time for several values of p. The obtained results may be now applied to determine the acceleration efficiency of thin foils impinged by an intense

ion beam.

REFERENCES

FERNANDEZ,A. and BARRERO, A.(1986) Plasma Physics and controlled Fusion 27,989
JACKSON,J.D.(1975)Electrodinamica Clasica, Wiley 3th Edition.
MELHORN, T.A. (1981) J.Appl. Phys.52,6522.
MIYAMOTO,K. (1980) Plasma Phys. for Nuclear Fusion,MIT Press, Cambridge.
NARDI,E.,PELEG,E. and ZINAMON,A.(1978) Physics of Fluids,21,574.
OLSEN,N., MELHORN,T.A.,MAENCHEN,J. and JHONSON; D.J. (1985)J.Appl.Phys58,2958.

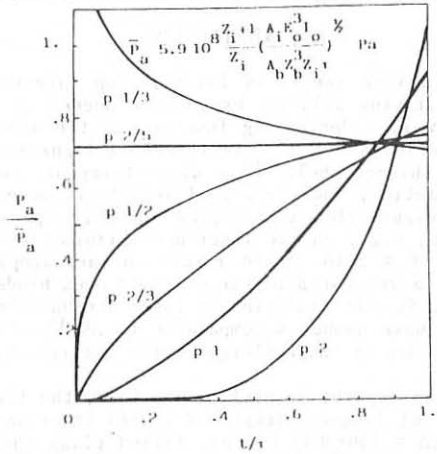

Figure 1.- Ablation pressure versus time for several values of p.

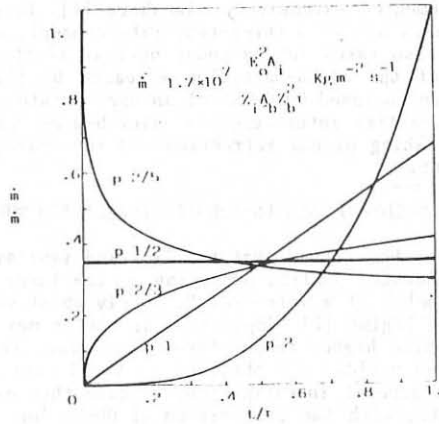

Figure 2.- Ablated mass rate versus time for several values of p.

2-D NUMERICAL STUDIES OF NON-UNIFORMILY IRRADIATED THIN SHELL TARGETS AND OF THE IGNITION OF ICF PLASMAS

S. Atzeni

Associazione EURATOM-ENEA sulla Fusione, Centro Ricerche Energia Frascati, C.P. 65, 00044 Frascati, Rome, Italy

1. INTRODUCTION

The interest in thin shells as laser fusion targets is motivated by the fact that the driving ablation pressure P needed to attain a certain implosion velocity v is a decreasing function of the aspect-ratio, or radius-to-thickness ratio, $A = R_o/\Delta R_o$ of the shell (approximately $P \propto v^2/A$). On the other hand, thinner shells pose more stringent requirements to the uniformity of irradiation, and are also likely to be more sensitive to the ablation-front Rayleigh-Taylor instability. Roughly speaking, long scale-length perturbations, e.g., due to laser non-uniformities corresponding to spherical harmonics $\ell = 2 \div 16$, could result in macroscopically asymmetric implosions, that in a reactor size target could even hinder the attainment of central ignition. Shorter scale-length laser non-uniformities and target imperfections (with wave number k comparable to ΔR_o^{-1}), could instead seed the most dangerous modes of the Rayleigh-Taylor instability of the ablation front.

In this paper we report, in preliminary form, the first numerical results on the effect of long-wavelength ($\ell = 2 \div 8$) laser non-uniformities on high aspect ratio ($A = 100 \div 300$) D-T gas filled glass shells, and also on the ignition of asymmetric, compressed target configurations.

For both studies we have used the 2-D Lagrangian fluid code DUED, which has been documented extensively elsewhere [1]. Here it suffices to recall that DUED makes use of a three-temperature model, with flux-limited conductivities. It also takes into account nuclear reactions and time dependent diffusion of the alpha-particles released by the D-T reactions. Matter properties are included by means of an appropriate real-matter Equation-of-State. Laser-matter interaction is described by means of a 2-D ray-tracing algorithm, taking plasma refraction and inverse-Bremsstrahlung absorption into account.

2. IMPLOSION OF NON-UNIFORMILY IRRADIATED SHELLS

Recently, it has been shown that two limiting implosion regimes exist for ablatively accelerated shells, depending on the laser pulse and target characteristics, namely, i) a more "soft", purely ablative regime, and ii) a shock-multiplexing regime [2]. Implosions in the former regime result in higher densities, while higher temperatures (and also, in current experiments, higher neutron yields) are obtained in the latter regime. In order to perform a rather general investigation, we have then made two series of numerical experiments, with the 2-T version of DUED, for a target imploded in regime i) (case a), and a for target imploded in a regime close to regime ii) (case b), respectively. Target a) has $R_o = 250$ μm, $A = 100$, and is

irradiated with a laser pulse with wavelength $\lambda = 0.53$ μm, energy E = 200 J and triangular time shape, with $\Delta t(FWHM) = 3$ ns and rise-time of 1 ns. According to 1-D simulations the shell maximum compression is attained at t = 5.0 ns, but the first shock already reaches the center at t = 4.2 ns. Most of the target implosion can be described as a free-fall. In case b) we have considered the target and laser parameters of a Rochester experiment [3], namely $R_o = 350$ μm, A = 250, $\lambda = 0.351$ μm, absorbed E = 1.6 kJ, $\Delta t(FWHM) = 700$ ps (in a Gaussian pulse with peak power at t = 1.2 ns and pulse duration of 1.4 ns). We have assumed centrally focused irradiation, with a perturbation (constant in time) described by Legendre polynomials with $\ell = 2,4,8$ and peak-to-valley relative amplitudes $\Delta I/I_o$ in the range 0.01-0.30. Since peak intensities for cases a) and b) are about 5×10^{12} and 8×10^{13} W cm^{-2}, respectively, absorption is efficient and classical; also, thermal conductivity smoothing of the irradiation non-uniformities should be poor. Since $P \propto I^{\beta}$, with $\beta = 0.6 \div 0.8$, we then expect pressure perturbations $\Delta P/P \propto \beta(\Delta I/I)$.

We measure the shell deformation at time t as the ratio $\varepsilon(t) = (R_{max} - R_{min})/R(t)$, where R_{max} and R_{min} are the maximum and the minimum value of the fuel-shell interface radius, respectively, and $R = (R_{max} - R_{min})/2$. The results of the simulations are found in agreement with a simple model, giving $\varepsilon = \beta(\Delta I/I)C$, where $C = R_o/R(t)$ is the convergence ratio of the shell. As a typical result, in Fig. 1 we show the mesh somewhat after shock reflection at the centre, but prior to the reflected shock-shell collision, for three targets of class a), for mode number $\ell = 4$, and $\Delta I/I_o = 0.02$, 0.06, and 0.10, respectively.

As far as the inner gas is concerned, a rather general feature is found, which is a also apparent in Fig. 1, namely, the convergence of the deformed shell induces jet-like perturbations of the gas, opposite in phase with the applied laser perturbation. It is worthy to observe that analogous structures have been observed in the numerical study of cylinders imploded by a non-uniform pressure [4].

The effect of this phenomenon has not in general be evaluated quanti-

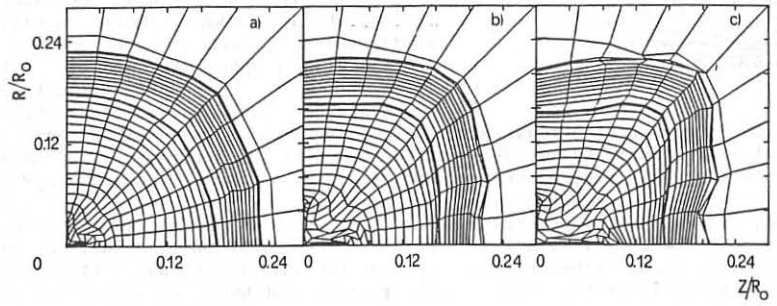

Fig. 1: Class a) targets (see main text) irradiated with a non-uniformity described by an $\ell = 4$ Legendre mode and peak-to-valley amplitudes of a) 2%; b) 6%; and c) 10%. The figures show the mesh of the imploded shells at t = 4.5 ns. The marked curve is the fuel-shell interface.

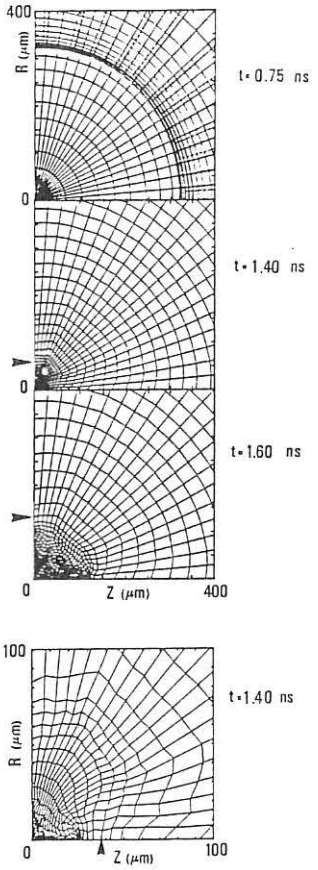

Fig. 2: Implosion of a class b) target (see main text) irradiated with non-uniformity described by a sum of ℓ=2,4,8 Legendre modes, resulting in a peak-to-valley amplitude of 17%. Solid lines:mesh; dashed lines:rays; the arrows indicate the fuel-shell interface.

tatively because in the presence of strongly sheared flows the mesh of DUED distorts substantially, thus leading to premature termination of the simulations. However, while for case a) implosions this occurs well before stagnation of the imploded shell even for very small values of $\Delta I/I_o$, for case b) implosions this only occurs for relatively large values of $\Delta I/I_o$ ($\Delta I/I_o$ about 0.20) and in any case not much before shell stagnation. For instance in Fig. 2 we show the implosion of a class b) shell irradiated with a perturbation consisting of a certain composition of the modes ℓ = 2,4 and 8, with global $\Delta I/I_o$ = 0.17.

An important effect which remains to be addressed is the Rayleigh-Taylor instability of the fuel-shell interface, and its interaction with the reflected shock.

3. IGNITION OF AN ASYMMETRIC, INITIALLY ISOBARIC TARGET

The fuel configuration of greatest interest for ignition studies [5,6] is that in which the fuel is isobaric, a central hot-spot with radius R_h, temperature T_h, and density ρ_h, being surrounded by cold fuel with density $\rho_c >> \rho_h$. As a first approach to the 2-D study of this problem we have simulated with the complete, 3-T version of DUED, two simple configurations, in which either an ellipsoidal hot-spot (with axes b_r and b_z) is contained in a spherical cold D-T system (with radius R_c) or a spherical hot-spot is contained in an ellipsoidal system. For the moment we have only considered cases in which 1-D ignition is non-marginal (e.g., by taking T_h = 6 keV, $\langle\rho_h R_h\rangle$ = 0.3 g cm^{-2}, $\langle\rho_c R_c\rangle \cong$ 3 g cm^{-2}, and ρ_h/ρ_c > 10). We have found that in these cases even a 2:1 deformation of either the hot-spot or the full target has little effect on ignition and burn. An example of such a study is reported in Fig. 3. Here initially the hot-spot has b_r = 62.5 μm, b_z = 125 μm, T_h = 6 keV and ρ_h = 30 g cm^{-3}, and is immersed in a sphere of D-T, with radius R_c = 154 μm, $T_c \cong$ 350 eV and ρ_c = 500 g cm^{-3}. Figures 3a and 3b show the evolution of the burn-wave, while Fig. 3c that of the in-

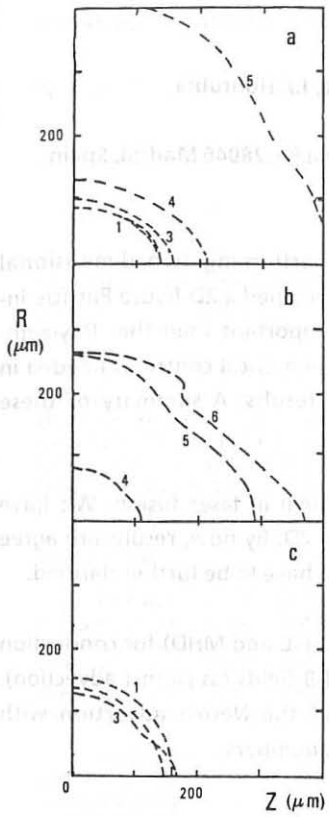

Fig. 3: Ignition of a D-T sphere, triggered by an ellipsoidal hot-spot (see main text). A) iso-temperature T_i= 5 keV; b) Iso-temperature T_i= 50 keV; c) front of the disassembling (rarefaction) wave, shown by the outer iso-density ρ=450 g/cm^3. 1) t=0; 2) t= 75 ps; 3) t=125 ps; 4) t=175 ps; 5) t=225 ps; 6) t=250 ps.

ward moving disassembling wave. In this case the fractional burn-up of the fuel is about 90% of that the equivalent 1-D case. Further studies are necessary to extend these preliminary results to a more general set of initial conditions and to shorther scale-length asymmetries (e.g., by taking ℓ = 4÷16 modes of perturbations of the hot-cold fuel interface).

4. CONCLUSIONS

The results of Sect. 3, if validated by further studied, would indicate that, in the absence of fluid instabilities and of quasi-turbulent fluid motion, a value of ε up to unity could perhaps be tolerated in a reactor size target. This, in turn, would limit the irradiation non-uniformity to $\Delta I/I_o < (C\beta)^{-1}$. Caution in using this result is however needed in view of the findings on the behaviour of the converging and reflected shock waves in the D-T gas. Indeed the latter phenomenology, which seems to be consistent with recent experimental [2,3] and numerical results [7], requires more accurate and specific studies.

REFERENCES

[1] S. Atzeni, Comput. Phys. Commun. 43, 107 (1986).
[2] C. Yamanaka et al., Phys. Rev. Lett. 56, 1575 (1986).
[3] M.C. Richardson et al. Phys. Rev. Lett. 56, 2048 (1986).
[4] S. Atzeni, A. Caruso and V.A. Pais, Phys. Lett. 120A, 343 (1987).
[5] S. Atzeni and A. Caruso, Phys. Lett. 85A, 345 (1981).
[6] S. Atzeni, "The Physical Basis for Numerical Fluid Simulations in Laser Fusion", invited review paper submitted to Plasma Phys. Controlled Fusion (1987).
[7] R.L. Mc Crory et al. in "Twenty Years of Plasma Physics" ed. by B. McNamara, World Scientific, Singapore (1985), p. 204.

INSTABILITIES AND SYMMETRY EFFECTS IN LASER PLASMA INTERACTION

P.M. Velarde, J.M. Aragonés, L. Díaz, J.J. Honrubia

Instituto de Fusión Nuclear (DENIM). Pº Catellana 80, 28046 Madrid, Spain

Several instabilities are studied in some extent performing two dimensional simulations. For mixing of two materials we have developed a 2D-hydro Particle-in-Cell (PIC) code (ARWEN). This effect can be more important than the Rayleigh-Taylor instability in some high-gain targets. Strong numerical control is needed in order to limit the numerical diffusion for reliable results. A summary of these properties is presented.

Actually Raman Scattering (SRS) remains as a problem in laser fusion. We have continued with the simulations with WAVE code in 2D. By now, results are agree qualitatively with the reported ones, but some points have to be further clarified.

We have implemented the ANTHEM code[2] (implicit PIC and MHD) for conduction problems with the produccion and amplification of B-fields (as Nernst advection). We are continuing the previous simulations about the Nernst advection with inertia, higher frecuency lasers and differents atomic numbers.

REFERENCES

1. D. FORSLUND: "Fundamentals of plasma simulation "LA-UR-85-413 (1985)
2. R. J. MASON: "An Electromagnetic Field Algorithm for 2-D Implicit Plasma Simulation" LA-UR-1391 (1986)

TRANSMUTATION PRODUCTS AT FUSION REACTOR FIRST-WALLS

Perlado, J.M., Sanz, J., de la Fuente, R.

Instituto de Fusión Nuclear (DENIM) Univ. Politécnica Madrid

1.-INTRODUCTION

The effect of radiation-induced transmutation products in the mechanical responses and bulk material properties of the structural materials in fusion environments has been remarked by different authors and experimental evidences have been obtained [1,2,3].

Among the different produced elements the most considered and studied has been the helium, and that was started in the mid-sixties with the research of the (n,α)-produced helium in structural, material of the fision reactors [4]. However, the main effect in fision, and even in fast fision reactors is the displacement damage because the cross reactions of the neutron induced reactions are relatively small. When the neutron spectra of the fusion reactors are considered an important increase of the current cross sections is obtained and the effect of the transmutated product by neutron reactions can be very significative.

The mechanism of the incidence of helium production in the material properties must be viewed through the atomic behaviour of the metal structures where the helium is implated, and the nucleation and growth of helium bubles [1]. Experimental results under equivalent conditions to fusion reactors show the existing dependance of the changes in tensile strength, creep rupture, fatigue and sweeling whit the generation of helium in the structures.

As it was pointed out in other works [5], the general strategy that has been adopted follows the above ideas in the sense to separate clearly the determination of the primary damage state (initial defect production due to displacement damage and transmutation reactions) and the succesive mechanisms of the diffusion and interaction of the created defects.

The aim of this work is to present the results obtained with three different neutron spectra on two stainless steels which are candidate to be structural materials in the future NET device. We analyze the generation of transmuted elements in general and particularly the helium generation. The use of our computational codes allows us to obtain general results for each component elements which can be easily treated. The significance of the helium production in comparison with other elements is presented together with the main contributors for the different cases to the helium generation.

2.-CALCULATIONAL PROCEDURE

In the calculations presented here, we use the general procedure developed in our Institute for activation problems, but properly adapted for the

analysis of transmuted elements. The scheme has been reported [6] and applied to the activation of some stainless steels [7]. It makes use of an activation code ACAB [6] which has a central algorithm from ACFA [8]. The UKCTRIIIA [9] data library has been used in our calculations. The selected response functions (gas, solid impurities generation) are analyzed with a fast and general module, PAC [6], which is here appropriatte to this transmutation problem, PACTR.

3.-RESULTS

The three different spectra that we analyze in this work can be represented by their typical mean energy: vessel of a fision reactor $<E>$ = 0.31 MeV, magnetic confinement fusion $<E>$ = 4.856 MeV, inertial confinement fusion assuming a final compression of ρR = 4 g/cm^2 $<E>$ = 1.59 MeV.

The two stainless steels that we have been studied correspond to the denomination: DIN 1.4914 and 316 L SS, and the two both are considered in the design of the NET project.

Let us first start with the considerations on the relations of the total transmuted elements with the helium production. In fig. 1, and 2, the increase

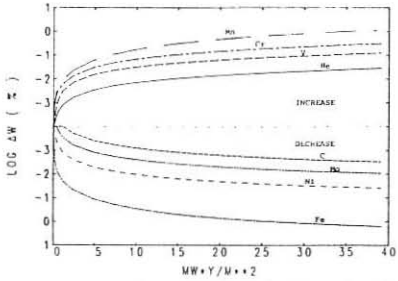

Fig. 1.- Weight variation (DIN1.4914)

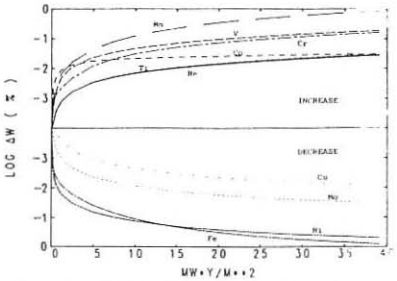

Fig. 2.- Weight variation (316LSS)

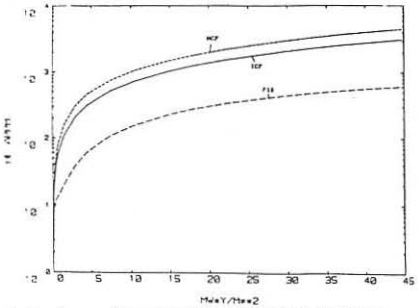

Fig. 3.- He-production (APPM) for different spectra vs. exposure (DIN 1.4914)

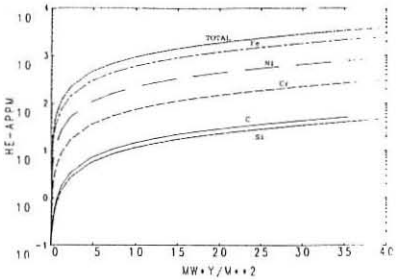

Fig. 4.- He-production (APPM) from different initial element vs. exposure (316LSS, magnetic spectrum)

and decrease of the element concentrations in the lograrithmic of the percentage of the weight variation versus the total exposure (MW x Y/m2) is represented. In both cases, a fractional helium production less than that for other elements (Mn, Cr, V, Co, Ti) is observed.

In order to give a representation of the spectrum influence in the helium generation, the fig. 3 represents the helium concentration in appm versus the exposure for the three different spectra. A large difference is observed among the fision and fusion which in any case is larger for magnetic spectrum. These conclusions shown for DIN 1.4914 can be extended to 316 L SS.

The main contributors for helium production for the two steels are represented in fig. 4 and 5 which give the helium concentration versus exposure in the case of the total amount and the corresponding for each one of the

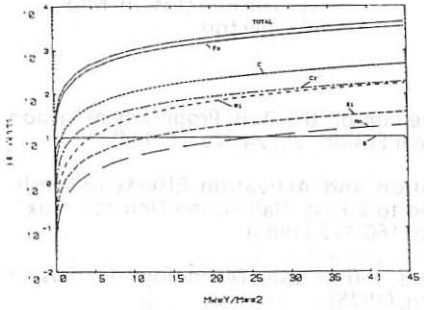

Fig. 5.- He-production (APPM) from different initial element vs. exposure (DIN 1.4914, magnetic spectrum).

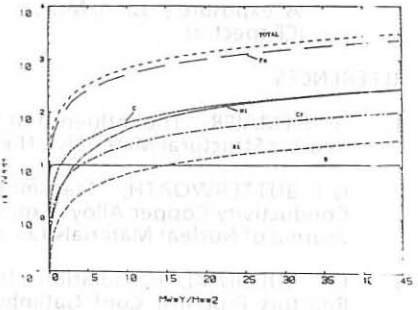

Fig. 6.- He-production (APPM) from different initial element vs. exposure (DIN1.4914, inertial spectrum)

significative component element. In both cases, the iron is the most important initial element, which in the case of the DIN1.914 represents almost the totality of the helium existance. The same effect is also noted in Fig. 6 where the ICF spectrum is considered. Nickel contribution in this last case becomes more important than in magnetic environment, and under MCF spectrum and 316 L SS should be the second important element.

The unit concentration curves for iron and nickel initial components are shown in fig. 7 and 8. They represent, the helium production motivated by these two initial components versus exposure, with different spectra. The influence of the spectrum is remarkable when observing the contrary effect for iron and nickel in the helium generation.

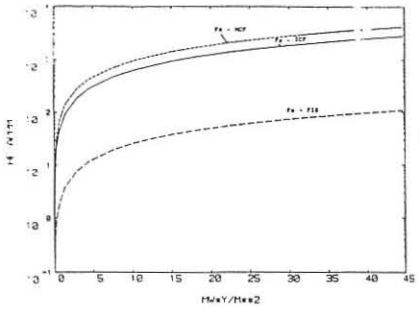

Fig. 7.- He-production (APPM) per unit concentration of iron. vs. exposure (fission, MCF, ICF spectra)

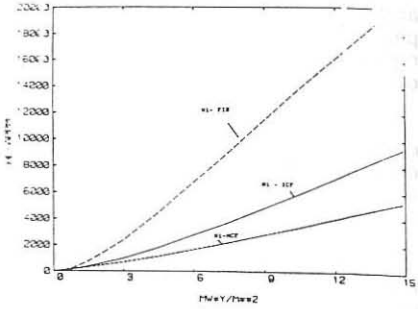

Fig. 8.- He-production (APPM) per unit concentration of nickel vs.exposure (fission, MCF, ICF spectra)

REFERENCES

1.- H. ULLMAIER, "The Influence of Helium on the Bulk Properties of Fusion Reactor Structural Materials", Nuclear Fusion, Vol 24. No.8 (1984)

2.- G.J. BUTTERWORTH, "Transmutation and Activation Effects in High-Conductivity Copper Alloys Exposed to a First Wall Fusion Neutron Flux", Journal of Nuclear Materials 135, pg. 160-172,(1985)

3.- G.L. KULCINSKI, in Radiation Effects and Tritium Technology for Fusion Reactors, Proc. Inst. Conf. Gatlinburg, (1975).

4.- R.S. BARNES, Nature 206, pg. 1307 (1965)

5.- J. SANZ, R. DE LA FUENTE, J.M. PERLADO, "Numerical Simulation of Radiation Damage in Fusion Reactors at DENIM", Workshop on Radiation Damage Correlations and Dosimetry, CEA, Paris, October 1986, DENIM 097.

6.- J.M. PERLADO, P. HERNAN, J.M. SANTOLAYA, J. SANZ,"Comparative Analysis of ICF Blankets: Data and Methodology Requeriments", Proceedings of the 4th ICENES, 45, Madrid, (1986).

7.- P. HERNAN, J.M. PERLADO, J.M. SANTOLAYA, J. SANZ "Low Activiation Studies Considering Candidate Steels: Calculational Procedures and Evaluation", Fusion Technology 10,3, 1489 (1986).

8.- H. BROCKMANN, U. OHLIG, "ACFA: A General Purpose Activation Code" JÜLICH-1866, September (1983).

9.- O.N. JARVIS, "Description of the Transmutation and Activation Data Library UKCTRIIIA", AERE R-9601, Atomic Energy Research Establishment Harwell (1980).

X-RAY AND OPTICAL SHADOWGRAPHY OF LASER HEATED CAVITIES

I.B. Földes(*), R. Sigel, Chen Shi-Sheng(+), K. Eidmann, R.F. Schmalz, G.D. Tsakiris, S. Witkowski

(*) Max-Planck-Institut für Quantenoptik, D-8046 Garching, FRG
(*) on leave from Central Research Institute for Physics, Budapest, Hungary
(+) Shanghai Institute of Optics and Fine Mechanics, Shanghai, People's Republic of China

The transformation of pulsed laser radiation into thermal soft x-rays becomes possible with the application of the closed geometry of small cavity targets. The hollow gold spheres are excellent tools for laboratory studies of radiation hydrodynamics, and they also have a possible future application for inertial confinement fusion. Radiation confinement and temperature is generally investigated by soft X-ray spectroscopy |1|. A complementary method, i.e. the investigation of the outward motion of the cavity wall is presented here in order to obtain information on the mass ablation and pressure at the inner wall of the cavity.

The third harmonic, λ=0.44 μm radiation of the Asterix III. iodine laser system was focussed into the center of the entrance hole of the gold cavities (Fig. 1). Cavities of 250-300 μm diameter were preferentially used, the wall thickness was varied between 2 and 8 μm. The laser pulse duration was 300 ps and the maximum absorbed energy 15 J.

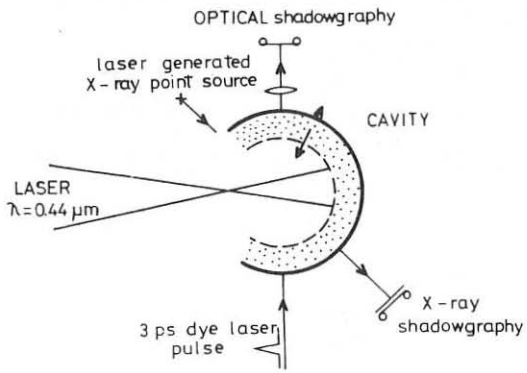

Fig. 1
The scheme of the experiment

The optical shadowgraphy used 3 ps dye laser pulses of 0.58 μm wavelength |2|. Images of the cavities were obtained in each of the six frames (relative delay: 3 ns) from a direction approximately perpendicular to the main laser beam. The observation angle was 135° in the case of X-ray shadowgraphy.

The point projection method [3] was used for X-ray shadowgraphy. A 4-5 J pulse was split off the main laser beam and tightly focussed onto the Cu backlighter after an optical delay of 3 or 6.5 ns. A spatial resolution of 30 μm was obtained. The detector was a Kodak 101-01 film with Al filter. The optical density on the film was caused partly by the 1.5 keV, partly by the 8 keV radiation of the backlighter. Whereas the cavities were expected to remain opaque for the 1.5 keV radiation, it was observed that the ones with the thinnest, 2 μm wall thickness became partially transparent for the backlighter radiation. This observed transparency is explained by the stronger penetration capability of the strong K-band emission of the backlighter at 8 keV.

There are some general features in the optical and X-ray shadowgrams. The rear wall which is directly hit by the λ=0.44 μm radiation is preferentially accelerated. The local intensity here can be much higher ($\sim 5 \cdot 10^{14}$ Wcm^{-2}) than the average absorbed laser intensity ($S_L \leq 2.6 \cdot 10^{13}$ Wcm^{-2}), thus the local ablation and acceleration is high. The other part of the wall shows a remarkably uniform but slower outward motion. The uniform motion is attributed to the ablation caused by the X-rays received from the primary spot. These characterics are visible on Fig. 2a.

An interesting observation can be done in the case of X-ray shadowgrams for cavities of 2 μm wall thickness, 6.5 ns after the heating laser pulse. The cavities become strongly transparent by that time, and the density of the highly transparent wall material seems to be decayed. An internal, less transparent, not spherical structure can be distinguished. This is explained to be caused by the stalk which disturbs the spherical symmetry and causes a more complicated hydrodynamical behaviour of the ablated material inside the cavity.

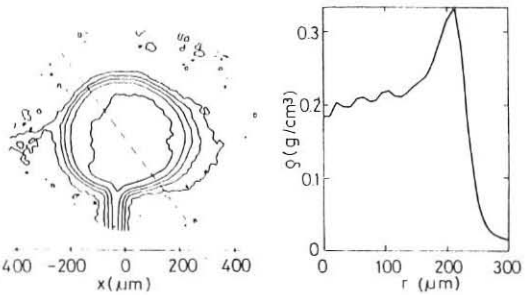

a) Isointensity curves b) Density profile

Fig. 2
X-ray shadowgram 3ns after the heating pulse. Direction of laser beam: from left to right.
Wall thickness: 2 μm

A lot of information can be derived using this transparency of the thin wall cavities. It is possible to obtain the density profile of the moving wall the first time from the X-ray shadowgrams. We used the fact that the cavity expansion is basically spherical. After digitizing the film density and converting it to X-ray intensity the 2D isointensity curves could be plotted in Fig. 2a. Now the radial density profile was deter-

mined in the upper hemisphere along the dotted line with an Abel inversion (Fig. 2b).

An average velocity of $(2.3\text{-}2.5)\cdot 10^6$ cm/s of the density maximum is obtained. Besides the density maximum a large amount of material can be observed inside the cavity. This refers to high ablation which can be caused by the X-ray drive only. Even the maximum density appears to be approximately 2 orders of magnitude less than solid density.

Fig. 3 shows the increase of the radius with time for cavities with 2 µm wall thickness, heated by $2.1\cdot 10^{13}$ Wcm^{-2} average laser flux. The displacement of the outer contours of the cavity determined from the X-ray shadowgrams (x) is in good agreement with that obtained from the optical shadowgrams (o). The position of the density maximum from the X-ray pictures (Δ) corresponds to a smaller velocity.

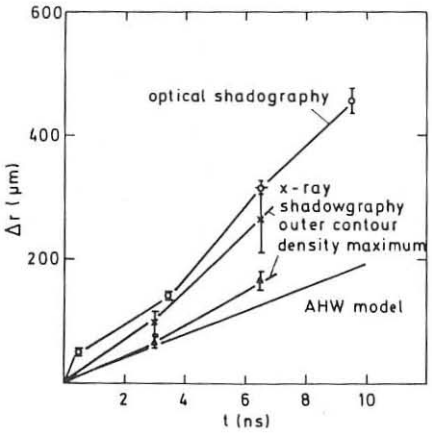

Fig. 3
The increase of cavity radius with time

The results are interpreted in terms of the ablative heat wave (AHW) model [4]. This is based on the ablative heat wave driven by the soft X-rays into the cavity wall, and assumes thermalization of laser radiation to black-body radiation field which is in equilibrium with the wall. The results of the AHW model which are in agreement with that of a multigroup radiation hydrocode are plotted in Fig. 3. The agreement between the AHW model and the motion of the density maximum is satisfactory, with the model slightly underestimating the experimental results.

The experimental scaling with absorbed laser flux is also well described by the $v \sim S_L^{10/13}$ scaling law of the calculations [4]. The maximum accelerating ablation pressure was ~1Tpa and the mass ablation rate $\sim 1.2\cdot 10^{-3}$g cm^{-2}. The deviation between experiment and theory is more con-

siderable in the case of cavities with thicker walls, where only the outer contours can be seen (they are not transparent). The difference can be explained by the kinetic pressure of the plasma filling up the finite sized cavities and causing a post-acceleration of the wall which was not taken into account in the calculations. The AHW velocity drops with the initial wall thickness, d_o and the kinetic pressure effects scale with $d_o^{-1/2}$, therefore the relative importance of the latter increases for thicker walls.

The wide density profile and the low measured densities can be understood neither within the frames of the model, nor by the simulations which predict high densities and low temperatures even when they take into account radiation transport. A density decay is expected if the wall becomes heated during expansion. Radiation preheat is a possible mechanism, but not too probable for the rather thick gold walls [5]. Our simulations show that the accelerated material is left in the condensed state.

We suggest fragmentation of the expanding cavity wall as a possible explanation. Obviously such fragmentation must occur if the material remains in the condensed state because the surface area of the cavity cannot increase so much, consequently the wall simply breaks. The fragmented wall may then expose a larger surface to the radiation and to the outstreaming plasma, thus an enhanced flow of energy steams into the fragments. It could happen that in this way the wall material becomes vaporized during expansion. The effect can be called enhanced preheat due to fragmentation. Additional evidence for fragmentation is served by the detection of long X-ray pulses (3-7 ns) from the cavity, which refer to a rather high, 10-20 eV radiation temperature. This might be caused by the leakage of radiation through the wall fragments or radiated by the wall if it is heated after fragmentation.

It can be concluded that in the future attention should be paid also to fragmentation, i.e. the exact equation of state of the material. This effect may be namely present in other types of laser targets as a consequence of deformation by beam nonuniformity or Rayleigh-Taylor instability. The observed symmetry and velocity of the cavity expansion supports the spectroscopical results and confirms the predictions based on an ablative heat wave driven by the thermal soft X-rays in the cavity.

This work was supported in part by the Commission of the European Communities in the framework of the Association Euratom/IPP.

References

[1] R. Sigel; this conference (invited)
[2] A.G.M. Maaswinkel et al.; Rev. Sci. Inst. 55, 48 (1984)
[3] M. Miyanaga et al.; Appl. Phys. Lett. 42, 166 (1983)
[4] R. Pakula, R. Sigel; Phys. Fluids 28, 232 (1985) and 29, 1340 (1986)
[5] J.L. Bocher et al.; Phys. Rev. Lett. 52, 823 (1984)

ABSORPTION OF LASER RADIATION IN THE COLLISIONLESS REGION OF THE PLASMA AT LASER FUSION EXPERIMENTS

F. F. Körmendi

Institute H .T. M., Belgrade,Yugoslavia

It is well known that the appearance of suprathermal electrons /1/ in laser fusion experiments, whose origin is also a subject of theoretical investigations, reduces the effectiveness of implosion /2/ and thus represents a con - siderable problem. In order to give an appropriate explanation of the generation of energetic electrons in laser produced plasmas, we shall analyze the nonlinear interaction of laser radiation with truly free electrons which form the collisionless part of the created plasma at high temperatures on the basis of our results in nonlinear quantum elec - trodynamics obtained earlier /3,4/.

Let us assume that at the interaction of laser radiation with a free charged particle of initial and final four momenta p_o, p, respectively, n monochromatic photons of four momenta k_o are elastically scattered to k with a simultaneous absorption or emission of N photons. T he conservation law

$$p_o + nk_o = p + nk + Nk_o \qquad / N = \pm 1, \pm 2 .. / \quad /1/$$

determines the necessary number of scattered photons n ,

$$n = P_0(k_0 - k)/2k_0k + \frac{N}{2} \pm \left\{ \frac{[P_0(k_0-k)]^2}{4(k_0k)^2} + \frac{N^2}{4} + \frac{NP_0(k_0+k)}{2k_0k} \right\}^{1/2} . \qquad (2.)$$

The transition probability per unit time P' at optical frequencies may be factorized in the form /4,5/

$$P' = P_n P'_N ,$$

with $P_n = K^n$, $K \to 1$. This condition determines the threshold incident beam intensity I_c

$$I_c = \hbar w_o^3 / r_o c 2\pi ,$$

w_o being the angular frequency of the photons, r_o - the classical radius of the particle, above which the absorption becomes probable. At incident laser beam intensities

$$I = 10^{15} \text{ W/cm}^2 - 10^{17} \text{ W/cm}^2$$

and $w_o = 10^{15}$ rad/s the effective cross section for the absorption of one photon by a free electron is

$$\sigma \approx 10^{-19}\text{cm}^2 - 10^{-17}\text{cm}^2 ,$$

respectively. With the help of these results one may evaluate the energy exchange rate between the photon field and the electron

$$\frac{\partial E}{\partial t} = c \int n(k_o) \frac{d\sigma}{d\Omega} \cdot n(\vec{p}_o) \hbar\omega_o \, d\vec{p}_o \, d\Omega \,, \qquad [3]$$

where $n/\vec{p_o}/$ is the electron distribution, $n/k_o/$- the photon density. At incident laser beam intensity

$$I = 10^{15} \text{ W/cm}^2 - 10^{16} \text{ W/cm}^2$$

$w_o = 10^{15}$ rad/s, a single pulse of $\Delta t = 10^{-8}$ s duration may accelerate an electron to

$$\Delta E = 10^5 \text{ eV} - 10^6 \text{ eV}$$

respectively, if the initial kinetic energy of the free electron does not exceed $E_K = 10^4$ eV.

References:

/1/ Armstrong C. et al., Journ. Appl. Phys.50,5233/1979/

/2/ DuderstadtJ.,Moses G.,Inertial Confinement Fusion. J. Wiley, N.Y. /1982/

/3/ Körmendi F., Optica Acta 28,1559 /1981/

/4/ Körmendi F., Optica Acta 31,3011 /1984/

/5/ Körmendi F., in III Int. Conf. ICOMP,Iraklion /1984/

PRELIMINARY MEASUREMENTS OF PLASMA TEMPERATURE AND CONFINEMENT TIME IN THE REXIMPLO SPHERICAL PINCH

E. Panarella* and V. Gilv
National Research Council of Canada
Ottawa, Canada K1A 0R6

ABSTRACT - In a pilot experimental program of modest initial condenser bank energy (~ 1KJ), the spherical pinch mechanism of plasma containment and compression leads to: 1) a plasma temperature of 730 eV, and 2) a containment time of 5.4 μsec. Moreover, the plasma is stable during the containment time. In discharges in deuterium, neutrons are emitted close to 10^7 per shot. From the experimental parameters of the plasma, one can derive a particle density for the shocked gas equal to 3.21×10^{19} cm^{-3} and a product $n\tau = 1.73 \times 10^{14}$ cm^{-3}·sec.

1. Experiment

The spherical pinch configuration is characterized by a hot, dense plasma in the center of a sphere, plasma which is contained and compressed by spherical shock waves created by strong discharges at the periphery of the metal vessel. Figure 1 reports in schematic form the discharge vessel. Both the central plasma and the peripheral shock waves are created by electrical discharges through electrodes. In the pilot experimental program that we have carried so far, in order to visualize the plasma motion, we have adopted a cylindrical configuration, rather than spherical. In other words the vessel is at present a cylinder of 1.15 cm height and 2 cm radius, closed on one side with a metal plate and open on the other side from where the plasma can be observed. 36 electrodes are radially accommodated along the peripheral circle of the cylinder, so as to have 36 sparks. All discharges, including the central one, are individually fed by 0.5 μF condensers charged to 10.5 KV. By carefully adjusting the gap of the central spark, self-breakdown of this gap occurs first, the UV radiation from the plasma so created triggering all peripheral discharges.

Figure 2 shows three streak records of the central plasma when it is compressed by the imploding shocks. The first record at left is a record of the plasma luminosity time history, as observed with an image converter camera. The original pressure of the hydrogen gas in the chamber was 6000 Torr, corresponding to a density of 2.14×10^{20} cm^{-3}. This record shows that the central plasma is being compressed by the imploding shocks.

Since the plasma luminosity can only provide a general indication of the events occurring in a plasma, we reduced the plasma luminosity recorded by the camera and obtained the streak record shown in the center of Fig. 2. We observe now that the central plasma seems to disappear at $t \cong 6$ μsec from the initiation of the discharge. In other words, the plasma becomes black at the time of maximum compression. Clearly, this effect is a manifestation that the plasma blockbody radiation, because of the compression and subsequent temperature rise, shifts towards the XUV range.

---

*Also with Advanced Laser and Fusion Technology, Research Division.

In order to have a confirmation of this we placed in front of the camera a narrow band interference filter centred at λ = 3900 Å, bandwidth 60 Å. We virtually rejected in this way all visible light except that at λ = 3900 Å. The streak record at the right of Fig. 2 shows the final plasma. Clearly, this is the hottest plasma formed during the compression phase. This remarkably stable plasma lasts ~ 5.4 μsec.

The same experiment was then repeated by fully enclosing the cylindrical discharge chamber with a metal plate and working with deuterium. Four calibrated silver activation neutron detectors were radially and symmetrically placed on a 60° solid cone angle having apex at the central plasma. Neutrons were detected in this experiment. Within the above solid angle, and within the experimental errors, the neutrons were symmetrically emitted. Their average number was 7.11×10^6 per shot.

2. Analysis

The imploding shock wave, as shown in Fig. 2 (left and central photographs), reach the central plasma after ~ 0.8 μsec. At this time compression begins. Knowing that the radius of the cylindrical vessel is 2 cm, the shock wave velocity is therefore $V_s = 2.50 \times 10^6$ cm·sec^{-1}. The shock wave velocity V_s is related to the energy density deposited at the periphery of the vessel through the following relation [1] $V_s = 42.16 (E_s/M_s)^{1/2}$. We find $E_s/M_s = 3.52 \times 10^5$ J/g. The volume of the hot plasma is assumed to be a small sphere whose radius $r = 7.94 \times 10^{-2}$ cm is obtained from the size of the plasma in Fig. 2 (right photograph). Hence, the volume V is: $V = 2.09 \times 10^{-3}$ cm^3. Finally, the containment time is assumed to be the time duration of the plasma shown in Fig. 2. It is τ = 5.4 μsec. We are now in a position to derive both plasma temperature T and average particle density $\bar{n}_p$, as follows. The final plasma pressure P_p is: $P_p = (\bar{n}_p/2)$ kT. This pressure must be equated to the imploding shock wave pressure P_i: $P_i = (4/3)\ \rho_o(E_s/M_s)$. Hence, we find: $\bar{n}_p = (8/3)\ \rho_o(E_s/M_s)(kT)^{-1}$, where $\rho_o = 10^{-3}$ gr. cm^{-3} is the initial gas density at 6000 Torr. On the other hand, the Maxwell average $\langle\sigma v\rangle$ is given by: $\langle\sigma v\rangle = 2Y_n/\bar{n}_p^2\ \tau\ V$, where Y_n is the total number of neutrons emitted by the plasma. Replacing the values of the parameters found before one gets: $\langle\sigma v\rangle = 3.67 \times 10^{-23} (kT)^2$, where kT is now expressed in KeV. On the other hand the dependence of $\langle\sigma v\rangle$ on kT is given by: $\langle\sigma v\rangle = 1.50 \times 10^{-14} (kT)^{-2/3} \exp[-18.6(kT)^{-1/3}]$. Equating this expression for $\langle\sigma v\rangle$ with the previous one, we find: kT = 0.73 KeV. This is therefore the plasma temperature. If we now insert in the formula for $\bar{n}_p$ the value of the parameters found before and the value of kT just found, we get: $\bar{n}_p = 8.03 \times 10^{18}$ cm^{-3}. This is the average particle density.

Clearly, the transmitted shock within the plasma compresses the gas by a factor of 4. Hence, the particle density of the shocked gas is $n_p = 3.21 \times 10^{19}$ cm^{-3}. With this value of n_p and for τ = 5.4 μsec one gets $n_p\tau = 1.73 \times 10^{14}$ cm^{-3} sec.

References

[1] E. Panarella and P. Savic, Jour. Fus. Energy 3, 199 (1983).

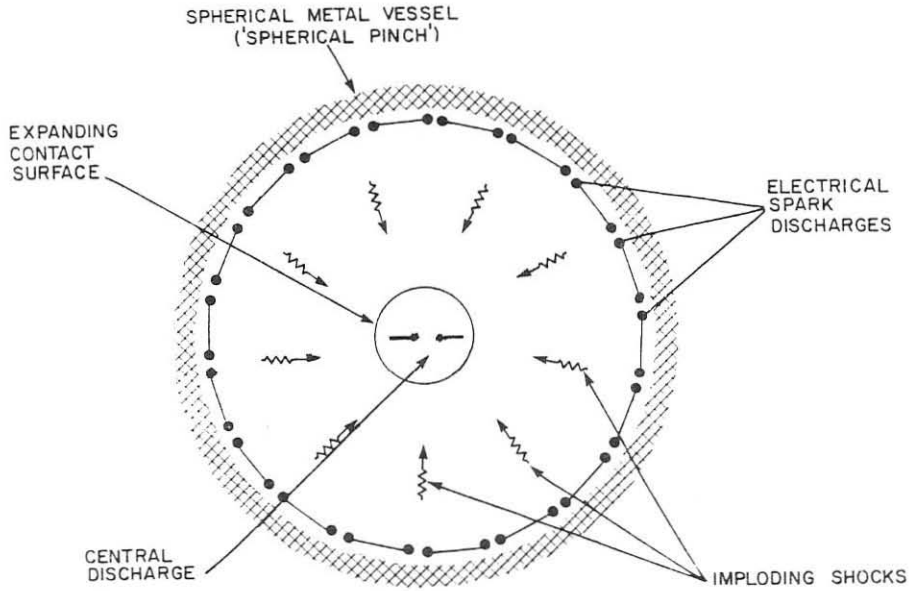

FIG. 1 - Spherical pinch apparatus for plasma formation and heating. The central discharge and the peripheral discharges are simultaneously fired.

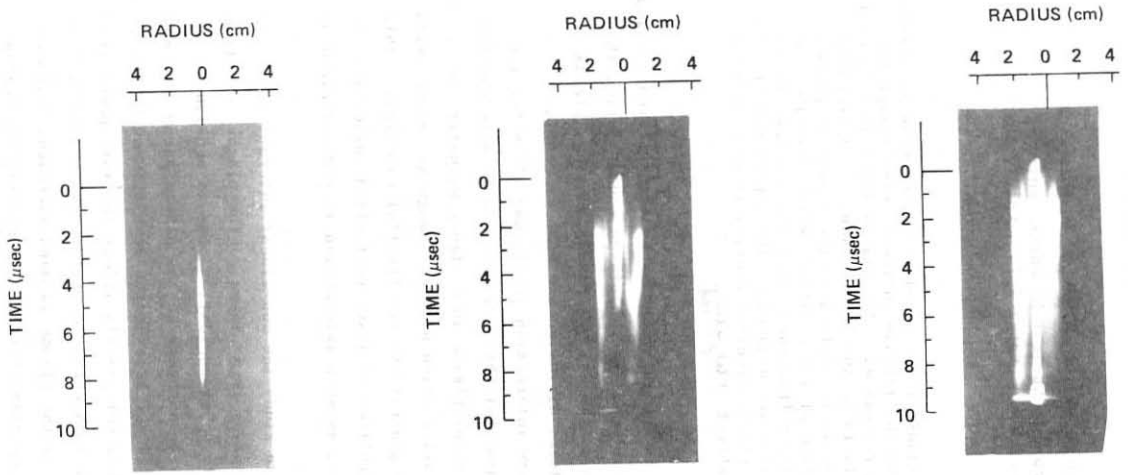

GAS: HYDROGEN

PRESSURE: 116 psi = 8 Atm = 6000 Torr

DENSITY: 2.14 × 10^{20} cm^{-3}

CONDENSER BANK ENERGY:

PERIPHERAL DISCHARGES ~ 1kJ

CENTRAL DISCHARGE ~ 30J

FIG. 2 - Streak record of the plasma, when it is compressed by the imploding shocks. The record at left is the time history of the plasma luminosity. The central record is the time history of the plasma, when its recorded luminosity has been greatly reduced. The record at right is the plasma as observed through a narrow band filter centered at λ = 3900 Å and bandwidth 60 Å. This is the hottest plasma, which is stable and lasts 5.4 μsec.

NON-LINEAR PHENOMENA IN ANISOTROPIC PLASMA

R.N. El Sherif, Sh.M. Khalil and M.A. Bourham

Plasma Physics Department, Nuclear Research Centre,
Atomic Energy Authority, Atomic Energy 13759, Cairo, Egypt

Abstract

The work is devoted to the study of the non-linear phenomena in plasmas where surface waves are coupled to the intense incident electromagnetic waves with maximum absorption at resonance. The plasma layer is subjected to a constant external magnetic field in the Z-direction. A proposed function for the density distribution is applied in the region of plasma inhomogenuity. Computer simulation of the equations which describe the generated wave has been made at laser frequency range for a dense plasma, and electron plasma density profiles are deduced. The dependence of the plasma electron frequency on the plasma electron density is also deduced, and the critical density is calculated at $\omega_p \sim \omega_{rad}$.

Introduction

Plasma, by its very nature, is a highly non-linear electric medium, and the investigation of the non-linear phenomena in plasma would clarify the importance of the kinds of plasma instabilities, plasma heating, plasma confinement, plasma radiation, plasma diffusion and wave generation[1].

The effects of non-linear wave interaction in plasmas allow for the possibility of extending the fundamental physical concepts to more complex situations, primarily to inhomogeneous plasma in a strong magnetic field, as well as to bounded plasma. The interaction of electromagnetic waves with plasma and the corresponding wave generations are fruitful examples. This is very important for practical problems of laser controlled fusion and it presents much fundamental interest, as such interaction is characterized by a number of non-linear phenomenae.

The purpose of this work is to study the non-linear interaction of the S-polarized radiation and surface waves in a plasma. The plasma electron density distribution is proposed to be sinusoidal. Due to non-linear interaction in a plasma, there may be a change in the plasma parameters and absorption of the waves occures[2,3]. At electron densities much less than critical ($n/n_c \ll 1$), the plasma does not greatly affect the wave propagation ($\varepsilon \approx 1$). As the density of the plasma aproaches the critical density (at which $\omega_p \sim \omega_{rad}$) the influence of the plasma is much increased as $\varepsilon \to 0$.

The critical density has an important role in determining the region where the influence of the plasma is great.

Theoretical Treatment and Numerical Calculations

The solution of the non-linear interaction of incident electromagnetic radiation on surface waves[4] in anisotropic plasma is computed, with a proposed plasma electron density of the form[5] :

$$n(x) = n_c \, \mathrm{Sin}(\pi x/a)$$

Numerical calculations for various values of $\omega_p^2(x)/\omega_{rad}^2$ in the range of a plasma layer $0 \leqslant x \leqslant a$ is performed. The absorption coefficient has been numerically calculated at resonance ($A \approx 1$). Strong absorption and plasma heating are expected at resonance ($\xi \approx 0$).

Starting from the equations which describe the interacting waves:

$$E_1 = \varkappa_{01} E_{01}\left[x + \int_0^x dx' \int_0^{x'} dx \, \varkappa_1^2 x\right] - E_{01}\left[1 + \int_0^x dx' \int_0^{x'} \varkappa_1^2 \, dx\right]$$

$$E_2 = E_{02}(1-r_s)\left[x - \int_0^x dx' \int_0^{x'} \varkappa_2^2 \, dx\right] + i\varkappa_{02}E_{02}(1+r_s)\left[x - \int_0^x dx \int_0^{x'} \varkappa_2^2 \, x dx\right]$$

Where,

$$\varkappa_{01} = \omega_1 \left(n_1^2 - 1\right)^{1/2} / c \quad , \quad n_1 = k_1 c/\omega_1$$

$$\varkappa_{02} = \omega_2 \left(1 - n_2^2\right)^{1/2} / c \quad , \quad n_2 = k_2 c/\omega_2$$

$$\varkappa_1^2(x) = (\omega_1^2/c^2)(n_1^2 - \xi_1(x)) \, , \; \xi_1(x) = 1 - (\omega_p^2(x)/\omega_1^2) \quad \text{for surface waves.}$$

$$\varkappa_2^2(x) = (\omega_2^2/c^2)(n_2^2 - \xi_2(x)) \, , \; \xi_2(x) = 1 - (\omega_p^2(x)/\omega_2^2) \quad \text{for incident wave.}$$

$$\omega_p^2(x) = 4\pi e^2 n(x)/m \quad , \quad n(x) = n_c \, \mathrm{Sin}(\pi x/a)$$

r_s is the reflection coefficient, and $A = 1 - r_s - t_s$, and A is the absorption coefficient, and t_s is the transmission coefficient.

$t_s = 4\mu_r/(1+\mu_r)^2$, and μ_r is the refractive index[5] and is given by:

$\mu_r = 1 - (\omega_p^2(x)/\omega_{rad}^2)^{1/2}$, and $r_s < 1$[6] .

ω_1 and ω_2 are the interacting wave frequencies and:

$$\omega_{rad}^2 = (\omega_1 \pm \omega_2)^2 - \omega_c^2$$

Numerical calculations have been carried out by computer to compute the refractive index and absorption coefficient for a plasma characterized by : $\xi = 1 - (\omega_p^2(x)/\omega_{rad}^2)$ within the layer $0 \leqslant x \leqslant a$.

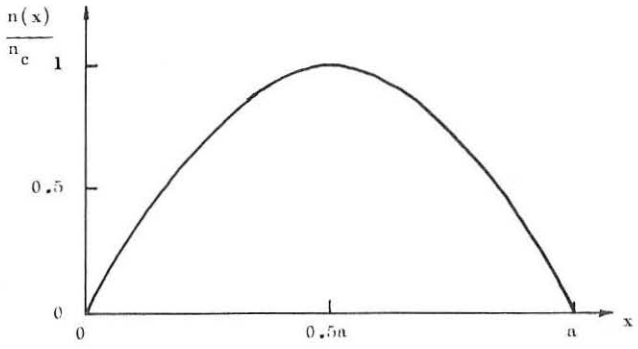

Fig.(1)

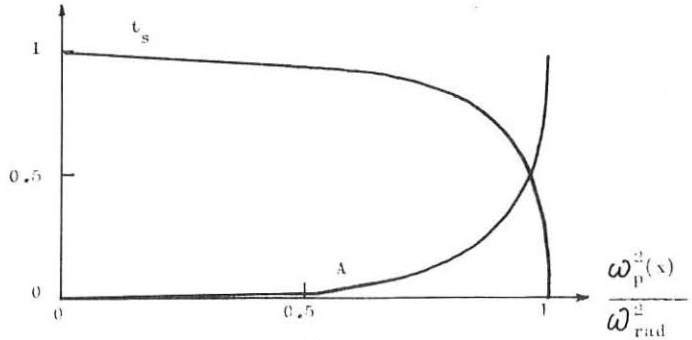

Fig.(2)

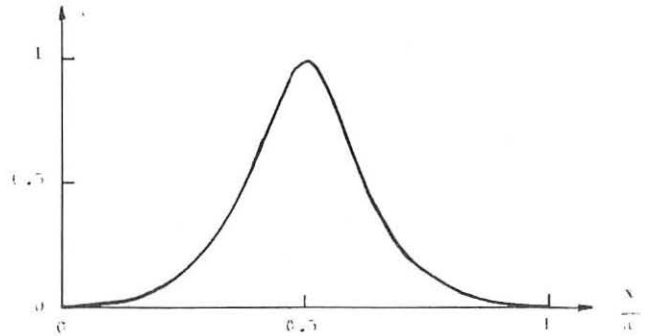

Fig. 3

Figure (1) shows the proposed electron density profile $n(x)=n_c \sin(\pi x/a)$, which exhibits a maximum electron density at the mid of the plasma layer.

Figure (2) shows the dependence of the refractive index t_s and the absorption coefficient A against the ratio $\omega_p^2(x)/\omega_{rad}^2$. It is clear that the maximum absorption occures at $\omega_p(x) \sim \omega_{rad}$, while the transmission coefficient approaches zero. This indicates that the maximum absorption of the generated power takes place at $\mathcal{E} = 0$, and the energy of the electromagnetic wave is transformed to the plasma.

Figure (3) shows the dependence of the absorption coefficient A on the spatial coordinate (x/a), showing a maximum absorption at x/a = 0.5, where the influence of the plasma is much increased.

Conclusion

The plasma electron density profile has been proposed to take the form $n(x) = n_c \sin(\pi x/a)$, and calculated numerically. By using the result $r_s < 1$, as given in reference number (6), it is concluded that the transmission coefficient is high at $0 \leqslant x$, and start to decrease approaching zero at x/a = 0.5, while the absorption coefficient is very small at $0 \leqslant x$ and starts to increase up to its maximum value during the space $0 \leqslant x \leqslant 0.5a$ as shown in fig.(3). Consequently, strong absorption and plasma heating are expected at $\mathcal{E} \sim 0$.

Referencec

(1) V.N. Tsytovich, "Non-linear Effects in Plasma", Plenum Press, New York, London (1970).

(2) Kaya Imre and Harold Weitzer, Phys.Fluids, 28, 1, January (1985).

(3) N.H. Burnett, Canadian J. Phys., 50, 3184 (1972).

(4) N.M. El Siragy, Sh.M. Khalil, Y.A. Sayed and R.N. El Sherif, Beitrage Aus der Plasmaphysik, 25, no.3 (1985).

(5) H. Huddleston and S.L. Leonard, "Plasma Diagnostic Techniques", Los Angeles, California, Academic Press New York, London (1965).

(6) I.G. Gekker, "The Interaction of Strong Electromagnetic Fields with Plasmas", Clarendon Press, Oxford (1992).

PROGRESS IN INERTIAL CONFINEMENT FUSION RESEARCH AT DENIM

Velarde, G., Aragonés, J.M., Honrubia, J.J., Martínez-Val, J.M. Mínguez, E., Ocaña, J.L., Perlado, J.M.

Instituto de Fusión Nuclear (DENIM). Univ. Politécnica Madrid

1.-INTRODUCTION

The research activities in Inertial Confinement Fusion (ICF) at DENIM are focused mainly in target physics, simulation and understanding of experiments. To this end, we have recently developed several models and numerical tools for the characterization of laser and ion beam-plasma interactions the target physics analysis, and material activ ation and damage.

Energy deposition by laser or ion beams to the plasma, radiation transport, atomic physics, charged particles, suprathermal and thermal electron transport have been the main improved topics, and a description of some of them will be presented.

Some results on the target analysis considering laser or ion beam with different pulse tailoring will be presented. In addition, numerical simulations were done to study the influence of different aspect ratios in the efficiency of the implosion and burnup of ICF targets.

2. SIMULATION MODELS

The ICF physics and computational developments at DENIM are incorporated or closely related to the NORCLA code for one-dimensional simulation of plane and spherical ICF targets. Figures 1 and 2 show the improved simulation models included in the NORCLA code [1].

The NORMA segment can compute the linear stopping of external ion beams using analytical stopping powers along radial tracks, with space dependent densities and temperatures at selected timesteps.

The laser interaction is considered at two simulation levels: ray tracing coupled to hydrodynamics and particle in cell (PIC). The ray tracing algorithm has been proved to be flexible, cheap in computer time and easy to implement. It includes current corrections for non Maxwellian electron distributions, approximate factors for stimulated Brillouin scattering and stimulated Raman scattering and radiation pressure projection in the radial direction. The PIC WAVE code [2] was used for more detailed simulations of laser interaction. In particular, the growth and saturation of SRS was simulated [1] showing its importance as mechanism in the hot electron production. Also, the WAVE code was used for simulating a neutralized beam impinging on a uniform plasma slab [1].

Braginskii fluid equations for thermal electrons have been included in the NORCLA code to be coupled to the charge particle transport through a self-consistent electric field. The diffusion approximation of the electron fluid equations is solved by the method of Chang and Cooper. This model provides a tool for the one dimensional simulation of hot electrons in laser produced plasmas.

Besides, we have implemented the ANTHEM code [3] (implicit PIC and MHD) for conduction problems with the production and amplification of B fields (Nerst advection), taking into account inertia effects, higher frecuency lasers and different materials.

The NORMA hydro solver has been extended to a fully implicit solution of the energy equations in 3 temperatures (electrons, ions and radiation). Radiation diffusion can be treated in a grey approximation, with Rosseland mean opacities. The multigroup radiation diffusion and discrete ordinates transport set of subroutines have been recently completed in a quasi-implicit coupling with the energy equations, and benchmarks are being completed [1]. For mixing of two materials, Rayleigh-Taylor instability and symmetry studies we have developed a 2D-hydro Particle-in-cell code (ARWEN).

Atomic data (EOS, ionization, conductivities and opacities) are available from the DENIM Atomic Tables which have been generated using a new family of atomic codes [1,4]. The PANDORA code uses the screened hydrogenic average atom model, whereas the ADELA code solves the DIRAC equation by the HFS method for average atom. The GEMINIS code computes the opacities. Recently, a new NLTE code (LIRA), which solves the time dependent rate equations, has been developed and tested.

A Thomas-Fermi code computes tabulated EOS and ionizations for elements in any T-ρ grid. This model provides also the mean ionization and the average ionization potential for partial ionized atoms in plasmas with any degeneracy, which are used to calculate ion stopping powers of the bound and free electrons of partially ionized plasmas. The model has been extended for calculations of the linear dielectric function in plasmas with any degree of ionization and degeneracy.

The time-dependent Fokker-Planck transport equation for charged particles is solved by a finite-element method [5]. Numerical benchmarks have shown that the method is very efficient.

The transport of knock-on deuterons and tritons by neutron scattering has been recently implemented in a coupled way to the neutron transport calculation [1,2]. The neutron distribution function provide the energy-angle dependent source of the recoil nuclei, which are transported by the same procedure as the alpha particles. The CLARA code has been extended for simultaneous transport of neutrons, alphas and knock-ons, calculating not only the energy deposition and momentum transfer but also the transport of mass (thermal ions) and the isotopic evolution by neutron reactions.

3.-ANALYSIS OF DIRECTLY DRIVEN TARGETS

Computer simulations have been carried out on heavy and light ion, and laser directly driven targets. The main purpose of these parametrical studies was to obtain a better understanding of the pulse shape, masses and aspect ratios influence in the high gain performance. The published works [1,6] related with this subject present more details about the characteristics of the energy deposition, implosion and burnup phases and show the range of variation of the driver energy for efficient power production. A synthesis of the results for light and heavy ions will be presented .

Some other related works have been performed in order to characterize the target with some well defined burnup parameter which allows a simple coupling of the neutronic responses of the ICF fusion blanket with the neutron spectra leaking from the target [7]. New simulation models and related works have been developed in order to take into account the activation of fusion materials, and a tentative scheme of material damage have been recently proposed.

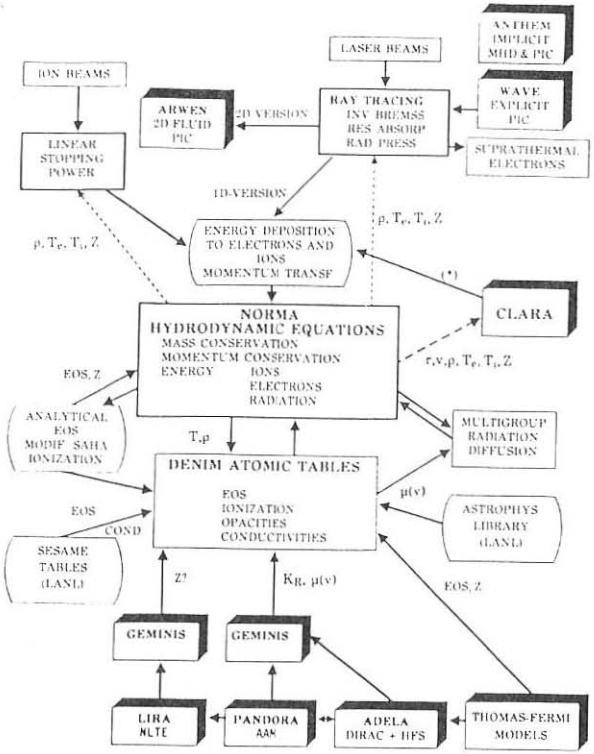

Fig 1. Simulation models for hydrodynamics in ICF plasmas

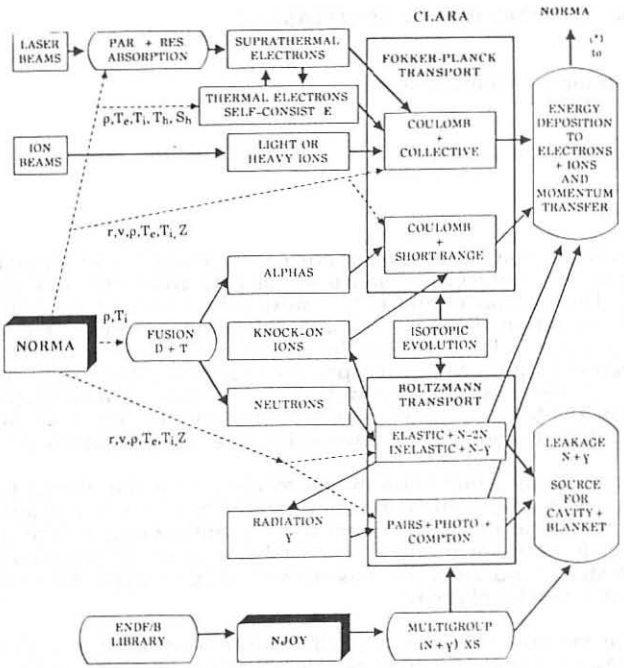

Fig. 2. Simulation models for particle transport in ICF plasmas

REFERENCES

1. VELARDE, G.,et al., Laser and Particle Beams, **4**, part 3&4, (1986), 349.
2. FORSLUND, D.W., in Los Alamos Nat. Lab. Report No. LA-UR-85-415 (1985).
3. MASON, R.J., "An Electromagnetic Field Algorithm for 2-D Implicit Plasma Simulation", LA-UR-1391 (1986)
4. VELARDE, G., et al., in Proc. 3rd International Conference Workshop on the adiative properties of Hot Dense Matter, Williamsburg (USA), (1985)
5. HONRUBIA, J.J., ARAGONES, J.M., Nucl. Sci. Eng. 93, (1986), 386.
6. VELARDE, G. et al., Trans. Am. Nucl. Soc. 49, (1985), 118
7. VELARDE, G., et al, Fusion Technology 8, 1, 2B, (1985) ,1850

DISTRIBUTION OF IONIZATION STATES IN PLASMAS

Mínguez E., Serrano J.F., and Gámez M.L.

Instituto de Fusion Nuclear [DENIM]

1.- INTRODUCTION

Low density plasmas, such as magnetic confinement fusion plasmas, are characterized by the reduced influence of particle collisions and photon reabsorptions. The corona model is the most useful tool to calculate the distribution of ionization states in this range of plasma densities. For higher density plasmas, such as laser and ion beam plasmas, Z-pinches, and other inertial confinement fusion [ICF] concepts, electron collisions and radiation interactions must be considered to determine a realistic distribution of ionization states. The Saha equation is usually applied in the higher range, and the collisional radiative model [1] must be used for the intermediate one.

This work contains a numerical model to determine the distribution of ionization states by solving the time-dependent rate equations. It is a useful tool to analyze atomic properties in ion beam plasma interactions, and to obtain radiation energy from bremsstrahlung and total energy in ICF targets. Also, it can be used to study laboratory plasmas, as well as to analyze the effects of impurities in fusion reactor plasmas.

Finally, the method has been applied to obtain results for argon and selenium plasmas, which have been compared with more detailed models.

2.- IONIZATION MODEL

The model used in this work solves the time-dependent rate equations. The processes considered are collisional ionization, radiative recombination, dielectronic recombination and 3-body recombination. The ionic states are coupled through the ground-state, and excited states are not considered in this case, although they can be determined with other model coupled with this one.

The energy levels for each ionization state used in the coefficients of the rate equations are determined by using a screened hydrogenic average atom model [2] with additional corrections given by pressure ionization, continuum lowering and spin-orbital effects, to the energy levels obtained through the analytical Dirac expressions for an isolated atom.

In a steady-state solution, the ratio of ion abundances at two ionization states, f_i and f_{i-1} is given by the ratio between the collisional ionization and recombination coefficients, yielding Z-1 coupled equations. The numerical solution used to solve both the time-dependent and steady state equations is provided to be very fast and stable. So, it should be used to work on-line with the hydrodynamic equations.

3.NUMERICAL RESULTS

The test cases chosen for comparing this model are two: one for argon plasma, and other for selenium one. In both cases the plasma is assumed in a steady-state, optically thin with negligible external photon flux.

The first case, reported by Stone and Weisheit [3] is an argon plasma, at ion density of $5{,}6 \times 10^{19}$ cm^{-3}, and temperatures from about 100 to 10,000 eV. A comparison between several NLTE codes, shows up importants deviations between them. The model here explained has been also compaired, essentially the average ionization and the ion abundances. The figure 1 represents the average ionization for the above conditions of temperature and ion density. The differences found came from the atomic model used for determining the coefficientes of the rate equations.

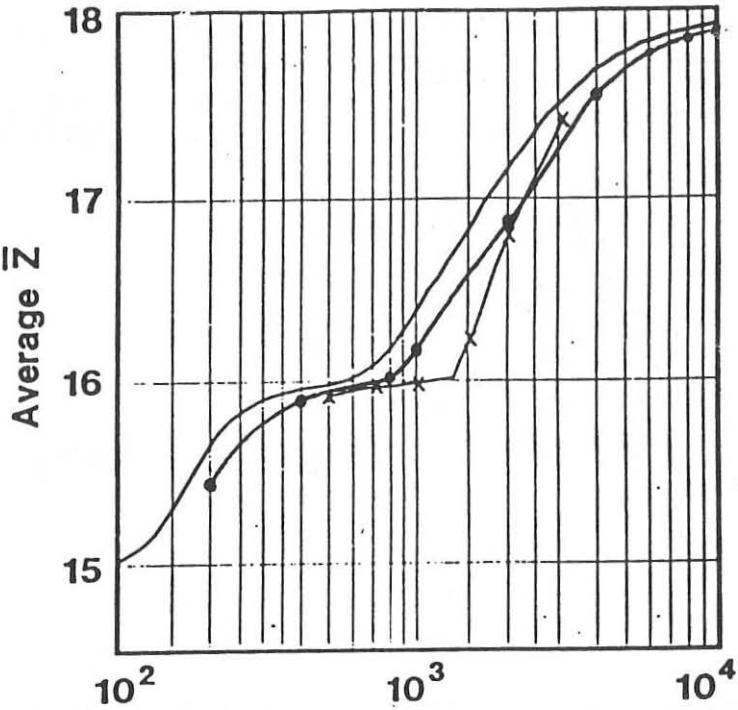

Fig. 1. Average ionization vs temperature for argon plasma, ion density of 5.6×10^{19} cm^{-3}.
(LINEZ ———; XSN –x–x–x–; LIRA (–●–●–●–)

The second case has been reported by Y.T. Lee [4] to check his program in a selenium plasma, used to study x-ray lasers. In the figure 2, the average ionization versus temperature for an electron density of 5×10^{23} cm^{-3}, calculated with this model shows a good agreament with the code reported by Lee, when the dielectronic recombination is taken into account. Finally because of the big differences found when the LTE and corona models are used, the conclusion must be focused to the use of NLTE models, more or less detailed depending of the analysis under studying.

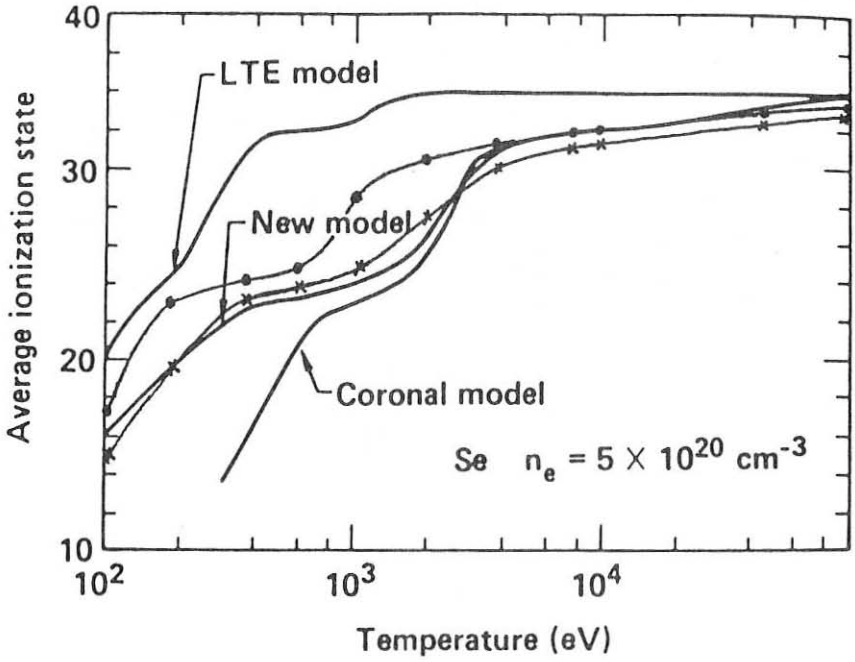

Fig. 2. Average ionization vs temperature for selenium plasma, electron density of 5×10^{20} cm^{-3}.
(YTL———new model; LIRA with DR –x–x–x–; LIRA without DR, –●–●–●–)

4.-CONCLUSIONS

It has been explained that in several ranges of interest, for instance: laser interaction with ICF targets, Z-pinch experiments, x-ray lasers and plasma spectroscopy experiments, models such as corona or LTE are very far of the real physical situation, so rate equations must be employed. The model here presented predicts average ionization and ion abundances within a permisible error, with a negligible calculation time. So, according to this, the model should be a preliminary candidate to be coupled to the hydrodynamic equations.

REFERENCES.

1.- R.W.P. McWhirter and T.F. Stratton, in Plasma Diagnostic Techniques, ed. by R.H. Hunddlestone & S.L. Leonard [Academic, NY, 1965].

2.- G. Velarde et al., in Radiative Properties of Hot Dense Matter III, ed. by B. Rozsnyai et al. World Scientific 1987.

3.- S.R. Stone & T. C. Wisheit, 5QSRT **35**, 67(1986).

4.- Y.T. Lee et al., in Radiative Properties of Hot Dense Matter III, ed. by B. rozsnyai et al. World Scientific 1987.

ANALYSIS OF RADIATION ENERGY TRANSPORT IN HIGH TEMPERATURE MEDIA. APPLICATION TO ICF TARGETS SIMULATION AND DIAGNOSIS

José Luis Ocaña.

Instituto de Fusión Nuclear (DENIM). Univ. Politécnica Madrid
Pº Castellana, 80, 28046 Madrid SPAIN.

1.- INTRODUCTION

A major problem in the analysis of radiation energy transport in dense, high temperature media (typical of ICF systems) is the strong non-linear character of the temperature dependent radiation source term, even under the assumption of local thermodynamic equilibrium (LTE)[1].

In addition, the coexistence of relatively optically thick and thin regions on both sides of the energy propagation front (typical in radiation dominated problems) difficults in a very important manner the calculation of energy fluxes across zone interfaces in a proper way, mainly because of the extremely different physical properties of cold and hot material[2,3].

In order to overcome some of these dificulties when using formally more simple treatments (diffusion codes, tipically), and as a way to obtain a prediction calculational tool for the analysis of experimental diagnostics, a radiation transport code has been developed, and some applications of it to characteristic problems have been made, including the generaly considered as a reference problem of propagation of thermal Marshak waves into cold, optically thick media with explicit consideration of the frequency dependence of the material photon cross sections.

2.- BRIEF QUALITATIVE ANALYSIS OF THE RADIATION TRANSPORT INFLUENCE ON THE DYNAMICS OF ICF TARGETS

Previous calculations carried out in the frame if the NORCLA code[4] (in which the energy transport by radiative processes is taken into account through diffusion conductivities) showed that radiation plays a major role in the ignition phase of ICF targets because at a few KeV it becomes an energy conduction mechanism dominant over electron + suprathermal particles conduction, a critical change happening over a short range of temperature[5].

According to these results, the success of the ignition seems to depend critically of the temperature evolution of the fusion fuel over that phase: if the fuel isothermalization resulting from the hydrodynamic compression attains a given temperature (say some KeV), ignition will presumably succeed and the fusion burst inmediately deploy.

In addition, the thermal radiation originating from the hot zones of the reacting fusion fuel has been acknowledged to play a not less important role in the process of fusion burn conditions propagation to relatively cold material surrounding them: In this process energy transport by charged particles + neutrons are recognized as the fundamental mechanisms in charge of

temperature feedback and energy delocalization[5] but energy transport by thermal radiation to more external zones has been observed to have an important effect over total fuel confinement time via thermal expansion of these layers.

3.- CALCULATIONAL TOOLS DESCRIPTION

In the non-linear radiation transport problem, the temperature and density dependent emitting and absorbing properties of the transport medium have to be obtained in terms of the past history of the radiation field and vice-versa: The knowledge of the radiation flux at any time allows for the direct determination of the energy an momentum sources to be included in the corresponding hydrodynamic equations characterizing the transport medium behaviour.

Further, in the cases in which local thermodynamic equilibrium (LTE) cannot be assumed, as, for example, in all those situations where the medium is optically thin (relatively transparent) to radiation (typical for diagnostic applications), the radiation field itself, including its detailed frequency (energy) dependence, influences to a critical extent the transport medium optical properties an emission dynamics and, consequently, the non-linear character of the problem is significantly strengthtened.

In the case of simplified geometries such as one-dimensional planar or spherical, it has been found more convenient (and so proceeds the developed code) to obtain the terms responsible for the energy and momentum contributions to the THD equations taking profit of the formal expression of the radiation transport equation itself, i. e. in the way:

$$\frac{\partial E}{\partial t} + \nabla.\mathbf{F} = \int_0^\infty d\nu \int_{4\pi} d\Omega \;\; \sigma_a' (B - I) \qquad [1a]$$

$$\frac{\partial \mathbf{M}_d}{\partial t} + \nabla.\mathbf{M}_f = \frac{1}{c}\int_0^\infty d\nu \int_{4\pi} d\Omega\Omega \;\; \sigma_a' (B - I) \qquad [1b]$$

instead of following the usual practice described for the general case in ref. 6

The developed code PLANCKY[7] solves the radiation transport equation in a multigroup frame for the energy (frequency) variable of the radiation specific intensity I (r, ν , Ω, t), with angular dependence taken into account through a discrete ordinates treatment, and uses the results obtained for this quantity to obtain the corresponding terms for coupling to the medium hydrodynamics in the way given by espressions (1).

For the appropriate treatment of the spatial variable discretization in order to yield the correct limits both in the cases of optically thick and optically thin media, an original scheme has been adopted based on the statement of the flux conservation over each spatial zone and the ensemble of discrete angular directions, and current correction at the zone interfaces in the case of optically thick medium to give the corresponding diffusion limit.

The time variable treatment is carried out in an semi-implicit way in the transport solution, and iteration is provided for accordance of the radiation

source to the transport resulting variation of the medium properties.

Originally the code has been developed for the solution of LTE problems, but simple modifications in the source term will allow, in connection with the radiation-hydrodynamics coupling phylosophy, for the resolution of non-LTE problems with strong energy dependence of the radiation source.

In addition, the program can treat without major dificulties radiation transport problems in which Compton scattering has a significant importance (i. e. very high temperature problems).

3.-APPLICATIONS

In order to test the results of the developed code, two different problems were chosen for which the code obtained the temperature profile evolution in a given medium and a comparison was established against the traditional references with indication of the computational effort required in each case. As a sample of the capabilities developed, we present here the corresponding results.

In a first case, the problem was analyzed of the propagation of a thermal Marshak wave into an initially cold slab of constant (non frequency or temperature dependente) opacity. The slab thickcness was 1.5 m.f.p., the spatial mesh 0,1 m.f.p. and the time step 0,05/c m.f.p. .A set of 4 discrete angular ordinates was used and the energy range (0,1 T_o - 10.1 T_o) was divided in 10 equally spaced groups.

The results obtained (see fig. 1) compare remarkably well with the reference provided by Campbell[8] (shown in solid line). The computational effort required scales as 0,0017. sec/time step/energy group/material zone/discrete direction in a CDC Cyber 170-835 computer, what gives a reasonably good code efficientcy even with a simplified transport-medium temperature coupling as the considered one.

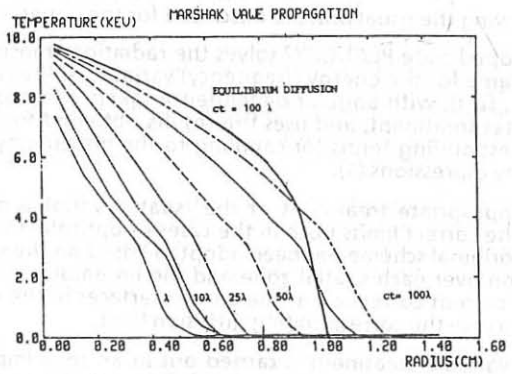

Figure. 1

The second problem analyzed was a similar one but with energy dependent opacities for the medium. In this case, a 100 m.f.p. (0) thick slab was chosen according to the same reference and a 50 zones spatial mesh was considered. The corresponding results (plotted in figure 2), were again reasonably good, the computational effort being in this case a bit higher than in the precedent one (~0,0022 sec. vs. 0,0017 sec. per unit calculational module).

In addition to the described kind of simple but rather critical problems, the described radiation transport analysis capability is being applied to the study of more realistic problems such as the dynamics of ICF targets, particularly in the field of analysis of planar and spherical targets compression experiments' diagnosis.

It is hoped that the capability provided by the detailed treatment of the energy and angle variables could serve as a useful tool for both the appropriate simulation and diagnostics interpretation of the treated kind of problems.

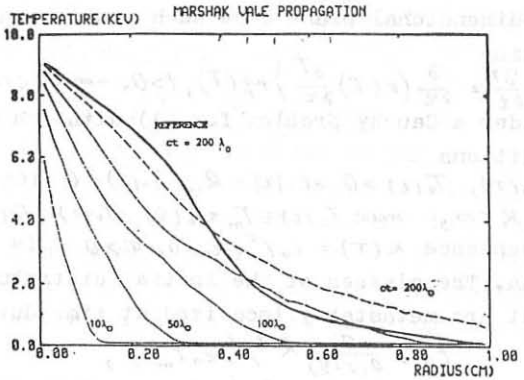

Figure. 2

REFERENCES.

1.- CAMPBELL, P.M., NELSON, R.G.:"Numerical Methods for Non-linear Radiation Transport Calculations". Report UCRL-7638. Lawrence Radiation Laboratory (1964)

2.- HANKIN, B.C. et al: J.Q.S.R.T. **11**, 949 (1971)

3.- BROWN, P.A.,et al: J.Q.S.R.T. **33**, 437 (1985)

4.- VELARDE, G., et al: Laser and Particle Beams **4**, 349 (1986)

5.- OCAÑA, J.L., et al: "Numerical Simulation of ICF targets driven by Heavy Ion Beams" 4th ICENES - Madrid June 30th-July 4th. 1986 p. 357

6.- POMRANING, G.C.:"The Equations of Radiation Hydrodynamics" Pergamon Press N. Y. 1973

7.- OCAÑA, J.L.:"Coupling of Radiation Transport Equations to the Hydrodynamics of High Temperature Media" 1984 DENIM Annual Research Report. Madrid 1985

8.- CAMPBELL, P.M.: J. Heat Mass Transfer **12**, 497 (1969)

DEVELOPMENT OF THE PEAKING REGIMES IN PLASMA AND EFFECTS OF THE ENERGY LOCALIZATION

N.V. Zmitrenko, S.P. Kurdyumov, A.A. Samarskii
Keldysh Institute of Applied Mathematics
USSR Ac.Sci., Moscow, USSR

The questions of the description of the energy balance taking into account the heat production and propagation processes (for example, by an electron heat conductivity) often play a decisive role in the study of plasma. The investigation of fusion ignition stage leads to situations like that both in the inertial confinement targets [1] and in the magnetic confinement systems [2].

On one-dimensional plane case such problems are described by the equation

$$\frac{\partial T}{\partial t} = \frac{\partial}{\partial r}\left(\kappa(T)\frac{\partial T}{\partial r}\right) + q(T), \quad t>0, \quad -\infty<r<+\infty. \qquad (1)$$

Let us consider a Cauchy problem for (1) with the following initial conditions

$$T(r,0)=T_0(r), \quad T_0(r)>0 \text{ at } |r|<R, \quad T_0(r)\equiv 0 \text{ at } |r|\geq R, \quad R<\infty, \quad \max T_0(r)\equiv T_m = T_0(0), \quad T_0(r)=T_0(-r). \qquad (2)$$

The dependence $\kappa(T)=\kappa_0 T^\sigma$, $\kappa_0>0$, $\sigma>0$ is characteristic of plasma. The classes of the initial distributions (2) $(q\equiv 0)$, that are metastably localized at time duration t_0,

$$t_0 \geq \frac{\sigma}{2(\sigma+2)} R^2/(\kappa_0 T_m^\sigma), \qquad (3)$$

$T(r,t)\equiv 0$ for all $|r|\geq R$ and $0<t<t_0$ are shown at [3]. Boundary regimes $T(0,t)$, that produce these localized profiles of temperature are peaking ones [3]: $T(0,t)=a_0(t_f-t)^n$, $a_0>0$, $-\frac{1}{\sigma}\leq n\leq 0$, $t<t_f<\infty$.

The peaking regimes originates in a natural way in a non-linear medium with $q(T)=q_0 T^\beta$, $q_0>0$, $\beta>1$. In this case the problem (1), (2) has a self-similar solution [4,5]

$$T(r,t)=q_0^n (t_f-t)^n \theta(\xi), \quad \xi = r\left[(\kappa_0 q_0^{n\sigma})^{1/2}(t_f-t)^m\right], \qquad (4)$$

where $n=-\frac{1}{\beta-1}$, $m=\frac{\beta-\sigma-1}{2(\beta-1)}$ and $\theta(\xi)$ is found from an equation

$$-n\theta + m\xi\theta' = (\theta^\sigma\theta')' + \theta^\beta \qquad (5)$$

with conditions $\theta'(0)=0$ and $\theta^\sigma\theta'\to 0$, $\theta\to 0$ at $|\xi|\to\infty$. These solutions describe an asymptotic stage of a process, when $\int_{-\infty}^{+\infty}\int_0^t q(T)\,dt\,dr \gg \int_{-\infty}^{+\infty} T_0(r)\,dr$.

For the case $\beta = \sigma+1$ $(m=0)$ (5) has [4,5] a solution (S-regime) $\theta_S(\xi) = \left[\frac{2(\sigma+1)}{\sigma(\sigma+2)}\cos^2(\pi\xi/\Delta\xi_T)\right]^{1/\sigma}$ which describes a localized heat structure with the invariable in time size of a burning region

$$L_T = \sqrt{K_0/q_0}\,\Delta\xi_T, \quad \Delta\xi_T = \frac{2\pi}{\sigma}\sqrt{\sigma+1}. \qquad (6)$$

L_T depends only on medium properties K_0, σ and q_0 (fundamental length (FL)). On case of HS-regime $(\beta<\sigma+1)$ the localization is absent, the burn region size $\sim(t_f-t)^m$ grows with the time $(m<0)$. At $\beta>\sigma+1$ (LS-regime) a half-width of a heat structure shortens, and $\theta(\xi)\to C(\xi^2)^{-\frac{1}{\beta-\sigma-1}}$ at $|\xi|\to\infty$. In this case (5) has a set of solutions ("eigen functions" (EF) of a non-linear problem). Their number is $N_{EF}=[a-[[a]/a]]$, $a=\frac{\beta-1}{\beta-\sigma-1}$, $[a]$ is an integer part of a [6]. Constant C_i is the analog of an eigen value for an i-th EF: $\theta_i(\xi)\to C_i\xi^{-\frac{2}{\beta-\sigma-1}}$, $C_i>C_j$, $i>j$. The form of EF $(1\le i\le 4,\ \sigma=2,\ \beta=3.18,\ N_{EF}=12)$ is shown in Fig. 1. If LS-regime is established with non-self-similar and finite initial data, the solution has a form of the first EF and is always strictly localized [7] (the asymptotics at $|\xi|\to\infty$ is not realized). This is connected with the majoration of the LS-regime by a certain S-regime, which has a finite burn region size (see Fig. 2).

Let us consider the case of an electron heat conductivity and a heat source $q_{\alpha T}(T)$, which is caused by a local absorption of α-particlies of DT-reaction. The power approximations [1,8] of $q_{\alpha T}(T)$ show that the source works in S-regime at $T\simeq 5\,keV$. The corresponding FL (6) is $\rho L_T \simeq 0.2\,g\,cm^{-2}$ [8]. The result of the computer simulation of the (1), (2) problem under $q_{\alpha T}(T)$ from [9] and taking into account the bulk emanation (which dominates for $T\le 4\,keV$) is shown at Fig. 3.

The investigation of HS, S and LS-regimes in a multi-dimensional case and for a density distributed in space is carried out in [10, 11].

The solutions of the following type

$$F_i(x,t) = B_{0i}(t_f-t)^{n_i} f_i(s), \quad s=\frac{x}{M_0} \qquad (7)$$

(M_0 is a plasma mass, x is a Lagrange mass coordinate, $B_{0i}=const$) are constructed [12, 13] for a system of one-

-dimensional equations, which describe plasma granting the ty-pical dissipative processes (heat conductivity, viscosity, sources and sinks of heat). These solutions are the generalization of a S-regime for this case, when gas dynamic motion is essential. Some of f_i are shown at Fig. 4 for the case when plasma in compressed by a cylindrical piston. Here $\xi = r[3\cdot10^{5} \times (t_f - t)^{4/5}]^{-1}$, $\theta = \kappa T[7.53\cdot10^{-14}(t_f - t)^{-2/5}]^{-1}$, density $\rho = \delta[1.67\cdot10^{-12}(t_f - t)^{-8/5}]$, magnetic field $H_z = h[0.388(t_f - t)^{-1}]$ in CGSE system, $M_0 \cong 0.94$g/cm. The heat structures, caused by a source action (ohmic heating, thermonuclear heat production) originate from (7) regime provided that adiabatic exponent $\gamma < \frac{5}{4}$ (axial) or $\gamma < \frac{4}{3}$ (spherical symmetry) [12, 13].

The realization of the (7) regime for a theta-pinch can eliminate the electron heat conductivity losses along the axis dew to the localization effect [14]. The estimation (3) gives for the pinch length $\ell_p = 2R$ the following value $\ell_p \cong \cong 4\cdot10^{10}\sqrt{\langle Te\rangle^{5/2} t_0 n_0^{-1}}$ cm, where $\langle \overline{Te} \rangle$ (eV) is a temperature in the middle of the pinch, t_0 (s) is the localization time, and density n_0 ($cc\,m^{-1}$) at the ends is constant (S-regime). The table of values ℓ_p, t_f and t_0 from [14] depending on parameter nt_0 is given below for $\langle Te\rangle = 1$ keV, $-8/5$ compression $\frac{n}{n_0} = 10^4$ and $n_0 = 10^{16}$ ccm^{-1}. If $n \sim (t_f - t)^{-8/5}$ along the entire pinch length, ℓ_p decreases $\sim$ 1,6 fold (LS-regime) [14].

REFERENCES

1. S.Yu. Gus'kov, V.B.Rozanov - Proc. Lebedev Phys. Inst., v.134, Moscow, Nauka, 1982, p.153-166.
2. A.D.Arinichev et al. - Plasma Physics,1986,v.12,N 12,p.1444.
3. A.A. Samarskii et al. - Doklady USSR Ac.Sci., 1975, v.223, N 6, p.1344.
4. A.A. Samarskii et al. - Ibid., 1976,v.227, N 2, p.321-324.
5. N.V. Zmitrenko et al. - Preprint N 74, Moscow, Keldysh Inst. Appl. Math., 1976.
6. A.A. Samarskii et al. - Doklady USSR Ac.Sci., 1977, v.237, N 6, p.1330-1333.
7. V.A.Galactionov - Diff.Equations, 1985, v.21, N 1, p.15-23.
8. N.V. Zmitrenko et al. - JETP Letters, 1977, v.26, N 9, p.620-624.
9. B.N. Kozlov - Atomic Power, 1962, N 12, p.238.
10. S.P. Kurdyumov et al. - Preprint N 16, Moscow, Keldysh Inst. Appl. Math., 1979.
11. S.P. Kurdyumov et al. - Journ. Comp. Math.Phys.,1986,v.26, N 8.
12. N.V. Zmitrenko, S.P. Kurdyumov - Doklady USSR Ac.Sci., 1974, v.218, N 6, p.1306-1309; v.219, N 3, p.578-581.

13. N.V,Zmitrenko, S.P.Kurdumov _ Journ.Appl.Mech.Techn.Phys., 1977, N 1, p.3-23.
14. N.V.Zmitrenko et al. - Preprint N 153, Moscow, Keldysh Inst. Appl. Math., 1980.

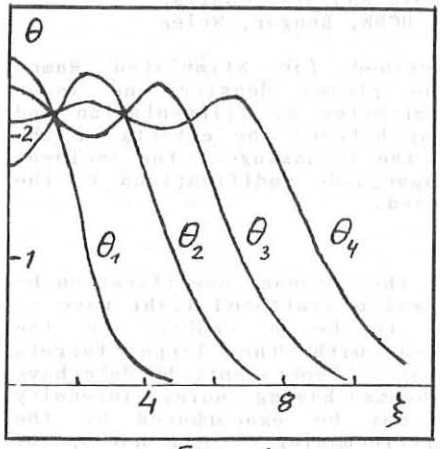

Fig. 1

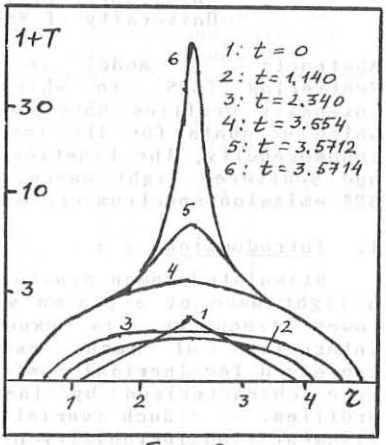

Fig. 2

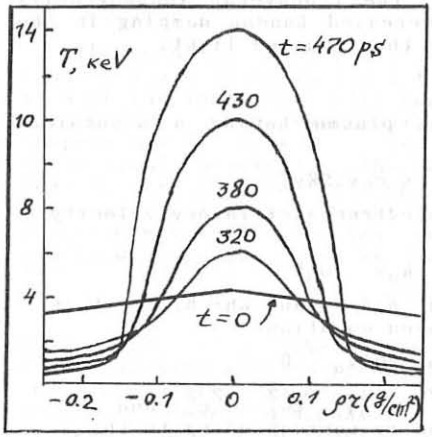

Fig. 3

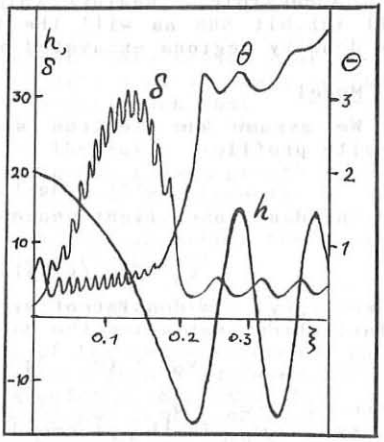

Fig. 4

nt_o (s/ccm)	10^{13}	10^{14}	10^{15}
L_p (m)	7.12	22.6	71.2
t_f (ms)	0.0316	0.316	3.16
t_o (μs)	0.10	1.00	10.0

STIMULATED RAMAN SCATTERING IN THE PRESENCE OF FILAMENTATION

H.C. Barr, T.J.M. Boyd and G.A. Coutts
University of Wales, UCNW, Bangor, Wales

Abstract: A model is described for Stimulated Raman Scattering (SRS) in which the plasma density and laser intensity profiles have been corrupted by filamentation and which accounts for the interplay between the effects of the inhomogeneity, the kinetics and the focussing of the incident and scattered light waves. Waveguide modifications to the SRS emission spectrum are discussed.

1. Introduction

Stimulated Raman Scattering, the resonant amplification by a light wave of a plasma wave and a scattered light wave of lower frequency, is expected to be a concern in the interaction of laser radiation with the large targets conceived for inertial confinement. Experiments to date have been characterized by laser beams having noisy intensity profiles. Such variations may be exacerbated by the filamentation instability or self-focussing of beam hot spots. Such locally intense laser radiation will make SRS thresholds more accessible; against this, the transverse inhomogeneity will inhibit SRS as will the increased Landau damping in the low density regions excavated by the focussed light.

2. Model

We assume an electron slab plasma having a sinusoidal density profile

$$n_o(y) = N_o(1 + \epsilon \cos 2Ky) \qquad (1)$$

and incident laser light whose electron oscillatory velocity is

$$\underline{v}_o = 2v_o(y) \sin (k_o x - \omega_o t)\hat{z} \qquad (2)$$

where $v_o(y)$ is consistent with $n_o(y)$ and which, for this polarization, satisfies the Mathieu equation

$$v_o'' + (a - 2q \cos 2\eta)v_o = 0 \qquad (3)$$

where $a = (\omega_o^2 - \omega_p^2 - k_o^2c^2)/K^2c^2$, $q = \epsilon\omega_p^2/2K^2c^2$ and $\eta = Ky$. ω_p is the plasma density corresponding to the mean density N_o . When $q < 1$, $v_o(y)$ is approximately uniform while, if $q > 1$, the light is strongly focussed or guided. The choice of (1) represents an infinite array of density channels. However, when $q > 1$, wave energy is localized or trapped within a single channel and hence we may expect the analysis to describe the behaviour of a single slab filament. The scattered light is polarized parallel to the laser light and described by a driven form of equation (3) . The plasma waves are described by the Vlasov equation

driven by the ponderomotive force of the beating light waves. Since the plasma wave energy is strongly localized, we need only use the appropriate local value of $v_o(y)$ as given by (3) and normalized to conserve energy and maintain pressure balance. Here we develop the theory assuming a uniform $v_o(y)$ and adjust the local value a posteriori when the location of the resonance is established.

The resulting equations then are the usual SRS equations which, when the sinusoidal density profile is included, become

$$\left[\omega_s^2 - \omega_p^2 - k_s^2\right] y_s(\underline{k}) - \frac{1}{2}\,\epsilon\,\omega_p^2\left[y_s(\underline{k}_+) + y_s(\underline{k}_-)\right] = ikv_o y_p(\underline{k}) \quad (4)$$

$$\left[1 + \chi^{-1}(\underline{k},\omega)\right] y_p(\underline{k}) + \frac{1}{2}\,\epsilon\left[\hat{\underline{k}}.\hat{\underline{k}}_+\, y_p(\underline{k}_+) + \hat{\underline{k}}.\hat{\underline{k}}_-\, y_p(\underline{k}_-)\right]$$

$$= i\,v_o\left[k\, y_s(\underline{k}) + \frac{\epsilon}{2}\,\hat{\underline{k}}.\hat{\underline{k}}_+\, y_s(\underline{k}_+) + \frac{\epsilon}{2}\,\hat{\underline{k}}.\hat{\underline{k}}_-\, y_s(\underline{k}_-)\right] . \quad (5)$$

All quantities are normalized to c,ω_o . y_s and y_p are proportional to the scattered and plasma wave electric fields respectively. $\chi(\underline{k},\omega)$ is the usual electron susceptibility . $\omega_s = 1 - \omega$, $\underline{k}_s = \underline{k}_o - \underline{k}$ and $\underline{k}_\pm = \underline{k} \pm 2\underline{K}$. It is the solution of the linear difference equations (4),(5) that constitutes the main result of this paper!

3. Results

The solution of (4),(5) for growth rate versus scattered frequency are shown in Fig.1 for a series of filament depths ϵ with the laser intensity kept uniform such that $v_o = 0.01c$. The mean density is $0.24n_c$ and the temperature is 2.5KeV . (n_c is the laser light cut-off, or critical, density). The homogeneous plasma growth rate ($\epsilon = 0$) of characteristic bandwidth γ_o is shown for reference. As the filament deepens SRS may occur at a discrete set of frequencies ($\epsilon = 0.25$) exhibiting the guided plasma wave normal modes in the density channel

$$\omega^2 = \omega_p^2\,(1 - \epsilon) + k_x^2 c^2 + \sqrt{6\epsilon}\,(2N + 1)K\,V_e\omega_p \quad (6)$$

($N = 0,1,2,\ldots$) . The focussing of the backscattered light at the density minimum strongly biases growth in favour of the most deeply trapped (low N) modes of equation (6). Growth is clearly dominant for resonance at the density minimum. When this density is low enough ($\epsilon = 0.75$) Landau damping becomes strong, washes out the plasma wave resonances and substantially inhibits growth. Ultimately ($\epsilon = 1$) SRS degenerates into stimulated Compton scattering at these low densities with optimum growth occurring at locations higher up the filament wall.

This maximum growth eigenstate is illustrated in Fig.2 for a temperature of 0.63KeV and a mean density of $0.1n_c$. Curve a) shows a rapid decrease as the resonance localizes such that the bandwidth associated with the density variation

exceeds that associated with the growth ($\epsilon \omega_{p2} \rightarrow \gamma_o$) . Thereafter a gentler decline occurs ($\gamma \propto \epsilon^{-1/3}$) which is purely a scalelength effect at the parabolic density minimum. The reduction in growth is accelerated when Landau damping becomes strong ($\epsilon \sim 0.4$) . Curve b) shows the enhancement in growth due to the focussing of the scattered wave. Finally, curve c) includes the focussing of the laser light leading to a modest net increase in growth, although less than might have been anticipated, until Landau damping becomes strong. Broadly, then, light wave focussing overcomes decreases due to plasma inhomogeneity but yields to those due to Landau damping.

4. Waveguide Effects

When the waves are guided within a channel, higher frequencies are needed to maintain propagation. Given the dominance of SRS at the density minimum of a filament, such waveguide corrections can restrict emission to a narrower band with minimum frequency greater than the expected $\omega_o/2$. To quantify this, neglect plasma temperature so that the plasma wave frequency at the density minimum is $\omega^2 = \omega_p^2(1 - \epsilon) = \omega_{p1}^2$ say; the focussed backscattered light has frequency ω_s given by

$$\omega_s^2 = \omega_{p1}^2 + k_s^2 c^2 + \omega_{p1} c/L \qquad (7)$$

where $L = (\omega_p/\omega_{p1})(2\epsilon)^{-\frac{1}{2}} K^{-1}$ is the transverse scale length at the density minimum. Frequency matching at the scattered wave cut-off gives the minimum scattered frequency

$$\omega_s = 0.5\ \omega_o(1 + c/\omega_o L)(1 + c/2\omega_o L)^{-1} \qquad (8)$$

If the filament focusses to a skin depth then $L \sim c/\omega_o$ and $\omega_s > 2\omega_o/3$ significantly higher than $\omega_o/2$. For a cylindrical Gaussian filament of diameter a , $\omega_{p1}/L \rightarrow 4c/a^2$ in (7) giving a cut-off frequency

$$\omega_s = 0.5\ \omega_o(1 + 4c^2/\omega_o^2 a^2) \ . \qquad (9)$$

Using the minimum radius for a self-trapped filament[2] $a = (2e)^{\frac{1}{2}} c/\omega_{p2}$, where ω_{p2} corresponds to the maximum plasma density n_M outside the filament, gives

$$\omega_s = 0.5\ \omega_o\ (1 + 2n_M/en_c) \ . \qquad (10)$$

This again may be substantially greater than $\omega_o/2$.

References

1. Barr, H.C., Boyd, T.J.M. and Coutts, G.A., Phys. Rev. Lett., 56, 2256 (1986).
2. Max, C.E., Phys. Fluids, 19, 74 (1976).

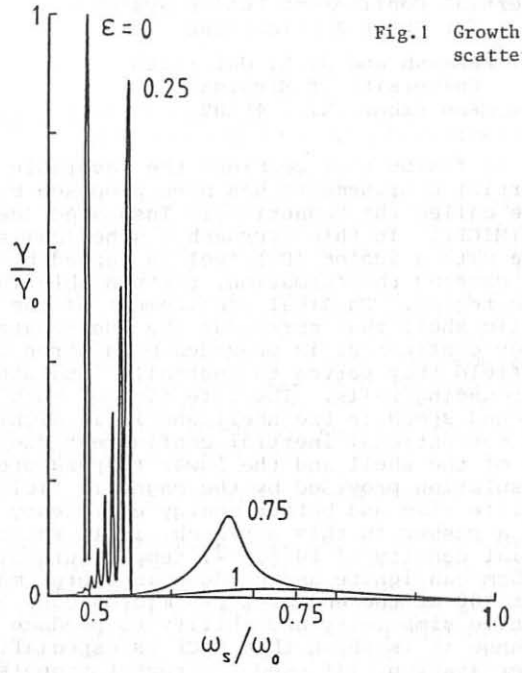

Fig.1 Growth rate versus scattered light frequency

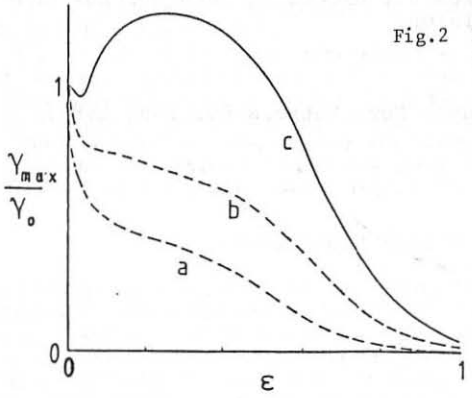

Fig.2 Maximum growth rate versus filament depth

An Inertial Confinement Fusion System for Space Applications

T. Kammash and D. L. Galbraith
University of Michigan
Ann Arbor, MI 48109

A new approach to fusion that combines the favorable aspects of magnetic and inertial confinements has been proposed by Hasegawa et al[1] in a scheme called the Magnetically Insulated Inertial Confinement Fusion (MICF). In this approach a spherical shell coated on the inside with a fusion (DT) fuel is zapped by a laser beam through a hole causing the formation, through ablation, of a plasma in the core region. Physical confinement of the plasma is provided a metallic shell that surrounds the fuel-coated inner surface, while energy confinement is provided by a strong, self-generated magnetic field that serves to thermally insulate the plasma from the surrounding walls. The life time of such a plasma is limited by the sound speed in the shell and it is significantly longer than that in conventional inertial confinement due to the higher mass density of the shell and the lower temperature arising from the thermal insulation provided by the magnetic field. Due to the increase in life time and better energy efficiency resulting from the absence of a pusher in this approach, it is shown that a plasma with an initial density of $10^{21} cm^{-3}$, temperature of 10 keV and a radius of 0.25cm can ignite and produce an energy multiplication factor of about 100 at the end of a two microsecond burn time. Because of its relative simplicity and ability to produce power in the multimegawatt range it is shown that MICF is especially attractive for space-based power station. If used for rocket propulsion it is also shown that MICF is uniquely suited for deep space missions requiring specific impulses far exceeding 1000 seconds that cannot be met by chemical propulsion.

1. A. Hasegawa et al, Phys. Rev. Letters 56, 139 (1986)

2-D SIMULATIONS OF LASER ACCELERATED THIN FOILS

S. Atzeni

Associazione EURATOM-ENEA sulla Fusione, Centro Ricerche Energia Frascati, C.P. 65 - 00044 Frascati, Rome (Italy)

INTRODUCTION

Experiments on laser acceleration of thin foils allow for the study of laser-matter interaction and of the process of ablative acceleration by using a simple, single beam, laser configuration [1-4]. Sufficiently thin foils can be accelerated to velocities about 100 km/s [1-4], even by using laser pulses with energy E of a few J [3-4]. Such experiments also allow for a number of transverse and rear-side diagnostics which are not feasible on spherical targets. On the other hand, significant departures from truly 1-D geometry may occur, due to the finite transverse size of the beam, to the non-uniform illumination, as well as to fluid and plasma instabilities. This motivates the present 2-D numerical study of the hydrodynamics of foils irradiated by low intensity, Nd: laser pulses, performed by means of the 2-D Lagrangian code DUED [5].

DEFINITION OF THE PROBLEM

We have performed numerical simulations for laser and target parameters approximating those of a series of experiments conducted at Frascati [3,4]. For the laser pulse we have assumed a triangular temporal shape, with peak power at t=1 ns, and width $\Delta t(FWHM)=3$ ns. The simulated beam is parallel (f/∞ optics), with a trapezoidal spatial shape, with flat-top radius $R_T=160$ μm and spot radius $R_s=240$ μm. The peak intensity is 10^{12} W cm^{-2}, and the energy on target is $E \simeq 4$ J. We have considered three plastic (CH) targets, with radius $R_0=500$ μm, and thickness $\Delta Z_0=1$ μm, 3 μm, and 20 μm, respectively (corresponding to fractional ablated mass about 65%, 20%, and 3%, respectively).

We have simulated the above experiments with a 2-T model, with flux-limited thermal conductivities, and a real-matter Equation-of-State. Laser-matter interaction is dealt with by means of a 2-D ray-tracing algorithm, taking plasma refraction and inverse Bremsstrahlung absorption into account. Such a model is adequate for the study of the kinematics of the process, but not for that of the status (temperature and density) of the dense, accelerated foil, which would require the treatment of X-ray transport.

COMPUTATIONAL ASPECTS

Despite of the simplicity of the model, the present simulations are computationally rather demanding. Indeed, at the moment, only Lagrangian fluid codes seem able to follow with a reasonable spatial resolution the evolution of both the accelerated part of the foil and of the highly sheared region at the edge of the laser spot (see, e.g., Fig. 1). Furthermore, given the small thickness of the ablated layer (0.6 μm), very thin zones (with initial axial spacing $\Delta Z_m \leq 0.03$ μm) are necessary for the description

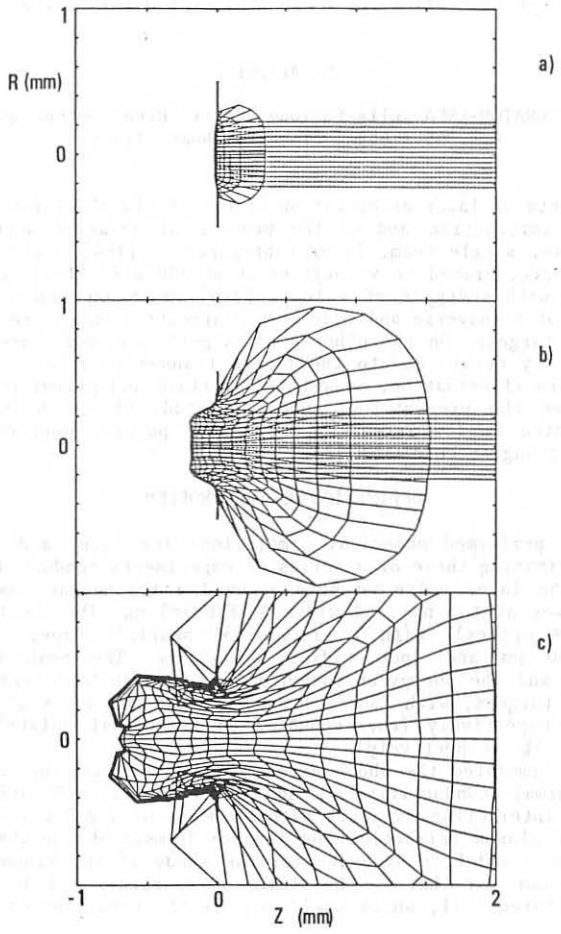

Fig. 1: Ablative acceleration of the 1 μm thick target. Mesh (solid) and selected rays (dashed) at a) t=1.5 ns; b) t=4 ns, c) t=8 ns. The 20x30 zone mesh at t=0 had uniform spacing in each direction.

of the ablation process. This results in a particularly severe Courant stability condition, as a consequence of which 5÷10 thousand steps are usually needed to simulate the evolution from 0 to 8 ns. Even using a rather coarse transverse zoning (20 radial zones) and a relatively small number of light rays for step (20÷30) the simulations described here have

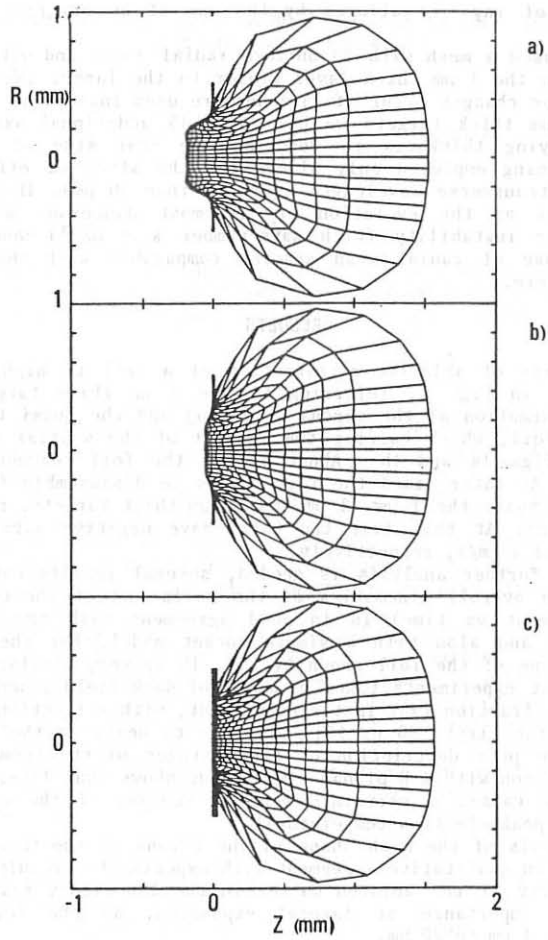

Fig. 2: Mesh plot at the same time t=4 ns for targets of different thickness: a) ΔZ_o=1 μm; b) ΔZ_o=3 μm; c) ΔZ_o=20 μm. To allow for an immediate comparison, the mesh in the laser ablated portion of the target had the same initial spacing for the three targets.

run in 600÷1500 CPU seconds on a CRAY-XMP 12 computer (the hydro-code is vectorized, but the ray tracing is essentially a scalar process, which in practice takes up to 70% of the CPU time; notice that the use of a

small number of rays is allowed by the use of an original ray-tracing method [5,6].

We have used a mesh with 20 uniform radial zones and with 30 uniform axial zones in the 1 μm thick layer closer to the laser. (We have tested that only minor changes occur if 45 zones are used instead of 30). For the 3 μm and 20 μm thick targets we have used 15 additional axial zones of gradually varying thickness to describe the rear side of the target. The radial zoning employed only allows for the study of effects with a rather large transverse wavelength (greater than 50 μm). The analysis of such processes as the evolution of the most dangerous modes of the Rayleigh-Taylor instability (with wave-number $k \sim \Delta Z_o^{-1}$) would in fact, require the use of radial mesh spacing comparable with the axial mesh spacing used here.

RESULTS

The process of ablative acceleration of a foil to high velocity is clearly shown in Fig. 1, referring to the 1 μm thick target. Here we observe the formation of the corona (Fig. 1a) and the quasi 1-D acceleration of the foil, which carries the imprint of the spatial shape of the laser beam (Figs 1a and 1b). About 4.2 ns the foil reaches a velocity v_z=-100 km/s. At later times the foil begins to disassemble (Fig. 1c). In Figure 2 we compare the 1 μm, 3 μm and 20 μm thick targets, respectively, at time t=4 ns. At this time the foils have negative axial velocities about 95,27 and 3 km/s, respectively.

Although further analysis is needed, several results can already be discussed. The overall kinematics of the foils and of the corona (e.g., foil displacement vs time) is in good agreement with the experimental results [3,4] and also with a simple rocket model. For the 1 μm thick target the shape of the foil shown by Fig. 1b is very similar to pictures of the relevant experiments taken by means of dark field shadowgraphy [4]. The absorption fraction (90% in the experiment, with reflection essentially occurring in the first 300 ps [4]) is close to unity in the simulations, because of the poor description of first stages of the formation of the corona. Comparison with 1-D planar simulations shows that lateral expansion of the corona causes a certain degree of cooling of the corona (about 15÷20% in the peak electron temperature).

The analysis of the mesh shape in the corona of the three targets of Fig. 2 shows, in qualitative agreement with experimental results [1,4], increased velocity of the ablated matter in the laboratory system, as well as increased importance of lateral expansion, as the foil thickness increases from 1 μm to 20 μm.

REFERENCES

[1] J. Grun et al., Phys. Fluids 26, 588 (1983).
[2] A.G.M. Maaswinkel et al., Opt. Comm. 51, 255 (1984).
[3] A. Caruso, in "Advances in Inertial Confinement Fusion" ed. by C. Yamanaka) ILE, Osaka , p. 121 (1984).
[4] Fusion Department 1985 Progress Report, ENEA C.R.E. Frascati, p. 43.
[5] S. Atzeni, Comput. Phys. Commun. 43, 107 (1986).
[6] S. Atzeni, Comments Plasma Phys. Controll. Fusion 10, 129 (1986).

DEVELOPMENT OF TRIANGLE-MESH PARTICLE-IN-CELL CODE FOR LIB DIODE SIMULATION

S. KAWATA and M. MATSUMOTO

The Technological University of Nagaoka
Nagaoka, Niigata 940-21, Japan

Abstract

The paper presents the development of a triangular-mesh particle-in-cell (PIC) code (TRIPIC) for a numerical simulation of a light-ion beam (LIB) diode and an LIB focusing in an inertial confinement fusion (ICF).

1. Introduction

In an LIB ICF one of important problems to be solved is a LIB focusing or to design a diode which produces a well-focused LIB. A PIC code is suitable in order to simulate a LIB diode and to design it. Up to now many PIC codes 1,2 have been developed to simulate plasma phenomena, a diode and so on. They have usually square meshes to describe such systems. But for the problem of a focused type of diode it is required to describe a complicated shape of computational region. Because the shape of electrodes of the diode is not simple. In our PIC code of TRIPIC triangular space meshes are employed to describe the complicated region.

The TRIPIC code consists of the following parts: mesh generator in which triangular meshes are generated by the mapping from a simple logical space to a complicated real space, particle generator to create ions or electrons at the electrodes surface with a condition of the space-charge limit, particle pusher in which a relativistic equation of motion is solved, field solver for electric fields by a finite differential method associated with the triangular space meshes. The interaction between particles and space meshes are accomplished by a weighting method.

2. TRIPIC code

The relativistic equation of motion for charged particles is solved by the Bunneman scheme.

The field solver for electromagnetic fields is based on the reference 3. In the real space the region covered by six triangles surrounding one point is a primary mesh region. The secondary mesh is also illustrated in Fig.1. Here we think about a generalized Poisson equation:

$$\kappa \frac{\partial \Phi}{\partial t} = \nabla \cdot (\lambda \nabla \Phi) + s$$

s: source term
(κ, λ : coefficients)

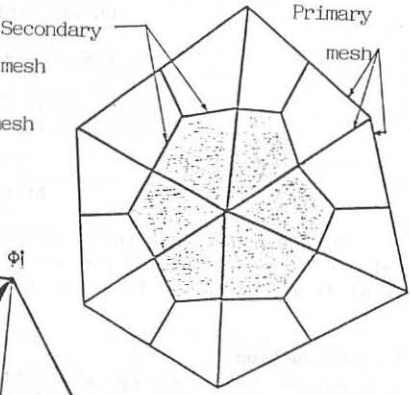

Fig.1 Space mesh construction

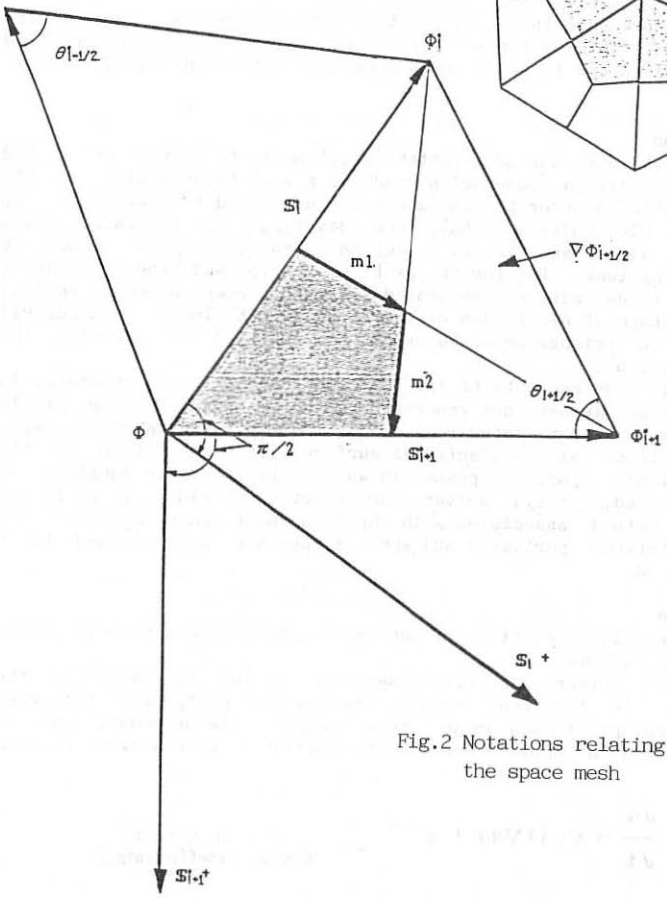

Fig.2 Notations relating to the space mesh

For the descretization the equation is integrated over the secondary meshes. In this case the gradient of physical quantities is constant in each triangles in the primary mesh. For the first term at the right hand side of the above equation, the Gauss law is adopted and the inward- and outward-fluxes are computed. In each triangles the gradient is described by the following expression:

$$\nabla\Phi_{l+1/2} = \frac{(\Phi_l - \Phi)\,\mathbb{S}_{l+1}^{\dagger} - (\Phi_{l+1} - \Phi)\,\mathbb{S}_l^{\dagger}}{\mathbb{S}_l \cdot \mathbb{S}_{l+1}^{\dagger}}$$

Each notations are defined in Fig.2. Finally we get the descretized equation of the generalized Poisson one on triangular meshes:

$$\frac{\delta\Phi}{\delta t} = \frac{1}{G}\left[\Sigma w_l\ (\Phi_l - \Phi) + S\right]$$

$$G = \Sigma \kappa_{l+1/2}\, a_{l+1/2} \quad , \quad S = \Sigma s_{l+1/2}\, a_{l+1/2}$$

$$w_l = \frac{1}{4}\left(\lambda_{l+1/2}\cot\theta_{l+1/2} + \lambda_{l-1/2}\cot\theta_{l-1/2}\right)$$

By using this method other basic equations are also descretized for the electromagnetic fields.

For searching a particle position the triangular mesh is not the best one. But if the triangular meshes are numbered in searies and we remember the position at the former time, to find the new particle position is accomplished by searching the several meshes just surrounding the mesh in which the particle was located at the former time. In addition, we need the interaction method between particles and meshes to compute the current and the charge densities. Each particles has a finite radius. Meshes located inside of this circle interact with the particle. In this weighting method the weight is defined by the inverse of the distance between the particle and the mesh point.

In the space-mesh generator two Poisson type of equations are solved, because the TRIPIC code is the 2.5 dimensional code. In the code two kinds of lines are employed to do numbering the triangular meshes. Each lines in the real space is considered to be like a equi-potential lines. If the two Poisson equations are solved inversely in the logical space with appropriate boundary conditions, the numbering of the space meshes can be accomplished.

In the particle generation the Gauss law is adopted to the mesh just besides of the electrodes with the space-charge-limit condition. The velocity of the particle is determined by the Maxwell distribution.

In Fig.3 one example of numerical results is presented: the generated space meshes and the static electric potential lines. Figure 4 shows the electron particle map for the code check of Child-Langmuir current in an anode-cathode gap; in this case the anode-cathode gap distance is 5 mm and the applied voltage is 1 volt.

3. Summary

By using triangular meshes TRIPIC code is developed for simulating the phenomena in the LIB diode or of the LIB focusing or relating to the plasma inside of the rather complicated region.

Previously many PIC codes have been developed by using square meshes. But recently we need to simulate a rather complicated problems especially in an LIB ICF, as mentioned above. For this purpose the TRIPIC code is fitted.

References

1 B. Goplen, et al., Mission arzesearch Corporation Document MRC/WDC-R-068,"User's Manual for MAGIC, Version-Sept. 1983".

2 S. Kawata, E. Halter, M. Sararu, K. Niu, E. Halter and E. Gabowitsch, "User's Manual for PCSKfK - Particle-in-cell Code for a Pulsed Diode", Kernforschungszentrum Karlsruhe(KfK) Primaerbericht, 14.04.01p44A, (1986).

3 A. M. Winslow, "Numerical Solution of the Quasilinear Poisson Equation in a Nonuniform Triangule Mesh", J. Comp. Physics 2(1967)149.

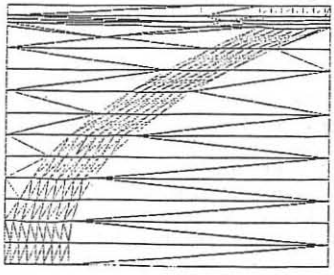

a) generated space mesh

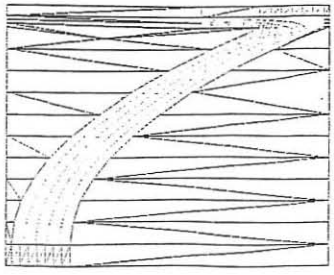

b) static electric potential

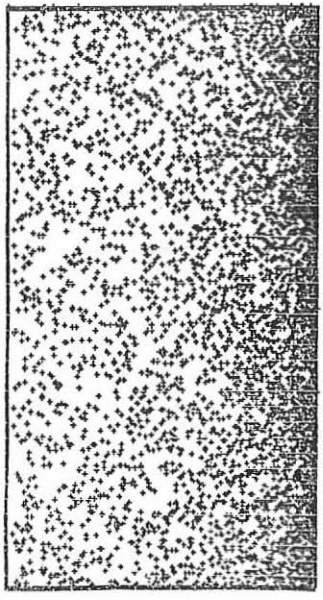

c) Electron map between anode-cathode gap

Fig. 3. Numerical results

SIMULATION OF LIGHT ION BEAMS FUSION CAPSULES

J.J. Honrubia, C. González, R. Otero

Instituto de Fusion Nuclear (DENIM), Univ. Politécnica Madrid.

1.-INTRODUCCION

The DENIM simulation capability for detailed analysis of light ion beam and ICF physics has been extended and experienced, including fully-EM 2D particle-in-cell simulation, beam-plasma and atomic interaction models and 1D charged particle transport coupled to fully implicit 3T hydrodynamics with radiation transport and improved atomic data.

This updated capability has been applied to the energy deposition by unfocused ion beams in different ICF fuel capsule concepts. Detailed calculations of the average ionization potentials, more accurate opacities and detailed radiation transport effects are taken into account. In addition, the collective effects and plasma regimes of the low density zones in the corona are studied by PIC simulations to assess the plausible instabilities or anomalous energy deposition processes, if any.

Specifically the works on numerical simulation of Light Ion Fusion (LIF) physics has been devoted to the characterization of the hydrodynamic and energy response of directly and indirectly driven targets. In this paper, our model for ion energy deposition is described and some results about target performance in the 1D simulation frame of the upgraded NORCLA code are presented [1, 2].

2.-MODEL FOR LIGHT ION ENERGY DEPOSITION

Charged Particle Transport

The starting point of our physical model is the linear Fokker-Planck equation in a Lagrangian frame:

$$\frac{1}{vV}\,\partial_t(V\psi)+\hat{\Omega}.\frac{\partial\psi}{\partial \mathbf{r}}=\frac{\partial[(S+D+D_\phi)\psi]}{\partial E}+T\frac{\partial}{\partial\mu}(1-\mu^2)\frac{\partial\psi}{\partial\mu}+\frac{\partial}{\partial\mu}(R+R_\phi)(1-\mu^2)\psi+\dot{Q}(\mathbf{r},E,\mu,t) \tag{10}$$

where $\psi = vn$ stands for the angular flux in transport notation, $\hat{\Omega}$ for the direction of particle motion, $\mathbf{v}(\mathbf{r},t) = \mathbf{v}_L - \dot{\mathbf{r}}(\mathbf{r},t)$ for the relative velocity of the particles to the plasma, and V for the volume of lagrangian intervals. The former equation is used for the transport of ion beams, suprathermal electrons produced in laser fusion and fusion products. The coefficients of the terms related to collisions, kinematics and self consistent fields have been published elsewhere [2,3].

From the physical viewpoint the major issue concerning the ion beam-plasma interaction is the stopping power and in less extent the mean straggling. As we are using the same computational model for problems so different

as ion beam and fusion product transport, a general formulation of the interaction coefficients has been used. For free particles, the linear dielectric response of a multi-component plasma including local field corrections is considered. In particular, the free-electron stopping is obtained for a degenerate gas following the prescriptions of Ichimaru [4] and using a Thomas-Fermi (TF) model for the average ionization degree and the degeneration parameter. For ion beam energy deposition the degeneration effects are not important in a wide range of cases, and the former formulation reduces to the linear response of a classical Vlasov plasma.

The bound-electron contribution plays an important role, especially in the next future ion beam interaction experiments with low-temperature plasmas. Its accurate determination from first principles requires a great deal of atomic information, so that. we have considered both the TF and full quantum frames, the last one by using our ADELA HFS code [2] The results obtained with those models are compared with the GOS results in Fig. 1 for the ground state of Al ions. In this picture we have considered the free electron gas (FEG), augmented free electron gas [5] (AFEG) and Bohr-like (B) approaches in the context of the TF theory [6], and the ADELA potentials in the frame of quantum theory.

The important issue of this picture is the fact that the B model in the TF frame fulfills the hydrogenic scaling as the GOS and ADELA results. Because the AFEG model leads to the GOS results when a quantum electron density is used [5] and the agreement of the B and AFEG potentials is good, we conclude that the B model gives accurate potentials up to the TF model precision. Therefore, in order to save computational effort, we have selected the average ionization potentials obtained by this model, but scaled to the experimental values corresponding to cold media. The fine structure of the potentials due to the shell structure of the average ion is not, however, represented in this way. As these effects can be important in the current low-temperature experiments, where the most important contribution is that of bound electrons [7], the full quantum calculations have to be considered in this case. In turn, we consider these results appropriate enough in LIF target simulations beyond the present experiments because of the more important role played by the free electrons and plasma effects.

Light Ion Beam-Plasma Interaction

The second issue that has been studied is the plasma regime in the corona under LIF conditions. Specifically, we have been looking for any plasma instability or anomalous energy deposition regime at the low density and high temperature zone of the corona for targets illuminated with high intensity ($>10^{14}$ W/cm^2) ion beams. Numerical simulation shows that under certain circumstances, such as those pointed out recently by Nardi and Zinamon [8], plasmas at these conditions can be obtained. The picture for ion beam energy deposition in such a corona is as follows: the ions lose a significant part of their energy by exciting plasma waves (b-e mode), the growing up of these waves is damped by collisions in the denser zones of the corona but, as the density scales approximately as exp(-r/l), this mode might not be stabilized at the outer low-density high-temperature zones. The result would be the production of suprathermal electrons. However, as the number of plasma electrons available

to be heated by this mechanism is small, no high levels of preheating should be expected.

Therefore, we have been looking for the hot electron production by the b-e mode under extreme conditions for both the beam and the plasma. Specifically, we assume the values $n_e \leq 10^{20}$ cm^{-3} (low Z elements), $T_e \geq 300$ eV and $n_b/n_e \leq 0.05$ as input to the PIC simulation via WAVE code [9]. Linear theory shows that for this parameters the growth rate fulfills the condition $\nu_e \ll \gamma \ll w_p$ (ν_e electron collision frequency), and the saturation levels reached are $\geq 70 n_e T_e$. The situation simulated is that of a current neutralized proton beam impinging on an uniform plasma slab. We have distinguished between the cases of cold ($\Delta E_b \sim o$) and hot ($\Delta E_b \sim 0.1\ E_b$) beams. The results for the cold beam case show that the amplitude of the plasma waves grow-up in space reaching high values. The electrons in resonance with the waves are accelerated up to suprathermal levels. Those electrons are trapped by the waves, stopping the growth of the waves. As reported in Ref. [2], the electron distribution function presents a suprathermal tail with a flat profile typical of particle trapping.

In the case of hot beams, the results show [2] that the amplitude of the plasma waves is not strong enough to accelerate electrons up to suprathermal levels, because of the modulation in the longitudinal electric field produced by the velocity spread of the beam.

In conclusion, we have not found an important fraction of suprathermal electrons in the cases analyzed. However more studies are needed to elucidate further this and other phenomena, such as beam stripping and density profiles.

3.-ANALYSIS OF DIRECTLY DRIVEN TARGETS

The model and new capabilities described in the previous sections have been applied to the study of directly driven targets. Our goal is to find optimized targets with minimum pulse power requirements to achieve a significant gain of energy.

We have considered a target with an external tamper of lead, to minimize the radiation leakages; an absorber of aluminium, to stop the ions; an internal tamper of gold, to avoid the radiation preheating of the fuel; a thin shell of aluminium, to mitigate the Rayleigh-Taylor (RT) instability growth rate; and finally, a layer of cryogenic deuterium-tritium. We have considered also two designs with different aspect ratios, that have been selected in a conservative (small) or optimistic (large) way for the RT instability. The maximum power has been chosen in order to reach reasonable values of the hydrodynamic efficiency.

In this kind of targets we have obtained that the energy available (without accounting focusing and radiation leakage) has to be $\geq$ 1.5 MJ/mg to obtain a significant yield of energy. Then, our simulations indicate a threshold near to 2.2-2.5 MJ/mg to obtain substantial energy gain for large aspect ratio targets, such as those required with the current pulse power diodes focusing. We consider this result somewhat conservative mainly because of the high values of radiation leakage obtained in our simulations.

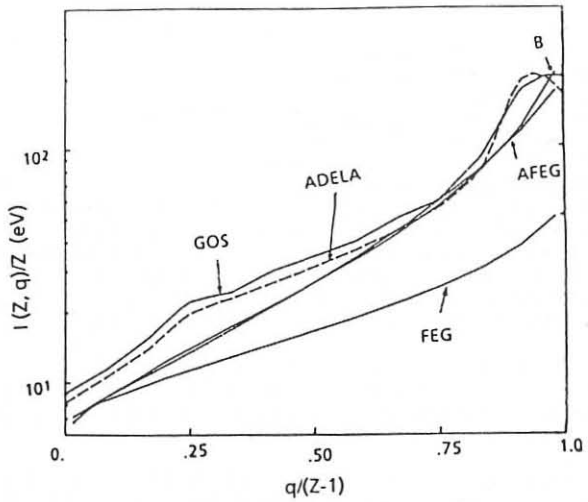

Fig. 1. Average ionization potentials vs ionization degree obtained by several models (for aluminum at 10^{-3} ρ_o)

REFERENCES

1. G. Velarde et al., Atomkernenergie, 44, 209, (1984).
2. G. Velarde et al., "Analysis of Directly Driven ICF Targets", Laser and Particle Beams **4**, 349, (1986).
3. J.J. Honrubia, J.M. Aragonés, Nucl. Sci. Eng. **93**, 386 (1986).
4. S. Ichimaru et al., Phys. Rev. A32, 3 (1985).
5. J.M. Peek, Phys. Rev. A26, 2 (1982).
6. G. Nardi, E. Peleg, Z. Zinamon, Phys. Fluids 21, 4 (1978).
7. T.A. Mehlhorn et al., "Current status of Calculations and Measurements of Ion Stopping Power in ICF Plasmas", SAND03-1519, (1983).
8. E. Nardi, Z. Zinamon, Phys. Rev. A56, 12 (1986).
9. D.W. Forslund, "Fundamentals of Plasma Simulation", LA-UR-85-413 (1985).

THE RAMAN INSTABILITY: NONLOCAL EFFECTS

H.C. Barr, T.J.M. Boyd and G.A. Coutts
University of Wales, UCNW, Bangor, Wales, U.K.

Abstract: A code has been developed to solve the full stimulated Raman scattering equations (SRS) in an arbitrary density profile which thereby overcomes the local nature of previous analyses, contains the coupled back and forward scatter resonances and wave reflections. This global solution elucidates the transition between absolute instability at the quarter critical density and convective instability at lower densities.

1. Introduction

Stimulated Raman Scattering, the resonant amplification by a light wave of a plasma wave and a scattered light wave of lower frequency, is expected to be a concern in the interaction of laser radiation with the large targets conceived for inertial confinement. Recent experiments indicate order of magnitude lower thresholds than predicted by linear theory; unexpected spectral features are observed.

SRS in an inhomogeneous plasma having a monotonic density profile admits two regimes. Below the quarter critical density surface $n_c/4$ (n_c , cut-off or critical density for the laser light) a W.K.B. analysis shows that, in a linear density profile, only convective amplification is possible for either back or forward scatter. A backscatter threshold is usually quoted as $(v_o/c)^2 k_o L > 1$ ($2v_o$, electron oscillatory velocity of the laser light; k_o , laser wavenumber; L , density scale length). Such a "threshold" is defined to give an amplification of $\exp(2\pi)$ over noise levels. In practice this threshold has been relaxed somewhat in an attempt to bring theoretical and experimental values into closer agreement. Both back and forward scatter are treated as independent resonances when clearly, as has been recognized elsewhere[1], they are not. For a given scattered frequency ω_s , they are separated by a small density difference

$$\frac{\delta n}{n_c} \simeq 12(V_e/c)^2 \left[\frac{\omega_s}{\omega_o}\left[2 - \frac{\omega_s}{\omega_o}\right]\left[2\frac{\omega_s}{\omega_o} - 1\right]\right]^{1/2} \qquad (1)$$

with forwardscatter occurring at the higher density of the two. If laser light propagates into a plasma of increasing density the plasma wave amplified in generating backscattered light will propagate to the forward scatter resonance and act as an enhanced noise source in generating forward scattered light. In turn if the plasma is overdense to this light it

will reflect and again be subject to amplification at the backscatter resonance. These nonlocal effects create a feedback loop which leads to temporal growth of the coupled back and forward scatter instabilities[1].

Near $n_c/4$ (or for sidescatter), the back and forward scatter resonances are degenerate as (1) indicates when $\omega_s \to \omega_o/2$; this is the scattered wave cut off hence WKB theory is invalid here. Neglect of plasma temperature retrieves a second order equation, the analysis of which[2] shows absolutely unstable eigenstates whose threshold is $(v_o/c)^2(k_oL)^{4/3} > 1$.

2. Model

The SRS equations, written here only for the (1D) back and forward scatter of laser radiation normally incident on an arbitrary density profile corresponding to plasma frequency $\omega_p(x)$, are

$$\left[\partial_t^2 + \omega_p^2(x) - \partial_x^2\right] v_s = v_o \, \partial_x E_p \tag{2}$$

$$\left[\partial_t^2 + \omega_p^2(x) - 3v_e^2\partial_x^2\right] E_p = - \omega_p^2(x) \, \partial_x(v_o v_s) \tag{3}$$

where $v_s(v_o)$ is the scattered (laser) light electron oscillatory velocity and E_p is the plasma wave electric field (all quantities normalized to c,ω_o ; damping terms are not shown). We have developed a code which treats the global SRS problem by solving these full wave equations, Laplace transformed in time and retaining only resonant terms, to obtain a) temporally growing eigenstates if these exist and, if they do not, b) reflectivities (convective amplification) from the nonhomogeneous equations with a noise source retained. The equations are solved in an inhomogeneous plasma slab $o \leq x \leq \ell$ with boundary conditions chosen to continuously match fields in homogeneous plasma for $x < o$ and $x > \ell$. The interaction region is assumed infinite although only resonant locally within $o < x < \ell$. The driven equations are solved analytically in the homogeneous plasma $x < o$, $x > \ell$ to obtain four independent solutions of which, in case a) above, only those two representing outward propagating waves are chosen in each region. For b) a variety of options for incoming waves is available to represent noise sources.

3. Results

So far, the code has been run to yield temporally growing eigenstates in a linear density profile $(n(x) = n(\ell/2) + (x - \ell/2)n_c/L)$ versus scalelength L or versus maximum density chosen to include/exclude reflections of forward propagating waves. Fig.1 shows the growth rate

versus inverse scalelength L^{-1} for three eigenvalues with frequencies $\omega_s \sim 0.56\ \omega_o - 0.60\ \omega_o$ ($\ell = 100c/\omega_o$) . The mean density ($n(\ell/2) = 0.15n_c$) is held fixed while the scale is reduced. $L^{-1} = 0$ retrieves the growth rate for absolute growth in an infinite homogeneous plasma, $\gamma = 2\gamma_o(V_sV_p)^{\frac{1}{2}}\ (V_s + V_p)^{-1}$ where $V_s(V_p)$ are the group velocities of the backscattered light (plasma wave) and γ_o is the usual growth rate for a homogeneous plasma. The plasma is resonant at all locations. As L^{-1} increases the resonance localizes and a sharp reduction in growth ensues until the resonance width is clearly within $0 \leq x \leq \ell$. Thereafter growth reduces more slowly. For these parameters the maximum density is still underdense to forward scattered light. Nevertheless temporal growth of the now coupled forward and backscatter signals occurs. The latter is strongly dominant especially when well above threshold or ω_s is different from $\omega_o/2$; nearer threshold back and forward scatter signals are more comparable. Fig.2 shows this case ($\gamma = 0.006\omega_o$, $\omega_s = 0.56\omega_o$, $L^{-1} = 0.0021\omega_o/c$ with $v_o = 0.01c$, $V_e = 0.15c$ and damping neglected) indicating small amplification within a narrow resonant region as well as the swelling of scattered (s) and plasma wave (p) as it propagates in the inhomogeneous plasma. Although absolute instability is possible in this case, thresholds are high relative to that for absolute instability at $\omega_o/2$. An empirical formula would suggest a threshold given by $(v_o/c)^2\ (k_oL)^{2/3} > \propto(\omega_s)$ where $\propto$ (~ 1) is a constant which increases with ω_s .

When the maximum density is increased (increased ℓ) maintaining a fixed scale length L such that forward scattered light is reflected, the growth rates (thresholds) rise (fall) substantially. Ultimately we anticipate that these thresholds will converge to that given above for absolute instability at $\omega_o/2$.

References

1. Koch, P. and Williams, E.A., Phys. Fluids 27, 2346 (1984).
2. Lui, C.S., Rosenbluth, M.N. and White, R.B., Phys. Fluids 17, 1211 (1974).

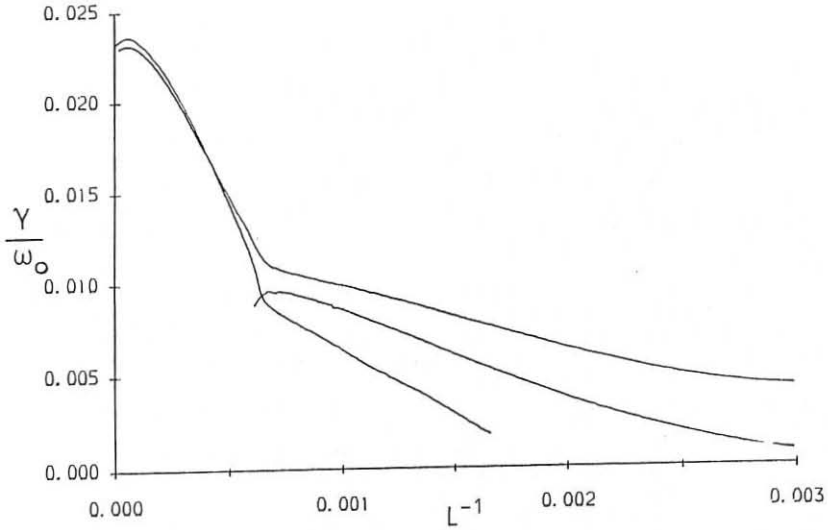

Fig.1 Growth rate versus inverse scale length

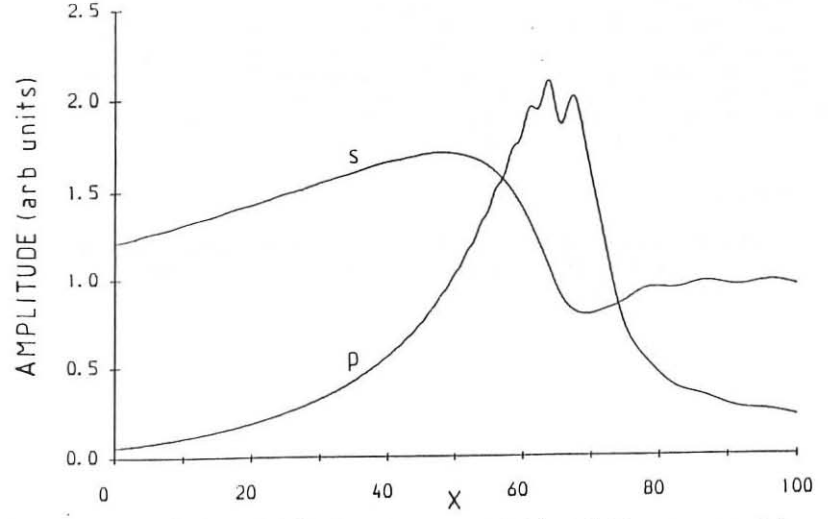

Fig.2 Amplitudes of scattered (s) and Plasma waves (p)

BEAM LOSSES IN THE ICF STORAGE RING HIBALL II DUE TO CHARGE CHANGING ION-ION COLLISIONS[+]

F.Melchert and E.Salzborn
Institut für Kernphysik, Universität Giessen, D-6300 Giessen
West-Germany

ABSTRACT

Beam intensity losses due to charge changing ion-ion collisions in the storage rings of the ICF scenario HIBALL II are estimated to amount up to 8 %, using absolute cross sections we have measured both for electron capture and for ionization in collisions between two Bi^+ ions in the cm-energy range from 9.9 keV to 56 keV.

INTRODUCTION

High current Bi^+ ion beams of 10 GeV energy, as projected in the HIBALL II scenario[1] for igniting a DT pellet, may suffer from severe intensity losses due to charge changing ion-ion interactions within the beam pulses in the storage ring. In order to calculate the expected loss rates the cross sections both for

electron capture (σ_c): $Bi^+ + Bi^+ \rightarrow Bi^0 + Bi^{2+}$ (1)

and for

ionization (σ_i) : $Bi^+ + Bi^+ \rightarrow Bi^+ + Bi^{2+} + e$ (2)

have to be known as a function of the relative velocity.

The total beam loss cross section σ_L is given by

$$\sigma_L = 2(2\sigma_c + \sigma_i) \qquad (3)$$

since 2 particles are lost per interaction in the electron capture reaction (1) and, furthermore, both ions simultaneously act both as projectile and target particles.

EXPERIMENTAL RESULTS

Employing the crossed-beams technique we have measured absolute cross sections σ_c and σ_i for collisions between two Bi^+ ions at center-of-mass energies ranging from 9.9 keV to 56 keV. A detailed description of the apparatus and the measuring procedures has been given previously[2,3]. In short, two momentum-analyzed Bi^+ ion beams of adjustable energies (up to 150 keV and up to 15 keV, respectively) are arranged to intersect at an angle of 45° in an ultra-high vacuum region of

[+]Work funded by BMFT under contract no. 06 Gi 658

about $1 \cdot 10^{-10}$ mbar. The collision products formed in both beams are analyzed with respect to their charge states by electrostatic deflection downstream of the interaction region. The parent Bi^+ ion beams are recorded by biased Faraday cups, whereas the reaction products (Bi^0 and Bi^{2+}) are counted individually by single-particle detectors.

Since the residual gas density, even at pressures of $1 \cdot 10^{-10}$ mbar, exceeds the ion beam densities by orders of magnitude, a low signal rate (Hz) has to be detected in the presence of a large background rate (kHz) due to reaction products originating from ion collisions with residual gas particles. A coincidence technique was employed to separate signal from background events in measuring the cross section σ_c for electron capture. The cross section σ_i for ionization is obtained from the difference $\sigma_i = \sigma_{2+} - \sigma_c$ with σ_{2+} being the cross section for the total Bi^{2+} ion production (sum of reactions (1) and (2)). In measuring σ_{2+} a beam pulsing technique was employed to discriminate signal from background events.

Fig.1 shows the measured cross sections σ_c and σ_{2+} together with the resulting calculated cross sections σ_i and σ_L. The beam loss cross section σ_L increased with collision energy from $2 \cdot 10^{-16}$ cm^2 to about $9 \cdot 10^{-16}$ cm^2 in the investigated energy range. There are no experimental or theoretical results available for comparison with the present data.

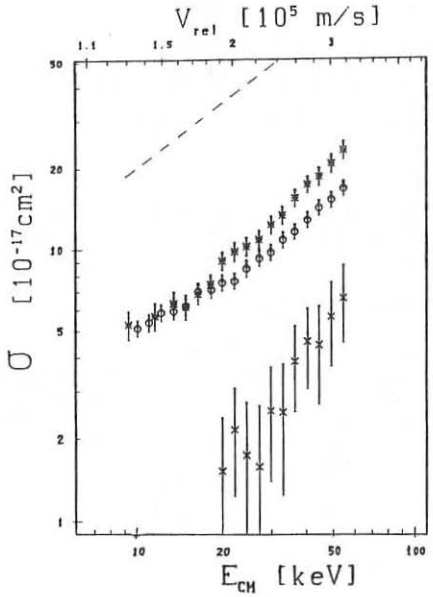

Fig.1: Cross sections for $Bi^+ + Bi^+$ collisions:
o: electron capture σ_c
x: ionization σ_i
*: Bi^{2+}-production
$\sigma_{2+} = \sigma_c + \sigma_i$
-: beam loss
$\sigma_L = 2(2\sigma_c + \sigma_i)$

ESTIMATE OF BEAM LOSS IN THE HIBALL II SCENARIO

In order to calculate the beam intensity loss we assume the ion density in the storage ring to be uniform and the ion relative velocities to be maxwellian. The rate coefficient for particle loss can be written[4]

$$\langle \sigma_L \cdot v \rangle \int_0^{E_{max}} \sigma_L (E) \cdot v \cdot f(E)\, dE \qquad (4)$$

with $\sigma_L (E) = 3.14 \cdot 10^{-17}\ cm^2 \cdot E^{0.812}$ (fit to exp.data)

$$f(E) = \frac{2}{T} \cdot \frac{E}{\pi \cdot T} \cdot e^{-E/T} \qquad \text{(Maxwell distribution)}$$

$$E_{max} = a \cdot T \qquad \text{(a: cut-off parameter)}$$

The average temperature T of ions in the HIBALL II storage ring is about T = 100 keV[5].

The reaction rate is given by

$$R(t) = \frac{1}{2} \int_V n^2 (\underline{r},t) \cdot \langle \sigma_L \cdot v \rangle dV = \frac{1}{2} \frac{N^2(t)}{V} \cdot \langle \sigma_L \cdot v \rangle \qquad (5)$$

since the ion density $n(\underline{r},t) = N(t)/V$ is assumed to be uniform ($N(t)$ = number of ions, V = volume of ion beam).

Solving the equation

$$N(t) = N_o - \int_0^t R(\tau)\, d\tau \qquad (6)$$

we obtain the solution

$$N(t) = \frac{\frac{2V}{\langle \sigma_L \cdot v \rangle}}{t + \frac{2V}{N_o \cdot \langle \sigma_L \cdot v \rangle}} \qquad (7)$$

Taking into account the HIBALL II parameters[1]

t = 4 ms (storage time)
$V = (\pi r^2) \cdot 2\pi R/4 = 1.31 \cdot 10^5\ cm^3$
with ion beam radius r = 1.5 cm
and storage ring radius R = 118 m

$N_o = 1.56 \cdot 10^{14}$ ions (12.5 A in one quarter of the ring)

we calculate beam intensity losses ranging between about 4 % for a = 2 (cut-off at E_{max} = 200 keV) and 8 % for a $\to \infty$ (no cut-off).

To obtain a more accurate estimate of the beam loss, numerical calculations should be performed using realistic density distributions of ions in 6-dimensional phase space.

The authores gratefully acknowledge fruitful discussions with Dr.R.W.Müller and Dr.V.P.Shevelko.

REFERENCES

1) HIBALL-II: An Improved Conceptual Heavy Ion Driven Fusion Reactor Study, Kernforschungszentrum Karlsruhe, Report KfK 3840, July 1985

2) K.Rinn, F.Melchert and E.Salzborn, J.Phys.B 18, 3783 (1985)

3) K.Rinn, F.Melchert, K.Rink and E.Salzborn, J.Phys. B 19 2717 (1986)

4) V.P.Shevelko (Moscow), private communication

5) R.W.Müller (GSI), private communication

ION OPTIC FUSION RESEARCH IN ŚWIERK

M.Gryziński, J.Stanisławski, J.Baranowski, S.Chyrczakowski
K.Czaus, E.Górski, A.Horodeński, L.Jakubowski, W. Komar,
M.Komarnicki, J.Langner, M.Sadowski, E.Składnik-Sadowska

Institute for Nuclear Studies, Swierk-Otwock, Poland.

Abstract: The paper reports on recent results of studies on a fusion energy release with intense ion beams produced by inductive plasma accelerators RPI-15, MAJA-60, and SOWA-400. Several hundred-kA ion beams with a mean energy ranging from several keV to several tenth keV and pulse duration of a $\sim 0.5\,\mu s$ were directed towards gaseous targets produced by fast high-pressure values. Evolution of the target was observed by means of a high-speed photography, time-resolved spectroscopy and X-ray diagnostics.

Introduction.

There are two key problems which must be solved to satisfy the basic Ion Optic Fusion criterions (1). They are:
- effective generation of powerfull ion beams,
- precise focusing of ion beams on appriopriately formed targets.

A solution of the first of the problems seems to be quite well advanced /JONOTRONS, which were orginally developed for IOF research are now successfully used for various technological applications/. The research on the beam-target interaction within the IOF concept has been undertaken not long ago and preliminary results of these investigations are briefly reported here.

According to the two basic variants of the IOF concept, two types of experiments have been carried out:the first directed towards construction a long-beam fusion system, and the second which has in view the ion-implosion fusion. To produce targets of the density high enough to satisfy the IOF requirements $/n_t \cdot L_t \simeq 10^{21}\,cm^{-2}/$ a high-pressure fast gas-valve /operating at 4 MPa/ has been constructed. To learn about the physics of the beam-target interaction various gases /deuterium, helium and argon/ were used and evolution of the targets was observed.

Research on the long-beam systems.

This research was carried out with RPI-15 and MAJA-60 ion beam accelerators (2,3). In front of the electrodes, at various distances from them, the gas target of various densities were produced with the fast

valve and illuminated with D^+ ion beams.

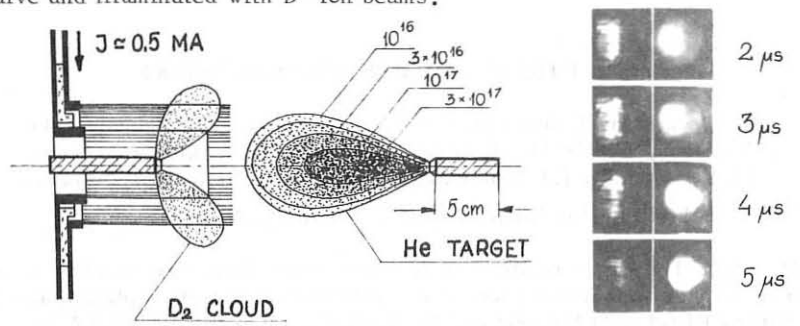

Fig.1. Schematic drawing of the beam-target experiments /on the left/ and evolution of the helium target as seen in the vissible radiation /on the right/.

To determine ion beam parameters: radial profiles and convergence, a system of 9 thermocouples was used and energy density in the beam was measured. To determine the time behaviour of ion beam pulses a Thomson mass-energy analyser equipped with photomultiplies was used. Typical energy density profiles and ion signals are shown in Fig.2.

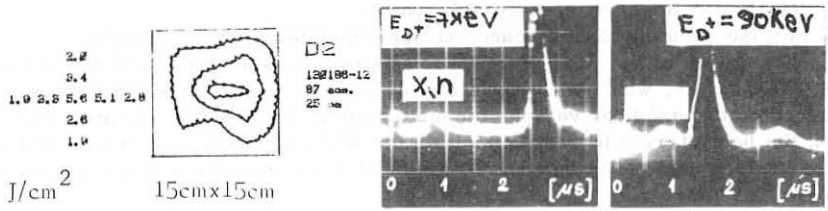

Fig.2. Energy density profile at the distance of 25 cm from the electrodes of RPI-15 device /on the left/ and signals of deuterons emmitted along the axis of MAJA-60 device /on the right/.

To estimate a correlation between the ion emmission and an accelerating potential, generated during the current breaking phase, the ion beam was directed on a heavy-ice target and neutrons were measured with scintilation detectors. It has been found that the neutron emission follows quite closely the acceleration potential.

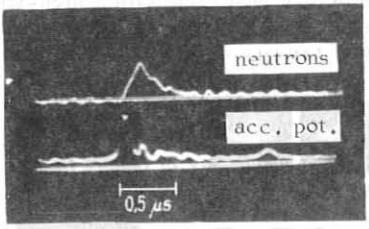

Fig.3. Typical oscilograms from RPJ-15 and MAJA-60 facilities showing the correlation between the neutron emission and the accelerating potential.

From absolute time-resolved neutron and accelerating potential measurements the absolute value of the ion beam current was estimated. In the case of the RPI-15 device the amplitude of the D beam current has reached 100 kA at the total current of the circuit equal to $\sim$250 kA.

Cylindrical Ion Implosion.

The main investigations on the ion-implosion fusion are being carried out with SOWA-400 facility, i.e. a modified SOWA-150 facility (3) in which energy of a supplying system has been increased from 150 kJ to 400 kJ. A gas target produced by two high-pressure fast gas-valves was illuminated by cylindrical radially-convergent D^+ ion beams, produced during the low pressure discharges between two cylindrical grid-type electrodes supplied from two sides, as shown on Fig.4. The most of experiments was carried out at 250 kJ.

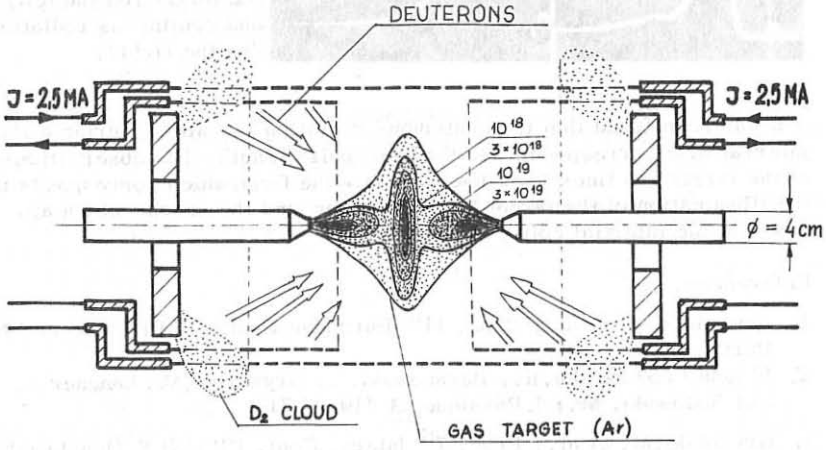

Fig.4. Scheme of the SOWA-400 ion-implosion experiment.

Evolution of the illuminated targets was observed with a high-speed photography. Depending upon the target density and the gas used a considerable differencies in the evolution of targets were observed. The typical evolution of the gas target is shown on Fig.5.

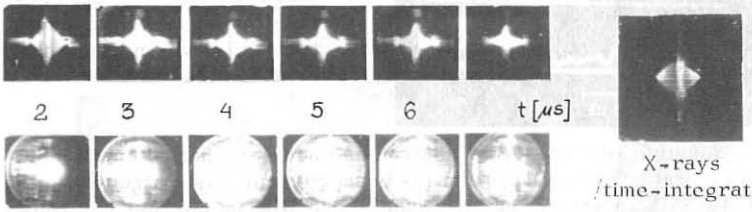

Fig.5. Implosion of the Ar target and X-ray emission.

To get more precise information about the dynamics of the implosion a time-resolved spectroscopy was used. There were observed the Balmer lines of the deuterium beam and the various spectral lines of the target gas as well as a continuous radiation at the given wave lengthes.

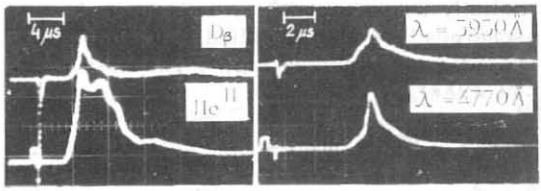

Fig.6. Time behaviour of the spectral lines of the D atoms from the beam and He atoms from the target /on the left/ and continuous radiation /on the right/.

It has been found that the continuous radiation is emitted during a short interval time corresponding to the beam pulse length. The observations of the target gas lines show two maxima - the first which corresponds to the illumination of the target by the D^+ beam and the second which appears at the intertial collapse phase.

References.

1. Gryziński, M. et al.; Proc. 11th European Conf. CF PP /Aachen 1983/ Part I, p.517.
2. Składnik-Sadowska, E., Baranowski, J., Gryziński, M., Langner, J, and Sadowski, M.; J. Physique 43 /1982/ 715.
3. Gryziński, M. et al.; Proc. 7th Intern. Conf. PP CNFR /Innsbruck 1978/. Vol.III. p.225.

ICF VOLUME COMPRESSION AND IGNITION CALCULATIONS

Hora H., Chicchitelli L., Eliezer* S., Stening, R.J. and Szichman H.

Department of Theoretical Physics
University of New South Wales, Kensington 2033, Australia

A re-evaluation of the difficulties and prospects of the central spark ignition of laser driven pellets is given in view of Yamanaka's highest gains where central compression had to be avoided in favor of a volume compression. The marginally treated volume compression theory, volume burn and the 1977 discovered volume ignition are re-evaluated and generalized fusion gain formulas and the self-ignition varying optimum temperatures derived. Reactor level DT fusion with MJ laser pulses and volume compression to 50 times the solid state are estimated. The surface tension caused by the double layers lead to stabilization. A further mechanism for generating suprathermal electrons by the dynamic electric fields in double layers is reported.

1) Introduction

The recent experiments on laser fusion [1] resulted in highest DT fusion gains and in a homogenous emission of x-rays only if a homogeneous volume compression of the pellet was achieved and any shock compression of the pellets center was avoided. This is contrary to the expectations of the scheme of the central core ignition with its well known difficulties [2] and revives the long years studies of the volume compression where the self-heat by the alphas resulted in the volume ignition [3].

Nevertheless there are various problems yet to be studied in both schemes: the spark and the volume ignition and the wel known fact that the total gain G for the pellet fusion has to be much larger than unity for the applicability of fusion reactors. Defining G as the ratio of the energy produced from a DT plasma [of initial (at time t=0)density n_0, volume V_0, and expansion velocitiy zero] per input energy E_0, and taking into account that the fusion burn works twice during compression and expansion, the gain for a fusion reactor has to be

(1) $\quad 2G > 1/(abcd) > 1 + W$

where a is the hydrodynamic efficiency (in best cases 20%), b is the power station efficiency (35%), c is the optical coupling of the laser energy into the pellet (80% in good cases), d is the laser driver efficiency (in extreme cases 80% e.g. in the cluster injection amplifyer scheme [4]), and W is the relative amount of output of usable electrical power which will be assumed of a value 1. Under these very positive - but technologically feasible - assumptions the value of G has to be larger than 22.3. This counts for the volume ignition only where the compression and the expansion will count for the burn; for spark ignition one has to take twice the gain, 44.6 as absolute minimum. For realistic considerations one may simply assume that the gain G has to be of a value of about 100.

2) Central Spark Ignition of Pellets

There were two initial arguments in favour of the spark ignition: (a) a volume burn of a fusion pellet even with 100% consumption of the fuel would result in a maximum gain of 421 only if the optimum temperature of the volume burn of 10.4 keV has to be used ,and (b) the mechanism of the transfer of the laser energy immediately suggested the spark mechanism: since the laser light can interact with the pellet in a shallow depth only, the heating of the pellet can be performed by thermal conduction from the heated corona to the interior only and the

mechanical action of compression is then obtained from the recoil of the ablated corona plasma. This recoil can be preferrably be used for a concentration of shocks in the center in order to reach densities beyond 1000 times the solid state density n_s. The reaction in the center has to produce a nuclear reaction intensity beyond 10^{19} W/cm^2 [5] for triggering the fusion wave.

The advantage with respect to (a) is the hope that the pellet can be of such size that the fusion wave can then burn a large amount of fuel such that higher gains than 380 can be achieved, however the problems of geometrical uniformity of irradiation and compression, and the then increasingly critical Rayleigh-Taylor instabilities are special problems. The spark ignition concept was promoted by K. Brueckner since 1969 [6] and it is so far the most predominantly discussed scheme in view of the first experimental success by KMS-Fusion [7] when the x-ray pin hole camera pictures showed the compressed high temperature pellet core in combination with fusion neutron generation. Nevertheless, spark ignition has never been achieved yet but only burn of the shocked fuel in the center.

Within the problems of the spark ignition theory remain the questions of the penetration depth of alphas as well as the interpenetration of the burning plasma into cold fuel. The precursing of an electron heat wave, long considered as dominating, has been shown to be of minor importance [8] in view of the new results of the electric double layers [9]. The threshold of the fusion wave of 10^{10} J/cm^2 for the solid state density could be lowered.

When calculating the necessary conditions for the spark ignition based on the improved conditions for triggering the fusion combustion wave with the optimum ratio bewteen density of the core and the density of the surrounding lower density plasma, based on a laser input energy of 1 MJ, the density of the compressed core has to have at least a density of 401 times the solid state density.

For more realistic conditions we recall earlier known results [10] that the compression of the core for the spark ignition has to be 1000 time of the solid state density. It further turned out that a minor deviation from the optimum temperature or the density of the compressed core by few percent only will not provide the conditions for triggering the fusion combustion wave. Other problems for spark ignition with respect to the double layer produced strong reduction of the thermal conduction [9] and the problems with the equation of state [2] are well known too.

3) Volume Compression and Volume Ignition

The computations for the optimized DT fusion gains G for a homogeneous distribution of an energy E_0 to a spherical volume V_0 of radius R_0 and density n_0 expanding adiabatically against vacuum was found [11] to be

$$G_0 = (E_0/E_{BE})^{1/3}(n_0/n_s)^{2/3} \tag{2}$$

if the initial temperature (averaged particle energy) at the begin of the expansion was

$$T_0 = 10.2 \text{ keV} \tag{3}$$

where E_{BE}= 1.6 MJ is the break even energy. Substituting volume by radius and expressing T_0 by (3), Eq.(2) is algebraically identical with Kidder's [12] value G=const.n_0R_0 with a difference of the constant by a factor of about 2 [13].

Adding to the computation of the volume compression and volume burn, the fuel depletion, the bremsstrahlung losses, and the alpha particle self-heat, the gain changes and it can happen that a nearly discontinuous increase in the gain plots appears by up to two orders of magnitude as discovered in 1977 [3][13] which was itentified as a volume ignition. A re-evaluation of the results was performed in view of the recent experimental realization of

the volume compression with avoiding any shock compression of the pellet center [1], and the following generalized gain formula was derived, valid for gains up to 200

$$(4)\quad G=G_0E_0/((6.32\times10^4 n_s/n_0)^2[1+E_0/(1.58\times10^4 n_s/n_0)^2]^{1/2}-1)$$

where a deviation by the saturation due to depletion occurs above the excluded range of this formula for gains above 200. The optimum temperature for the gains of Eq. (4) is then generalized into

$$(5)\quad T_{opt} = T_0[(25 + 10G_0)^{1/2} - 5]/G_0$$

Eqs. (4) and (5) change into Eq.s (2) and (3) for gains below 5. The fact that the optimum temperature decreases from 10.2 keV to values as low as 2 keV or less indicates that the limit of a total gain for volume compression of 421 - one main argument in favour of spark ignition - does not longer hold for volume ignition: the limit is then a gain of 2860 or more. Indeed the detailed computation [3][13] arrives at gain saturation of 1030. It further follows that the maximum burn at volume ignition is 39% only.

The result that the volume ignition always begins at a gain of 5 leads to a relation between compression volume and length which immediately reproduces the characteristic length for the stopping power of the fusion produced alphas in the pellet. For solid state density, a gain of 5 is reached for a pellet radius of 0.87 cm which with the geometrical factor of the stopping length for the self-heat results in a stopping range of 2.3 gcm^{-2} in agreement with the theoretical values (see Fig. 35 of Ref.[14]).

The most interesting conclusion is that Yamanaka's volume compression [1] needs densities between 30 and 50 times the solid state only for an irradiation of 1 MJ laser pulse energy according to Eq. (1) for achieving the conditions of a fusion reactor. The advantages of volume compression were observed also in computations with respect of minimizing of entropy production [15]

4) Double Layer Phenomena Improve Pellet Compression

While the Rayleigh-Taylor instability is very disadvantageous for the spark ignition and of less influence on the volume ignition, a stabilizing factor against this instability is possible by the surface tension due to electric double layers.

Contrary to the surface tension of liquids caused by intermolecular forces, fully ionized plasmas are compensated by attractive and repulsive Coulomb forces. However, the double layer at the surface, results in a surface tension of the value

$$(6)\quad \alpha = g(4\pi n)^{1/2}(kT)^{3/2}/e \quad erg/cm^2$$

where g is the strength of a thermal double layers which is of the value between 3/2 and 10, n is the electron density and T is the plasma temperature. The dispersion relation of surface waves was drived and stabilization was found for surface waves of the wave length

$$(7)\quad \lambda_{sw} < 8\pi^2\lambda_D/g$$

where λ_D is the Debye length. In nonlinear force dominated laser produced plasma, the effective Debye length can be 100 times and more than the thermal Debye length. A further stabilizing mechanism is due to the charging process of the plasma pellet.

For the illustration of the double layer phenomena we report here a recent result about the generation of energetic electrons in laser produced plasmas. The experimental observation of suprathermal x-ray emission from laser produced plasmas is well known [13] and is being

explained from the dielectrically increased (swelled) quiver motion of the electrons as known from nonlinear force action and as automatically reproduced from multiparticle codes [16]. Other possible explanations are given by resonance absorption or a special new resonance for perpendicular incidence [17], or simply by a local strong increase of the hydrodynamic temperature due to double layer caused inhibition of thermal conduction [18].

A further new mechanism is the fact that there are the mentioned very high longitudinal electric fields inside the

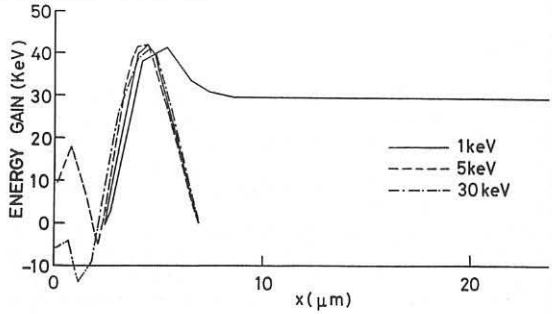

Fig. 1. 10^{17} W/cm^2 Nd glass laser irradiating a 0.025 mm thick plasma slab from the left. Computed traces of electrons of 1, 5 and 30 keV initial thermal energy moving collisionlessly to the left from a point of 7 μm from the left plasma border and showing an energy gain of more than 42 keV which can be slowed down too and retruned to be emitted at the rare side.

plasma in the area of the cavitons which are spread over several wave lengths and dynamically changing and ("slowly") alternating. If there are thermal electrons of 1 to 30 keV energy moving througth the fields caused by the laser manipulated plasma dynamics, computations show (Fig.1) that energies in the order of the measured suprathermal electrons are generated. The assumption of a collisionless penetration of the internal double layer speeding up thermal electrons is justified by the mean free path of 4 and 100 μm for 1 aqnd 5 keV electrons respectively.

*Gordon Godfrey Visiting Professor from SOREQ NRC Yavne, Israel

[1] C. Yamanaka and S. Nakai, Nature, 319, 757 (1986).-
[2] S. Eliezer, A.Ghatak, and H. Hora, Equations of State Cambridge University Press 1986.-
[3] H. Hora and P.S. Ray, Z. Naturforsch. 33A, 890 (1978)
[4] G.W. Kewntwell et al, J. Physique 47, No.10, C6-165 (1986).-
[5] J.L. Emmett, J. H. Nuckolls, and L. Wood, Sc.Am. 230,No.6, 24 (1974).-
[6] J. L. Bromberg Fusion MIT Press Cambridge,Mass.1983.-
[7] A.J. Glass, Laser Focus 19,No.2, 16 (1983).-
[8] H. Hora, Atomkernenergie 42, 7 (1983).-
[9] H. Hora, P. Lalousis, and S. Eliezer, Phys. Rev. Letters 53, 1650 (1984); H. Hora, Laser and Particle Beams 3, 59 (1985).-
[10] J. H. Nuckolls, Phys. Today 35, No. 9, 24 (1982).-
[11] H. Hora and D. Pfirsch, Laser Interaction and Related Plasma Phenomena H. Schwarz et al eds.(Plenum, New York, 1972) Vol.2, p.515.-
[12] R. E. Kidder, Nuclear Fusion 14, 797 (1974).-
[13] H. Hora, Physics of Laser Driven Plasmas, Wiley New York 1981.-
[14] K. Long and Tahir, Nuclear Fusion 26, 590 (1986).-
[15] G. Velarde et al. Laser and Particle Beams 4, 349 (1986) and priv. comm. Nov. 1986; M. Decroisette, J.P. Watteau et al, priv. comm. Nov. 1986.-
[16] E.J.Valeo,Phys.Fluids,17,1391 (1974);E.Valeo and W.Kruer Phys.Rev Lett.33,750 (1974).-
[17] H. Hora and A.K. Ghatak, Phys. Rev. 31A, 3473 (1985).-
[18] Y.V. Afanasyev et al, ECLIM 87 Conference Prague, May 1987.-

RECENT DEVELOPMENTS IN THE ANALYSIS AND DESIGN OF HEAVY ION BEAM DRIVEN ICF TARGETS

José L. Ocaña, José Mª Martínez-Val

Instituto de Fusión Nuclear (DENIM). Univ. Politécnica Madrid
Pº de la Catellana 80, 2806 Madrid, Spain

1.-INTRODUCTION

As a continuation of previous work on the analysis and optimization of ICF beam and target configurations [1,2], the influence of energy deposition profile by heavy ions in the different layers of multilayered ICF capsules has been analyzed.

For this purpose an attempt to establish physically based criteria different from a simple analysis of the aspect ratios of the different material zones has been made for the characterization of the ICF target dynamics.

A first result obtained from the calculations is that the hydrodynamic performance of the treated targets strongly depends of the particular ion energy deposition profile obtained along the different material zones. Furthermore, the possibility of continuously locating the energy deposition front at the appropriate penetration level would avoid, in a direct way, the undesirable fuel preheating resulting from the excessive penetration of optimized energy deposition profiles before the ion range shortening.

An attempt to demonstrate this fact in a practical way has been undertaken and the first positive results obtained, by comparing the evolution of a given target both with and without tailoring of the driver energy deposition profile in the described way and matching the corresponding hydrodynamic and burnup performances [3].

2.- ANALYSIS OF THE INFLUENCE OF PUSHER-TO-INTERNAL TAMPER MASS RATIO ON HIBALL TYPE TARGETS PERFORMANCE.

For the proposed study, reference heavy ion pulse and multilayered target configurations have been considered whose defining charateristics are compliled in figure 1 and table I.

In order to complete this study under more or less realistic assumptions on the characteristic working parameters of the ion accelerators (present or future), the properties of the ion beam driver have been highly altered in the sense of changing the peak power P_p of 720 TW or lower under which previous simulations have been performed, for a peak power of 500 TW (more reasonable in concern with the previewed capabilities of the HI accelerators).

The described analysis took as variable parameter the ratio mass of aluminium (pusher)/mass of internal lead (radiation shielding + explosion tamper) in order to establish the conditions under which a better compression

of the fusion fuel could take place in compatibility with a high enough mass of internal tamper needed in the burnup-phase

Material	Mass (mg)	Density ($g.cm^{-3}$)	External Radius (cm)
Pb	190	11.614	0,3
Al	60	2.707	0,2847754
Pb	15	11.614	0,2611145
DT	1	0,21	0,2595983
Void	-	-	0,2538489

Table I

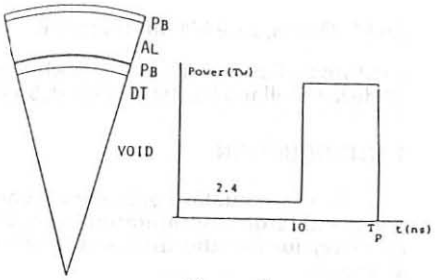

Figure 1

From previous simulations of the dynamics of ICF targets such as those considered (5), and also from a pure theoretical analysis of the conditions under which an efficient compression of the fusion fuel can take place, the bulk energy carried by the driver ions must be released on the "pusher" zone. In order to attain this condition, and if the energy of these ions has to remain constant, at the beginning of the compresion process (medium cold), one has to allow some part of this energy to penetrate to more deep zones, what, as a consequence of the conduction properties of the matter, can lead to an undesirable fusion fuel peheating.

If this peheating is to be avoided, one has to select the (pusher + internal shielding-tamper) thicknesses is such a way that the driver ion energy deposition profile is as a whole taken back to less deep zones in the pusher material, what, in turn, leads to a worse fuel compresion performance (more payload mass to be accelerated).

For a given set of data concerning the driver energy pulse and the geometry of the target under compression, the above mentioned ratio has been analyzed and optimal values have been obtained for different mass values of pusher material (aluminium) close to that of reference.

In figures 2 and 3 such collection of optimal values are represented along with the corresponding values of maximum fuel temperature and maximum fuel ρR parameter under these two separate criteria.

These figures not only provide the appropriate set of ratios under which an optimum compression takes place, but gives a singular value for the mass of pusher and the corresponding mass of internal shielding tamper under which the compression is absolutely optimum as it implies the minimum payload mass to be compressed together with the fuel to avoid its undersirable preheating.

This, is of great importance for the analysis under consideration, as it establishes the way to arrive to optimized target configurations without any regard to simple afficiency criteria such as those related to target and fuel aspect ratios, nevertheless useful for other kind of estimates.

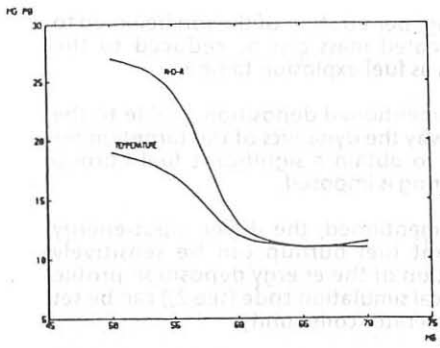

Figure 2

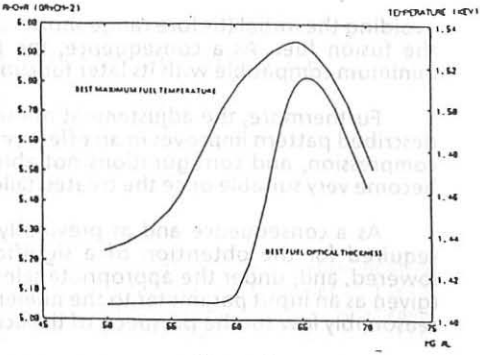

Figure 3

3.- HEAVY ION DRIVEN TARGET DYNAMICS IMPROVEMENT BY MEANS OF INCIDENT IONS ENERGY VARIATION IN TIME

For the proposed study on optimization of the energy deposition profile by continuous variation of the input ions energy, the subroutine STOP of the program NORMA[5] has been modified in order to allow for the possibility of fixing the set of material zones in which the ion energy deposition has to take place and prescribe the energy required for the incident ions as a function of time in order to fulfil this condition along the energy deposition phase.

This output profile (likely optimum regarding the target evolution) can be conveniently redefined from a simpler and technologically realistic point of view while conserving its approximate shape for the sake of an appropriate target dynamics.

Although the obtained profiles can be unfeasible from the experimental point of view while sensitively optimized for the target dynamics. Furthermore, the required accelerator current in no case departs substantially from the reference value or suffer large instantaneous variations, the case for the utilization of two separate storage rings being much more favourable.

In addition, in view of the really high fusion performances attainable under the described procedure, this seems a valuable way to obtain remarkably high gains and a signficant ignition energy thresholds reduction in HIF targets.

The main limiting point found in the analysis are the high driver power and energy still required to obtain a signficant gain, but more recent simulations indicate the possiblity of lowering these levels to others technolgically more realistic.

In addition, one can realize that upon tailoring, the mass of the internal shielding-tamper (internal lead) can be drastically reduced in comparison to the reference design as its shielding function can be practically elliminated by

avoiding the initial (before range shortening) penetration of the ion beam up to the fusion fuel. As a consequence, the treated mass can be reduced to the minimum compatible with its later function as fuel explosion tamper.

Furthermore, the adjustement of the mentioned deposition profile to the described pattern improves in an effective way the dynamics of the target under compression, and configurations not able to obtain a significant fuel burnup become very suitable once the treated tailoring is imposed.

As a consequence and as previously mentioned, the driver input-energy required for the obtention of a significant fuel burnup can be sensitively lowered, and, under the appropriate selection of the energy deposition profile (given as an input parameter to the numerical simulation code (see 2)) can be set reasonably low for the prospects of the accelerator community.

In figure 4 the gain curve obtained for the target family considered is plotted against the reference gain curves given by Lindl and Mark (7).The main conclusion to be extracted is that, in spite of the technological limitations envisageable for a compression pattern as the described (5), the suitability of HIF targets can be upgraded up to limits remarkably high.

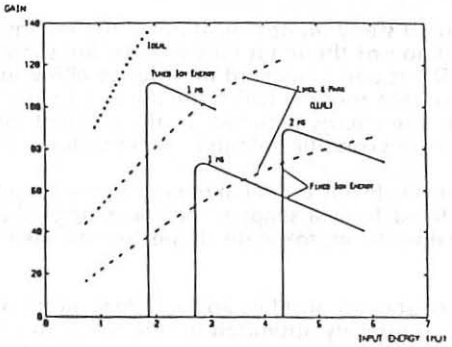

Figure 4

REFERENCES

1.- VELARDE, G. et al.:Trans. Am. Nucl. Soc. **46**, 190 (1984)
2.- VELARDE, G. et al.: Nucl. Fus. Supplement. 10 th IAEA **3**, 121 (1985)
3.- GERVAS, C. et al., "Analysis of the Influences of Pusher-to Internal Tamper Mass Ratio on HYBALL Type Target Performance" (1986) DENIM Annual Research Report
4.- VELARDE, G. et al.: Atomkernenergie **44**, 209 (1984).
5.- VELARDE, G. et al. : Laser and Particle Beams **4**, 349 (1986)
6.- OCAÑA, J.L. et al., "Numerical Simulation Result on Heavy Ion Target Dynamics Improvement by Means of Incident Ions Energy Variation in Time", (1986) DENIM Annual Research Report.
7.- LINDL, J.D., MARK,J.W.K.: Laser and Particle Beams **3**, 37 (1985)-.

LIGHT-ION BEAM FOCUSING BY SELF MAGNETIC FIELD IN ICF

S. KAWATA, M. MATSUMOTO and Y. MASUBUCHI

The Technological University of Nagaoka
Nagaoka, Niigata 940-21, Japan

Abstract

The paper shows the analyses for the focusing of the intense proton beam by the self magnetic field. In the analyses the self magnetic field is included for the computation of the beam trajectories. The analyses present that the self magnetic field can be used successfully for the good focusing of ion beam.

1. Introduction

In the light-ion beam (LIB) inertial confinement fusion (ICF), the experimental and theoretical researches have been done very actively 1-3. Especially the LIB diode has been developed very well to produce the intense LIB. On the other hand, the study for the LIB focusing is still required urgently in order to implode a small fuel pellet. In an LIB ICF reactor the LIB has about one mega ampere per one proton beam. Therefore the self magnetic field of the LIB is enough strong to pinch the LIB. It has been considered that the self magnetic field has a negative effect on the LIB focusing.

The paper presents the proton beam focusing by the self magnetic field 4. The self magnetic field is used positively in order to obtain the good LIB focusing.

2. Basic equation for beam trajectory

It is assumed that the beam is axially symmetric and has no azimuthal velocity. In a cylindrical coordinate the equation of motion for an ion is,

$$(dv_r/dt) = -(e/m)\, B\, v_z$$
$$(dv_z/dt) = (e/m)\, B\, v_r \,, \qquad (1)$$

where B is

$$B = \mu_0\, I(R_0)/(2\pi R) \qquad (2), \qquad I(R_0) = (R_0/R_a)^2\, I(R_a) \qquad (3),$$

Here m is the ion mass, e the ion charge and Ra the beam radius at the entrance (Z=0). The self magnetic field produced by the beam has only the azimuthal component. And I(Ra) is the total beam net current which is the unneutralized part of the LIB current, μ_0 the magnetic permeability in the vacuum and R0 the initial position of the particle normalized by Ra at the entrance (Z=0). The distribution of the beam current on the

initial surface (Z=0) is assumed to be uniform in the paper. It is assumed that the beam charge is neutralized perfectly and the beam current is retained.

Under the conditions, the components of the velocity are solved to be,

$$v_r = -\left(v_0^2-\{\Omega\ln(R/R_0)+v_0\cos\theta_0\}^2\right)^{1/2}$$

$$v_z = \Omega\ln(R/R_0)+v_0\cos\theta_0 \ , \qquad (4)$$

where $\Omega=eB/m$. At t=0 and Z=0 (the entrance point), the initial angle of the extracted particle is denoted by $\theta 0$ and the particle speed is v0. From the equations (4)

$$dR/dZ = -\left(1-\{\xi\ln(R/R_0)+\cos\theta_0\}^2\right)^{1/2}/\{\xi\ln(R/R_0)+\cos\theta_0\} \ . \qquad (5)$$

Here $\xi=\Omega/v0$ and is proportional to $I(Ra)/\sqrt{V}$ where V is the particle acceleration voltage ($eV=mv0^2/2$).

3. Numerical results

In the analyses the orbit is computed from Z=0 to the focal point(Z=Zf). In the paper only the steady state is considered. The initial angle of the extracted beam is computed. The value of $I(Ra)(Ampere)/\sqrt{V}$ (Volt) is 447. For example the value of 447 comes from the case of I(Ra)=1 MA and V=5 MV. The focal point is at Zf=Ra. Figure 1-(a) shows the relation between the computed initial angle and the normalized radius. In the figure the solid line presents the result at the surface (Z=0). At the surface (Z=0) it is assumed that there is no external magnetic field leaking from the diode gap. The beam is focused at the focal point as shown in figure 1-(b), if the relation shown by the solid line is satisfied. The result shown by the dotted line presents the same kind of relation at the diode electrode surface, that is, the cathode surface which is shown in figure 1-(b).

In the above case the crossing angle to the axis (R=0) is large for the most beam particles. A fuel pellet should be located at the focal point. This is the one way to implode a fuel pellet.

In the above case it is difficult to transport the beam through a z-discharged plasma channel. The incident angle to the plasma channel can be made small by using the gas cell. In the analyses it is assumed that the beam current is also neutralized in the gas cell besides the beam-charge neutrality. In the case $I(Ra)/\sqrt{V}=447$ and the focal point is set to Zf=5xRa. The region of the gas cell is after Z=0.2xRa in figure 2. Figure 2-(a) shows the relation between the incident angle and the radius at the surface of Z=0. The beam trajectories are shown in figure 2-(b).

4. Discussions

The paper presents that the LIB is focused well by using the self magnetic field successfully after the beam acceleration. This method

makes the focusing system simple and is fitted to the LIB focusing in ICF.

In the analyses, it is assumed that the charge neutrality of the LIB is uniform at the surface of Z=0 and the degree of the current neutrality is kept constant in the whole computational domain. A few works were done for the charge and current neutralizations 5 and showed that the degree of the neutralities can be controlled by changing the number density of the background gas. In addition, the nonuniformity of the LIB net current distribution is not essential in the analyses and can be included in the computations easily.

Near the focal point there is a possibility of the orbit crossing with each other. But this is not severe in these cases which are employed in this paper. Because in the LIB ICF a fuel pellet has a finite radius, typically about 5 mm. If the volume of the region in which the orbit crossing can be seen, is comparable to the volume of the pellet, this effect is not a problem on the results.

The steadiness in the phenomena is assumed. Typically the pulse duration time of the LIB is 50 nsec and the pulse length is about a few meters. Therefore the main body of the LIB pulse might be considered to be steady.

In order to clarify these unsolved problems, a computer simulation code is developed, whose name is TRIPIC, by the authors. The TRIPIC code is a particle-in-cell one, which is described in another paper 6 in this conference.

REFERENCES

1. J. R. Freeman, L. Baker and D. L. Cook, Nucl. Fusion, 1982, **22**, p. 383.
2. J. P. VanDevender and D. L. Cook, Sience, 1986, **232**, p. 801.
3. S. Kawata and K. Niu, J. Phys. Soc. Jpn. 1984, **53**, p. 3416.
4. T. P. Wright, Phys. Fluids, 1979, **22**, p. 1831.
5. T. Aoki, S. Kawata and K. Niu, Res. Report of Inst. of Plasma Phys. Nagoya Univ. 1985, IPPJ-742, p. 128.
6. S. Kawata, M. Matsumoto and Y. Masubuchi, "Development of triangle-mesh particle-in-cell code for LIB diode simulation", Proceedings of 14th European Conference on Controlled Fusion and Plasma Physics, 1326 b) D. Th. 5.

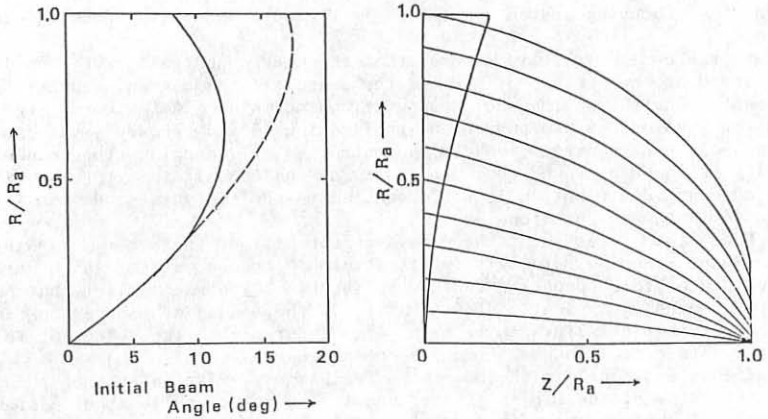

Figure 1. (a) Profile of the initial beam angle and (b) LIB particle path and predicted anode shape. In the case the focal point $Z_f=R_a$ and $I(R_a)/\sqrt{V}=447$.

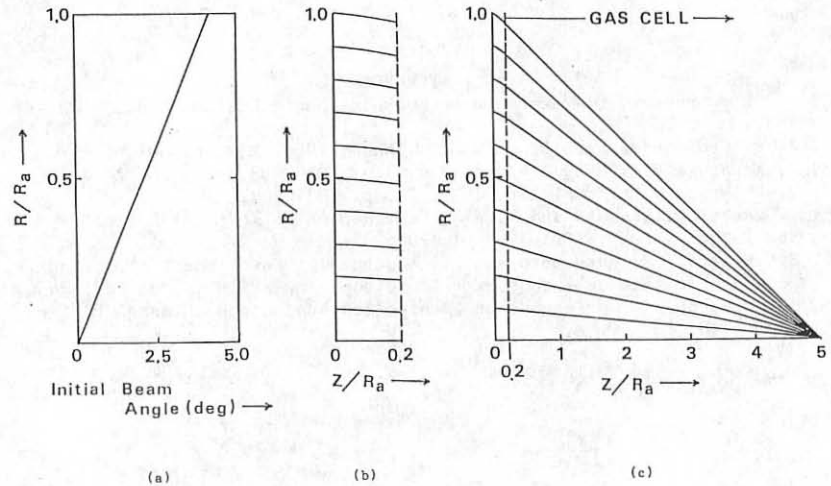

Figure 2. (a) Profile of the initial beam angle, (b) and (c) LIB particle path. In the case the focal point $Z_f=5xR_a$, gas cell is set after $Z=0.2xR_a$ and $I(R_a)/\sqrt{V}=447$.

E

PLASMA EDGE PHYSICS

LANGMUIR PROBE MEASUREMENTS IN THE ASDEX DIVERTOR PLASMA

N. Tsois[1], G. Haas, M. Lenoci, J. Neuhauser, and G. Becker, H.S. Bosch, H. Brocken, A. Carlson, A. Eberhagen, G. Dodel[2], H.-U. Fahrbach, G. Fussmann, O. Gehre, J. Gernhardt, G. v. Gierke, E. Glock, O. Gruber, W. Herrmann, J. Hofmann, A. Izvozchikov[3], E. Holzhauer[2], K. Hübner[4], G. Janeschitz, F. Karger, M. Kaufmann, O. Klüber, M. Kornherr, K. Lackner, G. Lisitano, F. Mast, H.M. Mayer, K. McCormick, D. Meisel, V. Mertens, E.R. Müller, H. Murmann, H. Niedermeyer, A. Pietrzyk[5], W. Poschenrieder, H. Rapp, A. Rudyj, F. Schneider, C. Setzensack, G. Siller, E. Speth, F. Söldner, K. Steinmetz, K.-H. Steuer, S. Ugniewski[6], O. Vollmer, F. Wagner, D. Zasche

Max-Planck-Institut für Plasmaphysik,
EURATOM Association, Garching, FRG

I. Introduction and apparatus: Langmuir probes have been used routinely in ASDEX divertor plasma diagnostics /1,2/. Recently, a fast movable probe carrier system was installed. Two fast sweeping movements with a speed of 1 m/s and 10 cm displacement were possible during a shot. The probe can also be kept, for an adjustable time interval, at the innermost position. The initial position of the probe can be adjusted by using the manipulator and a tilt mechanism. A large area of the divertor plasma can thus be scanned in the radial and vertical directions (see fig. 1).

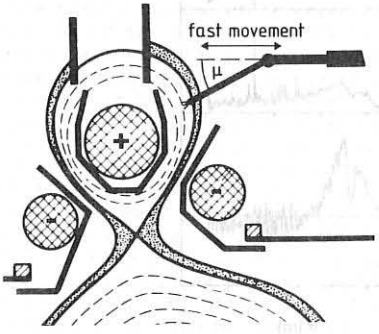

Fig.1: Probe arrangement and accessible area in the upper divertor.

The divertor probe system was used in all operation regimes of ASDEX. The triple-probe arrangement /3/ was mainly used but the probes were also operated as a double probe, especially for cross-check purposes. Up to four radial profiles of the ion saturation current, electron temperature and floating potential relative to the divertor plate were obtained during a shot.

II. Experimental results: Radial scans have revealed strong gradients of the plasma parameters across the flux surfaces, near the separatrix location. This fact is important since triple-probe operation is very sensitive to differences in plasma parameters seen by the three tips. In order to minimize the error introduced by these gradients in temperature and density evalu-

[1] N.R.C.N.S. "Democritos", Athens, Greece; [2] University of Stuttgart; [3] Ioffe Institute; [4] University of Heidelberg; [5] University of Washington, Seattle, USA; [6] Inst. for Nuclear Research, Swierk, Poland

ation, an optimum inclination of the probe arm was chosen so that the tips were as close as possible to the same flux surface. The data reported here were obtained with this optimum inclination ($\mu \approx 15^{o}$).

Ohmically heated discharges: Typical radial profiles of plasma parameters for two values of the main plasma densities are shown in fig. 2. The medium density profiles display the well-known characteristics of the ASDEX divertor plasma /1,2/: large maxima close to the separatrix, broad shoulders a few centimetres away in the ion saturation current and density profiles, and relatively flat temperature profile. The absolute values of the electron temperature and density are in good agreement with the double-probe cross-check measurements. The floating potential profiles are flat, with values slightly negative. At densities $\bar{n}_e \leq 5 \times 10^{13}$ cm^{-3}, a sharp negative "dip" develops close to the calculated position of the separatrix which cannot be attributed to a local temperature rise.

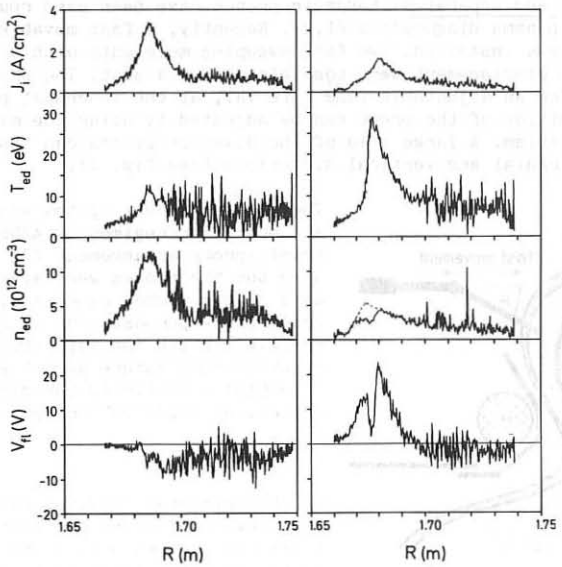

Fig.2: Profiles of ion saturation current, electron temperature, density and floating potential vs. major radius R for $\bar{n}_e = 4.3 \times 10^{13}$ cm^{-3} (left) and $\bar{n}_e = 1.4 \times 10^{13}$ cm^{-3} (right).

As the density is lowered, the floating potential becomes positive together with an increase of temperature around the separatrix, in a region which is more and more extended. Also the narrow "dip" is now well developed. Floating-potential gradients as high as ~100 V/cm can be observed in some low density shots. Even at the optimum inclination of the probe arm, floating

potential differences of 5 to 8 V between tips were measured in a narrow zone around the separatrix. These high gradients together with a presumably non-Maxwellian electron velocity distribution clearly affect the derivation of the electron temperature and density profiles (see fig. 2).

Additionally heated discharge: During the additional-heating phases of the discharges (NI, LH, ICRH) the divertor plasma also displays specific features. Besides the enhanced power flow (increased ion saturation current and electron temperature), some changes were also observed in the floating-potential and density profiles. In fig. 3 a few examples of floating-potential profiles are presented. In the L phase of a NI-heated discharge, the floating-potential profiles show positive charging of the plasma around the separatrix, similar to that in OH discharges of lower densities. The negative "dip" is also more pronounced.
In the H phase, the burst activity makes the interpretation of floating-potential data very difficult. The ion saturation current and electron temperature between bursts are comparable with the values for ohmic phases. The peak values of bursts are much larger and extend over the whole profile, including the shoulder.
The RF heating produces different effects on the density and floating-potential profiles, mainly depending on the plasma density and the injected power. At medium densities ($\sim 4 \times 10^{13}$ cm^{-3}) and high powers (~2 MW), all the divertor plasma is positively charged, as can be seen in fig. 3.

III. Discussion: As seen above, all profiles show a pronounced structure depending on the density, heating power and heating method. The dependence of the maximum values of the electron temperature, density and floating-potential of the divertor plasma on the main plasma density for ohmic discharges is presented in fig. 4. A smooth evolution in all three measured parameters can be seen with rising density. No step-like change of V_{fl} with density as in D-III /4/ was observed. The floating-potential profiles suggest different transport to the divertor plates for different plasma densities. So, at high and medium densities, the floating potential stays slightly negative, being compatible with locally ambipolar transport on each flux tube /5/, and with some (few eV) drop in the electron temperature between the probe position and the divertor plate. As the density is lowered or NI power is added, the floating potential around the separatrix starts to rise and extends radially, the whole cross-section of the divertor plasma being positively charged at densities below 1×10^{13} cm^{-3}. The positive values of V_{fl} suggest locally non-ambipolar transport to the divertor plates. The mechanism by which the divertor plasma is charged is not yet clear. Non-Maxwellian electrons close to the separatrix (see below) together with vertically asymmetric plasma position and divertor recycling etc. could be candidates for explanation. Further experiments are needed to clarify these aspects.
The negative "dip" displayed very close to the calculated position of the separatrix, although expected, was surprising in some respects. Firstly, it implies strong gradients in floating potential which perturbs any multiple-tip probe measurements. Then, it is very narrow so that we believe that it can be used for separatrix position determination (as done in Fig. 3) with a better accuracy than magnetic measurements.

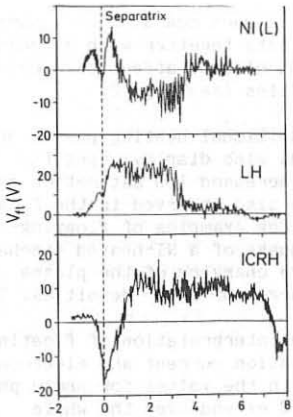

Fig.3: Floating potential profiles for different heating methods.

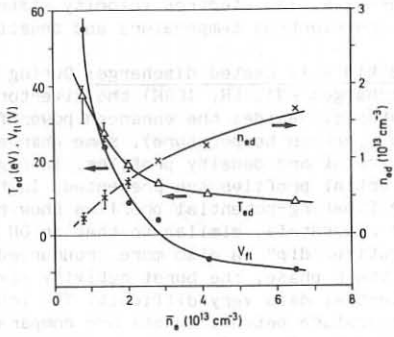

Fig.4: Peak values of electron temperature, density and floating potential vs. main plasma density $\bar{n}_e$.

Some estimation of the current density and energy of electrons responsible for the "dip" can be made by combining the available data. Values of 0.2 - 0.5 A/cm^2 and $E_e \geq 100$ eV were obtained in low-density discharges. At higher densities, these numbers are significantly lower and only upper limits can be estimated. The values obtained at low densities are in good agreement with those expected from a diffusive loss of fast electrons across the separatrix which can reach the divertor /6/. It is therefore concluded that the negative "dip" in floating-potential profiles as well as some distortion in ion saturation current profiles at very low densities are due to fast electrons which flow almost collisionless from the main chamber to the divertor very close to the separatrix.
The amounts of energy carried by these electrons can be locally important. Some comparisons with thermographic data have shown that the correction implied by these fast electrons has the right direction.

References

/1/ Y. Shimomura, M. Keilhacker, K. Lackner and H. Murmann, Nucl. Fus. 23, 869 (1983).
/2/ G. Fussmann et al., J. Nucl. Mater. 128/129, 350, (1984).
/3/ S.L. Chen, T. Sekiguchi, J. Appl. Phys. 36, 2363, (1965).
/4/ M. Shimada et al., in Plasma Phys. and Contr. Nucl. Fus. Res. 1984 (Proc. 10th Int. Conf. London, 1984), Vol. 1, IAEA, Vienna (1985) 281.
/5/ P.C. Stangeby, G.M. McCracken, S.K. Erents, J.E. Vince and R. Wilden, J. Vac. Sci. Technol. A1, (2), 1302 (1983).
/6/ U. Ditte, T. Grave, Probe and Thermographic Measurements in ASDEX Divertor, IPP Report, III/102 (1985).

THE EFFECT OF EDGE TEMPERATURE ON IMPURITY PRODUCTION UNDER A RANGE OF OPERATING CONDITIONS IN JET

J A Tagle, S K Erents*, G M McCracken*, R A Pitts*,
P C Stangeby+, C Lowry° and M F Stamp

JET Joint Undertaking, Abingdon, Oxon OX14 3EA, UK
* Culnam Laboratory, Abingdon, Oxon OX14 3EA, UK
+ Institute for Aerospace Studies, University of Toronto, Canada
° Imperial College of Science and Technology, London, UK

1. INTRODUCTION

The radial distribution of electron temperature and density in the edge of a Tokamak determines impurity production and transport. The impurity production by sputtering of the limiter and wall material is controlled by the particle fluxes and their energies. The subsequent transport of these impurity atoms back into the main plasma is controlled by the probability of ionization, which is again a function of the edge temperature and density. Finally this data allows one to convert the spectroscopically measured photon output from ionization states of the neutral impurity entering the edge plasma into atomic influx rates[1]. In this paper we show how the electron temperature and density in the scrape-off layer (SOL) of JET for ohmically heated plasmas in D and He scale with plasma currents I_p = 1-5 MA, toroidal field B_T = 2.1-3.5 T and line averaged density $\bar{n}_e$ = 1-4 x 10^{19} m^{-3}. These data are then used to calculate the carbon impurity production by physical sputtering from the limiter.

2. TEMPERATURE AND DENSITY SCALING

The results were obtained using Langmuir probes situated on an ICRH

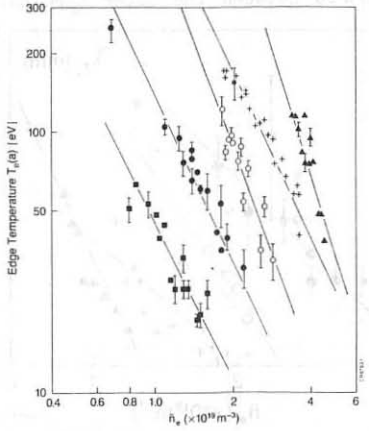

Fig. 1 Effect of line average density $\bar{n}_e$ on temperature T_e at LCFS.

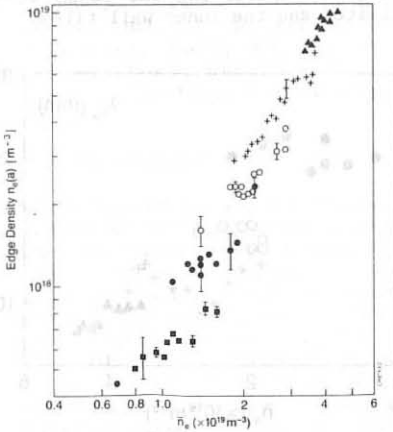

Fig. 2 Effect of $\bar{n}_e$ on density n_e at LCFS.

(■ = 1MA,2.1T; ● = 2MA,2.1T; o = 3MA,3.4T; + = 4MA,3.5T; ▲ = 5MA, 3.5T)

antenna protection tile, close to the torus midplane. Details of the diagnostic were reported elsewhere[2]. Assuming an exponential decay of the edge parameters in the SOL[1], the density and temperature profiles are extrapolated 15 mm to the last close flux surface (LCFS), defined by the carbon limiter. The scalings of edge temperature $T_e(a)$ and density $n_e(a)$ with line averaged central density ($\bar{n}_e$) for plasma currents 1 MA - 5 MA are shown in figure 1 and 2. Each data point represents steady state conditions during separate discharges and the parameters measured were averaged over a few seconds before the end of the plasma current flat top. Although the data were collected over several months, all are ohmic, limiter discharges in deuterium with fairly constant loop volts. The fraction of power radiated, (P_{RAD}/P_{OHM}) was ≈ 0.5. $T_e(a)$ falls with increasing $\bar{n}_e$ and increases with increasing input ohmic power ($P_{OHM} \alpha I_p^{0.8}$). The fitted lines in figure 1 gives us an approximate empirical scaling for the complete data set

$$T_e(a) \alpha \{I_p/\bar{n}_e\}^2 \qquad (1)$$

For a fixed I_p, the edge density $n_e(a)$ scales almost linearly with central density, $\bar{n}_e$. From figure 2

$$n_e(a) \alpha I_p \bar{n}_e \qquad (2)$$

An analytical model which considers particle diffusion and cooling of the edge by impurity sputtering [3,4] predicts that $n_e(a) \alpha \bar{n}_e^2$, and that $T_e(a) \alpha P_{OHM}/\bar{n}_e^2$. However this model assume a constant electron impact ionization rate ($\overline{\sigma v}_i$). In fact, ($\overline{\sigma v}_i$) $\alpha \bar{n}_e^{-1}$ over the temperature range shown in figure 1, hence the linear dependence of $n_e(a)$ on $\bar{n}_e$ is in agreement with the model. An exception to this scaling is the case of the 5 MA data which could be due either to the non-steady state plasma conditions (very short current flat-top) or to the close proximity of the plasma to the inner wall, causing the power to be shared between the outer toroidal limiter and the inner wall tiles.

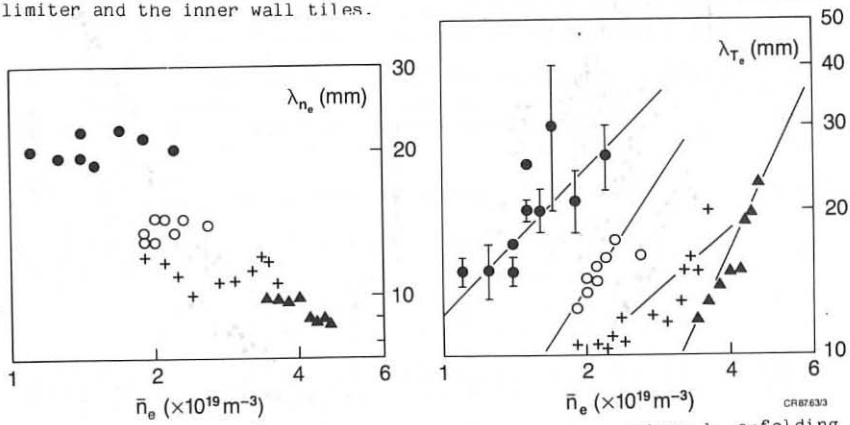

Fig. 3 The effect of $\bar{n}_e$ and I_p on density λ_n and temperature λ_T e-folding length in the SOL.
(● = 2MA,2.1T; o = 3MA,3.4T; + = 4MA,3.4T,▲ = 5MA,3.4T)

3. CHANGES IN THE SOL THICKNESS AND RADIAL DIFFUSION

In figure 3 we present the scaling of SOL thickness for edge temperature and density with $\bar{n}_e$ and I_p. The density e-folding length, λ_n, is practically independent of central density $\bar{n}_e$, but is almost inversely proportional to plasma current for a fixed toroidal field B_T. However, λ_T is rather less well defined due to scatter in the data points, but in general shows an increase with $\bar{n}_e$ and a decrease with I_p. Using the λ_n values and a formulation for the cross-field diffusion coefficient, $D_\perp$, deduced by Stangeby[5] we caluclate $D_\perp$ ($\bar{n}_e$). This is shown in figure 4 (for 2 MA and 3 MA discharges only), and the scaling

$$D_\perp \propto \bar{n}_e^{-1.3} \qquad (3)$$

is found. Since $D_\perp \propto \lambda_n^2 T_e(a)^{0.5}$, and λ_n is almost independent of $\bar{n}_e$, it follows that the inverse dependence of $D_\perp$ on $\bar{n}_e$ is largely due to the change of edge temperature with density. In fact we found that $D_\perp \propto T_e(a)^{0.7}/B_T^{1.5}$, although the power law dependence on B_T is only approximate because of a limited data set at different B_T. Nevertheless, it appears that the cross-field diffusion is not very different from Bohm.

4. IMPURITY PRODUCTION

The measured values of the ion flux and temperature have been used to calculate the local physical sputtering rate at the limiter as a function of radius, which after integration over the radial coordinate, gives the total carbon flux. The ion energy was deduced from the sum of the ion thermal energy plus the acceleration across the sheath potential, V_s ie. $E = 2T_e + qV_s$; where q is the charge state. To calculate V_s we use the value of the secondary electron emission coefficient $\bar{\gamma}(E)$ measured on typical limiter samples exposed to the JET plasma[4]. It is then assumed that all sputtered carbon is ionized, (q=4), and available for self-sputtering of the limiter. The total flux of carbon is then

$$\Gamma_c = \Gamma_D Y_D/(1 - Y_c) \qquad (4)$$

where Y_D and Y_c are the deuteron and carbon self-sputtering yields. The results of these calculations are presented in figure 5. The total carbon influx rate decreases with $\bar{n}_e$ for fixed plasma current, and increases with I_p for a constant $\bar{n}_e$. Even though $Y_D(E)$ only falls slightly with decreasing $T_e(a)$ over the energy range of interest (550 > E > 150 eV for D^+ ions), the fall in

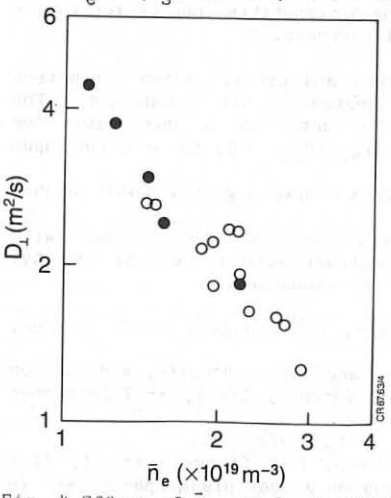

Fig. 4 Effect of $\bar{n}_e$ and I_p on cross field diffusion coefficient. (● = 2MA,2.1T, o = 3MA,3.4T).

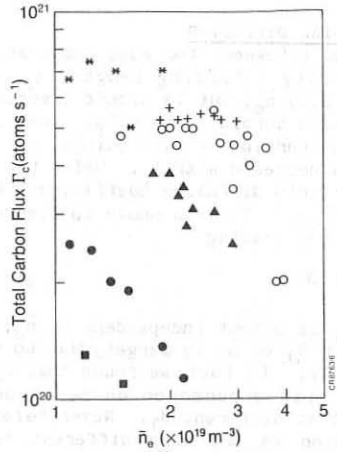

Fig. 5 Effect of $\bar{n}_e$ and I_p on total carbon flux sputtered from the limiter [■ = 1MA,2.1T; ● = 2MA,2.1T; ▲ = 3MA, 3.4T] [o = 2 MA,2.1T in He^4 plasma] [CIII flux (arb units): ✱ = 2MA,D; + = 2MA He]

self-sputtering $Y_c(E)$ is greater (over a higher energy range) and the combination in equation 4 results in the pronounced decrease of Γ_c with $\bar{n}_e$. We include a comparison for similar data for discharges in He^4, (2 MA, 2.1 T) and also with the spectroscopically determined CIII flux. Here $Y_{He^4} = 4\ Y_D$ at a given energy. There is also an increase in the ion energy due to a slightly higher sheath potential and because the helium ion is doubly ionised. The Γ_c calculated is = 4 times higher than in the D case, but remains quite flat for He^4 over the measured $\bar{n}_e$ range. This is due to the self-sputtering yield being almost constant over the He^4 ion energy range. The spectroscopy data are in good agreement for discharges in He^4. However in the case of D discharges the spectroscopically measured Γ_c remains constant with $\bar{n}_e$ and is higher than in He^4 discharge. Our calculations can not take into account the oxygen sputtering of carbon, charge-exchange and the screening of impurities due to ionization in the SOL, which could explain these differences.

CONCLUSIONS

- Empirical laws relating edge parameters and global plasma parameters have been found in JET for ohmically heated limiter discharges. The relations given in equations (1) and (2) determine a lower limit for density and upper limit for temperature ($P_{RAD}/P_{OHM} \to 0$) for a given input power (P_{OHM})
- The empirical laws can be explained by a simple a global power balance model.
- The limiter sputtering and total carbon release rates increase with input power for a given density, and decrease with increasing density. The model predicts that $\Gamma_c \propto T_e(a)^{0.6}$ for D discharges.

REFERENCES

1. S K Erents, J A Tagle, G M McCracken, P C Stangeby and L de Kock, Nuclear Fusion 26 (1986) 1591.
2. J A Tagle, S K Erents, G M McCracken and H Brinkschulte, Workshop on High Temperature Plasma Diagnostics, Varenna, Italy, 3-13 September 1986 (in press).
3. W Engelhardt et al, J Nucl Mater, 111-112 (1982) 337.
4. S K Erents, J A Tagle, G M McCracken, P C Stangeby et al, 'The dependence of tokamak edge conditions on global plasma parameters in JET', to be published.
5. P C Stangeby, J A Tagle, S K Erents and C Lowry (these proceedings).

Parametric Behavior of the Density Profile in the Scrape-off Layer of ASDEX for Neutral-Beam-Heated Plasmas in the L-Regime

K. McCormick, Z.A. Pietrzyk[4], H. Murmann and G. Becker, H.S. Bosch, H. Brocken, A. Carlson, A. Eberhagen, G. Dodel[1], H.-U. Fahrbach, G. Fussmann, O. Gehre, J. Gernhardt, G. v.Gierke, E. Glock, O. Gruber, G. Haas, W. Herrmann, J. Hofmann, A. Izvozchikov[2], E. Holzhauer[1], K. Hübner[3], G. Janeschitz, F. Karger, M. Kaufmann, O. Klüber, M. Kornherr, K. Lackner, M. Lenoci, G. Lisitano, F. Mast, H.M. Mayer, K. McCormick, D. Meisel, V. Mertens, E.R. Müller, J. Neuhauser, H. Niedermeyer, W. Poschenrieder, H. Rapp, A. Rudy, F. Schneider, C. Setzensack, G. Siller, E. Speth, F. Söldner, K. Steinmetz, K.-H. Steuer, N. Tsois[5], S. Ugniewski[6], O. Vollmer, F. Wagner, D. Zasche

Max-Planck-Institut für Plasmaphysik,
EURATOM Association, Garching, FRG

Abstract: Characterizing the scrape-off layer (SOL) density profile by the density at the separatrix n_s and the e-folding length λ_n, the SOL is described for a wide variety of conditions: $\bar{n}_e$=1-5x10^{13} cm^{-3}, I_p=250-440 kA, B_t~22 kG, q_a=2.4-4.3 for injected powers P_{NI}~0.4-1.7 MW, which lead to L-type discharges. Generally, λ_n increases with P_{NI}, these changes becoming more dramatic for lower I_p and $\bar{n}_e$. For OH and NI plasmas n_s is roughly proportional to $\bar{n}_e$; the constant of proportionality increases with NI and is independent of P_{NI} over the range investigated.

Introduction: This paper is designed to furnish an initial data base for the critical evaluation of SOL models, as well as to investigate the premise that the SOL behavior during NI reflects global plasma transport properties as has been observed elsewhere /1, 2/. Statements are limited to the SOL n_e profile in the outer midplane of doubly-null diverted discharges sustained by gas puffing. The ASDEX neutral lithium-beam probe /3, 4/ is used to determine λ_n and the relative changes in n_s; previous experience gained with the edge Thomson scattering system /5/ furnishes an approximate absolute calibration of n_s.

To place matters in context, fig. 1a illustrates the effect of high power (2.75 MW) $H^0 \rightarrow D^+$ injection on $\bar{n}_e$, $\beta_{p\perp}$ (taken from the diamagnetic loop) and D_α as well as the Li-beam light signal outside the separatrix. $\bar{n}_e$ decreases going into the L-phase, followed by the H-phase increase and subsequent clamping correlated with the D_α bursts. The characteristic D_α signatures are closely paralled by Li[2p-2s] (~ proportional to n_e) /3/. The SOL n_e profiles for OH, L and H (fig. 1b) indicate that $n_s^L < n_s^{OH} < n_s^H$. Further, λ_n^{OH}~1.95 cm, λ_n^L~2.8 cm and λ_n^H~1.1 cm. T_{es}~70, 130 and 250 eV for the OH, L and H-regimes respectively /5/. $R-R_s$ is the distance from separatrix; R_s is derived from magnetic signals and underlies an uncertainty of perhaps 1 cm. This has an important bearing on scaling statements made about n_s; thus if R_s were in fact one cm further outwards, then $n_s^{OH} > n_s^L \sim n_s^H$ would be deduced.

---

[1] University of Stuttgart; [2] Ioffe Institute; [3] University of Heidelberg; [4] University of Washington, Seattle, USA; [5] N.R.C.N.S. "Democritos", Athens, Greece; [6] Inst. for Nuclear Research, Swierk, Poland;

Results: Fig. 2b depicts for $H^0 \rightarrow He^{2+}$ injection, λ_n vs. the total absorbed input power $P_{TOT}=P_{OH}+P_{NI}^{abs}$ for $\bar{n}_e=1\text{-}4.9\times10^{13}$ cm^{-3} and I_p=420 kA; the energy confinement time "τ_E" deduced from the steady-state NI phase using $\beta_{p\perp}$ to determine the total energy W and "τ_E"=W/P_{TOT} (without correction for radiation effects) is plotted vs. $P_{TOT}/\bar{n}_e$ in fig. 2a.

Fig. 2b demonstrates that during OH (corresponding to the points at the left as in fig. 2a) λ_n is about constant for $\bar{n}_e>1.9\times10^{13}$ cm^{-3}, and is much larger for lower $\bar{n}_e$, as has been previously reported /6/. Auxiliary heating leads to an increase in λ_n, the changes becoming more apparent for lower $\bar{n}_e$ and higher P_{TOT}, τ_E decreases with $P_{TOT}/\bar{n}_e$. Thus, at $\bar{n}_e = 4\times10^{13}$ cm^{-3} (1.9×10^{13} cm^{-3}), over the power range λ_n increases by ~10% (22%) and τ_E goes from ~100 to 50 ms (63→45 ms). n_s exhibits the interesting behavior that it is described by an offset-linear law of the form $n_s=a\bar{n}_e+b$, the constants depending only on the type of heating (OH or NI). No parametrical dependence of n_s on P_{NI} is evident; however, for higher P_{NI} a relationship must exist, as documented in fig. 1b where n_s is reduced rather than increased in the L-phase for P_{NI} = 2.85 MW.

The $H^0 \rightarrow D^+$ series of fig. 3 involve a q_a-(I_p=270-420 kA) and $\bar{n}_e$-scan (2.2, 3.5×10^{13} cm^{-3}). For any given q_a the NI-induced changes in λ_n (see fig. 3b) have the same qualitative behavior as for He: lower $\bar{n}_e$ and higher P_{NI} are both conducive to large alterations in λ_n. The slope of the λ_n vs. q_a curves is about the same for all conditions. With respect to τ_E, for injection with 4 sources τ_E is the same for $\bar{n}_e$=2.2 or 3.5×10^{13} cm^{-3}, whereas λ_n increases by 25% ($\bar{n}_e$ = 2.2→3.5×10^{13} cm^{-3}), demonstrating that λ_n does not necessarily mirror changes only in τ_E.

In fig. 3c there is no convincing dependence of n_s on q_a; also, the largest absolute δn_s is small, of the order ~0.15×10^{13} cm^{-3}. Nevertheless, a plot of n_s vs. $\bar{n}_e$ (not shown here) also reveals an offset-linear relationship, switching from one slope to another as with He, depending on the type of heating used.

Fig. 4 shows the results of another $H^0 \rightarrow D^+$ power scan with either $\bar{n}_e$ (fig. 4b,c) or I_p (fig. 4d, e) being held constant. The familiar variation of λ_n with P_{NI} and $\bar{n}_e$ is again found, but the changes are more extreme. For example, at $\bar{n}_e\sim3\times10^{13}$ cm^{-3} and q_a=4.3 (fig. 4d), λ_n varies from 2.8 to 4.3 cm for P_{TOT}~0.25 → 1.2 MW. In addition, the λ_n^{OH} values are larger than those normally observed on ASDEX by ~0.5 cm. n_s^{NI} clearly increases more strongly with $\bar{n}_e$ for q_a=4.3 than for n_s^{NI}(He) at q_a=2.4 of fig. 2c; on the other hand, the n_s^{OH} values are nearly identical.

Discussion and Summary: It is a common feature of NI-heated plasmas in the L-regime that λ_n increases with P_{NI}, the increase being less pronounced for higher $\bar{n}_e$, and possibly higher I_p. In any case for both OH and NI, λ_n is augmented with q_a: The OH λ_n-q_a scaling of fig. 3b agrees well with previous results /6/, whereas λ_n^{OH} of fig. 4b and 4d is anomalously large for a D^+ plasma. This may be indicative of a deviant wall-conditioning of the divertor. Also, "τ_E" for the series of fig. 4 is noticibly lower. Hence, this series should be regarded in a more qualitative manner.

Whereas it is true that a degradation in τ_E is accompanied by larger λ_n, the reverse conclusion that larger λ_n are synonymous with lower τ_E cannot be universely drawn. It appears that the NI-induced degradation in the

cross-field diffusion coefficient $D_\perp$ also extends into the SOL, but that this is only one component in determining λ_n. With respect to τ_E, plotting vs $P_{TOT}/\bar{n}_e$ leads to a surprisingly orderly unification of the OH and NI values, at least for this limited data set. Further, the τ_E scalings for He^{++} of fig. 2a and D^+ of fig. 3a are virtually identical, and of the form $\tau_E \sim \alpha(P_{TOT}/\bar{n}_e)^{-\beta}$ msec (α = 31-32.3, β=0.48, 0.51).

For n_s vs. $\bar{n}_e$, a very clear feature which emerges is that the OH offset-linear scaling switches promptly to a steeper gradient upon initiation of NI, but beyond that shows no dependence on the magnitude of P_{NI}. Higher I_p might bring the OH and NI scalings closer together (compare fig. 2c and 4e): the data base is too small to allow definitive conclusions. As a comment, one of the quantities which should determine n_s for high recycling is the specific heat flux $q_\parallel$ into the divertor /7/, which is related to P_{TOT}, λ_n and λ_{Te}. λ_{Te} decreases ~10% /5/ over the P_{NI} range studied here, in contrast to the moderate (at low q_a and high $\bar{n}_e$) 10-20% enhancement in λ_n; therefore $q_\parallel$ should increase almost proportionately to P_{TOT}.

No Thomson data was available to calibrate the relative Li-beam determinations of n_s; to obtain n_s absolutely, experience from cross-calibrations of other series were used. Hence, strictly speaking, all absolute n_s values are provisional including the n_s vs. $\bar{n}_e$ scalings. Definitive conclusions can be drawn only with respect to the relative behavior of the switch in scaling between OH and NI discharges. λ_n is generally measured to an accuracy of $\pm$0.1 cm .

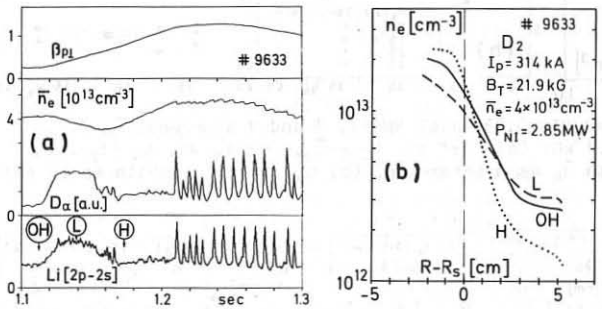

Fig.1 (a) Time behavior of $\beta_{p\perp}$, $\bar{n}_e$, D_α radiation in the divertor and the Li[2p-2s] light intensity several cm outside the separatrix, (b) n_e profiles for the OH, L and H-phases.

References

/1/ F. Wagner, Nucl. Fusion 25 (1985) 525.
/2/ F. Wagner, O. Gruber, et al. 12th EPS (Budapest 1985) 335.
/3/ K. McCormick, H. Murmann and El Shaer, J. Nucl. Mater. 121 (1984) 48.
/4/ K. McCormick, Rev. Sci. Instr. 56 (1985) 1063.
/5/ H. Murmann and M. Huang, Plasma Phys. 27 (1985) 103.
/6/ K. McCormick, Z.A. Pietrzyk, et al., J. Nucl. Mater. 145-147 (1987) 215.
/7/ J. Neuhauser and R. Wunderlich, in ref. /6/ (1987) 877.

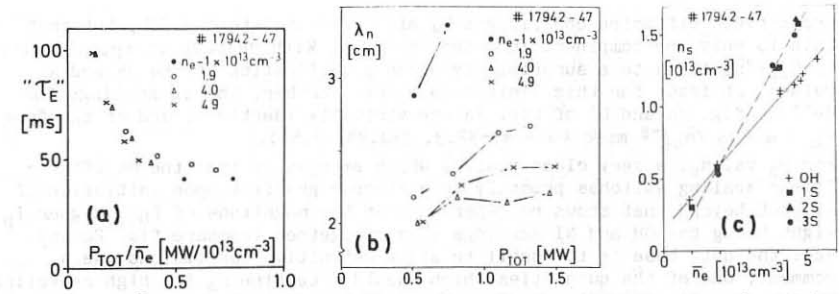

Fig.2 $H^0 \rightarrow He^{2+}$ with P_{NI}=0.41, 0.88, 1.24 MW (1, 2 and 3 NI sources), I_p=420 kA, B_t=21.7 kG: (a) energy confinement time "τ_E" vs. $P_{TOT}/\bar{n}_e$, (b) density e-folding length λ_n in the SOL vs. P_{TOT} with $\bar{n}_e$ as a parameter. (c) Separatrix density n_s vs. $\bar{n}_e$ during OH and NI.

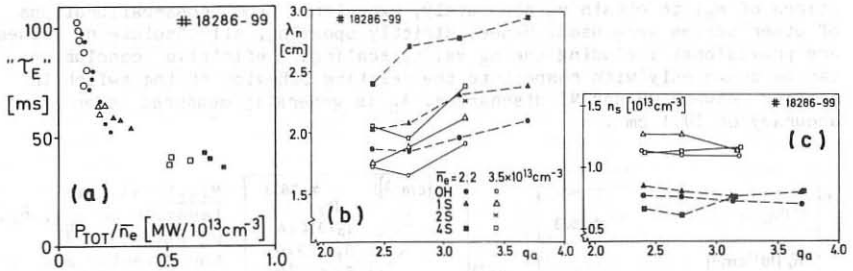

Fig.3 $H^0 \rightarrow D^+$ with P_{NI}=0.41, 0.83, 1.67 MW (1, 2 and 4 sources), $\bar{n}_e$=2.2, 3.5x10^{13} cm^{-3}, B_t=21.8 kG: (a) "τ_E" vs. $P_{TOT}/\bar{n}_e$, (b) λ_n vs. q_a (I_p=270, 320, 370, 420 kA) with $\bar{n}_e$ as a parameter, (c) n_s vs. q_a, symbols as in (b).

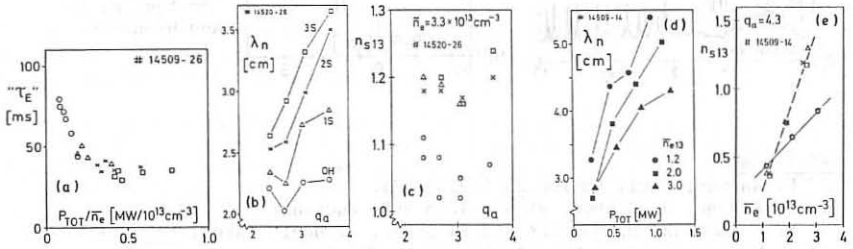

Fig.4 $H^0 \rightarrow D^+$ with P_{NI}=0.42, 0.87, 1.3 MW (1, 2 and 3 sources), B_t=22 kG: (a) "τ_E" vs. $P_{TOT}/\bar{n}_e$, (b) λ_n vs. q_a (I_p=290, 340, 390, 440kA) with P_{NI} as a parameter, $\bar{n}_e$-3.3x10^{13}cm^{-3}, (c) n_s vs. q_a for shots of (b); (d) λ_n vs. P_{TOT} with $\bar{n}_e$ as a parameter, q_a=4.3 (250 kA), (e) corresponding n_s vs. $\bar{n}_e$ plot.

OBTAINING VALUES OF $D_\perp$ FROM MEASUREMENTS OF THE EDGE SCRAPE-OFF LENGTHS IN JET

P. C. Stangeby*, J. A. Tagle, S. K. Erents** and C. Lowry***

JET Joint Undertaking, Abingdon, Oxon, OX143EA, U.K.
*and University of Toronto Institute for Aerospace Studies
4925 Dufferin Street, Downsview, Ontario, Canada, M3H 5T6
**EURATOM-UKAEA Association, Culham Laboratory
Abingdon, Oxon, OX143DB, U.K.
***and Imperial College, London University

It is necessary to establish the value of the cross-field diffusion coefficient $D_\perp$ which prevails in the edge plasma in order to predict central impurity densities from impurity influxes and to predict the scrape-off lengths which will result from the insertion of additional edge components.

Typically, the plasma density outboard of the last closed flux surface decays exponentially with radial distance. The decay length, λ_n, can be theoretically related to the hydrogen cross-field diffusion coefficient $D_\perp$. Thus measurements of λ_n, obtained by Langmuir probes and by optical viewing of the H_α footprint on the limiters, can be used to obtain $D_\perp$. The simplest edge modeling leads to the relation

$$\lambda_n = (LD_\perp/c_s)^{1/2} \qquad (1)$$

where L = connection length, i.e., the distance along $\vec{B}$ between limiters, $\sim \pi Rq$ for the JET limiter configuration,
and $c_s = [k(T_e + T_i)/m_i]^{1/2}$ the ion acoustic speed in the edge.

For JET this relation requires alteration to account for (a) the non-circular cross-section of the plasma, (b) the discrete nature of the limiters. In particular non-circularity causes poloidal variations in $\lambda_n(\theta)$ simply due to magnetic field effects. Additionally, one anticipates that fluid flow effects, associated with plasma transport along $\vec{B}$ to the limiters, would cause further poloidal variation in density $n(\theta)$ and $\lambda_n(\theta)$. With regard to the latter, fluid-flow effects, it appears that these may not be strong in JET, although the experimental basis for this conclusion is not substantial. This latter matter is addressed first before proceeding to the purely geometrical effects. For a few JET discharges probe measurements are available for two poloidal locations - the outer mid-plane ($\theta = 0$) and near the top of the torus ($\theta \approx 80°$). Experimental particle flux density (I^+_{sat}) results for such discharges are given in Fig. 1. Details of the probes and measuring techniques are given elsewhere [1]. As can be seen, the data from the two probes coincide if one accounts for the compression of the magnetic field lines between the two probe locations, Fig. 2. This does not mean that there is no density variation whatsoever along $\vec{B}$ between the two probes: the top probe is an isolated probe, 3 cm in diameter, for which

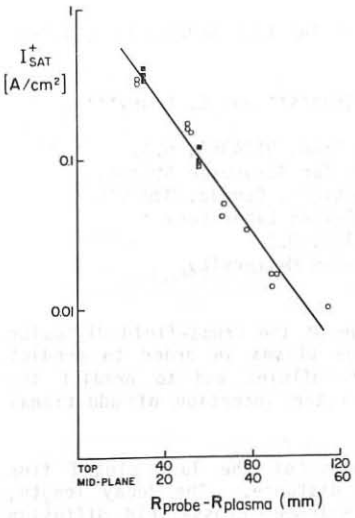

Fig. 1. Comparison of particle flux density measured by top Langmuir probe (O) and mid-plane probe (■). I_p = 3 MA, B_ϕ = 2.8T, $\bar{n}_e = 2.5\times10^{19}$ m^{-3}.

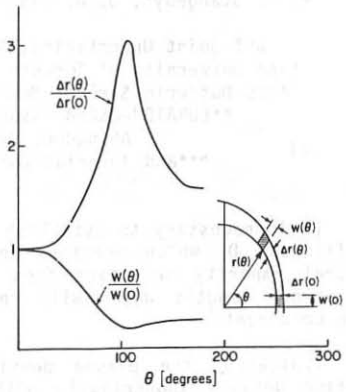

Fig. 2. Poloidal variation in flux tube cross-section for tube lying on last closed flux surface. I_p = 3.6 MA, B_ϕ = 3.4T, κ = 1.47.

the relation between particle flux and plasma density is $I^+_{sat} \simeq 0.5\, n_e e c_s$; the mid-plane probe is flush-mounted within a large, metre-size, RF antenna shield to which plasma is flowing regardless of the probe's presence, thus implying the relation $I^+_{sat} \simeq n_e e c_s$ where n_e is the density just near the antenna. Nevertheless, the density differences measured by the two probes on the same field line are equal for these discharges to within experimental error; the largest error is in establishing the location of a given field line which is computed from magnetic data and is only accurate to order cms. For the following, therefore, it will be assumed that variations of density along $\vec{B}$ are due to geometric factors only and not to fluid effects.

The limiters on JET [2] until 1987 were discrete rail limiters located at the outside mid-plane, approximately one metre high (poloidally) and 0.4 m wide (toroidally), of number varying up to 8. Consider a set of N discrete limiters located symmetrically (toroidal direction) around the outside mid-plane, each of poloidal height h, Fig. 3. There will be next-neighbour shadowing of limiters when

$$\frac{2\pi(R_m + a)}{Nh} < \frac{B_\phi(0)}{B_p(0)} \qquad (2)$$

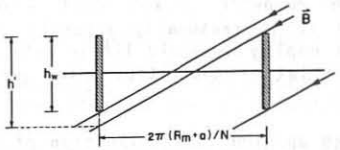

Fig. 3. Discrete limiter spacing.

where symbols have their usual definition. Toroidal width of limiters is neglected here which has a negligible effect for reasonable q values. Thus the discrete limiters are effectively a continuous toroidal belt limiter if $q_L > q_L^*$ where $q_L \equiv [r(0)\ B_\phi(0)]/[R(0)B_p(0)]$ and $q_L^* = [2\pi a]/[hN]$. Note that q_L, q_L^* are effectively field angles at the limiter, not safety factors. Limiter major radius = $R(0) = R_m + a$.

For a continuous belt limiter the relation between $D_\perp$ and $\lambda_n(0)$ is given by particle balance between inflow from the main plasma into the scrape-off layer at flux density $D_\perp dn/dr \simeq D_\perp n(0)/\lambda_n(\theta)$ and outflow to the limiter at a rate dependent on $n(0)$ and $\lambda_n(0)$. By accounting for the varying separation of magnetic field lines as a function of θ it can be shown [3] that

$$n(0)c_s\lambda_n(0)w(0)B_\phi(0)/B_{tot}(0) = \int_{\theta=0}^{\pi} D_\perp \frac{dn}{dr}\frac{B_\phi(\theta)}{B_p(\theta)}\, w(\theta)r(\theta)d\theta \qquad (3)$$

which gives

$$\lambda_n^2(0) = \frac{\pi D_\perp r(0)B_{tot}(0)f}{c_s B_p(0)} \qquad (4)$$

where

$$f \equiv \pi^{-1}\int_0^{\pi} \frac{w(\theta)}{w(0)}\frac{r(\theta)}{r(0)}\, d\theta \qquad (5)$$

is a magnetic field shape factor which, in principle, should be calculated for each discharge; $w(\theta)$ and $r(\theta)$ are defined in Fig. 2.

Turning to the case of $q_L < q_L^*$ when the limiters act discretely rather than as a continuous belt: h should now be replaced by h', Fig. 3, where

$$\frac{h'}{h} = \frac{B_p(0)}{B_\phi(0)}\ \frac{2\pi(R_m + a)}{Nh} \qquad (6)$$

This affects the outflow to the limiter which is accounted for by multiplying Eq. (4) by h'/h. Thus one has the simple relation between λ_n measured at the outside mid-plane and $D_\perp$:

$$\frac{c_s\lambda_n^2(0)}{fD_\perp\pi(R_m + a)} = \begin{cases} q_L \text{ for } q_L > q_L^* \\ q_L^* \text{ for } q_L < q_L^* \end{cases} \qquad (7)$$

While in principle f and q_L must be calculated from detailed calculations based on magnetic pickup coil measurements for each discharge, in practice it is reasonably accurate to use f = 0.5 (for $1.3 \lesssim \kappa \lesssim 1.6$) and to employ a simple linear relation, Fig. 4, between q_L and q_{cyl} or q_ψ, the latter quantities being generally available for each discharge on JET.

This model has been applied to a collection of ohmic JET discharges which were defined by a set of outer mid-plane discrete (usually 8) limiters, Fig. 5. The values of $D_\perp$ inferred in this way are about four times larger than would be obtained from the simple relation, Eq. (1), and generally fall within the INTOR-ALCATOR scaling of $D_\perp = (0.5\text{-}1.25\times10^{19})/\bar{n}_e$. As noted, the values of $D_\perp$ measured in this way are for the edge plasma, and it is therefore perhaps surprising that they are about the same as expected for the main plasma. Since it is found experimentally on JET [4] that $T_{edge} \simeq 25\text{-}100$ eV and decreases with $\bar{n}_e$, it is also true that these measured edge values of $D_\perp$ are approximately Bohm-like: $D_{Bohm} \simeq 0.06\ T_{edge}$ [eV]/B[T], i.e., for B ≃ 3T, $D_{Bohm} \simeq 0.5 - 2\ m^2/s$.

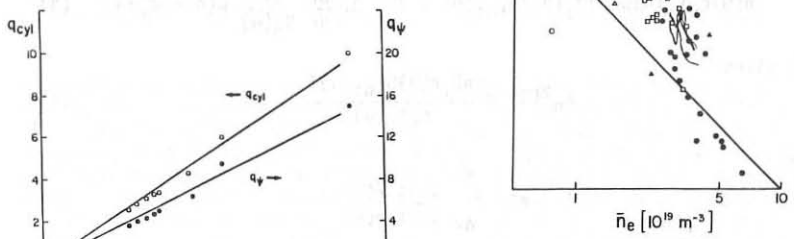

Fig. 5. $D_\perp$ obtained from measurements of τ_n. Ohmic discharges defined by outside mid-plane limiters. Probe data: (○) 1 MA, (△) 2 MA, (▲) 3 MA, (□) 4 MA, (●) 5 MA. H_α light: wavy lines, 5 MA discharges. Solid line $D_\perp = 10^{19}/\bar{n}_e$.

Fig. 4. Correlation between q_{cyl}, q_ψ and q_L for a range of JET discharges $\kappa \simeq 1.5$.

References

1. S. K. Erents, J. A. Tagle, G. M. McCracken, P. C. Stangeby, L. deKock, Nucl. Fusion, 26 (1986), 1591.
2. L. deKock, J. Nucl. Mater. 145 & 147 (1987), 26.
3. P. C. Stangeby, J. A. Tagle, S. K. Erents, C. Lowry, to be published.
4. J. A. Tagle, et al, this conference.

CALCULATION OF POLOIDAL ROTATION IN THE EDGE PLASMA OF LIMITER TOKAMAKS

H. Gerhauser, H.A. Claaßen

Institut für Plasmaphysik, Kernforschungsanlage Jülich GmbH
Association EURATOM-KFA, P.O. Box 1913, D-5170 Jülich, FRG

The existing 2-d two-fluid code /1/ for computing the plasma profiles in the scrape-off layer of limiter tokamaks has been further developed to include the effects of a poloidal rotation and of the associated non-ambipolar motion selfconsistently in the basic equations. The 2-d profiles of all relevant quantities are calculated and discussed for TEXTOR-typical parameters including also the effect of limiter recycled neutrals. The results agree well with the known experimental evidence on radial decay lengths, on electrostatic potential and on poloidal rotation.

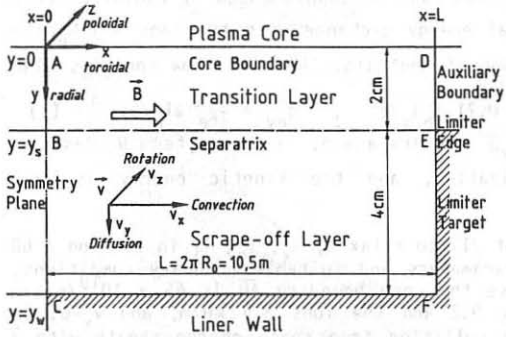

We consider the TEXTOR edge plasma in the rectangular integration domain ACFD. All variables are poloidally constant: $\partial/\partial z \equiv 0$. We avoid the usual assumption of local ambipolarity and allow for an electrical current density $\vec{j} = e\,n\,(\vec{v} - \vec{u})$, where $\vec{v}$ is the ion velocity and $\vec{u}$ that of the electrons. Quasineutrality entails $\nabla\cdot\vec{j} = 0$ and a stream function Ψ with $j_y = \partial\Psi/\partial x$ and $j_x = -\partial\Psi/\partial y$.

We use the full set of Braginskij's two-fluid equations including those terms that were omitted in previous treatments like /1/. The equation of continuity is unchanged and contains a source term S_n from the recycled neutrals, the ion equation of motion a source term $\vec{S}_p$:

$$\partial(mn\,\vec{v})/\partial t + \nabla\cdot(mn\,\vec{v}\vec{v}) = -\nabla p - \nabla\cdot\vec{\vec{\pi}} + \vec{j}\times\vec{B} + \vec{S}_p \qquad (1)$$

We retain only the parallel viscosity $\pi_{xx} = -4\,\eta\,\partial v_x/3\partial x$. Since diffusion $v_y = -D^{\perp}\partial n/n\partial y \lesssim 10^{-3} c_s$ (sound velocity), the dominant terms of the y-component of (1) reduce to the radial equilibrium condition:

$$j_z B = \partial p/\partial y = \partial p_e/\partial y + \partial p_i/\partial y = \partial(nT_e + nT_i)/\partial y \qquad (2)$$

The electron equation of motion leads to the generalized Ohm's law:

$$-\nabla p_e - e\,n\,(\vec{E} + \vec{u}\times\vec{B}) + \vec{R} = 0 \quad , \quad \vec{E} = -\nabla\Phi \qquad (3)$$

with the electric field $\vec{E}$, potential Φ and friction $\vec{R}$. The dominant part is the parallel thermal force R_x(for H^+ or D^+) $= -0.71\,n\partial T_e/\partial x$, and the electrical conductivity is practically infinite, so that $R_y, R_z \approx 0$. In the y-component of (3) we use $enu_z = env_z - j_z$ and (2) yielding

$$e\,n\,B\,v_z = e\,n\,\partial\Phi/\partial y + \partial p_i/\partial y \quad (+R_y) \qquad (4)$$

Hence in general a poloidal mass rotation velocity v_z of the plasma occurs, composed of an electric and a diamagnetic drift. In view of (4) the z-component of (1) determines the steady-state j_y in terms of the already known v_z:

$$Rj_y = R\partial\Psi/\partial x = -mn(v_x\partial/\partial x + v_y\partial/\partial y)v_z + S_{pz} - mv_z S_n \qquad (5)$$

This shows the close connexion between $\vec{j}$ and a spatially varying rotation. The non-ambipolar corrections $(j_x,\ j_y,\ v_z^2) \lesssim 10^{-2}(env_x,\ env_y,\ c_s^2)$ are taken into account in the energy balance equations. We eliminate $\vec{R}$ with Ohm's law:

$$\partial(1.5\ nT_e)/\partial t + \nabla\cdot(2.5\ nT_e\vec{u} + \vec{q}_e) = -en\vec{E}\cdot\vec{u} + \vec{R}\cdot\vec{v} + Q_{ei} + W_e$$
$$= \vec{j}\cdot\vec{E} + \vec{v}\cdot\nabla p_e + (v_z j_y - v_y j_z)B + Q_{ei} + W_e \qquad (6)$$

Thus even for $j_x = j_y = 0$ the $\vec{v}\cdot\nabla p_e$-term must be supplemented by radial Lorentz work $-v_y j_z B$. Q_{ei} is the thermal energy exchange with the ions and W_e the loss by ionization and excitation of neutrals. The heat flow contains also an ohmic term:

$$q_{ex} = -\chi_e^{\parallel}\,\partial T_e/\partial x - 0.71\,T_e j_x/e \quad , \quad q_{ey} = -\chi_e^{\perp}\,\partial T_e/\partial y \qquad (7)$$

In the ion energy equation $v_y j_z B$ appears again, a source term W_i describes charge exchange and ionization, and the kinetic energy is now $m(v_x^2+v_z^2)/2$, $m=m_i=m_D$.

We apply the numerical method of /1/ to relax n, v_x, T_e, T_i in time on a 60 x 33 grid for TEXTOR-typical parameters and suitable boundary conditions. The total particle inflow across the core boundary $\overline{AD}$ is 65 x 10^{19}/sec/m (poloidal), the electrons carry 9.2 and the ions 9.4 kW/m, and $v_x = 0$. In front of the limiter $\overline{EF}$ a thin collision free space charge sheath with a Langmuir potential drop $\Delta\Phi$ accelerates the ions and repels the electrons. The fluxes entering the sheath edge must be continuous and ensure a monotonous $\vec{E}$. We refer to /2/ and take Bohm's criterion with

$v_x = 1.0\ c_s = \sqrt{(T_e+T_i)/m_i}$, and the energy fluxes (convected + conducted) $Q_{ex} = 5.5\ T_e n u_x$, $Q_{ix} = 3.5\ T_i n v_x$. We have symmetry conditions at $\overline{AC}$ and $\overline{DE}$, low n and floating T_e, T_i at the wall $\overline{CF}$. η, $\chi_e^{\parallel}$, $\chi_i^{\parallel}$ are classical, but radial transport is anomalous: $D^{\perp} = 0.6\ m^2/sec$, $\chi_e^{\perp} = \chi_i^{\perp} = nD^{\perp}$.

The variables Φ, v_z, Ψ, j_x, j_y are computed by fast convergent iteration. At the limiter

$$e\Phi = e\Delta\Phi = -T_e\,\ln[\sqrt{2\pi m_e(1+T_i/T_e)/m_i}\,(1-j_x/enc_s)] \qquad (8)$$

Then Φ in the s.o.l. follows by integrating the x-component of (3): $e\partial\Phi/\partial x = \partial p_e/n\partial x + 0.71\,\partial T_e/\partial x$. Since $e\Phi \sim 3T_e$, considerable radial fields $-\partial\Phi/\partial y$ build up in the limiter shadow. The combined $\vec{E}\times\vec{B}$-drift and ∇p_i-drift enforce plasma rotation in (4). Assuming an exponential decrease of v_z along $\overline{BA}$ (core plasma at rest) defines $\Phi(x,y)$ and $v_z(x,y)$ everywhere. With $\Psi = 0$ at $\overline{AC}$ integrating (5) yields $\Psi(x,y)$, thus producing an iterated value j_x in (8), and so on.

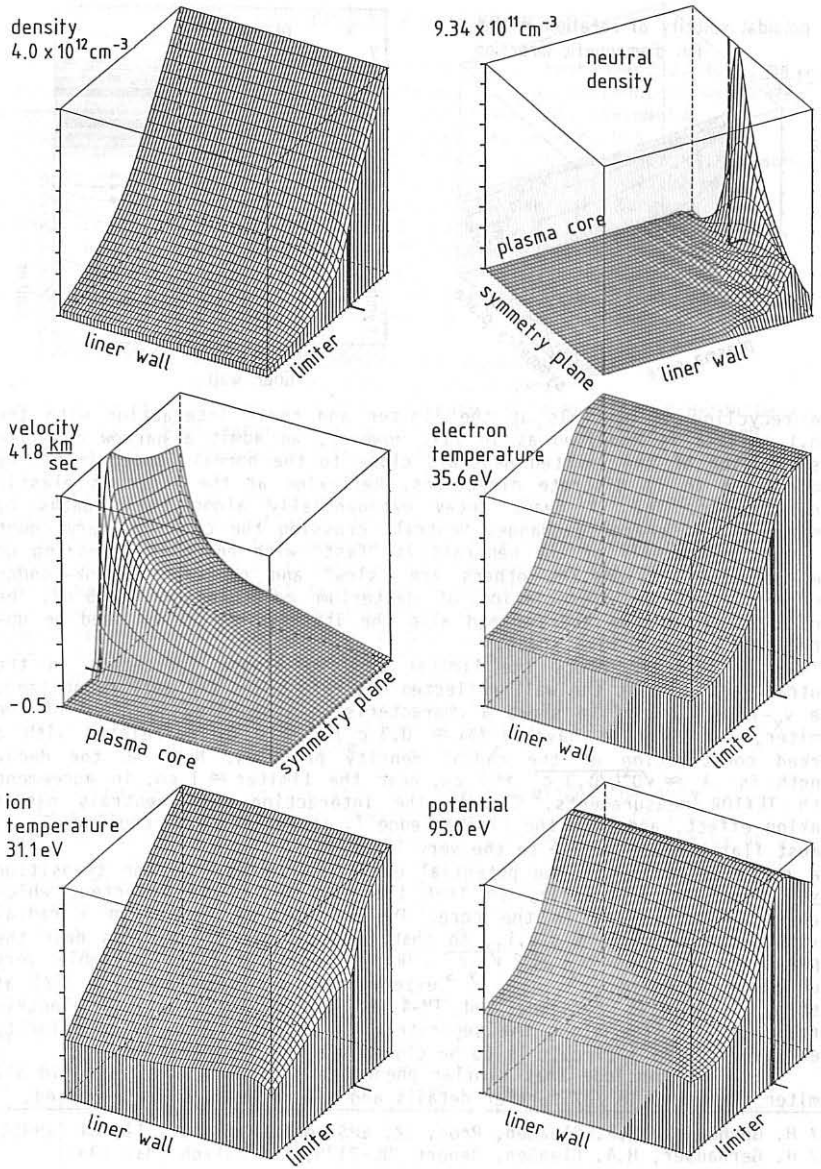
density
4.0 x 10^12 cm^-3
liner wall
limiter
9.34 x 10^11 cm^-3
neutral
density
plasma core
symmetry plane
liner wall
velocity
41.8 km/sec
-0.5
plasma core
symmetry plane
electron
temperature
35.6 eV
liner wall
limiter
ion
temperature
31.1 eV
liner wall
limiter
potential
95.0 eV
liner wall
limiter

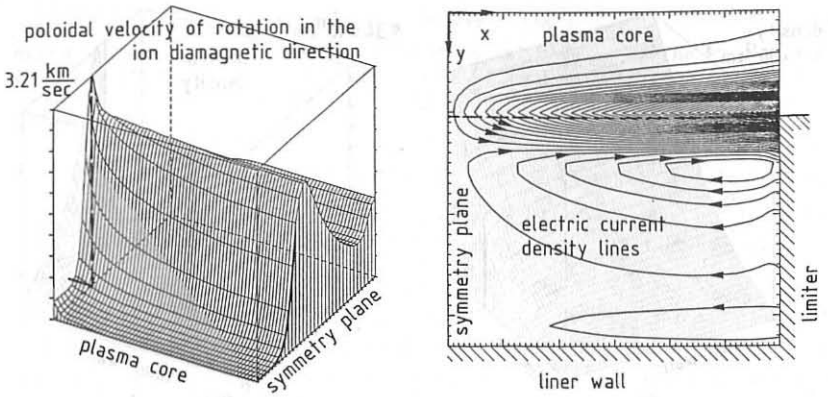

The recycling of neutrals at the limiter and their interaction with the s.o.l. plasma is modelled as in /1/. However, we admit a narrow cos-like distribution of the emitted neutrals close to the normal, approximated by propagation in 11 discrete directions. Reflexion at the liner is elastic and specular. The 11 beams decay exponentially along their paths by ionization and charge exchange. Neutrals crossing the core boundary count as lost. About half of the neutrals is "fast" with energies depending on the impinging D^+-ions. The others are "slow" and represent Frank-Condon neutrals from the dissociation of deuterium molecules with $\lesssim 5$ eV. The neutral density, the sources and also the iterated variables need be updated only every 20 time steps.

In the 8 computer plots the limiter edge is always indicated. In the neutral density plot the wall reflected discrete beams are well recognized. The v_x-velocity profile shows a characteristic steepening in front of the limiter, far away we have $\partial v_x/\partial x \approx 0.3\, c_s/L$. This is correlated with a marked constriction of the radial density profiles. Near $\overline{AC}$ the decay length is $\lambda \approx \sqrt{D^{\perp} L/0.3\, c_s} \approx 2$ cm, near the limiter ≈ 1 cm, in agreement with TEXTOR measurements.[s] Clearly the interaction with neutrals has a braking effect, and near the limiter edge T_i is depressed by cooling. T_e is almost flat toroidally due to the very large $\chi_e^{\parallel}$.

The radial profiles of the potential exhibit a maximum in the transition layer near the separatrix, so that the sign of E_r is inverted, which enables zero rotation in the core. The v_z-profiles show also a radial maximum, but inside the s.o.l., so that the steepest increase is near the separatrix. We find $|v_z| \lesssim 2\sqrt{v_y c_s}$. Our Φ- and v_z-profiles resemble very much those observed experimentally in the tokamaks TEXT at Austin, Caltech at Pasadena and TM-4 at Moscow. An elongated electric current vortex flow along the separatrix is caused by the large velocity shear $\partial v_z/\partial y$. The $\vec{j}$-circuit is to be closed via the limiter edge.

We conclude that similar phenomena should be observable in all limiter tokamaks. In /2/ further details and all references are reported.

/1/ H. Gerhauser, H.A. Claaßen, Proc. 12. EPS conf. Budapest, II,464 (1985)
/2/ H. Gerhauser, H.A. Claaßen, Report JÜL-2125, KFA Jülich (Mai 1987)

PLASMA EDGE EFFECTS WITH ICRF IN ASDEX

J.-M. Noterdaeme, G. Janeschitz, K. McCormick, J. Neuhauser, J. Roth, F. Ryter, E. Taglauer, N. Tsois, M. Brambilla, A.W. Carlson, F.Fussmann, G. Haas, F. Hofmeister, V. Mertens, C. Setzensack, K. Steinmetz, F. Wagner, F. Wesner, J. Bäumler, G. Becker, W. Becker, H.S. Bosch, F. Braun, H. Brocken, A. Eberhagen, G. Dodel[1], H.-U. Fahrbach, R.Fritsch, O. Gehre, J. Gernhardt, G. v.Gierke, E. Glock, O. Gruber, W. Herrmann, J. Hofman, A.Izvozchikov[2], E. Holzhauer, K. Hübner[3], F. Karger, M. Kaufmann, O. Klüber, M. Kornherr, K. Lackner, M. Lenoci, G. Lisitano, F. Mast, H.M. Mayer, D. Meisel, E.R. Müller, H. Murmann, H. Niedermeyer, A. Pietrzyk[4], W. Poschenrieder, S. Puri, H. Rapp, H. Riedler[6], A.Rudyj, F. Schneider, G. Siller, E. Speth, F. Söldner, A. Stäbler, G.Staudenmaier, K.-H. Steuer, S. Ugniewski[5], H. Verbeek, O. Vollmer, H. Wedler, D.Zasche

Max-Planck-Institut für Plasmaphysik
EURATOM Association, D-8046 Garching
[1] University of Stuttgart, [2] Ioffe Institute, [3] University of Heidelberg, [4] University of Washington, Seattle, USA, [5] Inst.for Nuclear Research, Swierk, Poland, [6] Schiedel-Stiftung, Austria

Introduction: The boundary plasma plays a major role in the understanding of the multiple aspects of an RF heated plasma: the coupling of RF waves, the impurity content of the plasma, or even its overall confinement properties. The difficulty to measure the boundary plasma especially with RF is compounded by the fact that machine specific aspects have a much larger impact on the plasma boundary than at the plasma center. Systematic tendencies are however recognized. In the following we give an overview of plasma boundary data (n_e,Te electric fields in the scrape off layer) and report on Fe flux measurements in the divertor and on evidence of a local impurity production mechanism. We then propose an explanation for the enhanced impurity content of the plasma during ICRF, which is also consistent with earlier measurements /1,2,3/.

Boundary density evolution: In standard ICRH discharges the density evolution, measured with the Li beam diagnostic /4/ is as follows: As the separatrix is moved outwards, due to β_p effects, the density at a fixed radial position increases (Fig. 1a). Normalised to the position of the separatrix, however, the density there is constant (Fig. 1b) with at low plasma current a small increase of the gradient length (Fig. 1c). The density at the antenna limiter stays constant. This results in a steepening of the density gradient close to the antenna.

Edge temperature evolution: In the last experimental period the Langmuir probes in the main chamber were disturbed by the ICRF and the edge laser scattering system did not cover in the case of ICRF the separatrix region (the plasma is shifted outward for a good antenna coupling). There is, however, substantial experience (incl. numerical simulation) from ohmic and neutral injection heated discharges with an unshifted plasma where all diagnostics are working. Taking the divertor data (density,

line intensities and the absolute X-ray signals can be converted into absolute Fe fluxes (Fig. 3a). In the case of NBI, the measured fluxes in the divertor, as well as the fluxes calculated by the code are in good agreement with those calculated /9,10/ from CX sputtering using data from the neutral particle diagnostics. In the case of ICRH, however, the fluxes calculated from the Fe XVI intensity are much higher than those measured by the divertor probe or calculated from CX sputtering. One has either to assume that the Fe flux measurements in the divertor were not representative of the fluxes in the main chamber or that the scrape off transport model in the code is incomplete in the case of ICRF heating.

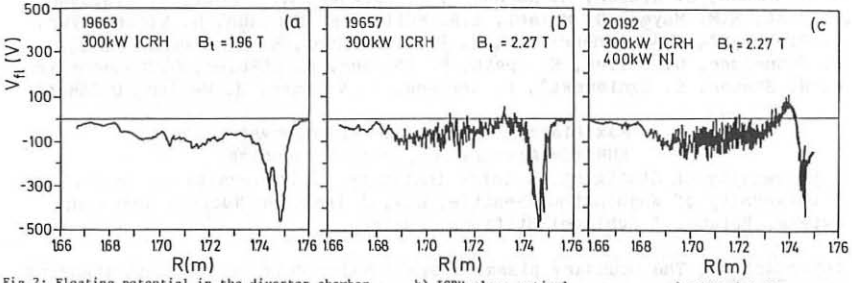

Fig.2: Floating potential in the divertor chamber
a) ICRH alone, non optimal position of resonance layer
b) ICRH alone, optimal position of the resonance layer
c) ICRH with NI

Evidence of local impurity production: There are several indications for localised impurity sources in the main chamber during ICRH. The development of the Fe XVI line intensity over a dozen of shots after wall carbonisation is shown in Fig. 4. The values for OH and ICRH were normalized at shot 18782. The faster shot to shot increase during ICRH, relative to the OH part of the pulse can only be explained by a strong local erosion due to the RF. Surface analysis of the carbon protection limiters of the antenna indicate the presence of a local Fe source /11/. A similar conclusion was reached by the JFT-2M group /12/, when they protected the antenna neighbourhood with graphite. The divertor probe could underestimate the amount of Fe originating from such local spots because much may be locally redeposited.

Discussion: In view of the now accumulated data we can propose an hypothesis for the increased impurity content in the plasma during ICRH. Earlier explanations, based mainly on the anticorrelation of wave absorption and the impurity content in the plasma /1,2,/ have emphasized increased impurity production with, however, the mechanism still to be identified. More recently, in view of the Fe measurements in the divertor, an increased penetration of neutrals through the scrape-off layer was put forward as an hypothesis/13/. Model calculations, however, show that this would require a major reduction of the boundary temperature which was not substantiated in normal discharges.
Consistent with earlier measurements and with both the measured Fe flux in the divertor, and the boundary parameters during RF, the higher impurity concentrations can be related to two effects: 1) a changed

temperature, CIII, bolometer etc.) and the main chamber edge density during ICRH, it is quite obvious that the power input into the divertor and hence the midplane temperature are substantially increased in normal ICRH discharges. This is in agreement with observations on JET and TEXTOR. RF theory /5/ also predicts that a few per cent of the power can be deposited in the boundary through collisional absorption on the electrons (the mechanism being that the electrons take up energy with their $\vec{E}$ x B drift and thermalize it if $\nu_{ei} >> \nu_{ICRH}$, cold electrons with large ν_{ei} are preferentially heated). Close to the separatrix this is a small fraction compared to the large power outflux from the main plasma. It can, however, strongly influence the temperature and potential in the low energy scrape off layer wing.

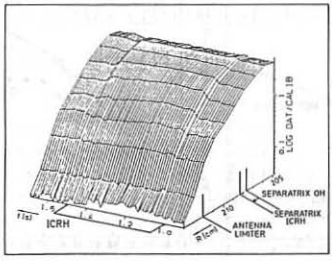

Fig.1a: Density evolution at the boundary

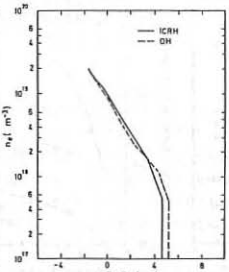

Fig.1b: Normalized to the position of the separatrix

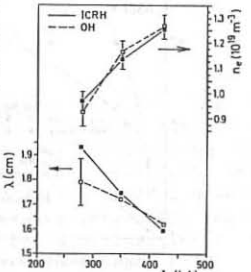

Fig.1c: Dependence of separatrix density and decay length at the separatrix with plasma current

Floating potential measurement in the divertor: In fact, a substantial influence is observed e.g. in the floating potential in the divertor /6/. During ICRH, a strong negative peak is observed in the outer scrape-off layer wing just inside the last flux surface entering the divertor (which is also the surface directly in front of the antenna). This may be connected with the spurious edge heating mentioned above. The detailed structure of the floating potential profile depends on the heating scenario (OH, $2\omega_c$, minority, addition of NI) and on the position of the resonance layer. There are indications that there is a correlation between enhanced impurity content of the plasma and the observed radial potential pattern: Figures 2 a,b,c show how this profile changes as one goes from a case (a) resulting in a large to a case (c) resulting in a much reduced impurity content of the plasma. Note the appearance of an intermediate region with a radially inward electric field. Those radial electric fields will affect the transport in the scrape off layer, the exact mechanism, however, remains unclear.

Measurements of Fe fluxes: A divertor collector probe was used to measure the Fe fluxes in front of the divertor target plate /7/. Assuming toroidal and poloidal symmetry, those fluxes can be related to the Fe fluxes originating from the main chamber walls (Fig. 3a). Spectroscopic measurements of the Fe XVI line intensity, as a function of power, are shown in Fig. 3b. Using an impurity transport code /8/, which neglect electric fields in the scrape-off, the absolute Fe XVII

transport in the SOL, because of radial electric fields at the edge, originating from a changed plasma potential, and 2) a strongly localised Fe source due to strong electric fields in the vicinity of the antenna. The anticorrelation between absorption and impurity production, seen for example in B_t scans /2/ and in the beneficial effect of NI can be explained as follows. Bad absorption would result in a strong local standing wave near the antenna /5/, which increases the impurity production directly in this region, and in larger RF fields at the plasma edge /14/, which, through acceleration of particles there, could change the plasma potential and thus the transport in the scrape off. In addition to changing the wave absorption, NI may also change the electric fields at the edge directly by the induced plasma rotation.

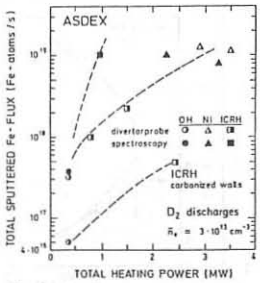

Fig.3a: Fe fluxes as calculated from the divertor probe and from the Fe intensity lines

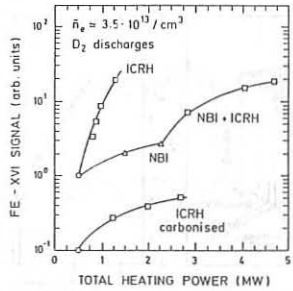

Fig.3b: Measured Fe XVI intensities

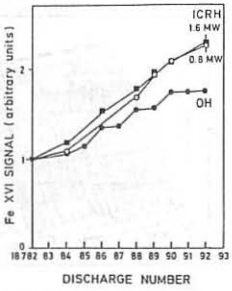

Fig.4: Normalized evolution of the Fe XVI signal

Summary: The evolution of n_e and T_e at the plasma boundary during the RF, together with measurements of the floating potential in the divertor, and the analysis of Fe collector probes in the divertor and of the antenna limiter indicate that the enhanced impurity concentration in a ICRF heated plasma is due to a combination of changed transport in the scrape-off layer because of electric fields, and an increased local production of impurities, related to large electric fields in the direct antenna neighbourhood.

References

/1/ G. Fussmann et al., Europhys.Conf.Abstr. (1985) Vol. 9F, I, 195
/2/ G. Janeschitz et al., Europhys.Conf.Abstr.(1986) Vol.10C,I, 407
/3/ C. Setzensack, IPP Report III Feb. 1987
/4/ K. McCormick, J.Nucl.Mat. 121 (1984) 48
/5/ M. Brambilla et al., this conference, and private communication
/6/ N. Tsois et al., this conference
/7/ E. Taglauer, J.Nucl.Mat. 128-129 (1984) 141
/8/ G. Fussmann, Nucl. Fus. 26 (1986) 983
/9/ H. Verbeek et al., as /1/, Vol. 9F, II, 583
/10/ G. Staudenmaier, J.Nucl.Mat. 145-147 (1987) 539
/11/ R. Behrisch et al., this conference
/12/ H. Tamai et al., JAERI-M 86-143, Tokai,Sept. 1986
/13/ J. Roth, IPP Jahresbericht 1986
/14/ R. Van Nieuwenhove et al., this conference

EXPERIMENTAL AND SIMULATED IMPURITY LINE RADIANCES DURING ECR HEATING AND PELLET INJECTION ON TFR

Equipe TFR and FOM ECRH Team* presented by B. Saoutic

Association EURATOM-CEA sur la Fusion Controlée
Centre d'Etudes Nucléaires de Cadarache
13108 Saint Paul Lez Durance CEDEX, FRANCE

* EURATOM-FOM Association on Fusion
Rijnhuizen, Nieuwegein, THE NETHERLANDS

1 ELECTRON CYCLOTRON RESONANCE HEATING:

1.1 Introduction:

Electron cyclotron resonance heating (ECRH) experiments on the TFR Tokamak have been previously described [1]. There, like in most of the papers published on ECRH experiments, impurity behaviour studies have been rather neglected, probably as a consequence of the relatively small increment of radiated power (measured by bolometry) during ECRH. However, on T-10, increased central iron densities have been observed [2] and the initial variation of the central radiated power during experiments at low n_e values was attributed to an increased impurity transport rate [3].

In this section, after a brief description of the plasma parameters and of the methodology used for simulations, we shall report the results of detailed comparisons between experiments and simulations for central heating of plasmas with two different n_e values. The contribution of impurities to energy balance (radiated power) and to effective charge Z_{eff} will be evaluated.

1.2 Plasma parameters:

The typical plasmas used for ECRH experiments had the following parameters: working gas hydrogen, plasma current 100 kA, toroidal field 2.14 T, graphite limiter radius 18 cm, central electron density $n_e(0)=1\text{-}3.5\ 10^{13}\ cm^{-3}$, central electron température $T_e(0)=850\text{-}1000$ eV, central ion température $T_i(0)=300\text{-}500$ eV.

In these heating experiments three 200 kW gyrotrons were used. They were successively switched on at 25 ms interval in such a way that the maximum power (500-550 kW) was applied to the plasma 50 ms after switching on the first gyrotron.

Due to the presence of a stainless steel calorimeter in the limiter shadow, the hardware conditions for these experiments were sensibly different from the ones described in [1]: as a consequence, the iron density in the plasma was larger and very sensible to horizontal displacements.

1.3 Simulation procedure:

The impurity transport simulation code has been previously discussed [4].The code considers independently the transport of any one atomic species and gives in cylindrical geometry the density of all charged ions as function of time and radius;line radiances (data available from experiments) are also calculated.

As discussed in [4], the code uses "ad-hoc" boundary conditions: the incoming neutral atom flux Γ_0 at the limiter radius is chosen, as a function of time, in such way that the absolute radiance of a non-central ion line (Fe XVI 335.4Å in the considered experiments) is correctly simulated.

Once this is done, the subsequent step is to adjust a diffusion coefficient D_A and an inward convection velocity V_A in such a way that the temporal behaviour of the radiances of central ions(Fe XIX 108.3Å, FeXX 121.8Å, Fe XXIII (blended with Fe XX) 132.9Å) is correctly simulated. It has to be pointed out that the uncertainty on the determination of the absolute value of the transport parameters with such a method is 50% for D_A and 100% for V_A. However, the uncertainty on possible variations of the transport parameters during ECRH is somewhat lower.

ECRH heating is simulated in the following way: the n_e and T_e profiles, measured (by interferometry and Thomson scattering) during the ohmic phase, give the steady state solution which is used as the starting point for the simulation. The n_e and T_e profiles resulting from one, two and three gyrotron heating are successively introduced during 25 ms each.

1.4 Comparison between experiments and simulations:

Figure 1 shows the comparison between experimental line radiances (left) and simulated ones (right) in the case of larger n_e ($3.5\ 10^{13}$ cm^{-3}).The best agreement is obtained when starting with D_A = 4000 cm^2/s and V_A = 600 cm/s during the ohmic phase and keeping constant these values for the ECRH phase (solid lines).The dashed lines show the result of a simulation where D_A and V_A are increased to 8000 cm^2/s and 1200 cm^2/s during the heating: the discrepancy with the experimental radiance of Fe XXIII confirms that the transport parameters can be considered as constant within the stated uncertainty.

Figure 2 deals with the case of lower n_e ($2\ 10^{13}$ cm^{-3}).In this case, keeping D_A and V_A constant to 6000 cm^2/s and 600 cm/s during the ohmic and heating phases (solid lines), clearly does not agree with the experimental measurements. Indeed, the best agreement is obtained when increasing D_A and V_A to 12000 cm^2/s and 1200 cm/s during one gyrotron heating and then to 18000 cm^2/s and 1800 cm/s during two and three gyrotron heating (dashed lines).This increase of the transport parameters is well above the uncertainty of their determination. It is therefore posible to conclude that, in the lower density case, the impurity confinement time decreases.

In both cases the incoming neutral atom flux Γ_0 has to be multiplied by a factor of 1.5-2 during the heating phase in order to correctly simulate the experimental radiance of Fe XVI.

1.5 Conclusion:

By applying the results of the simulations mentioned above to the main plasma impurities (O,C,Fe,Cr,Ni), it is possible to evaluate the radiated power and the effective charge Z_{eff}. In both cases, radiation losses do not vary outside the uncertainty during ECRH.

Larger density case: Pr=65 kW Z_{eff}=2.4 (Ω) Z_{eff}=3.1 (ECRH)
Lower density case: Pr=50 kW Z_{eff}=3.2 (Ω) Z_{eff}=3.0 (ECRH)

2 PELLET INJECTION:

Single pellet injection (PI) experiments on TFR have been previously reported [5]. Very few of the papers dealing with PI are concerned with impurity studies. However it was noticed on PDX [6], that the X-ray enhancement factor and Z_{eff} (measured from visible bremsstrahlung) were reduced much more that expected by simple dilution.It should also be recalled that centrally peaked impurity profiles occuring after PI were observed on Alcator C [7].

For these PI studies, the target plasma had the following parameters: working gas hydrogen, plasma current 200 kA, toroidal field 4.3 T, graphite limiter radius 18 cm, $n_e(0)=8\ 10^{13}\ cm^{-3}$, $T_e(0)=1.4$ keV.

The procedure used for the simulations is similar to the one described above. Figure 3 shows that the best simulation (solid line) is obtained when D_A and V_A are kept constant to 8000 cm^2/s and 1200 cm/s before and after PI. A simulation with constant D_A and V_A at 4000 cm^2/s and 600 cm/s (dashed line) shows that the evolution of the Fe XVI radiance is much too slow.

It must also be pointed out that six lines corresponding to six consecutive ionization degrees of iron (Fe XVIII to Fe XXIII) have been simultaneously obseved.Their evolution (increase of Fe XVIII,XIX and decrease of Fe XXII,XXIII with Fe XX,XXI staying roughly constant) can be satisfactorily simulated by the combined effect of plasma cooling, sudden variation (followed by slower evolution) of n_e and modification of the peripheral neutral flux.No modifications of the transport parameters are needed,but Γ_0 must be decreased by a factor of three following PI.This fact is quite consistent with the expected effect of the decreased temperature of the plasma on the sputtering rate.

Finally, the larger peripheral light impurity (C,O) radiances observed after PI were satisfactorily simulated by using the same transport parameters as above and increasing Γ_0 by a factor of 1.5. This increase of the input flux is probably due to a larger desorption occuring because of the increased density.

[1] De Esch H.P.L. et al,Proc. XIth Int. Conf. Plasma Phys. Contr. Fus. Res.,Kyoto 1986,Paper IAEA-CN-47/F-III-4
[2] Alikaev V.V. et al,Sov. J. Plasma Phys. 9 196 (1983)
[3] Abramov V.A. et al,Sov. J. Plasma Phys. 10 120 (1984)
[4] TFR Group,Nuclear Fusion 23 559 (1983)
[5] Equipe TFR,Euratom CEA Assoc.,Int. Rep. 1321,sub. to Nucl. Fus. (1987)
[6] Fonck R.J. et al,J. Nucl. Mater. 128&129 330 (1984)
[7] Petrasso M.D. et al,Phys. Rev. Lett. 57 707 (1986)

FIGURE 1

Experimental and simulated radiances
10^{15} ph/cm^2 s sr for Fe XVI
Arbitrary units otherwise

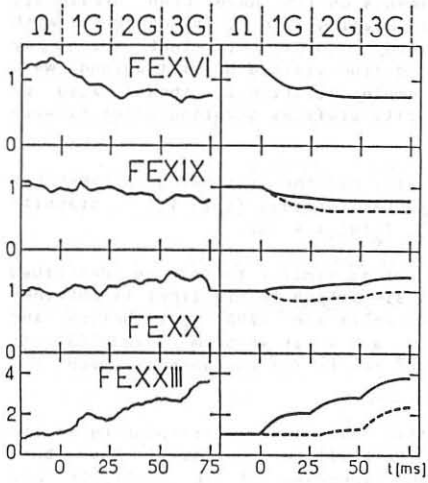

FIGURE 2

Experimental and simulated radiances
10^{14} ph/cm^2 s sr for Fe XVI
Arbitrary units otherwise

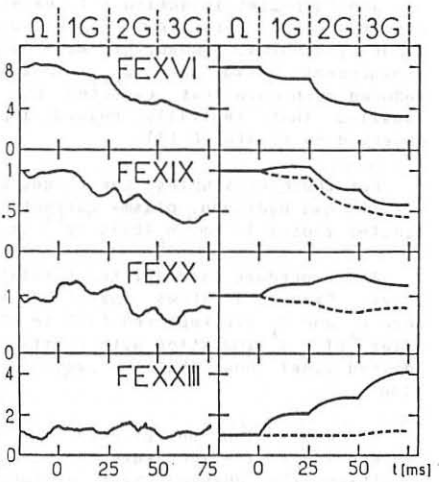

FIGURE 3

Experimental and simulated radiances
10^{15} ph/cm^2 s sr for Fe XVI;5 10^{14} ph/cm^2 s sr for Fe XXIII

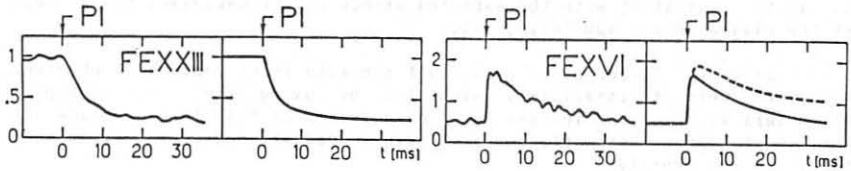

NON-LOCAL TRANSPORT IN THE SCRAPE-OFF PLASMA IN TOKAMAK

Igitkhanov Yu.L., Yushmanov P.N.
I.V.Kurchatov Institute of Atomic Energy, Moscow, USSR

ABSTRACT

The longitudinal heat and momentum transport of plasma particles from the main tokamak zone to the divertor or limiter plates is described within the frames of hydrodynamic equations with the classical coefficient of longitudinal heat conduction and viscosity [1] Even when the hydrodynamic approximation are satisfied on average, i.e. when the mean free path is much less than the characteristic longitudinal gradients, the expressions for classical heat conduction and viscosity coefficients turn out to be overestimated. This results in lower plasma temperatures and in greater densities at the separatrix than the experimental values [2] . This is due to the fact that the hydrodynamic heat and momentum flows are determined by the tails to the distribution function and become essentially non-local by nature. In this report the 20-moment Grad method, where, in difference from a traditional procedure, the derivatives of higher order moments are left is used to determine the transport structure. Such an approach allows to reduce the set of differential equations for the moments to one equation of higher order, from which the integral expressions for the longitudinal heat and momentum transport can be derived. For a thermal flux one gets

$$q(z) = \int dz' q_{SH}(z') G_q(z,z') \qquad (1)$$

where $q_{SH}(z')$ is the classical Spitzer-Härma heat conduction flux, G_q is the describing the non-local nature of heat transfer. The structure similar to (1) was postulated previously in [3] and can be naturally derived from the distribution function expansion.

REFERENCES

1. Yu.L.Igitkhanov, A.S.Kukushkin, A.Yu.Pigarov, V.I.Pistunovich Doklady Akademii Nauk SSSR, v.278, 1984, Issue 2, p.388.
2. Yu.L.Igitkhanov, et al. in 12th Europ.Conf.onContr.Fus. and Plasma Physics, Budapest, 2-3 Sept., 1985, part II, p.48.
3. J.F.Luciani, P.Mora, J.Virmont, Phys.Rev.Lett.v.51, 18, 1983.

MAGNETIC ISLAND EFFECT ON TOKAMAK EDGE PLASMA

Tokar' M.Z.

Institute for High Temperatures of the USSR
Academy of Sciences, Moscow, USSR

Abstract. The effect of the magnetic islands in configuration with EML on the edge tokamak plasma parameters is studied on the base of equations of single fluid hydrodynamics with taking into account the particle and heat flow along the magnetic field. The theoretical results are in good agreement with TEXT experimental results.

Introduction. The concept of Ergodic Magnetic Limiter (EML) /1/ is one of the interesting approaches to the problem of control of the tokamak edge plasma parameters. It's based on the theoretical notions that the plasma transport coefficients must increase with superposition of periodical perturbation on the tokamak magnetic field /2/ : overlapping of the magnetic islands created by the different harmonics of the perturbation results in the magnetic field lines stohastization. The heat and plasma particle flows along the ergodized lines of forces increase the transport across the unperturbed magnetic surfaces. As it's shown in Ref. /3/ the increase of transversal diffusivity up to Bohm level will reduce the temperature of the plasma being in contact with a tokamak-reactor wall lower than the threshold of the sputtering of such materials as molybdenum, stainless steel. The increase of the electron transversal heat conduction permits to realize the plasma configuration with so called expanded radiative boundary /4/ , where the substantial part of power transported from the tokamak core is radiated by light impurities on the first wall. In the stohastic region the enhanced consentration of impurities may be sustained due to their friction with the main ions flowing to the periphery along the magnetic field lines.
The experimental researches on TEXT device have shown /5/ that EML is actually the effective instrument for the effect on the edge plasma: recycling increases, the electron temperature drops and becomes more flatter with magnetic field perturbation. At the same time it has been shown that the substantial increase of the transversal transport coefficients may be attained at relatively low perturbations when the islands are not overlaped and the stohasticity is absent. In the present report the model for the description of the heat and plasma particles transport into the isolated chains of the magnetic islands without stohasticity is proposed. The effective coefficients of the plasma diffusion and heat conduction in configuration with the magnetic islands are obtained. The comparison of the theory results and TEXT experimental data is carried out.

Basic equations. When the tokamak magnetic field is perturbed with small disturbance $B_r = \ell \cdot B_r \cos(m\theta - k\varphi)$, where B_r is the toroidal component, $b \ll 1$, θ , φ are the poloidal

and toroidal angles, the system of the magnetic islands arises. Their axes are placed on the resonant surface with the safety factor $q_r = m/k$. Taking into account the spiral simmetry of the islands we introduce coordinates ξ, ℓ, where ξ numbers the magnetic surface and ℓ is the length of the magnetic field line from the point on the "top" of the surface O' - Fig. 1. The total length of the line between points O', O", L_0, is infinite at the island separatrixe with $\xi = \xi_m$. In the cylindrical approximation with small current density at the discharge edge where the islands are created $\xi_m = \sqrt{2 q_r \ell a R/m}$ (a,R are minor and major radii of the resonant surface). When $\xi \leq 0{,}8\,\xi_m$ L_0 depends on weakly: $L_0 = \pi/2 \cdot \xi_m/\ell$

The equation of the plasma motion along the magnetic field inside the islands has a form:

$$\frac{\partial}{\partial \ell}\left(m_i n V_\parallel^2 + 2nT\right) = \frac{\partial}{\partial \ell}\left(\frac{4}{3}\eta_\parallel \frac{\partial V_\parallel}{\partial \ell}\right) + \frac{1}{h_\xi}\frac{\partial}{\partial \xi}\left[\frac{1}{h_\xi}\left(\eta_\perp \frac{\partial V_\parallel}{\partial \xi} + m_i D_\perp \frac{\partial n}{\partial \xi} V_\parallel\right)\right] \quad (1)$$

where the density n, temperature T and longitudinal velocity $V_\parallel$ are assumed the same for ions and electrons, $\eta_{\parallel,\perp}$ are transversal and longitudinal coefficients of ion viscousity, h_ξ is Lame coefficient.

We consider the case of sufficiently small perturbations when the flow along the magnetic field lines inside the island results in additional transversal transport of heat and plasma particles not exceeded the anomalous heat conduction and diffusion with coefficients $\chi_\perp$ and $D_\perp$. In this case we seek a solution of Eq.(1) in the form $V_\parallel = V(\xi)\sin\pi\ell/L_0$ because $V_\parallel$ turns into zero at the point O', O", and for n, T dependences on ξ, ℓ we assume

$$n = n_0\left(1 + \frac{\xi}{\ell_n}\cos\frac{\pi\ell}{L_0}\right), \quad T = T_0\left(1 + \frac{\xi}{\ell_T}\cos\frac{\pi\ell}{L_0}\right)$$

where n_0, T_0 are the parameter values on the island axis and ℓ_n, ℓ_T are characteristic dimensions of their changes. The equation for $V(\xi)$ one may obtaine by integration of Eq.(2) over ℓ:

$$\frac{d^2V}{d\xi^2} = \left[\frac{4}{3}\frac{\eta_\parallel}{\eta_\perp}\frac{\pi^2}{L_0^2}V - \frac{2\pi n_0 T_0}{\eta_\perp L_0}\xi\left(\frac{1}{\ell_n} + \frac{1}{\ell_T}\right)\right]\langle h_\xi^2\rangle \quad (2)$$

where $\langle h_\xi^2\rangle = \int_0^{L_0} h_\xi^2\, d\ell/L_0 \simeq \pi^2/4$

Eq. (2) solution turning into zero at the island separatrixe and axis has a form:

$$V = V_0\left(\frac{\xi}{\xi_m} - \frac{sh\,\xi/\xi_0}{sh\,\xi_m/\xi_0}\right) \quad (3)$$

where

$$V_0 = \frac{\pi^3 n_0 T_0 \xi_m \xi_0^2}{4\eta_\perp L_0}\left(\frac{1}{\ell_n} + \frac{1}{\ell_T}\right), \quad \xi_0 = \frac{\pi\xi_m}{4\beta}, \quad \beta = \beta\sqrt{\frac{3\eta_\perp}{4\eta_\parallel}} \simeq \beta\omega_i\tau_i,$$

ω_i is ion Larmor frequency, τ_i is the time interval between ion collisions.

Let's average over θ and φ the equations of continuity and heat conduction for the plasma inside the islands:

$$\frac{1}{h_\xi}\frac{\partial}{\partial\xi}\left[\frac{1}{h_\xi}\left(-D_\perp\frac{\partial n}{\partial\xi}\right)\right]+\frac{\partial nV_\parallel}{\partial\ell}=S$$

$$\frac{1}{h_\xi}\frac{\partial}{\partial\xi}\left[\frac{1}{h_\xi}\left(-\varkappa_\perp\frac{\partial T}{\partial\xi}-5D_\perp\frac{\partial n}{\partial\xi}T\right)\right]+\frac{\partial}{\partial\ell}\left(5nV_\parallel T-\varkappa_\parallel\frac{\partial T}{\partial\ell}\right)=Q$$

where S is the particle source due to neutral ionization, Q is the energy losses.
As a result we obtaine the one-dimensional equations describing the plasma transport. At y = 0 they may be presented as follows:

$$\frac{d}{dy}\left(-D_n\frac{dn}{dy}-D_T\frac{n}{T}\frac{dT}{dy}\right)=S \qquad (4)$$

$$\frac{d}{dy}\left(-\varkappa_*\frac{dT}{dy}\right)=Q-5ST+5D_\perp\frac{dn}{dy}\frac{dT}{dy} \qquad (5)$$

Here we have neglected the turns of the order of $\frac{m\xi_m}{q}$, $D_n = D_\perp+\Delta D$, $D_T=\Delta D$, $\varkappa_*=\varkappa_\perp+\Delta\varkappa$, $\Delta D=0{,}53\frac{\xi_m^2}{\tau_i}\left(1-\frac{th\beta}{\beta}\right)$, $\Delta\varkappa=\frac{4}{3\pi}\beta^2\varkappa_\parallel$.
The additional turns in the transport coefficients averaged over island are

$$\overline{\Delta D}=0{,}35\frac{\xi_m^2}{\tau_i}\left(1+\frac{3}{4\beta^2}-\frac{3}{2\beta\,th2\beta}\right),\quad \overline{\Delta\varkappa}=\frac{8}{3\pi}\beta^2\varkappa_\parallel \qquad (6)$$

Results. It's interesting to compare Ex (6) with the plasma diffusivity D_{st} and heat conductivity $\varkappa_{st}$ in stohastic magnetic field obtained in paper /6/. Taking the width of stohasticity region and longitudinal length of perturbation correlations in Ref. /6/ are equal to the island width and the magnetic field line length, $2\xi_m$ and L_c, respectively, we obtaine $\overline{\Delta\varkappa}/\varkappa_{st}=\beta^4/3\pi\,\beta_c^2$, where $\beta_c^2=\Sigma\beta_{m,\kappa}$. To estimate β_c^2 we take into account that $\beta_{m,\kappa}$ are reduced exponentially on the resonant surface with m deviation from $m_\kappa=q_r\cdot k$. This $\overline{\Delta\varkappa}/\varkappa_{st}=1{,}25$. With small perturbations when $\beta\ll 1$ and the plasma flow velocity along the magnetic field is defined by the transversal viscousity $\overline{\Delta D}$ and D_{st} are also close one to another $\overline{\Delta D}/D_{st}\simeq 0{,}82$.

Thus inside the magnetic islands the additionals terms in the transport coefficients due to the heat and particle flow along the magnetic lines of forces are similar to those in the stohastic magnetic field.
The qualitative difference between $\overline{\Delta D}$ and D_{st} obtained in Ref. 6 takes place with $\beta\gtrsim 1$ when the flow velocity is defined by ion longitudinal viscousity: $\overline{\Delta D}\sim\beta^3$ with $\beta\ll 1$ and $\overline{\Delta D}\sim\beta$ when $\beta\gtrsim 1$. It's interesting to note that the condition $\beta\simeq 1$ is close to the boundary of applicability for D_{st} in Ref. /6/.
The modification of $\overline{\Delta D}$ dependence on the magnetic field perturbation amplitude has been observed in TEXT experiments with EML /5/. Fig. 2 represents the experimental and

computed dependences of the global particle time τ_p in TEXT device on the current in EML windings. According to the definition $\tau_p = \bar{n} a_L / 2 \Gamma_L$, where $\bar{n}$ is the averaged density in the tokamak, a_L is the radius of the magnetic surface touching the limiter, Γ_L is the particle flux into the scrape-off layer. As an estimate $\Gamma_L \sim D_n$, $\tau_p \sim D_n^{-1} \simeq 1/D_L \cdot (1 - \Delta D / D_L)$
The computation of the plasma parameters in the next-to wall region has been carried out on the base of Eq.(4), (5), with ΔD , $\Delta \chi$ given by Ex. (6). For conditions of Ref. /5/ $\beta = 1$ with $I_0 \simeq 1$ kA.
Experimental and theoretical results are in good qualitative and quantitave agreement and this fact is the evidence of adequacy of the proposed model for the describtion of plasma transport properties in configurations with magnetic islands

REFERENCES

1. Ohyabu N. e.a. J.Nucl.Mater. 1984, V. 121, p. 363.
2. Rechester A.B., Rosenbluth M.N. Phys.Rev.Lett. 1978, V.40, p.38.
3. Vasilyev N.N. e.a. in 8 Europ.Conf. on Contr. Fus. Plasma Phys., Prague, 1977, V.1, p.164.
4. Ohyabu N. Nucl.Fusion 1981, V.21, p.519.
5. Mc Cool S.C. e.a. J.Nucl.Mater 1986, V.145-146, p. 340.
6. Yamagishi T. e.a., J.Nucl.Mater. 1984, V.128-129, p.118.

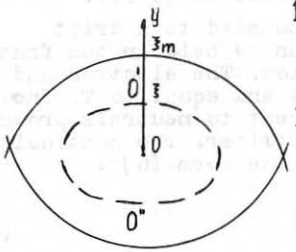

Fig. 1

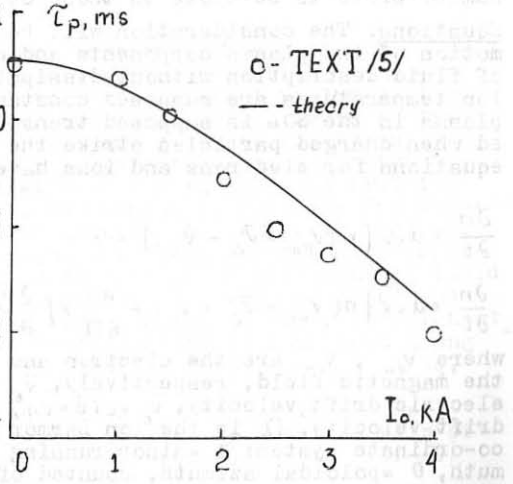

Fig. 2

PLASMA INSTABILITY IN THE SCRAPE OFF LAYER

V.G. Petrov

Institute for High Temperatures of the USSR
Academy of Sciences, Moscow, USSR

Abstract. Instability of the plasma flow in the poloidal limiter scrape off layer of a tokamak (SOL) is demonstrated in the frames of linear approach.

Introduction. Steady state plasma flow in the SOL has been considered in [1] . The primary cause of the flow is a toroidal drift of the ions and the electrons. The charge separation caused by the drift is compensated for by nonambipolarity of the plasma flux to the limiter. The electric current density to the limiter along with the Langmuir potential drop at the limiter proves to be a function of the poloidal azimuth. A poloidal electric field arises in the SOL and this leads to a radial plasma drift. It has been noted in [2] that plasma flutes stretched along the magnetic field in the SOL can be unstable relative to a displacement along the minor torus radius. In the present paper the plasma flow instability is investigated with boundary conditions for fluctuations, ion inertia and magnetic shear being taken into account. The real part of the oscillation frequency and the poloidal wave number prove to be close to those observed in [3-5] .

Equations. The consideration will be bounded to a drift motion of the plasma components and can be held in the frames of fluid description without dissipation. The electron and ion temperatures are supposed constant and equal to T. The plasma in the SOL is supposed transparent to neutrals produced when charged particles strike the limiter. The continuity equations for electrons and ions have the form [6] :

$$\frac{\partial n}{\partial t} + \mathrm{div}\left[n(v_{e\parallel} + \bar{v}_E - \bar{v}_L)\right] = 0 \qquad (1)$$

$$\frac{\partial n}{\partial t} + \mathrm{div}\left\{n(v_{i\parallel} + \bar{v}_E + \bar{v}_L) + \frac{n\vec{B}}{B\Omega} \times \left[\frac{\partial \bar{v}_E}{\partial t} + ((\bar{v}_E + \bar{v}_L)\cdot\nabla)\bar{v}_E\right]\right\} = 0 \qquad (2)$$

where $v_{e\parallel}$, $v_{i\parallel}$ are the electron and ion flow velocities along the magnetic field, respectively, $\bar{v}_E = c[\bar{B}\times\nabla\varphi]/B^2$ is the electric drift velocity, $\bar{v}_L = c[\bar{B}\times\nabla n]/eB^2 n$ is the ion Larmor drift velocity, Ω is the ion Larmor frequency. Introduce a co-ordinate system: r =minor running radius, ζ =toroidal azimuth, θ =poloidal azimuth, counted off from the outside torus circumference to the toroidal ion drift side. The limiter separates the magnetic field lines to helical sections which hit the lateral sides of the limiter. Each such section is fully defined by the minor running radius r and the poloidal azimuth α , which corresponds to the section point in the poloidal cross-section of the torus rotated through 180^0 in the toroidal direction with respect to the cross-section of the poloidal limiter. The field line section corresponding to

the azimuth α enters the limiter when $\theta = \alpha - (\pi/q)$ from the ion side and when $\theta = \alpha + (\pi/q)$ from the electron side. The boundary conditions on the lateral surface of the limiter (the limiter potential is equal to zero) are:

$$V_{e\parallel} = \sqrt{T/2\pi m_e}\, \exp(-e\varphi/T) \tag{3}$$

$$V_{i\parallel} = \sqrt{2T/M} \tag{4}$$

For the sake of simplicity we adopt n=const and φ =const along every magnetic field line section. We consider fluctuations streched along the magnetic field. Equations (1,2) are integrated along the field line sections with allowance for the boundary conditions (3,4) as has been done in [1], $a/R \ll 1$, $8\pi nT/B^2 < m_e/M$ are supposed (where a is the inner limiter radius, R is the major torus radius).
Thus equations for u=ln n and φ are obtained. We present $n = u_0 + u'$, $\varphi = \varphi_0 + \varphi'$ where u_0, φ_0 are the steady state solutions from [1] and u', φ' are the small perturbations. The equations are linearized in these perturbations and the perturbations themselves are presented in the form:

$$\begin{Bmatrix} u' \\ \varphi' \end{Bmatrix} = \begin{Bmatrix} u_1 \\ \varphi_1 \end{Bmatrix} \exp[-i\omega t + im\alpha - f(r-a)] \times \sin[g(r-a)], \quad r > a \tag{5}$$

$$u' = \varphi' = 0, \quad r < a$$

where u_1, φ_1 are the primary perturbation amplitudes, ω is the frequency, m is the poloidal wave number, g and f are the constants which determine a radial form of the perturbations corresponding to zero boundary conditions. With zero magnetic shear the quatities f and g can be sufficiently small. With nonzero shear a perturbation being stretched along the magnetic field at some $r = r_0$ deflects from the field direction at $r \neq r_0$. It happens so that the longitudinal wave number $k_\parallel$ becomes nonzero at $r \neq r_0$. If the wave number $k_\parallel$ reaches the meaning $1/R$ at some r than the longitudinal wave length reaches the length of the magnetic field line section in the SOL. With that the averages of u' and on each field line section become equal to zero. The highest possible radial length of perturbations is such that along it $k_\parallel$ changes from $-1/R$ till $1/R$. In this case $g = m/aq$, where $q = aB_\zeta/RB_\theta$
The dispersion equation is obtained from the linearized equations for the small perturbations (5) with the help of multiplying the equations by $\exp[-f(r-a)] \times \sin[g(r-a)]$ and integrating them from a to ∞.

Discussion of results. It follows from the dispersion equation that two physical mehanisms of the instability development take place. The first mehanism is connected with the ion inertia and manifests under large values of $\sqrt{g^2 + f^2}$, which are comparable to the inverse ion Larmor radius $1/\varrho = eB\sqrt{M/2T}/Mc$. When the plasma moovs radially in a disturbed radial electric field the ion density disturbes

due to the ion inertia with respect to the electron density. The charge accumulation and the amplification of the primary electric potential disturbance can take place. For the TOSCA parameters [5] the increment is 3×10^4 Hz and the real part of the frequency is 10^5 Hz.
The second mechanism of the instability proves to be of a flute tipe. If a plasma flute stretched along the magnetic field shifts radially the flute plasma density starts to differ from the adjacent regions. Due to the toroidal drift there appear charges on the lateral surfaces of the flute. Thus a poloidal electric field disturbance arises and the drift in this disturbed field can lead to the amplification of the initial flute displacement. The value of the disturbed electric field is determined by the flow of the disturbed charge to the limiter and also by the electric current which is transverse to the magnetic field and due to the ion inertia. The plasma is unstable on the outer contour of the torus that is natural for the flute instability. With the shear the maximum value of the increment is

$$\gamma = \frac{4}{3\tau}\left(q^{7/3}\sin\frac{\pi}{q}\right)(\pi^2+q^2)^{-2/3}\left[d\left(1+\frac{2\Lambda}{d}\sin\alpha\right)/\pi R\right]^{-1/3}\cos\alpha$$

where $\tau = \pi R\sqrt{M/2T}$, $\Lambda = Pq\sin(\pi/q)$, d is the radial scale length of change in the plasma density. The real part of the frequency $Re\,\omega = \gamma/2$. For the parameters [5] $Re\,\omega = 2\cdot10^5$ Hz and $mP/q = 0.2$ that is close to the experimental data. The increasing density perturbations shift poloidally to the side of the toroidal ion drift under the both instability mehanisms. A larger oscillation amplitude ought to be there. Such asymmetry is observed experimentally. The change in the plasma convection with the anomalous transport coefficients is considered in [7] .

References

1. Nedospasov A.V., Petrov V.G., Fidel'man G.N. Nucl.Fus. 1985, 25, 21.
2. Kolesnikov V.K., Nedospasov A.V. in Kinetic Theory of Microturbulence and Transfer in Edge Tokamak Plasma Workshop Proc., Moscow, 1986.
3. Zweben S.J., Gould R.W. Nucl.Fus., 1983, 23, 1625.
4. Levinson S.J., et al. Nucl.Fus., 1984, 24, 527.
5. Howling A., et al. XII Europ.Conf. on Contr.Fus. and Plasma Phys. Budapest 1985, pt 1, p.311.
6. Hinton F.L., Horton C.W. Phys.Fluids, 1971, 14, 116.
7. Nedospasov A.V., Petrov V.G. Nucl.Fus., 1986, 26, 1529.

EDGE DYNAMICS IN PELLET-FUELLED INNER-WALL JET DISCHARGES

S.A. Cohen*, J. Ehrenberg**, D.V. Bartlett, D.J. Campbell, A.D. Cheetham, L. de Kock, A. Gondhalekar, N. Gottardi, R. Granetz, W. Houlberg***, H. Jaeckel**, E. Lazzaro, P. Morgan, J. O'Rourke, M. Pick, M.F. Stamp, D.D.R. Summers, E. van der Goot, M. Watkins, and A. Weller**

JET Joint Undertaking, Abingdon, Oxon OX14 3EA, UK
* Visiting scientist, Plasma Physics Laboratory, Princeton University, Princeton, NJ, 08544, USA
** On attachment from Max-Planck-Institut fur Plasmaphysik, 8046 Garching bei Munchen, FRG
*** Oak Ridge National Laboratory, Oak Ridge, TN, 37831, USA

I. Introduction

Pellet fuelling has shown itself to be an effective means for obtaining low Z_{eff} peaked density profiles in ohmic plasmas [1]. Further uses of pellet fuelling may develop when tokamaks enter their DT burning phases. Then the above factors and the correct species mix become crucial for achieving the largest Q value. A necessary corollary for the success of sustained pellet fuelling is good hydrogen removal from the plasma edge. Methods to control the edge exhaust have included various wall conditioning techniques and special limiter or divertor configurations. For any of these approaches to be optimized, an understanding of the basic processes of hydrogen transport in the plasma and in the walls must be developed.

In this paper we report on the density behaviour in JET during pellet-fuelled inner-wall discharges without auxiliary heating. Certain discharges, characterized by minor disruptions at the q=2 surface, show a ten times more rapid decay of the plasma density than previously observed. We show that this is related to the combined effects of plasma and wall properties.

The time evolution of the plasma density is simulated by a 1-d plasma transport code which includes the effects of minor disruptions on both particle transport in the plasma and recycling behavior at the wall. As a starting point for the analysis we use transport coefficients from previous studies of the density profile evolution of neutral-beam and ICRF- heated JET outer-limiter discharges [2]. Several-fold changes in the particle transport and reflection coefficients during the minor disruptions are required to fit the present experiment. The detailed description of hydrogen transport in JET walls and limiters is in a companion paper [3].

II. Experiment

Deuterium pellets (4e21 atoms) were injected into deuterium discharges formed with JET in the inner-wall configuration [1]. The target plasmas had central electron densities and temperatures of 2e19 m^{-3} and 3 keV, respectively. Immediately after injection the plasma parameters were: B_ϕ =2.8T, I_ϕ =3.0-3.5 MA, R_0=3.00 m, a=1.15 m, b=1.61 m, $q_{cyl}(a)$=5.0, $T_e(0)$=1 keV, and $\langle n_e \rangle$=4-5e19 m^{-3}. The distance from the last closed flux surface to the outer limiter was 7 cm. The time evolution of the volume-average electron density (from a 5-chord IR interferometer array) and edge electron temperature (from 2-nd harmonic ECE) are shown in figure 1 for two discharges, 9226 and 9238, which had similar macroscopic plasma

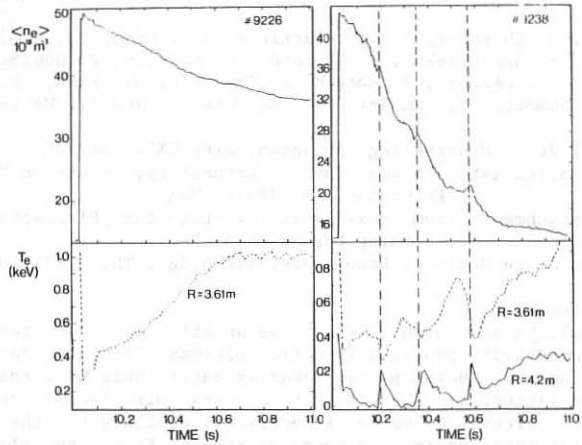

Fig. 1. Time evolution of the volume-average electron density, $<n_e>$, and the electron temperature at R=3.61 and 4.2 m for two discharges, 9226 and 9238. The latter was characterized by minor disruptions at the q=2 radius, R=3.85 m. The high edge temperature for 10.05>t>10.7 s is an artifact, known to be due to 2-nd harmonic overlap in ECE.

parameters. The first discharge is typical of those which did not have minor disruptions. The electron density decays smoothly with about a 2 s e-folding time. The electron temperature falls when the pellet is injected, and recovers slowly, in about 1 s.

In contrast, the density in discharge 9238 decays in a scallop-like manner, with an overall e-folding time of 0.25 s. As ascertained from both ECE and soft x-ray measurements, this discharge undergoes several minor disruptions (at t=10.195, 10.355, and 10.58 s) with phase inversion radii at R=3.85 m. This position is coincident with the location of the q=2 surface calculated from magnetics. The rapid decay of plasma density- at rates up to 3e21 atoms/s- occurs only if the disturbance from the disruption propagates to the inner-wall radius. Within 15 ms after the initiation of each disruption, the edge temperature has risen above 100 eV where it remains for about 50 ms. It is typical that a series of 3-4 such minor disruptions occurs following pellet injection into discharges of this type and that during each disruption $<n_e>$ falls about 0.7e19 m^{-3}. The electron density on axis falls about 15% during the first 15 ms after each disruption. Concurrent with the rise in $T_e(a)$ is a rise in $n_e(r>.8a)$, as shown in fig 2. However, the D-α emission from the inner wall decreases during the disruptive phase, indicating a decrease in deuterium reemission from the inner wall in spite of the expected increase in flux to the wall due to the increases in edge density and temperature.

Other mhd activity occurred in both types of discharges. Sawteeth preceded and followed pellet injection. "Snake" oscillations [4] were also present after the pellet but ended before the disruptions. No precursor

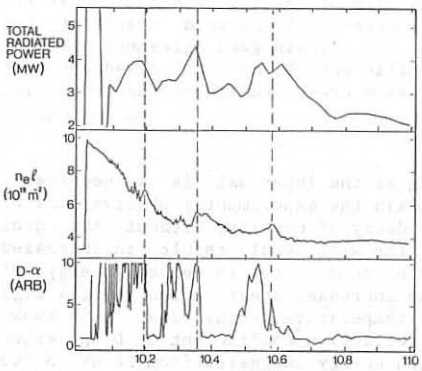

Fig. 2

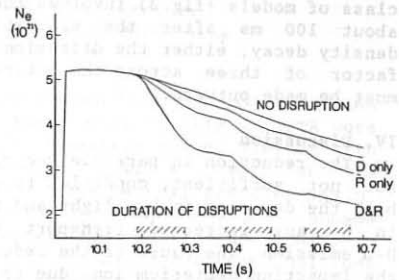

Fig. 3

Fig. 2. Line-integral electron density, $n_e l$, at R=3.75 m, D-α emission from the inner wall, and total radiated power for discharge 9238.
Fig. 3. Calculated time evolution of N_e for four cases: no disruptions; particle reflection,r, changed from 0.85 to 0.07 for 100 ms during the three disruptions; D changed a factor of 3 for 100 ms during the three disruptions ; and changing both r and D during the disruptions.

oscillations to the disruptions were observed, though minor sawteeth at q=1 immediately preceded many.

III. Modelling Plasma Behaviour

Previous studies of density evolution in JET showed the need for both diffusive and convective terms in the particle transport equation. The diffusion coefficient varied with radius from 0.3 m^2/s on axis to 1.0 m^2/s at the edge, and the convective term (inward) increased from 0 m/s on axis to 0.6 m/s at the edge. These combine to give a calculated global confinement time of about τ_p=0.35 s. The confinement of pellet-fuelled particles is 50% longer due to their (calculated) deposition near the plasma core. The apparent confinement time, $\tau_p^* = \tau_p/(1-R)$, due to the finite reycycling, R, is about 2 s, giving R=0.82. The observed rapid decay of density in the plasma core during the minor disruptions shows the need to increase the transport rate of particles out of the plasma. As noted earlier, the drop in D-α emission shows that the recycling (which includes direct particle reflection) drops. In all the models we have tried, agreement with the experiment is only obtained when R drops to $\leq$0.15.

We have considered two classes of models for particle transport by the disruptions. The first assumes an instantaneous rearrangement of the density. For this class we achieve reasonable agreement between the calculated and measured volume-average densities if either of two rearranged density profiles are used: a 15% drop on axis with those particles placed outside the q=2 surface; or a flattening of the density profile for $\pm$30 cm around the q=2 surface. However neither of these

satisfies the observed 15 ms decay time of density on axis. The second class of models (fig 3) involves the increase of outward transport for about 100 ms after the disruption. To obtain good agreement with the density decay, either the diffusion coefficient, D, must be raised about a factor of three across the entire plasma cross-section or the convection must be made outward.

IV. Discussion

The reduction in particle recycling at the inner wall is a necessary, but not sufficient, condition to explain the experimental observations of both the decrease in D-α light and the decay of density. Without the drop in R any increased transport to the wall would result in increased D-α emission. The cause of the reduced R could be the increased energy of the impacting deuterium ions due to the increased sheath potential ($\simeq 4.2T_e$) associated with the increased electron temperature at the edge. It is known from beam-solid studies [5] that the reflection coefficient of D on carbon does drop from about .7 to .1 as the ion energy increases from 20 eV to 500 eV. These energetic ions are then implanted about 10 nm into the carbon tiles of the inner wall. If the carbon there is sufficiently cool (T<400 C) the implanted deuterium will remain trapped until its concentration exceeds 0.1-0.4 of the carbon density. If the temperature of the carbon is slightly higher then it may serve as a temporary reservoir only [3], releasing the implanted deuterium at a rate determined by the diffusion of D in carbon.

Minor disruptions occur in JET in a variety of configurations including outer limiter discharges. In that case no drop in density is observed and the D-α emission is seen to rise. We speculate that the cause for this difference is the limiter temperature which is measured to be > 700 C. In contrast the temperature of the inner wall is < 350 C.

Theories of minor disruptions, under development [6], have magnetic reconnection only within the islands located at the q=2 surface. The islands are thought to be only a few cm in width. Hence these theories offer no explanation for the particle loss from the plasma core.

Discharges with minor disruptions do not have particularly good energy confinement. It thus does not appear desirable to provoke minor disruptions as a way to enhance pumping. However, the apparent connection between high sheath potentials and better wall pumping does suggest that edge plasma heating, or alternatively negative biasing of large area limiters, may provide a suitable solution, at least in the short term, to the problem of hydrogen exhaust at the plasma edge.

V. References

1. A. Gondhalekar, A. Cheetham, M. Bures, et al., Proc. 11-th Int. Conf. on Plasma Physics and Contr. Fusion, Kyoto, 1986.
2. A. Cheetham, J.P. Christiansen, S. Corti, et al., Proc. 13-th Eur. Conf. on Contr. Fusion and Plasma Physics, Schliersee, V.1, (1986) 420.
3. J. Ehrenberg, S.A. Cohen, L. de Kock, et al., this conference.
4. A. Weller, A.D. Cheetham, A.W. Edwards, et al., this conference.
5. G.M. McCracken and P.E. Stott, Nucl. Fusion 19 (1979) 889.
6. J. Wesson, private communication.

WALL PUMPING AND PARTICLE BALANCE IN TFTR

H.F. Dylla, D.B. Heifetz, M.A. Ulrickson, K.W. Hill,
P.H. LaMarche, A.T. Ramsey, B.C. Stratton
Plasma Physics Laboratory, Princeton University
Princeton, NJ 08544 USA

INTRODUCTION. Plasma pumping effects with carbon limiters have been seen in TFTR [1], JET [2], and TEXTOR [3]. The pumping effects in TFTR were induced by conditioning the large area axisymmetric bumper limiter with low density, helium initiated discharges. As a result of the conditioning, significant decreases in the edge neutral pressure and D_α emission have been observed. Analysis of the D_α emission data [1] showed the global particle recycling coefficient was reduced from near unity to values as low as 0.5 for ohmic plasmas. The low recycling conditions were not a permanent effect. A pumping capacity of ~ 100 torr liters (0.2 Pa m^3) for ohmic plasma has been determined by a wall loading experiment described below. A preliminary analysis of the capacity of the conditioned limiter to pump higher energy particles, such as the outflux from neutral beam fueled discharges, is presented here. The limiter pumping effect, with its commensurate reduction in recycling, is a prerequisite for the enhanced confinement neutral beam heated discharges observed in TFTR [4,5].

THE WALL LOADING EXPERIMENT. In order to quantify the gas loading of the limiter (and any contributed pumping by the wall) a previously conditioned torus was exposed to a sequence of identical, gas-fueled, ohmic discharges. The experiment consisted of a conditioning sequence of seven 1.4 MA He^{++} discharges, followed by eleven 0.8 MA D^+ fiducial discharges. These discharges were programmed to a density of $\bar{n}_e = 1.25 \times 10^{19} m^{-3}$ then the deuterium gas feed was turned off to allow the density to decay to the recycling limit.

The particle confinement time, τ_p, and global recycling coefficient R, were calculated by solving the global particle balance equation

$$\frac{dN^+(t)}{dt} = S + G - \frac{N^+(t)}{\tau_p} \quad , \qquad (1)$$

at time t. Here $N^+(t)$ is the total core ion population at time t, G is the measured gas fueling rate, S is the source in the core due to ionization of neutral particles, and τ_p is the average time that an ion stays in the core. Given N^+ and dN^+/dt, Eq. (1) can be solved for τ_p. Further, given the global density decay time, τ_p^*, when the external sources are zero, so that $dN^+(t)/dt = N^+/\tau_p^*$, the global recycling coefficient of deuterium, R, is determined from $R = 1 - \tau_p/\tau_p^*$.

The total density can be expressed as $N^+ = f_{D+} \langle n_e \rangle V_{pl}$ where f_{D+} is the average ratio of the deuterium density to the electron density determined from spectroscopic data, $\langle n_e \rangle$ is the volume average electron density, and V_{pl} is the plasma volume. Assuming a parabolic density profile, then $\langle n_e \rangle$ is 0.75 times the measured line-averaged electron density. During the entire sequence $f_{D+} = 0.85$ and $\bar{n}_e = 1.25 \times 10^{19} m^{-3}$, so that $N^+ = 2.35 \times 10^{20}$. The density decay rate, $dN^+(t)/dt$, was calculated using this value of N^+ and the measured values of τ_p^* during the gas loading sequence (Fig. 1).

The remaining term in Eq. (1), the ion recycling source S, was

calculated from D_α measurements using a three-dimensional calculation of D_α emission and ionization distributions. These were computed using the multi-dimensional DEGAS neutral transport code [6] which was used to simulate recycling at the TFTR inner limiter for three discharges during the gas loading sequence. The DEGAS model contains a comprehensive description of D_α emission from both atomic and molecular dissociation excitation. The limiter ion flux distribution was simulated using a model which has been experimentally calibrated using data from moveable limiter discharges. Plasma elongation was insignificant during the gas loading sequence. The toroidal variation of D_α emission was found to be relatively small and so was ignored. The plasma scrape-off was also assumed to be poloidally symmetric, although there are indications that the plasma edge density may rise near the limiter.

The calculated D_α distributions were integrated along chords, and then compared with D_α emission measured by the H_α Interference Filter Array [7]. By scaling the calculated D_α distributions to agree with the measurements, the resulting recycling sources, S, were then calculated.

The resulting values of τ_p varied from 0.16 to 0.18 s. Using an average τ_p of 0.17 s, the computed global recycling coefficients varied from 0.61 at the beginning of the sequence to 0.82 at the end (Table I). The calculated ion particle current Γ^+ increased correspondingly from 2.17×10^{21} D^+/s to 3.1×10^{21} D^+/s. The calculated limiter pumping efficiency, ρ, which is the fraction of particle flux removed by the limiter, decreased over the sequence from 0.085 to 0.025.

The particle inventory in the limiter and wall during the gas loading sequence was obtained from calibrated measurements of the required gas input per discharge (Q_{in}) and the integrated vessel outgassing (Q_{out}) for an 80 s period after a discharge. Figure 2 shows the measured values of Q_{in}, Q_{out}, and the computed wall inventory, $W = Q_{in} - Q_{out}$, during the gas loading sequence. At the beginning of the sequence 40 torr-liters of D_2 was required to reach the fiducial plasma density ($1.25 \times 10^{19} m^{-3}$). At the end of the sequence, the required gas input decreased to an asymptotic value of ~20 torr-liters, as the limiter became loaded and the recycling coefficient increased. For the entire sequence, the amount of D_2 outgassed from the vessel between discharges was a relatively constant value of $Q_{out} \approx 4$ torr-liters. Thus, the wall loading also showed a decrease to an apparent asymptotic value of W = 16 torr-liters/discharge during this shot sequence. The total wall loading minus the asymptotic value for the entire sequence was ~ 70 torr-liters, which can be equated to the pumping capacity of the limiter which was induced by the initial He discharge conditioning. This pumping capacity is consistent with the wall pumping model described in Ref. 1, where the capacity for pumping ohmic plasma is estimated to be equal to the saturation capacity of the limiter volume contained within the scrape-off area (~ 5 m^2) and the mean range of incident D^+.

The asymptotic value of W = 16 torr-liters per discharge is apparently not related to plasma pumping by the limiter, because W was relatively constant during the shot sequence, while the recycling coefficient changed from R = 0.6 to R = 0.8. The residual pumping of deuterium may have been due to pumping of deuterium by molecular components (C_xD_y), or deuterium incorporation into sputtered carbon films on low flux areas of the torus. Such redeposition phenomena have been

invoked to explain carbon pumping effects in tokamaks [1-3] and glow discharge experiments [8]. For redeposition to have been responsible for the residual (16 torr-liter/discharge) pumping seen in TFTR, the effect would have had to dominate during the non-steady state (i.e., formation and/or termination) phases of the discharge. It appears that the observed residual pumping is related to deuterium/carbon chemistry because similar particle balance measurements with He-gas-fueled discharges showed that $Q_{in} = Q_{out}$.

PARTICLE BALANCE DURING NEUTRAL BEAM INJECTION. During neutral beam injection we typically observe that the plasma density rises rapidly early in the beam pulse but after about 0.5 sec the density has reached a new equilibrium. A typical example of the line integral plasma density during neutral beam injection is shown in Fig. 3. The time constant for relaxation to the new equilibrium has been determined by fitting a function of the form $n(t) = n_o + \Delta n e^{-t/\tau}$ to the data shown in Fig. 3. The time constants determined from such fits are between 180 and 240 msec. There is no observable systematic variation of the relaxation time with plasma current, beam power, or ohmic particle confinement times. The rate of rise of the number of plasma particles at the beginning of the beam pulse is plotted versus the beam fueling rate in Fig. 4. A parabolic squared plasma density profile was assumed.

Figure 3 shows that early in the beam pulse nearly all of the beam particles are being absorbed by the plasma. However, later in the beam pulse when the new equilibrium has been reached an as yet unknown mechanism is removing particles at a rate approximately equal to the beam fueling rate. We find that for beam powers up to 17 MW, plasma currents between 0.8 and 1.4 MA, and 1 sec beam pulses, only 26 ± 3% of the total injected beam particles stay in the plasma.

ACKNOWLEDGMENT. This was supported by the U.S. Department of Energy Contract No. DE-AC02-76-CHO-3073.

REFERENCES

(1) H.F. Dylla et al., Princeton University Plasma Physics Laboratory Report, PPPL-2448 (1987), submitted to Nucl. Fusion.
(2) S.A. Cohen, in Proceedings of the XIV European Conference on Controlled Fusion and Plasma Physics, Madrid (1987).
(3) J. Winter, J. Vac. Sci. Technol. (in press).
(4) R.J. Goldston et al., in Proceedings of the 11th International Conference Plasma Physics and Controlled Fusion Research, Kyoto, November 1986 (IAEA, Vienna), in press.
(5) J.D. Strachan et al., Phys. Rev. Lett. 58 (1987) 1004.
(6) D. Heifetz et al., Comput. Phys. 45 (1982) 309.
(7) A.T. Ramsey and S.L. Turner, Rev. Sci. Instrum. (in press)
(8) W.L. Hsu and R.A. Causey, J. Vac. Sci./Technol. (in press).

TABLE 1: GAS LOADING RESULTS AT t = 2s

SHOT	S (10^{20}/s)	G (10^{20}/s)	τ_p^* (s)	R	Γ^+ (10^{21}/s)	ρ
27634	8.2	4.8	0.44	0.61	2.17	0.085
27637	11.6	1.9	0.69	0.75	2.81	0.043
27645	13.2	1.5	0.94	0.82	3.10	0.025

*The recycling coefficient R was calculated using $\tau_p = 0.17$

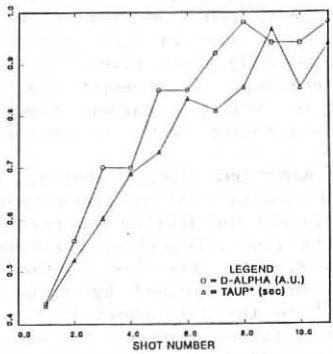

FIG. 1. Variation of the mid-plane D_α emission and τ_p^* during gas loading sequence of ohmic discharges.

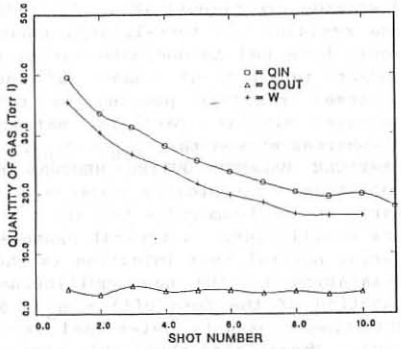

FIG. 2. Required gas fueling (Q_{in}), integrated vessel outgassing after a discharge (Q_{out}), and the wall loading, $W = Q_{in} - Q_{out}$, during the gas loading sequence.

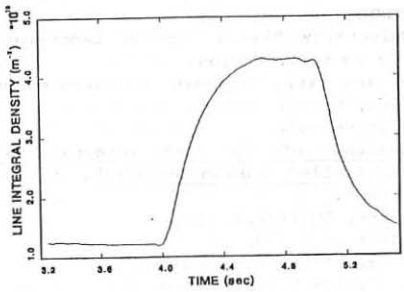

FIG. 3. Typical electron density rise during neutral beam injection.

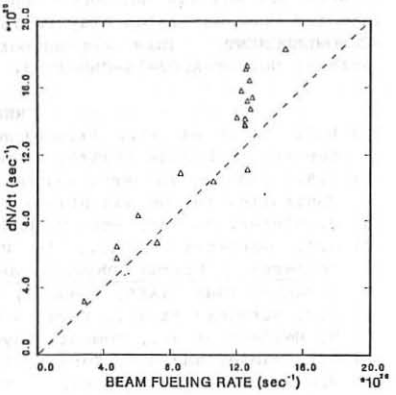

FIG 4. A comparison of dN/dt with the beam fueling rate.

Wall Pumping Experiments in TEXTOR

J. Winter, H.G. Esser, F. Waelbroeck, P. Wienhold

Institut für Plasmaphysik, Kernforschungsanlage Jülich GmbH,
Association EURATOM/KFA, Postfach 1913, 5170 Jülich, FRG

Abstract

The global hydrogen recycling in TEXTOR with carbonized graphite limiters and carbonized Inconel liner ("all carbon" machine) /1, 2/ has been investigated. The wall properties can be modified in a controlled way from a status in which the plasma is fuelled (recycling coefficient $R > 1$) to one in which it is pumped ($R < 1$) by the wall. This is achieved by adjusting the hydrogen concentration in the near surface layer of the carbon material. This concentration decreases e.g. when the wall is outgassed in-situ at temperatures $T_W \gtrsim 350°C$; it can be increased by short glow discharges at $T_W = 150°C$ or lower. The wall pumping effect is strongly enhanced when a previously centered plasma is shifted towards the inside wall during part of the discharge. Reproducible wall pumping - i.e. no shot to shot n_e variation for a given parameter setting - has been observed in TEXTOR when the wall and limiters are at $T_W = 350°C$. Glow discharges in hydrogen do not significantly affect then the hydrogen recycling /2/. It will be shown here that a wall surface previously outgassed at $T_W \sim 350°C$ but operated at $T_W = 150°C$ is recharged with hydrogen by tokamak and/or short glow discharges and can change its behaviour from "pumping" to "fuelling".

Introduction

The phenomenon of wall pumping by inward plasma shifts in an all carbon tokamak has recently attracted great interest. The effect has first been observed in JET /3/ and since then been systematically studied in JET and TEXTOR /2/. Its importance as an operational tool for controlling the density, e.g. during neutral beam or pellet injection is obvious. It also seems to help achieving the modes of good energy confinement (supershots in TFTR). The subject of wall pumping is being adressed in an invited paper during this conference /4/.

The properties of carbonization films (a-C:H) are nearly identical to those of graphite surfaces which have been irradiated with high doses of energetic hydrogen ions /1, 5, 6/ (amorphous structure, similar outgassing and chemical reactivity, same saturation concentration of hydrogen, etc.). Thus the results from a carbonized tokamak are of relevance also to machines with large area graphite wall components.

It is important to explore and understand the mechanisms which govern the wall pumping effect both from the confined plasma and from the materials interaction point of view in order to assess its limits. Due to the lack of space, only a phenomenological description of some TEXTOR experiments will be given here; a more detailed discussion will be published elsewhere.

Experiments and Discussion

The experiments discussed here were made several hundreds of discharges after the last carbonization. The liner (r = 55 cm), poloidal antenna protection limiters (r = 48.8 cm) and the main limiters were regularly outgassed during the nights for eight hours at temperatures between 350°C and 420°C, and then adjusted to the desired operation temperature. In most cases the same parameters, in particular an identical gas feed program, were used for all discharges of one series. Differences in the evolutions of the plasma densities display then changes in recycling properties. During some discharges the plasma has been shifted from its initially centered position at R = 1.75 m by 10 cm to the inside torus wall.

When the wall and limiter temperatures after outgassing are reduced to 150°C operation temperature, strong sorption of hydrogen by the wall occurs during the first discharge # 25887, see fig. 1. A rapid decrease of the density is observed, after termination of the external gas feed at 500 ms. This caused radiation from runaway electrons. In order to avoid this, the duration of the gas puff was extended to 1900 ms for the second discharge # 25888, the gas flow rates remaining unchanged. Already shortly after the ignition phase higher density and a steeper slope of the density rise during current ramp up, are observed compared to the first discharge. The third discharge # 25889 shows a further increase of the start up density and of the density slope during the current rise. The density remains constant during the current flat top, after the end of the external fuelling at 1200 ms, indicating that $R \approx 1$.

The experiments at T_W = 150°C demonstrate that the pumping action of the previously outgassed wall is strong and that it decreases rapidly from shot to shot. The carbon surfaces are progressively filled up with hydrogen of which only a fraction is released before the next discharge. This leads to increased density rises and total densities from discharg to discharge.

After a number of discharges with constant parameters, and in particular with the same amount of gas let in a "stationary" and reproducible density evolution is observed, the form of which depends on the scenario (I_p-program, gas feed, a), see fig. 2a # 26887-89. The current program was similar to that of fig. 1c, the gas feed extended to 500 ms, and the minor radius was a = 44 cm for all discharges shown in fig. 2.

Under otherwise identical conditions, the plasmas in # 26890-93 were shifted at 1.0 s by 10 cm to the inside wall of the torus. A rapid density decrease within about 700 ms is observed, thereafter the slope of the density follows closely that of the unshifted plasmas (wall pumping effect). Within the errors of the measurement no shot to shot n_e-variation is observed. This supports the conclusions drawn from the analysis of many additional experiments that the wall pumping behaviour depends on the amount of gas introduced rather than on the scenario (plasma shift or soft landing) by which the plasma is eventually sorbed by the wall.

The tokamak operation was interrupted and molecular D_2-gas was bleeded through TEXTOR for 10 min at the pressure required for a RG discharge. The vessel was evacuated and plasma operation resumed under the same conditions. Identical density traces both for unshifted and shifted plasmas as in fig. 2a were measured. Then a RG discharge of 5 min duration was made, followed again by tokamak discharges with identical external parameters. As measured previously at this T_W /2/, a significant increase of n_e is found for the unshifted plasmas; during the flat top phase $R > 1$. The recycling has increased, the wall cannot pump as much particles as before. This is also manifest from the density traces of shifted discharges # 26907-9 which exhibit an initial density increase after the position change at 1.0 s, followed by density decreases at much smaller rates than those shown in fig. 2a. Additional 10 minutes of RG-discharge conditioning (fig. 2c) lead to further increased values of n_e for the centered plasma (# 26913) and progressive density increases when the plasma is shifted. After three shifted discharges the density traces became reproducible. The data show that a large amount of hydrogen is retained by the wall at a temperature of 150°C, i.e. a pronounced memory effect exists in contrast to the behaviour at 350°C.

Experiments at T_W = 350°C which have been discussed in detail elsewhere /2/ show a very reproducible density evolution with $R < 1$ during the current flat top (I_p = 340 kA, ohmic heating, a = 46 cm). Radiofrequency assisted dc glow (RG)-discharges in deuterium for 20 min and for 40 min do not affect the recycling behaviour significantly. Inward plasma shifts lead to reproducible wall pumping actions. The wall pumping capability remains the same from discharge to discharge.

Measurements in which the temperature of the limiters which are in contact with the plasma was increased from 150 °C to 330 °C and in which the liner was kept at 150°C, do not show an influence on the hydrogen recycling. From this we conclude, that the temperature of the (large area) wall is more important than that of our (small area) limiters.

In order to achieve reproducible density evolution rapidly and to achieve a large pumping capacity of the wall, operation temperatures of 350°C appear to be favourable.

References

/1/ J. Winter, J.Nucl.Mater. 145-147 (1987), 131

/2/ J. Winter, J. Vac. Sci. Techn. A (1987), in press (Proc. 10th Int. Vac. Congress, Baltimore, Oct. 1986)

/3/ K.J. Dietz, private communication

/4/ S.A. Cohen et. al., invited lecture, this conference

/5/ J. Winter el. al., J.Nucl.Instr.Meth. in Physics Res. (1987), in press

/6/ E. Vietzke et. al., this conference

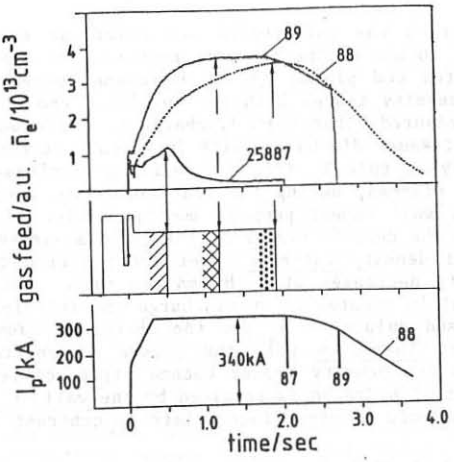

Fig. 1

Evolution of n_e, of the fuelling rate and of I_p during the first three discharges made at T_W = 150°C following a bake out of liner and limiters of 8 h at 350°C and 400-420°C respectively.

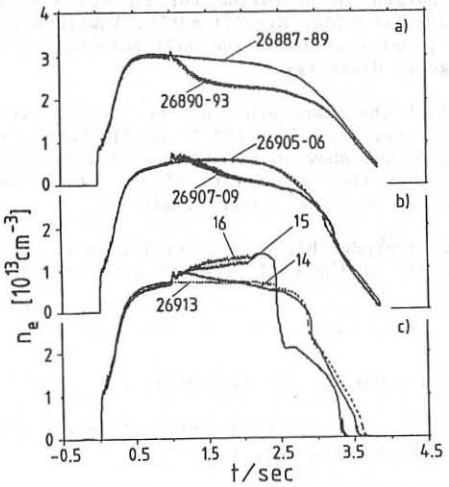

Fig. 2

Evolution of n_e for discharges at T_W = 150. Current and gas feed programs were the same during these and preceding experiments. An inwand plasma shift by 10 cm was made at t = 1.0 s during some discharges. (a) without additional conditioning, (b) after 5 min RG discharge conditioning in D_2, (c) after 10 min RG discharge conditioning in D_2.

THE EFFECTS OF WALL AND LIMITER MATERIAL PROPERTIES ON HYDROGEN RECYCLING IN JET

J Ehrenberg°, S A Cohen*, L de Kock, P J Harbour,
P D Morgan, M F Stamp and D D R Summers

JET Joint Undertaking, Abingdon, Oxon OX14 3EA, UK
° On attachment from Max-Planck-Institut für Plasmaphysik,
8046 Garching bei München, FRG
* Visiting scientist from Plasma Physics Laboratory,
Princeton University, Princeton NJ 08544, USA

I INTRODUCTION

The recycling of hydrogen at the limiters and walls of a fusion machine is important in controlling the particle and power balance of the plasma.

The problem may be subdivided into two parts: the transport of particles in the plasma and the transport of particles in the limiters and walls. In this paper we concentrate on the transport in the limiters and walls, treating plasma transport in a global way.

We present a numerical model which predicts, as a function of time during a simulated plasma discharge, the number of plasma particles and the particle fluxes to and from limiters and walls. We study with this model a JET discharge in which the plasma was moved from the outer limiter onto the inner wall and back to the limiter. We find good agreement between experiment and simulation.

II EXPERIMENTAL ASPECTS OF RECYCLING IN JET

JET limiter discharges are initiated with a hydrogen or deuterium gas prefill. A subsequent dosing raises the density. When the dosing valve is closed the density stays approximately constant /1/. The number of particles found in the plasma, compared to the number admitted into the machine (the fuelling efficiency) depends on the conditions of the limiters and walls. However, the walls and limiters soon reach a steady state in which the fuelling efficiency is below one.

In some JET discharges, the plasma is moved from the outer carbon limiter onto the inner carbon wall. Subsequently the plasma density drops. This pumping at the inner wall is not reduced after a series of similar discharges, excluding the saturable trapping of hydrogen implanted into carbon as a pumping mechanism. Also, we estimate that pumping due to deuterium/carbon codeposition /2,3/ contributes less than 30%, otherwise the required erosion rate of carbon would have to exceed that from known processes by a factor of three. When the plasma is moved back to the outer limiter, the density rises again. An example is shown in Fig. 1. This indicates that changes in the plasma position may be considered as changes in the balance between the particle fluxes out of the plasma and those out of walls and limiters.

III THE RECYCLING MODEL

The walls and limiters in a fusion machine are a reservoir for hydrogen atoms in the same way as the plasma is a reservoir for ions /4,5/. The neutral gas phase is unimportant as a reservoir because its confinement time for neutrals is of the order 10^{-3} s and thus much smaller than the particle confinement time τ_p in the plasma. Walls and limiters, in order to be an important reservoir, must have a particle confinement time τ_w similar to the plasma particle confinement time. The plasma is the source for energetic ions and neutrals which impact the walls. τ_w can be considered as the time these particles need to diffuse back to the surface and to desorb into the plasma. This effect is well-known for the case of hydrogen in metals and is called transient or dynamical retention /6/. However JET has carbon limiters, carbon inner walls and inconel vessel walls which are covered with a carbon layer (> 10 nm) /7/. In addition the carbon is saturated with deuterium, contaminated with metallic impurities and may have cracks at the surface. Little is known about dynamical retention in such materials. Nevertheless, we use the concept of hydrogen diffusion in solids and develop a model to calculate the number of plasma particles as well as particle fluxes from walls and limiters.

We assume that the change in the number of plasma particles (N_p):

$$\frac{dN_p}{dt} = - \frac{N_p}{\tau_p} + f \cdot \phi, \qquad (1)$$

where ϕ is the total flux of deuterium atoms from walls and limiters and f is a factor taking into account that part of this flux returns directly to the limiters and walls due to atomic processes, ionisation in the scrape-off layer, or due to the escape of neutrals. The magnitude of f has to be estimated.

Plasma losses, N_p/τ_p, are assumed to stream either to the outer-limiters or to the inner wall, depending on where the plasma resides. The flux $(1-f)\phi$, which is that part which does not fuel the plasma, is shared between the limiter, the inner wall, and the rest of the vessel wall. It is assumed that 50% of this flux goes to the surface where the plasma resides (limiter or inner wall) and 50% to the rest of the wall and the inner wall or limiter (i.e. depending on where the plasma is not). The latter 50% is assumed to be shared according to the ratio of the respective surface areas. The partition is somewhat arbitrary, however it simulates roughly the situation that the probability of creation of "daughter"-neutrals by charge exchange processes is largest near surfaces where recycling is large. Thus "daughter"-neutrals have a good chance to return to that surface where the initial neutrals have been born.

The particles which impinge onto surfaces are either reflected (with reflection coefficient, r) or penetrate into the material up to a depth d. r and d depend on the impact energy of particles, which is derived from Langmuir probe measurements in the plasma boundary of JET /8/. For simplicity we assume monoenergetic particles. The penetrating particles are the source for the diffusion in walls and limiters. The diffusion equation is solved numerically, using an assumed diffusion coefficient, a

recombination coefficient, and appropriate boundary conditions. The diffusive losses as well as the reflected flux from all surfaces then fuel the plasma (see equ 1). From the dependence of the experimental fuelling efficiency on the number of particles admitted to the machine, it can be shown that the release of particles from JET limiters and walls is most likely determined by diffusion. Thus we have to know the diffusion coefficient only. We also have to know whether diffusion takes place within the entire wall thickness ($\leq 10^{-2}$ m) or only within a surface layer with a thickness L. Assuming a simple triangular concentration profile of diffusing particles in limiters and walls (peaked at the range d and zero at either surface of the layer L) it can be shown that the wall confinement time τ_W is approximately:

$$\tau_W \sim \frac{d \cdot L}{D} \text{ if } L > d \text{ and } L << (t_{max} \cdot D)^{1/2} \qquad (2)$$

where t_{max} is the duration of particle bombardment. If $L \geq (t_{max} \cdot D)^{1/2}$, τ_W is larger than in (2) and depends on time. In this case (or when $d > L$) it can be shown that the plasma is still pumped by the walls, however, the number of particles cannot increase during a discharge as is shown to occur in Fig. 1. Good agreement between experiment and calculation was found by taking L to be around 20 nm. This suggests that the material structure of wall and limiter surfaces prevents the diffusion of a significant fraction of deuterium into the bulk material.

IV RESULTS

For the calculation presented in Fig. 2 we took a reflection coefficient, r, of 0.3 and a particle range, d, in walls/limiters of 5 nm corresponding to an impact energy of about 100 eV for deuterium on carbon. According to previous investigations /1/ τ_p was taken to be proportional to $1/N_p$. To simulate the higher temperature at the limiter (> 700°C) compared to the walls (300°C) and the different materials (carbon, carbonized inconel), we assumed the diffusion coefficient D to be different on these surfaces. D and the factor f (see Fig. 2) were varied until satisfactory agreement with the experiment was achieved. The discharge scenario simulated in Fig. 2 is as follows: an external gas source with 10^{21} particles/s for the first 4 s, fills the plasma while it rests at the limiter. The total particle input is the same as in the experiment of fig. 1. At 6 s the plasma interaction is shifted from the limiter to the inner wall. At 10 s this is reversed. To simulate the detached plasma phase at 6 s and 10 s the plasma particle confinement at these times was enhanced for 0.2 s by a factor of 2. Good agreement between calculation and experiment was achieved with $D = 2.10^{-11}$ cm²/s at the limiter, $D = 1.10^{-11}$ cm²/s at the inner wall, and $D = 1.10^{-12}$ cm²/s at the rest of the wall. The set of values for d, L, D and f is not unique. The limiter flux, deduced from the data in Fig. 1 agrees within a factor of 2 with that in Fig. 2. However the measured inner wall D_α-signals show toroidal variations, probably caused by non-uniformities in the surface of the inner wall, making a quantitative comparison difficult.

V CONCLUSION

A model has been developed to describe the complementary processes of pumping and fuelling of plasma by diffusion of deuterium in limiters and walls. Also account is taken of non-fuelling processes which increase particle fluxes to walls/limiters and subsequently the particle inventory therein. Comparison with experimental results shows good quantitative agreement. The model indicates the importance of plasma and wall properties for the balance of particle fluxes.

VI REFERENCES

/1/ P Morgan et al, Proceedings 12th Europ Conf Contr Fus Plasma Phys, Budapest, 2-6 September 1985, Vol II, 535.
/2/ R Behrisch et al, Journal of Nucl Mat, 145+147 (1987) 723.
/3/ H Bersaker et al, Journal of Nucl Mat, 145+147 (1987) 727.
/4/ G M McCracken and P E Stott, Nuclear Fusion, Vol 19, No 7 (1979) 889.
/5/ T Jones et al, this conference.
/6/ F Waelbroek et al, Journal of Nucl Mat, 111+112, (1982) 185.
/7/ P Coad et al, Proceedings 12th Europ Conf Fus Plasma Phys, Budapest, 2-6 Sept 1985, Vol II, 571.
/8/ T Tagle et al, this conference.

FIGURES

Fig. 1 Plasma current I_p, total number of electrons N_e, and D_α signals from limiters and inner wall of a JET discharge which was moved onto the inner wall at t=6s and removed back to the limiter at 10 s and again moved to the inner wall at 14 s. To compare N_e with N_p of fig. 2, N_e has to be reduced by approximately 20% due to $Z_{eff} = 2$, assuming carbon as the only impurity.

Fig. 2 Calculated number of plasma particles N_p and particle fluxes from limiter, Γ_L and inner wall, Γ_{IW} for a discharge with a similar total particle inventory as in Fig. 1.

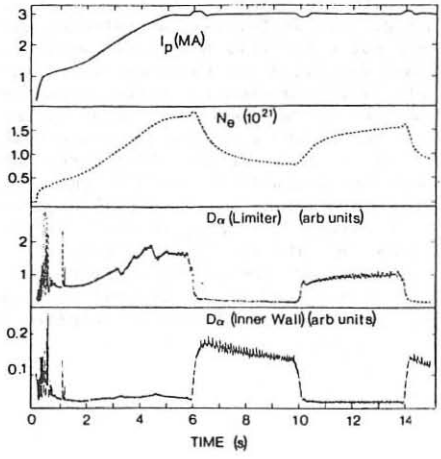

Fig. 1

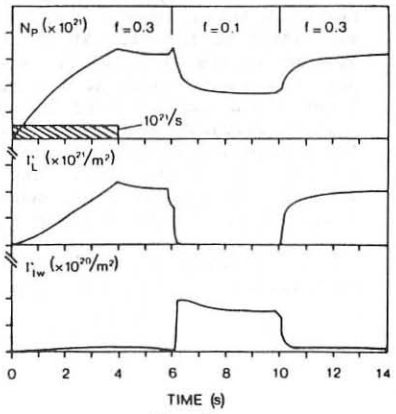

Fig. 2

SPATIAL AND TEMPORAL EVOLUTION OF BERYLLIUM CONCENTRATIONS IN THE TOKAMAK UNITOR

M. Bessenrodt-Weberpals, J. Hackmann, I. Lakicevic*, C. Nieswand, and J. Uhlenbusch

(Institut für Laser- und Plasmaphysik, Universität Düsseldorf, Universitätsstrasse 1, D - 4000 Düsseldorf, FRG
*on leave from Inst. Phys., Beograd, Yugoslavia)

INTRODUCTION

The use of beryllium as limiter material has led to a reduction of metallic impurities and an improvement of the plasma parameters [1,2]. In the investigations reported here, the local transport of neutral and ionized beryllium released from a poloidal limiter is studied, both numerically and experimentally at the small-scale tokamak UNITOR. The UNTIOR vacuum vessel with the arrangement of two poloidal beryllium limiters is shown in fig. 1. The beryllium limiters can be retracted behind the torus wall, which then serves as toroidal limiter (fig. 1, left). By moving the beryllium limiters radially into the torus, UNITOR is operated in the poloidal limiter mode (fig. 1, right).

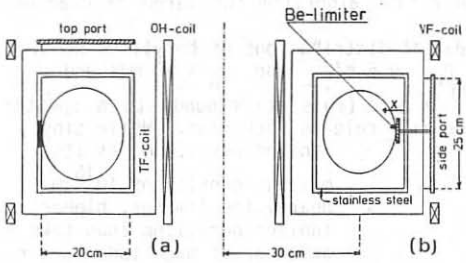

Figure 1

The discharges have a plasma current of 50 kA, a toroidal magnetic field of 1.7 T, and an electron density of 2×10^{19} m^{-3} at discharge times of 50 ms. The plasma temperatures at the centre reach 200 eV and 50 eV for the electrons and ions, respectively. The energy deposition on the limiters is of the order of 1MJ/m² per discharge with a peak power load of 20 MW/m².

IMPURITY TRANSPORT ALGORITHM

In order to study the dynamics of the different impurity ions, their diffusive and convective motion is described by the corresponding flux

$$\Gamma_i = - D_A \, d_r n_i - v_A \, n_i \, r/a \quad (i=1,\ldots,Z)$$

with diffusion coefficient D_A and convective velocity v_A. In the transport equations the divergence of this flux is balanced by the production and loss terms of charge carriers via ionization (S_i) and CX recombination processes (R_i), respectively. Summing up, the impurity transport algorithm

in cylindrical geometry reads

$$(1/r)\, d_r(r\,\Gamma_1) = -S_1 n_1 - R_1 n_1 + R_2 n_2 + d$$
$$(1/r)\, d_r(r\,\Gamma_i) = S_{i-1} n_{i-1} - S_i n_i - R_i n_i + R_{i+1} n_{i+1}$$
$$(1/r)\, d_r(r\,\Gamma_Z) = S_{Z-1} n_{Z-1} - R_Z n_Z \quad ,$$

where the source term d takes the influx of neutral particles into account. These may be released by either sputtering or evaporation. The differential equations of the second order are completed by the boundary conditions $n_i(r=a) = 0$ and $d_r n_i(r=0) = 0$ $(i=1,\ldots,Z)$; that implies no impurity ions at the limiter and symmetry in the centre. The system is solved iteratively using an alternating symmetric treatment of ionization and recombination [3]. In each step, the second-order equations are converted into tridiagonal linear equations by a finite difference method. Hence, the simulation is based on a fast algorithm for large tridiagonal systems [4].

These calculations yield the spatial distributions of beryllium densities and fluxes. Here, we choose $D_A = 0.5$ m²/s and $v_A = 10$ m/s and assume a neutral influx $d = 10^{20}$ m^{-3}/s. (This corresponds to a sputter yield of 0.001 if sputtering is the main release mechanism.) While singly ionized beryllium has its maximum density of 10^{16} m^{-3} nearby the limiter, higher ionized beryllium ions take an order of magnitude larger values at smaller radii. Fully stripped Be V dominates in the plasma core and reaches about 8×10^{17} m^{-3} which corresponds to 4% n_e. On the basis of this density distribution, the contribution of beryllium to Z_{eff} is evaluated to be at most 0.6 in the centre with a strong decrease towards the edge. In fig. 2, the fluxes of beryllium ions are presented. Nearby the limiter, where very small densities with very large negative density gradients prevail, all ionic fluxes are dominated by diffusion and show positive sign. Hence, all ions diffuse outwards towards the limiter. As can be seen, the sum of all ionic fluxes equals

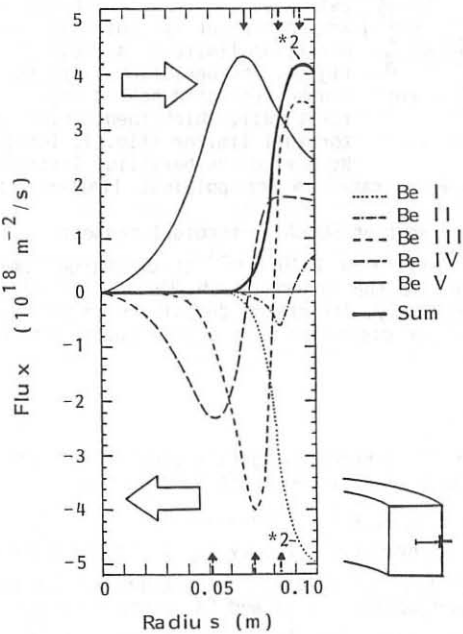

Figure 2

approximately the influx of neutral beryllium. At those radial positions, where the densities take their maximum values, the sign of the corresponding flux changes. Beyond this radius, convection and diffusion both drive the ions from the limiter towards the centre. Approximately the same flux of fully stripped Be V in opposite direction from the centre to the limiter prevents the impurity accumulation.

LASER INDUCED FLUORESCENCE AND SPECTROSCOPY

To study the behaviour of beryllium in a tokamak discharge experimentally two poloidal beryllium limiters are installed in UNITOR. They can be moved radially up to 30 mm from the outer side of the torus into the plasma (cf. fig. 1).

In front of one of the limiters, laser induced fluorescence is performed to determine the densities of neutral beryllium in the ground state and in a metastable level and of singly ionized ground state beryllium. The corresponding lines investigated are 234.9 nm and 332.1 nm for Be I and the doublet at 313.0 nm and 313.1 nm for Be II. The light source is a frequency doubled, pulsed dye laser with energies up to 1 mJ, 15 ns pulse duration, and about 5 pm spectral width. The saturation parameter of 1000 is obtained for the Be I transitions (saturation intensity 0.5 kW mm^{-2} nm^{-1}) and 10000 for the Be II transitions (saturation intensity 0.2 kW mm^{-2} nm^{-1}). The scattering volume of 7 mm^3 is adjusted at a distance of 5 mm from the surface of the limiter, which is positioned 10 mm in front of the outer wall. The scattered light is observed perpendicular to the laser beam. The signals are calibrated with Rayleigh scattering in argon with an accuracy of a factor of 2. The detection limit for this set-up is 10^{14} m^{-3} for beryllium ground state atoms.

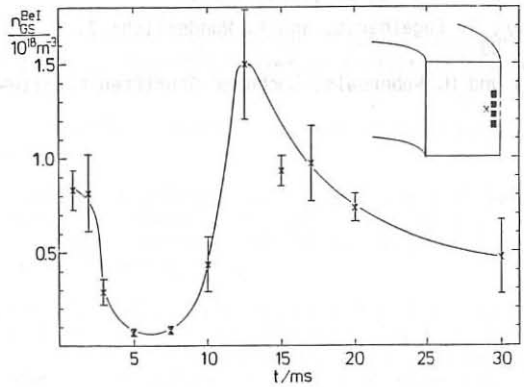

Figure 3

In fig. 3, the time dependence of the ground state density of Be I is shown. During the first milliseconds the density decreases according to the lowering of the proton flux onto the limiter (no pulsed gas feed). A maximum of 1.5×10^{18} m^{-3} is observed 13 ms after ignition of the discharge. This strong increase of beryllium release cannot be explained by proton sputtering. An additional release mechanism, e.g. evaporation, must play an important role when the limiter is heated up du-

ring the discharge. Retracting the limiter to the outer wall by 5 mm, we observe a decrease of the density at the beginning of the shot while later on the maximum density is higher by a factor of 2.

The spectroscopic measurements show the same temporal behaviour for the lines at 234.9 nm (Be I), 332.1 nm (Be I), 313.0 nm (Be II), and 372.2 nm (Be III).

SUMMARY

Transport calculations reveal that the ionization states of beryllium are rapidly run through. When sputtering is the main release process, even for the relatively cold edge plasma of UNITOR (<10 eV) fully stripped Be V dominates beyond a distance of 50 mm from the limiter. The contribution of the beryllium contamination to Z_{eff} is below 1. The beryllium fluxes give no indication for impurity accumulation.
Laser induced fluorescence has shown to be a sensitive diagnostic for impurity distributions with high temporal and spatial resolution. When during the discharge the limiter is heated up and thermal loads are increasing, the results make clear that besides sputtering additional erosion plays an important role. Screening of the beryllium impurities by the edge plasma is not observed. The additional release mechanism has not yet been identified in detail. Further elaborate investigations are in progress.

This work was performed as part of a cooperation with the JET laboratories, Culham.

REFERENCES

[1] J. Hackmann and J. Uhlenbusch: Nucl. Fusion. 24 (1984) 640.

[2] P. Mioduszewski et al.: Nucl. Fusion 26 (1986) 1171.

[3] K. Lackner, K. Behringer, W. Engelhardt, and R. Wunderlich: Z. Naturforsch. 37a (1982) 931.

[4] M. Bessenrodt-Weberpals und H. Weberpals: Bochumer Schriften Parallele DV 10 (1986) 25.

MONTE CARLO MODELLING OF IMPURITY TRANSPORT FOR A LIMITER SOURCE/SINK

P. C. Stangeby,* L. Wood and S. Hoskins

JET Joint Undertaking, Abingdon, Oxon, OX143EA, U.K.
*and University of Toronto Institute for Aerospace Studies
4925 Dufferin Street
Downsview, Ontario, Canada, M3H 5T6

Introduction

In order to relate [1-3] impurity influxes, Γ_I (atoms/sec), from walls and limiters to central impurity densities, n_I (ions/m^3), it is necessary to know the sink strength of the scrape-off layer, SOL, for impurity ions. The SOL sink is represented in the impurity particle balance equation by the loss term n_I/τ_I where n_I represents the local impurity density and τ_I represents the loss time for impurity ions as they move along $\vec{B}$ to the limiters.

The problem addressed here is the one of calculating τ_I. If one makes the simplest assumption that the impurity ions are coupled to the hydrogenic flow, which reaches the limiters at the hydrogenic ion acoustic speed $c_s = [k(T_e + T_H)/m_H]^{1/2}$, and that the impurities enter the SOL uniformly along its connection length L_c (due either to ionization within the SOL or diffusion from the main plasma) then $\tau_I \simeq L_c/c_s$ and the radial scrape-off layer thickness would be $\lambda_I \simeq (D_I\tau_I)^{1/2} \simeq (D_I L_c/c_s)^{1/2}$, i.e., the same as λ_H, if $D_H = D_I$. The impurity sink strength appears in the relation [1-3] between influx Γ_I and $n_I(0)$:

$$n_I(0) = \frac{\Gamma_I}{A_p D_\perp}(\lambda_{iz} + \lambda_I) \qquad (1)$$

assuming uniform distribution of source and sink around the plasma periphery of area A_p. λ_{iz} is the average ionization distance inside the limiter. For outboard ionization, $(\lambda_{iz} + \lambda_I) \rightarrow \lambda_I \exp(-\lambda_{iz}/\lambda_I)$.

Clearly a number of the assumptions in the foregoing can be questioned:

1. Even for a uniform, e.g., wall, source of impurity ions distributed along the SOL, does $v_I = v_H$? i.e., is the coupling strong between the impurities and the main plasma flow? If the impurities simply diffuse along $\vec{B}$ then $v_I \ll c_s$.

2. For impurities released from the limiters the effective length of the return path to the limiter sink $L_{eff} \ll L_c$. On JET, for example, $L_c \simeq \pi Rq \simeq 50$ m while the distance moved by an impurity atom away from the limiter before ionizing is of order cms.

These questions are examined here using a Monte Carlo impurity particle code which tracks a large number of impurity particles launched either

uniformly along the SOL, or near a limiter as they move through the background plasma until finally returning to the limiter (sink). The following types of output are sought:

1. For the uniform (wall) source, the values of τ_I, thus λ_I.

2. For the localized (limiter) source, there are two types of output:

   (a) The sizes of the impurity "clouds" of the successive ionization states each centred toroidally at the limiter but extending radially and toroidally by greater amounts for Z ranging upward from unity. Impurity cloud sizes can be observed spectroscopically permitting, in principle, a measurement of the value of $D_\perp$ by comparing experimental and model results.

   (b) As in the uniform (wall) source case, the values of τ_I or λ_I are sought. This value of τ_I is then used to calculate the Reduction Factor applied to the analytical result obtained by Fussmann [3] for uniform impurity influx and assuming $\tau_I = L_c/c_s$. That is, for a given impurity flux, ionized at a given radius, the central impurity density $n_I(0)$ will be less for the limiter source than for the same uniform (Fussmann) case by a Reduction Factor which is found as a function of background plasma conditions.

Method of Calculation

Only results from the base code, LIM.1 (Limiter Impurity), are reported here. In LIM.1 the impurities are started as Z = 1 ions rather than as neutrals, and the limiter geometry is idealized as a flat plate extending from the limiter tip outward and of negligible toroidal thickness, Fig. 1.

The analysis follows that of J. N. Brooks' ZTRANS 2-D Monte Carlo code [4], but with certain modifications and giving as output the two results indicated in the last section. A number of other impurity transport codes and models have been developed to describe behaviour near divertor plates and limiters, including fluid, analytic and test particle ones, but the Monte Carlo approach seems best suited to incorporating impurity heating and parallel diffusion.

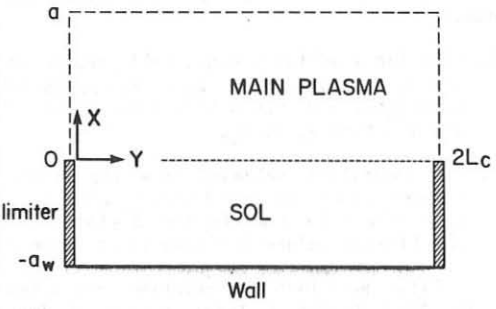

Fig. 1. Geometrical arrangement. $\vec{B}$ is in y-direction. Centre-line of main plasma at x = a, wall at x = $-a_w$. Last closed flux surface at x = 0. Separation of limiters $2L_c$. Impurity ions are collected at limiter and wall surfaces, reflected at other surfaces. Impurity ions are launched as Z = 1 ions at specified point (x_0, y_0) or homogeneously along y for specific x_0.

In LIM.1 impurity particles are launched as Z=1 ions at assigned position (x_0, y_0) and with single velocity v_0 along y, i.e., $\vec{B}$. The background plasma density, n_B, and temperature, T_B, are fixed and are constant spatially. Each ion is followed in time allowing for: (a) ionization to higher states (recombination is neglected), (b) finite heating rate, (c) parallel diffusion (thermalizing) collisions with the background, (d) frictional collisions with the background, (e) acceleration in the ambipolar electric field (when in the SOL), (f) cross-field diffusion for an assumed value of $D_\perp$. Thus the 2D spatial dispersal of impurity ions can be followed in time from an instantaneous injection for comparison with the analytic Fussmann [3] result for a uniform source/sink. Also, by time integration the steady-state 2D cloud shapes are obtained for each charge state. Two different models are used for the ambipolar electric field, E, and the background flow velocity, $v_B = Mc_s$, in the SOL: a fluid model [5] result designated as SOL.1:

$$M = (y/L_c - 1)^{-1} + [(y/L_c - 1)^{-2} - 1]^{1/2} \quad \text{and} \quad E(y) = \frac{T_B}{L_c} \frac{M(1 + M^2)}{1 - M^2}$$

and a linear model [6], designated as SOL.2:

$$M(y) = \frac{3\sqrt{\pi}}{4} (y/L_c - 1) \quad \text{and} \quad E(y) = \frac{T_B}{\pi L_c} (y/L_c - 1)$$

Results and Comments

1. Figure 2 shows the sizes of successive ionization clouds of carbon released near the limiter ($x_0 = +1$ cm, $y_0 = 0$) with launch velocity away from the limiter ($E_0 = 2$ eV). Figure 2a gives the x-integrated particle density profiles, Fig. 2b the y-integrated ones. Conditions: D^+ plasma, $n_B = 2\times10^{18}$ m^{-3}, $T_B = 50$ eV, $L_c = 40$ m, a = 1.2 m, $a_w = -1.3$ m, $D_\perp = 1$ m^2/s, no inward pinch, SOL.1.
2. Figure 3 assumes same plasma as Fig. 2 but with impurity ions launched at $x_0 = -1$ cm, i.e. within the scrape-off layer. The sink action of the limiter is clearly stronger than for $x_0 = +1$ cm. Figure 3a assumes SOL.1, Fig. 3b SOL.2.

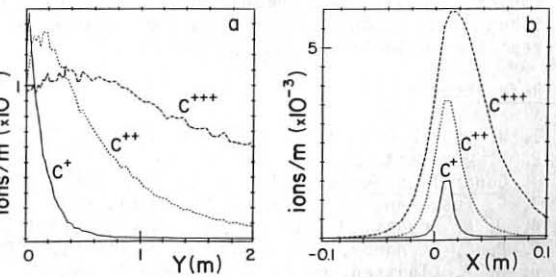

Fig. 2. Size of ionization clouds for release near limiter. (a) One half of profile along $\vec{B}$ (limiter is at y = 0), (b) cross-field profiles (last closed flux surface at x = 0). Plasma conditions specified in text. Ions launched at x = +1 cm.

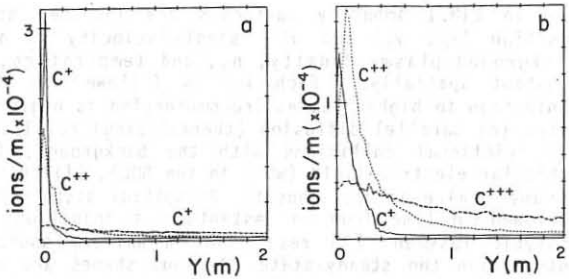

Fig. 3. Conditions as above but ions launched at x = -1 cm. (a) Same (nonlinear) SOL ambipolar field as in Fig. 2, i.e. SOL.1, (b) linear ambipolar field, i.e., SOL.2.

With regard to the relation between impurity influx and central impurity density a case is considered here which is sufficiently simplified that the Monte Carlo results can be compared with a simple analytic formulation. This serves both to test the code and to illustrate the method. More realistic cases will be reported later. Thus the following conditions are assumed: homogeneous influx ionized within SOL.2, $D_\perp = 0$, heating and diffusive collisions turned off, ionization to higher stages turned off. Friction with the plasma flow and the ambipolar field are included, $T_B = 50$ eV, $L_c = 40$ m. It can be shown [7] that for the SOL.2 E and v_B, $n_I(y) = \text{const.}$ and that the terminal impurity ion velocity for this case is

$$v_I(0) = \frac{L_c}{4\tau_s}\left[-1 + (1 + 8\alpha\,\tau_s^2)^{1/2}\right] \quad \text{with} \quad \alpha = \frac{\pi Z_I k T_B}{\pi m_I L_c^2} + \frac{3c_s}{4\sqrt{\pi}\,\tau_s L_c}$$

where τ_s is the C^+-D^+ stopping time. Thus $\tau_I = L_c/v_I(0)$ can be compared to the reference value $\tau_r = L_c/v_B(0)$ (= 0.44 ms for this case). Results are as shown in the table:

n_B (m^{-3})	Monte Carlo $v_I(0)$ (m/s)	Analytic Value $v_I(0)$ (m/s)	τ_I (ms)
2×10^{18}	3.26×10^4	3.18×10^4	1.23
2×10^{19}	6.78×10^4	6.5×10^4	0.59
2×10^{20}	8.81×10^4	8.7×10^4	0.45

Clearly for toroidally distributed ionization within the SOL the limiter sink action can be weaker than the reference value and thus the central impurity density will be higher than for the reference case. This must be taken into account when comparing limiter to wall influxes, as will be reported on subsequently.

References

1. W. Engelhardt and W. Feneberg, J. Nucl. Mater. 76 & 77 (1978), 518.
2. P. E. Post and K. Lackner in Physics of Plasma-Wall Interactions in Controlled Fusion, Eds. D. E. Post and R. Behrisch (Plenum Press, 1986).
3. G. Fussmann, Nucl. Fusion 25 (1986), 983.
4. J. N. Brooks, J. Nucl. Mater. 145-147 (1987), 837.
5. P. C. Stangeby, Physics Fluids 27 (1984), 2699.
6. H. A. Claassen and H. Repp, Nucl. Fusion 23 (1983), 597.
7. P. C. Stangeby, to be published.

Power Balance in the Bulk Plasma and in the Scrape-off Layer during H and L Mode Divertor Discharges in JET

H J Jaeckel[(a)], P J Harbour, N Gottardi,
E B Deksnis, P D Morgan, D D R Summers, J A Tagle
JET Joint Undertaking, Abingdon, Oxon OX14 3EA, United Kingdom
[(a)] *Permanent address : EURATOM-IPP Association, Garching, W. Germany*

Introduction – In JET a magnetic separatrix can be formed inside the vacuum vessel at plasma currents up to 3 MA with one ("single null", SN) or two ("double null", DN) stagnation points ("X-point") [1,2]. In SN discharges a transition from L- to H-mode has often been observed with neutral beam (NB) heating in the range 5–10 MW. A significant fraction of the total radiation power loss is dissipated from the the X-point region(s). Using bolometer measurements an attempt is made to estimate the power radiated from the confinement region and the divertor region(s). The radial emissivity profiles of the confined plasma show broad radiation shells during the H-mode. The poloidal distribution of the radiation flux near the X-point is compared with the poloidal distribution of the D_α emission. The power flow to the divertor target tiles is estimated using infrared thermography. The occurence of the H-mode appears to be related to the heating of the plasma edge.

Experimental Setup: The relationship between the JET X-point null, the divertor target tiles and the relevant diagnostics is shown in Fig. 1 in plan view. The eight sets of carbon target tiles were installed as protective tiles for the octant joints.

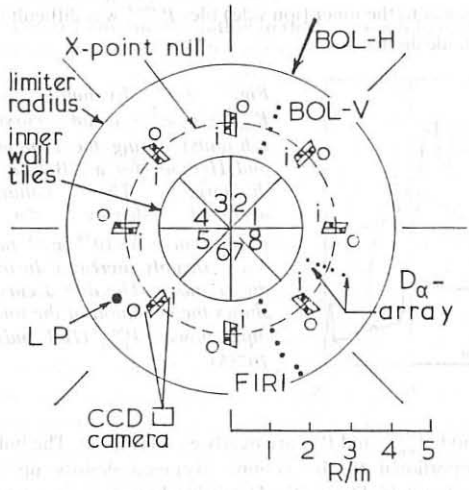

Fig. 1 : Schematic plan-view of the JET vacuum vessel showing the relationship of the diagnostics to the eight sets of divertor target tiles. The scrape-off layer impinges at a glancing angle of 9.5 ° on an outer (o) and an inner (i) location of each set. The horizontal (BOL-H) and vertical (BOL-V) bolometer cameras, the D_α array, the far infrared interferometer (FIRI) and the moveable Langmuir probe (LP) are all located in mid-octant as shown. The CCD camera, mounted midplane, views directly the top target tiles on octant joint 5/6.

The total radiation power is measured by two bolometer camera systems, located in mid-octant, one horizontal the other vertical [3]. Camera chords looking into the X-point regions at the top and/or the bottom of the plasma show enhanced radiation. The detection range of the bolometers is $3 \leq E_{ph}[eV] \leq 9000$, so that all radiation which might contribute substantially to the total power loss is detected. By choosing channels not affected by the X-point radiation and assuming toroidal symmetry one can estimate the radiation P_{rad}^{bulk} from

the bulk plasma (confinement region). The radiation from the X-point region P_{rad}^{xp} is defined as $P_{rad}^{xp} = P_{rad}^{tot} - P_{rad}^{bulk}$. Fig 2 shows P_{rad}^{bulk}, P_{rad}^{tot} and P_{rad}^{xp} for a discharge with H-mode.

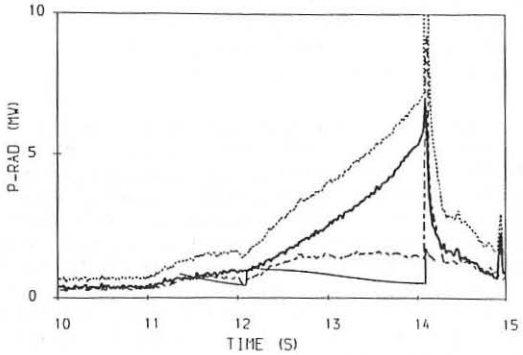

Fig. 2 : Radiation power P_{rad}^{bulk} (bold solid curve), P_{rad}^{xp} (dash-dotted) and P_{rad}^{tot} (dotted) for a SN-discharge with H-mode from 12 to 14.1 s (JET pulse 10755). Also shown is the power flow to the outer divertor target P_t^{outer} (thin solid curve).

One set of target tiles is viewed directly with an infrared CCD camera (Fig.1), filtered to be sensitive from 0.98 – 1.02 μm. For many pulses the camera had insufficient dynamic range to measure the surface temperature of the tiles ($\leq 1800\ ^\circ C$) throughout the pulse. However it has been possible to estimate both the power flux to the outer (electron side) tiles P_t^{outer} (Fig. 2), and the area of the SOL. The power to the inner (ion side) tiles P_t^{inner} was difficult to estimate but it was $\leq P_t^{outer}/2$ in all H-mode discharges.

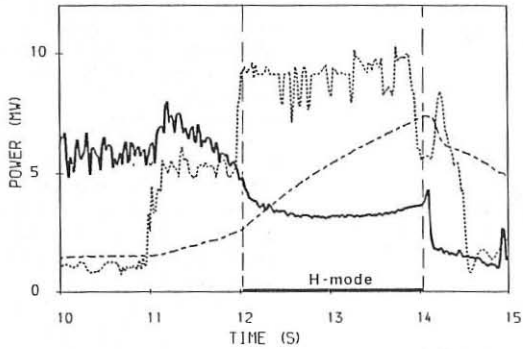

Fig. 3 : Evolution of $P_{rad}^{bulk}/<n_e>^2$ (solid curve; arb.units) during the L-mode and H-mode for a NB-heated discharge. The volume averaged density $<n_e>$ (dash-dotted; $6\times10^{19}\ m^{-3}$ full scale) steadily increases during the H-mode. The dotted curve shows the evolution of the total input power, P_{heat}^{tot} (JET pulse 10755).

Bulk Radiation Loss: During the L-mode P_{rad}^{bulk} and P_{rad}^{xp} are nearly equal (Fig. 2). The bulk radiation power is about linearly proportional to the volume averaged density up to $<n_e> \leq 1.5\times10^{19}\ m^{-3}$, achieved in the L-mode. During the H-mode when $<n_e>$ increases steadily up to $\leq 4\times10^{19}\ m^{-3}$ a strong increase in P_{rad}^{bulk} is observed, roughly proportional to $<n_e>^2$ in pure NB heated discharges (Fig. 3). Disregarding changes in temperature and in profiles of density and of impurities this implies constant impurity concentration. In the few cases when the H-mode was sustained for some time with the addition of slight RF-heating ($P_{ICRH} \leq 2\ MW$) a more rapid increase of P_{rad}^{bulk} with $<n_e>$ was observed.

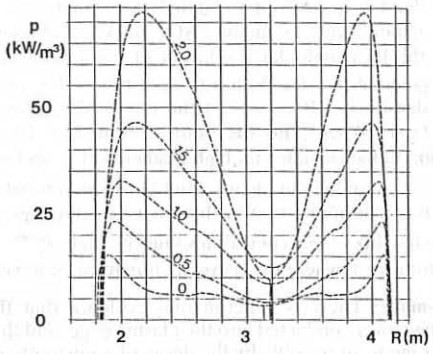

Fig. 4 : Evolution of the radial emissivity profile during the H-mode. Although the main impurity species are carbon and oxygen, very broad radiation shells are observed. The number at each curve gives the time of the profile with respect to the start of the H-mode. Curve 0 shows the profile during the preceding L-mode (JET pulse 10755).

The dominant impurities in purely NB heated discharges are carbon and oxygen; metals are negligible [4]. Radial emissivity profiles derived from the bolometer measurements show a radiation shell much broader than predicted by coronal equilibrium. Furthermore the width of the radiating shell broadens during the H-mode although the plasma density in the outer region grows faster than in the centre. This behaviour is not understood at present. Fig. 4 shows the evolution of radiation emissivity profiles during one of the longest H-modes ($\sim 2.1\ s$) achieved so far in JET.

Power Flow and Radiation in the Scrape-off Layer: The power conducted into the SOL (the heating power of the SOL) is given by

$$P_{heat}^{SOL} = P_{heat}^{tot} - dW_p/dt - P_{rad}^{bulk} - P_{cx}^{bulk} .$$

The charge exchange losses P_{cx}^{bulk} are not measured and are neglected thus overestimating P_{heat}^{SOL} which is typically 40 to 60 % of P_{heat}^{tot} and does not vary significantly during the H-mode. The power loss from the SOL is given by

$$P_{loss}^{SOL} = P_{rad}^{xp} + P_t^{inner} + P_t^{outer} + P_{cx}^{SOL} + P_{cx}^{xp} + P^{lim} .$$

An upper bound for the charge exchange loss may be estimated, using the measured D_α-influx from the walls ($\leq 10^{22}\ s^{-1}$), to be $P_{cx}^{SOL} \leq 0.3\ MW$; P_{cx}^{xp} is estimated to be smaller. Using data from the Langmuir probes the power conducted to the limiters and wall, P^{lim}, is negligible. The largest power losses measured from the SOL are by radiation and conduction to the target tiles, and these are maintained during the H-mode, in contrast to observation in ASDEX [6]. At the onset of the H-mode in JET, P_{rad}^{xp} usually decreases suddenly and then increases with $<n_e>$ until it reaches ~ 15% of P_{heat}^{tot} and then becomes stationary, although both $<n_e>$ and P_{rad}^{bulk} grow steadily. In contrast P_t^{outer} appears to show an increase to about 15% of P_{heat}^{tot} at the onset of the H-mode and then decreases to ~10% before termination. Immediately after the H-mode is terminated, there is a remarkable increase in P_{rad}^{xp}, P_t^{outer} and P_{heat}^{SOL} (Fig. 2) for ≤ 40 ms. The poloidal distribution of P_{rad}^{xp} shows a maximum at the inner wall side of the X-point in its immediate vicinity (Fig.5). This distribution deviates appreciably from the D_α distribution [5] indicating that Lyman-α emission (to which the bolometers are still sensitive) only partially accounts for the observed emissivity. With carbon target tiles, C is expected to be mainly responsible for the radiation loss in the divertor region. The observed maximum mean emissivities lie between 1 and 5 $MW\ m^{-3}$. An estimate on the basis of coronal equilibrium gives the lower limit of the possible carbon

concentration, showing that it must be at least 5 to 10% at (assumed) local densities of $5\times10^{19}\ m^{-3}$ to account for the observed radiation levels, assuming a SOL thickness of about 2 cm at the maximum of P_{rad}^{xp}. However the local poloidal resolution of the bolometers ($\sim 0.4\ m$) may lead to a flattening of the poloidal profile. With a steeper profile the peak emissivity may be larger, suggesting local densities $\leq 10^{20}\ m^{-3}$ at the target tiles. This is consistent with the observed power flux ($\leq 1\ kW\ cm^{-2}$)to the outer tiles if $T_e \leq 10\ eV$ locally. The fast poloidal decay of the X-point radiation indicates high gradients of T_e and n_e, as have been observed in other tokamaks [6,7]. These high gradients would be more probable with the higher value of n_e ($10^{20} m^{-3}$). It is worth noting that in the inner divertor region, where P_{rad}^{xp} and D_α radiation are high and so the flux of recycling atoms must be high, P_t^{inner} is low. The opposite is true in the outer divertor region where the recycling flux must be lower.

Triggering and Termination of the H-mode: There is experimental evidence that the H-mode is triggered by increasing the heating power conducted into the plasma edge, and that this can be achieved by increasing the power input, or possibly by the decay of a sawtooth, or alternatively by decreasing the edge radiation loss by reducing local impurity sources. At present it is not quite clear if an increase of P_{heat}^{SOL} triggers the L/H-transition. In many cases an increase of P_{heat}^{SOL} preceded an H-mode but there were also cases observed where the H-mode was achieved at constant P_{heat}^{SOL}. Apart from those cases where the additional heating power was switched off the termination of the H-mode always occured when $P_{rad}^{bulk}/P_{heat}^{tot}$ reached about 60%.

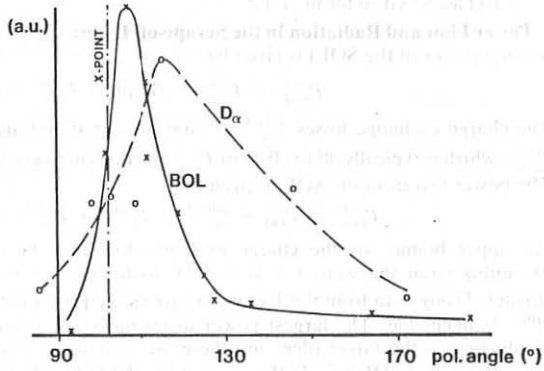

Fig. 5 : Poloidal distribution of P_{rad}^{xp} and of the D_α radiation in the X-point region. The graph covers the upper half of the plasma cross section for a SN discharge (JET pulse 10755) during the H-mode ($\theta = 0$ at the outer midplane).

References

[1] A Tanga et al., Proc. 12th European Conf. on Contr. Fus. and Plasma Phys., Vol I P 267, Budapest 1985

[2] A Tanga et al., Proc. 11th Int. Conf. on Plasma Phys. and Contr. Nucl. Fus. Res., Kyoto, IAEA-CN-47/I-6, (1986)

[3] K F Mast and H Krause, Rev. Sci. Instr. 56(5)(1985)969

[4] B Denne et al., this conference

[5] P D Morgan et al., this conference

[6] F Wagner, M Keilhacker et al., J. Nucl. Mat. 121(1984)103

[7] S Sengoku et al., Nucl. Fusion 24(1984)415

BEHAVIOUR OF PARTICLE INFLUXES AND EDGE RECYCLING DURING ICRF HEATING ON JET

M. Bureš, V.P. Bhatnagar*, M.P. Evrard*, A. Gondhalekar, J. Jacquinot, T.T.C. Jones, P.D. Morgan, D.F.H. Start

JET Joint Undertaking, Abingdon, Oxon, OX14 3EA, UK
* LLP-ERM/KMS; EUR-EB Association, 1040 Brussels, Belgium

INTRODUCTION

During ICRF heating in JET, the main species and the impurity neutral influxes always increase. The magnitude of influxes and also the density increase is proportional to the RF power. The important parameter is the number of neutral atoms available for desorption from the wall and limiters. This depends strongly on the conditioning of the vessel and after glow discharge cleaning or carbonisation the neutral influxes are substantially enhanced. The global particle confinement, which is the ratio of the electron content and the total influxes, is thus always decreasing with the input power.

The density evolution is appropriately described by the incremental confinement time τ_p^{RF} of the additional density and by the time dependent additional influxes $\Delta\phi^{\perp}$.

NEUTRAL INFLUXES AND DENSITY EVOLUTION

The neutrals are released typically with two time scales. The flux from the wall is seen to rise rapidly ($\tau \lesssim 10$ msec). The flux from the

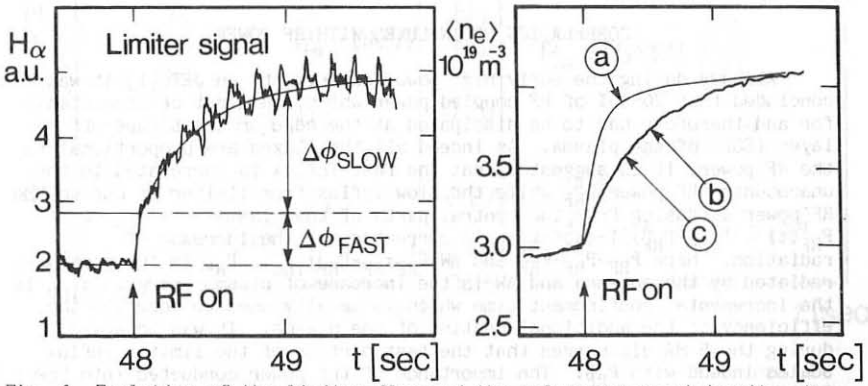

Fig. 1 Evolution of the limiter flux and the volume averaged density at the onset of the RF power. (c) and (b) curves represent the measured and simulated (eq. 1) density traces. Curve (a) shows the evolution if the total neutral influx is assumed to vary as a step function.

limiter also rises rapidly but its final value approaches on approximately the confinement time scale for energy. An example of limiter flux is shown in Fig 1.

The fast flux from the wall is ≈ 40% of the fast limiter flux. The particle balance then becomes

$$\dot{N} + \frac{N}{\tau_p^{RF}} = \Delta\phi^T = \Delta\phi \left(1 + \frac{Z_{eff} - 1}{Z_I + 1 - Z_{eff}}\right) [s^{-1}] .$$

$\Delta\phi = \Delta\phi_F + \Delta\phi_S$ are the particle fluxes deduced from the absolute H_α measurements. The typical values of Z_{eff} measured by the visible bremsstrahlung are in the range 2.5 - 3.5. $Z_I = 7$ is assumed in simulation, which represents well the JET dataset on Z_{eff}. Assuming the fast flux to vary as a step function and taking $\Delta\phi_S(t) = \Delta\phi_S(1-\exp(-t/\tau_1))$ the evolution of the total electron content from the ohmic value can be expressed

$$N(t)=\Delta\phi^T\tau_p^{RF}(1-\exp(-t/\tau_p^{RF}))-\Delta\phi_S^T\tau_p^{RF}\tau_1(\exp(-t/\tau_p^{RF})-\exp(-t/\tau_1))\ /(\tau_p^{RF}-\tau_1) \quad (1)$$

Here $\tau_p^{RF} = \Delta N/\Delta\phi^T$. The measured and calculated densities are shown in Fig 1, curves c and b. We conclude that the density evolution is determined not only by the confinement time τ_p^{RF} but also by the evolution of fluxes. Eq. 1 can be used to define the recycling coefficient $R = \frac{\Delta\phi(t)}{N(t)/\tau_p^{RF}}$. It always increases at the onset of RF power indicating a rapid neutral desorption. The importance of the flux evolution for the density build-up is also observed in cases where the RF power is ramped up. Correspondingly the influxes become slower and the density build-up longer.

CORRELATION OF INFLUXES WITH RF POWER

Already during the early high power experiments on JET [1] it was concluded that 20-30% of RF coupled power which could not be accounted for and therefore had to be dissipated at the edge or the scrape-off layer (SOL) of the plasma. As indeed all the fluxes are proportional to the RF power, it is suggested that the fast influx is correlated to the unaccounted RF power P_{RF}^A while the slow influx from limiter is due to the RF power diffusing from the central parts of the plasma $P_{RF}^I(t) = (P_{RF}-P_{RF}^A)(1-\exp(-t/\tau_{RF}))$ corrected for the increase of radiation. Here $P_{RF}=P_{RF}^I+P_{RF}^A$ and $\Delta W=P_{RF}\tau_{RF}=P_{RF}\tau_{inc}$. P_{RF} is the power radiated by the antenna and ΔW is the increase of plasma energy. τ_{inc} is the incremental confinement time which is usually used to describe the efficiency of the additional heating of the plasma. It was observed during the 5 MA discharges that the fast portion of the limiter influx scales indeed with P_{RF}^A. The importance of the power conducted into the SOL is shown in Fig 2. The influx from the limiter is not proportional to the plasma density, as observed in OH cases [2].

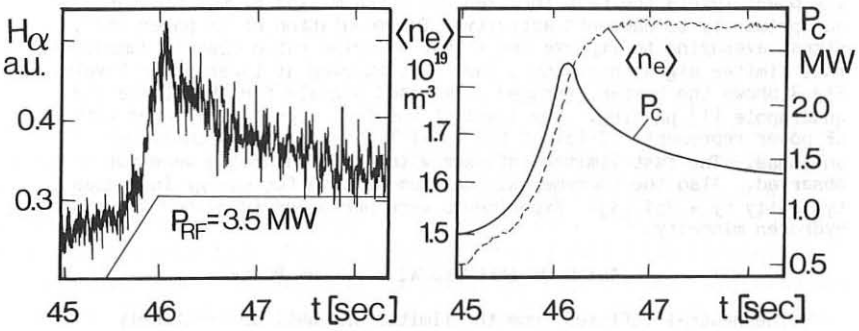

Fig. 2 Time evolution of the conducted power into the SOL, H_α signal from limiter and the average density.

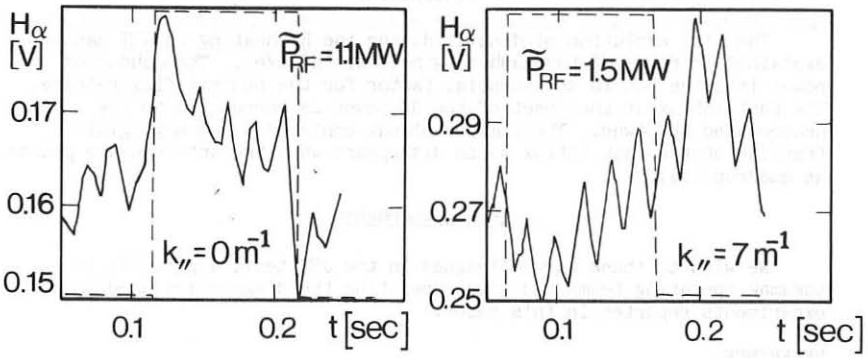

Fig. 3 Boxcar averaged limiter flux signal with the RF power modulated by 5 Hz in D(H) scenario. The signals are shown for the cases of the dipole and quadrupole phasing of the antennae.

EFFECTS OF THE ANTENNA PHASING

The 5 MA high RF power discharges show the fast limiter influx. At low power levels the fast influxes are often masked by the fluctuations due primarily to sawteeth activity. The modulation of RF power and signal averaging to improve the signal to noise ratio clearly demonstrate that limiter signal contains a fast portion even at lower power levels. Fig 3 shows the boxcar averaged normalised signals for the dipole and quadrupole [1] phasing. The level of the fast signal correlated with the RF power represents 10-15% of the total limiter signal with dipole antennae. The fast limiter influxes with the quadrupoles were not observed. Also the incremental confinement time for energy increases typically by ≈ 25% [3]. Experiments were performed in deuterium with the hydrogen minority.

SCALING OF INFLUXES WITH THE RF POWER

The neutral influxes from the limiter and wall are routinely measured on JET. The main results of scaling with the power in RF equilibrium can be summarised as follows:

(a) both limiter and wall influxes increase roughly linearly with the RF power up to the maximum levels achieved so far, $P_{RF} \approx 8$ MW.

(b) the density increase is correspondingly also linear, except for the lower power levels, where it increases faster.

(c) the ratio of wall to limiter flux scales with the plasma current and is independent of the RF power in accordance with the expected evolution of the SOL profiles.

CONCLUSIONS

The time evolution of density during the RF heating on JET can be explained in terms of fast and slow neutral influxes. The conducted power into the SOL is an essential factor for the neutral flux release. The fast influx at the onset of the RF power is correlated to the unaccounted RF power. The limiter signal contains a non-negligible fraction of the fast influx which disappears when the antennae are phased as quadrupoles.

ACKNOWLEDGEMENTS

We wish to thank our colleagues in the JET team, especially the tokamak operating teams and those operating the diagnostics used in the experiments reported in this paper.

REFERENCES

[1] J. Jacquinot et al, Plasma Phys. and Contr. Fusion, Vol. 28, No 1A, pp.1-15, 1986

[2] P. Morgan et al, 12th Europ. Conf. on Contr. Fusion and Plasma Phys., Budapest 1985, Vol. 9F, Part II, p. 535

[3] M. Bureš et al, submitted for publication.

THE CALCULATION OF A NONEQULIBRIUM ION DISTRIBUTION FUNCTION NEAR A LIMITER

T.F.Volkov, Yu.L. Igitkhanov
I.V.Kurchatov Institute of Atomic Energy
Moscow

Abstract

A distribution function of ions outcoming from plasmas near divertor plates or limiter is essentially non-equlibrium one due to a surface absorption of ions and charge exchange collisions with neutral atoms. For diagnostic purposes it is important to know the real ion distribution function because the value of a saturation current for probe measurments is determined by the ion distribution function. The calculations show that there is a deple tion of ion distribution function comparatively to equlibrium one in high energy range due to escape of ions to the wall. This deple tion leads to the fact that the averange energy of ion incoming to the wall appears less than 2T. The dependence of the charge exchange rate upon the relative velocity leads also to the depletion in a high energy range and to the enrichment in a low energy range.The last effect is proportional to the neutral atom concentration near the limiter (or divertor plate). The heat flux is calculated from the obtained ion distribution function. The momentum fluxes for ion and neutral components at the plasma surface are calculated.

ON RADIATION TRANSPORT IN SUPERHIGH DENSITY OPERATION OF DIVERTOR IN TOKAMAK-REACTOR.

Krasheninnikov S.I., Pigarov A.Yu.

In [1] it has been shown that with a rise in plasma density at the separatrix N_s up to $\sim 2 \cdot 10^{20} m^{-3}$, the plasma temperature in the neighbourhood of divertor plates drops to ≤ 1 eV and a complete, volumetric plasma recombination occurs. In this case, the energy flux onto the plate is transferred by radiation, the spectrum of which is determined by the parameters of a plasma in the local thermodynamical equilibrium. In [1] the radiation transport effect L_α is neglected. Therefore the results obtained there are top estimates. The account of L_α-transport allows to make the conditions for the divertor operation close to that of a gaseous blanket much softer and studied in a given paper. A kinetic equation for the intensity of radiation $I(\vec{\Omega}, \omega)$ in the L_α-line and the heat conduction equation are solved:

$$\partial I(\vec{\Omega}, \omega) / \partial s = - K'(\omega) \left[I(\vec{\Omega}, \omega) - I_p(\vec{\Omega}, \omega) \right]$$

$$C_p \frac{\partial T}{\partial t} = \frac{\partial}{\partial y} \varkappa_\Sigma \frac{\partial T}{\partial x} - Q_\alpha - Q_R - Q_h$$

where: $Q_\alpha = - \int d\vec{\Omega}\, d\omega\, K'(\omega) \left[I(\vec{\Omega}, \omega) - I_p(\vec{\Omega}, \omega) \right]$, Q_R, Q_h are the losses in recombination radiation and in the radiation of higher series; $\varkappa_\Sigma$ is the plasma heat conduction coefficient under pressure P; $K'(\omega)$ is the L_α-absorption coefficient. The plasma temperature in the neighbourhood of the plates (X=0)is considered to be equal 0.3 eV; the energy flux entering the zone of radiative losses $q_\infty = \varkappa_\Sigma \frac{dT}{dy} \Big|_{x \to \infty}$ is varied from 0.03 to 0.3 kW/cm^{-2}. The dependences of a conductive energy flux onto the divertor plates, q_d, on P and q_∞ are obtained.

1. Krasheninnikov S.I., Pigarov A.Yu. 11 Int. Conf. on Plasma Phys. and Contr. Nucl. Fusion Res., Kyoto, 13-20 nov. 1986, IAEA-CN-47/H-III-10.

INDIRECT STUDIES OF EROSION AND DEPOSITION ON GRAPHITE PROBES IN THE LIMITER SHADOW IN TOKAMAKS.

H. Bergsaker[♠], S. Nagata[▽], B. Emmoth[♠], J.P. Coad [◇] and P. Wienhold [♣].

[♠] Research Institute of Physics, S-104 05 Stockholm, Sweden

[▽] Department of Nuclear Engineering, Tohoku University, Sendai, Japan

[◇] JET Joint Undertaking, Abingdon, OX14 3EA, United Kingdom

[♣] Institut für Plasmaphysik, KFA, POB 1913, D-5170 Jülich, FRG

1. Introduction

A major part of both hydrogen recycling and impurity production in tokamaks takes place at limiters and other protruding structural parts which absorb high heat load and particle flux. Consequently, it is valuable to study how limiter surfaces are modified by the plasma, and to develop and test models which describe the actual surface conditions at limiters during tokamak operation and predict e.g. impurity source distributions. Erosion, deposition and hydrogen retention at graphite surfaces are of particular interest, since graphite is presently the preferred choice of limiter material.

As a part of the preliminary collector probe experiments at JET /1/, cylindrical probe shields of graphite, Inconel and shields which were made partly of graphite and partly of Inconel have been introduced in the limiter shadow and exposed to one or more discharges. A limiter-like graphite probe was moved into position 9 mm outside the main limiter in TEXTOR and exposed to eleven complete disharges. The surface composition of these various probes has been investigated afterwards, using ion beam analysis techniques.

This report shows that the amount of carbon which has been deposited by the plasma on the graphite probes can be indirectly determined from depth distributions of deuterium, oxygen and metals.

The lateral distribution of collected deuterium and impurities is related to the intensity of the plasma contact, and it is proposed that, within the frames of a simple model, this can be used to infer the relative importance of erosion and deposition, as a function of distance to the plasma edge.

2. Results and discussion.

Figure 1 shows an RBS spectrum from a graphite probe shield which has been exposed to five 10 s discharges in the limiter shadow at JET. The spectrum is from a point 60 mm outside the plasma edge. The spectrum (dots) indicates that an overlayer with more or less uniform composition has been deposited on top of the graphite substrate. The solid line in the figure is a theoretical spectrum, simulated for a hypothetical target

with a 165 nm thich layer of composition $C_{1.0}O_{0.04}D_{0.4}Cr_{0.002}Ni_{0.008}$, situated on top of a homogenous $C_{1.0}O_{0.001}Ni_{0.0005}$ bulk substrate. Depth profiles of deuterium from Nuclear Reaction Analysis likewise suggest a layer with more or less uniform hydrogen concentration. Deuterium or impurities which are implanted into graphite at energies which might be expected (in the lower 100 eV range) can not penetrate substantially below the surface, and are not expected to diffuse at low temperature. It thus appears that oxygen, metallic impurities and deuterium can be used as markers for carbon which has been deposited on the graphite surface. A second probe shield which was exposed at JET was made partly of graphite, partly of inconel. It was exposed to seven discharges, three of which were disruptive. Simulated RBS spectra were fitted to spectra from the graphite parts by adjusting the thickness of uniform carbon layers containing a few percent impurities. On the inconel parts the amount of carbon could be determined directly, by non-Rutherford proton backscattering. Figure 2 shows an example where the indirect determination of carbon deposition on graphite can be compared to carbon deposition on inconel substrate. The fact that there is a fairly smooth passage, going from one substrate to the other, supports the arguments where depth profiles were used. There is a comparatively small mismatch, in that the amount of carbon collected on graphite seems to be 20 - 100 percent higher than on inconel. However, the same discontinuity is visible in the areal density of deuterium, and it is likely that there is indeed smaller deposition of both carbon and deuterium on the inconel substrate. This could be due to higher backscattering, or lower sticking of molecular species. It may also have to do with a difference in surface roughness.

At the surface of limiters or probes which are large compared to the expected Larmor radii, it is reasonable to assume that plasma particles, heat and ionised impurities are transported macroscopically along the magnetic field lines. Insofar as erosion and deposition mechanisms are directly related to heat flux and ion impact, they are thus expected to increase monotonously with $|\cos\theta|$, where θ is the field inclination with respect to the surface normal. Due to the surface sheath potential, the microscopic angle of incidence of ions and electrons is expected to be rather weakly dependent on θ /2/, particularly at a rough surface. Apart from the θ-dependence, erosion and deposition at a probe which is inserted in a symmetrical environment should only be a function of the distance r to the plasma core. This suggests that interesting information may be gained from studying the results of plasma surface interaction at a probe where θ varies continously at constant r.

In the experiment at TEXTOR a graphite cylinder of 25 mm radius was used. At the end which was facing the plasma, the cylinder is terminated with a half-sphere with the same radius. With its cylinder axis along a tokamak minor radius, the probe was moved in stepwise, until the spherical tip reached a position 9 mm outside the main limiter position. At the intermediate positions between the wall and the final position,

it was exposed to eleven discharges, three of which were disruptive. It was then exposed at the final position to eleven discharges with 3 s duration, plus one disruption.

Figures 3 and 4 show the collected amounts of metals (Cr+Fe+Ni) and deuterium on the probe, at three different distances from the plasma. The angular coordinate is chosen such that the plasma contact is large at 90° (electron drift side) and 270° (ion drift side). The solid lines are least squares fits to the expression $c(r,\theta) = A(r)+B_1(r)\cdot f_1(\theta)+B_2(r)\cdot f_2(\theta)$, where $f_1(\theta) = |\cos\theta|$ on the ion drift side and zero on the electron drift side, and conversely for f_2. Apparently the distributions of collected material change from a $|\cos\theta|$ deposition pattern at 40 mm from the plasma to a more uniform distribution closer, at 16 mm outside the main limiter. In the case of deuterium, there is even an inversion, in the sence that there is at $r - a = 16$ mm a minimum where $|\cos\theta|$ is maximal on the electron drift side. The same behaviour is visible for oxygen (not shown).

The observed surface concentrations $c(r,\theta)$ must result from a balance between deposition and erosion. A simple, linearized balance equation may be written:

$$\frac{dc}{dt} = (D(r) - E(r)) \cdot |\cos\theta| - K(r) \cdot c \cdot |\cos\theta| \qquad (1)$$

The last term allows for erosion processes which may be proportional to the surface concentration, such as sputtering of a very thin layer, or particle induced detrapping and release of molecules. If $K = 0$, there will be an accumulation proportional to $|\cos\theta|$ at positions where $D > E$, and any initial surface concentration c_0 will be eroded where $D < E$ /3/. If $K > 0$ then:

$$c = (1 - e^{-K|\cos\theta|\cdot t}) \cdot (D - E)/K + c_0 e^{-K|\cos\theta|\cdot t}, \qquad (2)$$

which is initially a $|\cos\theta|$ distribution, but tends to become a uniform distribution when equilibrium is approached. In the present case, only the amplitude and not the width of the maxima in the angular distributions seems to change with r, suggesting an accumulative, rather than equilibrium behaviour. An initial areal density c_0 may have been deposited by disruptions while the probe was brought in. The fitting parameters B go negative at about $r - a = 22$ mm for both deuterium and oxygen, indicating that $D < E$. At the tip of the probe, where the areal density of metals is about a monolayer, the uniform distribution may possibly be an equilibrium distribution.

References.

/1/ H. Bergsaker, J P Coad, L de Kock et al. These Proc.

/2/ R. Chodura, J. Nucl. Mat. 111/112(1982)420.

/3/ G. McCracken,J. Ehrenberg,P. Stott et al., J. Nucl. Mat. 145-147(1987)621.

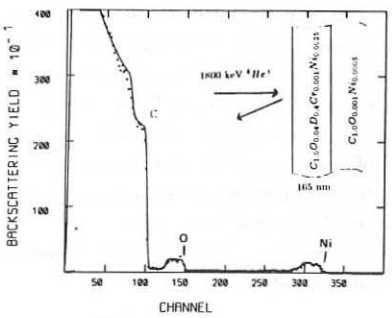

Figure 1.

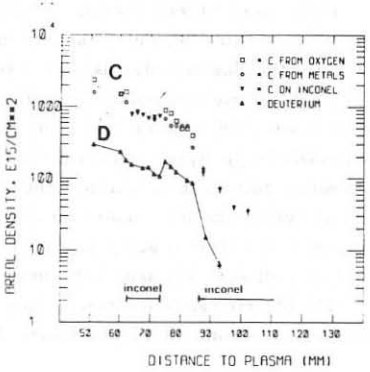

Figure 2.

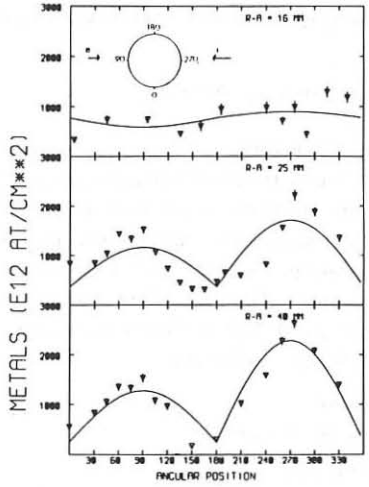

Figure 3.

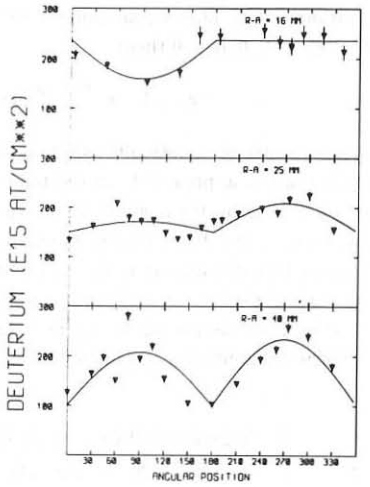

Figure 4.

PRELIMINARY MEASUREMENTS OF IMPURITY FLUXES USING TIME RESOLVED COLLECTOR PROBES IN JET

H Bergsaker*, J P Coad, L de Kock, B Emmoth*,
J Hancock, A Stevens and J Vince

JET Joint Undertaking, Abingdon, Oxon OX14 3EA, UK
* Research Institute of Physics, 10405 Stockholm 50, Sweden

1. INTRODUCTION

Two probe systems have been developed to collect impurities in the boundary region during selected tokamak pulses, the Fast Transfer System (FTS) which exposes probes near the outer midplane and the Plasma Boundary Probe System (PBPS) which inserts probes near the top of the vessel. The preliminary results of the first exposures with each of these systems are presented here, and the results are compared with Langmuir probe data obtained from similar shots.

2. EXPERIMENTAL

The PBPS is a vertical shaft mounted on top of the torus in Octant I, the probe entering the vessel at a major radius of 3.25 m, just outside the plasma centre (at 3.15 m). The probes are cylinders (initially of graphite) which can rotate within a carbon shield with two slits, one on the ion drift side and one on the electron drift side of the probe axis. Connection lengths on the electron drift side were about 9 metres, and on the ion drift side were about 60 metres, for the types of pulses considered below.

The first PBPS probe was exposed during shots 9657 to 9661 (inclusive). The shots were 3 MA, 2.8 T pulses, with 10 second flat tops. The plasma was in contact with the limiters during the flat-top, but was pushed onto the inner wall at the start of the rampdown. The probe did not rotate for pulse 9657, but for the others it rotated at constant angular velocity during 8 seconds of the flat top.

The FTS enters the torus horizontally 385 mm above the median plane, and uses the same collector probes as the PBPS. The connection length on the electron-drift side is 2.5 m to a graphite limiter in octant 6D, and on the ion-drift side is typically 55 to 80 metres if the field lines clear the inner wall, or 25 to 35 metres if they do not. The probe was exposed without rotation to eight 3 MA discharges (8927 to 8934), so that deposition only occurred under the two slits, whilst two other probes were exposed to single pulses when the collector was rotated throughout the pulse.

3. RESULTS

The analysis of the deposit in the flat-top region of the PBPS probe as a function of vertical distance from the plasma is shown in Fig. 1. The area analysed was exposed for a total of 2.2 secs(~ ½ sec from each of four discharges) approximately half way through the flat top period The observed amounts of deuterium, oxygen and metal (small amounts of the elements Cr, Fe and Ni are not separately resolvable by the technique

used, Rutherford Backscattering Spectroscopy) decrease exponentially with distance into the scrape-off layer (SOL). Careful analysis of the deposits on this probe, the first silicon probe and various shields indicates that the deuterium is not related to the incident deuterium flux, but to the amount of carbon collected. This conclusion is reached from analysis of the thicker deposits, eg. in the two slit images wherein deuterium and oxygen are found to be at a constant level of about 20 and 5% respectively, the remainder being carbon. Thus, the collected amounts of carbon, oxygen and metal impurities are at approximately, 20, 1 and 0.1% of the total ion fluence at a vertical distance of 64 mm from the plasma boundary, the flux being taken from Langmuir probe data measured for these shots. Also on figure 1 are shown as dashed lines similar plots of concentration versus distance from the plasma for the rampdown image. The distributions are much flatter than for the flat top and the amounts of deposit much larger.

The first probe exposed on the FTS was not rotated so gave integrated data from eight similar discharges. It showed much greater amounts of deposition on the ion drift side than on the electron-drift side, so the latter is probably affected by the short connection length. To gain more direct information on the relative amounts of carbon and deuterium collected in the SOL, the second probe exposed on the FTS was made from silicon (the collector) and inconel (the shield). The probe was rotated throughout a single 5 MA pulse(10903) in a step-wise manner, each point being exposed for 1.33 seconds. Figure 2 shows the analyses of deuterium and carbon as a function of distance from the plasma from a part of the collector exposed to the ion-drift direction at the beginning of the flat-top: the amount of deuterium is approximately a constant fraction of the amount of carbon (at 25 to 30%). The metal impurity levels are a similar proportion of the deuterium concentration to that found on carbon probes, but at these low levels could also be influenced by local sputtering from the sides of the inconel shield. On this probe the greatest deuterium and carbon levels were found on areas exposed during the flat-top, the levels falling away from these values in both the ramp-up and ramp-down phases. If the Langmuir probe data recorded much nearer the plasma boundary at the midplane are extrapolated to this distance from the boundary they suggest the ion saturation current is similar to the deposition rate of carbon as deduced from figure 2. Clearly there is an inconsistency here which requires elucidation.

The last rotating collector probe to be exposed in 1986 was exposed using the FTS to a 2 MA plasma (flat-top from 45 to 55 secs) with 4 MW of auxiliary RF heating from 48 to 51.5 seconds (shot 11149). Carbon and deuterium concentrations found on the collector 66 mm from the plasma boundary as a function of time in the pulse are shown in Figure 3. The area was exposed through the ion-side slit and each point was exposed for 1.33 secs. Prior to rotation during shot 11149 the probe was parked in position in the torus during shots 11143 to 11148 (some of which disrupted). Thus deposits accumulated at the zero positions during these pulses, which accounts for the high apparent levels near 40 and 60 seconds in Fig. 4 (the image points for the ion and electron-side slits, respectively). Although there is some scatter in the data, the carbon level is higher than the deuterium level as usual except during the period of RF heating. During RF heating the deuterium level greatly

increases (by a factor of about 10) and then clearly exceeds the carbon concentration, which only increases marginally. Langmuir probe data (') suggest that closer to the plasma the ion density increases and the ion temperature does not fall off as rapidly as one moves out into the SOL during RF heating. If the Langmuir probe data is extrapolated to 66 mm from the boundary (ie. the distance at which the data of Fig. 3 is taken) then one might expect a greater ion (deuterium) flux and temperatures of ~ 20 eV rather than ~ 5 eV.

4. DISCUSSION

During the flat top phases impurity fluxes decrease radially into the SOL with e-folding lengths of typically 10-20 mm. Differences in folding lengths have been observed between carbon (as inferred from deuterium where necessary) and other impurities (oxygen and metals), and between ion side and electron side. However, not enough measurements have been made to be sure these differences are systematic, and connection length effects have not been evaluated. A clearly different folding length was observed during rampdown (combined with moving to the inner wall) using the PBPS. As two probes exposed using the FTS have not shown such effects during simple rampdowns, it seems reasonable to assume a strong flux of carbon which is almost constant in the region probed (from 60 to 120 mm vertically above the plasma) associated with the move to the inner wall. This may be of relevance to the phenomena of "wall pumping" and will be investigated further.

For all the probes exposed during ohmic heating there is no evidence of implantation of deuterium into the probes. All the deuterium levels observed can be explained by trapping within the associated carbon deposits, for example by co-deposition, and in many cases the deuterium concentrations are too high to have occurred by implantation. The situation during RF heating is totally different, however. The deuterium concentration suddenly increases and exceeds the carbon level while the RF heating is on. The majority of this deuterium must be implanted into the silicon substrate, or else be combined on the surface with some element which is undetected. In order to implant ~ 2.5 x 10^{16} atoms cm^{-2} of deuterium at the fluence of ~ 10^{18} atoms cm^{-2} predicted from Langmuir probe data, an ion temperature of 30-50 eV is required, assuming a Maxwellian distribution, or an ion energy of ~ 180 eV for monoenergetic ions ([2],[3]). During ICRH the predicted average ion temperature is ~ 20 eV at 66 mm from the boundary, so average ion energies of ~ 80 to ~ 120 eV might be expected, allowing for the sheath potential ("): this approaches the order of magnitude needed and the energies deep in the boundary may be sufficient to explain the implantation observed.

5. CONCLUSIONS

Four collector probes were exposed using either the PBPS or FTS systems at JET towards the end of the 1986 campaign, of which three gave time-resolved information. As a variety of plasma parameters and conditions were involved, the results merely provide a foretaste of the information that may be gained in more comprehensive studies.

It is already clear that important information can be obtained relating to wall pumping, connection lengths, diffusion and RF heating effects in the SOL.

ACKNOWLEDGEMENTS

The authors are indebted to D Wilson, M Green and K Slavin for software support, the Culham and GEC staff involved in the installation of the FTS, the JET teams which provide technical support and the JET operations team who permitted exposure of the probes. The probes were designed by C Dorn and J Ehrenberg (Max-Planck Institut für Plasmaphysik, 8046 Garching-bei-München, FRG).

REFERENCES

1. S K Erents, J A Tagle et al, J Nuclear Materials, 145-147 (1987) 231.
2. G Staudenmaier et al, J Nuclear Materials 84 (1979) 149.
3. S Cohen and G McCracken, ibid, p157.
4. R Chodura, J Nuclear Materials 111 and 112 (1982) 420.

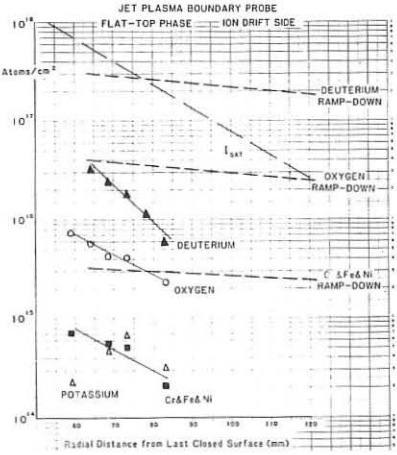

Fig. 1 PBPS probe results.

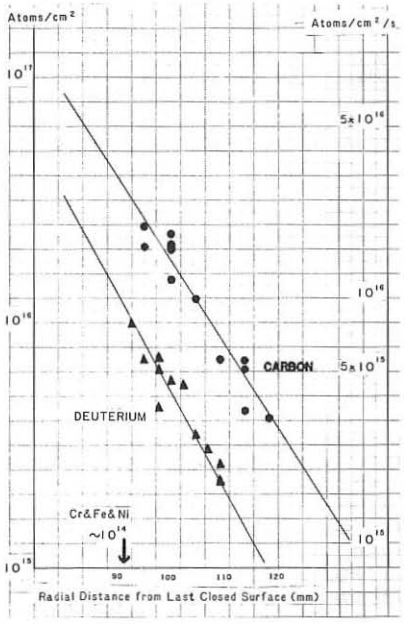

Fig. 2 D and C during a 5 MA flat top.

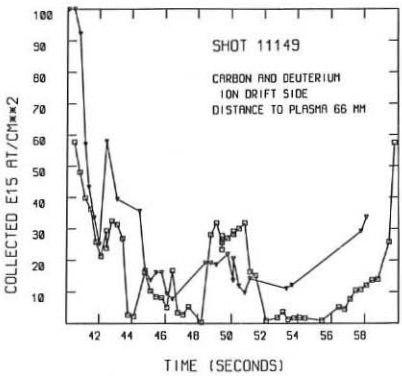

Fig. 3 D and C during an RF heated discharge.

OBSERVATIONS OF NON-AMBIPOLAR FLOW TO LIMITERS IN THE DITE TOKAMAK

C S Pitcher*, D H J Goodall, G F Matthews, G M McCracken, P C Stangeby*
Euratom/UKAEA Fusion Association
Culham Laboratory, UKAEA, Abingdon, Oxon. OX14 3DB
* Institute for Aerospace Studies, University of Toronto, Canada

1. Introduction

It is normally assumed in tokamaks that plasma flow to limiters and divertor plates is both globally and locally ambipolar in nature. Although global ambipolarity is required for charge conservation no equivalent restriction is placed on local particle fluxes. Local deviations from ambipolar conditions, if they exist, could significantly change the power and particle fluxes incident on limiters/divertor plates. In this paper we present experimental evidence of significant local non-ambipolar effects observed for limiters in the DITE tokamak.

2. Experiment

Experiments are performed with a movable graphite probe limiter (PL) in ohmically-heated DITE discharges, fig. 1 [1]. Four built-in Langmuir probes are voltage scanned with respect to the PL body, which electrically floats with respect to the main fixed limiter. The fixed limiter defines a circular plasma of nominal radius a = 26.0 cm and the PL is moved between discharges from a minor radius r_{PL} = 27.5 cm to r_{PL} = 22.5 cm, entering from the top of the machine. In addition to the built-in Langmuir probes the PL is diagnosed with an infra-red (IR) camera and a CCD camera.

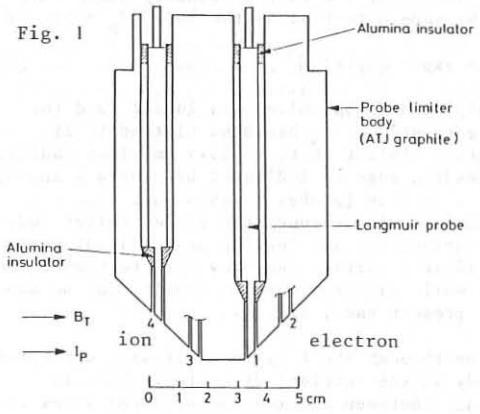

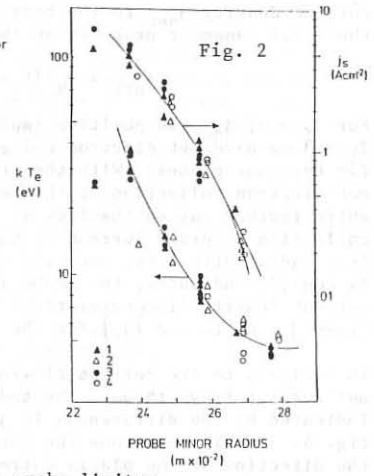

Fig. 1 Toroidal cross-section through the probe limiter.
Fig. 2 Incident plasma conditions as a function of Langmuir probe radius.

3. Results

The experiments are performed in deuterium discharges with a plasma current I_p = 150 kA, toroidal field B_t = 2T, a line average density $\bar{n}_e \sim 3 \times 10^{19}\ m^{-3}$, a loop voltage V_ℓ = 2.7 V, approximately 75% radiated power and a central electron temperature of $T_e(0) \sim 700$ eV. Langmuir probe data is fitted to a simple characteristic for the current density j [2]

$$j = j_s \left[1 - \exp\left(\frac{e(\Phi_p - \Phi_f)}{kT_e}\right)\right] \qquad (1)$$

where j_s is the ion saturation current density, Φ_p the probe voltage and Φ_f the floating voltage. Plotted in fig. 2 are the results for j_s and T_e obtained by the four probes during the current flat-top (t = 375 ms) as functions of the radial position of the particular Langmuir probe. At minor radii less than 26 cm, eg, inside the fixed limiter, probes on the electron drift side (1 and 2) agree with those on the ion drift side (3 and 4). In addition, the inner probes (1 and 3) agree with the outer probes (2 and 4) for the same radial position. The latter agreement indicates that insertion of the probe limiter into the plasma is not significantly altering the edge conditions further out. In addition to the values of j_s and T_e, data for Φ_f and the body potential Φ_{PL} are taken (fig. 3). As the probe limiter is pushed in, the body floats negative with respect to the torus, while the inner probes (1 and 3) float negative with respect to the body and the outer probes (2 and 4) float positive. With the probe limiter at $r_{PL} > 26$ cm the body and probes float at approximately the fixed limiter potential.

The fact that the probes do not float with the probe limiter body (eg, $\Phi_f \neq 0$) means that net current is flowing into the body. The local net current density j_{net} to the body is simply the current density drawn when the local Langmuir probe is at the same potential as the body ($\Phi_p = 0$), eg

$$j_{net} = j_s \left[1 - \exp(-e\Phi_f/kT_e)\right] \qquad (2)$$

For $\Phi_f > 0$, j_{net} is positive implying net ion collection locally and for $\Phi_f < 0$ we have net electron collection; j_{net}/j_s has been plotted in fig. 4 for the four probes. With the probe limiter at $r_{PL} \sim 23.5$ cm minor radius, net electron collection at the leading edge is indicated by probes 1 and 3, while farther out on the body at r ~ 25 cm (probes 2 and 4) net ion collection occurs. Current is thus flowing through the probe limiter body in a radial direction, entering further out and leaving at the leading edge. As eqn.(2) indicates, the probe limiter surface can draw no more than j_s ion current density (ion saturation) while electron current density can be many times j_s, up to $\sim 2\,|j_s|$ for the present case, fig. 4.

In addition to the current flowing through the body in the radial direction, net current flows through the body in the toroidal direction. This is indicated by the differences in j_{net} between the ion and electron sides in fig. 4. At all positions the toroidal currents within the limiter flow in the direction of the plasma current. This was also observed in T10 [3].

4. Effect on Power Density and Sputtering: IR and CCD Cameras

Although the non-ambipolar flow to the probe limiter has little effect on the ion flux, it does however affect the sheath potential and thus, the power flux and sputtering. The Langmuir probe measurements are correlated with the IR camera (for the power) and CCD camera measurements of CI emission (for the sputtering), table 1. While the plasma conditions (j_s,T_e) are symmetric on the two sides, significantly different electron currents ($j_e = j_s - j_{net}$) are drawn. The sheath potential and the power densities (P_e, P_i) are calculated using

$$\left|\Phi_s\right|^{i,e} = \left|\Phi_s^{amb}\right| + \Phi_f^{i,e} \tag{4}$$

$$P_e = \frac{2kT_e}{e}\ (1 - \gamma_e)^{-1}\ j_e \tag{5}$$

$$P_i = (\frac{2kT_e}{e} - \Phi_s)\ j_s \tag{6}$$

neglecting particle energy reflection and assuming $T_i = T_e$, $Z = 1$. Φ_s^{amb} has been calculated using secondary electron emission data from Woods et al [6] for tokamak-exposed graphite ($\gamma_e \approx 0.5$). The resulting total power P_{tot} is significantly enhanced on the electron side and this agrees well with the IR camera measurements. The larger sheath voltage on the ion side results in enhanced sputtering and this is in qualitative agreement with the CI emission which is $\sim 40\%$ more intense. As expected from the probe measurements, the D_α emission is symmetric on the two sides. On both sides of the leading edge the sheath voltage is, in relative terms, reduced compared with further out on the body. This enhances the power flux at the leading edge but reduces the sputtering.

5. Conclusions

Strong non-ambipolar flow to a probe limiter is observed which is in qualitative agreement with a simple model. Toroidal currents are apparently driven through the limiter by the toroidal electric field while radial currents flow because the limiter is in contact with a spatially varying plasma. Similar observations have been made for the larger ICL limiter [7] to be discussed in a later paper [5]. The general effects associated with the currents are, in the case of the toroidal current, to enhance power and suppress sputtering for the electron side relative to the ion side, and in the case of the radial current, leading edge sputtering is reduced but power flux is enhanced.

References

1. C S Pitcher et al, Nucl Fusion 26 (1986) 1641.
2. P C Stangeby, J Phys D: Appl Phys 15 (1982) 1007.
3. V A Vershkov et al, J Nucl Mat 145-147 (1987) 611.
4. P C Stangeby, in "Physics of Plasma-Wall Interactions in Controlled Fusion", eds D E Post and R Behrisch, Plenum, New York (1986).
5. C S Pitcher et al, in preparation.
6. M E Woods et al, J Phys D: Appl Phys (1987), to be published.
7. D H J Goodall et al, these proceedings.

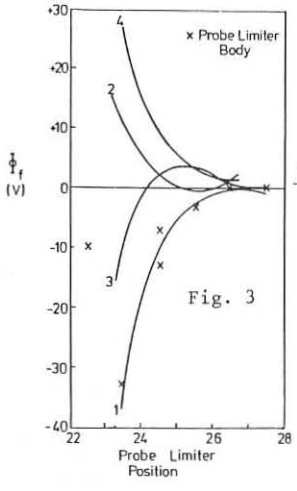

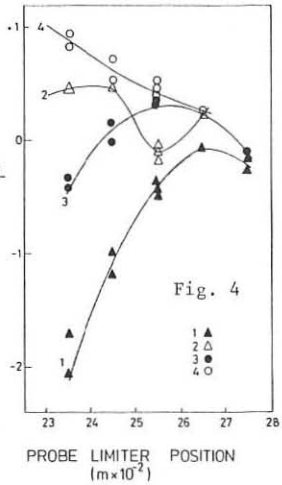

	units	f(LP3)	e(LP1)
probes (exp)			
j_s	A/cm^2	3.7	3.7
T_e	eV	37	37
Φ_f	V	-18	-43
j_{net}	A/cm^2	-2.3	-8.1
probes (cal)			
j_e	A/cm^2	6.0	11.8
Φ_s	V	-63	-38
P_e	W/cm^2	850	1680
P_i	W/cm^2	510	410
P_{tot}	W/cm^2	1360	2090
IR camera (exp)			
P_{tot}	W/cm^2	1130	1700
CCD camera (exp)			
CI	a.u.	1.4	1.0
D_α	a.u.	1.1	1.0

Fig. 3 Probe and body potentials as functions of probe limiter radius.
Fig. 4 Net current density flowing into the body.
Table 1 Experimental and calculated conditions at the leading edge.

Both the toroidal and the radial currents are caused by electron flows that are enhanced or suppressed compared with the ion flow, which is approximately symmetric on the two sides as is shown by the results in fig. 2. The toroidal asymmetry in the electron flux is caused by the difference in plasma potential $\Delta\Phi_{sp}$ on either side of the probe limiter, with the potential being less on the electron side. This strongly increases the electron flux on the electron side while having little effect on the ion flux, as with simple Langmuir probe operation [2]. The opposite effect occurs on the ion side, the electron flux is reduced. The potential difference arises because the body partially interrupts the current that would be flowing in the plasma in the absence of the PL.

The radial current is nearly independent of the toroidal asymmetry and flows because the equipotential body is in contact with a spatially varying plasma ($n_e(r)$, $T_e(r)$, $\Phi_{sp}(r)$). In general, the plasma to body potential at the leading edge is less than the sheath potential $|\Phi_s|$ required for ambipolar flow [4], eg

$$\Phi_s^{amb} = \tfrac{1}{2}\,\frac{kT_e}{e}\,\ln\left[(2\pi\frac{m_e}{m_i})(Z + \frac{T_i}{T_e})(1 - \gamma_e)^{-2}\right] \qquad (3)$$

where $\gamma_e(T_e)$ is the secondary electron emission coefficient. As a result, net electron collection occurs at the leading edge with the situation being reversed at greater minor radii. More detailed modelling will be presented in a subsequent paper [5].

DENSITY AND TEMPERATURE CHANGES IN THE JET EDGE PLASMA DUE TO NEUTRAL BEAM INJECTION

S K Erents,* J A Tagle, and G M McCracken*

JET Joint Undertaking, Abingdon, Oxon OX14 3EA, UK
* Culham Laboratory, Abingdon, Oxon OX14 3DB, UK
(Euratom/UKAEA Fusion Association)

1. Introduction

A knowledge of the scaling of edge parameters with neutral beam power is important for predicting the plasma behaviour as the beam power is increased.

In ohmically heated discharges in JET it has been found that the edge temperature and density vary in a predictable way with the line average density and the input power[1,2]. In this paper the effects of neutral beam heating on the edge parameters has been investigated. The edge temperature and density have been measured over a wide range of conditions using the Langmuir probes in the scrape-off layer (SOL). The temperature and density profiles are normally exponential falling with e-folding lengths of between 5 and 50 mm. From these measurements estimates have been made of the total carbon sputtering yield from the limiters. Scaling of the impurity production to higher beam powers is discussed.

2. Experiment

The mode of operation of the Langmuir probes in JET to obtain ion current density ($I_S(r)$), and electron temperature ($T_e(r)$) is described in previous publications. From these measurements the electron density ($N_e(r)$) is obtained.

Data are taken from an extensive neutral beam heating campaign in which various NBI powers were injected into 1-5 MA reference plasmas. Measurements were made as close to steady state as possible, during the plasma current flat-top just before NBI, and one second into NBI when the temperature is near to a maximum (for 2 MA discharges) and the internal energy is no longer changing, ($\dot{W} = 0$). However, the mean plasma density and the radiated power is still changing rapidly at this time, so a true steady state has not been reached.

3. Results

Results for average plasma density (n_e), ion current density (I_S) and temperature (T_e) at the first Langmuir probe position are plotted as a function of time in figure 1. The edge density 15 mm behind the LCFS (last closed flux surface) calculated from I_S and T_e, is also shown. A NBI power level of 5.3 MW is injected at 9 seconds during the plasma current (2 MA) flat-top. This figure illustrates the type of result which is obtained for a high NBI power injected into a low ohmic power (1.2 MW) discharge. The edge temperature, which before injection is falling due to a slowly rising density, increases immediately after injection with a time constant of ~ 0.3 to 0.5 seconds, then falls again as the edge density continues to rise. Very little increase in T_e is observed when the ohmic and NBI power are of a

similar level; indeed one second after NBI, T_e is often lower than that during the ohmic phase of the discharge.
Data extrapolated to the LCFS is plotted as a function of total power input (ohmic + NBI) in figure 2, for plasma currents of 2 MA and 4 MA. The mean plasma density, which rises due to particle fuelling by the beams, is also shown. The edge temperature data is more scattered at the higher plasma currents (4 MA), but has clearly fallen below its ohmic value one second after NBI switch on, for the higher NBI power levels. Both particle flux and edge density continue to rise with increasing total input power.
The effect of neutral beam heating on the edge profiles is presented in figure 3. The e-folding length of both density (λ_n) and temperature (λ_T) remain almost constant as the NBI power is increased for a given plasma current. This is in contrast to both ohmic heating [2] and ICRH [4]. In ohmic heating as the plasma current is increased the profiles become progressively steeper i.e. λ_n decreases. For ICRH the profiles become flatter as the heating power is increased.

4. Discussion

The slow increase in edge parameters at NBI switch-on, ($\tau \approx 0.3$ to 0.5 seconds, figure 1), demonstrates that the disturbance is due to particles diffusing from the core plasma rather than a directly induced edge effect as observed with ICRH, (4).

The edge temperature increases, but then quickly falls again as the edge density rises. The rise is due to the instantaneous power input at constant density. There are two possible explanations for the falling edge temperature. The first is that as the plasma density rises due to beam fuelling, the particle flux and edge density (via re-cycling) rise. As the particle flux to the limiter rises the average energy per particle, and the edge temperature, decrease. The second explanation is that when the edge temperature rises for a given flux the number of impurity atoms sputtered from the limiters increases. This initial increase is mainly due to carbon self-sputtering - the sputtering yield due to deuterons is almost constant for ion energies corresponding to the T_e range shown in figure 2. The impurity density then increases, and so even at constant density the total radiation increases. This feed back mechanism results in less power being conducted to the edge and so the temperature reaches a new equilibrium.
Both these processes are likely to occur when the neutral beam heating is turned on: An analytical model of these processes has been proposed, [2] and an approximate expression is derived that

$$T_e(a) \propto \frac{P_{TOT}}{\langle n_e \rangle^2}$$

Where P_{TOT} is the total power input. This is in reasonable agreement with the neutral beam heating results.
Both particle flux and density show an increase with total power input, (figure 2), and each show an almost linear increase with plasma current.

The total power conducted to the edge, P_c is given by

$$P_c = (P_\Omega + P_{NBI} - P_{RAD}) = \int_{r=a}^{r=wall} L_w \cdot \gamma_s \cdot I_s \; (a).e^{-r/\lambda_I.T_e(a)} \; e^{-r/\lambda_T}.dr \quad (1)$$

where a is the radius of the LCFS, γ_s is the sheath energy transmission factor and L_w is the wetted height of the limiters.
The power conducted to the limiters has been calculated using the experimental density and temperature profiles. It has been found that $P_c + P_R$ is directly proportional to P_{TOT} and that the data is in good agreement with the data for ohmically heated discharges, (2).
The total impurity production rate resulting from physical sputtering of the limiters has been calculated using the measured particle flux and temperature profiles. It was assumed that the deuterium energy was the sum of the thermal energy plus that resulting from acceleration in the sheath potential. Physical sputtering only was assumed since no evidence of chemical sputtering has been observed in JET, (5). The results are shown as a function of NBI power in figure 4. Both deuteron sputtering and carbon self sputtering have been included assuming that all carbon atoms enter the plasma and return in an average charge state 4. It is seen that the carbon impurity influx increases roughly linearly with total power input. This increase is predominantly due to the increase in edge density.

5. Conclusion

Measurements of the edge parameters have been made over a range of neutral beam heating powers and a range of plasma operating conditions. A reasonable energy balance between the heating power and the power radiated and convected to the limiters has been established. Initially when neutral beam heating is turned on the edge temperature rises but it quickly falls again as the plasma mean density and edge density rise. A notable feature of the edge condition during NBI is that the edge profiles do not change significantly. This is in contrast to the situation during ohmic heating and ICRH.
From the measured edge profiles calculations of the flux of carbon sputtered from the limiter have been made. The impurity flux increases approximately linearly with the neutral beam power. This is expected to lead to a less than linear increase in the impurity density due to increased screening of the impurity flux at higher plasma densities.

References

1. J.A. Tagle, S.K. Erents, G.M. McCracken, R. Pitts, P.C. Stangeby, C. Lowry and M.F. Stamp. These proceedings.
2. S.K. Erents, J.A. Tagle, G.M. McCracken, P.C. Stangeby, et al, 'The dependence of Tokamak edge conditions on global plasma parameters in JET', to be published.
3. S.K. Erents, J.A. Tagle, G.M. McCracken, P.C. Stangeby and L. De Kock. Nuclear Fusion 26 no 12 (1986) 1591-1603.
4. H. Brinkschulte, J.A. Tagle, M. Bures, S.K. Erents, P.J. Harbour, T. Huld, A.S. Kaye, C. Lowry and G.M. McCracken. Proc. 13. Eur. Conf. on Controlled Fusion and Plasma heating, Schliersee, April 14-18 1986.
5. M.F. Stamp et al, J. Nucl. Mat. 145/147(1987) 236-240.

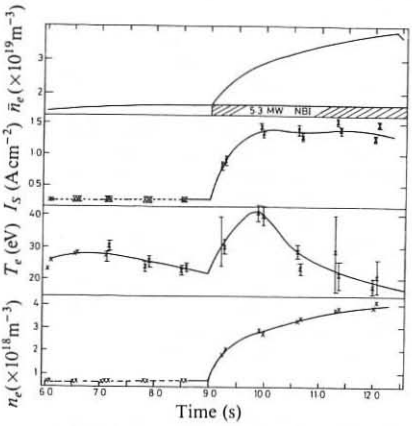

Fig.1 Time dependence of edge parameters 15mm behind LCFS. $I_p = 2$MA, $B_T = 3.4$T.

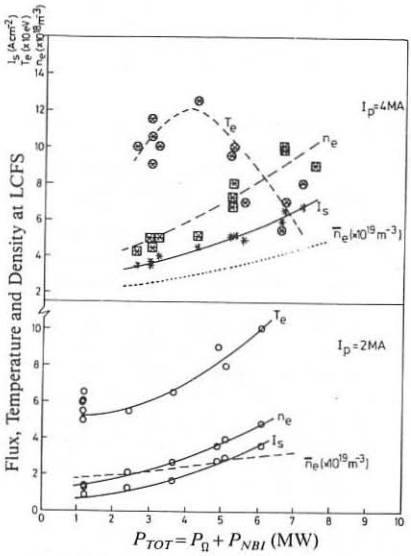

Fig.2 Effect of total input power on edge parameters at LCFS. The average plasma density is also shown.

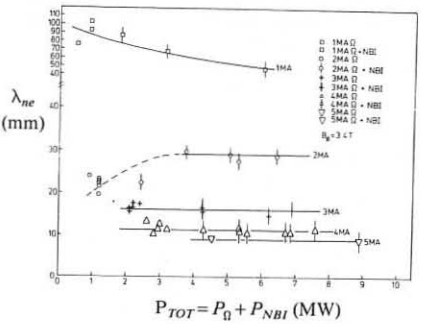

Fig.3 Effect of total input power on density e-folding length for plasma current $I_p = 1$-5MA.

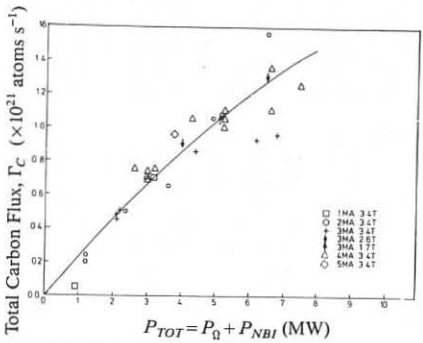

Fig.4 Effect of total input power on total carbon flux sputtered from all limiters.

CARBON EROSION AND DEPOSITION AT THE JET LIMITERS

J P Coad, R Behrisch*, J Roth*, L de Kock, J Ehrenberg**, G Israel, D H J Goodall+, W Wang* and M Wielunski*

JET Joint Undertaking, Abingdon, Oxon OX14 3EA, UK
* Max-Planck Institut für Plasmaphysik, 8046 Garching-bei-München, FRG
+ Culham Laboratory, Abingdon, Oxon OX14 3DB, UK
** on attachment to JET from the Max-Planck Institut für Plasmaphysik

INTRODUCTION

Carbon is the major impurity in the JET plasma, and may limit the ultimate temperatures and densities obtained. To understand the carbon levels observed it is important to assess the production mechanisms at the limiters and walls, and transport in the plasma. This paper describes studies of carbon erosion and deposition at the carbon limiters in JET in 1986, performed by marker experiments. The pattern of erosion from and deposition observed on the limiters represent a starting point for impurity transport calculations and are also important for predictions about erosion in future plasma machines with higher temperatures and larger pulses.

EXPERIMENTAL

Before the 1986 operations a carbon limiter tile was implanted with ^{13}C at 1.4 MeV to a mean depth of ~ 2 μm at a number of points on the surface facing the plasma. The shape of the limiter tile was also accurately measured using a coordinate measuring machine to show up larger changes in dimensions (>a few microns). The limiter tile was placed adjacent to the plasma midplane on the limiter in octant 1D. Altogether there were eight limiters in operation for almost all 3200 discharges of the 1986 campaign, the limiters being effectively 12mm in front of the protection tiles of the three RF antennae.

While the investigation of limiter erosion can only give a global result after many discharges, erosion in one discharge was also investigated with a special limiter probe which was also implanted with ^{13}C, however at 40keV (0.1μm mean depth). The limiter probe was a 50mm diameter cylinder of POCO graphite mounted on one of the manipulators of the Fast Transfer System (FTS) which allows samples to be inserted into the shadow of the limiters just above the outer midplane of the vessel (in Octant 7) (Fig.1a). From this position, the probe has a short connection length on the electron drift side of ~2.5m to a graphite limiter in octant 6D, whilst on its ion-drift side it has a long connection length of either ~25m to the inner wall or ~55m to a limiter, depending on the size of the plasma.

After exposure the limiter tile and the probe were analysed by Secondary Ion Mass Spectroscopy (SIMS) to determine the depth of the ^{13}C marker.

In addition nuclear reaction techniques were used to measure deuterium, and Rutherford Backscattering (RBS) and Proton Induced X-ray Emission (PIXE) were used to determine metallic deposits.

RESULTS AND DISCUSSION

On the limiter tile the ^{13}C marker had disappeared in the central part, while it could still be detected on the edges. On the ion drift side ^{13}C was discovered 22μm beneath the surface, being covered by a deposited layer of ^{12}C containing of the order of 0.5% Ni impurity and several per cent of hydrogen isotopes (5% H, 1% D). On the electron drift side even heavier deposition was observed with some flaking of the deposit: flake thicknesses were about 100μm. This is consistent with the physical measurement of the limiter tile (Fig.2). It shows that over the central region of the tile erosion of over 200μm occurred. Fig.2 includes the results from three scans across the tile, each of which gives a similar profile. Three tiles of another limiter have also been measured yielding similar depths of erosion. Computer calculations of erosion and redeposition on limiter surfaces predict large erosion and redeposition (‘). However, the net changes appear to be small, so that the 200 μm observed here may only be a small fraction of the total erosion.

The erosion of the limiter tile is the result of about 3200 discharges including many different modes of operation and other events such as glow discharge cleaning and disruptions. In order to determine the erosion and deposition during a well-defined discharge the special probe was exposed using the FTS. The probe was inserted to within 10mm of the last closed surface for two identical 5MA shots with 5 secs flat tops: a section of this limiter probe is shown in Fig. 1b. The surface at all points on the section of the probe marked in Fig. 1b with circles was analysed for D, Ni and Cr by nuclear techniques, and points also marked with squares were profiled with Secondary Ion Mass Spectroscopy (SIMS) to look for the ^{13}C marker, and study the depth distribution of other elements. The probe shows a similar erosion pattern to that at the main limiter. At points furthest from the plasma the marker was present at a depth larger than prior to exposure, while nearer the plasma

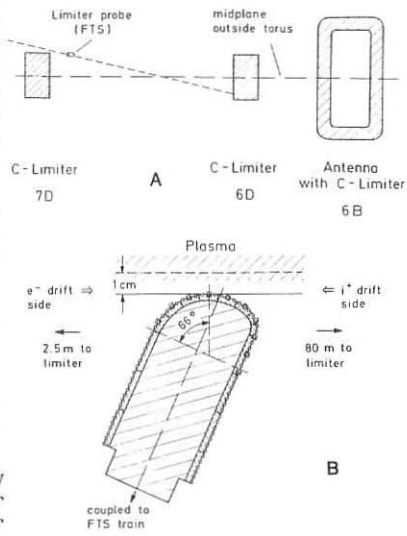

Fig. 1(a) Relative positions of components in the JET vessel.
(b) Geometry of the limiter probe.

the markers could not be detected. However, at the surface tangential to the field lines ^{13}C was detected but in a somewhat modified distribution. Fig.3 shows the results of the nuclear analyses of the probe. For each analysis point the areal elemental concentration is plotted against the distance from the plasma, taking into account the angle between the surface normal and magnetic field lines. Large fluences of deuterium are observed of up to 10^{18} atoms cm^{-2}, disregarding the anomaly at the centre which is due to the angle correction. The Ni and Cr are plasma impurities and on the ion side are in total about 0.5% of the collected deuterium. The amounts collected on the electron-drift side are considerably less, probably due to the shorter connection length. From the large amount of D observed even in the eroded regions it has to be assumed that after erosion, codeposition of carbon and deuterium plus hydrogen occurred in a later phase of the discharge. A trapped D fluence of 8×10^{17} atoms cm^{-2} cannot be due to ion implantation ([2]) at a plasma edge temperature of about 100-200 eV ([3]), but indicates a deposited layer of about 0.2 µm of saturated carbon ([4]).

CONCLUSIONS

The JET limiters show both large amounts of erosion and deposition, according to the proximity to the plasma. Close to the plasma ~ 200 µm have been eroded in 1986, corresponding to about 60 nm (net) per discharge, whilst a few centimetres from the plasma up to 100 µm nas been deposited onto the original surface: this is the cumulative result of exposure throughout the 1986 campaign.

The limiter probe was exposed to just two identical 5 MA discharges to show what happens at the limiter on a much shorter timescale. It is found that erosion and deposition patterns are very similar to the main limiters in that erosion of > 0.1 µm occurs near the plasma edge, and deposition occurs a few centimeters away from the edge. However, there is also as much deposition on the surface in the eroded zone as elsewhere: this must occur in a later part of the discharge. It is therefore necessary to investigate this on a smaller time scale, so that one can ascertain within a single discharge when erosion and deposition occur.

Globally, one finds that most of the carbon from the limiters (and from the inner wall) is deposited on the sides of the limiters and on the RF antennae, whilst a relatively thin layer of carbon (with some co-deposited D and H, and a low concentration of metals) covers the vessel walls. This layer was not maintained on the inner half of the vessel in 1985, and carbonisation was found to reduce the metallic impurities in the plasma. However, the thin layer of carbon on the vessel wall in 1986 may simulate an all-carbon wall in JET, explaining the low metal concentrations found in the plasma.

ACKNOWLEDGEMENTS

The authors are indebted to staff at the Chalk River Laboratory, Canada for the high energy ^{13}C implants.

REFERENCES

1. J N Brooks, J Nuclear Materials 111/112 (1982) 457.
2. W R Wampler, D K Brice and C W Magee, J Nuclear Materials 102 (1981).
3. S K Erents, J A Tagle et al, J Nuclear Materials 145-147 (1987) 231.
4. W R Wampler and C W Magee, J Nuclear Materials, 103/104 (1981) 509.
5. J Roth et al, J Nuclear Materials 145-147 (1987) 383.

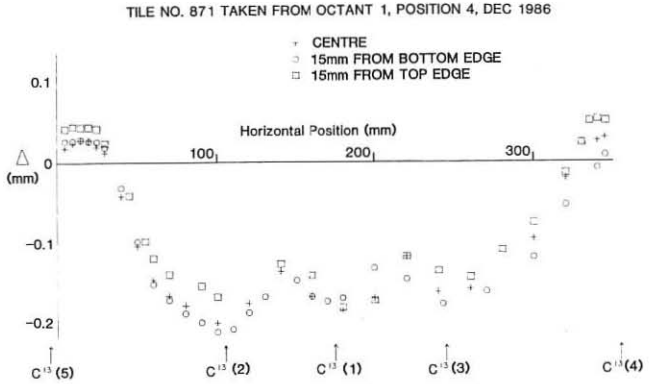

Fig. 2 Topographical changes in a limiter tile after use in 1986.

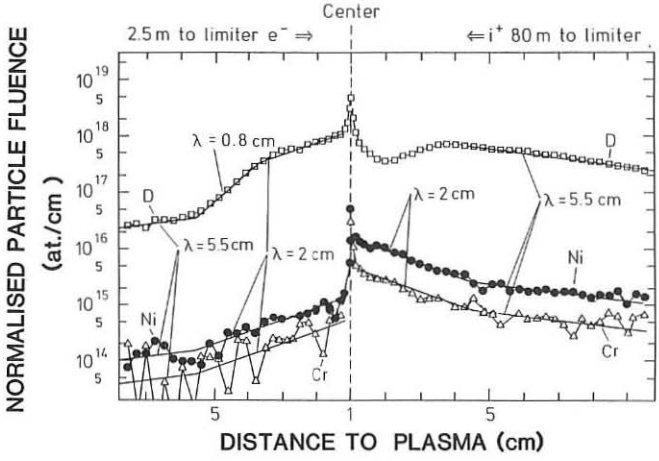

Fig. 3 Nuclear analysis of the limiter probe.

A COMPLETE NEOCLASSICAL TRANSPORT MODEL FOR THE TOKAMAK SCRAPE-OFF LAYER

W. Feneberg, R. Zanino

Max-Planck-Institut für Plasmaphysik, EURATOM Association, D-8046 Garching, Fed. Rep. of Germany

Abstract. We describe here the macroscopic momentum equations necessary to be solved numerically in a scrape-off layer code which govern the particle transport of a pure plasma. Energy transport usually based on classical heat conductivity along field lines and anomalous heat conduction perpendicular to the magnetic field is not considered here.
The transport model given here is basis of the 2-D JET boundary code /1/.

A self-consistent model for the scrape-off layer of a toroidal limiter respectively divertor is studied using the classical two-fluid equations. In a extension of earlier calculations /1/, where only the contribution of the coefficient of thermal diffusion to the perpendicular transport has been taken into account we give here also expressions for the electric potential distribution and the currents flowing in the scrape-off layer. These are driven mainly by a difference in the wall potential between the two positions where a field line hits the limiter respectively the divertor plates. The potential depends from the temperature which is different on both sides of the limiter due to the asymmetry caused by the neoclassical effects, as it is shown by code calculations /1/.

Due to the Langmuir probe characteristic there exists a connection between wall potential and electric currents from which we obtain for given wall temperatures the self consistent corresponding potentials which are influenced by currents only being in the order of the ion saturation current.

We discuss the poloidal plasma rotation caused by the radial electric field which can overcome the parallel motion of the fluid near a X-point and in regions with Mach number $M \simeq 0.1$.

The pressure gradient along the field lines in the scrape-off layer produces a current perpendicular to the magnetic surfaces depending also from the parallel viscosity neglected here assuming the free mean path small compared to the parallel decay length of the flow velocitz near the wall.

The theory presented here is an extension of the work given by Singer and Langer /2/.

We start with the classical Braginskii two fluid equations, which give a complete set of 8 equations for the quantities $\vec{v}$, $\vec{\tau}$, n, and ϕ, that is flow velocity, electric currents, particle density and the electric potential in the sheath. Aim of the work is to derive analytic expressions for most of the quantities to enter in the remaining two equations to be solved numerically, which are the equation of continuity for the density

$$\nabla \cdot n \vec{V} = Q \qquad (Q = \text{source term}) \qquad (1)$$

and the equation for the toroidal component V_φ of the flow velocity, which follows from the parallel component of the equation of motion:

$$\frac{1}{\sqrt{g}\,R}\frac{\partial}{\partial\theta}\left(\frac{\sqrt{g}}{H_\theta}V_\varphi V_\theta n m_i R\right)+\frac{1}{\sqrt{g}}\frac{\partial}{\partial\varrho}\left(m_i n V_\varphi V_\varrho \frac{\sqrt{g}}{H_\varrho}\right)$$

$$-\,n m_i \frac{V_\varphi^2}{R H_\theta}\frac{\partial R}{\partial\theta} f_p + \vec{b}\cdot\nabla\cdot\vec{\vec{\pi}} + f_p\frac{\partial p}{\partial l_p} = 0 \qquad \text{- - - - - - - (2)}$$

($P = n(T_e + T_i)$ is the total pressure, $f_p = B_p/B_\varphi$ the ratio of poloidal to toroidal magnetic field, V_ϱ, V_θ the perpendicular and poloidal component of the flow velocity, $\vec{b}$ = unit vector of B, R the major radius).

We use here an axisymmetric coordinate system fixed on the magnetic surfaces with

$$\delta^2 s = H_\varrho^2\,\delta\varrho^2 + H_\theta^2\,\delta\theta^2 + R^2\,\delta\varphi^2 \qquad \sqrt{g} = R H_\varrho H_\theta$$

(ϱ is a flux quantity; $\delta_\psi = H_\varrho\,\delta\varrho$ and $\delta l_p = H_\theta\,\theta$ are the radial and poloidal distances).

In the expression for the viscosity $\vec{b}\cdot\nabla\cdot\vec{\vec{\pi}}$ we add to the parallel viscosity which is necessary to impose boundary conditions for the flow at the limiter respectively the divertor plates also an expression for gyroviscosity as given in ref. /3/:

$$\vec{b}\cdot\nabla\vec{\vec{\pi}}_{3,4} = -\frac{1}{R^2 H_\theta}\frac{\partial}{\partial\psi}\left(R^3 H_\theta \eta_4\right)\frac{\partial}{\partial l_p}\left(V_\varphi R^{-1}\right)+\frac{B_p}{R}\frac{\partial}{\partial l_p}\left(\eta_4\frac{R^2}{B_p}\right)\frac{\partial}{\partial l_\psi}\left(V_\varphi R^{-1}\right)$$

$$\eta_4 = n_i T_i m_i/(eB) \qquad (3)$$

Equation (1) and (2) are considered in a region where the sources Q are present, extending over the scrape-off layer and reaching also inside the separatrix in X-point geometry up to a last magnetic surface called the plasma side where we pose conditions on n and V_φ.

In cases of neutral injection the coefficient of gyroviscosity which contains the perpendicular derivates of $(V_\varphi R^{-1})$ describes the transport of toroidal momentum into the scrape-off layer where this effect can change the flow pattern completely compared with all code calculations up to now which have neglected it. By this also the impurity transport will be influenced.

Because of friction the impurity flow is coupled strongly to the flow velocity of the bulk plasma ions.

The inertial term and the viscosity in the toroidal component of the momentum equation give rise to currents perpendicular to the magnetic surfaces, which can be expressed using also the parallel momentum balance (2) by:

$$i_\varrho B_p = n m_i \frac{V_\varphi^2}{R}\frac{\partial R}{\partial l_p} f_p + f_p\left(\nabla\cdot\vec{\vec{\pi}}_{//}\right)_p - f_p\frac{\partial p}{\partial l_p} \qquad (4)$$

That means that the perpendicular current is produced mainly by the parallel pressure gradient in the scrape off layer. Viscosity and the centrifugal force entering in equ. (4) are considered as small quantities and will be neglected in future corresponding to an ordering $M_\varphi^2 << f_p^{-1} R/\Delta_{//}$ respectively $M_\varphi \lambda_i/\Delta_{//} << 1$, where M_φ is the Mach number of the toroidal flow velocity, $\Delta_{//}$ the parallel decay length of V_φ respectively p, λ_i the free mean path of the ions due to ion-ion collisions. Gyroviscosity being much smaller than the parallel viscosity was not taken into account

here.

The currents in the scrape-off layer have to flow divergence free, therefore the perpendicular currents produces a return current along field lines such, that

$$\nabla \vec{i} = 0 \tag{5}$$

As usual the return current deduced from (5) contains a free flux function:

$$\sqrt{g}\, i_\theta / H_\theta - \frac{\partial}{\partial \varrho} \int_{(1)}^{\theta} \left(\frac{R}{B_\varphi} \frac{\partial p}{\partial \theta} \right) \delta\theta = \alpha(\varrho) \tag{6}$$

(Here we have integrated along a field line from position (1), where it starts at the wall to an arbitrally poloidal position - θ -. i_θ is the poloidal component of the current.)

The expression for the parallel current can be found completely from Ohm's law parallel to $\vec{B}$:

$$-\nabla_{\parallel} \phi = \vec{i}_{\parallel} \eta_{\parallel} - \frac{0.71}{e} \nabla_{\parallel} T_e - \frac{1}{ne} \nabla_{\parallel} p_e \tag{7}$$

The electric field we are using is $\vec{E} = -\nabla\phi$ and $\eta_{\parallel}$ is the parallel resistivity. The coefficient of thermal diffusion being $-\frac{0.71}{e}\nabla_{\parallel} T_e$ is also taken into account here.

From this and the force balance perpendicular to the magnetic surfaces

$$\nabla_{\perp} p = (\vec{i} \times \vec{B})_{\perp} \tag{8}$$

where inertial effects are ordered to be very small compared to the pressure gradient, we obtain the final expression for the return current by integrating along the field:

$$\alpha(\varrho) \int_{(1)}^{(2)} \frac{H_\theta^2 \eta_{\parallel}}{f_p^2 \sqrt{g}}\, \delta\theta = \int_{(1)}^{(2)} \left(\frac{H_\theta \eta_{\parallel}}{B_\varphi H_\varrho} \frac{\partial p}{\partial \varrho} \right) \delta\theta + \phi_{(2)} - \phi_{(1)} +$$
$$\frac{0.71}{e} \left(T_e^{(1)} - T_e^{(2)} \right) - \int_{(1)}^{(2)} \frac{1}{ne} \frac{\partial p_e}{\partial \theta}\, \delta\theta - \int_{(1)}^{(2)} \frac{H_\theta^2 \eta_{\parallel}}{f_p^2 \sqrt{g}} \frac{\partial}{\partial \varrho} \left(\int_{(1)}^{(\theta)} \frac{R}{B_\varphi} \frac{\partial p}{\partial \theta}\, \delta\theta \right) \delta\theta \tag{9}$$

In opposite to the bulk plasma, where the electric potential can only be found up to free constant, in the scrape-off layer the electric potential depends from the values at the two positions (1) and (2) where a field line hits the wall. As long as the electric currents flowing into the wall are smaller than the ion saturation current we obtain the boundary conditions from probe theory /3/ to be $\phi_{1,2} = 3.5\, T_e(1,2)$.

The return current in equ. (9) is mainly a thermoelectric current driven by the differences between the wall temperatures. We neglect in the following the contribution of the resistivity on the right hand side of equ. (9) and give the expression for the radial electric field:

$$E_\varrho = -\nabla_{\perp} \Phi(\varrho, v) = \frac{\partial}{\partial \varrho} \left(\frac{0.71}{e} T_e^{(1)} - \phi_{(1)} - \frac{0.71}{e} T_e + \right.$$
$$\left. \int \frac{1}{e} \frac{\partial p_e}{\partial \theta}\, \delta\theta + \int \alpha(\varrho) \frac{H_\theta^2}{f_p^2 \sqrt{g}} = \delta\theta \right) \tag{10}$$

The toroidal component of Ohm's law contains the perpendicular flow velocity:

$$V_\vartheta B_\rho = f_\rho^{-1} \frac{H_\vartheta}{\sqrt{g}} \eta_{\parallel} \alpha(\varrho) - \frac{f_\rho}{n e} \frac{\partial p}{\partial L_\rho} - \frac{0.71}{e} f_\rho \frac{\partial T_e}{\partial L_\rho} \qquad (11)$$

The radial electric field enters the poloidal flow velocity in the well known equation:

$$V_\Theta = f_\rho V_\varphi - E_\varrho / B_\varphi + \frac{1}{n e B_\varphi} \frac{\partial p_i}{\partial \psi} \qquad (12)$$

The equs. (9), (10), (11) and (12) together with the equations of continuity (1) and the parallel momentum equation (2) describe a complete self-consistent neoclassical transport model for the scrape-off layer.

/1/ R. Simonini, W. Feneberg, A. Taroni, 12th Europ. Conf. on Contr. Fusion and Plasma Phys., Budapest, 2-6 September 1986.
/2/ C.E. Singer, W.D. Langer, Phys. Rev. A, 28, 2, 1983.
/3/ D.M. Manos, G.M. McCracken, Nato ASI Series, Proceedings of Nato Summer School, 1984, Quebec.

TWO-ZONE MODEL FOR THE TRANSPORT OF IMPURITIES INJECTED INTO THE EDGE OF A TOKAMAK PLASMA

H.A. Claaßen, H. Gerhauser

Institut für Plasmaphysik, Kernforschungsanlage Jülich GmbH

Association EURATOM-KFA, P.O.Box 1913, D-5170 Jülich, FRG

One method of studying the transport of impurities in the edge plasma of a tokamak is to inject non-intrinsic metal atoms from the torus wall into the plasma and to follow their ionization sequence and their space-time evolution. The migration of impurity ions of specified charge in the edge plasma is determined by the simultaneous action of a variety of processes: gain and loss by electron impact ionization (and eventually recombination and charge-exchange), cross-field ($\perp B$) diffusion due to the correlated effect of density and electric field fluctuations, cross-field drift due to friction with the poloidally rotating plasma, as well as parallel-field ($\parallel B$) convection due to friction and electrostatic forces in the scrape-off layer (s.o.l.). The relative importance of these processes and the attainable population densities of the various ionization levels depend, of course, on the injection parameters (pulse duration, energy and angular distribution as well as species of the injected impurity atoms) and the background plasma.

It is the aim of this paper to present some preliminary results concerning the influence of some of the aforementioned processes on the transmission of a toroidally uniform metal injection pulse with a Gaussian time-dependence assuming a two-zone model for the edge plasma. This model (see fig.1) subdivides the edge plasma into s.o.l. and outer region of the plasma core and treats in a very simplified form two-dimensional (radial-toroidal) variations of the plasma parameters. The radial plasma profiles are simulated by step functions, the steps being located at the separatrix. In contrast to the core region the s.o.l. is characterized by low values of plasma density and electron-ion temperatures and subject to $\parallel B$ components of electrostatic forces and plasma flows. The latter are assumed to increase linearly in toroidal direction towards a limiter or a divertor throat. This implies constant values of plasma source and plasma density, but presupposes that the electron and ion temperatures undergo slight to-

roidal variations, which are neglected in this study.

The analytical treatment of the present time-dependent impurity transport problem, which ignores recombination and charge-exchange as well as impurity-impurity interactions, is given in detail in ref. [1]. It proceeds basically in three steps. In the first step the drift-kinetic equation for each ionization level is averaged over the velocity component $v_\perp$ and then transformed into a set of transport equations by expanding the averaged guiding-centre distribution functions in eigenfunctions of the $\parallel$B convection-collision operator similar to the method outlined in ref. [2]. In the second step the transport equations for the expansion coefficients are decoupled in zero order approximation assuming a collision-dominated scrape-off plasma and a toroidally uniform impurity source function, which is even in $v_\parallel$. The first two zero-order expansion coefficients $A_m^o(\varrho,t)$ related to the density (m=0) and the $\parallel$B particle flux (m=1) satisfy the following equation written in Cartesian coordinates:

cross-field diffusion and convection — source function

$$\frac{\partial A_m^o}{\partial t} + \frac{\partial}{\partial \varrho}\left(-D_\perp \frac{\partial A_m^o}{\partial \varrho} + V_\perp A_m^o\right) + \left(\nu_I + \underbrace{\lambda_m \nu_C}_{\text{ionization and convection losses } \parallel B} + \frac{\delta_{m1}}{\tau_\parallel^*}\right) A_m^o = Q_m^o \qquad (1)$$

time variation due to time-dependent surface and volume sources

Q_m^o refers to stepwise electron impact ionization of the injected impurity atoms. δ_{m1} is the Kronecker symbol. ν_C and λ_m are respectively the frequency of impurity-hydrogen ion collisions and the eigenvalues of the $\parallel$B convection-collision operator, both determining the effective convection time $\tau_\parallel^*$. Eq.(1) holds for each ionization level. It also applies to the sum of all charge states (taking $\nu_I = 0$), if the charge-dependence of $D_\perp$, $V_\perp$ and $\tau_\parallel^*$ is ignored. In the third step eq.(1) is solved by Laplace transformation with respect to the time (a different method was given in ref. [3]) using the boundary conditions $A_m^o(\pm\infty,t) = 0$, which at the torus wall $\varrho = \Delta$ yields a boundary value somewhat in between specular ion reflection and complete ion absorption (an approximate solution satisfying $A_m^o(\Delta,t) \tilde{=} 0$ has also been derived). Due consideration is given to the continuity conditions for density and $\perp$B particle flux in the presence of plasma discontinuities at the separatrix $\varrho = 0$. The solution contains the source function and the ini-

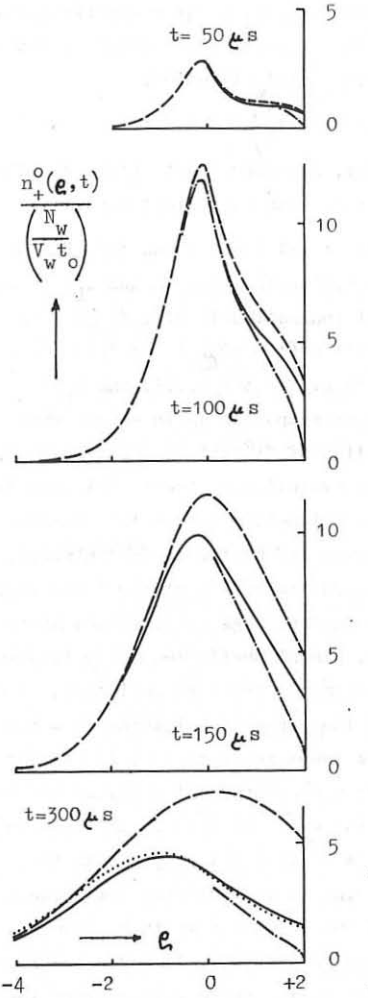

fig.2 :time evolution of the radial density profiles for kT_w=25eV and $V_\perp$=0 (...$V_\perp$=10m/s)

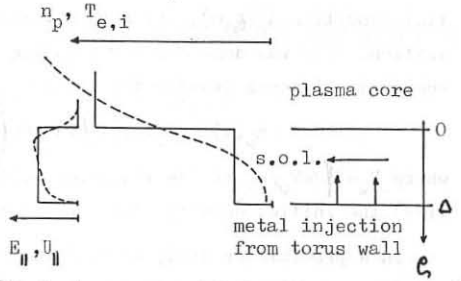

fig.1 :two-zone model for the edge plasma

---- actual, —— model

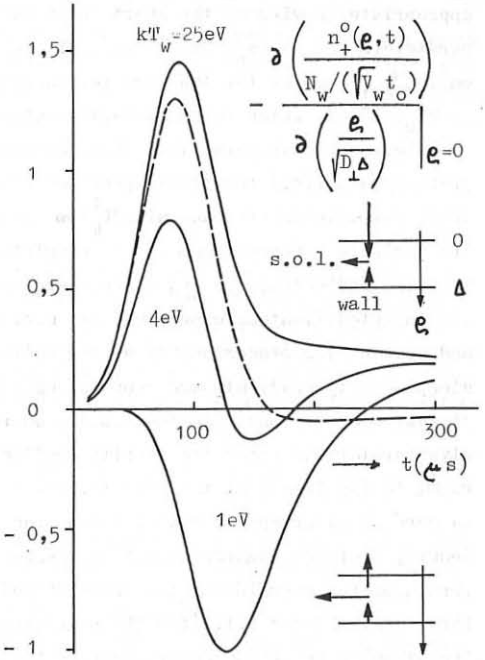

fig.3: particle flux across the separatrix as a function of time $V_\perp$=0, kT_w= 1..25 eV

$\tau_\parallel^*$ { $= \infty$ ---} $n_+^o(\infty,t)=0$

Z_{eff}=5 { —— / -.- } $n_+^o(\Delta,t)\approx 0$

tial condition $A_m^o(\varrho,0)$, which had still to be specified for a numerical evaluation. This was done for m=0 assuming a Gaussian injection pulse of monoenergetic Ti-atoms leaving the torus wall in radial direction,

$$n_w(t) = N_w/(V_w t_o \sqrt{\pi}) \exp\left(-(t-t_1)^2/t_o^2\right) \qquad (2)$$

where $V_w = \sqrt{2kT_w/m_z}$ is the injection velocity. Assuming $t_1 = 2t_o$ (to save CPU-time) the initial density could be set to zero with sufficient accuracy.

In a preliminary study we calculated the total density and the $\perp$B flux of Ti-ions (summed over all charge states) taking the same values $D_\perp = 1 m^2/s$, $V_\perp = 0$ or 10 m/s and $\tau_\parallel^*$ with $Z_{eff} = 5$ for all ionization levels. $Z_{eff} = 5$ is appropriate in view of the short pulse duration ($t_o = 40\,\mu s$) and the plasma parameters chosen ($n_p = 2 \times 10^{12}/cm^3$, $kT_{e,i} = 10$ eV for the s.o.l. and $n_p = 10^{13}/cm^3$, $kT_{e,i} = 100$ eV for the core periphery) presupposing an injection energy $kT_w = 25$ eV, which causes a fast penetration of Ti^o into the plasma core.

Fig.2 shows in normalized form the time evolution of the radial density profiles and fig.3 the time-dependence of the ion-flux across the separatrix. Comparisons are made with $\tau_\parallel^* = \infty$ in case the $\parallel$B forces in the s.o.l. are neglected. Corrections due to complete ion absorption at the torus wall are also indicated. For injection energies in the range of 10 eV and above the injected Ti-atoms cross the cold s.o.l. almost unaffected to be ionized and accumulated predominantly at the hotter and denser core periphery. Thus steep density gradients are soon formed at the separatrix leading to a back-diffusion of Ti-ions into the s.o.l., where they are swept to a limiter or divertor target. Later the density profiles are smeared out decaying to zero due to ion losses at the targets, the torus wall and deep inside the plasma core. A superimposed radial convection (≤ 10 m/s) slightly shifts the density profiles inwards or outwards according to the velocity direction. For injection energies of the order of 1eV and below a density maximum forms inside the s.o.l. (for the same plasma parameters). It moves towards the plasma core in the decay phase of the injection pulse and reverses the ion flux across the separatrix during an intermediate time interval.

[1] H.A.Claaßen, H.Gerhauser, Report JÜL-2115, KFA Jülich (Febr.1987)
[2] H.A.Claaßen, H.Repp, Nuclear Fusion 21(5), 589 (1981)
[3] G.Fußmann, Nuclear Fusion 26(8), 983 (1986)

A KINETIC MODEL OF A SCRAPE-OFF LAYER WITH RECYCLING

R. Chodura

Max-Planck Institute für Plasmaphysik,
EURATOM Association, D-8046 Garching, Fed. Rep. of Germany

Abstract

A 1d particle model with a Fokker-Planck collision term is used to describe the energy flow in a scrape-off layer with particle recycling. Hot particles from the core plasma and relatively cold recycled particles from the target plate form a velocity distribution with a low energy maxwellian bulk distribution and a tail in target direction of energetic particles which cannot be maxwellized within the path length along the layer. The energy flux is mainly carried by these tail particles, whereas the other flow quantities are determined by the bulk particles.

Introduction

In toroidal plasma configurations the core of closed, nested magnetic surfaces is surrounded by a scrape-off region, where magnetic field lines end on material walls, i.e. limiters or divertor plates. Particles and energy, diffusing perpendicularily to the magnetic field out of the core into the scrape-off layer flow there mainly parallel to field lines to the target plates. Plasma ions reaching the target are recycled as cold neutrals and eventually become reionized. Thus a cloud of cold plasma in front of the target is formed. The energy flux along the scrape-off layer has to provide the energy for ionization and heating of the recycled partices, for the kinetic energy of the ions and for the energy of some electrons to overcome the potential barrier of the sheath at the target.

The scrape-off layer contains hot core particles as well as relatively cold recycled particles. The hot core particles may have mean free path lengths for relaxation which are comparable or larger than their path lengths from the place of their appearance in the scrape-off layer to the target plate. The velocity distribution of these particles is thus expected to be strongly non-Maxwellian. The relatively cold particles, on the other hand, have mean free path lengths of a small fraction of their total path length and are Maxwell distributed. A kinetic model is thus demanded to describe the relaxation process between hot and cold particles and the energy flux along the scrape-off layer.

Model

The numerical model is a 1d electrostatic particle-in-cell code for the plasma electrons and ions including a Fokker-Planck representation of the velocity change by Coulomb collisions [1]. The magnetic field is assumed perpendicular to the target plate along x (Fig. 1). The particle flow originates from a source of hot particles with temperature $T_i = T_e = T_h$ near the symmetry plane x=0. Ions reaching the target plate at $x = L$ are redeposited as cold electron-ion pairs with $T_i = T_e = 0$ in front of the target plate. An amount of energy representing the ionisation energy of the recycled particles is withdrawn from the already existing electrons.

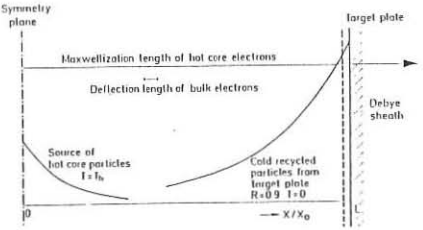

Fig. 1: Schematic situation of a 1d scrape-off layer with recycling.

The code resolves the electrostatic Debye sheath. In a real scrape-off layer the sheath thickness λ_s is 4-5 orders of magnitude smaller than the mean free path lengths λ of bulk particles and even more orders of magnitude smaller than the lengths L of the layer. In order to keep these quantities in scale λ_s was artificially enlarged relative to λ and L. Thus, as in reality,

$$\lambda_s \ll \lambda \ll L \leq \lambda_h$$

where λ_h is the mean free path length of hot core particles, but the numerical relation of λ_s to the other quantities is unrealistic.

Results

Figure 2 shows steady-state profiles of flow quantities and electric potential over x for a hydrogen plasma. Hot core particles are fed in at constant rate near x=o with an e-folding length 5 at a temperature $T_h = 10$ (in arbitrary units). Ions reaching the target are recycled with an recycling coefficient R=0.9 as electron-ion pairs over a e-folding length of 20 in front of the target plate at L=80. An ionization energy of $W_{ion} = 0.4$ is withdrawn from background electrons. The source distribution determines the particle flux Γ. The other curves of Fig. 1 show density n and mean velocity V of ions and electrons (which differ only in the sheath) together with the isothermal sound speed $C = [(T_i + T_e)/m_i]^{1/2}$. At the sheath edge V=C. Electron and ion "temperatures" (parallel and perpendicular to the flow direction, $T_\parallel$ and $T_\perp$ respectively) are much lower than T_h of source particles. The energy input of electrons or ions in the source, $Q_h = \frac{3}{2}\Gamma_h T_h = \frac{3}{2} 0.00233 \cdot 10 = 0.035$ is mainly transported as heat flux $q = \frac{m}{2} \cdot \langle (v-V)^2 (v_x - V_x) \rangle$ in the pre-recycling region and is partly transformed in ionization energy rate, convective and ion kinetic energy flux in the recycling region.

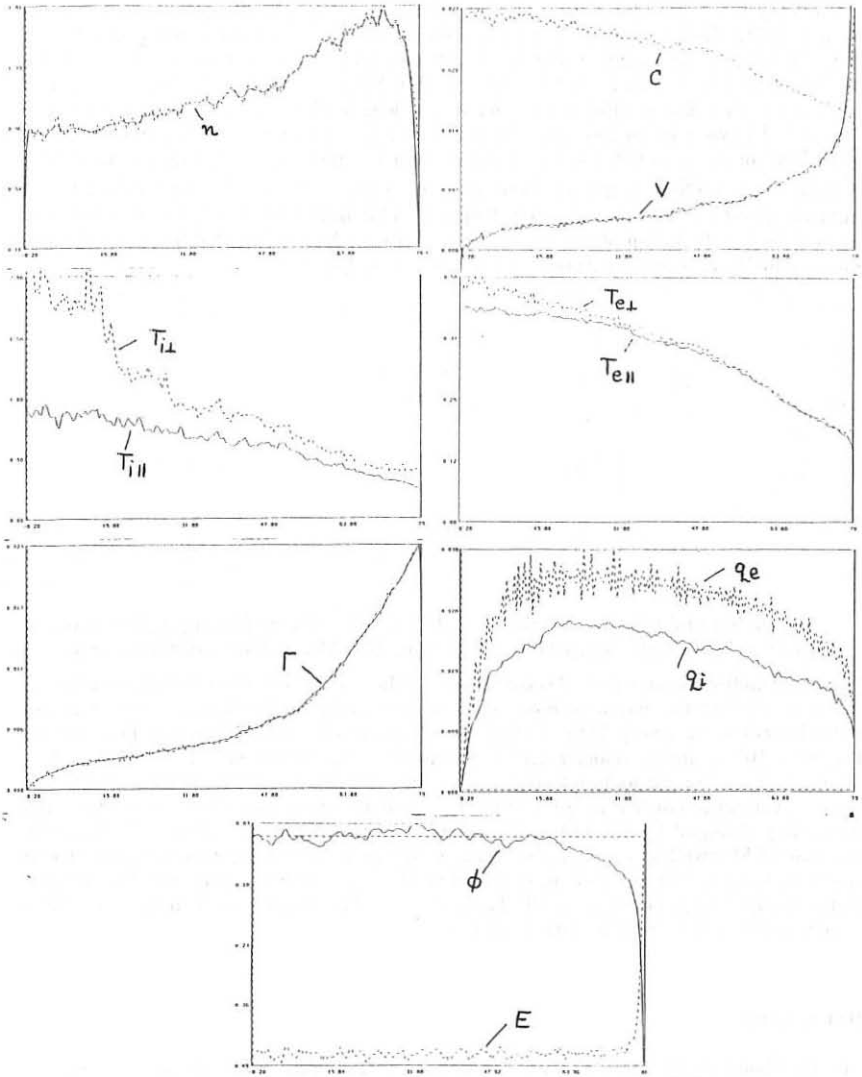

Fig. 2: Density n, mean velocity V and isothermal sound speed C, temperatures $T_{\parallel}$ and $T_{\perp}$ parallel and perpendicular to the flow direction for ion and electrons, particle flux Γ, heat flux q, potential o and electric field E as function of x for steady state.

The energy transport of electrons and ions through the scrape-off layer is characterized by a velocity distribution of relatively cold Maxwellian bulk particles and a tail in the direction to the target of energetic particles from the hot source. This is shown in Fig. 3 for the ion and electron distribution $F(v_x) = \int\int dv_y dv_z f(v_x, v_y, v_z)$ at 4 locations x on a logarithmic scale. Source particles with their thermal velocity $v_{th} = (T_h/m)^{1/2}$ have a mean free path length for energy transfer to bulk particles of the same kind of $\lambda_h = 5 \cdot 10^2$, i.e. much larger than L. Since $\lambda_h \propto v^4$, only particles with velocities $v < 0.63 v_{th} = 2.0$ for electrons and 0.05 for ions can be thermalized to the bulk temperature within the system length L. This limit can clearly be recognized by inspecting the deviation of the distribution F from a Maxwellian (of the same density, mean velocity and temperature). For bulk particles $\lambda \sim 4$.

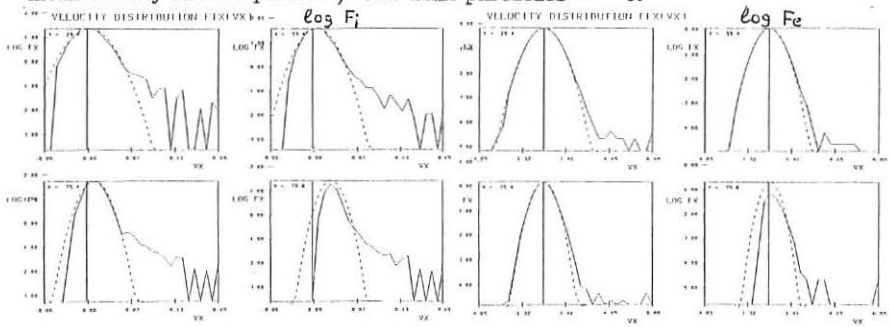

Fig. 3: Ion and electron distributions $F(v_x) = \int\int dv_y dv_z f(v_x, v_y, v_z)$ at 4 locations x = 29.4, 59.4, 75.4, 79.8 and corresponding Maxwellians (dashed lines).

Only thermalized source particles contribute to the heating of the cold recycled plasma, whereas the fast tail particles move more or less freely to the target plate. The tail particles contribute very little to the low moments of the distribution, i.e. density $(n_h/n \sim 10^{-3})$, mean velocity and temperature, but carry most of the heat flux q. Thus, in the situation at hand no local or non-local relation between heat flux q and temperature gradient ∇T is applicable. The potential drop Δo_s over the sheath is not noticeably changed by the tail in the electron distribution, i.e. $e\Delta o_s = 2.8 T_{es}$ as in the case of Maxwellian electron distribution, where T_{es} is the electron temperature at the sheath edge. But the elctron energy flux $Q_{es} =< \frac{1}{2} m_e v^2 v_x >$ at the sheat edge is significantly larger, i.e. $Q_{es} = \delta_e \Gamma_s T_{es}$ with $\delta_e = 7.6$, as compared to $\delta_e = 4.8$ for a purely Maxwellian electron distribution [2].

References

/1/ R. Chodura, 12th Europ. Conf. on Contr. Fusion and Plasma Physics, Budapest, Europhysics Conf. Abstracts 9F, Part II, p.472 (1985).

/2/ P.C. Stangeby, J. Nucl. Mat. 128&129, 969 (1984).

DESCRIPTION OF IMPURITIES WITH ARBITRARY CONCENTRATION IN THE SCRAPE-OFF TOKAMAK PLASMA

Igitkhanov Yu.L., Pozharov V.A., Pistunovich V.I.
I.V.Kurchatov Institute of Atomic Energy, Moscow, USSR

ABSTRACT

A 2D-self-consistent model of impurity ion transport in the scrape-off layer and in the divertor volume has been developed. In difference from the previous models of test particles [1], the concentration of impurities in the divertor can be rather large ($\sum n_z z^2 > n_i$) and determine the parameters of the main plasma. The main plasma is described within the frames of 2D-hydrodynamical transport equations and it is consistent with the impurity problem: the plasma flow to the divertor plate provides the impurity ion flux from the plate due to sputtering, plasma electron and ion transport coefficients as well as the longitudinal electric potential depend on the impurity concentration. The 20-moment Grad method is used to describe the impurity ions. The expressions in the explicit form have been derived for the transport coefficient in the equations of multifluidal hydrodynamics, describing the longitudinal transport of impurity ions for all charge states. The transversal transport for all the components is simulated as a diffusive one with the anomalous (Bohm) transport coefficient. It is shown that a thermal force affectin a highly-ionized impurity ion weakly depends on its charge state (in difference from the test-particle approximation), when the relaxation of protons in a plasma is determined mainly by the collisions with impurities. The last effect results in the reduced pushing of such impurities by a thermal force in comparison with the friction force due to the streaming plasma flow onto the plate (this friction force remains to be proportional to Z^2). This results in the possible impurity circulation within the divertor volume, with due regard for transversal diffusion, and in the impurity localization near the divertor plates.

1. Igitkhanov Yu.L., Pistunovich V.I., Pozharov V.A. IAE Preprint 4217/8.

14 European Conference on Controlled Fusion and Plasma Physics.

IMPURITY TRANSPORT AT THE PLASMA EDGE IN TOKAMAK

Krupin V.A., Yushmanov P.N.
I.V.Kurchatov Institute of Atomic Energy, Moscow, USSR

The generalized transport in the Pfirsch-Schluter regime for arbitrary perturbations in the impurity concentrations has been derived. The Coulomb collisions at the plasma column edge are found to be so effective that longitudinal flows cannot equalize the impurity ion density upon the magnetic surface. As a result, a poloidal asymmetry in concentration observed in the experiment emerges. Under these conditions the neoclassical theory, assuming the smallness of perturbations upon the magnetic surface $\tilde{n}/n_0 \ll \varepsilon$,turns out to be inapplicable. The calculation of impurity densities in the hydrodynamical approximation with the account of a radial diffusive flux and ionization sources is carried out in the paper. The necessity of the diffusive flux account, which follows from the violation of the approximation $\tilde{n}/n_0 \ll \varepsilon$, results in a rise in the order of equations in comparison with the traditional approach. Under these conditions the Pfirsch-Schluter radial fluxes, generalizing the known neoclassical expressions, have been calculated. The additional terms are shown in the expression for the flux to be important in the transient processes only. An equilibrium state with a zero flux is described by an expression close to the neoclassical one.

THE IMPURITY CONTROL LIMITER EXPERIMENT ON DITE

G F Matthews, G M McCracken, D H J Goodall, C S Pitcher*, P C Stangeby*, J Allen, R Barnsley**, R C Bissel, S J Fielding, N Hawkes, J Hugill, P C Johnson, L N Khimchenko***, A M Ternopol****

Culham Laboratory, Abingdon, Oxon OX14 3DB, UK
(Euratom/UKAEA Fusion Association)

* Institute of Aerospace Studies, University of Toronto, Canada
** Department of Physics, University of Leicester, Leicester, UK
*** Kurchatov Institute, Moscow, USSR
****Physicotechnical Institute, Kharkov, USSR

1. Introduction

In this paper we present results from the impurity control limiter (ICL) experiment which is installed on the DITE tokamak. Unlike a conventional limiter the ICL is toroidally concave on the side facing the plasma. It is designed so that the majority of the incident ions strike the back of its carbon tiles which are at an angle of 35° to the toroidal magnetic field. Impurities sputtered from these surfaces are directed towards the walls and have a low probability of ionisation. Also, the ionisation which does occur is strongly localised in the scrape-off layer (SOL) where impurities are more likely to be driven back to the limiter. Quantitative predictions of the relative importance of these effects have been made by Matthews, et al (1987) using a 2-D Monte-Carlo sputtering code. These calculations showed that a significant reduction in the carbon impurity content could be achieved in situations where sputtering from the limiters is the dominant source of contamination.

2. The Experiment

The ICL consists of a 180° poloidal sector of 21 cm radius made from 9 poco-graphite tiles. Figure 1(a) shows a section through one of the tiles and 1(b) the complete assembly. Twelve flush Langmuir probes are used to diagnose the plasma local to the ICL. This information can be combined with

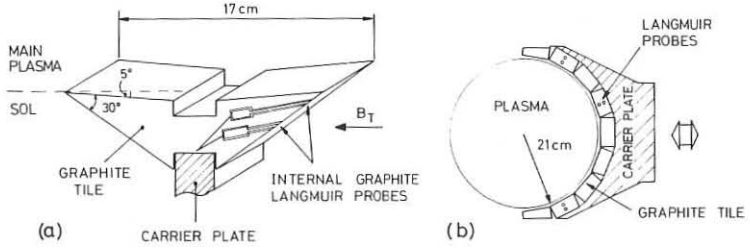

Figure 1 The ICL (a) tile cross section (b) the assembly

the measurements of line radiation from specific neutral impurities, made with CCD cameras imaging the ICL, and used to test the predictions of the 2-D code. An infra-red camera enables thermographic studies of the vulnerable leading edges of the ICL (Goodall, 1987).

The ICL can be withdrawn completely from the torus and two graphite rail limiters located at the top and bottom of the machine driven into the same radius for comparison. These rails are of conventional geometry with a 30° chamfer at the leading edge. On a nearby port a rapid movement Langmuir probe measures the plasma parameters in the shadow of the rail limiters. Imaging of the rails with the CCD camera is also possible through a tangential window on an adjoining octant of the torus.

3. Results

3.1 Global Behaviour

Comparisons are made between the rails and ICL in both helium and deuterium plasmas. A standard ohmic discharge is described with a plasma current of 100 kA and a toroidal magnetic field of 2 T. In helium the ICL reduces the

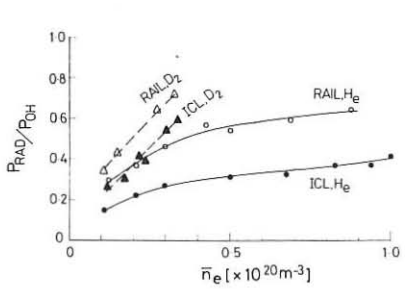

Figure 2 Radiated fraction P_R/P_{OH} as a function of $\bar{n}_e$.

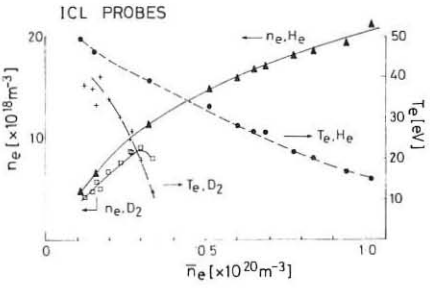

Figure 3 Electron density and temperature, at the ICL radius, versus $\bar{n}_e$.

total radiation (P_R) to less than one half of that seen with the rails at all densities. In addition, the loop voltage falls by 10% (from 2V to 1.8V at $\bar{n}_e = 3\times10^{19}m^{-3}$), consequently reducing the ohmic input power (P_{OH}). The radiated fraction P_R/P_{OH}, which is plotted in figure 2 as a function of line average electron density $\bar{n}_e$, is 45% lower with the ICL than with the rails in helium plasmas.

In deuterium, where the disruptive density limit is almost three times lower than in helium, the ICL has a smaller effect on global parameters; it reduces the total radiation by 20% and the loop voltage by 4% (from 2.3V to 2.2V at $\bar{n}_e = 3\times10^{19}m^{-3}$).

3.2 Local Behaviour

In figure 3 the poloidally averaged electron density and temperature at the leading edge of the ICL are plotted as functions of line average density. These measurements are made with the Langmuir probes embedded in the ICL. Helium and deuterium plasmas have very similar edge electron density profiles at a given line average density. However, the electron temperature in deuterium falls much more rapidly with increasing line average density than in helium, and in both cases the density limit is reached with the edge temperature in the region of 10 to 15 eV.

The Langmuir probe measurements have been used as input data for the 2-D sputtering code. This model calculates the energies of the incident ions from the specified plasma conditions and determines the physical sputtering yield (Bohdansky, 1984), self sputtering and chemical sputtering are neglected (Pitcher, 1986). It then generates trajectories with the energy and angular distribution specified by Thompson (1981) and computes the ionisation of the sputtered atoms in each plasma cell. In the case of carbon the photon efficiency (Pospieszczyk, 1987) is used to compute the CI emission at each point and this is then integrated torodially along the lines of sight. The results of this procedure are shown in figure 4 along with the normalised radial distributions measured with a CCD camera fitted with a CI (9050 Å) interference filter. Theory and experiment are in good agreement considering that there are no arbitrary parameters. As predicted, the ICL pushes the CI source into the scrape-off layer, in complete contrast to the rail limiter where the bulk of the emission is located inside the limiter radius. These observations apply equally to deuterium and helium plasmas.

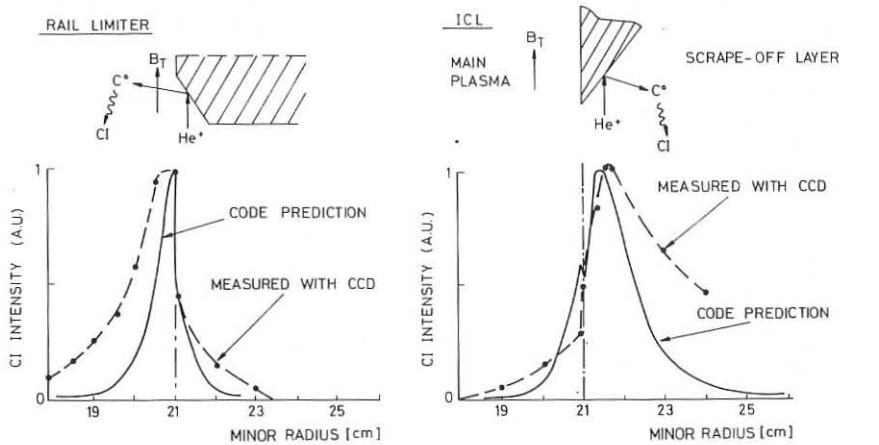

Figure 4 Measured and predicted radial CI intensity distributions for rails and ICL.

4. Spectroscopy

A wide variety of spectroscopic data is available. Intensities of Fe XVII(15A°) and OVIII(19A°) near the centre of the plasma are measured with a Bragg rotor spectrometer (Barnsley, 1986). In the ultra-violet region of the spectrum OVI(1037A°), OV(629.7A°), CV(2271A°) and CIII(1176A°) are monitored. An analysis of this data using a $1\frac{1}{2}$-D transport code (Behringer, 1986), shows that the radiated power is dominated by oxygen and carbon in all cases. Far from either limiter, a visible spectrometer is focused on the wall and observes CII(4267A°), OII(4351A°) and CrI(4274A°). When there is a change from deuterium to helium the wall influxes of carbon and oxygen are reduced by a factor of 10.

In helium plasmas the impurity concentrations deduced from the OVIII and CV shows only a small reduction when the rail limiters are replaced by the ICL. However, the lower ionisation states OII, OV, OVI and CII, CIII indicate a halving of the influx. This inconsistency cannot be resolved by a $1\frac{1}{2}$-D impurity transport model and so a definitive analysis of the impurity control cannot yet be provided.

5. Discussion

Significant global impurity control has been demonstrated with the ICL in helium plasmas but it is not as great in deuterium. We believe that this difference is due to the dominance of the impurity influx from the walls in deuterium. Support for this view is provided by spectroscopy of the wall sources of carbon and oxygen which show a ten fold reduction when the switch is made from deuterium to helium. This behaviour is probably associated with the charge exchange flux which is found in ASDEX to be 5-15 times lower in helium than deuterium (Verbeek, 1987). However, the physical sputtering yields are too low to explain the influxes and so charge exchange induced desorption must be postulated (McCracken, 1987).

The physical sputtering of carbon from the ICL and rails and its subsequent ionisation is well described by our 2-D computer model. This aspect of the problem is in accord with our predictions and is well understood.

References

Barnsley, R, et al, (1986) Rev. Sci. Instrum Vol. 57 p2159.
Behringer K H, et al, (1986) Nuclear Fusion Vol. 26 No 6 P751.
Bohdansky, J (1984), Nuclear Fusion Data Compendium for PSI, pp 55-72.
Goodall, D H J (1987), this Conference.
Matthews, G F, McCracken, G M, Stangeby, P C, Pitcher, C S, Sewell, P, Goodall, D H J (1987), Plasma Physics and Cont Fus. Vol.29, No.2, p 189.
McCracken, G M, (1987) this Conference.
Pitcher C S, et al, (1986) Nuclear Fusion Vol. 26 p1641.
Pospieszczyk, A, private communication.
Thompson, M W (1981), Physics Report No.69, 335.
Verbeek, H, and the ASDEX team (1987), J Nuc Mats, 145-147 p 523.

THE THERMAL PERFORMANCE OF THE IMPURITY CONTROL LIMITER GRAPHITE TILES IN SIMULATION EXPERIMENTS AND IN THE DITE TOKAMAK

D H J Goodall, G F Matthews, G M McCracken, C S Pitcher* and D A Hughes

Culham Laboratory, UKAEA, Abingdon, Oxon. OX14 3DB
(Euratom/UKAEA Fusion Association)
* Institute for Aerospace Studies, University of Toronto, Canada.

1. Introduction

The impurity control limiter (ICL) in the DITE tokamak is made from 9 individual graphite tiles which have a thin tapered leading edge shaped to minimise the sputtering of impurities into the plasma[1]. The cross sectional profile is unlike that found for typical limiters which are designed to spread the incident heat flux uniformly over their surface. Fig. 1 shows a single ICL tile with a JET limiter tile for comparison. The maximum heat load for the ICL is at the leading edge unlike the JET tile where the maximum surface temperature and erosion are observed in the region shown in Fig. 1 on either side of the tile centre[2]. In addition to the normal heat flux, the tips of the ICL tile are vulnerable to runaway electrons and a suitable graphite must be chosen to minimise this type of damage.

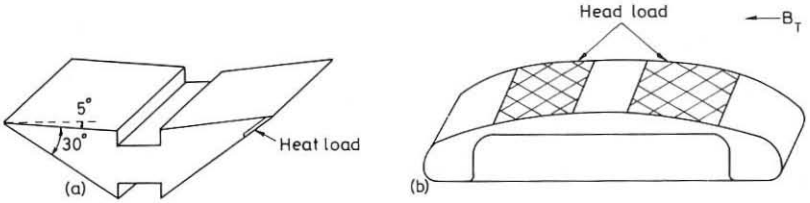

Fig. 1 (a) an ICL limiter tile (b) a JET limiter tile.

2. Choice of Graphite

From the many possible graphites, three types were selected for heat load simulation experiments using a high power laser which could provide ~ 10 kW continuously. These were a pyrolitic graphite[3], Poco[4] and 5890PT[5]. The thermal properties of the pyrolitic graphite differs markedly from the other two, having a thermal conductivity which is a factor of 3 higher in one plane and only ~ 0.005 of this value orthogonal to the high conductivity direction. Tests on rectangular samples with peak laser power density of 3.6 kw cm^{-2} for 5 sec showed least surface damage for the pyrolitic graphite, but delamination occurred at low power levels when the initial temperature was > 300°C. Surface damage and weight loss for the other types were similar but with Poco performing slightly better than the 5890 PT graphite.

In addition to the rectangular samples, small triangular samples of Poco graphite similar to the design of the ICL tile leading edge were tested using the laser beam incident on the apex of the triangle with a power density ~ 3 kw/cm^2 over an area of 1 cm^2 for 0.5 secs, simulating the expected heat load in DITE. No significant damage was observed under these conditions.

To simulate runaway electron damage triangular samples were placed in a vacuum chamber with an electron beam incident on the apex of the triangle. The samples were moved through the beam at uniform velocity. The experimental arrangement enabled a large number of graphite types to be compared including carbon reinforced graphites. Beams from 60-80 kV with current densities up to 5 A cm^{-2} were used. Again it was found that Poco graphite showed the least erosion at the apex of the samples and this material was therefore selected to fabricate the ICL.

3. Thermal and Stress Analysis of an ICL tile

A 2D finite element analysis using the computer program PAFEC (6) was undertaken to evaluate the temperature and stress distribution and to calculate peak temperatures. A 216 element mesh is used in the computation with very small elements at the tip of the tile, increasing in size towards the base (Fig. 2). The analysis is divided into two parts, a transient pulse heating phase followed by a cooling period equal to the pulse length. Stress calculations are made at the end of the heating phase using the computed thermal data. For the heat calculations, an incident heat flux $F(r) = F_0 \exp(-\frac{r}{\lambda})$ is assumed where $F_0 = 3$ kWcm^{-2} and $\lambda = 1$ cm with radiative cooling to 0 K and a tile base temperature of 300K for both heating and cooling cycles. The thermal properties of 5890PT graphite are used as these are known as a function of temperature. Once the incident heat flux is removed the hot tip acts as a heat source which conducts to the rest of the body giving a peak temperature stress at the end of the heating pulse. The calculations show that the tip reaches 2620K at the end of a 0.5 sec pulse cooling to 1375K after a further 0.5 sec. A large proportion of the tile, however, remains at the base temperature with the maximum thermal gradient at the tip along the face OA.

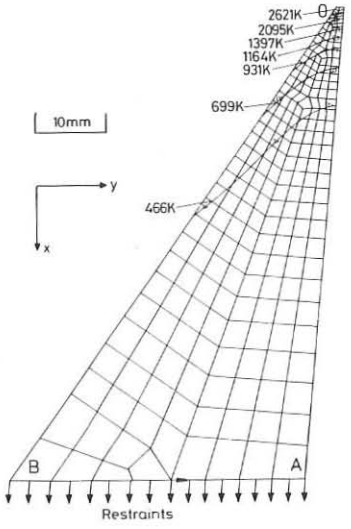

Fig. 2 The mesh and the temperature gradients after 0.5 secs heating.

For the stress calculations the same mesh is used with the tile base AB constrained not to move in the x direction and the mid-point of AB constrained not to move in any direction. The analysis is in two parts, a plane strain and a plane stress boundary condition with zero displacement in the Z direction orthogonal to the plane in fig. 2. Although this can cause artificially high out-of-plane stress it is considered in practice this would not occur in a finite object. The computations show that there is some stress relief by the bending of the thin tip of the tile and that both faces OA and OB are in compression with tensile stress in the tile centre. The in-plane stresses calculated are considerably below the failure stress giving a high factor of safety.

4. The Performance of the ICL

The local conditions at the ICL are monitored using integral Langmuir probes and thermocouples and remotely by a scanning infrared camera and CCD cameras fitted with interference filters. The IR camera at the back of the ICL drive views the apex and part of the outer sloping face on both sides of the tile immediately below the median plane tile. A similar view but centred on the tile immediately above the mid-plane is obtained using a CCD camera. A vertical view of the back of the mid plane tile is obtained by a miniature CCD camera and a complete view of the ICL is available from a CCD camera using a tangential window. All the CCD cameras could monitor CI, CII, CIII, OI, OII and H_α line emission.

The Langmuir probes are in pairs at three different poloidal positions, and at two minor radii. This provides in addition to the local T_e and n_e measurements the e-folding length for the power to the ICL, λ_p, from which the power density at the tile apex can be extrapolated. The nearest Langmuir probe pair to the tile observed by the IR camera is on the electron drift side of the tile immediately above the median plane. Thus a comparison of the heat flux above and below the median plane can be made.

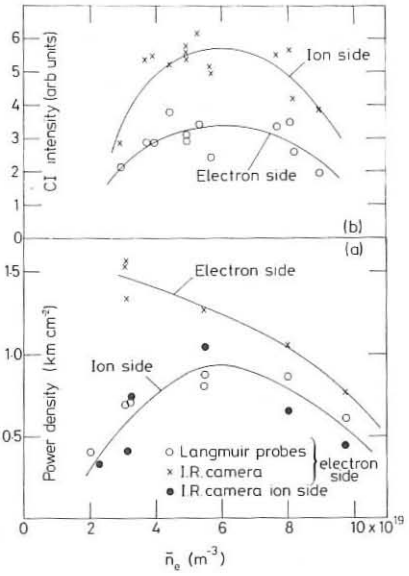

Fig. 3(a) The power density on ICL tiles above and below the median plane tile. (b) Intensity of CI radiation above median plane, as a function of line average line density.

The ICL consists of discrete straight sided tiles forming a polygon which does not exactly match the circular flux surfaces (1). The maximum plasma

surface interaction therefore, occurs at the centre of the flat face of each tile. Fig. 3 shows the power density at the centre of the tile apex as a function of the line average density for a 100 kA helium discharge with a toroidal field of 2T. There is a marked difference between the two sides of the tile for the IR results at low density probably due to a contribution to the power from supra thermal electrons and non-ambipolar current flow (7) on the electron side. (Both the IR and CCD cameras show very localised interactions which decrease and eventually disappear as the density increases). When the mapping of the ICL on to itself for a rotational transform of q = 3.8 is considered, it is found the electron side of the upper tile containing the probes is connected after 4 toroidal rotations to the ion side observed by the IR camera. Fig. 3 shows that the power density for these two positions is in good agreement both in magnitude and density dependence. This is partly fortuitous since a sheath transmission factor of 10 has been assumed and non-ambipolar currents are ignored.

The CI line intensity at the upper tile for a helium discharge shows a similar density dependence to the power density and also reaches a maximum at 6 x 10^{19} m^{-3} (fig. 3b). There is also an asymmetry between the two sides, with the ion drift side having twice the intensity of the electron side which is again consistent with the mapping between the upper and lower tiles.

5. ICL Damage

Slight damage was observed on the tiles above and below the median plane tile and on the median plane tile itself. This damage consists of the removal of about 1-2 mm from the original apex of the tile for a few cm of tile height. This damage occurred during low density discharges and is thought to be mainly due to runaway electrons. Once damaged, the tiles did not deteriorate further during normal density discharges and there was no noticeable effect on the distribution of sputtered atoms as seen by the CCD cameras.

6. Conclusions

The power density observed at the ICL tiles was within the limits anticipated for the stress analysis computations and confirmed that the type of graphite selected from simulation tests is a suitable material for the ICL geometry and the plasma conditions during the experiment. Some minor runaway electron damage was observed but this did not affect the performance of the limiter in the control of impurities.

References

(1) G.F. Matthews et al. This conference.
(2) J.P. Coad al. This conference.
(3) Pyroid graphite manufactured by PFIZER, USA.
(4) Poco AXF5Q manufactured by ERODEX, USA.
(5) 5890PT manufactured by Le Carbonne, France.
(6) PAFEC finite element program written by PAFEC Ltd. Nottingham U.K.
(7) S. Pitcher et al. This conference.

ENHANCED PARTICLE FLUX CONTROL IN A TOKAMAK WITH A RESONANT HELICAL DIVERTOR

T.E. EVANS, J.S. deGRASSIE, G.L. JACKSON, N. OHYABU
(GA Technologies Inc., P.O. Box 85608, San Diego, Calif. 92138 USA)
F. KARGER and G. HAAS
Max-Planck-Institut für Plasmaphysik, EURATOM, D-8046, Garching, Fed. Rep. of Germany)
A.J. WOOTTON, K.W. GENTLE, S.M. McCOOL, W.L. ROWAN,
R.D. BENGTSON, T. RHODES, B. RICHARDS, C.P. RITZ, P. PHILLIPS, R. DURST,
S.B. ZHENG*, X.H. YU*, S. FAN**, and the TEXT GROUP
(The University of Texas at Austin, Fusion Research Center, Austin, TX 78712 USA)

1. INTRODUCTION

A series of experiments designed to demonstrate the efficacy of the Resonant Helical Divertor /1/ (RHD) concept in a tokamak have been completed. These proof-of-principle experiments utilized a small scoop limiter and a simple modular coil set /2/ to produce an $m = 7$, $n = 2$ RHD configuration for controlling the particle efflux and edge refueling rate in the Texas Experimental Tokamak (TEXT). The coils were designed to generate a quasi-ergodic edge layer using a few modes. Nevertheless at small perturbation levels intact islands are produced. See Fig. 1 for the relative positions of the perturbation coils and the scoop limiter module. A description of the movable scoop limiter, the diagnostics used for analyzing the RHD performance, and the TEXT island topology have been given in a previous paper /3/. Typical TEXT RHD parameters are $\bar{n}_e \approx 2 - 3 \times 10^{13}$ cm^{-3}, with an ohmic plasma current (I_p) between 230 kA and 295 kA depending on r_ℓ. The results, for scoop limiter minor radii (r_ℓ), between 20 cm and the primary TEXT limiter at $r = a = 26$ cm ($R_o = 1.0$ meter) clearly demonstrate greater flux control than had been expected for this simple RHD geometry. Conditions necessary for optimal particle collection are: the scoop limiter at the o-point of a 7/2 magnetic island, a 4 kA current in the coils producing islands of ~ 1.0 cm full width, and helium discharges at high toroidal magnetic field ($B_T = 2.8T$). The neutral density (n_o) within the scoop limiter head is increased by up to 500% and recycling on the front scoop face can be reduced as much as 80%. Under optimal collection conditions the central electron density ($\bar{n}_e$) is reduced by 20% indicating enhanced global particle control. Experimental results and implications of cross-field particle diffusion are presented. A comparison of RHD efficiencies in hydrogen and helium discharges is discussed.

The RHD concept was proposed in 1977 after experiments in Pulsator /4/ suggested that magnetic islands could be resonantly driven with external coils and used to guide plasma flux into a collection aperture. This is conceptually similar to the poloidal divertor but with the advantage that resonant helical magnetic islands may be driven using relatively modest currents in a simple external coil. Operational advantages of the RHD approach include an ability to adjust the flux collection efficiency on a short time scale for feedback control during a discharge and dynamic island shielding of sensitive material collector components. An ideal RHD configuration may be capable of providing plasma unloading efficiencies from 10%, a typical value for conventional pump limiters, up to values approaching 100%, which are expected with full poloidal divertors.

Demonstration experiments on TEXT have produced better than expected particle flux control results. The relatively small poloidal and radial extent of the magnetic islands, shown to scale in Fig. 1, restrict the size of the limiter head and neutralization plate which means

* Institute of Plasma Physics, Chinese Academy of Sciences, Beijing, PRC.
** Institute of Plasma Physics, Hefei, PRC.

that particles must make many toroidal circuits before transiting an island and striking the neutralizer. In high cross-field diffusion dominated discharges the full benefit of coherent island RHD flux control mechanisms are lost to local effects which dominate near the limiter. Extreme radial diffusion washes out the island effects completely. In this limit the RHD concept has little or no useful purpose in terms of flux control. Although the TEXT configuration is somewhat less than ideal with its small radial island widths and closely spaced multiple mode resonances, (see Fig. 1), the experiments demonstrate very large improvements in the scoop collection efficiency during RHD operation. The increase in efficiency is so dramatic that additional mechanisms must be invoked to explain the rapid circulation of particles around the islands. The case shown in Fig. 1 implies that particles must make about 10 toroidal circuits in order to travel from the inner 7/2 island separatrix to the outer separatrix where they will be collected by the limiter. This corresponds to a toroidal transit length of ~60 meters or roughly a 1 ms transit time. In TEXT $D_r \approx 10^4$ cm^2/sec gives an average radial diffusive velocity $\langle v_r \rangle_{diff} = \langle \Delta r \rangle_{diff}/t$ =3 cm/ms. Thus radial diffusion carries particles across the primary resonant islands faster than it takes them to make a normal island circuit assuming only parallel flow. The effective rate of circulation can be increased if the island o-points are at a different potential than the separatrix. 50 V/cm radial island electric fields have been observed on CSTN-11 /5/ with externally imposed magnetic islands and would provide a sufficient $\mathbf{E}\times\mathbf{B}$ island circulation velocity to compensate for the effect of radial diffusion and explain the large efficiency increases which are observed with the TEXT RHD.

2. FLUX CONTROL RESULTS FROM THE RHD DEMONSTRATION ON TEXT

In the demonstration experiments on TEXT a measure of the effectiveness of the RHD is obtained from neutral density measurements behind the scoop limiter head. During the steady state RHD period, a parallel particle flux $\Gamma_\parallel \propto n_i v_\parallel$ enters the scoop aperture, hits the neutralizer and is collected for measurement as neutral gas in the scoop chamber. When the helical current is pulsed (typically with a pulse length of several hundred milliseconds) any neutral density change in the scoop chamber reflects a change in $\Gamma_\parallel$.

The typical data signature of interest is a drop in the recycling light on the limiter face with a corresponding rise in the scoop chamber neutral density as $q_\ell \left(\equiv q_{cyl} \left[1 + \frac{\epsilon^2}{2} \gamma \right] \right)$, the safety factor on the scoop limiter face, nears 7/2. Here $\epsilon = r_\ell / R_o$ and $\gamma = 2(\Lambda - 1) + (\Lambda - 1)^2 + 3$ account for the reduced plasma size and toroidal effects with $\Lambda = \beta_p + \ell i/2$. These signatures are consistently observed with 20 cm $\leq r_\ell \leq$ 24 cm and with the helical coil current (I_H^-) phased to produce a fundamental $m/n = 7/2$ island o-point on the limiter head. Figure 2 shows the neutral density time response. Figure 2(a) shows n_o^H for a hydrogen discharge with $r_\ell = 24$ cm while 2(b) shows n_o^{He} for a helium discharge with $r_\ell = 22$ cm. As q_ℓ increases through 3.3, n_o^H goes up by approximately a factor of two. $\delta n_o(q_\ell)$ is clearly a resonant phenomenon. Given a plasma density of $\bar{n}_e = 4 \times 10^{13}\ cm^{-3}$ this increase in scoop neutrals corresponds to roughly 2.5% of the total plasma ions. A reduction in the recycling source at the face of the scoop limiter accounts for an additional loss of fueling. Although the exact nature of this change in recycling is complex we expect that an increase in recycling takes place inside the scoop chamber as flux is diverted away from the face into the aperture.

The combined effect of enhanced particle flux collection with loss of limiter face refueling are shown in Fig. 3. A multi-chord FIR laser interferometer is used to obtain plasma density profiles, $n_e(r)$, just prior to the I_H^- pulse (*i.e.*, at t = 300 ms), and at four subsequent times during the I_H^- pulse. Figure 3(a) shows the n_e profiles during the RHD pulse at t = 345 ms, 465 ms, 390 ms, and 428 ms respectively. Shown in Fig. 3(b) are the time evolution of $\bar{n}_e$ and the H_α light from the scoop limiter face. These results are from a hydrogen discharge which had a n_o^H response similar to that shown in Fig. 2(a). A $n_e(r)$ profile modification occurs as the scoop collection efficiency is increased and the scoop limiter recycling begins to drop. This

causes a decrease in n_{eo}, the central electron density, with relatively little change in the shape of the $n_e(r)$ profile. One-quarter of 20% reduction in n_{eo} is accounted for with the increased flux collection of the scoop limiter while the remainder is due to a drop in the limiter face recycling and a reduction in the particle confinement time due to a partial ergodization of the edge /6/.

3. COMPARISON OF RHD EFFICIENCY IN HYDROGEN AN HELIUM DISCHARGES

RHD induced neutral density increases in the scoop limiter chamber are observed for both hydrogen and helium discharges. Typically the increase in the scoop efficiency is more pronounced for helium, in some cases a 500% increase is observed. The best results in hydrogen are limited to slightly better than 100%. Figure 2(b) shows a typical RHD induced n_o^{He} increase. This may be compared with the results shown in Fig. 2(a) for hydrogen. Figure 2(a) shows data for $I_H^- = 3$ kA while Fig. 2(b) $I_H^- = 5$ kA. Allowing for differences in r_ℓ in these two cases and the perturbation field intensity decay typical of our $m = 7$ coils there remains a slight difference between the optimal I_H^- for hydrogen and that for helium discharges. The difference in I_H^- may be related to a difference in the radial diffusion coefficients (D_r) for hydrogen and helium.

As yet data on the radial diffusion coefficients (D_r), scrapeoff layer widths (λ_n), and particle confinement times (τ_p) for these two species is incomplete. Relatively complete electron temperature profiles have been measured and measurements of τ_p in hydrogen and deuterium have been regularly obtained. These τ_p measurements indicate a $m^{1/2}$ /7/ scaling suggesting that a factor of two increase in τ_p from hydrogen to helium may be reasonable. All the data now support a model which indicates that the flux steering capacity of the RHD configuration depends strongly on D_r.

4. CONCLUSION

The effectiveness of the RHD concept for enhanced particle flux control has been demonstrated on TEXT. Different RHD efficiencies have been found for hydrogen and helium discharges. These differences are believed to be related to the diffusion coefficient, D_r, as well as variations in other discharge parameters. Correlations with other parameters are being investigated both experimentally and with numerical particle transport simulations. Enhanced island circulation velocity due to radial electric fields in the island and $\mathbf{E}\times\mathbf{B}$ drift can explain the better than expected efficiency of the RHD on TEXT. The full potential of the RHD awaits demonstration on a large auxiliary heated tokamak using an optimized perturbation coil to generate coherent islands of width ~0.1 a.

ACKNOWLEDGEMENTS

Work supported in part by the U.S. Department of Energy Contracts DE-AC05-78ET-53043 and DE-AC03-84ER53158.

REFERENCES

/1/ F. Karger and K. Lackner, *Phys. Lett.* 61A (1977) 385.
/2/ N. Ohyabu, J. S. deGrassie, *et al.*, *Nucl. Fusion* **25** (1985) 1684.
/3/ T. E. Evans, J. S. deGrassie, G. L. Jackson, N. Ohyabu, *J. Nucl. Mater.* **145-147** (1986) 812.
/4/ F. Karger, *et al.*, in: 5^{th} Conf. on Plasma Phys. and Contr. Nuclear Fusion Research, Tokyo, 1974, IAEA-CN-33/PD-2; F. Karger, *et al.*, in: 6^{th} Conf. on Plasma Phys. and Contr. Nuclear Fusion Research, Berchtesgaden, 1976, IAEA-CN-35/A-7.
/5/ S. Takamura, N. Ohnishi, H. Yourada and T. Okuda, *Phys. Fluids* **30**, 144 (1987).
/6/ A. J. Wootton, R. D. Bengston, *et al.*, in: 11^{th} Inter. Conf. on Plasma Phys. and Contr. Nuclear Fusion Research, Kyoto, IAEA-CN-47/A-111-6.
/7/ W. L. Rowan, private communication.

Fig. 1.

a.) Relative positions of the RHD perturbation coils and movable scoop limiter. b.) Partial Poincaré section showing the magnetic island topology with the scoop head positioned in the $\theta = 90^0$, m/n = 7/2 island o-point.

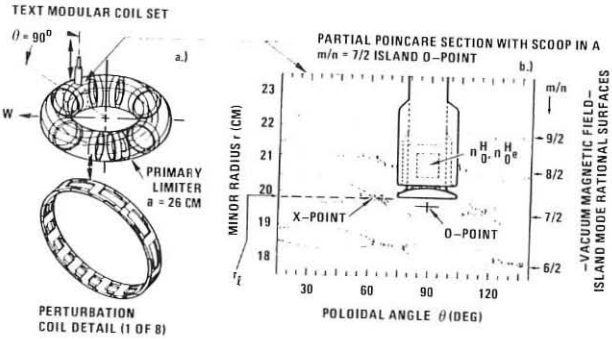

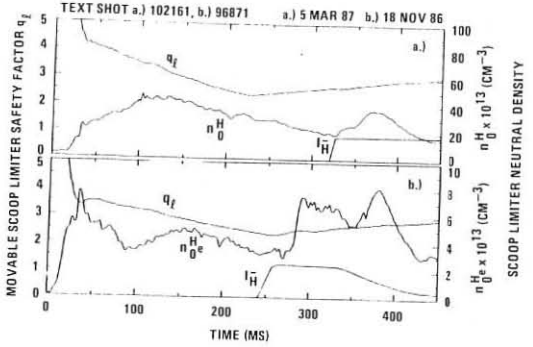

Fig. 2.

a.) Time evolution of the scoop neutral density n^H_0 in hydrogen. b.) Time evolution of n^H_0e for similar conditions as a.) but in helium. Note the larger δn^H_0e but lower ambient n^H_0e value.

Fig. 3.

a.) Density profile n_e (r) at five times during the discharge as indicated by the arrows from b.). b.) Time evolution of $\bar{n}_e$ and the scoop H_α with I^-_H = 5 kA in hydrogen.

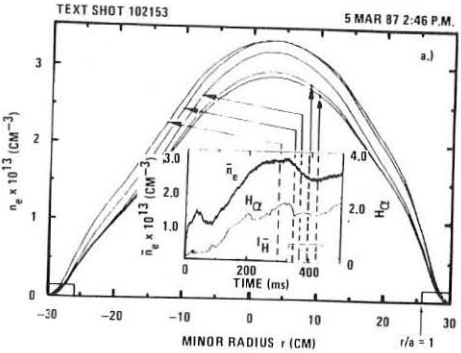

ICRH INFLUENCE ON DEUTERIUM AND IMPURITY DEPOSITION, MEASURED BY COLLECTOR PROBES.

B. Emmoth[♠], H. Bergsaker[♠], S. Nagata[♡], M. Rubel[◇], P. Wienhold[♣], J. Winter[♣], and F. Waelbroeck[♣].

[♠] Research Institute of Physics, S-104 05 Stockholm, Sweden

[♡] Department of Nuclear Engineering, Tohoku University, Sendai, Japan

[◇] Space Research Centre, Polish Academy of Sciences, 01-237 Warszawa, Poland

[♣] Institut für Plasmaphysik, KFA, POB 1913, D-5170 Jülich, FRG

1. Introduction

The deposition rate of deuterium and impurity fluxes have been studied by analysis of rotating collector probes, exposed at TEXTOR in the scrape-off layer. Details of the probe system were described earlier /1/. The collected deuterium was measured by using the nuclear reaction $D(^3He,p)^4He$. Impurities were determined by Rutherford backscattering analysis.

The TEXTOR discharges were additionally heated by ICRH. The input power varied in the range 0.2 - 0.9 MW. The collector probe was exposed for one single discharge on several occasions, but twice two discharges were overlayed in order to study the scaling of deposited particles. A typical discharge lasted 3-4s, with a flat top current of 350-500 kA and a central electron density of $2\text{-}4\cdot10^{13}$ atoms/cm^3.

For the interpretation of the deuterium measurements we use experience from other experiments at TEXTOR and at JET, where it was found that deposited deuterium concentrations should be explained by two different effects. One contribution would be implantation of deuterium and another effect would be the codeposition of deuterium and carbon impinging at the probe surface. In the latter case every new layer of carbon deposits reach saturation, and a measure of deuterium surface concentration corresponds to deposited carbon flux. Data collected in a time-resolved way are critically influenced by the exposure time, and due to limited of measurements the reported results should be considered as preliminary.

The impurities oxygen and metals were also detected on the probes. Oxygen was only found in small quantities or less than one tens of deuterium. Measured metal concentrations were even smaller.

2. Results.

Increased deposition of deuterium in form of a peak when ICRH acted on the plasma, Fig. 1*a*, can be compared with the evolution of the density, Fig. 1*b*, and the corresponding change in central electron temperature, Fig. 1*c*. This behaviour is typical in a number of shots, although in a few cases these features in the deuterium deposition was obscured by

a "fine structure". A slower increase in density, Fig. 1*b*, appears to be slightly delayed as compared to the ICRH pulse. From our deuterium data, there is no consistant support for a delayed deposition of deuterium.

In the next figure it is shown that an increased metal deposition i Fig. 2*a* comes with an increase in oxygen deposition, Fig. 2*b*, simultaneously with an increased deuterium deposition, Fig. 2*c*. Both deuterium and impurities increase during the ICRH pulse, suggesting that the same responsible processes are acting. Collected metals are expected to be directly related to the fluxes of metal impurities in the scrape-off layer. The deposition mechanisms for oxygen are not yet fully investigated.

In Fig. 3 seven radial decay curves are shown for deuterium. The average e-folding length is approximatly 40-50 mm. The two top curves seem to have a longer decay for the first part which is closer to the plasma. These curves were taken within and at the end of an ICRH pulse, but data are not sufficient for definite conclusions concerning a different e-folding length inside and outside ICRH, as was earlier shown in Langmuir data /2/.

3. Discussion and Conclusions.

Deposited deuterium surface concentrations on the collector probes can, since these measurements were made in a time-resolved mode, be converted to deposition rates of deuterium, which next can be compared to other calculations where deuterium fluxes were determined in the scrape-off layer by other methods like the lithium beam device at TEXTOR /3/. For a single discharge exposure of the probe, with an exposure time on each point of the collector of 0.13 seconds, we find the deposition rate of deuterium to be $4 \cdot 10^{17}$ atoms/ $cm^2 \cdot s$, whilst calculations based on density and temperature measurements with lithium beam experiments, give a deuterium flux at the probe position of $1\text{-}2 \cdot 10^{18}$ atoms $cm^{-2} \cdot s^{-1}$. Kinematic particle reflection, erosion induced by sputtering or thermal release, and diffusion due to the heat flux may partly be responsible for this discrepancy, but first the relation between the measured surface concentration of deuterium on the probes and the retained level in graphite at deuterium energies and fluences expected in the scrape-off layer should be considered.

Carbon which is subjected to deuterium implantation can only incorporate about 40 at. percent deuterium, which is retained in a surface layer, the width of which corresponds roughly to the range of the ions. Through the range, the maximum attainable areal density depends sensitively on the implantation energy. It has been shown that if the energy distribution of incident ions is known, the retained areal density can be calculated reliably using a simple local saturation model /4,5/in combination e.g. with TRIM depth profiles. Due to acceleration through the surface sheath, ions reaching the surface are essentially monoenergetic with average energies $E_{av} = K \cdot k_B T_e$, where K is a factor

between 3 and 6 /6/. In order to account for the influence of an energy spread $\sim k_B T_e$ we introduce an effective energy E_{eff} slightly higher than E_{av}, which would give rise to the same saturation level in monoenergetic implantation as is observed for the actual energy distribution. With electron temperatures T_e in the range 15-20 eV /3/, deuterium should saturate in graphite at 2-3·10^{16} atoms/cm^2, which is far below the areal concentrations measured on the probes.

For the general feature (e.g. Fig. 1a which can be compared with the feature of two overlayed discharges), disregarding the fine structure, the collected areal density of deuterium , A, during a specified fraction of the discharge is measured and can be written $A = \Phi \cdot \tau$, where Φ is the deposition rate and τ the exposure time. For a single discharge the areal density can be written $A^{(1)} = A_{imp} + A_c$, where the first term is the implanted part and the second the amount of deuterium related to codeposition with carbon. For two overlaid discharges, assuming the same n_e (0), we measure $A^{(2)} = A_{imp} + 2A_c$. The relations between the collected areal densities in the two cases give $A^{(2)} - A^{(1)} = A_c$, or $A^{(2)} = F \cdot A^{(1)}$, where F may vary from $F = 1$ if implantation only is responsible, up to $F = 2$ if the deposition is only determined by codeposition. In principle this is a way to measure the carbon flux Φ_c, since $A_c = b \cdot \Phi_c \cdot \tau$, where b is approximatly 0.4 or at least in the interval 0.2-0.5. In our investigated cases the factor F is found to be 2 or somewhat less. We can therefore conclude that the collected amount of deuterium is mainly determined by carbon codeposition.

Simultaneously with the ICRH we found an increase of the deposition of deuterium. If this increase ΔA in surface concentration on the probes is to be attributed to a raise of T_e, then $\Delta A = K \cdot \frac{dC}{dE_{eff}} \cdot k_B \Delta T_e(r)$. From the local saturation model or from experiments the factor $\frac{dC}{dE_{eff}}$ can be estimated, and from measurements at TEXTOR, $k_B \Delta T_e$(r) is approximatly known. Although some uncertainity still exists we can preliminary conclude that the observed increase during ICRH is mainly due to increasing codeposition and hence in carbon flux.

References.

/1/ B. Emmoth et. al. J. Nucl. Mat. 145-147 (1987)637

/2/ S.K. Erents et. al. J. Nucl. Mat. 145-147 (1987)231

/3/ G. Ross, TEXTOR, private communication

/4/ W.R. Wampler et. al. J. Nucl. Mat. 102 (1981)304

/5/ S.A. Cohen et. al. J. Nucl. Mat. 84 (1979)157

/6/ R. Chodura, J. Nucl. Mat. 111-112 (1982)420

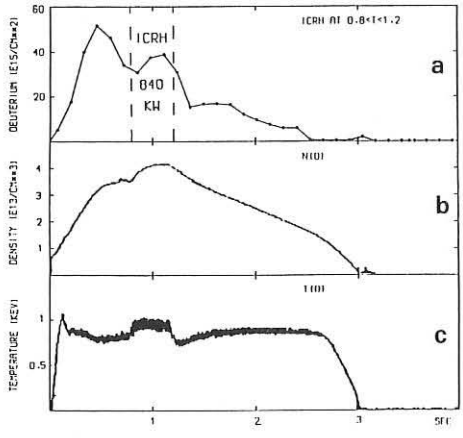

Figure 1

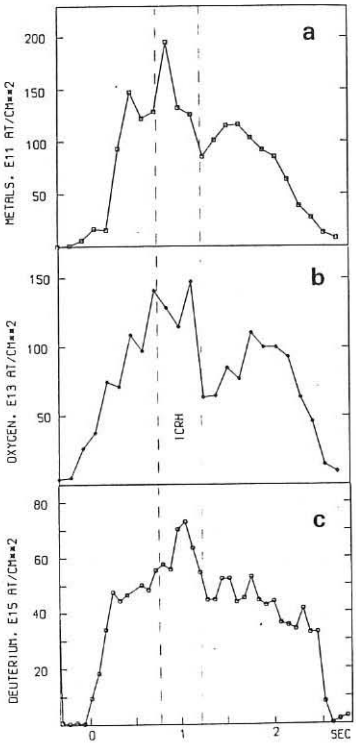

Figure 2

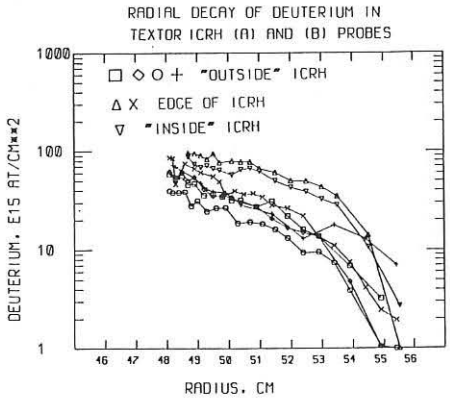

Figure 3

DEPOSITION AND EROSION AT THE OPEN AND CLOSED ICRH ANTENNAE OF ASDEX

R. Behrisch, F. Wesner, M. Wielunski[1], J.-M. Noterdaeme, E. Taglauer,
Max-Planck-Institut für Plasmaphysik,
EURATOM Association, D-8046 Garching

1. INTRODUCTION

In the ASDEX tokamak ICRH has been applied with two antennae and a total RF generator power of 3 MW for about one and a half years between 1984 and April 1986. Second harmonic and minority heating modes in Deuterium and Deuterium-hydrogen mixture plasmas have been investigated /1/. In April 1986 the antennae were dismanteled to be exchanged by watercooled ones. This gave the possibility to investigate the surface composition of the internal and external surfaces of antenna elements and of the carbon tiles of the antenna protection limiters using ion beam techniques as RBS, PIXE and Nuclear Reactions /4/ as well as SIMS and Auger Electron Spectroscopy. These surface compositions are the time integrated result of deposition and erosion processes during the different operation modes of ASDEX as glow discharge conditioning, carbonization and decarbonization processes as well as tokamak discharges in the L and H mode with NI, ICRH and LH heating and pellet injection.

2. GEOMETRY AND MATERIAL OF THE ANTENNA ELEMENTS

Two low field side loop antennae with Faraday screens and protecting limiters have been installed in ASDEX (Fig. 1, lower part). Central and return conductors of the loops and the antenna side wall elements were silver coated. The limiters were made of graphite mushrooms brazed into copper blocks, the copper being protected against particle bombardment by stainless steel plates at the side seen by the plasma. The Faraday screen was composed of TiC coated rods with different cross sections: the screen of one antenna consisted of T-shaped rods and was almost opaque while at the other antenna circular rods formed an optically open array /2,3/.

3. EXPERIMENTAL RESULTS

The surfaces of the dismanteled limiter elements and Faraday rods showed almost no visible modifications due to the plasma operation, while all parts below the Faraday screen of the optically open antenna - mainly the central conductor - showed a remarkable pattern of dark and bright stripes correlated with the position of the Faraday rods.
The distribution of metals and deuterium found on the TiC-coated Faraday rods and on the center conductor of the optically open antenna are shown in Fig. 2. In contrary to initial expectations carbon due to carbonization processes is almost homogeneously distributed and the dark stripes located in the shadow regions of the Faraday rods on the central conductor show a deposition of Fe and O. The bright stripes show clear maxima of D-implantation.
The distribution of wall material (Fe + Cr + Ni) and of Deuterium on the different Faraday rods is shown in Fig. 3. The concentration of both is clearly larger in front of the plasma than behind. The maxima of metals

---

[1] Guest scientist from Institute of Nuclear Research, Warshaw - Poland

are found at the sides or at half-shadowed surface parts of the rods while Deuterium shows a more homogeneous distribution with maxima rather in front of the plasma.
The deposition of silver on the inner surface of the opaque screen is much smaller than in the case of the optically open one (Fig.3) indicating that silver from the Ag-plated inner antenna surfaces is only eroded by particles coming from outside and not by arcing in the antenna. This is in agreement with the result, that the electrical strength in the open antenna is not worse compared to the closed one up to the tested level /2/.
The small content of tantalum and tungsten is possibly an impurity originating from the TiC coating process.
Figure 1 (upper side) shows the toroidal variation of the surface composition of the Faraday screen elements and of the protection limiters facing the plasma. While the D-concentration is similar for screen and limiter elements, the concentration of wall material (Fe + Cr + Ni) on the screen is considerably smaller than on the limiters.
The amount of Ti, Cu and Ag, measured on the carbon limiter blocks is much larger than at other areas of the torus, thus indicating sources in the direct neighbourhood: the TiC-coated Faraday screen, copper blocks of the limiter elements and the antenna side walls (Fig. 1).

4. POSSIBLE INTERPRETATIONS

The measured surface composition is the integrated result of deposition and erosion processes during tokamak operation and conditioning glow dicharges. Figure 4 shows schematically the relevant particle fluxes for both cases. During tokamak operation electrons and ions follow predominantly the mgnetic field lines, superposed by drift and plasma rotation movements. In addition, there are runaway electrons, energetic ions on drift orbits and charge exchange (D) neutrals moving in random directions. During the glow discharge the plasma (D^+) ions are accelerated in the sheath potential and move perpendicularly towards the wall and antenna structure. Their energy is of the order of a few 100 eV and thus sufficient to cause sputtering. Shadowing is only possible for charged particles.
The stripes inside the open antenna (Fig. 2) can be explained as being the result of random deposition of sputtered, not ionized wall material (Fe+Ni+Cr), possibly predominantly during glow discharges, and erosion at the unshadowed areas below the slits between Faraday rods by D-ions during the glow discharges. The profiles shown in Fig. 3 can also be explained by this shadow effect.
In order to explain the surface composition shown in Fig. 1, glow and tokamak discharges have to be taken into account. Since D-ions at plasma operations would be shadowed from the screen by the limiters, the almost homogeneous D content, implanted with energies below about 1 keV, is obviously the result of glow discharge ions and/or CX-neutrals in tokamak discharges. The small maxima at the ion side of the limiters can be due to an additional ion implantation in tokamak discharges.

The small Fe + Cr + Ni content on the screen situated more than 5 mm behind the first unshadowed magnetic surface could in principle be the result of an ion deposition during tokamak discharges, which is largely

reduced due to the shadowing limiters. But the maxima at the sides of the screen rods (Fig. 3) and limiter elements (Fig. 1, mainly at the left one) may rather indicate a homogeneous deposition and a subsequent erosion during tokamak discharges (the erosion during glow discharges should be similar at Faraday rods and limiters). In this case a special ion accelerating process by ICRH just in front of the active antenna area would have to be assumed to explain the erosion.This would be in agreement with the increase of antenna material impurity observed at ICRH operation in JET /5/. The Fe+Cr+Ni maxima at the outer limiter sides are comparable with the deposition on carbon limiters previously used in ASDEX /6/. They may be enlarged by the direct neighbourhood of the stainless steel plate protecting the copper blocks, while Cu and Ag may originate from the Cu blocks and the Ag coating of the Faraday screen support.

SUMMARY
The measured surface composition of the ICRH antenna and protecting limiter elements, dismanteled after an operation time of one and a half year, showed an implanted Deuterium and metal content which can only be explained by combined deposition and erosion processes during tokamak operation and glow discharge conditioning. Some results also indicate a special ion accelerating process during ICRH just in front of the active part of the antenna.

REFERENCES
/1/ K. Steinmetz et al., Proc. 11th Conf. on Plasma Phys. and Contr. Nucl. Fusion Research, Kyoto (1986).
/2/ J.-M. Noterdaeme et al., Proc. 13th Europ. Conf. on Contr. Fus. and Plasma Heating, Vol. II, 137 (1986)
/3/ J.-M.Noterdaeme et al., Proc.14th Symp.on Fus.Techn.,Vol.I, 795 (1986)
/4/ R. Behrisch et al., J.Nucl.Mat. 145-147, 731 (1987)
/5/ K.H. Behringer et al., see Ref. /2/, Vol. I, 176 (1986)
/6/ R. Behrisch et al., J. Nucl. Mat. 128-129, 470 (1984).

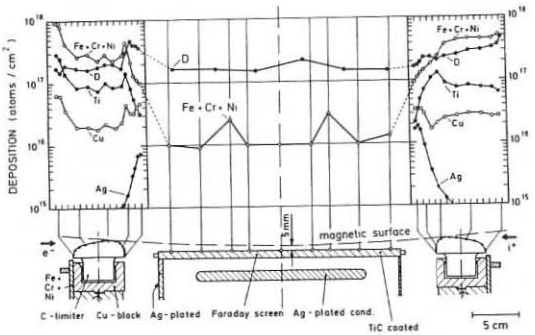

Fig. 1:
Cross section of the antenna and protection limiters (lower part), and distribution of deuterium and metal depositions in toroidal direction.

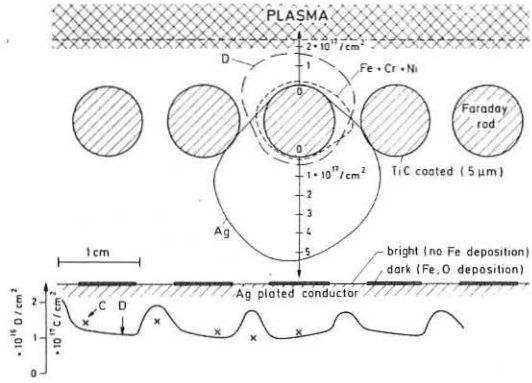

Fig. 2

Stripe pattern on the central conductor and surface composition on central conductor and on the rods of an open Faraday screen.

Fig. 3

Surface composition on the rods of the opaque and the optically open Faraday screen. The maxima at the sides and at shadowed parts can be explained by the lower density of eroding particles. Silver is found at the central conductor of the open antenna only.

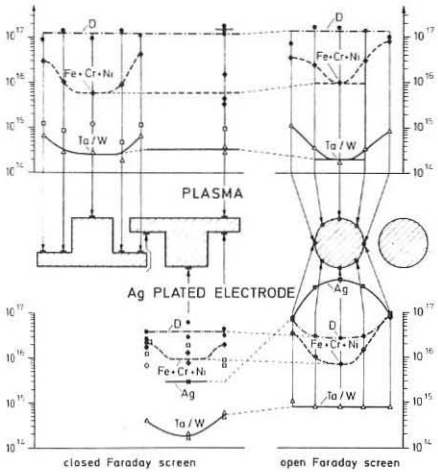

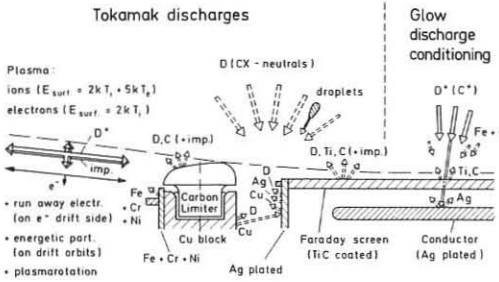

Fig. 4

Fluxes of neutrals (dotted lines) and charged particles in tokamak and glow discharges.

DETERMINATION OF CARBON FLUXES IN THE LIMITER SHADOW OF TEXTOR BY ANALYSIS OF CARBON DEPOSITS ON STEEL TARGETS

P. Wienhold, F. Waelbroeck, H. Bergsåker+, B. Schweer, H.G. Esser, J. Winter

Institut für Plasmaphysik, Kernforschungsanlage Jülich GmbH, Ass. EURATOM/KFA, D-5170 Jülich, FRG

+ Research Institute of Physics, Ass. EURATOM/EFN, S-10405 Stockholm, Sweden

1. Introduction

The inner wall of TEXTOR is covered with an amorphous hydrogen-containing carbon layer /1/. Nevertheless, the C concentration in the plasma does not exceed ~ 1% of the average electron density $\bar{n}_e$ /2/. It originates from the graphite limiters /3/ and from the carbonized liner where hydrocarbons are formed /4/ (Frank-Condon atoms and charge exchange neutrals).

The Stockholm-TEXTOR probe has been used to measure time resolved the carbon fluxes in the scrape-off layer (SOL) /5,6/. The C deposition occurs mainly during the flat top phase and is practically constant during the discharge. The C flux density is then about 2×10^{16} C · cm^{-2} s^{-1}. The RBS-technique is time consuming. Therefore, a complementary method was used to determine carbon impurity fluxes in the SOL from the thickness of carbon deposits on steel targets. This method can be used because the transparent deposits exhibit interference colours from which their thickness, hence the areal density of carbon can be deduced. We report here on preliminary experiments made between september and november 86 to test the applicability of this method during typical TEXTOR experimental series.

2. Experimental situation at TEXTOR

The four main limiter segments (ML, r = 46 cm) and the two poloidal protection limiters (PL, r = 48.8 cm) of the ICRH-antennae were made of graphite; the inconel liner (r = 55 cm) was covered with an amorphous deuterated carbon layer (a-C:D). Liner and limiter temperatures were 150 and 200 °C, respectively. Polished stainless steel targets (8 cm x 6.5 cm, 1 cm thick) were positioned with their edge 2.5 cm above the plasma and oriented perpendicular to the toroidal direction.

In total, four targets have been exposed to between 33 and 184 discharges under different plasma conditions. The results are almost identical, and we focus here on target 2. 70 discharges were made with the following parameters for most of the discharges: I_p = 350 kA, $\bar{n}_e = 3 \times 10^{13}$ cm^{-3}, B_T = 2.6 T, average duration = 3.2 s. A few shots were made at plasma currents of 480 kA and 287 kA and at different B_T (2.0, 1.6 T). Five discharges ended disruptively. ICRH-power between 150 and 500 kW was coupled in by minority heating (3 % ^{3}He) in 52 discharges.

3. Results and discussion

All targets showed similar radial deposition profiles as measured from the interference colours. But much less material was deposited on the e-drift side. (compare fig. 1 and 2). The material has been identified as deuterium containing carbon (a-C:D) by the absolute determination of the C and D concentrations at AFI, Stockholm using RBS - and NRA - technique.

The target 2 results (e-drift side) are shown in fig. 1. The measured areal densities A are plotted as a function of the radial positions r; r = 48.5 cm corresponds to the tip of the target. Three curves are shown: C (carbon) and D (deuterium) as measured by RBS and NRA respectively and C_E determined from the colour pattern /7,8/. All three increase with increasing distance from the liner reaching at r = 49 cm a maximum which corresponds to about 120 nm. The circular edge (radius 5 mm) was not covered. The ratio D/C is 0.4 ± 0.1 as in a-C:D layers formed by RG-discharges in CD_4/D_2 mixtures /1/. Because of the good agreement between the C and C_E curves the other targets were inspected via their colour patterns only.

The deposited layers are much thicker on the i-drift sides. The

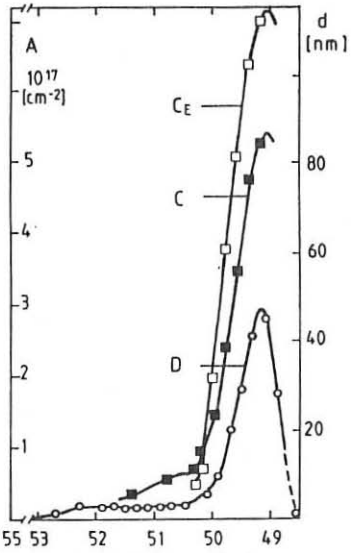

fig.1 radial distance r [cm]

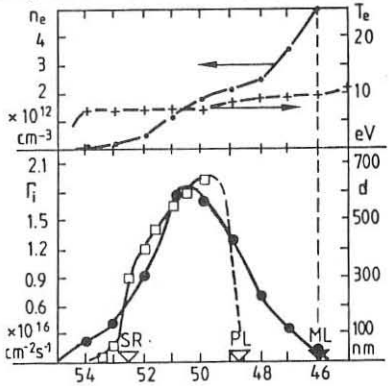

Fig. 2 radial distance r [cm]

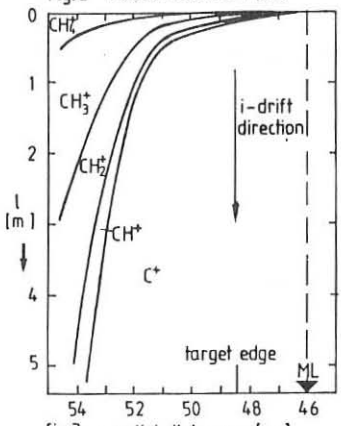

fig.3 radial distance r [cm]

integrated amount is about 10 times larger than on the e-drift side. The radial dependance found on target 2 is given in fig. 2 (squares). Obvious is the shadow effect of a protruding stiffening ring (SR) at r = 52.5 cm and at a toroidal distance of about 25 cm from the target. The fact that the deposits observed on the e-drift sides are thinner may result from a shielding effect of the upper segment of the main limiter which is 1.37 m apart only, compared with 9.62 m in the i-drift direction.

The maximum value reaches 650 nm at r = 50 cm, i.e. 4 cm in the SOL. Taking into account the 70 discharges of about 3 s duration, this value corresponds to a deposition rate of 2×10^{16} C-atoms/cm² s which agrees well with the results from the Stockholm-TEXTOR probe. Surprisingly, at r = 52 cm, i.e. 6 cm in the SOL, the deposition is still one half of the maximum value.

We will show in the following that this carbon originates most probably from the carbonized liner and not from the plasma. Assuming that a flux $\Gamma_W = 8 \times 10^{20}$/s of neutral deuterium reaches the wall /9/ and that hydrocarbons (mainly methane) are formed with a yield $Y = 3 \times 10^{-2}$ /10/, CD_4 will enter the SOL at a rate of 2.4×10^{19}/s. These molecules penetrate radially inward with thermal velocities until they become ionized by collisions with plasma particles and follow henceforth the toroidal field lines (plasma diffusion is neglected here). Taking into account the ionization cross sections for collisions with electrons and protons given by W.D. Langer /11/ and the measured profiles of electron density n_e and temperature T_e in the SOL /12/ (top of fig. 2), the ionization rate of methane can be calculated as a function of r if $n_i = n_e$ and $T_i = T_e$ are assumed. If the CH_4^+ ions were to fly along field lines, their flux density at the probe is then the Γ_i curve plotted in the figure (dots). It shows a maximum at nearly the same position than the deposited layer and an extinction at the plasma edge (ML). The quantitative agreement is, as shown below, somewhat fortuitious.

Similar ion profiles in the SOL have been calculated for discharges where ICRH-power was coupled in (~ 300 kW) and with lower current (285 kA) using the corresponding measured distributions of n_e and T_e. But, for a detached plasma (I_p = 285 kA, $\bar{n}_e = 2.6 \times 10^{13}$ cm^{-3}), the maximum of Γ_i is shifted to r = 47 cm and the decreasing tail ends at r = 42 cm, i.e. 4 cm into the plasma.

Not all ions reach the target in their original form: further dissociative collisions occur. An estimation based on the model of Langer for the depletion of CH_4^+ to C^+ using the measured TEXTOR parameter is given in fig. 3. It shows the average distances l covered in toroidal directions by an ion CH_n^+ before it dissociates into CH_{n-1}^+ as a function of the radial distance from the plasma center. Except in the very vicinity of the liner, where n_e and T_e are low, most of the carbon should reach the target as C^+ unless it escapes radially by known reactions as C^0. It seems likely, therefore, that the layers are formed by codeposition of carbon and hydrogen ions rather than by hydrocarbons, whereby the results show that the ratio D/C does not exceed 0.4. Taking the above mentioned losses of carbon in the form of C^0, the agreement found in fig. 2 is only by a factor of two. It is still satisfactory if one conciders

the uncertainties in the assumptions, Γ_W , Y and on the cross-sections.

4. Conclusions

The observations show, that the material which has been collected on steel targets in the SOL of TEXTOR is amorphous carbon (a-C:D) and suggest that it originates mainly from the methane released at the carbonized liner. Most likely the layers are formed by codeposition of carbon and hydrogen ions.

The thickness profiles of the deposits and also the absolute deposition rates can be understood when this assumption is made, although the origin of the difference between the deposition rates observed on the ion and electron drift sides is still somewhat unclear. It might be due to the shielding by a neighbouring segment of the main limiter. The deposition rate presents a maximum of 2×10^{16} C/cm² s at a radial position 4 cm into the SOL. These results agree well with observations with the Stockholm- TEXTOR probe. On the e-drift side of the target, only about 1/10 is deposited.

It is important to note that the ionization of the methane molecules by collisions with electrons and deuterons in the SOL should lead to a screening effect: most of the carbon released (as methane) from the liner does not reach the confined plasma, since the resulting ions, following the toroidal field lines, end upon the limiters or other obstacles. The screening seems less effective in case of a detached plasma: the lower electron temperature in the SOL does not lead than to a full ionization of CD_4 during its transit between liner and confined plasma.

References

/1/ J. WINTER, J. Nucl. Mat. 145-147 (1987) 131

/2/ J. SCHLÖTER, E. GRAFFMANN, L. KÖNEN, F. WAELBROECK, G. WAIDMANN, J. WINTER, and TEXTOR team, 12th Eur. Conf. on Contr. Fusion and Plasma Physics, Sept. 2-6, 1985, Budapest, Hungary

/3/ A. POSPIESZCZYK, H.L. BAY, P. BOGEN, H. HARTWIG, E. HINTZ, L. KÖNEN, G.G. ROSS, D. RUSBÜLDT, U. SAMM, B. SCHWEER, J. Nucl. Mat. 145-147 (1987) 574

/4/ E. VIETZKE, K. FLASKAMP, V. PHILIPPS, H.G. ESSER, P. WIENHOLD, J. WINTER, J. Nucl. Mat. 145-147 (1987) 443.

/5/ P. WIENHOLD, J. WINTER, H.G. ESSER, F. WAELBROECK, H. BERGSÅKER, B. EMMOTH, H.E. SÄTHERBLOM, J. Nucl. Mat. 145-147 (1987) 642

/6/ to be published

/7/ P. WIENHOLD, H.G. ESSER, U. LITTMARK, A. KALECK, J. WINTER, Conf. of E-MRS, June 2-5, 1987, Strasbourg, France, to be published in J. de Physique

/8/ J. WINTER, H.G. ESSER, P. WIENHOLD, V. PHILIPPS, E. VIETZKE, K.H. BESOCKE, W. MÖLLER, B. EMMOTH, J. Nucl. Instr. and Meth. in Physics Research (1987), in press

/9/ U. SAMM, P. BOGEN, H.A. CLASSEN, H. GERHAUSER, H. HARTWIG, E. HINTZ, K. HÖTHKER, L. KÖNEN, Y.T. LIE, A. POSPIESZCZYK, G.G. ROSS, J. Nucl. Mat., 145-147 (1987) 206

/10/ E. VIETZKE, V. PHILIPPS, K. FLASKAMP, P. WIENHOLD, H.G. ESSER, this conference

/11/ W.D. LANGER, Nucl. Fusion 22, No. 6 (1982), 751

/12/ A. POSPIESZCZYK, G.G. ROSS, this conference.

RADIAL AND POLOIDAL DISTRIBUTION OF IMPURITIES AND DEUTERIUM DEPOSITED ON THE FT LIMITER DURING OHMIC DISCHARGES

G. Maddaluno
Associazione EURATOM-ENEA sulla Fusione, Centro Ricerche Energia Frascati, C.P. 65 - 00044 Frascati, Rome, Italy

A.P. Martinelli
Max Planck Inst. für Plasmaphysik, EURATOM Association, 8046 Garching F.R.G.

INTRODUCTION

In a machine with limiter operation, such as the Frascati Tokamak (FT), the limiter is the main source of foreign atoms affecting the plasma purity and makes a large contribution to the total recycling of the working gas [1]. In turn the surface composition and topography of the limiter are changed, erosion-redeposition phenomena taking place because of the plasma flux. The knowledge of the radial and poloidal distributions of impurities and deuterium deposited on the limiter can be of great importance for understanding the complex plasma-limiter interaction, particularly with regard to the observed asymmetries of the scrape-off parameters [2].

In this work the stainless steel full poloidal limiter of FT [3] was equipped with six graphite targets in order to study the spatial distributions of impurities and deuterium within larger radial and poloidal ranges with respect to previous investigations [4,5].

EXPERIMENT

Three 15×10×2 mm^3 graphite (grade EK98, Ringsdorff) targets were mounted on the ion side and three on the electron side of the stainless steel limiter support and poloidally distributed all around the limiter circumference, as shown in Fig. 1.

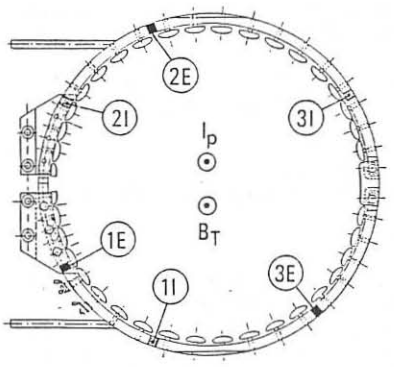

Fig. 1: Schematic view of the main poloidal FT limiter showing the position of graphite targets.

The collecting surfaces of the targets were oriented perpendicularly to the toroidal magnetic field. The reliable measurement point closest to the plasma edge was at r-a = 1.3 cm, where a = 20 cm is the plasma radius.

All the targets but one were exposed to 623 ohmic discharges in the April/May 1986 experimental period; once, when the limiter was temporarily extracted after 494 shots, the target mounted on the bottom ion side (1I in Fig. 1) was removed. The main plasma parameters were I_p = 300÷600 kA, B_T = 6÷8 T, n_e 0.7÷2.7×10^{14} cm^{-3}. The toroidal field was parallel to the plasma current. After removal from the limiter the targets were surface analysed by SEM, PIXE and NRA.

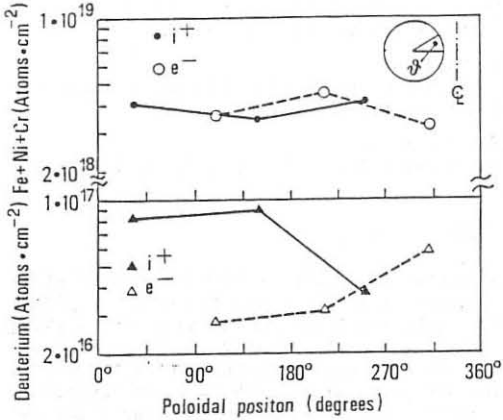

Fig. 2: Radially averaged poloidal distribution of metal and deuterium deposited on the graphite targets.

RESULTS

Metal Deposit Analysis - The metal coverage (Fe+Cr+Ni), averaged over the seven experimental points radially measured by PIXE on each of the six graphite targets, was found to be $3 \div 5 \times 10^{18}$ atoms cm^{-2} (more than a thousand monolayers) with no large poloidal or directional (electron vs ion side) differences (Fig. 2).

The chromium concentration on all the targets was about twice as large as in the stainless steel used as limiter (AISI 316) and wall (AISI 304) material. The target subjected to fewer discharges than the other ones showed the same amount of metal deposit.

With respect to the radial distribution of metallic impurities, a concentration continuously decreasing with the distance from the plasma edge was found in the inner part of the limiter on the electron side (target 3E), with an e-folding length of ~ 1 cm, and, less clearly, on the ion side (Fig. 3). In the other parts of the limiter the radial distribution was almost uniform, with a smooth maximum at intermediate positions between the top and bottom of the targets.

Deuterium Analysis - Higher radially averaged deuterium concentrations were measured on the ion side ($8 \div 9 \times 10^{16}$ atoms cm^{-2}) than on the electron side (~ 3×10^{16} atoms cm^{-2}) by the D(^{3}He, p)^{4}He nuclear reaction on the targets which had been subjected to an equal number of discharges and showed similar impurity distributions (Fig. 2).

Unlike metallic impurities, lower D concentration by a factor 2÷3 was found on the target 1I with respect to the other targets facing the ion side.

The radial distribution was rather uniform (Fig. 3), with shallow maxima and minima occurring at different positions, but the target 4E showed a D concentration clearly increasing with the distance from the plasma.

DISCUSSION

The general pattern observed in the metal deposit (as well as in the deuterium concentration) is the result of several hundred both normal and disruptive discharges. The evaluation of impurity fluxes in the scrape-off from the measured concentrations is to be carefully considered because of the different impurity amounts released in such a large number of discharges.

Erosion action of the plasma and nonlinear dependence of the deposit thickness on the number of discharges can also lead to misleading results.

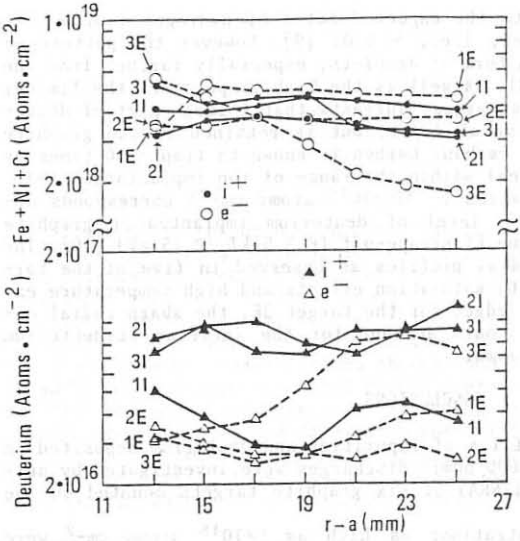

Fig. 3: Metal and deuterium concentration on the graphite targets as a function of the radial distance from the plasma. See Fig. 1 for the poloidal position of the different targets.

In effect a nonlinear dependence is inferred by comparing target 1I with the other ones.

Moreover the metallic impurities collected by deposition probes mounted on the limiter sides are largely the result of local redeposition close to the erosion area.

According to the measured values of density and temperature in the FT scrape-off [6] ($\tilde{n}_e \sim 1\times10^{12}$ cm^{-3}, $T_e \cong 15$ eV at 1÷2 cm outside the plasma edge) and the calculated ionization rate coefficients (i.e. $\langle\sigma v\rangle \sim 1\times10^{-7}$ cm^3 s^{-1} for a Cr atom [7]), a particle sputtered from the limiter side with an energy of a few eV has a mean free path for electron impact ionization as short as ~ 1 cm. Therefore it has a high probability of being ionized and of returning to the limiter under the combined action of the friction with the background plasma and the acceleration by a pre-sheath electric field. Atoms released with thermal energies by evaporation have an even higher probability of redeposition owing to their shorter ionization mean free path. Therefore the large Cr/(Fe+Ni+Cr) ratio observed on all the targets is probably due to preferential Cr evaporation from the neighbouring hot zones of the limiter.

The decrease of metal deposition with increasing distance from the plasma as found on the inner targets (especially on the electron side) could be related to a poloidally asymmetric radial profile of energy flux to the limiter. A minimum density (and energy) e-folding length has been found in the inner part of the poloidal cross section of Alcator-C by Langmuir probes [2].

Particle and energy fluxes concentrated on the upper part of the elliptically shaped mushrooms (see Fig. 1) cause a release of metal atoms minly directed onto closed flux surfaces inside the limiter radius [8].

On the other hand, longer energy and particle e-folding lengths cause the release of metal impurities which are ionized in the scrape-off and directly collected by the limiter and overlap the impurity outflux from the main plasma. The result could be a nearly constant deposit as observed on the targets apart from those on the inside of the poloidal cross section.

With respect to the working gas concentrations, the deuterium implanted in the targets within ~ 1 μ from the surface (the depth range of NRA ana

lysis) seems to correspond to the expected ratio of hydrogen isotopes to host atoms in stainless steel, i.e., ~ 0.01 [9]. However the pattern of metal deposition, which is in form of droplets, especially farther from the plasma edge (as found by SEM), as well as the high temperature the limiter surface reachs during the discharges, suggests that a large part of deuterium is not trapped in the metal layer, but is retained in the graphite substrate or in co-deposited carbon. Carbon is known to trap ~ 40 times as much hydrogen as stainless steel within the range of ion implantation [9].

The measured D concentration (~ $3 \div 9 \times 10^{16}$ atoms cm^{-2}) corresponds approximately to the saturation level of deuterium implanted in graphite with the energy expected in the FT scrape-off ($E \cong 5\ kT_e \cong 75$ eV) [10]. The flatness of the deuterium radial profiles as observed in five of the targets could be ascribed to both saturation effects and high temperature excursions close to the plasma edge. For the target 3E, the sharp radial decrease of the metal deposit could account for the increase of deuterium with the distance from the plasma.

CONCLUSIONS

Radial and poloidal profiles of impurities and deuterium deposited on the FT limiter during about 600 ohmic discharges were investigated by surface analyses (SEM, PIXE and NRA) of six graphite targets mounted on the SS limiter support.

Metal (Fe+Cr+Ni) concentrations as high as 5×10^{18} atoms cm^{-2} were found with no large poloidal or directional differences. The chromium concentration was twice as large as in stainless steel, probably due to preferential evaporation from the limiter.

The radial profile of impurities was rather flat apart from on the inside of the poloidal cross section, especially on the electron side ($\lambda_{Fe+Ni+Cr} \sim 1$ cm), perhaps as a result of asymmetry in the density and energy scrape-off lengths.

The overall deuterium concentration was higher on the ion ($8 \div 9 \times 10^{16}$ atoms cm^{-2}) than on the electron side (~ 3×10^{16} atoms cm^{-2}) and poloidally uniform.

The radial deuterium distribution did not exhibit any decay with the distance from the plasma.

Further analyses on a new set of targets mounted on a limiter with INCONEL mushrooms are in progress.

FOOTNOTE AND REFERENCES

[1] F. De Marco et al., Nucl. Fusion 26, 1193 (1986)
[2] B. La Bombard, M.I.T. Plasma Fusion Center Report PFC/RR-86-6 (1986)
[3] C. Alessandrini, C. Ferro and M. Samuelli, 11th Symposium on Fusion Technology, Oxford (1980) p. 1067
[4] C. Ferro et al., 12th European Conf. on Controlled Fusion and Plasma Physics, Budapest (1985), Part II, p. 555
[5] E. Franconi, F. Brossa, J. Nucl. Mater. 145-147, 691 (1987)
[6] V. Pericoli-Ridolfini, Plasma Physics Controlled Fusion 27, 493 (1985)
[7] M.A. Lennon, K.L. Bell et al., Culham Report CLM-R-270 (1986)
[8] G.F. Matthews et al., Plasma Physics Controlled Fusion 29, 189 (1987)
[9] R.A. Langley et al., Nucl. Fusion, special Issue 1984
[10] S.A. Cohen, G.M. McCracken, J. Nucl. Mater. 84, 157 (1979)

EROSION OF A-C:H FILMS AND REDEPOSITED CARBON LAYERS BY ATOMIC AND ENERGETIC HYDROGEN

E. Vietzke, V. Philipps, K. Flaskamp,*P. Wienhold,*H.G. Esser
Institut für Chemie 1 (Nuklearchemie),*Institut für Plasmaphysik
Kernforschungsanlage Jülich, Ass. Euratom-KFA
D-5170 Jülich, FRG

Introduction

Deposition of amorphous hydrogenated carbon films [a-C:H films] on the first wall is used in several fusion devices to improve plasma operation [1]. Redeposited carbon layers on first wall components have been observed since carbon materials are used in fusion devices either in form of compact protection tiles or as thin carbon film [2,3]. Both types of carbon films have been investigated in simulation experiments to evaluate their chemical reactivity by thermal and energetic hydrogen impact. In addition, hydrogen saturated carbon surfaces have been prepared by implanting energetic hydrogen until the saturation level (0.4 H/C at R.T.) and are compared with the films with respect to their reaction with thermal atomic hydrogen. Besides the evaluation of the erosion yields and the product spectra these results are also helpful for understanding the recycling behaviour of the hydrogen species in devices with carbon walls.

Experimental

The a-C:H films with a typical thickness of 100 nm are prepared in the TEXTOR tohamak by a radiofrequency assisted glow discharge at a substrate temperature of 200°C (more details in [4]). Redeposited carbon layers used in this experiment were taken from a stainless steel tube which was exposed to the scrape-off region of the TEXTOR plasma. During plasma operation of 300 discharges a carbon layer has been built up with a thickness up to about 1 µm at the end of the tube (about 2 cm behind the limiter edge). The thickness has been estimated from the interference colours [5]. All three types of carbon samples were exposed later either to a beam of thermal hydrogen atoms or energetic ions (typical fluxes 10^{16} H^0 atoms/cm^2sec and 10^{14} H^+ ions/cm^2sec respectively). Volatile reaction products as well as sputtered species have been detected mass-spectrometically in the direct beam method [6].

Results and discussion

The total erosion yields of the different carbon materials are shown in Fig. 1. The yields found at the a-C:H films and the redeposited layers are determined by a complete eroding of the film from the substrate and a scaling of the atom flux to the thickness of the films. The most striking effect is the fact that the erosion of the a-C:H films by thermal hydrogen atoms reaches yields close to 10^{-1} C/H^0 which is about two orders of magnitude larger than on pure graphite.

However, this remarkable difference levels off when the graphite surface is saturated with hydrogen. The erosion increases in this case drastically and reaches values only a factor three smaller than for the film. As can be seen in fig. 1 the erosion due to energetic ion impact is only about twice that of the thermal atoms and similar to erosion of pure graphite with ions. It has to be noted that the differences in the erosion yield of the a-C:H films and the redeposited carbon layers which are also shown in fig. 1 is probably due to a temperature excursion of the redeposited layers during the plasma exposures which results in a partial annealing of the reactivity.
At temperature above about 800K, the amount of produced hydrocarbons due to thermal hydrogen impact decreases during the exposure due to a thermal annealing of the film structure. An evaluation of an erosion yield above 800K remains therefore doubtful. Summarising the results, the differences in the erosion of a-C:H films and redeposited carbon layers by hydrogen impact are not very drastic. No large difference exists to the erosion of hydrogen saturated graphite surfaces by atomic hydrogen. From this point of view other criteria then the chemical erosion may be considered when carbon materials have to select. We have furthermore to conclude that the chemical erosion of the low energy Frank-Condon-atoms hitting the inner walls with overall fluences similar to the overall ion fluences is a significant contribution for the carbon production in the SOL region.

Fig. 2 shows the measured mass-spectrum of detected ions in the reaction of thermal hydrogen with an a-C:H film (open bars). Beside the main reaction product which is the radical CH_3 a wide spectrum of higher hydrocarbons is formed. The main other species are C_2H_4 together with the radicals C_2H_3 and C_2H_5 as well as C_3H_x species where a detailed identification remains more difficult. Taking into account the experimental uncertainties, equal product distributions are obtained on the redeposited carbon layers as well as on the hydrogen saturated graphite.

When energetic hydrogen ions are used to erode the different graphite substrates, the observed ion spectrum is changed. The main product is now the saturated CH_4 molecule, the amount of the C_2H_x species are reduced (roughly by a factor of three) and the formation of higher hydrocarbons is negligible small.

A remarkable behaviour is observed when thermal deuterium atoms were used to erode an hydrogenated carbon film. In this case, the spectrum of produced species consists predominantly of deuterocarbon molecules and very few molecules containing hydrogen atoms. The bonded hydrogen is released in this case in form of an HD molecule. Recent experiments have shown that this small mixing is typical for "hard" a-C:H films which are produced when the impact energy is sufficiently high [7]. "Soft" films (produced by impact energies below 100 eV) show a significant enhancement of the mixed molecule formation.

In the extreme case that no mixed molecules are formed and that the maximum erosion level of 10^{-1} C/H^0 is reached, about 40 % of the

impinging deuterium atoms are released as deuterocarbonmolecules. The recycling way of the low energy Frank-Condon-atoms proceeds so to a significant amount via the production of low energy hydrocarbon molecules. These molecules have low velocities and their way when they penetrate from the walls to the plasma has to evaluate. The transfer of 40 % incoming hydrogen atoms to a hydrocarbon molecule (in the maximum) can also act as a way to pump away the hydrogen when the molecules are redeposited before the hydrogen atoms are stripped. We have to assume furthermore, that the redeposited molecules can build up carbon films containing more then 0.4 D/C. This has already been demonstrated by producing "soft" polymerlike carbon films [8]. Only about 5 % of the incoming hydrogen atoms are necessary to transfer the bonded hydrogen in the film to a hydrogen molecule when the film is eroded away. The remaining 55 % of the incoming atoms may recombine to molecules or directly be reflected. All these numbers have to be used with caution due to uncertainties of the assumptions of the model used.

Summary

- The chemical reactivity of the a-C:H films against thermal hydrogen atoms impact reaches yields of 10^{-1} C/H and is similar to that obtained by energetic ion impact
- The observed redeposited carbon layers show a similar chemical erosion behaviour as the a-C:H films
- Thermal hydrogen atoms react on a-C:H films, redeposited carbon as well as hydrogen saturated graphite producing CH_3 and a wide spectrum of higher hydrocarbons. When these carbon films are irradiated with energetic hydrogen ions, the methane formation becomes dominant.
- From the viewpoint of the chemical erosion by thermal atomic and energetic hydrogen there are no large differences between a-C:H films, redeposited carbon as well as hydrogen saturated graphite.
- The chemical erosion of the low energy Frank-Condon-atoms have also to be considered in all devices where graphite or other carbon materials are used.

[1] J. Winter, J. Nucl. Mat. 145-147 (1987) 131

[2] J. Roth, J. Ehrenberg, K. Wittmaack, et al., J. Nucl. Mat 145-147 (1987) 383

[3] P. Wienhold et al., this issue

[4] J. Winter, H.G. Esser, P. Wienhold et al., Nuclear Instr. and Meth., in press

[5] P. Wienhold et al., to be published in Journal de Physique

[6] E. Vietzke, K. Flaskamp, V. Philipps, J. Nucl. Mat. 145-147 (1987) 443

[7] E. Vietzke, V. Philipps, K. Flaskamp, to be published in Journal de Physique

[8] C. Angus, P. Koidl, S. Domitz, Plasma Deposition of thin films, CRC press, 1986

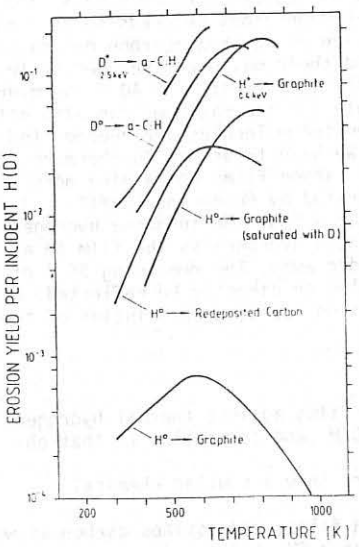

Fig. 1: Comparison of the total erosion yields as a function of temperature for eroding different carbon materials with thermal hydrogen (deuterium) atoms (H^0,D^0) and energetic ions (H^+,D^+)

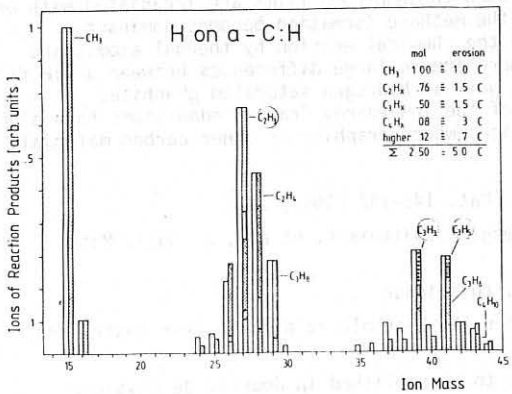

Fig. 2: Measured mass spectrum of detected ions in the reaction of thermal hydrogen with a-C:H films (open bars) compared with the resulting ion spectrum assuming the formation of the hydrocarbons indicated in the figure

GRAPHITE EROSION IN CONTACT WITH A HYDROGEN PLASMA AND A COMPARISON TO ION BEAM EROSION DATA

J. Bohdansky[+], R.W. Conn[++], D.M. Goebel[++]
Y. Hirooka[++], W.K. Leung[++], J. Roth[+]

[+] Max-Planck-Institut für Plasmaphysik, EURATOM Association D-8046 Garching/München, Fed. Rep. of Germany

[++] Center for Plasma Physics and Fusion Engineering, University of California, Los Angeles, CA 90024, USA

Introduction

Graphite bombardment by energetic hydrogen ions shows a high erosion yield due to chemical reactions (methane formation). This chemical sputtering depends on the graphite temperature as found in beam experiments /1/. In spite of this significant effect, carbon impurities in a tokamak plasma are not influenced by the temperature of a carbon limiter /2/. Ion flux dependence of the chemical sputtering, metal impurities at the limiter surface and redeposition of sputtered species were considered as the main reason for this discrepancy.

In this work chemical sputtering and its temperature dependence is investigated by an ion beam (flux 1.5 10^{15} cm^{-2} sec^{-1}) and in contact with a plasma (flux 1.5 10^{18} cm^{-2} sec^{-1}). The plasma experiment also shows the importance of redeposited carbon layers created at certain plasma parameters for the net erosion yield.

Experimental

Chemical sputtering with D^+-ions of 50 eV, 100 eV and 200 eV was measured in the IPP high current ion source /3/ and in the plasma generator PISCES /4/. The graphite temperature was varied between RT and 900°C. The sputtering yield was gained by the weight loss method /3/ and the target temperature was measured either by a thermocouple (plasma experiment) or by an imfrared pyrometer (beam experiment). The targets were cleaned in an ultrasonic bath and outgassed well above the operating temperature before each test.

Results and discussion

In Fig. 1 yield data for 100 eV D^+ at normal incidence gained by beam and plasma experiments are compared. Redeposition is avoided also in the plasma experiment by a proper choice of the plasma parameters /4/. The corresponding ion fluxes for beam and plasma experiments are 1.5 10^{15} cm^{-2} sec^{-1} and 1.5 to 10^{18} cm^{-2} sec^{-1}, respectively. In the beam experiment two different types of graphite (Pyrolytic and POCO graphite) are tested. The same POCO graphite samples are tested also in the plasma experiment. For temperatures up to 300°C the beam data

are higher by a factor 1.5 which may be explained even by the uncertainties in the data gained from the plasma experiments. At higher temperature the difference is larger and even the beam data for the different types of graphite are different. A possible explanation may be seen in the different bulk structure (dense and porous) for pyrolytic and POCO graphite. However, also for the high ion flux the yield data depend on the graphite temperature.

The lowest yield values are measured at the highest temperature of 900°C investigated in these experiments. This is more significant for lower ion energies as shown in fig. 2. In this figure yield data versus target temperature are given for three different D^+-ion energies (50 eV, 100 eV and 200 eV) measured for POCO in PISCES. The extrapolations (dashed lines) point to the expected values for physical sputtering as methane cannot be formed at these temperatures.

For temperatures above 900°C an increase in the erosion yield by radiation enhanced sublimation has been measured in beam experiments /5/. However, this effect may be small for ion energies below 100 eV /6/.

The net erosion yield is reduced in plasma experiments by redeposition if the ionization length for methane is smaller than the plasma dimensions (in PISCES 10 cm). This is shown in fig. 3. Erosion yields for 100 eV H^+-ions are given for the same flux but two different ionization length (5 cm and $>$ 15 cm). Although the ionization length is still larger than the diameter of the graphite sample ($\sim$ 1 cm) the yield is reduced up to a factor 2. Experiments with an ionization length of less than one cm gave net erosion yields below the detection limit. However, the surface structure changed significantly due to the redeposited layer.

According to the plasma parameters of scrape-off layers in tokamaks ($n \gtrsim 10^{12}$ cm^{-2} sec^{-1}, Te $\gtrsim$ 10 eV) high redeposition take place at the graphite limiter /7/ and this effect may mask the chemical erosion effect.

Conclusion

The chemical sputtering yield of graphite is not significantly reduced at typical ion fluxes to a carbon limiter ($\sim 10^{18}$ cm^{-2} sec^{-1}) compared to the data gained by beam experiments (flux $\sim 10^{15}$ cm^{-2} sec^{-1}). Also at the high flux the yield depends on the graphite temperature. Such a temperature dependence of the carbon impurities in the main tokamak plasma has not been observed /2/. It is proposed that methane formed in the chemical sputtering process is ionized in the scrape-off layer and redeposited at the limiter. Therefore impurities cannot penetrate into the main plasma. At temperatures above 800° C the erosion yiel is low and reaches values expected for physical sputtering.

References

/1/ J. Roth, J. Bohdansky, Nucl. Instr. Meth. in Phys. Res. (1987) in press

/2/ C.S. Pitcher, G.M. McCracken, D.H.J. Goodall, G.F. Matthews, P.C. Stangeby, Nucl. Fus. (1986) in press

/3/ J. Roth, J. Bohdansky, W. Ottenberger IPP (Garching) 9/26 (1979)

/4/ D.M. Goebel, R.W. Conn, J. Nucl. Mater. 128/129 (1984) 249

/5/ J. Roth, J. Bohdansky, K.L. Wilson J. Nucl. Mat. 111/112 (1982) 775

/6/ J. Roth, W. Möller, Nucl. Instr. Meth. in Phys. Res. B 7/8 (1985) 788

/7/ C.S. Pitcher, G.M. McCracken, P.C. Stangeby, J. Allen, S.J. Fielding, D.H.J. Goodall, G.F. Matthews, J. Nucl. Mater. 145-147 (1987) 539

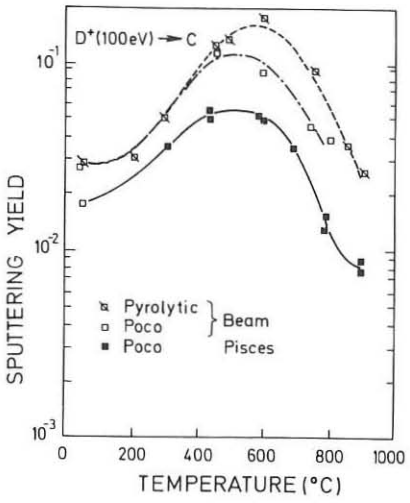

Fig. 1 Chemical sputtering yield versus temperature for 100 eV D^+ ions and two types of graphite

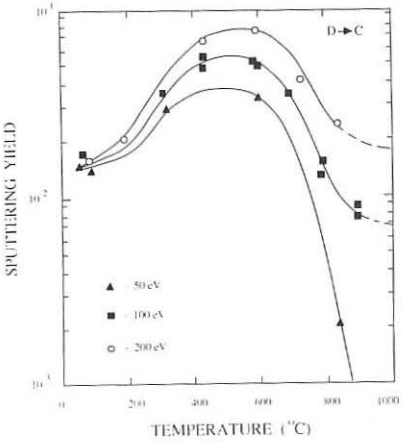

Fig. 2 Chemical sputtering yield of POCO graphite versus temperature for D^+ ions of three different energies

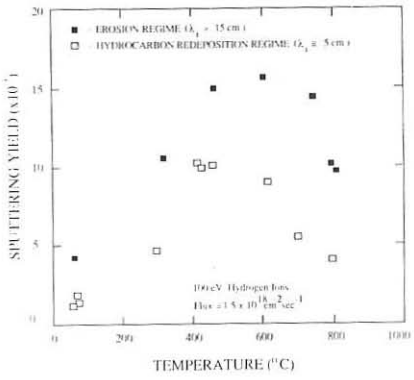

Fig. 3 Chemical sputtering yield of POCO graphite versus temperature for 100 eV H^+ ions in the erosion and redposition regime

CARBONISATION OF T-10 TOKAMAK LINER FOR THE ECRH EXPERIMENTS.

S.A.GRASHIN, Yu.A.SOKOLOV, G.E.NOTKIN, V.M.CHICHEROV
KURCHATOV INSTITUTE OF ATOMIC ENERGY, MOSCOW, USSR
V.H.ALIMOV, I.I.ARHIPOV, D.V.BOGOMOLOV, A.E.GORODETSKY, S.Yu.RHYBAKOV
A.P.ZAKHAROV
INSTITUTE OF PHYSICAL CHEMISTRY, MOSCOW, USSR

In 1985 T-10 tokamak was rebuilded and its vacuum chamber was substituted by new one. After that the amount of metal atoms in a plasma tremendously rised. High level of heavy impurities led to desruption of the high density discharges. As a consequence we failed to investigate high density regimes during the last ECRH experiments in spring 1986[1]

To reduce high Z impurities influx from the wall material in plasma we used the carbonisation of inner surface of T-10 liner. Beside of standard procedure developed at TEXTOR and JET 50 Hz discharges in pure methane as a method of carbonisation were under study. To control the carbonisation procedure a set of samples both of metal and silicon was introduced into tokamak vessel and a systematical analysis was made on samples by surface physics techniques as AES, SIMS, EIXE, ESCA and RHEED. The films formed by carbonisation were highly amorphous and possessed of different kinds of structure and composition depending upon the procedure of deposition.

The effect of carbonisation on level of metal impurities in plasma under high power ECR heating is under investigation.

1. V.V.Alikaev, A.A.Bagdasarov et.al. 11th Int. Conf. on Plasma Phys. and Contr. Fusion. Kyoto. Japan 1986 IAEA-CN-47/A-II-4.

ASYMMETRY IN POTENTIALS AND NON-AMBIPOLARITY OF PLASMA FLUXES ONTO THE LIMITER SURFACE IN T-10 TOKAMAK.

Vershkov V.A., Chankin A.V.
I.V.Kurchatov Institute of Atomic Energy, Moscow, USSR

The limiter in T-10 has a few Langmuir/Heat flux probes located on both ion and electron sides. The pair of probes, closest to the plasma column, is set at a distance 4.6mm from the plasma column surface; the next pair is located at a distance 40mm from the plasma column. It is shown that the difference of floating potentials on both sides of the limiter is about 50 V for the near-plasma probes; for other probes it is about a few volts. A difference in the current density to the ion and electron sides of the limiter surface corresponds to a current through the limiter equal to the Spitzer one for the measured plasma parameters. An average floating potential for both near-plasma probes is about -30 V, an average potential on other probes is positive and equal to a few volts. Such a potential distribution should result in the ambipolarity of the total flux of charged particles from the plasma to the limiter. Both the asymmetry in floating potentials and an average potential for the plasma-close probes are proportional to $Jd/\bar{n}_e$, where J is the plasma current, d is width of a scrape-off layer, $\bar{n}_e$ is the plasma electron density averaged over the plasma column diameter. The relationship between the non-ambipolar flux to the limiter and the asymmetry in heating of the ion and electron sides, measured with infrared technique, is discussed.

ON THE MECHANISM OF STEADY-STATE BURN OF UNIPOLAR MICROARCS IN THE SCRAPE-OFF TOKAMAK PLASMA

Yu.L.Igitkhanov
I.V.Kurchatov Institute of Atomic Energy,Moscow,USSR

ABSTRACT

The model of a steady-state arc spot burn in the scrape-off tokamak plasma due to the non-uniformity of the surfaces (first wall, limiter etc.) is proposed. The principal difficulty in the theory of unipolar arc burn [1] under a magnetic field is related with the impossibility of providing the arc current short circuiting with the current from plasma without using additional mechanisms of transversal electron spread from the spot. The role of such a mechanism can be played by the so-called surface conduction related with the electron spread upon a non-uniform surface. The current provided by this effect turns out to be distributed within a thin surface layer. Spreading from the spot area across the surface, electrons enter the adjacent magnetic field lines and reduce the potentials there. Thus the current commutation area on the surface is increased and the condition for a steady-state arc burn is provided. Some estimates show that the reflection of 1% of electrons only from an uneven surface provides a minimal current necessary for the cathode spot existence for typical parameters of scrape-off plasmas. The treatment of a surface up to a degree of roughness equal to 10^{-4}cm results in the reduction of scrape-off conduction and in the impossibility of sustaining the steady-state burn of a unipolar arc.

REFERENCES

1 G.M.Mc Craken et al. GLM, p.492, 1977.

FIRST AUTHOR ALPHABETICAL INDEX